University of Bath

PHD

New Multifunctional Ligands for Transition Metals Coordination and Investigations into their Biomedical Applications for the Molecular Imaging of Prostate Cancer Cells

Casarsa, Federico

Award date:
2020

Awarding institution:
University of Bath

Link to publication

Alternative formats
If you require this document in an alternative format, please contact:
openaccess@bath.ac.uk

Copyright of this thesis rests with the author. Access is subject to the above licence, if given. If no licence is specified above, original content in this thesis is licensed under the terms of the Creative Commons Attribution-NonCommercial 4.0 International (CC BY-NC-ND 4.0) Licence (https://creativecommons.org/licenses/by-nc-nd/4.0/). Any third-party copyright material present remains the property of its respective owner(s) and is licensed under its existing terms.

Take down policy
If you consider content within Bath's Research Portal to be in breach of UK law, please contact: openaccess@bath.ac.uk with the details. Your claim will be investigated and, where appropriate, the item will be removed from public view as soon as possible.

Download date: 05. May. 2023

New Multifunctional Ligands for Transition Metals Coordination and Investigations into their Biomedical Applications for the Molecular Imaging of Prostate Cancer Cells

Federico Casarsa

A thesis submitted for the degree of Doctor of Philosophy

University of Bath

Department of Chemistry

September 2019

Copyright Notice

Attention is drawn to the fact that copyright of this thesis/portfolio rests with the author and copyright of any previously published materials included may rest with third parties. A copy of this thesis/portfolio has been supplied on condition that anyone who consults it understands that they must not copy it or use material from it except as licenced, permitted by law or with the consent of the author or other copyright owners, as applicable.

Table of contents

Acknowledgements

As this adventure is coming to an end, I would like to finish this work by thanking all the people who made this journey a very enjoyable one. First, I'd like to thank Prof Sofia Pascu for giving me the opportunity to work on this project. I would also like to thank my second supervisor, Dr Ian Eggleston, for the precious advices and meetings.

A big thank you goes to all the SIP group: Vincenzo, Fernando, Haobo, Marina, Sophia, Sam and Giuseppe. Arguably, the best lab mates in the Department! Thank you for all the long days (and longer nights!) we have spent together not only as colleagues, but also as friends. These years spent with you all will be unforgettable.

I'd like also to mention Maia, Lucia, Sara and Eva for all the good time spent together and the countless nights out, usually beginning at the Parade and with a good pint firmly in our hands. I would also like to thank Simone for the innumerable pub crawls and the endless Friday's night conversations.

Thank you to all the people who made my time in Bath most enjoyable: the St Pauls crew, especially Marco and Cecilia, for giving me the chance to be part of the most colourful house in the city.

A special mention is for Marina, wonderful colleague and now my lovely half. Thank you for your constant support and for cheering me up all the times. T'estimo molt!

Vorrei anche ringraziare sentitamente, mamma e papà, per il vostro supporto incondizionato durante tutti questi anni. Mi ritengo davero fortunato ad avervi come genitori! Ringrazio anche mia sorella, Alice, e Mauro, per il tempo speso assieme (specialmente durante le ottime cene) ogni qualvolta ridiscendo dalla perfida Albione, e per aver fatto di me un felicissimo zio per i bellissimi nipoti Eleonora e Gabriele. Grazie a voi tutti, la parte più bella dell'Italia per me è tornare a casa.

Abstract

This project investigates the possibility to develop organometallic complexes of transition metals possessing biomedical applications, so as to develop potential theranostic agents. Specifically, this work describes the development of tripodal systems and their related metal complexes with relevance for prostate cancer diagnosis using cellular imaging techniques.

Chapter 1 presents the context of this work. The concept of coordination compounds possessing biomedical applications is introduced, and a literature review regarding the latest transition metal complexes displaying biological activities is presented. Molecular imaging techniques are described together with examples of metal complexes designed for imaging applications. An overview of cellular hypoxia and its role in tumour development is given, along with a description of prostate cancer, its features and how these can be exploited in diagnosis and therapy.

Chapter 2 describes the syntheses of tripodal systems based upon a hexasubstituted benzene scaffold, and their potential for biomedical applications is probed. In this chapter, two series of nitrogen-based and one series of anthracene-thiosemicarbazone-based tripodal systems were successfully synthesised and characterised spectroscopically, and their biological activity probed with MTT assay and confocal microscopy experiments on PC3 prostate cancer cells.

Chapter 3 describes the development of a series of tripodal N-heterocyclic carbene-based compounds with the potential to act as ligands for a variety of transition metals. In this chapter, the synthesis and characterisation of nine tripodal systems, which incorporate unsymmetrical imidazole arms is described. Crystals suitable for X-ray diffraction were successfully obtained for four compounds described hereby, allowing an appreciation of how these systems present dynamic conformational equilibria, and are able to form polymeric associations *via* network of interactions between the tripodal systems and their anions.

Chapter 4 describes the syntheses of novel tripodal systems with unsymmetrical substituents, so to develop ligands capable of binding metals as well as other functionalities. The unsymmetrical tripodal systems presented in this work are based upon the tripodal NHC-based compound **76** described in Chapter 3, in which one of the three NHC arms is modified either with carboxylic acid-based linkers, as well as with the introduction of an anthracene-thiosemicarbazone derivative.

Chapter 5 describes the complexation attempts between a series of transition metals that have known biomedical potential and selected tripodal systems discussed in the previous chapters. Two anthracene-thiosemicarbazone based tripodal systems, previously reported in Chapter 2, were metallated by exploiting microwave technology to obtain rhenium and ruthenium complexes. The development of metal complexes of group 11 transition metals and tripodal NHC-based ligands reported in Chapter 3 is discussed and their biological activities are probed in PC3 cells using MTT assays and confocal microscopy experiments.

Chapter 6 summaries the work described throughout the thesis and future work emerging from the project results.

Chapter 7 contains all the experimental details and characterisation data for the compounds obtained in this work.

The *Appendices* provide supporting spectroscopic data and X-ray diffraction data for the compounds developed during this project.

List of abbreviations

^{18}F-FACBC	1-amino-3-^{18}F-fluorocyclobutane-1-carboxylic acid
^{18}F-FDG	^{18}F-fluorodeoxyglucose
^{18}F-FMISO	^{18}F-fluoromisonidazole
A	Alanine
Ag_2O	Silver(I) oxide
AIF	Apoptotic inducing factor
AO	Acridine orange
AR	Androgen receptor
AST	Androgen Suppression Therapy
ATSC	Anthracene thiosemicarbazone
BBN	Bombesin
C	Cysteine
catB	Cathepsin B
CB-TE2A	1,4,8,11-Tetraazabicyclo[6.6.2]hexadecane-4,11-diacetic acid
cdc2	Cell division cycle protein 2
CO	Carbon monoxide
CORMs	Carbon monoxide-releasing molecules
COSY	Correlation spectroscopy
Cu-ATSM	Copper(II)-diacetyl-*bis*(N_4-methylthiosemicarbazone)
DABCO	Diazabicyclo[2.2.2]octane
DCE	Dichloroethane
DCM	Dichloromethane
DIC	Differential interference contrast (microscopy)
DLC	Delocalised lipophilic cation
DMEM	Dulbecco's Modified Eagle Medium
DMSO	Dimethyl sulfoxide
DNA	Deoxyribonucleic acid
DOTA	1,4,7,10-Tetraazacyclododecane-1,4,7,10-tetraacetic acid
DSA	Di(stearylamide)
DTPA	Diethylenetriaminepentaacetate
EIF4F	Eukaryotic initiation factor 4F
EPO	Erythropoietin
EPR	Enhanced permeation and retention principle
ESI	Electrospray ionization
ESI-MS	Electrospray ionisation mass spectrometry
FCS	Foetal calf serum
FITC	Fluorescein isothiocyanate
FT-IR	Fourier-transform infrared spectroscopy
GRP	Gastrin-Releasing Peptide

GRPR	Gastrin-Releasing Peptide Receptor
HDL	High-density lipoprotein
Her-2	Human Epidermal Growth Factor Receptor 2
HIF-1	Hypoxia-inducible factor-1
HREs	Hypoxia-response elements
HSPs	Heat Shock Proteins
Hz	Hertz
IC	Internal conversion
IC_{50}	Half maximal inhibitory concentration
ISC	Intersystem crossing
J	Coupling constant
K_2CO_3	Potassium carbonate
KHMDS	Potassium bis(trimethylsilyl)amide
LECs	Light-emitting electrochemical cells
LPS	Lipopolysaccharide
LUMO	Lowest unoccupied molecular orbital
m/z	Mass-to-charge ratio
MeCN	Acetonitrile
MIC	Minimum inhibitory concentration
MLCT	Metal-to-ligand charge-transfer
MRI	Magnetic resonance imaging
MTR	MitoTracker Red
MTT	2-(4,5-dimethyl-2-thiazolyl)-3,5-diphenyl-2H-tetrazolium bromide
MW	Microwave
MXI1	MAX-interactor 1
NADH	Nicotinamide adenine dinucleotide
NADPH	Nicotinamide adenine dinucleotide phosphate
NCs	Nanoclusters
NH_4PF_6	Ammonium hexafluorophosphate
NHC	N-heterocyclic carbene
NIRF	Near infrared fluorescence
NMR	Nuclear magnetic resonance
NO	Nitric oxide
NSAID	Nonsteroidal anti-inflammatory drug
ODD	Oxygen-dependent degradation domain
OI	Optical imaging
ORTEP	Oak Ridge Thermal Ellipsoid Plot
PAH	Polycyclic aromatic hydrocarbon
PBS	Phosphate-buffered saline (buffer)
PCa	Prostate Cancer
PDK1	Pyruvate dehydrogenase kinase 1
PDT	Photodynamic therapy
PET	Positron emission tomography
PF_{6^-}	Hexafluorophosphate anion

PIN	Prostate intraepithelial neoplasia
PSA	Prostate-specific antigen
PSGR	Prostate Specific G-Protein Coupled Receptor
PSMA	Prostate-Specific Membrane Antigen
PTP	Protein tyrosine phosphatases
RF	Radiofrequency
RGD	Arginylglycylaspartic acid peptide
RNA	Ribonucleic acid
ROS	Reactive oxidative species
S	Serine
SEM	Standard error of the mean
SOCTA	Succinimidyl 3,6-diaza-5-oxo-3-[2-(triphenylmethyl)thioethyl]-8-[(triphenylmethyl)thio]octanoate
SPECT	Single-Photon Emission Computed Tomography
STEAP	Six-Transmembrane Epithelial Antigen of the Prostate
*t*BuOK	Potassium *tert*-butoxide
TEM	Transmission electron microscopy
terpy	Terpyridine
Tf	Transferrin
TfR	Transferrin Receptor
THF	Tetrahydrofuran
$timteb_{dipp}$	1,3,5-{tris({2,6-diisopropylphenyl}imidazol-2-ylidene)methyl}- 2,4,6-triethylbenzene
$timtmb_{tBu}$	1,3,5-[tris(3-tert-butylimidazole-2-ylidene)methyl]-2,4,6-trimethylbenzene
TLC	Thin-layer chromatography
TrxR	Thioredoxin reductase
UPR	Unfolded protein response
UV	Ultraviolet (radiation)
VEGF	Vascular endothelial growth factor
β^+	Positron
δ	Chemical shift

List of compounds

Chapter 2

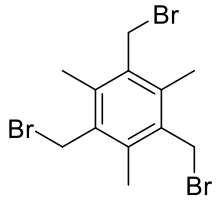

60

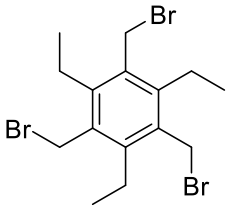

61

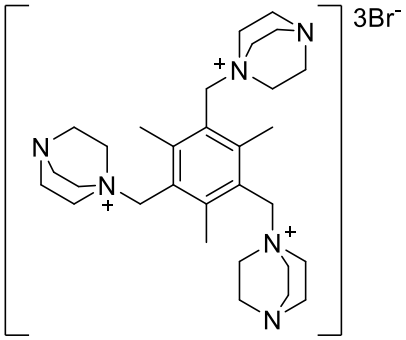

62

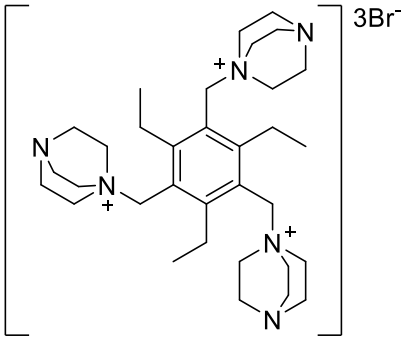

63

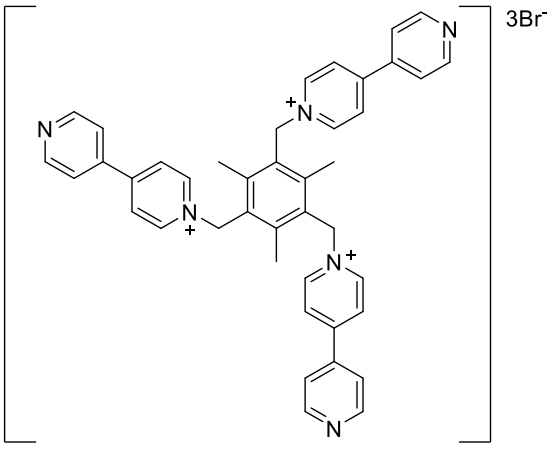

64

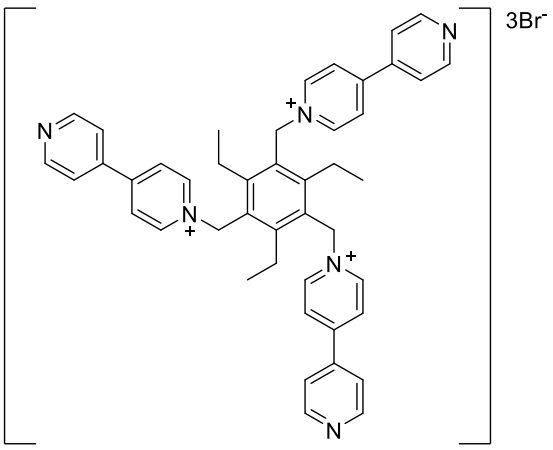

65

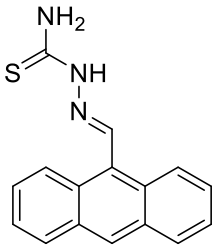

66

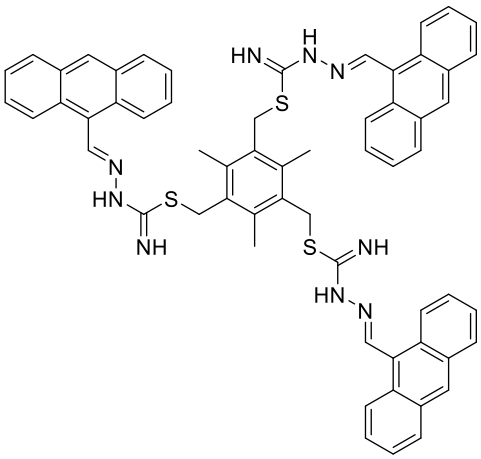

67

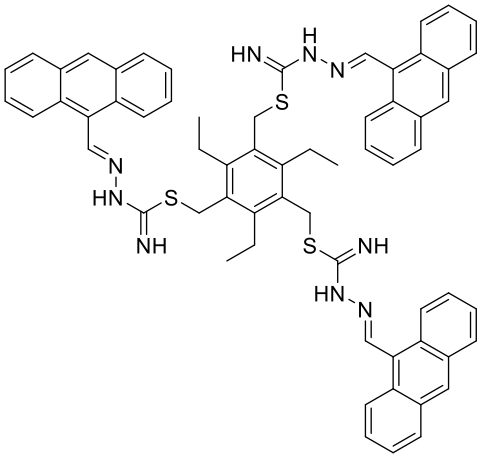

68

Chapter 3

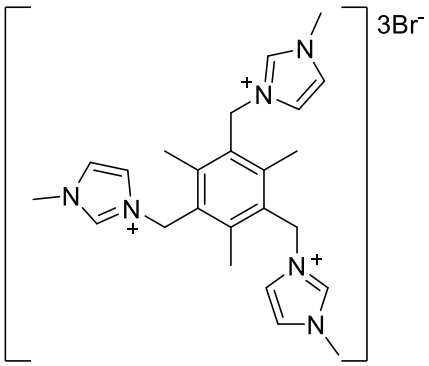

69

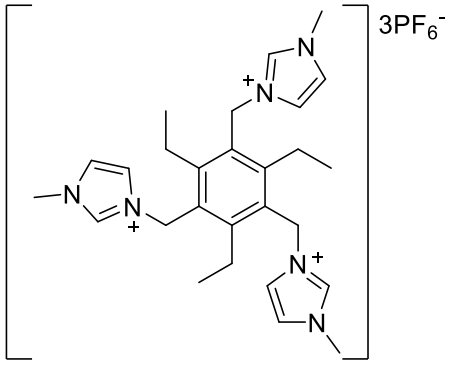

70

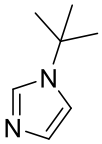

71

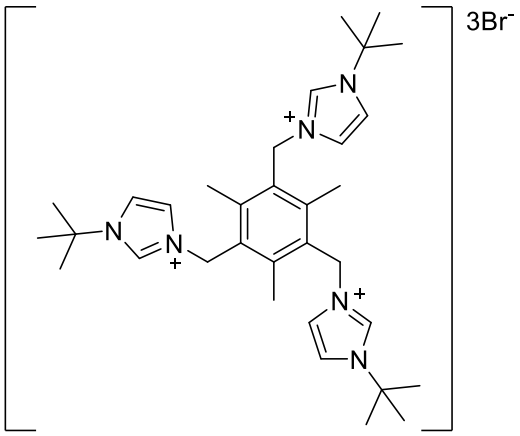

72

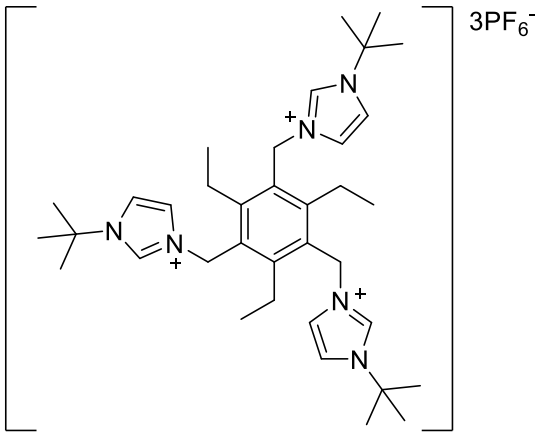

73

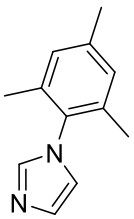

74

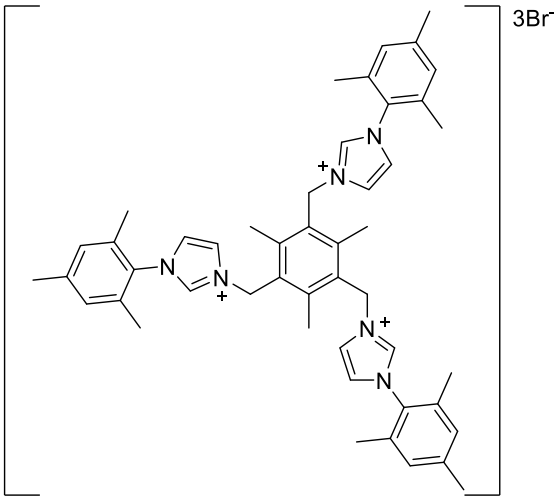

75

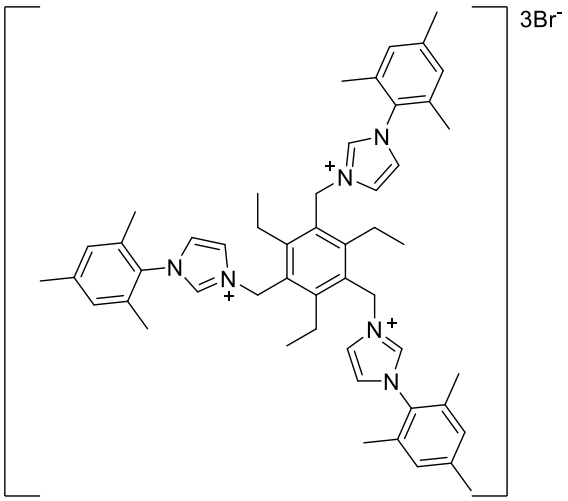

76

Chapter 4

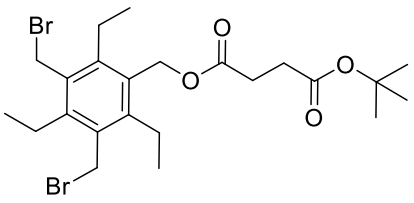

77

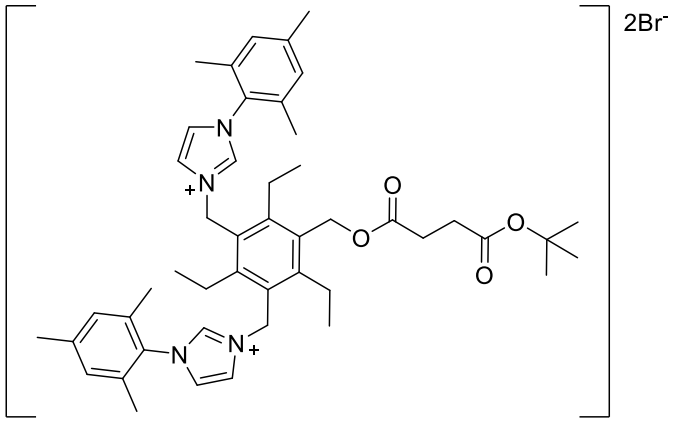

78

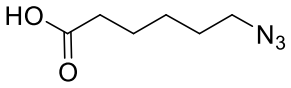

79

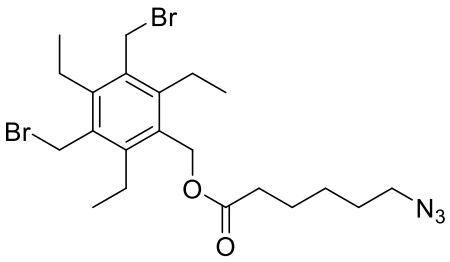

80

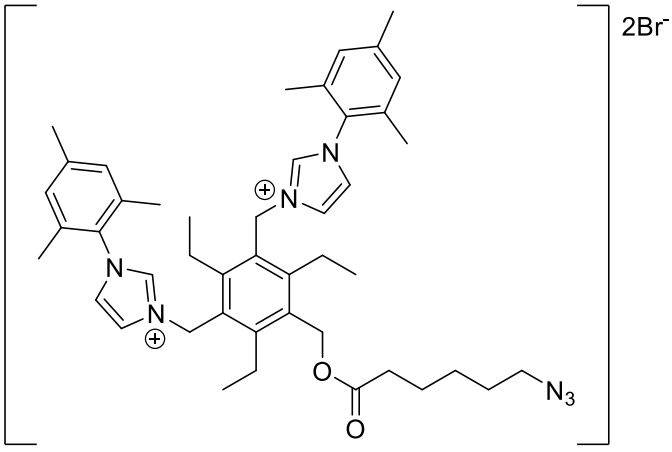

81

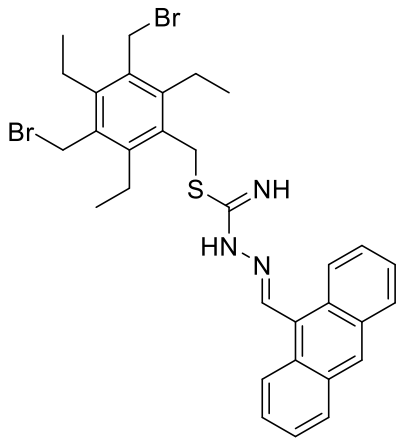

82

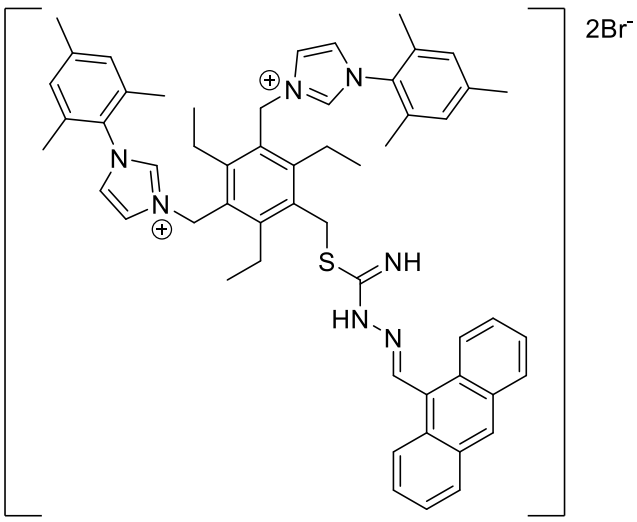

83

Chapter 5

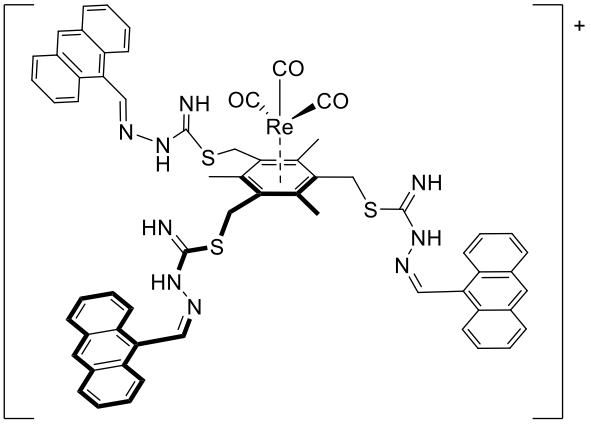

84

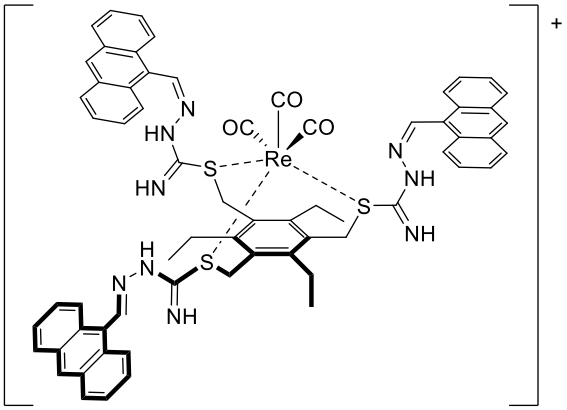

85

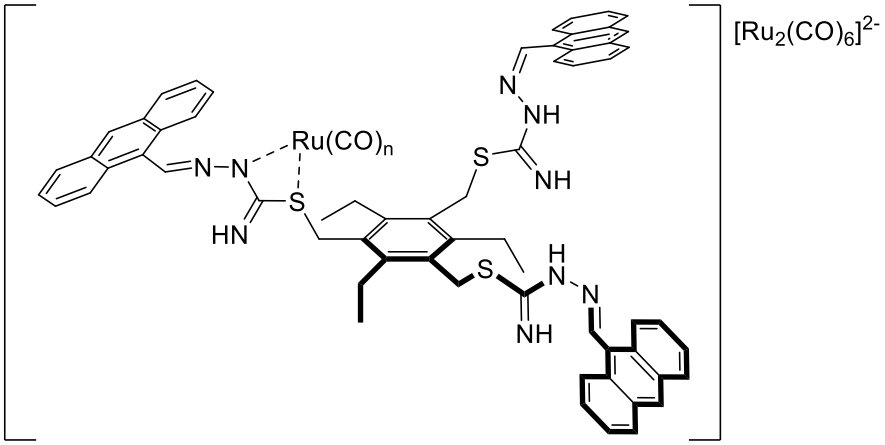

86

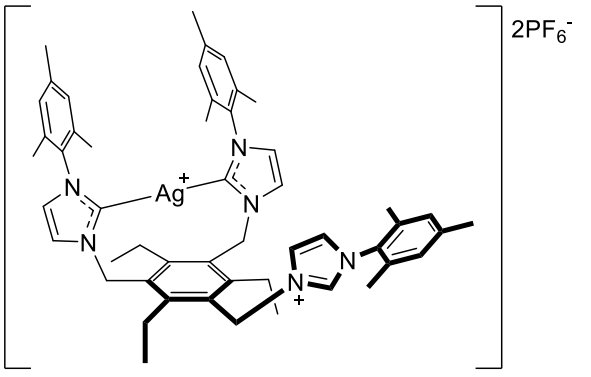

87

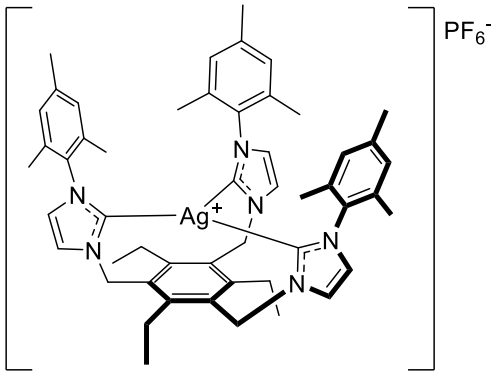

88

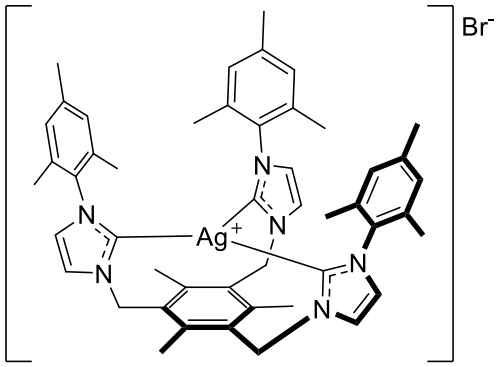

89

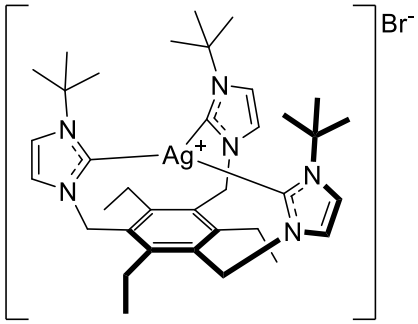

90

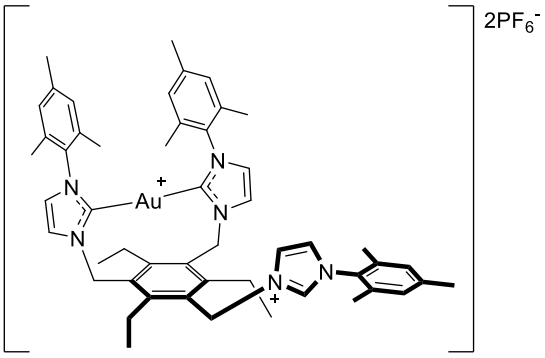

91

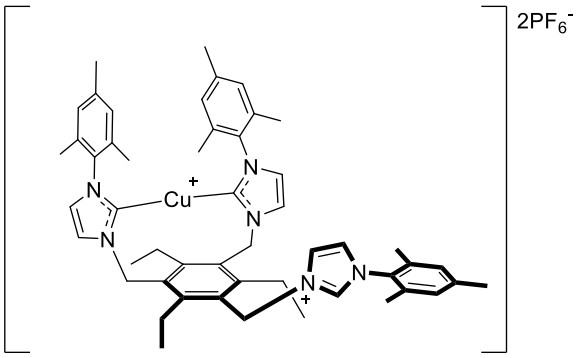

92

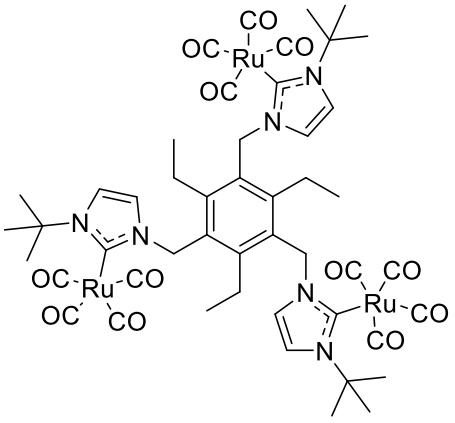

93

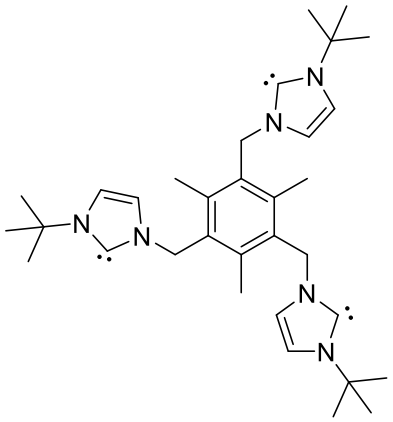

94

1. Introduction

1.1. Coordination chemistry for cancer therapy and other biomedical applications

In 1893, the Swiss chemist Alfred Werner (1866−1919) was the first to propose the correct geometry of transition metal complexes when he described the structure of hexamminecobalt(III) chloride.[1, 2] This seminal work led to the establishment of coordination chemistry, the branch of inorganic chemistry that studies coordination complexes. Generally, a coordination compound consists of a molecule composed of a central atom or ion, usually a metal, surrounded by molecules or anions, known as ligands.[3] The ligands are attached to the central atom by dative bonds, also known as coordinate bonds, in which both electrons in the bond are supplied by the same atom on the ligand.

A coordination complex whose centre is a metal atom is called a metal complex. The use of transition metal complexes as chemotherapeutic agents began with the discovery of the anticancer activity of the platinum(II)-based drug cisplatin in 1965 (Figure 1.1).[4] Since then, the use of metal complexes for sensing and medicinal purposes has been increasing noticeably.[5-7]

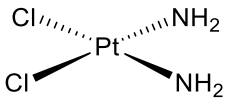

Figure 1.1. Structural representation of cisplatin.

One of the main characteristics of coordination complexes is their capacity to undergo a process called “ligand exchange” which denotes a chemical reaction whereby one ligand in a complex ion is replaced by a different one.[8] A typical example regarding the way in which this ligand exchange may be used in medicinal chemistry is the mode of action of cisplatin: this complex exchanges its chloride substituents with N7-guanine residues of DNA strands, causing the formation of crosslinks between the two DNA strands.

A different way to exploit the ligand exchange effect in coordination complexes is the possibility to bind the metal with a releasable ligand that presents a medicinal effect on its own. A suitable example is the recent development of carbon monoxide-releasing molecules (CORMs), which may be used to perform a selective and specific delivery of carbon monoxide

(CO) to the site of interest. Even though carbon monoxide holds the bad reputation of a "silent killer", its diverse effects as a second messenger (like nitric oxide, NO) include reduction of inflammation, heart protection from reperfusion damage following surgery and improvement of organ functionality after transplantation.[9, 10] Some representative examples of CORMs are shown in Figure 1.2.

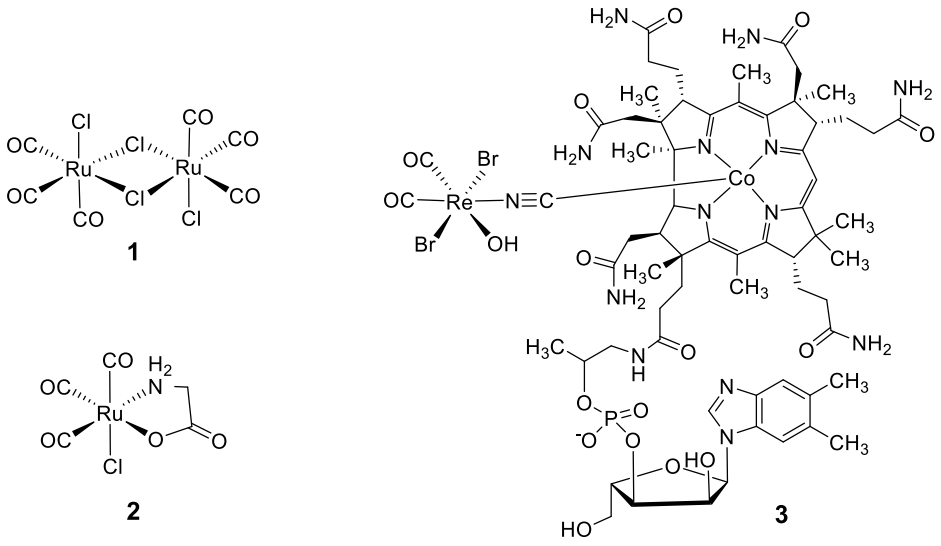

Figure 1.2. Some examples of currently investigated CORMs. $[Ru(CO)_3Cl_2]_2$ (**1**), $[Ru(CO)_3Cl(glycinate)]$ (**2**), and the biocompatible vitamin B_{12}-rhenium complex B_{12}-ReCORM-2 (**3**).[9, 11]

Organometallic complexes, which are chemical compounds containing one or more metal-carbon bonds, are a class of chemical compounds widely used in homogenous catalysis. For this reason, several research groups have started to develop organometallic complexes that are able to catalyse chemical reactions in cells.[12-14] One of the first studies in this direction comes from Sadler and co-workers,[15] by using a series of ruthenium-arene ethylenediamine complexes **4** (Figure 1.3) that catalyse a redox reaction involving glutathione. The result is a net increase of reactive oxidative species (ROS), which is found to be highly toxic towards human lung and ovarian cancer cells.

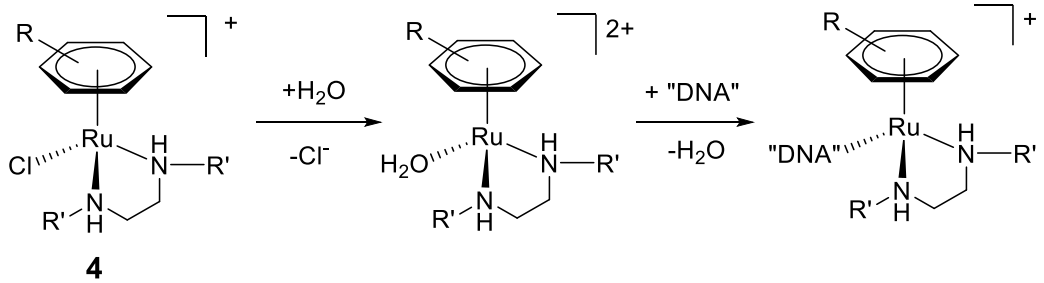

Figure 1.3. A schematic representation of the mechanism of action of Ru-arene ethylenediamine complex **4**.

Following the discovery of several radioisotopes, the development of organometallic compounds has become a crucial part of radiochemistry. These complexes usually consist of a radioisotope linked to a simple chelator, which can be further attached to a targeting molecule to increase the specificity for the tissue of interest. An example of how such a strategy can be applied comes from a paper by Schibli and co-workers: in their work, the group synthesised a series of biomolecules containing the targeting molecule folic acid, functionalised with a tridentate picolylamine-monoacetic acid chelating system which ultimately binds an atom of ^{99m}Tc (see compound **5** displayed in Figure 1.4).[16] The resulting radiopharmaceuticals were able to accumulate in cancer cells where the folate receptor is overexpressed, thus allowing the visualization of the tumours.[17]

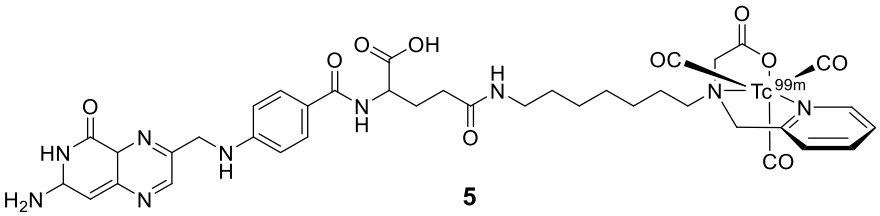

Figure 1.4. Structural representation of compound **5**.

With the aim of developing treatment strategies that are minimally invasive and considerably less toxic, the emerging field of photodynamic therapy (PDT) has seen an extensive application of coordination compounds. PDT involves a combination of three elements: light, photosensitiser and a substrate.[18] Upon light irradiation, the photosensitiser at ground singlet state (S_0) may be excited to the first excited singlet state (S_1) and then undergoes intersystem crossing (ISC) to reach the first excited triplet state (T_1) (see Figure 1.5). The excited photosensitiser directly interacts with substrates (typically oxygen) to produce ROS, which in turn elicit cell death.[19]

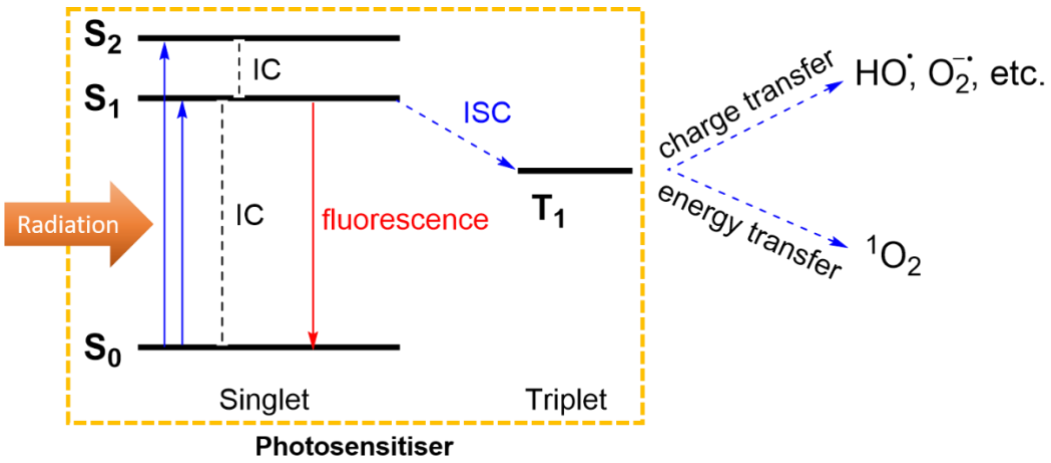

Figure 1.5. Generation of reactive oxygen species due to absorption of electromagnetic radiation by a photosensitiser molecule. The absorption leads to population of excited singlet states, which are rapidly converted into an S_1 population via internal conversion (IC). The excited photosensitiser can return to the ground state (S_0) by release of energy as heat (IC) or by fluorescence. Alternatively, through intersystem crossing (ISC), the molecule moves to the metastable triplet T_1 state, which then allows energy or charge transfer to other molecules such as oxygen. Adapted from Ref.[20] with permission from the Royal Society of Chemistry.

Cyclic tetrapyrrolic molecules (such as porphyrins) are good examples of fluorophores and photosensitisers.[21] A wide range of metals have been used to form complexes with photosensitiser macrocycles, particularly transition metals, although a number of photosensitisers coordinated to group 13 and group 14 metals have also been synthesised.[22, 23] The nature of the central metal ion greatly influences the photophysical properties of the photosensitiser.[24-26] For example, the zinc phthalocyanine photosensitiser ($ZnPcS_4$, Figure 1.6) has a singlet oxygen quantum yield of 0.70 in water;[21] nearly twice that of most other metallated phthalocyanines. $ZnPcS_4$ was found to be active against several cancer cell lines,[27] as well as pathogenic microorganisms such as *Staphylococcus aureus* and *Candida albicans*.[26]

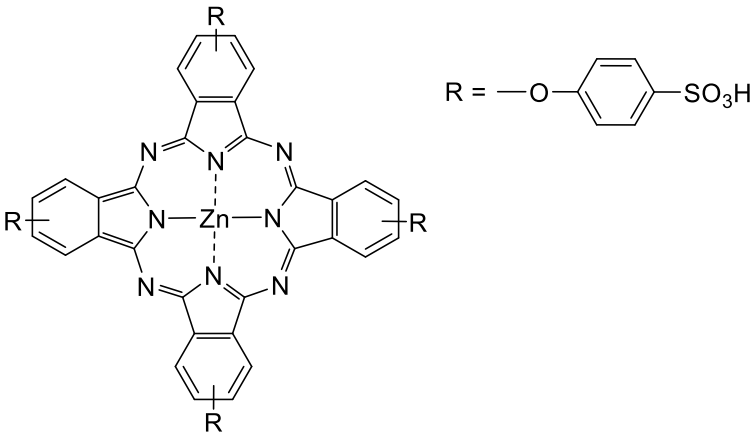

Figure 1.6. Structural representation of the zinc phthalocyanine photosensitiser $ZnPcS_4$.

The versatility of coordination complexes can also be exploited to develop combination agents,[28] a class of compounds obtained by combining two or more active agents to form a molecule capable of modulating multiple targets simultaneously. An example of such a compound is the bifunctional heterobimetallic copper-ruthenium complex **6** (Figure 1.7) developed by Reedijk and co-workers.[29]

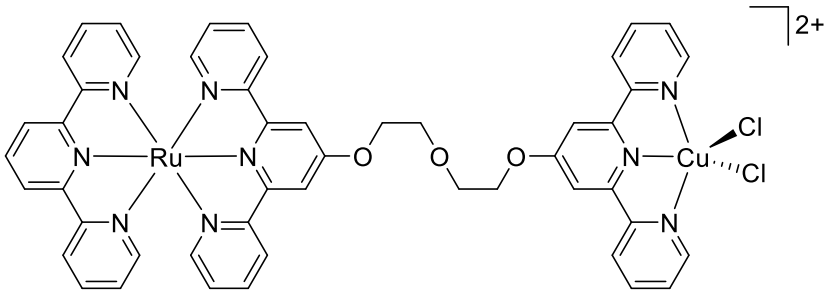

Figure 1.7. Structural representation of the bifunctional heterobimetallic copper-ruthenium complex **6**.

Compound **6** is composed of the DNA-cleaving agent copper terpyridine (Cu(terpy)), linked by a flexible bridge to a high affinity ruthenium metallo-intercalator. The bimetallic combination agent **6** demonstrated a superior DNA-cleavage activity compared to the Cu(terpy) agent alone.

Overall, coordination complexes display numerous properties that can be used to design drugs that present both therapeutic and diagnostic capabilities, thus becoming a powerful tool for several biomedical applications.

1.1.1. N-Heterocyclic carbene complexes with biomedical applications

N-Heterocyclic carbenes (NHCs) are cyclic compounds containing a divalent carbon atom bound to at least one nitrogen atom within the heterocycle.[30] There were many attempts to isolate such species over the 20th century and, in 1991 Arduengo *et al.* reported the isolation and characterisation of the first free carbene unit incorporated into a nitrogen heterocycle.[31] N-heterocyclic carbenes (NHC, Figure 1.8) contain the lone pair of electrons of the carbon atom stabilised by two geminal nitrogen atoms within the heterocyclic ring. Their electronegativity withdraws σ-electron density away from the carbene, while at the same time the nitrogen atoms donate π-electron density into the empty p orbital of the sp^2 hybridised carbon.[32]

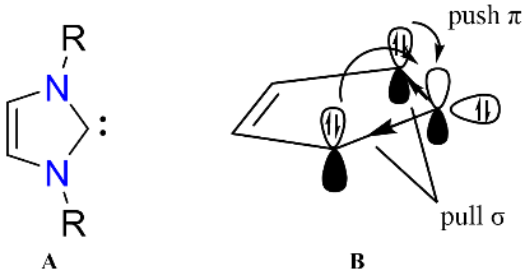

Figure 1.8. General structure of an N-heterocyclic carbene (**A**) and representation of the electronic stabilising effects (**B**).

Thanks to these stabilising effects, NHCs have become extremely popular for complexing various transition metals. Many research articles show that NHC complexes are used as catalysts in a variety of chemical transformations, such as Suzuki coupling, Diels-Alder reactions and many others.[33-35] In the last 20 years though, the application of NHC-based metal complexes in the area of medicinal chemistry has seen a steady increase, with their position being reinforced by the discoveries of tuneable biological activity. The application of NHC-metal complexes as antimicrobial agents is a good example, with the gold imidazoline derivative **7** (Figure 1.9) being active against several bacterial species.[36]

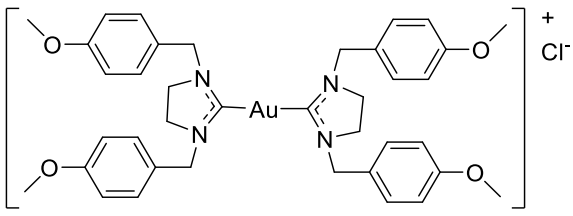

Figure 1.9. Structural representation of the gold imidazoline complex **7**.

However, most progress made in this field has been achieved by using the innate antimicrobial properties of silver and its carbene complexes.[37] Several research groups have successfully developed silver-based NHC chemotherapeutics that have shown minimum inhibitory concentration (MIC) values against bacteria under 10 µg/ml. In a study led by Youngs *et al.*, two pyridine-linked pincer silver NHC complexes **8** (Figure 1.10) were even more active than $AgNO_3$ against several bacterial strains.[38] Another study conducted by Roland and Jolivalt *et al.* in 2011 reported a series of halido Ag(I)-NHC complexes **9** (Figure 1.10) that were found to be active even against *S. aureus* MsrA (a bacterial strain with constitutive resistance to erythromycin).[39]

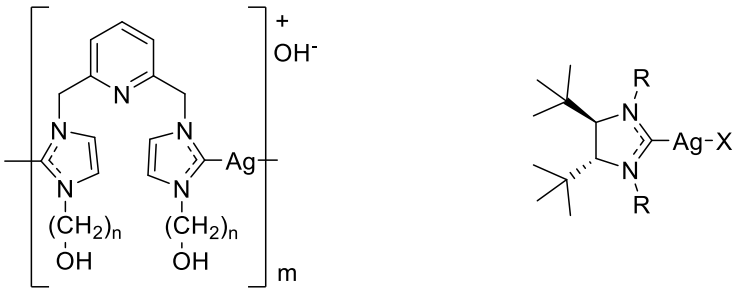

Figure 1.10. Structural representations of the pyridine-linker silver(I)-NHC complex **8** and the halido-silver(I) NHC complex **9**.

Although most antimicrobial metal complexes are silver-based, the use of gold-based NHC complexes is predominant in cancer therapy. Gold-based biomolecules have also been tested in various inflammatory diseases, such as rheumatoid arthritis, and they have been found to interfere with common biochemical pathways that are also relevant for cancer.[40]

One of the first studies that analysed the cytotoxic activity of some dinuclear gold(I) NHC complexes reported the induction of mitochondrial membrane swelling triggered by intracellular Ca^{2+} increase.[41] The study, conducted by Berners-Price and co-workers and published in 2008, revealed that gold(I) NHC complexes, such as compound **10** (Figure 1.11), act as mitochondria-targeted agents by interacting with selenoproteins (such as thioredoxin reductase) as preferential targets.[42] The antimitochondrial activity of these Au(I)-NHC complexes could also be due to their delocalised cationic charge and their lipophilicity. Such attributes allow the gold complexes to accumulate in the mitochondria of the cancer cells which is characterised by an enlarged mitochondrial membrane potential.[43]

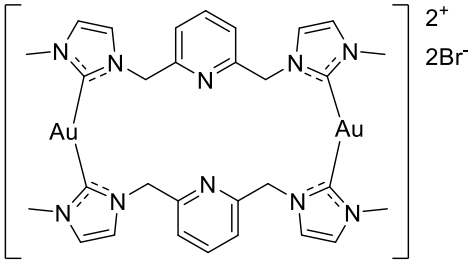

Figure 1.11. Structural representation of the dinuclear gold(I) NHC complex **10**.

Aiming to investigate the uptake and intra-cellular distribution in the PC3 human prostate cancer cell line of gold(I) NHC complexes Gautier, Cisnetti and co-workers developed the Au(I)-NHC complex **11** bearing a fluorescent coumarin moiety (Figure 1.12).[44] This functionalised Au-NHC complex was synthesised by a straightforward synthetic route, combining an 'auto-click' reaction with a transmetallation process. Interestingly, a significant blue fluorescence was detected in the cytoplasm but not in the nucleus after 18 hours incubation of PC3 prostate cancer cells with 10 μM of the compound **11**. Furthermore, compound **11** appears to specifically localise in the mitochondria in a similar manner to the mitochondria-targeted Au(I)-NHC complexes **12** and **13** developed by Li and co-workers (Figure 1.12).[45]

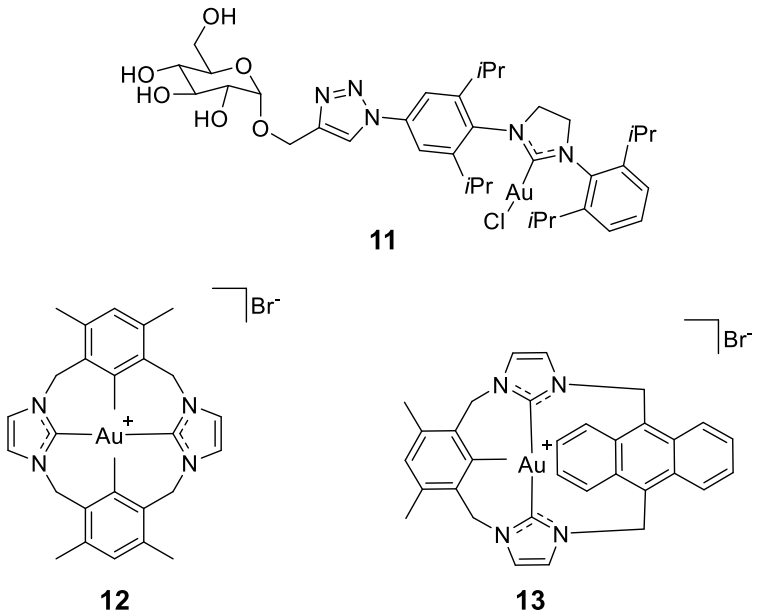

Figure 1.12. Structural representations of the gold(I) NHC complex **11** and the mitochondria-targeted Au(I)-NHC complexes **12** and **13**.

A series of amino-functionalised Au(I)-NHC complexes (such as compound **14**, Figure 1.13) were tested for their antiproliferative activity in the PC3 prostate cancer cell line by Gornitzka and co-workers.[46] The observed anti-tumour effects were attributed to the lipophilic properties of these complexes. Complex **14** was also found to be active towards several other cancer cells,

again highlighting the intriguing anti-mitochondrial properties of gold and its complexes. Moreover, compound **14** was found to be insensitive to normal primary human umbilical vein endothelial cells (HUVECs) at the highest concentration tested (5 μM). All these results indicate that **14** is active against multiple cancer cell lines while having restricted effects on normal human endothelial cells.

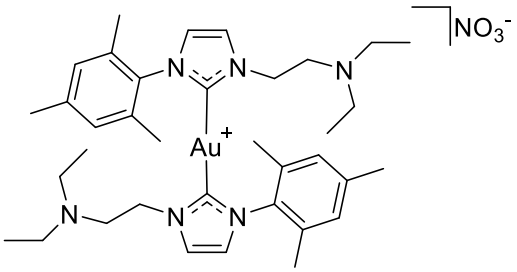

Figure 1.13. Structural representation of the gold(I) NHC complex **14**.

However, selenoproteins are not the only targets of gold NHC complexes. A study from Barrios and co-workers reported that various gold(I) NHC complexes are capable of strongly inhibiting several protein tyrosine phosphatases (PTP), which are involved in several pathways relevant not only to cancer but also diseases such as diabetes and obesity.[47] Another paper by Che *et al.* reported a series of gold(III) NHC complexes (*e.g.* compound **15**, Figure 1.14) that are capable of interacting with topoisomerase I, thus producing DNA strand breaks.[48]

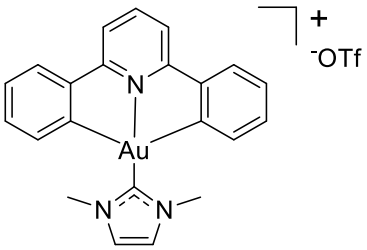

Figure 1.14. Structural representation of the gold(III) NHC complex **15**.

In the last few years, various research groups have studied the possibility of developing anticancer metal NHC complexes with other transition metals.[49] A significant number of platinum-based NHC complexes have been studied and showed good activity against cancer cell lines.[50-53] For example, a comparative study between the *cis*-platinum NHC complex **16** (Figure 1.15) and cisplatin showed that two compounds had similar antiproliferative activity, and a strong interaction between compound **16** and DNA strains was observed. However, the study also outlined that compound **16** shares a similar level of interaction with glutathione to cisplatin, which lowers the bioavailability of the drug.[54]

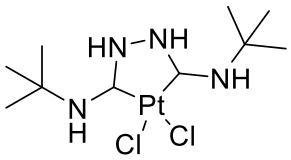

Figure 1.15. Structural representation of the *cis*-platinum based NHC complex **16**.

A series of *trans*-platinum NHC complexes such as compound **17** (Figure 1.16) have been investigated and their antiproliferative activity was found to be comparable to cisplatin.[55] Cyclometalated platinum(II) NHC complexes, such as compound **18** (Figure 1.16), displayed strong cytotoxic activity and useful fluorescent properties, which allowed a completely different biological profile to be discovered. *Trans*-platinum complexes were found to be potent inhibitors of the anti-apoptotic protein survivin, thus promoting the activation of caspase-3, a protease which plays a fundamental role in programmed cell death.[56]

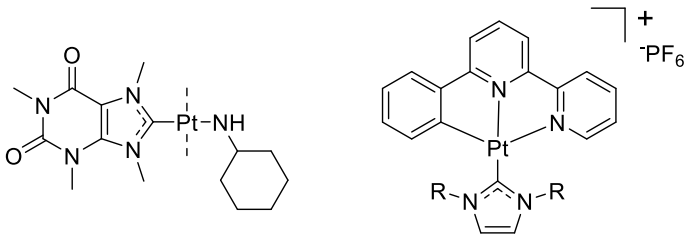

17 **18**

Figure 1.16. Examples of *trans*-platinum(II) NHC complexes: compounds **17** and **18**.

As well as being widely known for their anti-infective properties, silver-based NHC complexes have also demonstrated cytotoxic effects in cancer cells. Compound **19** (Figure 1.17) demonstrated IC_{50} values comparable to cisplatin.[57] A study published in 2012 by Eloy and co-workers demonstrates that silver NHC complexes such as compound **20** (Figure 1.17) act as antimitochondrial agents: these complexes can trigger membrane depolarization, damage of the endoplasmic reticulum and liberation of apoptotic inducing factor (AIF) from the matrix, ultimately causing apoptosis in cancer cells.[58]

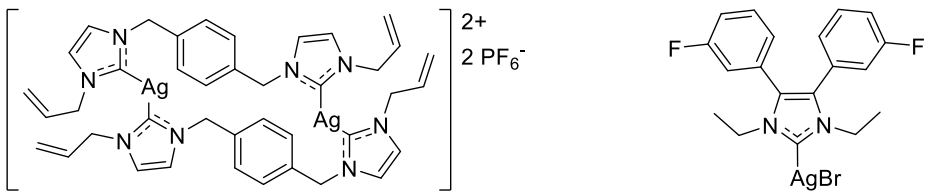

19 **20**

Figure 1.17. Structural representations of silver NHC complexes **19** and **20**.

Although the vast majority of studies on the antiproliferative activity of group 11 transition metals involved the use of gold, several copper(I) NHC complexes have also been investigated. An extensive study by Tacke *et al.* involved nine symmetrically substituted (**21a-i**) Cu(I)-NHC bromide complexes and one unsymmetrically substituted (**21j**) derivative (Figure 1.18). These complexes were synthesised via the transmetallation reaction of *p*-benzyl substituted imidazolium halides with Cu(I) bromide dimethylsulfide over Ag(I) oxide.[59] The Cu(I)-NHC bromido complexes (**21a-i**) showed high cytotoxicity against MCF-7 breast cancer and Caki-1 renal cancer cell lines with IC_{50} values in the micromolar and sub-micromolar range.

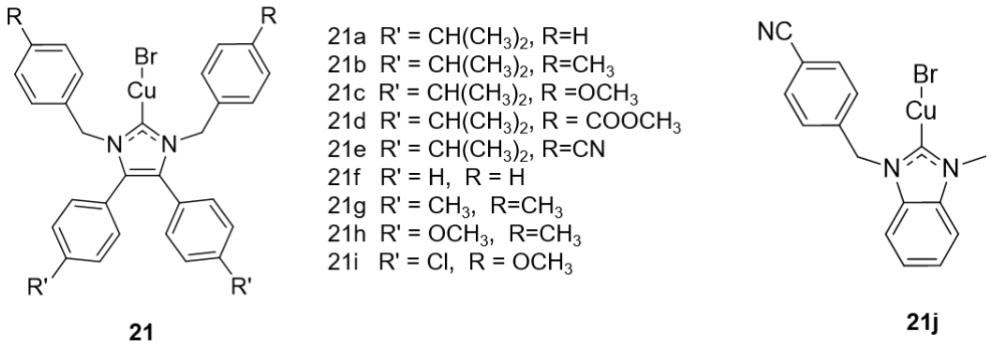

Figure 1.18. Structural representations of Cu(I)-NHC complexes **21a-j**.

A study in 2015 from Gandin and co-workers on 1,2,4-triazolium-based group 11 NHC-based metal complexes led to the development of the Cu(I)-NHC complex **22** (Figure 1.19). The newly synthesised copper(I) complex was assessed for cytotoxicity in various human cancer cell lines, including cisplatin-sensitive and resistant cells. Compound **22** was found to be between 3- to 7-fold more effective than cisplatin against A431 cervical, A549 lung, HCT-15 colon and BxPC3 pancreatic cancer cells.[60]

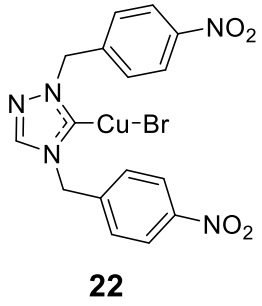

Figure 1.19. Structural representation of the 1,4-bis(4-nitrobenzyl)-1H-1,2,4-triazol-4-ium bromide-based Cu(I)-NHC complex **22**.

Interestingly, **22** displayed higher cytotoxicity than its corresponding gold and silver complexes against all tested cancer cell lines. Furthermore, transmission electron microscopy (TEM)

analyses suggested that compound **22** could enter and consequently accumulate in cancer cells leading to cell death through the impairment of the ubiquitin-proteasome degradation pathway. This study reinforces the rationale that the biological activity of specific NHC complexes may be properly tuned and modified by the nature of the metal centre, thus giving useful direction to the development of clinically relevant NHC-based metal complexes.

A more recent study conducted by Bertrand and co-workers on a series of complexes of cyclic (alkyl)(amino)carbene (CAAC) of group 11 metals found that Cu(I)-NHC complexes such as compound **23**, and the *bis*-carbene complex $[(Me_2CAAC)_2Cu(I)]^+$ **24** (Figure 1.20), displayed noticeable cytotoxicity against a panel of cancer cell lines (including the cisplatin-resistant A549 lung cancer cells), with IC_{50} in the low sub-micromolar range.[61]

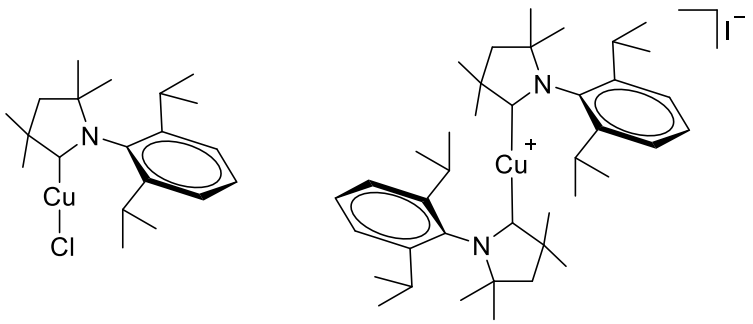

23 **24**

Figure 1.20. Structural representations of the Cu(I)- CAAC complex **23** and the bis-carbene $[(Me_2CAAC)_2Cu(I)]^+$ complex **24**.

Further mechanistic studies revealed that compound **23** was able to induce about the same amount of reactive oxygen species (ROS) production as the positive control H_2O_2. ROS overproduction can induce cellular stress, which ultimately leads to cell death.[62] Interestingly, the cationic *bis*-CAAC complex **24** did not trigger ROS formation, suggesting that the higher steric hindrance, as well as the lack of readily available coordination sites on the metal centre of **24**, might play a role in the generation of ROS compared to the more labile NHC ligand of the compound **23**.

The latest study on the cytotoxic activity of copper complexes, conducted by Gaillard and collaborators., involved a panel of cationic Cu(I)-NHC bearing 2,2′-dipyridylamine (dpa)-type ligands.[63] These metal complexes were previously investigated for their emissive properties as blue light-emitting electrochemical cells (LECs) based on copper(I) complexes.[64]

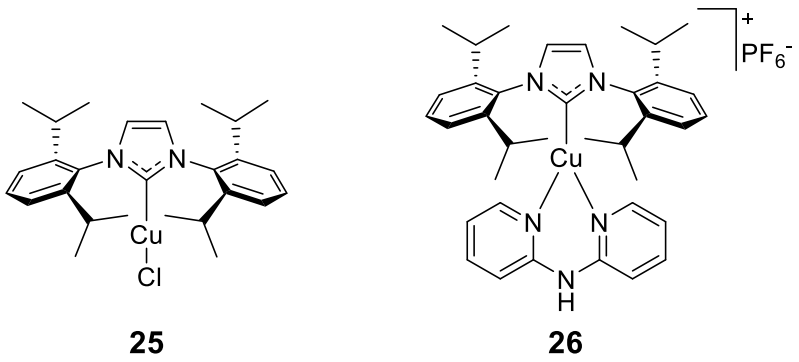

25 **26**

Figure 1.21. Structural representations of the neutral Cu(I)-NHC complex **25** and the cationic complex $[Cu(I)(NHC)(dpa)]^{+}[PF_6]^{-}$ compound **26**.

From the comparative study between the neutral complexes (*e.g.* compound **25**, Figure 1.21), previously screened by Gautier and co-workers,[65] and the cationic Cu(I)(NHC)(dpa) complexes, compound **26** emerged as the most active against a panel of four cancer cell lines and with IC_{50} values lower than the commercial drugs, Etoposide and 5-fluorouracil. These results indicate that copper complexes are currently an attractive area of investigation in the pursuit for novel, potent anticancer compounds based on earth-abundant elements.

The antiproliferative activity of palladium-based NHC complexes has been investigated and some promising results have also been obtained.[66] The antiproliferative activity of compounds **27** and **28** (Figure 1.22) may be related to the electron donating nature of their substituents and also appears to depend upon their stereochemistry, with the *trans*- derivatives being more cytotoxic than the *cis*-.[67] The mechanism of action of such complexes has been proposed in a paper by Ray *et al.*: it appears that compound **28** triggers an overexpression of the mitotic protein cyclin B1, thus arresting the cell cycle at the G2-M transition phase, as well as blocking mitosis by avoiding the translocation of the cell division cycle protein 2 (cdc2) into the nucleus.

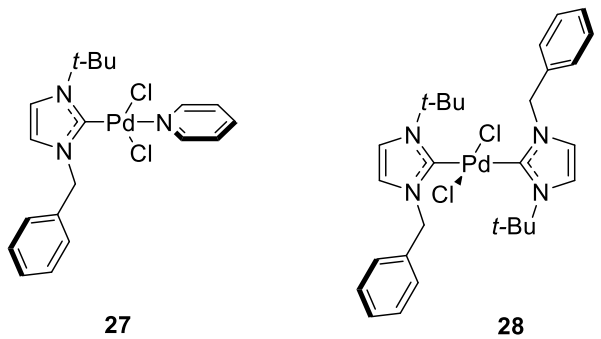

27 **28**

Figure 1.22. Structural representations of the palladium-NHC complexes **27** and **28**.

Ruthenium NHC complexes with biological activity have been successfully identified in various recent reports.[68, 69] Among these, the well-known Grubbs and Hoveyda-Grubbs

catalysts (such as compounds **29** and **30**, Figure 1.23) were screened as antiproliferative agents.[70] However, limiting factors such as poor solubility in biological system contributed to their weak efficiencies against tumour proliferation. Compound **30** instead displayed significant antiproliferative effects with IC_{50} values of 9.9 μM against MCF-7 breast adenocarcinoma, as well as strong inhibiting efficiency against the tumour biomarkers cathepsin B (catB) and thioredoxin reductase (TrxR).

Following these first results, research conducted by Ott and co-workers involved a series of arene-ruthenium(II) benzimidazolylidene carbene complexes such as compound **31** (Figure 1.23). These compounds displayed greater activity against catB and TrxR, as well as noticeable antiproliferative effects. Furthermore, mechanistic studies confirmed the interaction between the ruthenium centre and thioselenols through ligand exchange reactions.

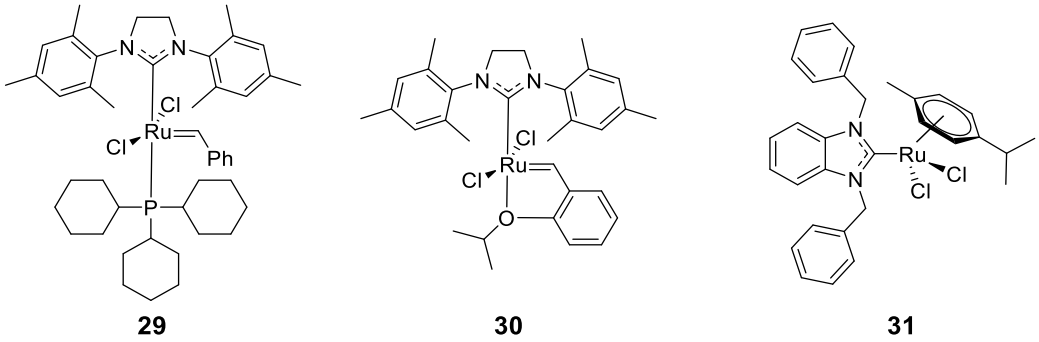

Figure 1.23. Structural representations of ruthenium-NHC complexes.

Another recently studied class of metal-carbene complexes in the 'metals in medicine' field involves those having iridium(III) as the metal core. These complexes are characterised by an octahedral configuration, which allows wider structural modification, thus allowing greater possibilities for the design of new biomolecules.[71]

In 2014 Mao and co-workers developed a series of phosphorescent cyclometallated Ir(III) complexes containing *bis*-NHC ligands **32** (Figure 1.24) that showed remarkable antiproliferative activity, acting as antimitochondrial agents. Furthermore, their photophysical properties might be exploited for diagnosis and therapy at the same time.[72] For example, the group was able to monitor the cellular localisation of the complexes *via* confocal microscopy in HeLa cells, demonstrating that **32** was able to cross the cellular membrane and localise in the mitochondria, where it demonstrated a high degree of co-localisation with the conventional mitochondrial dye MTR (Figure 1.25).

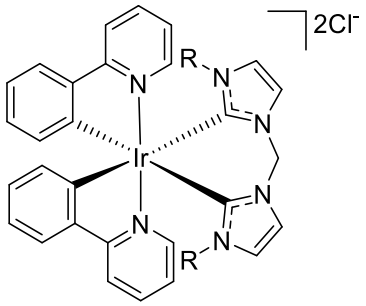

Figure 1.24. General structural representation of the cyclometalated Ir(III) complexes **32**.

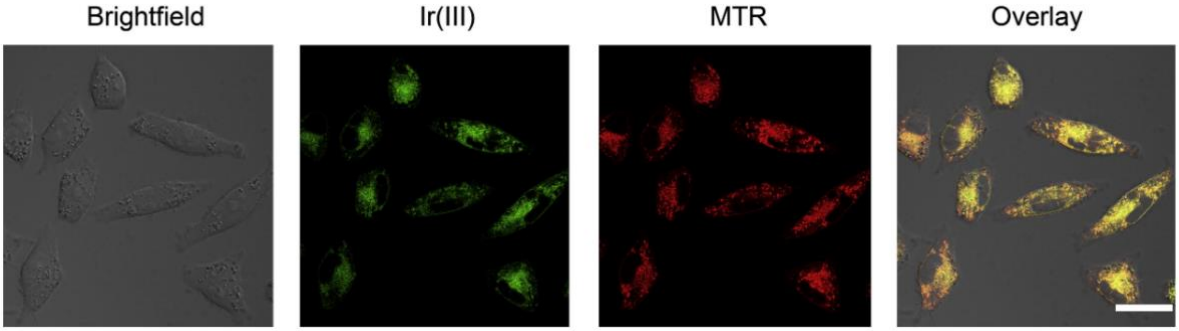

Figure 1.25. Determination of intercellular localisation of complex **32** by confocal microscopy. HeLa cells were incubated with the mitochondrial dye MTR (100 nM) for 20 min and then co-incubated with 32 (20 μmol) for 10 min at 37°C. The Ir(III) complex 32 was excited at 405 nm and the emission was collected at 520±20 nm. MTR was excited at 543 nm and the emission was collected at 600±20 nm. Scale bar: 20 μm.[72]

In recent years several groups have begun to investigate the biological properties of the group 7 transition metal rhenium. The profound interest in this research area is due to the fact that rhenium is cheaper than most of the noble metals previously described and its two isotopes, ^{186}Re and ^{188}Re, can be easily produced and employed for radiotherapeutic purposes.[73-75] However, the synthesis of the first radiolabelled ^{188}Re(V) N-heterocyclic carbene complex (compound **33**, Figure 1.26) was reported by the groups of Reiner and Kühn only in 2014, following the development of the "cold" analogue by Lum and co-workers.[76, 77]

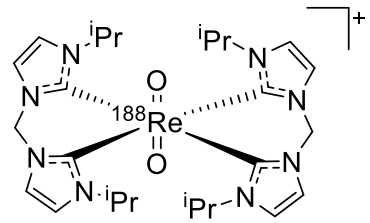

Figure 1.26. Structural representation of the radiolabelled cationic ^{188}Re(V)-*bis*-NHC complex **33**.

Following the synthesis of compound **33**, the Reiner group conducted a series of stability tests under various conditions, starting with water at 37 °C in a pH range from 5 to 8, with phosphate buffered saline solutions (37 °C; pH: 5, 6 and 7), and also bovine serum (which is reasonably similar to the *in vivo* environment). Although its "cold" precursor was found to be rather stable in such media, compound **33** was found to undergo decomposition.

Investigation of the luminescent properties of the Re(CO)$_3$-NHC complexes have been carried out by several research groups. In 2012, Li and co-workers, inspired by the pioneering works of Wrighton and Morse,[78] reported the syntheses of a panel of rhenium(I) tricarbonyl chloride complexes with pyridine-functionalized N-heterocyclic carbenes (such as compounds **34** and **35**, Figure 1.27). These were obtained following the transmetallation reaction of a set of ligand precursors with rhenium(I) pentacarbonyl chloride over Ag_2O. The complexes exhibit blue-green emission characterised by metal-to-ligand charge-transfer transitions (MLCT) influenced by the strong electron donor capability of the bound NHC.[79]

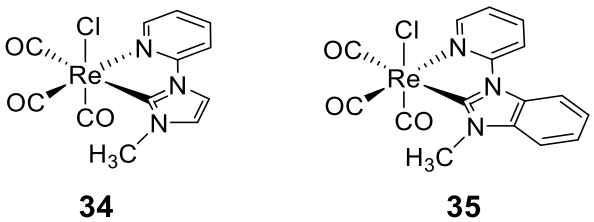

34 **35**

Figure 1.27. Structural representations of the Re(CO)$_3$Cl pyridine-functionalised N-heterocyclic carbene complexes **34** and **35**.

In parallel with this work, an extensive study carried out by Brown, Stagni and Massi *et. al.* thoroughly investigated the photophysics and photochemistry of related rhenium(I) tricarbonyl complexes of general formula *fac*-[Re(CO)$_3$(N^C)X] such as compounds **36**, **37** and **38** (Figure 1.28).[80, 81]

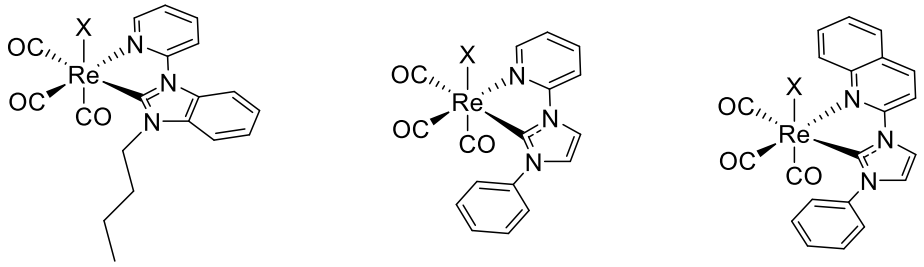

Figure 1.28. Structural representations of the fac-[Re(CO)$_3$(N^C)X] compounds **36**, **37** and **38**. X = Cl, Br.

It was demonstrated that the coordinated NHC ligands of **36**-**38** act as π^*-acceptors, thus directly influencing the energy of the LUMO level, in a similar fashion to the well-known diimine-based rhenium complexes.[82, 83] Moreover, compound **37** was found to undergo photochemical CO dissociation after excitation to its lowest excited state,[84] which makes such complexes an interesting benchmark for new phosphorescent rhenium(I) carbonyl-based complexes as photoactivated CO-releasing molecules for the treatment of inflammation-related pathologies.[85]

More recently, an extensive study carried out by Barnard and co-workers investigated the synthesis and characterisation of several rhenium and technetium tricarbonyl complexes with NHC ligands, suitable for both biological imaging and sensor applications (compounds **39** and **40**, Figure 1.29).[86] The Barnard group reported the successful radiolabelling of one such complex (compound **41**, Figure 1.29) with ^{99m}Tc *via* a Ag(I) transmetallation reaction by treating the ligand precursor with Ag_2O, followed by the addition of $[^{99m}Tc(H_2O)_3(CO)_3]^+$.[87]

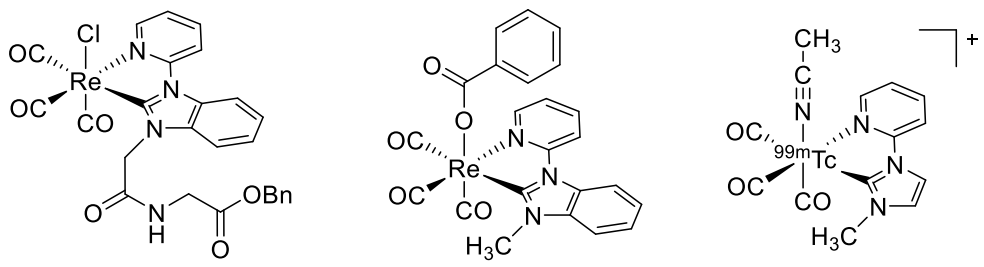

Figure 1.29. Structural representations of a carboxylic acid-functionalised *fac*-[Re(CO)$_3$(N^C)Cl] complex coupled with the benzyl ester-protected glycine (compound **39**), *fac*-[Re(CO)$_3$(N^C)OBn] compound **40** and the ^{99m}Tc-labelled compound **41**.

In order to further enhance the complex stability of rhenium and technetium tricarbonyl complexes, the same group prepared a number of bidentate, *bis*-bidentate and tridentate NHC pro-ligands and their corresponding Re(I) complexes (Figure 1.30).[88] Although these complexes represent building blocks for the development of more biologically relevant metal complexes, mainly due to the poor stability of the bidentate complexes,[89] the tridentate complex **44** was stable in the presence of metal-binding amino acids (L-histidine or L-cysteine) and showed no evidence for displacement of the tridentate NHC ligand.

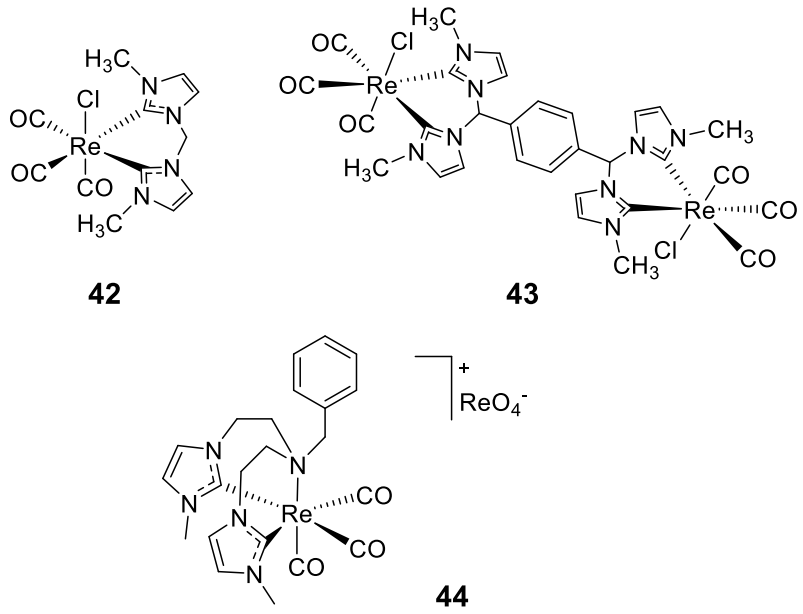

Figure 1.30. Structural representations of the bidentate (compound **42**), *bis*-bidentate (compound **43**) and tridentate (compound **44**) rhenium tricarbonyl complexes developed by Barnard and co-workers.

A study in 2017 published by Simpson and co-workers investigated the anticancer properties of rhenium and ruthenium complexes containing NHC ligands conjugated to the nonsteroidal anti-inflammatory drug (NSAID) indomethacin (compounds **45-a** and **46-a**, Figure 1.31).[90]

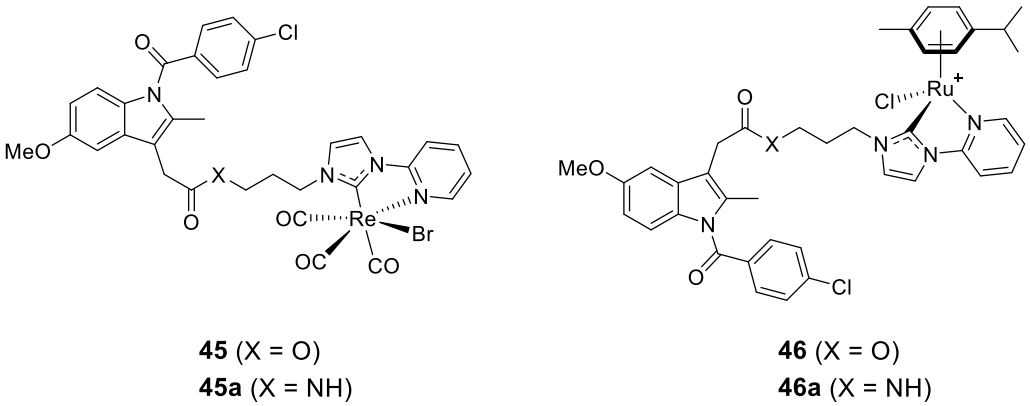

Figure 1.31. Structures of rhenium and ruthenium NHC-indomethacin conjugated complexes **45-a** and **46-a**.

The antitumoral activity of these complexes was probed against a panel of pancreatic cancer cell lines. The ruthenium complexes (compounds **46** and **46a**, Figure 1.31) were found to be inactive against the pancreatic cancer cell lines, while their rhenium analogues demonstrated remarkable antiproliferative activity. Moreover, it was demonstrated that the cytostatic activity, promoted by the metal, was triggered by the arrest of the cell cycle at the G2/M phase, associated with inhibition of the phosphorylation of the Aurora-A kinase gene, which is usually overexpressed in several cancers.[91]

Finally, a study, conducted in 2018 by Luengo *et al*, involved the synthesis and application of the first cationic heterobimetallic complex of the type *fac*-$[Re(CO)_3(NHC)(LAuPPh_3)]^+$ (compound **47** , Figure 1.32). The aim was to couple the valuable emissive properties of the previously described compound **34**,[78] with the antiproliferative activity of gold, so as to generate a multimodal agent suitable for both imaging and therapeutic purposes. Compound **47** exhibited remarkable antiproliferative activity against the A549 lung tumour cell line. Moreover, confocal microscopy experiments showed that **47** was able to penetrate the cellular membrane and localise throughout the cytoplasm (Figure 1.33), further demonstrating the appealing properties of transition metal complexes for the development of multimodal agents suitable for biomedical applications.

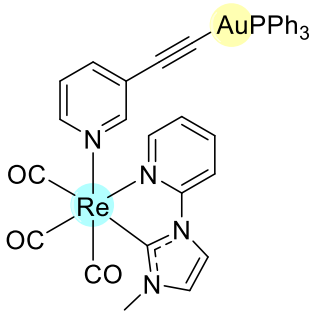

Figure 1.32. Structural representation of the heterobimetallic Re(I)/Au(I) complex **47**.

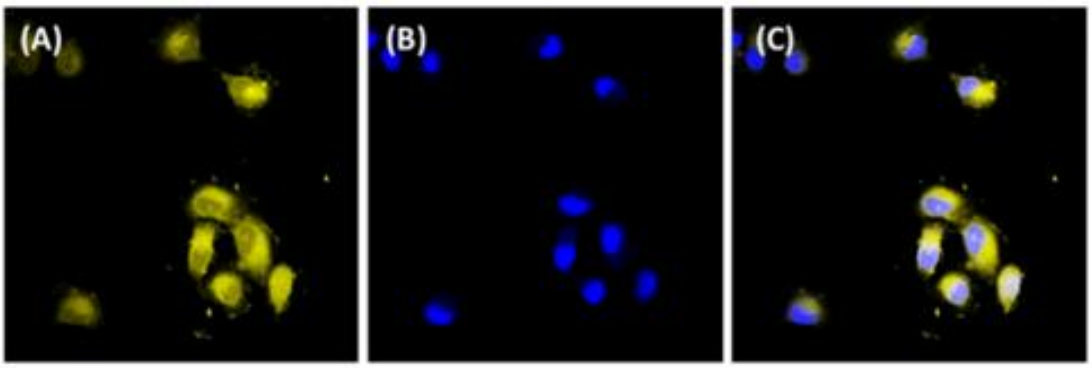

Figure 1.33. Images of compound **47** incubated with A459 cells and Draq5 (a nuclear dye used as an internal standard) at 37 °C for 4 h: (**A**) after irradiation at 405 nm; (**B**) after irradiation at 647 nm; (**C**) superimposed image.

Over the last few years, research on the medical applications of metal NHC complexes has brought us many different ligands and metals. Considering the wide chemical diversity amongst the various complexes described, it is highly unlikely that a unique target for metal NHC complexes exists.

Overall, the possibility to tune the biological activity of both ligands and metals, as well as the useful characteristics of some transition metals to be used as imaging agents, confers this recent class of compounds with exciting possibilities for NHC-metal complexes in medicinal chemistry. One of the main aims of this thesis is to investigate new carbene-based ligands for their capacity to bind transition metals forming new coordination complexes with relevance in biomedical applications, including for the molecular imaging of cancers.

1.2. Molecular imaging of cancer

Molecular imaging is a set of various techniques that allows the *in vivo* characterisation and quantification of biological processes at a cellular level. It exploits chemical tracers as well as intrinsic tissue features in order to obtain "images" that can give crucial information for detection and progression of a disease and evaluation of the treatment.[92] The key features of some of the most important molecular imaging techniques are summarised in Figure 1.34.

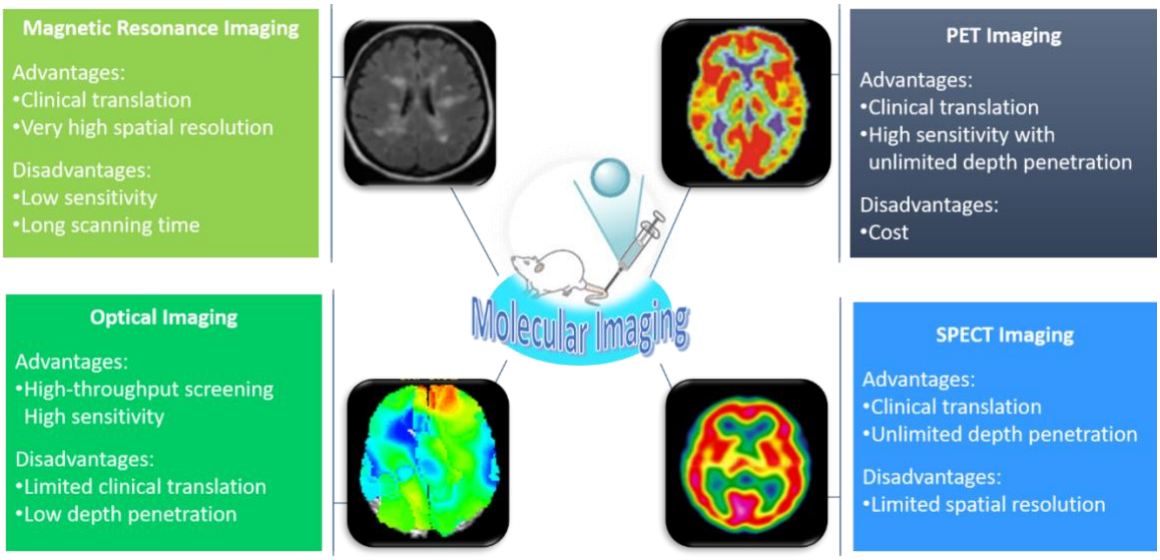

Figure 1.34. A summary of techniques used for molecular imaging.[92]

1.2.1. Magnetic Resonance Imaging (MRI)

Magnetic resonance imaging (MRI) relies on the principles of nuclear magnetic resonance (NMR), a spectroscopic technique that allows chemical and physical information to be obtained regarding the structure of a molecule. MRI produces images based on spatial variations in the phase and frequency of radiofrequencies (RF) being absorbed and emitted by the imaged object.

The human body is composed primarily of water and fat, both rich in hydrogen atoms, which therefore constitutes up to 63% of the human body.[93] The nuclei of hydrogen atoms (protons) are comparable to small magnets, each possessing its own magnetic moment which is randomly oriented. By applying a strong, external magnetic field, the protons assume a non-random alignment, resulting in a measurable magnetic moment in the direction of the external magnetic field. Upon application of RF pulses, it is possible to reconstruct images deriving from the discrepancies in signal from protons in different types of tissue.

The main advantages of MRI over other imaging techniques include a very high spatial resolution, especially due to a superior soft tissue contrast resolution and multiplanar imaging capabilities.[94] Since MRI does not require the use of ionising radiation, this technique is widely used in hospitals and clinics for medical diagnosis, staging of disease and follow-up, without exposing the body to potentially harmful radiation. The main disadvantage of MRI is its very low sensitivity, usually around 10^{-3} mol/L to 10^{-5} mol/L, well below that of other imaging techniques such as PET and SPECT.[95]

The use of contrast agents in MRI allows enhancement of the signal for certain types of tissues, organs or molecules by altering the longitudinal and transverse relaxation time (T1 and T2) of water protons. This is achieved by using paramagnetic metal ions such as gadolinium (Gd^{3+}).[96] The enhanced sensitivity makes it possible to take advantage of the great spatial and temporal resolution of the MRI imaging modality, thus allowing a detailed picture of the biological microenvironment to be acquired at a cellular and molecular level. An example of such an agent is shown below in Figure 1.35: the ferrocene-conjugated complex Gd-DTPA, developed by Kim and co-workers in 2010,[97] which demonstrated high relaxivity as well enhanced thermal and kinetic stability in the target tissue.

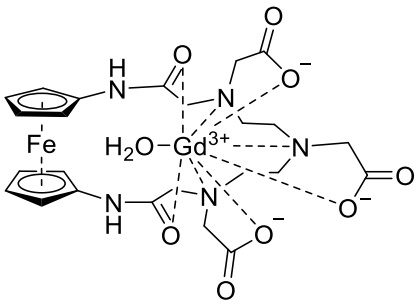

Figure 1.35. Structural representation of the ferrocene-conjugated Gd-DTPA, used as MRI contrast agent. Adapted from citation[97]

1.2.2. Positron Emission Tomography (PET)

Positron emission tomography is a technique that exploits compounds (drugs or biomolecules) attached to a positron emitting radioisotope (Table 1.1). The antiparticle generated undergoes an annihilation process with an electron from a nearby molecule, thus producing two γ-rays that move in opposite direction. The event is detected, and a 3D image of the tracer concentration is obtained by software reconstruction.[98]

Table 1.1. Most common radioisotopes used in PET and SPECT. The average energy of the positron (β^+) is given along with the percentage of decays in which the β^+ is emitted. The energy of γ-rays that occur in more than 1% of decays is given along with the percentage of decays in which that γ-ray is emitted.[99]

Isotope	Half-life	β^+ Energy (MeV)	γ Energy (MeV)
^{11}C	20.4 min	0.385 (99.8%)	
^{13}N	9.97 min	0.492 (99.8%)	
^{15}O	122 s	0.735 (99.9%)	
^{18}F	110 min	0.250 (100%)	
^{38}K	7.64 min	1.216 (99.3%)	2.167 (99.8%)
^{62}Cu	9.74 min	1.315 (97.6%)	
^{64}Cu	12.7 h	0.278 (17.9%)	
^{68}Ga	68.1 h	0.836 (8.79%) 0.352 (1.12%)	1.077 (3.0%)
^{82}Rb	75 s	1.523 (83.3%) 1.157 (10.2%)	0.776 (13.4%)
^{124}I	4.18 d	0.686 (11.3%) 0.974 (11.3%)	1.691 (10.4%), 7.228 (10.0%), 1.509 (3.0%), 1.376 (1.7%), 1.325 (1.43%)

In order to obtain the best outcome from PET imaging, the choice of the radiotracer is crucial. In recent years, many radiolabelled compounds have been synthesised in order to improve their localisation and the detection of cancers.[100-102] The most commonly used radiotracer for PET imaging is ^{18}F-fluorodeoxyglucose (^{18}F-FDG - Figure 1.36). This radiolabelled analogue of glucose was developed as a tracer selective for high-glucose-utilising cells such as brain, kidney and cancer cells. In the context of prostate cancer, ^{18}F-FDG use is generally limited to the detection of primary forms of this disease because of the small size and slow growth rate of the prostate gland. However, ^{18}F-FDG may be used for the detection of hidden metastatic lesions in patients with biochemical recurrence (a state characterised by an increasing level of prostate-specific antigen), and also the evaluation of the treatment response in advanced prostate cancer.[103]

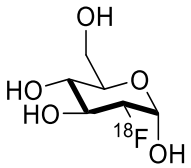

Figure 1.36. Structural representation of ^{18}F-FDG.

Another characteristic shared by many types of tumour cells is increased lipogenesis followed by abnormal cellular membrane synthesis. ^{11}C-acetate, ^{11}C-choline and ^{18}F-fluorocholine have been synthesised in order to target phospholipid biogenesis.[104] Acetate is incorporated in the synthesis of fatty acids by fatty acid synthetase, which is found to be overexpressed in several malignancies.[105] ^{11}C-acetate may therefore be useful in detecting lymphatic metastases and in the localisation of tumour recurrences. Choline is transported into the cells via its dedicated transporter and it is used as a building block for the biosynthesis of phosphatidylcholine (a component of the cellular membrane) through the action of choline kinase, which is upregulated in prostate cancer cells.[105] Various studies have reported that choline-based radiotracers may be exploited for the detection of metastatic diseases in patients with biochemical relapse who are subject to increasing prostate-specific antigen (PSA) levels (Figure 1.38).[106-108]

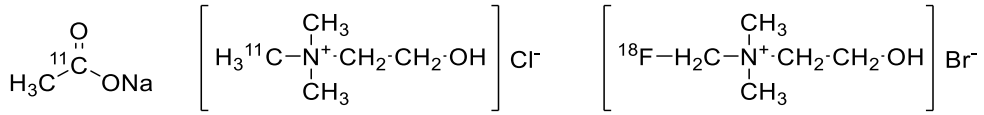

48 **49** **50**

Figure 1.37. Structural representations of ^{11}C-acetate (**48**), ^{11}C-choline (**49**) and ^{18}F-fluorocholine (**50**).

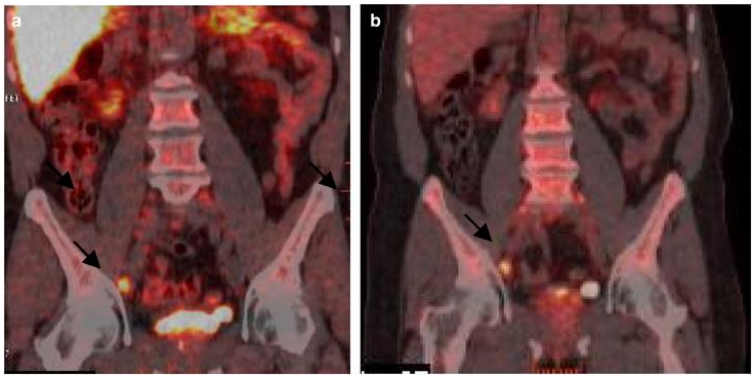

Figure 1.38. Instance of a PET-positive pelvic nodal area in a patient with biochemical relapse following prostate radiotherapy and androgen ablation therapy. (**a**) PET/CT scan with ^{18}F-FDG. (**b**) PET/CT scan with ^{18}F-choline.[109]

Among many upregulated pathways in prostate cancer cells, the overexpression of various amino acid transport systems are emerging as suitable targets for PET imaging. *Anti*-1-amino-3-^{18}F-fluorocyclobutane-1-carboxylic acid (*anti*-^{18}F-FACBC, Figure 1.39) is a synthetic amino acid analogue that accumulates in prostate cancer cells following the overexpression of the ACS (Alanine, Cysteine & Serine) transport system.[110] A study from Nanni and co-workers proposed that *anti*-^{18}F-FACBC may be more efficient than ^{11}C-choline for localisation of metastatic recurrences.[111]

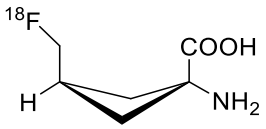

Figure 1.39. Structural representation of *anti*-^{18}F-FACBC.

Surface receptors that are generally upregulated in cancer cells are emerging as attractive targets for therapy and diagnosis. For example, various Prostate-Specific Membrane Antigen (PSMA)-based radiotracers have been developed, including peptidomimetic PSMA inhibitors and radiolabelled antibodies.[112] Promising derivatives include the bombesin-based ligand ^{68}Ga-DOTA-CHCO-Gly-4-aminobenzyl-Gln-Trp-Ala-Val-Gly-His-Leu-Met-NH_2 **51** that binds to the overexpressed Gastrin-Releasing Peptide (GRP) receptor, the ^{89}Zr-5A10 monoclonal antibody **52** that targets free Prostate-Specific Antigen (PSA) and the 1-(2'-deoxy-2'-fluoro-b-D-arabinofuranosyl)thymidine **53**, specific for thymidine kinase, which was developed for assessing cellular proliferation and as a cellular stress marker.[113] All these recent approaches are currently under investigation in the preclinical stages for the molecular imaging of prostate cancer with PET.

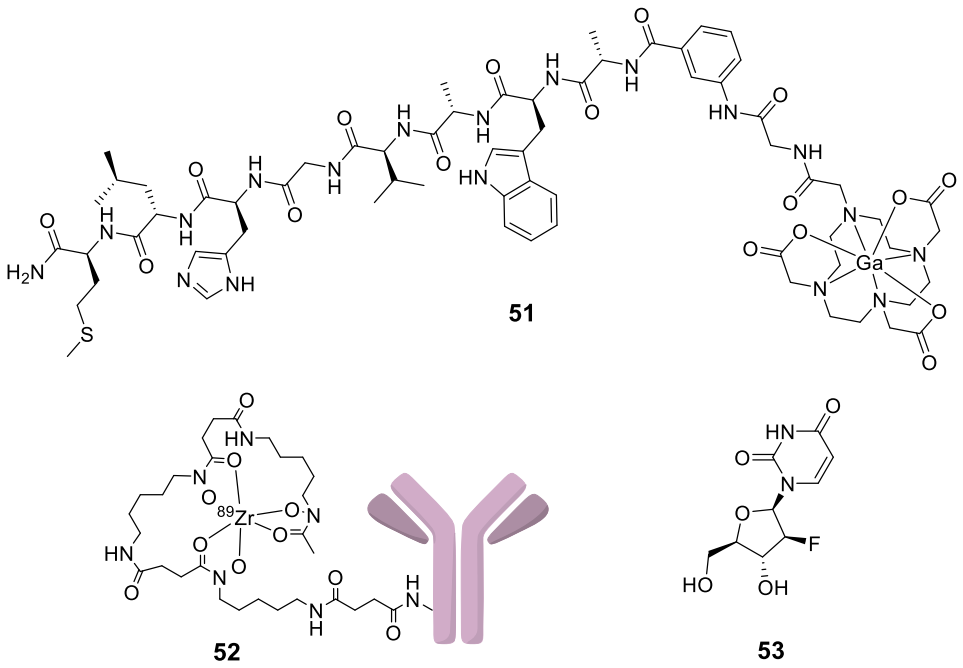

Figure 1.40. Structural representations of ^{68}Ga-DOTA-CHCO-Gly-4-aminobenzyl bombesin analogue (**51**), ^{89}Zr-5A10 monoclonal antibody (**52**), and 1-(2'-deoxy-2'-fluoro-b-D-arabinofuranosyl) thymidine (**53**).

1.2.3. Single-Photon Emission Computed Tomography (SPECT)

In the same manner as PET, SPECT imaging makes use of a radioisotope that emits one or more γ-rays of characteristic energies which are directly measured by an instrument.[114] The advantages of this technique, compared to PET, are lower cost, thanks to the longer half-lives of the radioisotopes used (*e.g.* $t_{1/2}$ ^{99m}Tc = 6 hours), and the possibility of using different isotopes in the same study (Table 1.1). In contrast, SPECT imaging suffers from lower spatial resolution and the use of heavier isotopes may alter the biochemical properties of the labelled compound.

In clinical practice, SPECT has been used to detect bone metastases in patients with advanced prostate cancer. Various radiolabelled phosphonates (for example the ^{99m}Tc-diphosphonate represented in Figure 1.41) have been developed and used in diagnosis.[115, 116]

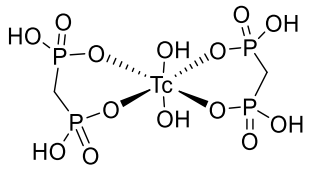

Figure 1.41. Structural representation of ^{99m}Tc-diphosphonate.

1.2.4. Optical imaging

Optical imaging (OI) is a non-invasive imaging technique that allows one to follow the biodistribution of fluorescent molecules in living organisms.[117] OI makes use of an external excitation light source (usually a laser) that excites a selected fluorescent probe which emits light at a longer wavelength of lower energy. This type of imaging is particularly useful for monitoring the targeted accumulation of fluorophore-labelled drugs thanks to its high sensitivity and resolution, as well as the possibility to perform multimodal imaging by coupling OI with other imaging techniques, such as computed tomography and PET. Lack of deep tissue penetration, auto-fluorescence and diffusive scattering phenomena and the lack of anatomical information are the main limitation of OI.

While the majority of optical imaging applications are in preclinical research (using techniques such as confocal microscopy), it is possible to exploit OI for clinical purposes.[118] A paper published by Dam *et al* reported a methodology to exploit the near-infrared fluorescent dye derivative named Folate-FITC (compound **54** shown in Figure 1.42), which consists of fluorescein coupled with a targeting molecule specific for the folate receptor-α (overexpressed

in ovarian cancer cells). In this pilot study, the folate-FITC in an intravenously injected formulation enhances the fluorescence imaging over the time course from 2 to 8 h after injection (Figure 1.42). This could be used to help surgeons to detect and remove malignant lesions while keeping as much healthy tissue as possible.[119]

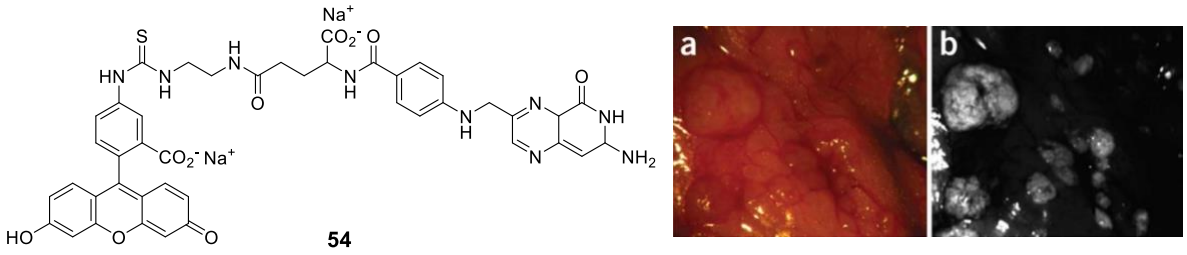

Figure 1.42. Left: Structural representation of Folate-FITC (**54**). Right: Colour image (**a**) of a representative area in the abdominal cavity (**b**) with the corresponding tumour-specific fluorescence image.[119]

As mentioned before, OI displays excellent sensitivity, and it is particularly suitable for non-invasive imaging of drug localisation in superficial tumours. Unfortunately, due to the excessive light scattering effect of deep tissues, such a technique is usually restricted to superficial tissues where the light can easily penetrate.

Chen and co-workers[120] reported a near infrared fluorescence (NIRF) labelled high-density lipoprotein (HDL) nanoparticle **55** to assess both active specific targeting to blood vessels in tumours and passive accumulation (due to the enhanced permeability and retention effect). The results showed that nanoparticles functionalised with a specific targeting system accumulate immediately after administration, while passive targeted accumulation of a nonspecific probe is the main event over a longer time period. This study gives an insight into how OI can be used for the kinetic assessment of drugs accumulation in tumours.

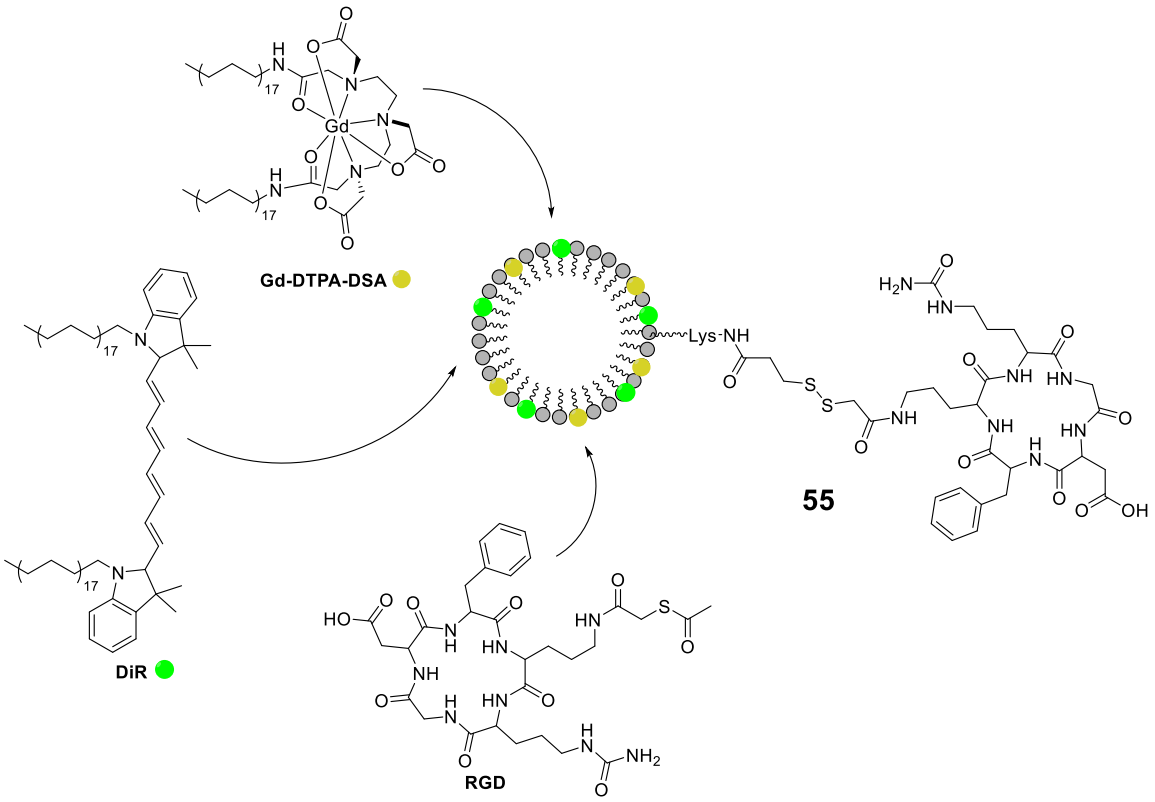

Figure 1.43. Structural representation of the functionalised nanoparticle **55** and its constituents: Gadolinium diethylenetriaminepentaacetate-di(stearylamide) (Gd-DTPA-DSA, yellow dot) as MRI contrast agent, 1,1'-dioctadecyl-3,3,3',3'-tetramethylindotricarbocyanine iodide (DiR, green dot) as NIR dye and the cyclic RGD-containing pentapeptide (c(RGDf(S-acetylthioacetyl)K) (RGD) as specific targeting agent.

The possibility to exploit OI for detecting alterations in the tumour environment has been reported by Kim *et al.* in 2011[121] by assessing the accumulation of a hydrocyanine-labelled nanoparticle (Hydrocyanine-NC) in subcutaneous mice xenografts. The principle behind this study is that tumours are often involved in inflammatory and immune responses that are characterised by an increase of reactive oxygen species (ROS). In the presence of such an oxidative environment, the hydrocyanine moiety undergoes an oxidation reaction that produces a fluorescent cyanine dye (see Figure 1.44). Strong fluorescence intensity could be developed from hydrocyanine NC in a dose-dependent manner with ROS, and the nanoparticles showed strong intracellular fluorescence after treatment of macrophage cells (RAW 264.7) with the cytotoxic agent lipopolysaccharide (LPS), whereas in non-treated cells no fluorescence image was obtained (Figure 1.45).

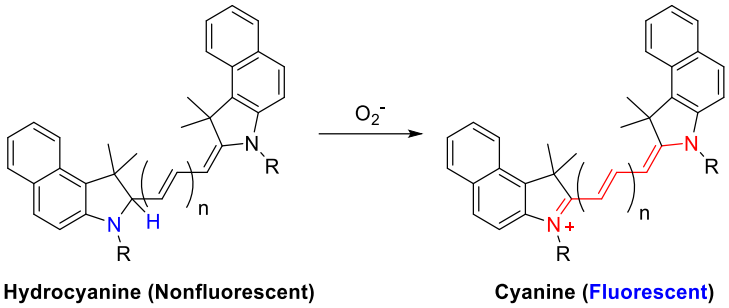

Figure 1.44. The oxidation of a hydrocyanine to a fluorescent derivative due to the presence of intracellular ROS.

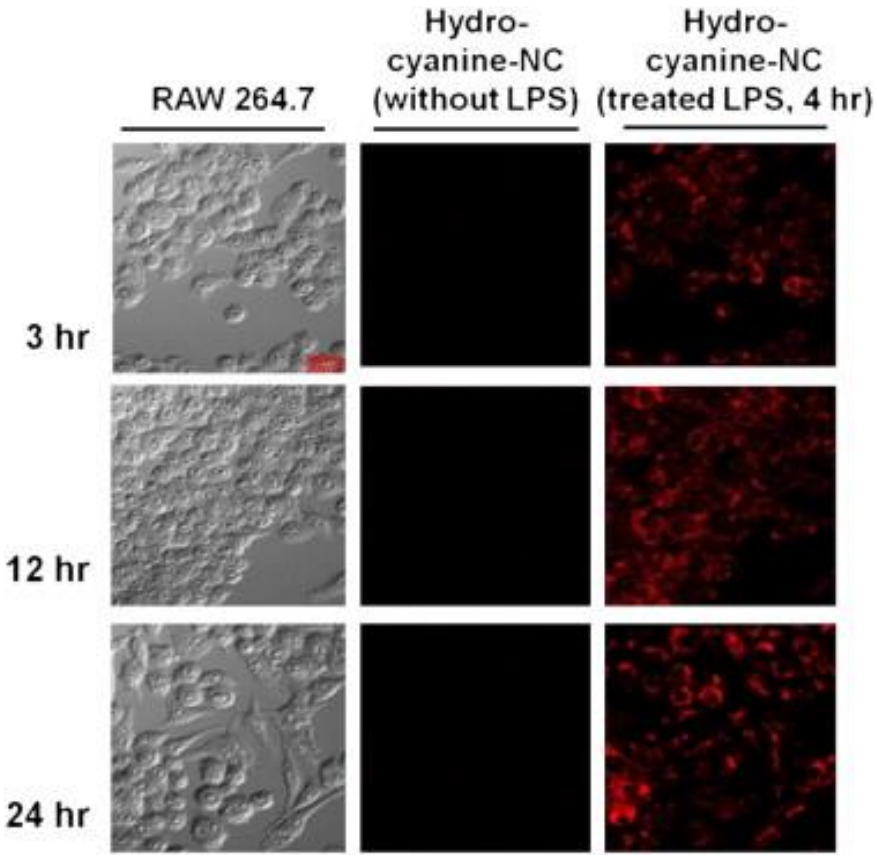

Figure 1.45. Confocal microscopy images of cellular uptake of Hydrocyanine-NC in RAW 264.7 macrophage cells after 3 h, 12 h, and 24 h of LPS stimulation at 500 ng/mL.[121]

1.3. Hypoxia and cancer

Hypoxia is a microenvironment condition characterised by decreased oxygen content at the cellular level. This particular condition is present in the microenvironment of many tumours, due to an imbalance between the quantity of oxygen available and its enhanced consumption rate by cancer cells.[122] Another cause is due to the physiological characteristics of the tumour microvasculature which is often undeveloped, thus limiting oxygen diffusion in deep tissues.

Prolonged hypoxic states in tumour cells produce a marked decrease in protein synthesis, which results in a reduced cell proliferation and cell death: these phenomena are generally considered a way for the tumour to reduce its overall energy consumption.[123] The inhibition of protein translation is achieved through two distinct pathways:

I) Unfolded protein response (UPR) that leads to the inhibition of mRNA translation in the endoplasmic reticulum;
II) Disruption of the mRNA capping complex (EIF4F) that causes the loss of recruitment of translatable mRNA.[124]

Another important consequence of tumour hypoxia is the increase in expression of the hypoxia-inducible factor-1 (HIF-1), an important element in tumour progression and resistance to radio- and chemotherapy.[125] HIF-1 is a transcription factor composed of two subunits: a hypoxia-regulated α subunit and an oxygen-dependent β subunit, the latter binding to DNA through hypoxia-response elements (HREs) responsible for controlled target gene transcription. The hypoxia-sensitive subunit α is mainly regulated through a degradation pathway that involves various members of the prolyl hydroxylase family of enzymes. These enzymes mediate the hydroxylation of proline residues in the oxygen-dependent degradation domain (ODD) of HIF-1α. This modification is then recognised by the von Hippel-Lindau complex that ensures HIF-1α degradation via proteosomal activity. Thus, under normoxia conditions HIF-1α levels are kept low. However, deficiencies of oxygen lead to prolyl hydroxylase malfunction, producing a decrease of proteosomal degradation and a consequent increase of HIF-1α levels. HIF-1α accumulation leads to the formation of the HIF-1 heterodimer by binding to the β subunit: the resulting enzyme is then able to upregulate several genes to promote survival in low-oxygen conditions (Figure 1.46).[126]

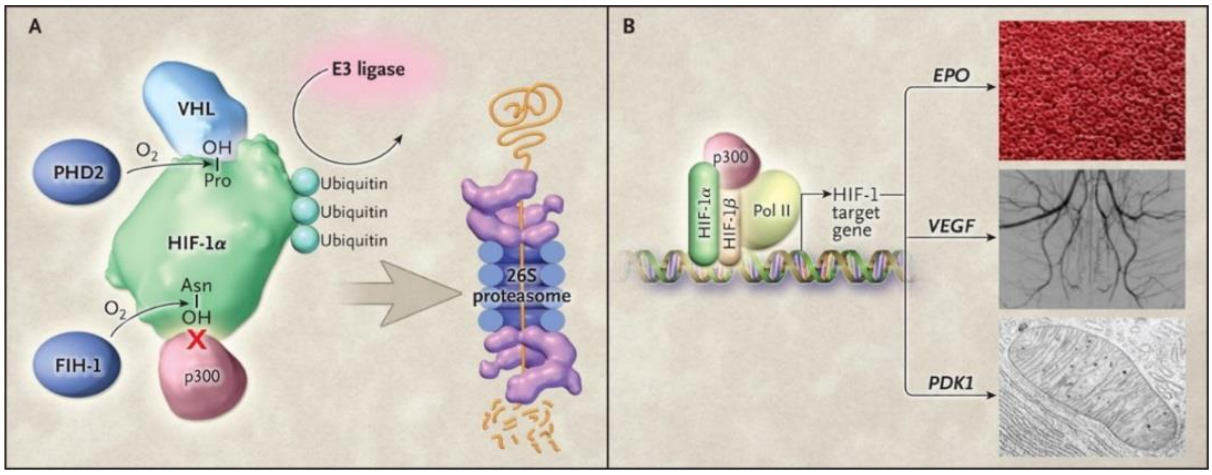

Figure 1.46. HIF-1α inhibition pathway in normoxic conditions (**A**) and response to hypoxic condition (**B**).[126]

HIF-1 activation plays an important role in sustaining cell growth by stimulating energy production in cancer cells via aerobic glycolysis. This phenomenon, known as the Warburg effect, is largely dependent on HIF-1 and induces the expression of various enzymes and transporters responsible for internalisation and degradation of extracellular glucose. HIF-1 promotes the activation of pyruvate dehydrogenase kinase 1 (PDK1) and MAX-interactor 1 (MXI1), causing a steady reduction of oxidative phosphorylation in mitochondria. Both effects ultimately lead to a reduction of oxygen consumption in cancer cells.[127] HIF-1 also promotes the expression of vascular endothelial growth factor (VEGF) and erythropoietin (EPO), increasing angiogenesis and resupply of oxygenated blood to the hypoxic tumour region.[128]

1.3.1. Imaging cellular hypoxia in cancer

The capacity to determine the extent of tumour hypoxia in solid cancers is vital for the evaluation of an anti-tumour therapy, since cellular hypoxia plays a pivotal role in resistance to therapy, increased aggressiveness and metastaticity.[129-131]

Cellular hypoxia cannot be predicted from biopsies or by conventional imaging methods. Direct measurements of hypoxia tend to be invasive procedures (often undertaken at the time of surgery) and are subject to sampling errors. Instead, non-invasive methods such as PET may offer a better solution while using hypoxia-specific tracers.[132]

An imaging method for *in vivo* measurement of hypoxia was developed by radiolabelling various nitroimidazoles. These compounds are known to undergo chemical reduction at low oxygen levels,[133] and the most extensively studied nitroimidazole for *in vivo* PET imaging is [^{18}F]fluoromisonidazole (^{18}F-FMISO).[134, 135] The main advantage of ^{18}F-FMISO is due to the fact that its reduction is directly affected by tumour oxygenation, however, ^{18}F-FMISO imaging is limited by the relatively low tissue uptake of the compound *in vivo*. Furthermore, the slow cellular washout of this tracer results in low-count-rate studies and images of limited quality.[136]

The development of suitable alternatives to ^{18}F-FMISO has brought copper(II)-diacetyl-*bis*(N^4-methylthiosemicarbazone), or Cu-ATSM, a metal complex that is able to overcome many of the limitations of ^{18}F-FMISO. Cu-ATSM shows rapid delineation of tumour hypoxia (< 1 hour) and high tumour-to-background tissue ratios, greatly improving the imaging quality that can be achieved.[137]

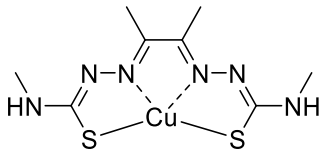

Figure 1.47. Structural representation of Cu(II)-diacetyl-bis(N^4-methylthiosemicarbazone), or Cu-ATSM.

The anti-tumour properties of dithiosemicarbazones were first identified in the 1960s, followed by the discovery of an enhancement of this capability by complexation with copper(II).[138] Compared to other established radionuclides, the use of copper presents several advantages: copper chemistry is restricted to two main oxidation states (I and II) and its redox properties are well known. Furthermore, the relatively simple coordination chemistry and the increasing

availability of positron-emitting isotopes of copper (^{60}Cu, ^{61}Cu, ^{62}Cu and ^{64}Cu) makes this element an attractive option on which to base new imaging agents.

The first report of the hypoxia selectivity of Cu-ATSM was in an isolated rat heart model of ischemia in 1997. The proposed mechanism of action of Cu-ATSM as a hypoxia tracer relied on its behaviour as a copper transporter in cells: the complex crosses the membrane due to its high lipophilicity. Once inside, the hypoxic condition favours the reduction of Cu(II) to Cu(I), thus determining its intracellular accumulation.[139]

Cu-ATSM was first used in clinical trials in 2000,[140] and further clinical studies have provided useful information in patients with lung,[140, 141] cervical[142, 143] and rectal[144] cancers. Since then, several derived bis(thiosemicarbazonato) complexes, designed with the purpose of serving as multimodal imaging agents, have been used in pre-clinical research for PET, SPECT and confocal microscopy.[145-147] Furthermore, given the interest that theranostics are currently generating in the scientific community, bis(thiosemicarbazonato) metal complexes will keep attracting many research groups aiming to discover new and more efficient hypoxia-selective anti-tumour agents.

1.4. Prostate Cancer

With more than 47,600 estimated new cases in the UK in 2016, Prostate Cancer (PCa) is one of the most commonly diagnosed types of cancer in men, and the second most common cancer overall. In 2016, around 11,600 men died from prostate cancer in the UK, which means 31 people die every day from this common form of cancer.[148] If detected in its first stages, the localised disease can be effectively cured by radical surgery or radiation therapy (stages 1-2 in Figure 1.48). On the other hand, locally advanced and metastatic forms (stages 3-4, Figure 1.48) can be treated with Androgen Suppression Therapy (AST). AST is capable of inducing tumour regression for a period of two years, but unfortunately this approach is not sufficient to prolong the survival rate.[149] PCa gradually progresses to a castration-resistant state, which presently remains incurable. Thus, the lack of treatments for this type of cancer have to be addressed with novel targeted therapies.[150]

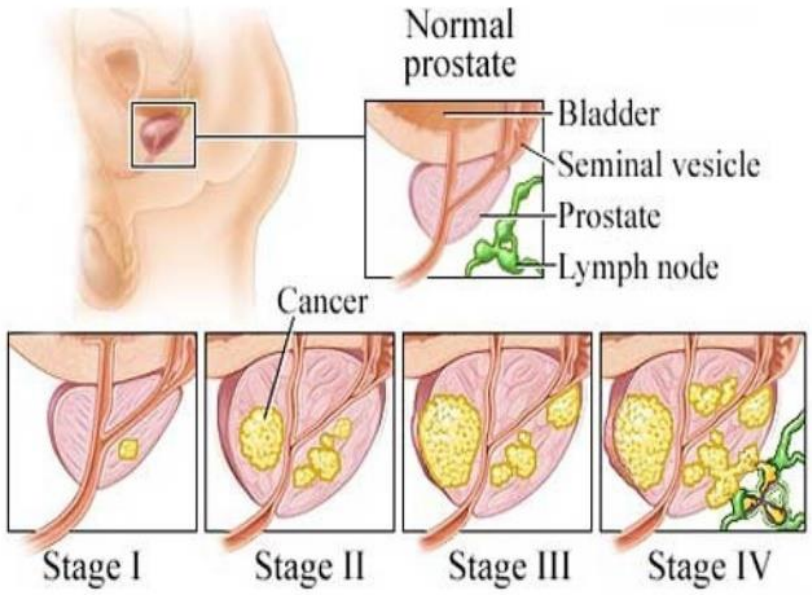

Figure 1.48. Anatomy of the prostate and different stages of PCa. Stages 1-2 correspond to early stages of PCa in which the malignancy is localised only within the prostate gland. Stage 3 represents an advanced form that is beginning to spread outside the prostate gland. The final, stage 4, is generally incurable due to the presence of metastasis, spreading into the lymph nodes.[151]

The development of new therapies follows an increased understanding of the molecular mechanisms that drive the development of PCa, its progression, and resistance to the different therapies.[152] Given the molecular and clinical heterogeneity displayed by castration-resistant PCa among patients, suitable therapeutic approaches are likely to require personalised therapy with various targeting agents and a combination of treatments.[153-155] In this context, there is

various evidence that molecular therapeutics developed in the last few years (for example antiangiogenic agents, proteasome and growth factor receptor inhibitors) may selectively hinder certain biochemical pathways activated in tumours as compared to conventional chemotherapeutic agents. It is crucial to consider also pharmacokinetic issues, such as poor distribution through the circulatory system, rapid clearance, scarce accessibility to the tumour area and excessive toxicity.[150]

The recent emerging branch of nanomedicine, based on the use of tumour-targeted nanotherapeutics, which are drugs of a size comparable to one hundred thousandth of a human hair, may represent a promising approach to overcome such challenges.[156] The main characteristic of tumour-specific nanotherapeutics is to be capable to deliver the active drug molecules preferably to the tumour site rather than to the normal tissues, thus assuring improved antitumoral activity and reduced toxicity towards healthy tissues.[157] The targeted delivery of a bioactive molecule to the tumour site is possible through either active or passive targeting.[156] Passive targeting is based on the principle of the enhanced permeation and retention (EPR) effect and makes use of both the locally increased vascular permeability in the tumour area and the reduced lymphatic drainage directed to the tumour tissue, thus accumulating the drugs in the desired site. Active targeting bases its actions on ligands bound to delivery systems that act as homing agents and which interact with specific surface receptors widely expressed on the target cells, thus ensuring uptake (*via* receptor-mediated endocytosis) and achieving the specific delivery of the therapeutic agent.

For optimum drug delivery, the choice of specific targeting ligand is crucial to achieve successful therapy. Simple moieties like growth factors and cytokines are usually advantageous in terms of production, handling and availability. An example is the widely used folate system that targets the related folate receptor, overexpressed in a wide range of tumours.[158] Alternatively, antibodies are attractive targeting systems due to their specificity and stability towards biological systems.[159] Another class of ligands suitable for targeting are peptides: these molecules are characterised by their relatively small size, low immunogenicity and high stability, and are fairly easy to manufacture.[160]

1.4.1. Targeting Prostate Cancer

Following an increased understanding of the molecular pathways responsible for tumorigenesis in PCa, a variety of suitable targets (*e.g.* receptors, antigens) are emerging. These targets are generally overexpressed on the outer membrane of PCa cells (Figure 1.49) and could be used to improve the delivery of the treatment. A brief description of these targets is presented in Table 1.2 below.

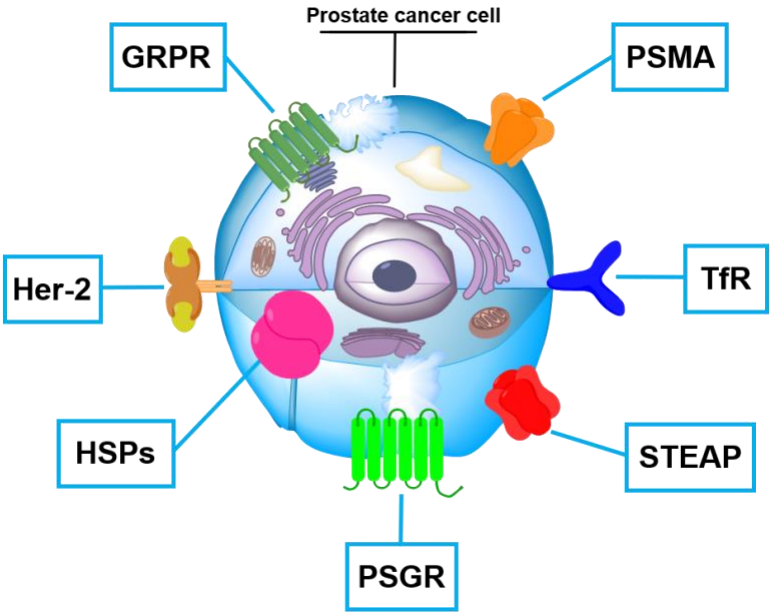

Figure 1.49. Pictorial representation of the possible targets on a prostate cancer cell.

Table 1.2. A summary of possible targets for targeted delivery of therapeutics in PCa.

Target	Role	Tumour involved
Prostate Specific Membrane Antigen (PSMA)	metallopeptidase	prostate
Transferrin Receptor (TfR)	iron uptake, cell growth	prostate, breast, pancreas
Six-Transmembrane Epithelial Antigen of the Prostate (STEAP)	iron homeostasis	prostate, bladder, lung, colon, ovary, Ewing's sarcoma
Prostate Specific G-Protein Coupled Receptor (PSGR)	negative regulation of cell proliferation	prostate
Gastrin-Releasing Peptide Receptor (GRPR)	cell growth	prostate, breast, lung
Human Epidermal Growth Factor Receptor 2 (Her-2)	cell growth, survival, adhesion, migration, cell differentiation	prostate, breast, pancreas, gastric
Heat Shock Proteins (HSPs)	cell cytoprotection, survival	prostate, breast, colon, lung, ovary, pancreas

Prostate Specific Membrane Antigen (PSMA)

The Prostate Specific Membrane Antigen is a type II integral membrane glycoprotein (a transmembrane protein that displays its N-terminal residue towards the cytosol) which is currently used as a marker for PCa cells and therapy progression. PSMA overexpression is correlated with all types of prostate tumours, especially metastatic and castration-resistant forms.[161] This characteristic, coupled with its high internalisation rate, makes PSMA an attractive target not only for diagnosis, but also for therapeutic approaches.[162-165]

A paper published by Banerjee and co-workers in 2014 reported the synthesis and application of a series of ^{64}Cu-labelled inhibitors for PSMA, based on a lysine-glutamate urea scaffold and a variety of macrocyclic chelators.[166] Their most potent ligand comprised the CB-TE2A chelator for complexation of ^{64}Cu (compound **56**, Figure 1.50), which demonstrated improved biodistribution with rapid clearance from healthy tissues, resulting in significantly improved image contrast.[167]

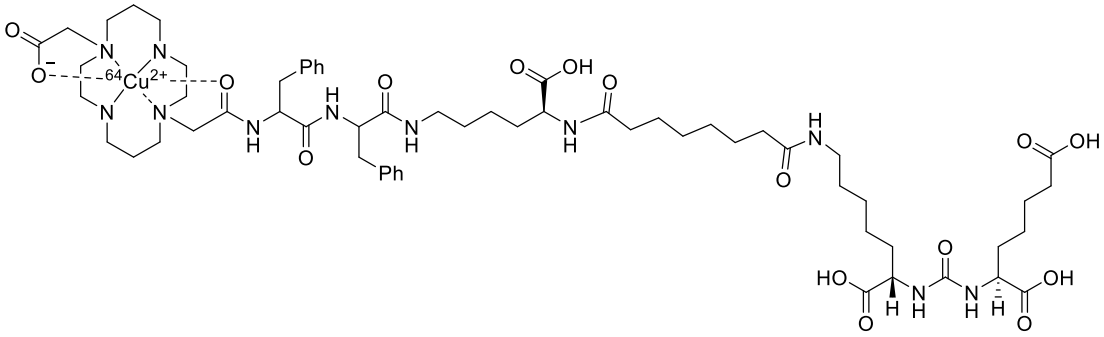

Figure 1.50. Structural representation of the urea-based, ^{64}Cu-labelled, PSMA-targeted radiotracer **56**.

Transferrin Receptor (TfR)

The transferrin receptor (TfR) is a membrane transport glycoprotein that regulates iron homeostasis and is widely expressed in rapidly proliferating cells.[168, 169] As a target for therapies, TfR shows two important characteristics:

I) TfR is overexpressed (2 to 10-fold) in PCa cells,

II) The clathrin-mediated endocytosis, responsible for the internalization of this receptor, may be exploited for selective delivery of transferrin-conjugated systems.[170]

An example of how TfR could be exploited in the context of molecular imaging comes from the work of Zhao *et al* published in 2015.[171] The group successfully synthesised transferrin (Tf) stabilised gold nanoclusters (Tf-Au NCs, Figure 1.51) by adapting a procedure previously outlined by Yan and co-workers.[172, 173] The obtained Tf-Au NCs were successfully applied in the near-infrared (NIR) targeted fluorescence imaging of PCa-overexpressing Tf receptors *in vivo*, demonstrating a remarkable ability for these probes to detect early-stage small tumours in mice.

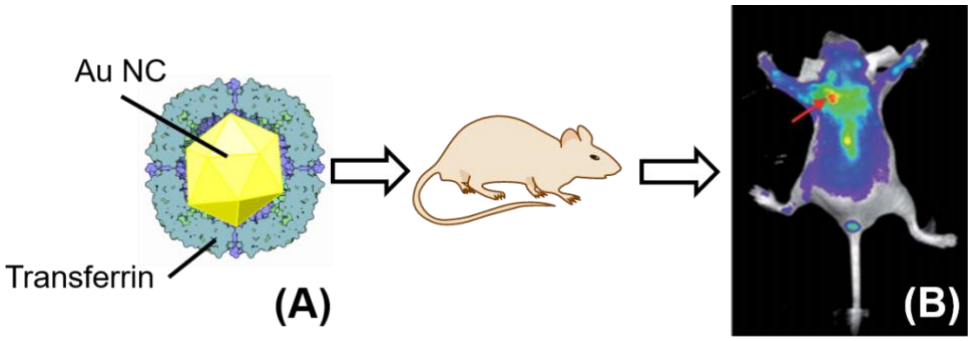

Figure 1.51. (**A**) Pictorial representation of a Tf-Au NC prepared by Zhao *et al.* (**B**) In vivo NIR fluorescence imaging of PC3 tumour xenograft mice after 2 hours from the injection of Tf-Au NCs (8 µg Au per mouse).[171]

Six-Transmembrane Epithelial Antigen of the Prostate (STEAP)

The six-transmembrane epithelial antigen of the prostate (STEAP) is a metalloreductase significantly expressed in various tumours.[174, 175] Challita-Eid and co-workers observed that STEAP is particularly overexpressed in prostate metastases to bone and lymph node. *In vitro* data from the same group also suggested that STEAP may be involved in intercellular communication between cancer cells.[176] Thus, STEAP could represent a useful tool for targeting advanced PCa.

In a study published in 2015, Doran and co-workers developed a formulation designated MSTP2109A (Figure 1.52), which consists of an antibody-^{89}Zr radiotracer conjugate that recognizes STEAP1 extracellular epitopes.[177] The radiolabelled complex exhibited a significant percentage of immunoreactivity for human STEAP1 and it was also capable of accumulating at the tumour site and accurately detecting metastatic PCa cells.[178]

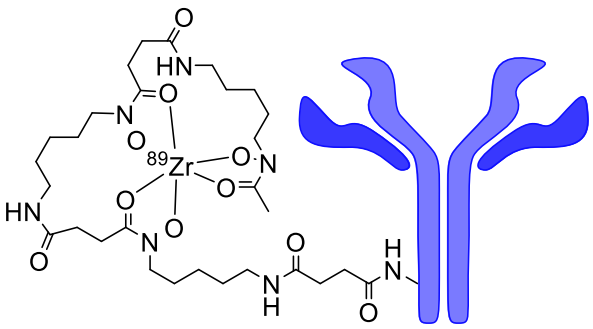

Figure 1.52. Pictorial representation of the ^{89}Zr-antibody complex MSTP2109A.

Prostate Specific G-Protein Coupled Receptor (PSGR)

The prostate-specific G-protein coupled receptor (PSGR) is a 7-transmembrane domain receptor, specific for prostate tissue, part of the bigger family of G protein odorant receptors.[179] Its overexpression has been observed in prostate intraepithelial neoplasia (PIN) and in prostate cancer, implying that PSGR may be crucial for the development and progression of the tumour.[180-182]

Heat Shock Proteins (HSPs)

The heat shock proteins (HSPs) are a large family of highly conserved proteins whose expression is triggered by a wide range of physiological and environmental insults.[183] HSPs are crucial for cell cytroprotection and survival: these proteins I) act as catalysts for proper protein folding, avoiding protein aggregation and proteosomal activation; II) interfere with the apoptotic machinery by inactivation of the caspase pathway. These two characteristics are also exploited by cancer cell for their survival: high levels of expression of HSP90, HSP70, GRP78 and HSP27 are found in cancer cells resistant to chemotherapy.[184] Numerous therapeutic approaches involving the targeting of HSPs have been explored,[184-186] including the possibility to develop vaccines: HSPs have been found expressed on the cell surface of tumour cells, where they act as modulators of the immune system.[187, 188]

Human Epidermal Growth Factor Receptor 2 (Her-2)

The human epidermal growth factor receptor 2 (Her-2) is a transmembrane tyrosine kinase receptor, part of the HerB family, which is found to be overexpressed in numerous malignancies.[189, 190] It positively regulates cell growth, survival, adhesion, migration and cell differentiation.[150] The Her-2 signalling pathway stimulates the activation of the androgen receptor (AR) pathway, thus influencing the progression of aggressive prostate cancer.[191] Clinical attempts to exploit Her-2 as a target have led to the development of the Her-2 monoclonal antibody, trastuzumab, for the treatment of breast cancer.[192, 193] Therapeutic approaches for the treatment of hormone-refractory prostate cancer have shown that targeting HerB kinases indeed has beneficial effects. However, a study conducted by Lara and co-workers observed that upregulation of Her-2 occurred only in less than one fifth of the patients,

thus hindering the clinical applications.[194] An example of how the targeting of Her-2 could be exploited in therapy was published by Lin and co-workers in 2013.[195] The group made use of a ^{188}Re labelled chelator SOCTA (succinimidyl 3,6-diaza-5-oxo-3-[2-(triphenylmethyl)thioethyl]-8-[(triphenylmethyl)thio]octanoate) that was conjugated to trastuzumab (compound **57**, Figure 1.53). As noted above, trastuzumab is a humanized anti-Her2 monoclonal antibody widely used for the treatment of patients with Her2-overexpressing breast cancer.[196] Treatment of DU145 (an androgen receptor-negative prostate cancer cell line) with **57** resulted in a reduction in proliferation of DU145 cells in a dose- and time-dependent manner. These promising results suggest that combined radio- and immuno-therapy could prove beneficial to treat patients with advanced tumours.

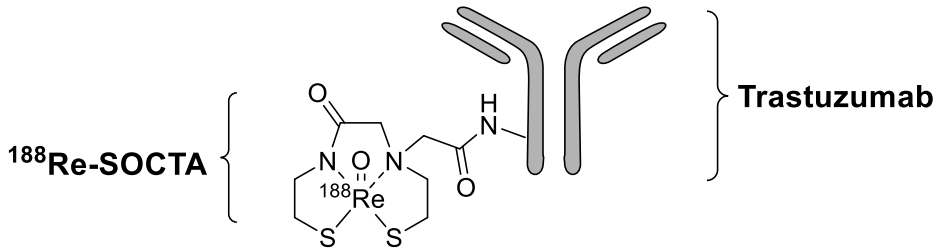

Figure 1.53. Pictorial representation of the ^{188}Re-SOCTA – Trastuzumab conjugated compound **57**.

Gastrin-Releasing Peptide Receptor (GRPR)

The gastrin-releasing peptide receptor (GRPR) is another 7-transmembrane G-protein coupled receptor whose main ligands are the gastrin-releasing peptide (GRP) and bombesin (Figure 1.54). While negative in normal conditions, high levels of GRPR expression are found in PCa, as well as in breast cancer and small-cell lung carcinoma.[197-199]

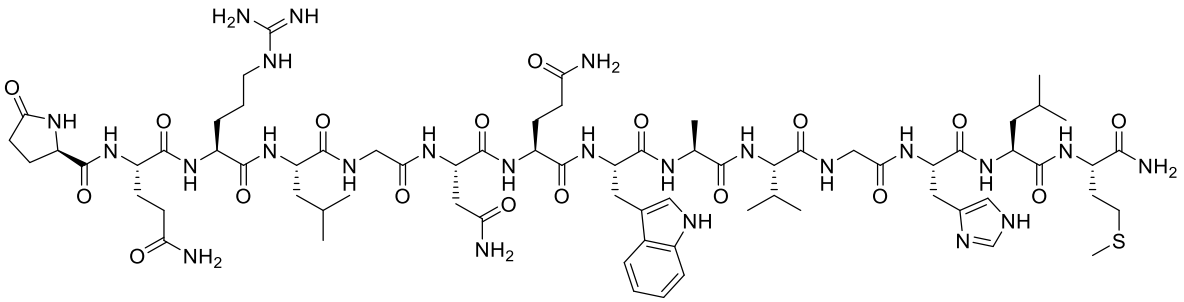

Figure 1.54. Structural representation of the naturally occurring peptide, bombesin.

Bombesin is a 14-amino acid peptide, originally isolated from the skin of the European fire-bellied toad (*Bombina bombina*).[200, 201] Similarly to GRP, bombesin has a C-terminus ending

in Gly-His-Leu-Met-NH_2. Therefore, the two peptides present similar biological activities. There is a growing consensus among the scientific community that GRP and bombesin (and other bombesin-like peptides) may operate as growth factors in these types of cancer.[202] Thanks to these characteristics, various labelled bombesin-based molecules have been synthesised for therapy and imaging applications.[203-205]

The first GRP receptor targeting compound used for molecular imaging was the ^{64}Cu DOTA-Aoc-BBN(7-14) complex **58** (Figure 1.55), developed by Rogers *et al.*[206] This work demonstrated for the first time that it was possible to incorporate the PET imaging isotope ^{64}Cu into a bombesin derivative with high efficiency. Furthermore, compound **58** demonstrated a rapid internalisation rate into PC3 cells and good tumour localisation.

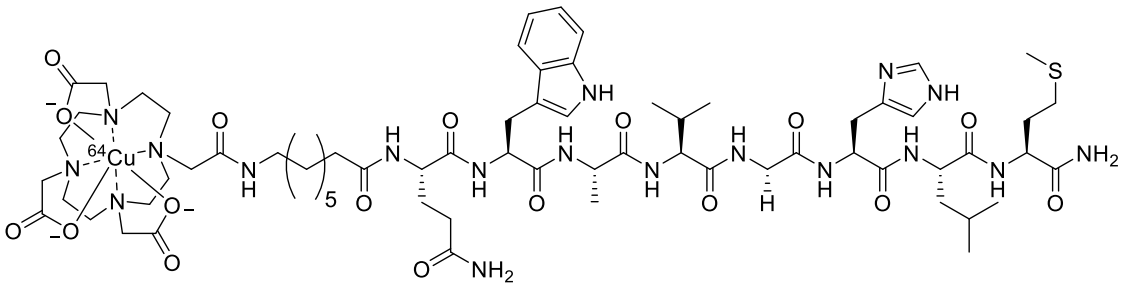

Figure 1.55. Structural representation of the ^{64}Cu radiolabelled GRP receptor targeting compound **58**.

An innovative way to combine target selectivity, therapeutic and imaging applications in a single scaffold has been reported in 2011 by Santos and co-workers.[207] The group developed a novel multifunctional agent (compound **59-Re** and **59-^{99m}Tc**, Figure 1.56) comprising:

(1) a pyrazolyl-diamine framework bearing a set of donor atoms, to stabilise the $[M(CO)_3]^+$ (M = Re, ^{99m}Tc) metal centre;

(2) a DNA intercalating moiety based upon acridine orange (AO), to ensure close proximity of the radionuclide to DNA and to allow the internalization of the compound to be followed by confocal fluorescence microscopy;

(3) a bombesin analogue as targeting unit, so as to provide prostate cancer cell-selectivity.

Compound **59-^{99m}Tc** demonstrated high cellular internalization and nuclear uptake in GRPr-positive PC3 human prostate tumour cells, while the congener **59-Re** showed a considerable accumulation of fluorescence in the nucleus and high kinetic stability, which makes these compounds promising agents for targeted radiotherapy.

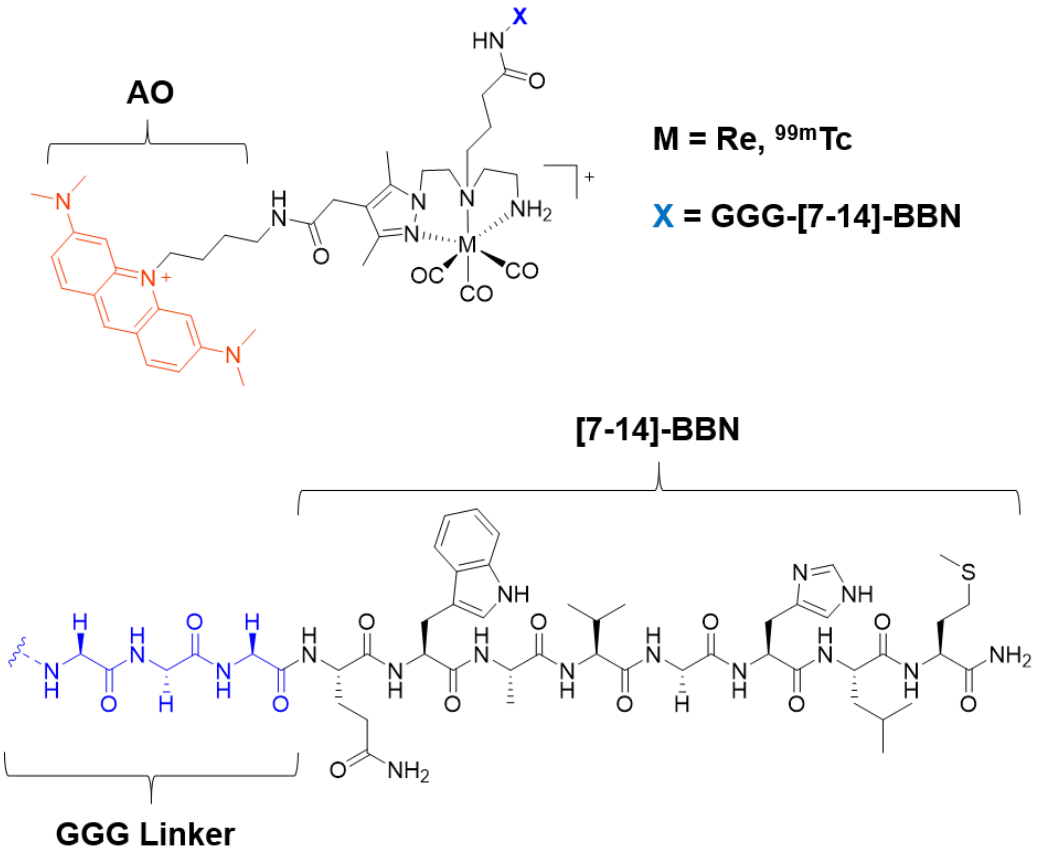

Figure 1.56. Structural representation of the targeted multifunctional tricarbonyl complexes **59-Re** and **59-^{99m}Tc**.

In summary, in the last few years, many possible targets against prostate cancer have been studied and various practicable pathways have been discovered. However, given the complexity and the high degree of heterogeneity displayed by prostate cancer, multiple therapeutic approaches are needed. Effective methodologies, such as personalised medicine and rapidly evolving imaging techniques, will require more effort to accomplish the ultimate aim of developing selective and effective therapies.

1.5. Aim and objectives

This project involves the design, synthesis and study of highly kinetically stable molecular systems ready for cellular uptake, so as to be of relevance to prostate cancer diagnosis using cellular imaging techniques.

Such systems can also be incorporated into the synthetic scaffold of future therapeutics through:

- incorporation of transition metals that demonstrate anticancer properties;
- controlled carbon monoxide (CO) releasing properties, so to create a CO-releasing molecule (CORM) able to deliver a defined and therapeutic quantity of CO in a selective way.

The molecular systems described in this work are based upon a tripodal organic core that can be functionalised with a wide range of functionalities (*e.g.* linkers, fluorophores, targeting groups). These systems will be tested for their suitability to act as ligands for a variety of transition metals possessing biomedical applications, so as to develop potential theranostic agents.

In summary, the specific objectives of this work are:

1. the development of nitrogen and thiosemicarbazone-based tripodal systems with potential biomedical applications;
2. the synthesis and characterisation of N-heterocyclic carbene-based tripodal systems potentially able to bind transition metal ions;
3. to explore the possibility to synthesise a tridentate system with unsymmetrical substituents in order to develop ligands capable of binding metals as well as attaching other functionalities;
4. to test the possibility to develop novel metal complexes containing metal centres of relevance to imaging and/or therapy of prostate cancer.

1.6. References for Chapter 1

1. A. Werner, *Z. Anorg. Allg. Chem*, 1893, **3**, 267-330.
2. K. H. Ernst, F. R. Wild, O. Blacque and H. Berke, *Angew. Chem. Int. Ed.*, 2011, **50**, 10780-10787.
3. G. A. Lawrance, *Introduction to coordination chemistry*, John Wiley & Sons, 2013.
4. B. Rosenberg, L. Vancamp and T. Krigas, *Nature*, 1965, **205**, 698-699.
5. M. E. Moragues, A. Toscani, F. l. Sancenón, R. n. Martínez-Máñez, A. J. White and J. D. Wilton-Ely, *J. Am. Chem. Soc.*, 2014, **136**, 11930-11933.
6. A. K. Renfrew, A. D. Phillips, A. E. Egger, C. G. Hartinger, S. S. Bosquain, A. A. Nazarov, B. K. Keppler, L. Gonsalvi, M. Peruzzini and P. J. Dyson, *Organometallics*, 2009, **28**, 1165-1172.
7. C. S. Allardyce and P. J. Dyson, *Dalton Trans.*, 2016, **45**, 3201-3209.
8. D. Astruc, in *Organometallic Chemistry and Catalysis*, Springer Berlin Heidelberg, Berlin, Heidelberg, 2007, DOI: 10.1007/978-3-540-46129-6_7, pp. 121-134.
9. B. E. Mann, in *Medicinal Organometallic Chemistry*, Springer Berlin Heidelberg, 2010, pp. 247-285.
10. R. Motterlini and L. E. Otterbein, *Nat. Rev. Drug Discov.*, 2010, **9**, 728-743.
11. F. Zobi, O. Blacque, R. A. Jacobs, M. C. Schaub and A. Y. Bogdanova, *Dalton Trans.*, 2012, **41**, 370-378.
12. P. Schluga, C. G. Hartinger, A. Egger, E. Reisner, M. Galanski, M. A. Jakupec and B. K. Keppler, *Dalton Trans.*, 2006, 1796-1802.
13. A. Levina, A. Mitra and P. A. Lay, *Metallomics*, 2009, **1**, 458-470.
14. M. D. Hall and T. W. Hambley, *Coord. Chem. Rev.*, 2002, **232**, 49-67.
15. S. J. Dougan, A. Habtemariam, S. E. McHale, S. Parsons and P. J. Sadler, *Proc. Natl. Acad. Sci. U. S. A.*, 2008, **105**, 11628-11633.
16. C. Müller, C. Dumas, U. Hoffmann, P. A. Schubiger and R. Schibli, *J. Organomet. Chem.*, 2004, **689**, 4712-4721.
17. C. Muller, A. Hohn, P. A. Schubiger and R. Schibli, *Eur. J. Nucl. Med. Mol. Imaging*, 2006, **33**, 1007-1016.
18. W. Fan, P. Huang and X. Chen, *Chem. Soc. Rev.*, 2016, **45**, 6488-6519.
19. Y.-Y. Wang, Y.-C. Liu, H. Sun and D.-S. Guo, *Coord. Chem. Rev.*, 2019, **395**, 46-62.
20. W. Bäumler, J. Regensburger, A. Knak, A. Felgenträger and T. Maisch, *Photochem. Photobiol. Sci.*, 2012, **11**, 107-117.
21. L. B. Josefsen and R. W. Boyle, *Met.-Based Drugs*, 2008, **2008**.
22. M. Ambroz, A. Beeby, A. MacRobert, R. Svensen and D. Phillips, *J. Photochem. Photobiol. B: Biol.*, 1991, **9**, 87-95.
23. A.-M. Manke, K. Geisel, A. Fetzer and P. Kurz, *Phys. Chem. Chem. Phys.*, 2014, **16**, 12029-12042.
24. H. Ali and J. E. Van Lier, *Chem. Rev.*, 1999, **99**, 2379-2450.
25. D. J. Ball, S. R. Wood, D. I. Vernon, J. Griffiths, T. M. Dubbelman and S. B. Brown, *J. Photochem. Photobiol. B: Biol.*, 1998, **45**, 28-35.
26. V. Mantareva, V. Kussovski, I. Angelov, E. Borisova, L. Avramov, G. Schnurpfeil and D. Wöhrle, *Biorg. Med. Chem.*, 2007, **15**, 4829-4835.
27. D. Wöhrle, N. Iskander, G. Graschew, H. Sinn, E. Friedrich, W. Maier-Borst, J. Stern and P. Schlag, *Photochem. Photobiol.*, 1990, **51**, 351-356.
28. L. Chiang, M. R Jones, S. L Ferreira and T. T. Storr, *Curr. Top. Med. Chem.*, 2012, **12**, 122-144.
29. S. van der Steen, P. de Hoog, K. van der Schilden, P. Gamez, M. Pitié, R. Kiss and J. Reedijk, *Chem. Commun.*, 2010, **46**, 3568-3570.

30. M. C. Jahnke and F. E. Hahn, in *N-Heterocyclic Carbenes: From Laboratory Curiosities to Efficient Synthetic Tools (2)*, The Royal Society of Chemistry, 2017, DOI: 10.1039/9781782626817-00001, pp. 1-45.
31. M. N. Hopkinson, C. Richter, M. Schedler and F. Glorius, *Nature*, 2014, **510**, 485-496.
32. W. A. Herrmann, J. Schütz, G. D. Frey and E. Herdtweck, *Organometallics*, 2006, **25**, 2437-2448.
33. R. S. Menon, A. T. Biju and V. Nair, *Chem. Soc. Rev.*, 2015, **44**, 5040-5052.
34. N. Wang, J. Xu and J. K. Lee, *Org. Biomol. Chem.*, 2018, **16**, 8230-8244.
35. R. Song and Y. R. Chi, *Angew. Chem. Int. Ed.*, 2019, **58**, 8628-8630.
36. İ. Özdemir, A. Denizci, H. T. Öztürk and B. Cetinkaya, *Appl. Organomet. Chem.*, 2004, **18**, 318-322.
37. S. Medici, M. Peana, V. M. Nurchi and M. A. Zoroddu, *J. Med. Chem.*, 2019, **62**, 5923-5943.
38. A. Melaiye, R. S. Simons, A. Milsted, F. Pingitore, C. Wesdemiotis, C. A. Tessier and W. J. Youngs, *J. Med. Chem.*, 2004, **47**, 973-977.
39. S. Roland, C. Jolivalt, T. Cresteil, L. Eloy, P. Bouhours, A. Hequet, V. Mansuy, C. Vanucci and J. M. Paris, *Chem.: Eur. J.*, 2011, **17**, 1442-1446.
40. S. J. Berners-Price and A. Filipovska, *Metallomics*, 2011, **3**, 863-873.
41. P. J. Barnard, M. V. Baker, S. J. Berners-Price and D. A. Day, *J. Inorg. Biochem.*, 2004, **98**, 1642-1647.
42. J. L. Hickey, R. A. Ruhayel, P. J. Barnard, M. V. Baker, S. J. Berners-Price and A. Filipovska, *J. Am. Chem. Soc.*, 2008, **130**, 12570-+.
43. S. Sundelacruz, M. Levin and D. L. Kaplan, *Stem Cell Rev*, 2009, **5**, 231-246.
44. H. Ibrahim, C. Gibard, C. Hesling, R. Guillot, L. Morel, A. Gautier and F. Cisnetti, *Dalton Trans.*, 2014, **43**, 6981-6989.
45. Y. Li, G.-F. Liu, C.-P. Tan, L.-N. Ji and Z.-W. Mao, *Metallomics*, 2014, **6**, 1460-1468.
46. L. Boselli, I. Ader, M. Carraz, C. Hemmert, O. Cuvillier and H. Gornitzka, *Eur. J. Med. Chem.*, 2014, **85**, 87-94.
47. D. Krishnamurthy, M. R. Karver, E. Fiorillo, V. Orru, S. M. Stanford, N. Bottini and A. M. Barrios, *J. Med. Chem.*, 2008, **51**, 4790-4795.
48. J. J. Yan, A. L. F. Chow, C. H. Leung, R. W. Y. Sun, D. L. Ma and C. M. Che, *Chem. Commun.*, 2010, **46**, 3893-3895.
49. N. J. Sweeney, O. Mendoza, H. Müller-Bunz, C. Pampillon, F.-J. K. Rehmann, K. Strohfeldt and M. Tacke, *J. Organomet. Chem.*, 2005, **690**, 4537-4544.
50. E. Chardon, G. Dahm, G. Guichard and S. p. Bellemin-Laponnaz, *Organometallics*, 2012, **31**, 7618-7621.
51. E. Borré, G. Dahm, G. Guichard and S. Bellemin-Laponnaz, *New J. Chem.*, 2016, **40**, 3164-3171.
52. J. K. Muenzner, T. Rehm, B. Biersack, A. Casini, I. A. de Graaf, P. Worawutputtapong, A. Noor, R. Kempe, V. Brabec and J. Kasparkova, *J. Med. Chem.*, 2015, **58**, 6283-6292.
53. J.-Y. Lee, J.-Y. Lee, Y.-Y. Chang, C.-H. Hu, N. M. Wang and H. M. Lee, *Organometallics*, 2015, **34**, 4359-4368.
54. G. Alves, L. Morel, M. El-Ghozzi, D. Avignant, B. Legeret, L. Nauton, F. Cisnetti and A. Gautier, *Chem. Commun.*, 2011, **47**, 7830-7832.
55. M. Skander, P. Retailleau, B. Bourrie, L. Schio, P. Mailliet and A. Marinetti, *J. Med. Chem.*, 2010, **53**, 2146-2154.
56. R. W. Y. Sun, A. L. F. Chow, X. H. Li, J. J. Yan, S. S. Y. Chui and C. M. Che, *Chem. Sci.*, 2011, **2**, 728-736.
57. T. J. Siciliano, M. C. Deblock, K. M. Hindi, S. Durmus, M. J. Panzner, C. A. Tessier and W. J. Youngs, *J. Organomet. Chem.*, 2011, **696**, 1066-1071.

58. L. Eloy, A. S. Jarrousse, M. L. Teyssot, A. Gautier, L. Morel, C. Jolivalt, T. Cresteil and S. Roland, *ChemMedChem*, 2012, **7**, 805-814.
59. W. Streciwilk, F. Hackenberg, H. Müller-Bunz and M. Tacke, *Polyhedron*, 2014, **80**, 3-9.
60. M. Pellei, V. Gandin, M. Marinelli, A. Orsetti, F. Del Bello, C. Santini and C. Marzano, *Dalton Trans.*, 2015, **44**, 21041-21052.
61. B. Bertrand, A. S. Romanov, M. Brooks, J. Davis, C. Schmidt, I. Ott, M. O'Connell and M. Bochmann, *Dalton Trans.*, 2017, **46**, 15875-15887.
62. U. Jungwirth, C. R. Kowol, B. K. Keppler, C. G. Hartinger, W. Berger and P. Heffeter, *Antioxid. Redox Signal.*, 2011, **15**, 1085-1127.
63. M. Elie, G. U. Mahoro, E. Duverger, J.-L. Renaud, R. Daniellou and S. Gaillard, *J. Organomet. Chem.*, 2019, **893**, 21-31.
64. M. Elie, F. Sguerra, F. Di Meo, M. D. Weber, R. Marion, A. l. Grimault, J.-F. o. Lohier, A. l. Stallivieri, A. Brosseau and R. B. Pansu, *ACS Appl. Mater. Interfaces*, 2016, **8**, 14678-14691.
65. F. Lazreg, D. B. Cordes, A. M. Slawin and C. S. Cazin, *Organometallics*, 2015, **34**, 419-425.
66. A. Gautier and F. Cisnetti, *Metallomics*, 2012, **4**, 23-32.
67. S. Ray, R. Mohan, J. K. Singh, M. K. Samantaray, M. M. Shaikh, D. Panda and P. Ghosh, *J. Am. Chem. Soc.*, 2007, **129**, 15042-15053.
68. A. L. Noffke, A. Habtemariam, A. M. Pizarro and P. J. Sadler, *Chem Commun (Camb)*, 2012, **48**, 5219-5246.
69. C. G. Hartinger, N. Metzler-Nolte and P. J. Dyson, *Organometallics*, 2012, **31**, 5677-5685.
70. L. Oehninger, H. Alborzinia, S. Ludewig, K. Baumann, S. Wölfl and I. Ott, *ChemMedChem*, 2011, **6**, 2142-2145.
71. A. Wilbuer, D. H. Vlecken, D. J. Schmitz, K. Kraling, K. Harms, C. P. Bagowski and E. Meggers, *Angew. Chem. Int. Ed. Engl.*, 2010, **49**, 3839-3842.
72. Y. Li, C. P. Tan, W. Zhang, L. He, L. N. Ji and Z. W. Mao, *Biomaterials*, 2015, **39**, 95-104.
73. F. Knapp Jr, *Cancer Biother. Radio.*, 1998, **13**, 337-349.
74. T. Mindt, H. Struthers, E. Garcia-Garayoa, D. Desbouis and R. Schibli, *CHIMIA*, 2007, **61**, 725-731.
75. G. R. Morais, A. Paulo and I. Santos, *Organometallics*, 2012, **31**, 5693-5714.
76. R. Lum, H. Zhang, W. Zhang, S.-Q. Bai, J. Zhao and T. A. Hor, *Dalton Trans.*, 2013, **42**, 871-873.
77. T. Wagner, B. M. Zeglis, S. Groveman, C. Hille, A. Pöthig, L. C. Francesconi, W. A. Herrmann, F. E. Kühn and T. Reiner, *J. Labelled Compd. Radiopharm.*, 2014, **57**, 441-447.
78. M. Wrighton and D. L. Morse, *J. Am. Chem. Soc.*, 1974, **96**, 998-1003.
79. X.-W. Li, H.-Y. Li, G.-F. Wang, F. Chen, Y.-Z. Li, X.-T. Chen, Y.-X. Zheng and Z.-L. Xue, *Organometallics*, 2012, **31**, 3829-3835.
80. L. A. Casson, S. Muzzioli, P. Raiteri, B. W. Skelton, S. Stagni, M. Massi and D. H. Brown, *Dalton Trans.*, 2011, **40**, 11960-11967.
81. J. G. Vaughan, B. L. Reid, S. Ramchandani, P. J. Wright, S. Muzzioli, B. W. Skelton, P. Raiteri, D. H. Brown, S. Stagni and M. Massi, *Dalton Trans.*, 2013, **42**, 14100-14114.
82. D. Stufkens, *Comments Inorg. Chem.*, 1992, **13**, 359-385.
83. A. Kumar, S.-S. Sun and A. J. Lees, in *Photophysics of Organometallics*, Springer, 2009, pp. 37-71.
84. H. Takeda, K. Koike, T. Morimoto, H. Inumaru and O. Ishitani, in *Adv. Inorg. Chem.*, Elsevier, 2011, vol. 63, pp. 137-186.

85. A. E. Pierri, A. Pallaoro, G. Wu and P. C. Ford, *J. Am. Chem. Soc.*, 2012, **134**, 18197-18200.
86. C. Y. Chan, P. A. Pellegrini, I. Greguric and P. J. Barnard, *Inorg. Chem.*, 2014, **53**, 10862-10873.
87. R. Alberto, R. Schibli, A. Egli, A. P. Schubiger, U. Abram and T. A. Kaden, *J. Am. Chem. Soc.*, 1998, **120**, 7987-7988.
88. C. Y. Chan and P. J. Barnard, *Dalton Trans.*, 2015, **44**, 19126-19140.
89. R. Schibli and A. P. Schubiger, *Eur. J. Nucl. Med. Mol. Imaging*, 2002, **29**, 1529-1542.
90. P. V. Simpson, I. Casari, S. Paternoster, B. W. Skelton, M. Falasca and M. Massi, *Chem.: Eur. J.*, 2017, **23**, 6518-6521.
91. J.-H. Mao, D. Wu, J. Perez-Losada, T. Jiang, Q. Li, R. M. Neve, J. W. Gray, W.-W. Cai and A. Balmain, *Cancer Cell*, 2007, **11**, 161-173.
92. J. K. Willmann, N. van Bruggen, L. M. Dinkelborg and S. S. Gambhir, *Nat. Rev. Drug Discov.*, 2008, **7**, 591-607.
93. L. L. Seeger, *Clin. Orthop. Relat. Res.*, 1989, **244**, 7-16.
94. E. Ngen and D. Artemov, *Int. J. Mol. Sci.*, 2017, **18**, 198.
95. M. E. Ladd, P. Bachert, M. Meyerspeer, E. Moser, A. M. Nagel, D. G. Norris, S. Schmitter, O. Speck, S. Straub and M. Zaiss, *Prog. Nucl. Magn. Reson. Spectrosc.*, 2018, **109**, 1-50.
96. P. Caravan, *Chem. Soc. Rev.*, 2006, **35**, 512-523.
97. H.-K. Kim, J.-A. Park, K. M. Kim, N. S. Md, D.-S. Kang, J. Lee, Y. Chang and T.-J. Kim, *Chem. Commun.*, 2010, **46**, 8442-8444.
98. D. L. Bailey, M. N. Maisey, D. W. Townsend and P. E. Valk, *Positron emission tomography*, Springer, 2005.
99. H. Jadvar and J. A. Parker, Springer Science & Business Media, 2006.
100. K. Smolarz, B. J. Krause, F.-P. Graner, F. M. Wagner, C. Hultsch, C. Bacher-Stier, R. B. Sparks, S. Ramsay, L. M. Fels and L. M. Dinkelborg, *J. Nucl. Med.*, 2013, **54**, 861-866.
101. K.-M. Kälkner, C. Ginman, S. Nilsson, M. Bergström, G. Antoni, H. Ahlström, B. Långström and J.-E. Westlin, *Nucl. Med. Biol.*, 1997, **24**, 319-325.
102. D. Denoyer, L. Kirby, K. Waldeck, P. Roselt, O. C. Neels, T. Bourdier, R. Shepherd, A. Katsifis and R. J. Hicks, *Eur. J. Nucl. Med. Mol. Imaging*, 2012, **39**, 703-712.
103. H. Jadvar, B. Desai, L. Ji, P. S. Conti, T. B. Dorff, S. G. Groshen, J. K. Pinski and D. I. Quinn, *J. Nucl. Med.*, 2013, **54**, 1195-1201.
104. J. Suburu and Y. Q. Chen, *Prostaglandins Other Lipid Mediat.*, 2012, **98**, 1-10.
105. A. B. Apolo, N. Pandit-Taskar and M. J. Morris, *J. Nucl. Med.*, 2008, **49**, 2031-2041.
106. M. H. Umbehr, M. Muntener, T. Hany, T. Sulser and L. M. Bachmann, *Eur. Urol.*, 2013, **64**, 106-117.
107. L. Evangelista, F. Zattoni, A. Guttilla, G. Saladini, F. Zattoni, P. M. Colletti and D. Rubello, *Clin. Nucl. Med.*, 2013, **38**, 305-314.
108. P. Castellucci and M. Picchio, *Eur. J. Nucl. Med. Mol. Imaging*, 2013, **40 Suppl 1**, S36-40.
109. C. Greco, G. L. Cascini and O. Tamburrini, *Prostate Cancer Prostatic Dis.*, 2008, **11**, 121-128.
110. H. Okudaira, T. Nakanishi, S. Oka, M. Kobayashi, H. Tamagami, D. M. Schuster, M. M. Goodman, Y. Shirakami, I. Tamai and K. Kawai, *Nucl. Med. Biol.*, 2013, **40**, 670-675.
111. C. Nanni, R. Schiavina, S. Boschi, V. Ambrosini, C. Pettinato, E. Brunocilla, G. Martorana and S. Fanti, *Eur. J. Nucl. Med. Mol. Imaging*, 2013, **40 Suppl 1**, S11-17.
112. R. C. Mease, C. A. Foss and M. G. Pomper, *Curr. Top. Med. Chem.*, 2013, **13**, 951-962.
113. H. Jadvar, *J. Nucl. Med.*, 2013, **54**, 1685-1688.

114. R. J. Jaszczak and R. E. Coleman, *Invest. Radiol.*, 1985, **20**, 897-910.
115. G. Subramanian, J. McAfee, R. Blair, F. Kallfelz and F. Thomas, *J. Nucl. Med.*, 1975, **16**, 744-755.
116. L. Qiu, W. Cheng, J. Lin, S. Luo, L. Xue and J. Pan, *Molecules*, 2011, **16**, 6165-6178.
117. S. M. Erturk, C. Johnston, C. Tempany-Afdhal and A. D. Van den Abbeele, in *Clinical and Translational Science*, eds. D. Robertson and G. H. Williams, Academic Press, San Diego, 2009, DOI: https://doi.org/10.1016/B978-0-12-373639-0.00006-6, pp. 87-104.
118. S. Kunjachan, J. Ehling, G. Storm, F. Kiessling and T. Lammers, *Chem. Rev.*, 2015, **115**, 10907-10937.
119. G. M. van Dam, G. Themelis, L. M. Crane, N. J. Harlaar, R. G. Pleijhuis, W. Kelder, A. Sarantopoulos, J. S. de Jong, H. J. Arts, A. G. van der Zee, J. Bart, P. S. Low and V. Ntziachristos, *Nat. Med.*, 2011, **17**, 1315-1319.
120. W. Chen, P. A. Jarzyna, G. A. F. v. Tilborg, V. A. Nguyen, D. P. Cormode, A. Klink, A. W. Griffioen, G. J. Randolph, E. A. Fisher, W. J. M. Mulder and Z. A. Fayad, *FASEB J.*, 2010, **24**, 1689-1699.
121. J. Y. Kim, W. I. Choi, Y. H. Kim and G. Tae, *J. Controlled Release*, 2011, **156**, 398-405.
122. E. J. Hall and A. J. Giaccia, *Radiobiology for the Radiologist.*, Lippincott Williams & Wilkins, 2006.
123. M. Koritzinsky, M. G. Magagnin, T. v. d. Beucken, R. Seigneuric, K. Savelkouls, J. Dostie, S. Pyronnet, R. J. Kaufman, S. A. Weppler, J. W. Voncken, P. Lambin, C. Koumenis, N. Sonenberg and B. G. Wouters, *EMBO J.*, 2006, **25**, 1114-1125.
124. C. T. Lee, M. K. Boss and M. W. Dewhirst, *Antioxid. Redox. Signal.*, 2014, **21**, 313-337.
125. B. J. Moeller, R. A. Richardson and M. W. Dewhirst, *Cancer Metastasis Rev.*, 2007, **26**, 241-248.
126. G. L. Semenza, *N. Engl. J. Med.*, 2011, **365**, 537-547.
127. N. C. Denko, *Nat. Rev. Cancer*, 2008, **8**, 705-713.
128. G. L. Semenza and N. R. Prabhakar, *Antioxid. Redox. Signal.*, 2007, **9**, 1391-1396.
129. T. G. Graeber, C. Osmanian, T. Jacks, D. E. Housman, C. J. Koch, S. W. Lowe and A. J. Giaccia, *Nature*, 1996, **379**, 88.
130. M. Höckel, K. Schlenger, B. Aral, M. Mitze, U. Schäffer and P. Vaupel, *Cancer Res.*, 1996, **56**, 4509-4515.
131. D. Shweiki, A. Itin, D. Soffer and E. Keshet, *Nature*, 1992, **359**, 843.
132. L. Hoigebazar and J. M. Jeong, in *Theranostics, Gallium-68, and Other Radionuclides*, Springer, 2013, pp. 285-299.
133. P. Kumar, E. Naimi, A. J. McEwan and L. I. Wiebe, *Biorg. Med. Chem.*, 2010, **18**, 2255-2264.
134. A. Nunn, K. Linder and H. W. Strauss, *Eur. J. Nucl. Med.*, 1995, **22**, 265-280.
135. J. G. Rajendran, D. A. Mankoff, F. O'Sullivan, L. M. Peterson, D. L. Schwartz, E. U. Conrad, A. M. Spence, M. Muzi, D. G. Farwell and K. A. Krohn, *Clin. Cancer Res.*, 2004, **10**, 2245-2252.
136. M. H. Cherk, S. S. Foo, A. M. Poon, S. R. Knight, C. Murone, A. T. Papenfuss, J. I. Sachinidis, T. H. Saunder, G. J. O'Keefe and A. M. Scott, *J. Nucl. Med.*, 2006, **47**, 1921-1926.
137. A. L. Vāvere and J. S. Lewis, *Dalton Trans.*, 2007, 4893-4902.
138. D. H. Petering, *Bioinorg. Chem.*, 1972, **1**, 255-271.
139. Y. Fujibayashi, H. Taniuchi, Y. Yonekura and H. Ohtani, *J. Nucl. Med.*, 1997, **38**, 1155.
140. N. Takahashi, Y. Fujibayashi, Y. Yonekura, M. J. Welch, A. Waki, T. Tsuchida, N. Sadato, K. Sugimoto and H. Itoh, *Ann. Nucl. Med.*, 2000, **14**, 323-328.

141. F. Dehdashti, M. A. Mintun, J. S. Lewis, J. Bradley, R. Govindan, R. Laforest, M. J. Welch and B. A. Siegel, *Eur. J. Nucl. Med. Mol. Imaging*, 2003, **30**, 844-850.
142. J. S. Lewis, R. Laforest, F. Dehdashti, P. W. Grigsby, M. J. Welch and B. A. Siegel, *J. Nucl. Med.*, 2008, **49**, 1177-1182.
143. F. Dehdashti, P. W. Grigsby, M. A. Mintun, J. S. Lewis, B. A. Siegel and M. J. Welch, *Int. J. Radiat. Oncol. Biol. Phys.*, 2003, **55**, 1233-1238.
144. D. W. Dietz, F. Dehdashti, P. W. Grigsby, R. S. Malyapa, R. J. Myerson, J. Picus, J. Ritter, J. S. Lewis, M. J. Welch and B. A. Siegel, *Dis. Colon Rectum*, 2008, **51**, 1641.
145. I. S. Alam, R. L. Arrowsmith, F. Cortezon-Tamarit, F. Twyman, G. Kociok-Köhn, S. W. Botchway, J. R. Dilworth, L. Carroll, E. O. Aboagye and S. I. Pascu, *Dalton Trans.*, 2016, **45**, 3650-3650.
146. S. I. Pascu, P. A. Waghorn, B. W. Kennedy, R. L. Arrowsmith, S. R. Bayly, J. R. Dilworth, M. Christlieb, R. M. Tyrrell, J. Zhong and R. M. Kowalczyk, *Chem. Asian J.*, 2010, **5**, 506-519.
147. P. A. Waghorn, M. W. Jones, M. B. Theobald, R. L. Arrowsmith, S. I. Pascu, S. W. Botchway, S. Faulkner and J. R. Dilworth, *Chem. Sci.*, 2013, **4**, 1430-1441.
148. Cancer Research UK, http://www.cancerresearchuk.org/health-professional/cancer-statistics/statistics-by-cancer-type/prostate-cancer#heading-One, (accessed July, 2019).
149. N. Sharifi, J. L. Gulley and W. L. Dahut, *JAMA*, 2005, **294**, 238-244.
150. M. Katsogiannou, L. Peng, C. V. Catapano and P. Rocchi, *Curr. Cancer Drug Targets*, 2011, **11**, 954-965.
151. N. C. Institute, Prostate Cancer Treatment (PDQ®)–Patient Version, https://www.cancer.gov/types/prostate/patient/prostate-treatment-pdq#_120, (accessed February, 2020).
152. F. Stavridi, E. M. Karapanagiotou and K. N. Syrigos, *Cancer Treat. Rev.*, 2010, **36**, 122-130.
153. R. B. Shah, R. Mehra, A. M. Chinnaiyan, R. L. Shen, D. Ghosh, M. Zhou, G. R. MacVicar, S. Varambally, J. Harwood, T. A. Bismar, R. Kim, M. A. Rubin and K. J. Pienta, *Cancer Res.*, 2004, **64**, 9209-9216.
154. J. Lapointe, C. Li, J. P. Higgins, M. v. d. Rijn, E. Bair, K. Montgomery, M. Ferrari, L. Egevad, W. Rayford, U. Bergerheim, P. Ekman, A. M. DeMarzo, R. Tibshirani, D. Botstein, P. O. Brown, J. D. Brooks and J. R. Pollack, *Proc. Natl. Acad. Sci. U. S. A.*, 2004, **101**, 811-816.
155. D. Bianchini, A. Zivi, S. Sandhu and J. S. d. Bono, *Ann. Oncol.*, 2010, **21**, vii 43-vii 55.
156. T. Lammers, W. E. Hennink and G. Storm, *Br. J. Cancer*, 2008, **99**, 392-397.
157. M. E. Davis, Z. G. Chen and D. M. Shin, *Nat. Rev. Drug Discov.*, 2008, **7**, 771-782.
158. D. Zhao, X. Zhao, Y. Zu, J. Li, Y. Zhang, R. Jiang and Z. Zhang, *Int. J. Nanomedicine*, 2010, **5**, 669-677.
159. A. Beck, J. F. Haeuw, T. Wurch, L. Goetsch, C. Bailly and N. Corvaia, *Discov. Med.*, 2010, **10**, 329-339.
160. E. Vives, J. Schmidt and A. Pelegrin, *Biochim. Biophys. Acta*, 2008, **1786**, 126-138.
161. G. P. Murphy, A. A. Elgamal, S. L. Su, D. G. Bostwick and E. H. Holmes, *Cancer*, 1998, **83**, 2259-2269.
162. H. Jadvar, *J. Nucl. Med.*, 2015, **56**, 1131-1132.
163. S. Lutje, S. Heskamp, A. S. Cornelissen, T. D. Poeppel, S. A. v. d. Broek, S. Rosenbaum-Krumme, A. Bockisch, M. Gotthardt, M. Rijpkema and O. C. Boerman, *Theranostics*, 2015, **5**, 1388-1401.
164. H. Aloysius and L. Hu, *Med. Res. Rev.*, 2015, **35**, 554-585.
165. M. I. Davis, M. J. Bennett, L. M. Thomas and P. J. Bjorkman, *Proc. Natl. Acad. Sci. U. S. A.*, 2005, **102**, 5981-5986.

166. S. R. Banerjee, M. Pullambhatla, C. A. Foss, S. Nimmagadda, R. Ferdani, C. J. Anderson, R. C. Mease and M. G. Pomper, *J. Med. Chem.*, 2014, **57**, 2657-2669.
167. T. Wüstemann, U. Haberkorn, J. Babich and W. Mier, *Med. Res. Rev.*, 2019, **39**, 40-69.
168. T. R. Daniels, T. Delgado, J. A. Rodriguez, G. Helguera and M. L. Penichet, *Clin. Immunol.*, 2006, **121**, 144-158.
169. C. M. Lawrence, S. Ray, M. Babyonyshev, R. Galluser, D. W. Borhani and S. C. Harrison, *Science*, 1999, **286**, 779-782.
170. J. Wang, S. Tian, R. A. Petros, M. E. Napier and J. M. Desimone, *J. Am. Chem. Soc.*, 2010, **132**, 11306-11313.
171. Y. Zhao, J. Peng, Y. Niu, X. Zhang, N. Jiang, R. Jia, J. Li, Z. Shang, S. Zhu and L. Sun, *RSC Advances*, 2015, **5**, 64076-64082.
172. Y. Wang, J.-T. Chen and X.-P. Yan, *Anal. Chem.*, 2013, **85**, 2529-2535.
173. S.-K. Sun, L.-X. Dong, Y. Cao, H.-R. Sun and X.-P. Yan, *Anal. Chem.*, 2013, **85**, 8436-8441.
174. R. S. Hubert, I. Vivanco, E. Chen, S. Rastegar, K. Leong, S. C. Mitchell, R. Madraswala, Y. Zhou, J. Kuo, A. B. Raitano, A. Jakobovits, D. C. Saffran and D. E. Afar, *Proc. Natl. Acad. Sci. U. S. A.*, 1999, **96**, 14523-14528.
175. A. K. Sendamarai, R. S. Ohgami, M. D. Fleming and C. M. Lawrence, *Proc. Natl. Acad. Sci. U. S. A.*, 2008, **105**, 7410-7415.
176. P. M. Challita-Eid, K. Morrison, S. Etessami, Z. An, K. J. Morrison, J. J. Perez-Villar, A. B. Raitano, X. C. Jia, J. M. Gudas, S. B. Kanner and A. Jakobovits, *Cancer Res.*, 2007, **67**, 5798-5805.
177. M. G. Doran, P. A. Watson, S. M. Cheal, D. E. Spratt, J. Wongvipat, J. M. Steckler, J. A. Carrasquillo, M. J. Evans and J. S. Lewis, *J. Nucl. Med.*, 2014, **55**, 2045-2049.
178. J. Barroca-Ferreira, J. Pais, M. Santos, A. Goncalves, I. Gomes, I. Sousa, S. Rocha, L. Passarinha and C. Maia, *Curr. Cancer Drug Targets*, 2018, **18**, 222-230.
179. The Protein Model Portal, http://www.proteinmodelportal.org/?pid=modelDetail&provider=SWISSMODEL&template=4xesA&pmpuid=1000967922656&range_from=1&range_to=320&ref_ac=Q9H255&mapped_ac=Q9H255&zid=async, (accessed June, 2019).
180. J. Wang, J. Weng, Y. Cai, R. Penland, M. Liu and M. Ittmann, *The Prostate*, 2006, **66**, 847-857.
181. J. Weng, J. Wang, Y. Cai, L. J. Stafford, D. Mitchell, M. Ittmann and M. Liu, *Int. J. Cancer*, 2005, **113**, 811-818.
182. L. L. Xu, B. G. Stackhouse, K. Florence, W. Zhang, N. Shanmugam, I. A. Sesterhenn, Z. Q. Zou, V. Srikantan, M. Augustus, V. Roschke, K. Carter, D. G. McLeod, J. W. Moul, D. Soppett and S. Srivastava, *Cancer Res.*, 2000, **60**, 6568-6572.
183. N. Sung, J. Lee, J.-H. Kim, C. Chang, T. F. Tsai and S. Lee, *Acta Crystallogr. D*, 2016, **72**.
184. G. Jego, A. Hazoumé, R. Seigneuric and C. Garrido, *Cancer Lett.*, 2013, **332**, 275-285.
185. M. M. Centenera, A. K. Fitzpatrick, W. D. Tilley and L. M. Butler, *Biochim. Biophys. Acta*, 2013, **1835**, 211-218.
186. H. M. Specht, N. Ahrens, C. Blankenstein, T. Duell, R. Fietkau, U. S. Gaipl, C. Gunther, S. Gunther, G. Habl, H. Hautmann, M. Hautmann, R. M. Huber, M. Molls, R. Offner, C. Rodel, F. Rodel, M. Schutz, S. E. Combs and G. Multhoff, *Front. Immunol.*, 2015, **6**, 162.
187. M. Gehrmann, G. Liebisch, G. Schmitz, R. Anderson, C. Steinem, A. D. Maio, G. Pockley and G. Multhoff, *PLoS ONE*, 2008, **3**, e1925.
188. M. Ni, Y. Zhang and A. S. Lee, *Biochem. J*, 2011, **434**, 181-188.
189. V. Renard and D. R. Leach, *Vaccine*, 2007, **25 Suppl 2**, B17-23.

190. C. J. Novotny, S. Pollari, J. H. Park, M. A. Lemmon, W. Shen and K. M. Shokat, *Nat. Chem. Biol.*, 2016, **12**, 923-930.
191. R. Berger, D. I. Lin, M. Nieto, E. Sicinska, L. A. Garraway, H. Adams, S. Signoretti, W. C. Hahn and M. Loda, *Cancer Res.*, 2006, **66**, 5723-5728.
192. D. Grimm, J. Bauer, J. Pietsch, M. Infanger, J. Eucker, C. Eilles and J. Schoenberger, *Curr. Med. Chem.*, 2011, **18**, 176-190.
193. F. Montemurro, S. Redana, G. Viale, G. Sanna, M. Donadio, G. Valabrega, B. d. Curto, A. Bottini, G. Botti, A. P. d. Tos, M. E. Jacomuzzi, M. D. Bonito, S. Danese, M. Clavarezza, J. Kulka, S. D. Palma, A. Durando, A. Sapino and M. Aglietta, *Clin. Breast Cancer*, 2008, **8**, 436-442.
194. P. N. J. Lara, K. G. Chee, J. Longmate, C. Ruel, F. J. Meyers, C. R. Gray, R. G. Edwards, P. H. Gumerlock, P. Twardowski, J. H. Doroshow and D. R. Gandara, *Cancer*, 2004, **100**, 2125-2131.
195. H.-Y. Wang, W.-Y. Lin, M.-C. Chen, T. Lin, C.-H. Chao, F.-N. Hsu, E. Lin, C.-Y. Huang, T.-Y. Luo and H. Lin, *Int. J. Radiat Biol.*, 2013, **89**, 346-355.
196. J. Albanell, J. Codony, A. Rovira, B. Mellado and P. Gascón, in *New Trends in Cancer for the 21st Century: Proceedings of the International Symposium on Cancer: New Trends in Cancer for the 21st Century, held November 10–13, 2002, in Valencia, Spain*, eds. A. Llombart-Bosch and V. Felipo, Springer US, Boston, MA, 2003, DOI: 10.1007/978-1-4615-0081-0_21, pp. 253-268.
197. R. P. Schroeder, M. d. Visser, W. M. v. Weerden, C. M. d. Ridder, S. Reneman, M. Melis, W. A. Breeman, E. P. Krenning and M. d. Jong, *Int. J. Cancer*, 2010, **126**, 2826-2834.
198. M. Gugger and J. C. Reubi, *Am. J. Pathol.*, 1999, **155**, 2067-2076.
199. M. Toi-Scott, C. L. Jones and M. A. Kane, *Lung Cancer*, 1996, **15**, 341-354.
200. N. Gonzalez, T. W. Moody, H. Igarashi, T. Ito and R. T. Jensen, *Curr. Opin. Endocrinol.*, 2008, **15**, 58.
201. A. Anastasi, V. Erspamer and M. Bucci, *Experientia*, 1971, **27**, 166-167.
202. D. B. Cornelio, R. Roesler and G. Schwartsmann, *Ann. Oncol.*, 2007, **18**, 1457-1466.
203. Z. Yu, G. Carlucci, H. J. Ananias, R. A. Dierckx, S. Liu, W. Helfrich, F. Wang, I. J. de Jong and P. H. Elsinga, *Amino Acids*, 2013, **44**, 543-553.
204. B. R. Sah, I. A. Burger, R. Schibli, M. Friebe, L. Dinkelborg, K. Graham, S. Borkowski, C. Bacher-Stier, R. Valencia, A. Srinivasan, T. F. Hany, L. Mu, P. J. Wild and N. G. Schaefer, *J. Nucl. Med.*, 2015, **56**, 372-378.
205. G. Carlucci, A. Kuipers, H. J. K. Ananias, D. d. P. Faria, R. A. J. O. Dierckx, W. Helfrich, R. Rink, G. N. Moll, I. J. d. Jong and P. H. Elsinga, *Peptides*, 2015, **67**, 45-54.
206. B. E. Rogers, H. M. Bigott, D. W. McCarthy, D. D. Manna, J. Kim, T. L. Sharp and M. J. Welch, *Bioconjug. Chem.*, 2003, **14**, 756-763.
207. T. Esteves, F. Marques, A. Paulo, J. Rino, P. Nanda, C. J. Smith and I. Santos, *J. Biol. Inorg. Chem.*, 2011, **16**, 1141-1153.

2. Novel developments into the synthesis, characterisation and cellular interactions of nitrogen and thiosemicarbazone-based tripodal ligands

2.1 Tripodal scaffolds as host-guest compounds and supramolecular systems

The last three decades have seen a noticeable increase in the development of tripodal ligands, which can be defined as tri-dentate ligands characterised by C_3 symmetry. These systems were found to be particularly useful in a variety of supramolecular assemblies, particularly in the context of ion sensing.[1-4] As many of such host molecules make use of non-covalent interactions (such as hydrogen bonds), their preorganisation plays a pivotal role in the activity of the sensor.

In 1997, Anslyn and co-workers introduced a series of guanidinium-based hosts able to bind tricarboxylate ions.[5] Preorganisation is achieved by incorporating these guanidinium-based recognition groups into a trisubstituted 1,3,5-triethylbenzene core, generating a cone shaped cavity due to the steric bulk around the benzene core. Following Anslyn's work, several research groups developed an array of hosts based upon the preorganised hexasubstituted benzene core.[6]

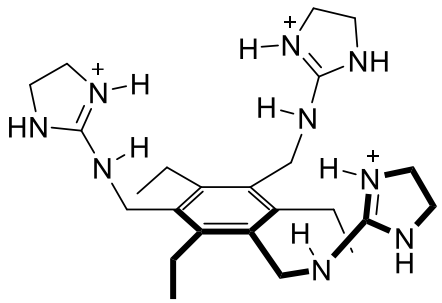

Figure 2.1. An example of a guanidinium-based host developed by Anslyin and co-workers.

Metal complexes have also been successfully used as anion binding sites for the development of chemosensors that also display optical properties.[7, 8] Cabell and co-workers developed a

tripodal receptor consisting of Cu(II) bound by a 1,10-phenanthroline ligand, which in turn is attached to a bis(aminoimidazolium) receptor (Figure 2.2).[9] The receptor is able to interact with the citrate anion through its positively charged moieties and the copper(II) centre, which in turn determine an increase of the phenanthroline-based fluorescence when the anion interacts with the metal.

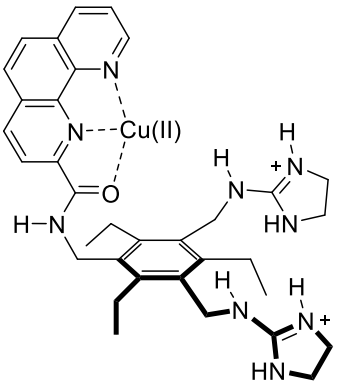

Figure 2.2. Structural representation of the Cu(II)-based chemosensor prepared by Cabell et al.

The ability of tripodal systems to bind anions could be also exploited for therapeutic purposes. For example, two research groups, led by Gale[10] and Davis,[11] explored the possibility of influencing cellular homeostasis by increasing intracellular chloride anion levels using thiourea-based tripodal anion transporters (Figure 2.3). The tripodal host **A** developed by Gale and co-workers was found to be able to strongly bind several ions and permeate the cellular membrane due to its increased lipophilicity. Moreover, subsequent cytotoxicity studies revealed that compound **A** was active towards several cancer cell lines. The group ascribed the cytotoxicity of **A** to the alteration of intracellular pH caused by the molecule.

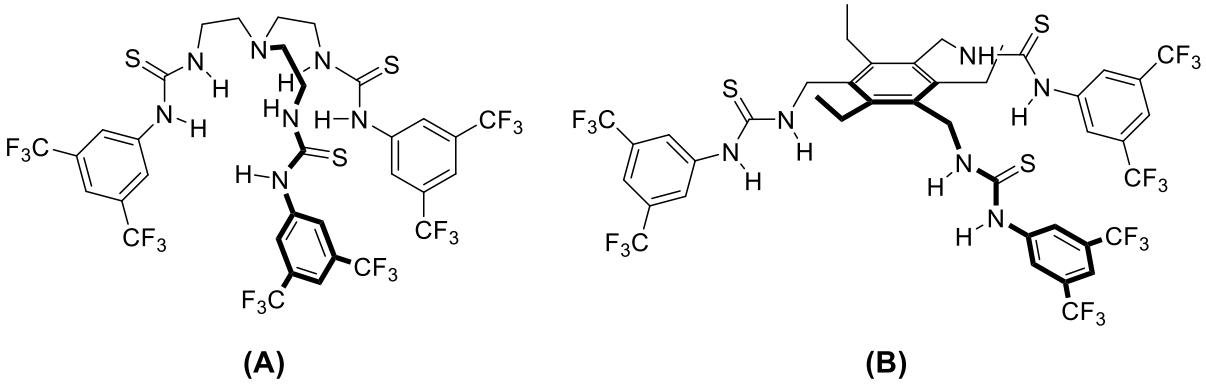

Figure 2.3. Structural representations of the thiourea-based tripodal receptors developed by Gale (compound **A**) and Davis (compound **B**)

The usage of a hexasubstituted benzene scaffold by Davis *et al* allowed this research group to easily develop a more accessible tripodal receptor. Compound **B** was found to be among the most effective anion carriers reported in literature.[11, 12] Interestingly, characterisation by X-ray crystallography revealed that compound **B** existed as a dimer, forming a cage surrounding a cyclic $(Cl\cdots H_2O)_2$ dianionic cluster (Figure 2.4).

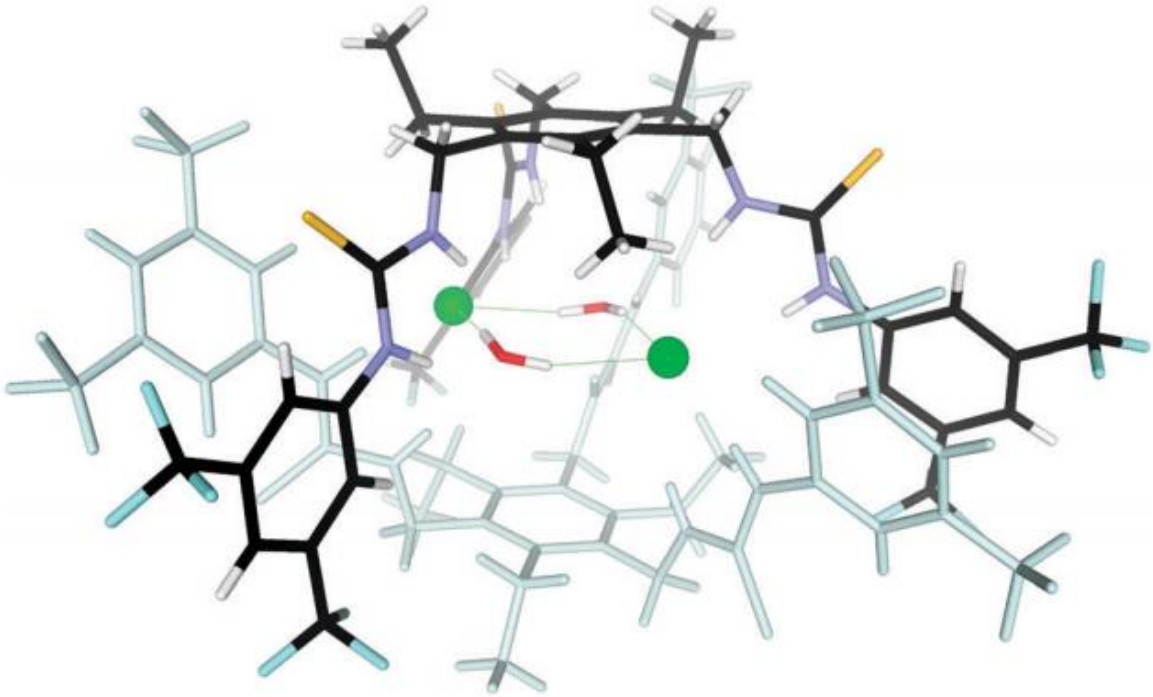

Figure 2.4. Structure of the compound **B** forming a dimeric cage around the dianionic cluster $(Cl\cdots H_2O)_2$. Adapted from ref.[11] with permission from The Royal Society of Chemistry.

Many more tripodal systems based upon the hexasubstituted benzene scaffold were extensively studied in the search for effective ion sensors.[3, 13, 14] However, very little emphasis has been placed on their biological activity and their potential as ligands for biologically relevant transition metals. The aim of this chapter is to provide an insight into how such molecules could be employed for biomedical applications.

2.2 Synthesis of the tripodal core

The first part of this project involved the synthesis of a library of multidentate systems suitable for the accommodation of the metal centre. To achieve this, the "pinwheel" hosts tris(bromomethyl)-trialkylbenzene derivatives were chosen as a starting point, as these an extensively explored synthetic tools for the construction of 1,3,5-trisubstituted cationic tripodal ligands. The rationale behind using hexasubstituted benzene scaffolds is to ensure a small, rigid backbone able to maintain a predetermined conformation upon insertion of the metal.

The synthesis of the hexasubstituted scaffolds including alternating Me/-CH_2Br and Et/-CH_2Br units were performed following the procedures outlined by van der Made for compound **60**,[15] and Anslyn for compound **61** (Scheme 2.1).[16]

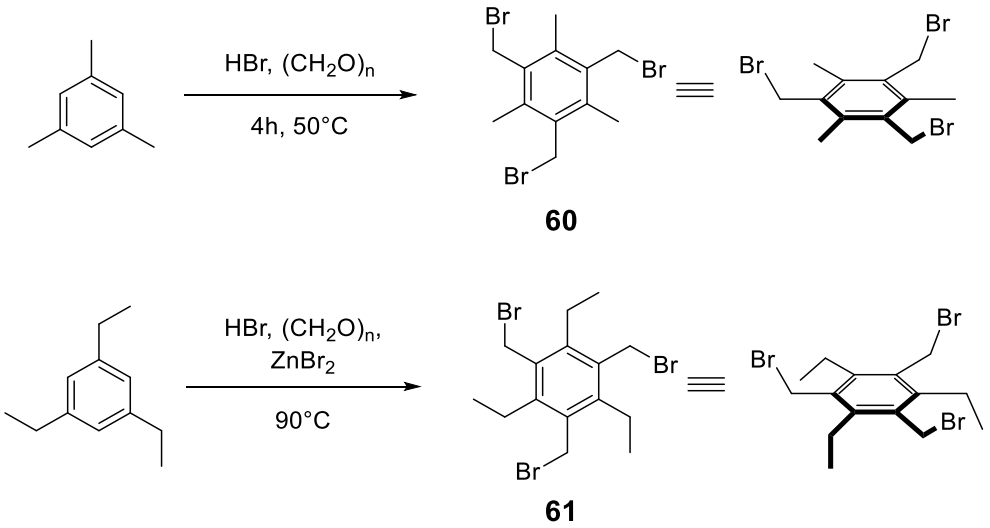

Scheme 2.1 Synthetic pathways for 1,3,5-tris(bromomethyl)mesitylene (compound **60**) and 1,3,5-tris(bromomethyl)-2,4,6-triethylbenzene (compound **61**).

Both products were characterised by ^{1}H NMR spectroscopy. For compound **60**, the ^{1}H NMR spectrum showed two series of signals, one singlet at 4.58 ppm, with an integration of 6H, corresponds to the three pairs of C*H*$_2$Br groups. The other peak, placed at 2.47 ppm, is a sharp singlet integrating for 9 protons, which represents the three methyl groups of the mesityl core (for the full ^{1}H NMR spectrum of **60** see Appendix A). ^{1}H NMR spectrum of compound **61**, reported in Figure 2.5, shows three sets of ^{1}H resonances, where the sharp singlet at 4.58 again corresponds at the six protons of the three C*H*$_2$Br as for compound **60**. The other two signals are a quartet placed at 2.94 ppm, with an integration of 6H, and at 1.34 ppm a triplet of intensity 9H, belonging respectively to the C*H*$_2$ and C*H*$_3$ of the three ethyl arms around the benzene core.

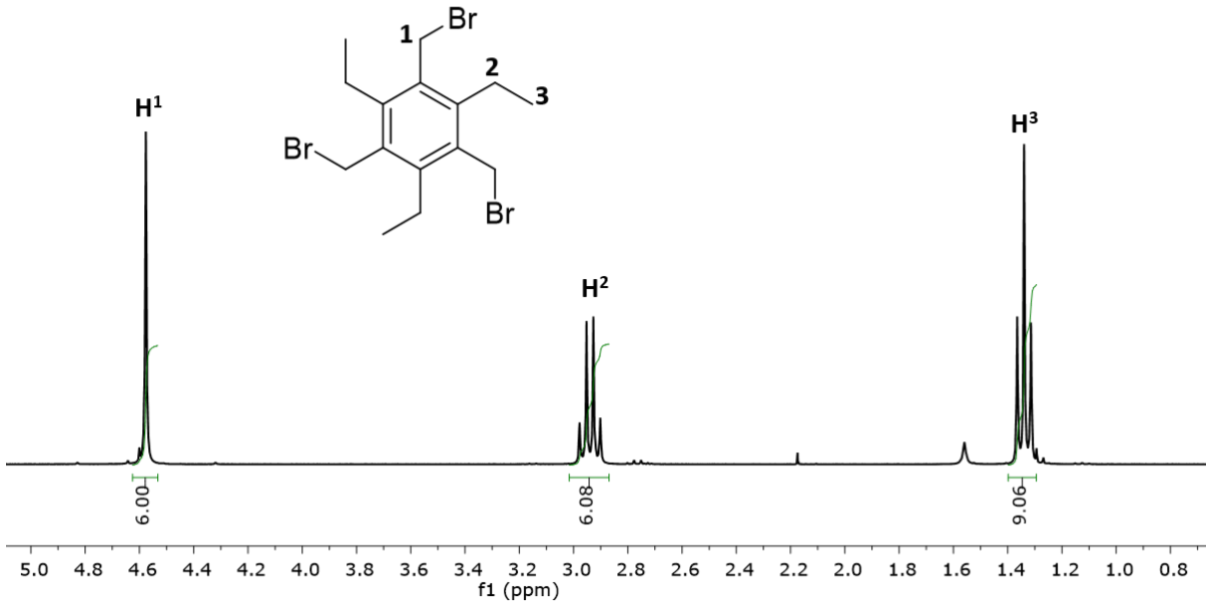

Figure 2.5. $_1$H NMR (300 MHz, $CDCl_3$, 298 K) spectrum of compound **61**. For clarity, magnetically equivalent nuclei within the same NMR spin system are labelled once.

2.3 Tripodal nitrogen-based systems

2.2.1 DABCO-based tripodal systems

With the aim of developing a simple tripodal system which includes characteristics such as predetermined conformation and solubility in aqueous solvents, a series of lipophilic cations of diazabicyclooctane (compounds **62** and **63**, Scheme 2.2) were investigated, and it was envisaged that these would be capable of forming metal complexes through host-guest interactions.

The reactions were carried out by reacting the two tribromo-substituted trialkylbenzene derivatives **60** and **61** with an excess of diazabicyclo[2.2.2]octane (DABCO). The two reactants were heated in refluxing acetonitrile for up to 36 hours until the formation of a cloudy suspension was observed. For both reactions, the precipitated products were filtered and carefully washed with aliquots of acetonitrile and diethyl ether in order to obtain a white water-soluble powder.

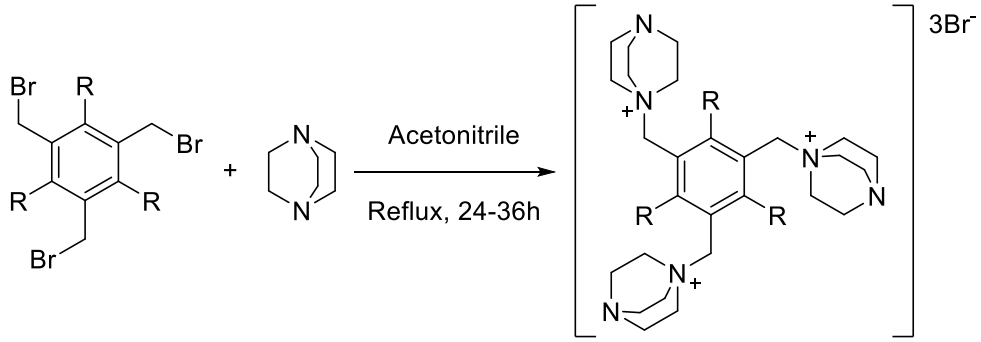

62, R = Me (85%)
63, R = Et (73%)

Scheme 2.2. Synthetic pathway for compounds **62** and **63**.

Both compounds were subsequently characterised by ^{1}H and ^{13}C NMR spectroscopy (see Figure 2.6 and Figure 2.7). The proton spectrum of compound **62** showed four main peaks corresponding to the four different groups of protons. The peak at 4.79 corresponds to the CH_2 that separates the hexasubstituted benzene and the quaternary amine of the bonded DABCO. The two intense peaks respectively at 3.51 and 2.97 ppm confirmed the presence of the DABCO substituents. Furthermore, the integration of these two peaks confirmed the presence of three

DABCO residues attached to the central core. Finally, the singlet at 2.59 indicates the presence of a methyl moiety attached to the benzene core.

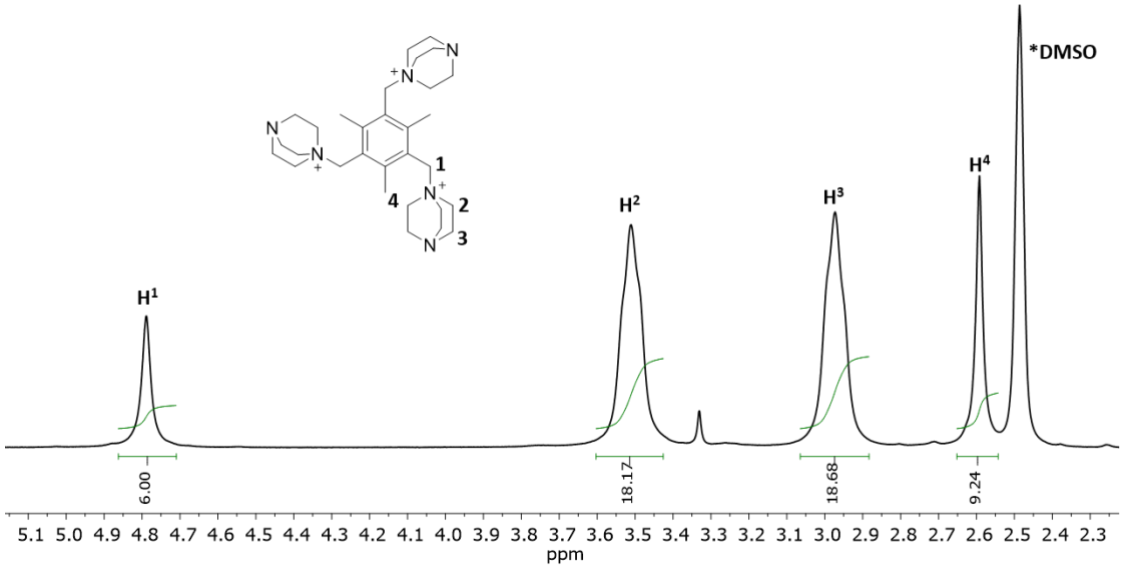

Figure 2.6. $_1$H NMR (300 MHz, DMSO-d$_6$, 298 K) spectrum of compound **62**. For clarity, magnetically equivalent nuclei within the same NMR spin system are labelled once. * CD_3SOCD_2H.

The proton spectrum of the compound **63**, displayed below in Figure 2.7, shows comparable chemical shifts to the spectrum of the compound **62**, with an additional peak at 0.82 ppm of intensity 9H that indicates the presence of the three C*H*$_3$ resonances, assignable to the ethylene "arms".

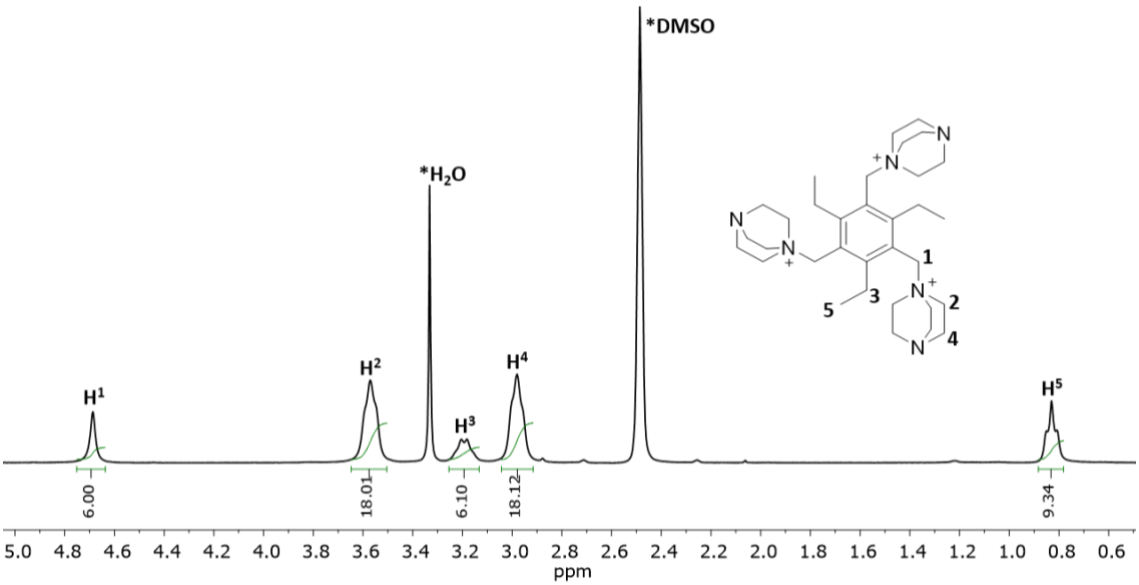

Figure 2.7. $_1$H NMR (300 MHz, DMSO-d$_6$, 298 K) spectrum of compound **63**. For clarity, magnetically equivalent nuclei within the same NMR spin system are labelled once.

The ^{13}C NMR spectrum for compound **63** is reported in Figure 2.8 below, and shows the presence of 7 signals, which were assigned as following: two low-fields signals, respectively at 154.90 and 122.70 ppm correspond to the two sets of quaternary carbons of the aromatic core; another two intense signals at 50.35 and 45.14 ppm were assigned to the methylene groups of the DABCO arms. Signals corresponding to the methylene groups are at 59.79 ppm for the C*H*$_2$ bridging the aromatic core to the quaternary nitrogen of the DABCO arms, and 25.60 ppm for the C*H*$_2$ groups of the ethylene arms. Finally, one up-field signal at 18.25 ppm was assigned to the C*H*$_3$ groups belonging to the ethylene arms.

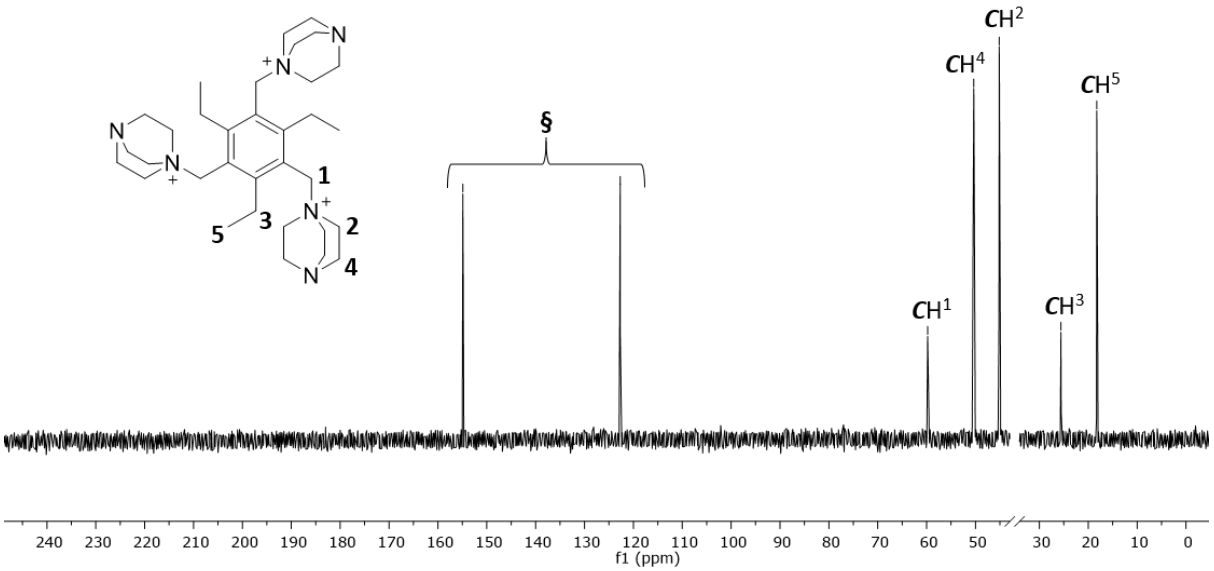

Figure 2.8. ^{13}C NMR (75 MHz, DMSO-d_6, 298 K) spectrum of compound **63**. **§** refers to aromatic **C** within phenyl ring. For clarity, magnetically equivalent nuclei within the same NMR spin system are labelled once.

From the mass spectrometry analysis carried out on compound **63** (reported below in Figure 2.9) it was possible to identify two ion species: the base peak of m/z = 697.3017 belonging to the singly charged species $[M+2^{79}Br]^+$, and the doubly charged ion fragment $[M+^{79}Br]^{2+}$ at m/z = 309.1903. This result may suggest that compound **63** possesses strong affinity for its counterion.

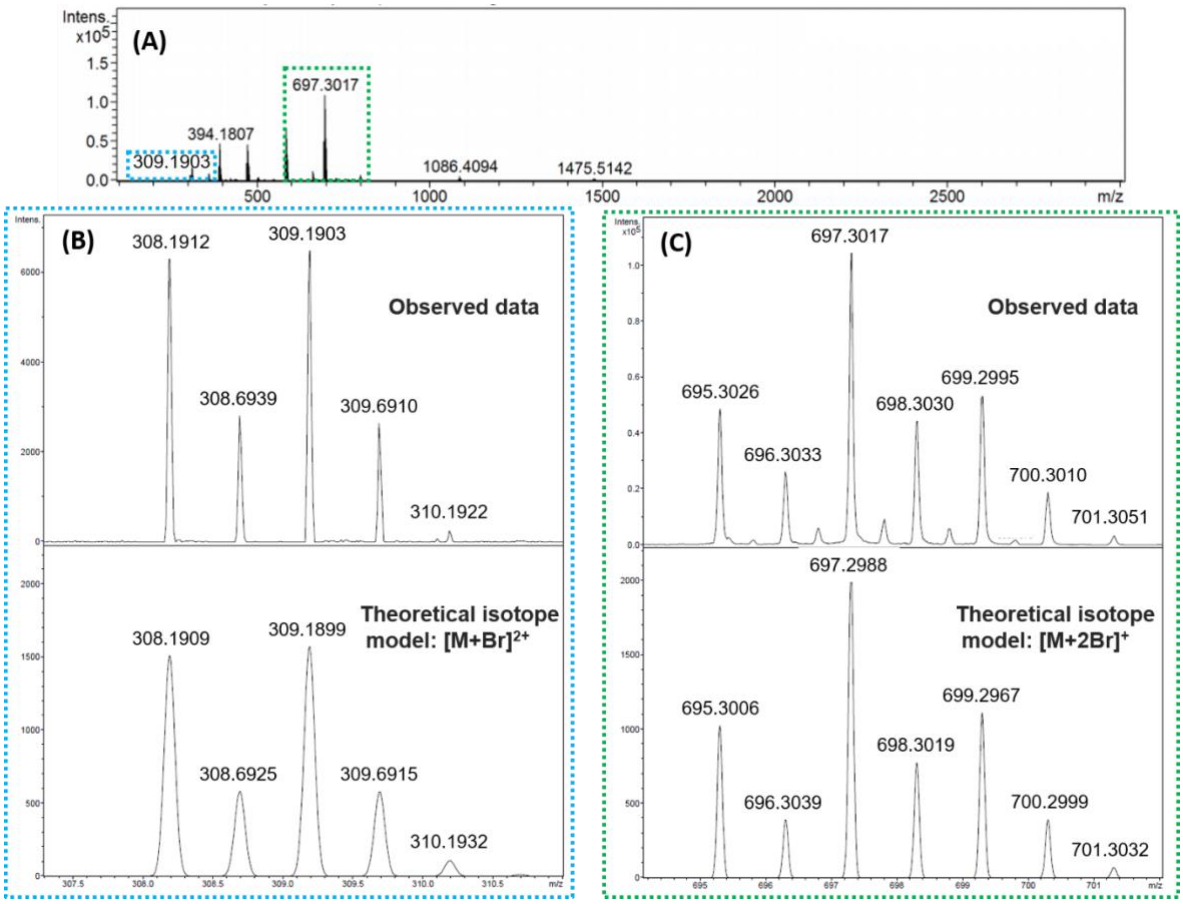

Figure 2.9. (A) Mass spectrum of compound **63**. **(B)** Ion species $[M+^{79}Br]^{2+}$ at m/z = 309.1903. **(C)** ion species $[M+2^{79}Br]^{+}$ at m/z = 697.3017.

In order to gain some preliminary evaluations on the activity of the synthesised tripodal systems in the cellular environment, cell viability assays were performed. In this work, cell viability was tested with the 2-(4,5-dimethyl-2-thiazolyl)-3,5-diphenyl-2H-tetrazolium bromide (MTT) assay, a widely accepted method to measure cell viability.[17, 18]

In this assay, the tetrazolium salt (MTT), a yellow-coloured dye, is taken by viable cells and may be reduced to Formazan (purple-coloured) by NADH/NADPH-dependant reductases in the cytoplasm and mitochondria (Scheme 2.3). A solvent (usually dimethyl sulfoxide) is then added to dissolve the insoluble purple formazan product and the absorbance of this coloured solution is measured. This can then be correlated with the number of metabolically active (thus viable) cells.[19]

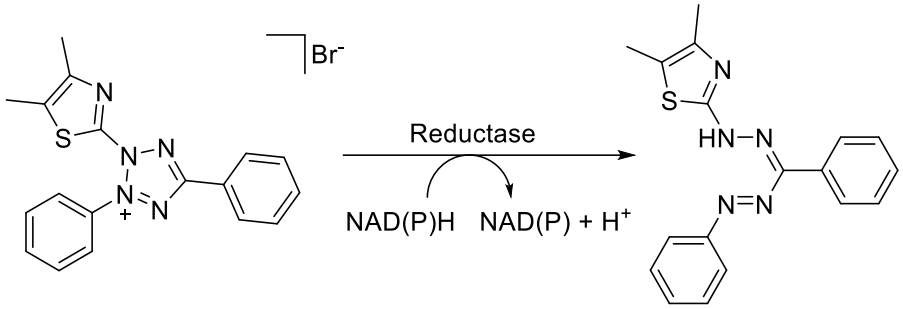

Scheme 2.3. Reduction of MTT into formazan by cellular reductases.

Cellular viability assays were carried out in PC3 cells in 96 well plates incubated with compounds **62** and **63** in serum medium (1% DMSO) at different concentrations and times (30 minutes, 24, 48 and 72 hours) at 37°C. MTT was then added and the treated cells incubated for 2 hours before recording the absorbance with a plate reader. The MTT assays showed herein were carried out by Dr Haobo Ge at the University of Bath.

Treatment of PC3 cells with **62** did not significantly perturb the cell viability at any concentration tested. Moreover, cell viability recovered to pre-treatment levels after 48 hours. Treatment with compound **63** produced a small loss in viability at the highest concentrations studied after 24 hours, with recovery of viability being observed after 72 hours.

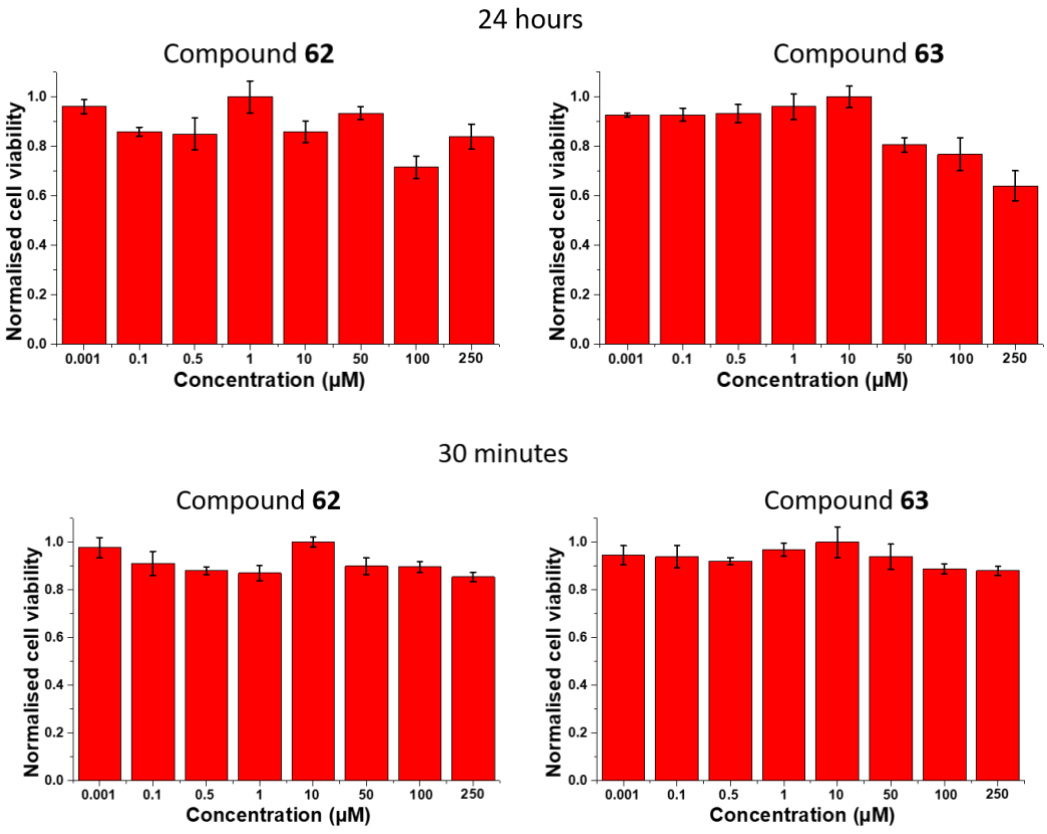

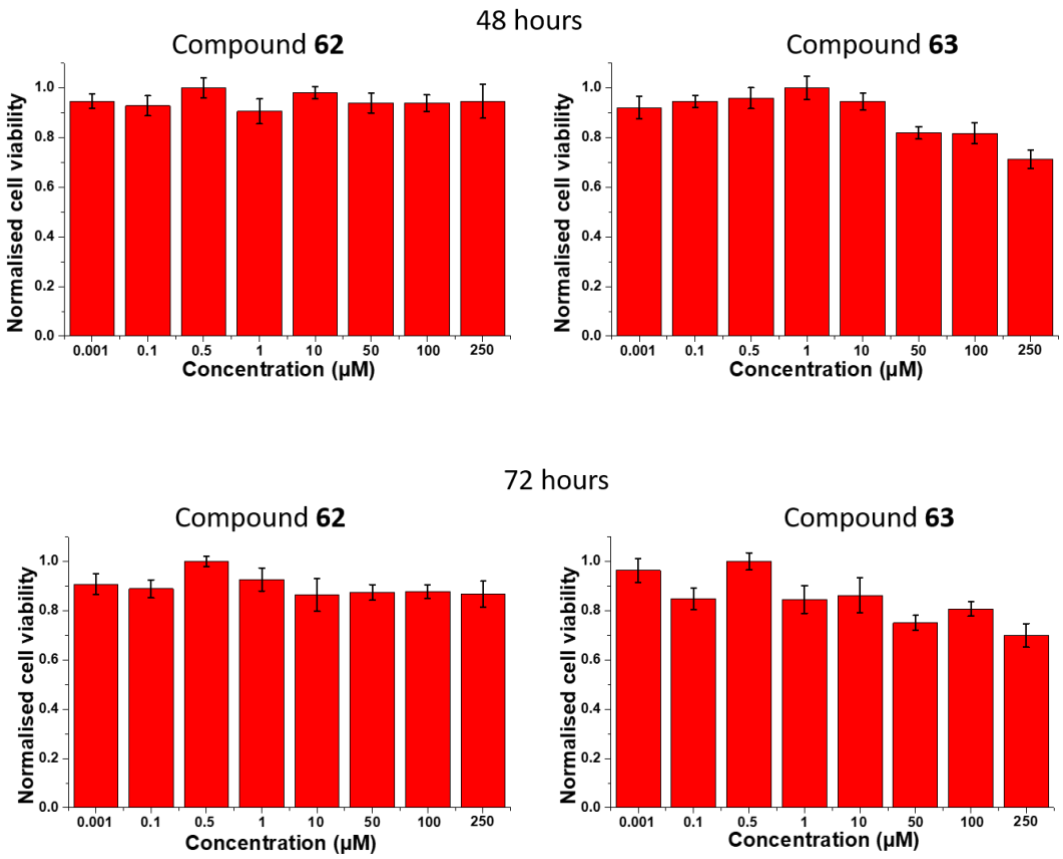

Figure 2.10. Cell viability studies of PC3 cells incubated at 37°C with compounds **62** (left) and **63** (right) for 30 minutes, 24, 48 and 72 hours. (The data were collected from six repeated measurements on the same day, N = 1).

2.2.2 Bipyridine-based tripodal systems

With the aim of increasing the cavity size as well as introducing valuable spectroscopic properties (such as luminescence), we attempted the synthesis of more flexible ligands by varying the "arms" attached to the trialkylbenzene unit. Tripodal ligands such as 1,3,5-tris(3-pyridylmethoxyl)benzene, 1,3,5-tris(2-pyridylmethoxyl)benzene, and 1,3,5-tris(4-pyridylmethoxyl)benzene have been successfully used previously to generate metalorganic cages in the presence of metal halides emitting between 400 and 550 nm.[20]

We, therefore, opted for 4,4'-bipyridine as a binding moiety in order to obtain a series of tripodal ligands characterised by an enhanced flexibility with the potential to generate luminescent supramolecular assemblies with a bigger cavity (see Scheme 2.4). Furthermore, the highly delocalised positive charge of the three bipyridinium arms was expected to make these compounds potential delocalised lipophilic cations (DLC).[21-24]

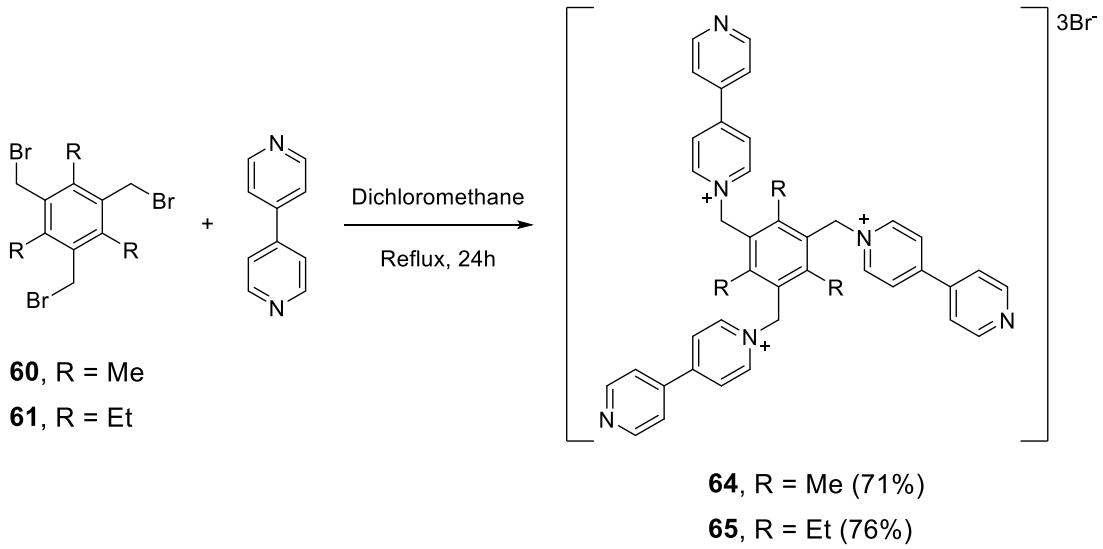

Scheme 2.4. Synthetic pathway for compounds **64** and **65**.

The two compounds (**64** and **65**) were synthesised following an adapted procedure outlined by Steed *et al.*[25], by reacting the bromomethyl benzene compounds **60** and **61** with a 10-fold excess of 4,4'-bipyridine in refluxing dichloromethane for 24 hours. The resulting precipitates were collected by filtration and washed thoroughly with dichloromethane to give in both cases a hygroscopic yellow powder. For compound **65**, ^{1}H and ^{13}C NMR showed chemical shifts comparable to literature values[25], and its mass spectrum, acquired with a Nano-ESI instrument at the EPRSC UK National Mass Spectrometry Facility in Swansea, showed a base peak at 223.1230 m/z corresponding to the triply-charged molecular ion $[M]^{3+}$ (see appendix A).

For the newly synthesised compound **64**, the ^{1}H NMR spectrum (reported in Figure 2.11) shows four series of multiplets between 8 and 9 ppm belonging to the 4,4'-bipyridinium arms, a singlet at 6.17 ppm corresponding to the six protons of the methylene linkers connecting the 4,4'-bipyridyl arms to the mesitylene core and an intense singlet at 2.40 ppm belonging to the three mesityl C*H*$_3$ resonances.

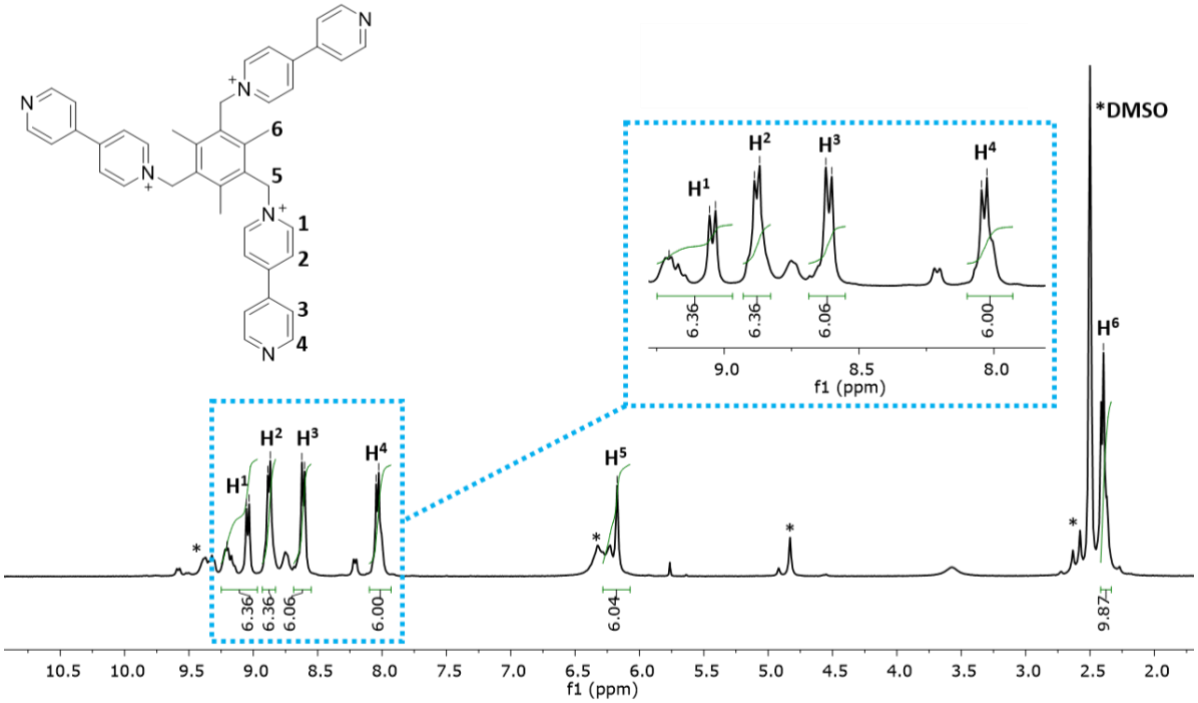

Figure 2.11. ^{1}H NMR (300 MHz, DMSO-d$_6$, 298 K) spectrum of compound **64**. For clarity, magnetically equivalent nuclei within the same NMR spin system are labelled once. * residual solvents and impurities traces.

UV-Visible and fluorescence spectroscopy were subsequently carried out to investigate the emissive properties of **64** in DMSO solution. The UV-visible spectrum (blue curve in Figure 2.12) showed an absorption maximum of 267 nm, while the fluorescence emission spectrum (red curve in Figure 2.12) presented a minimal Stokes shift, with an intensity maximum at 280 nm.

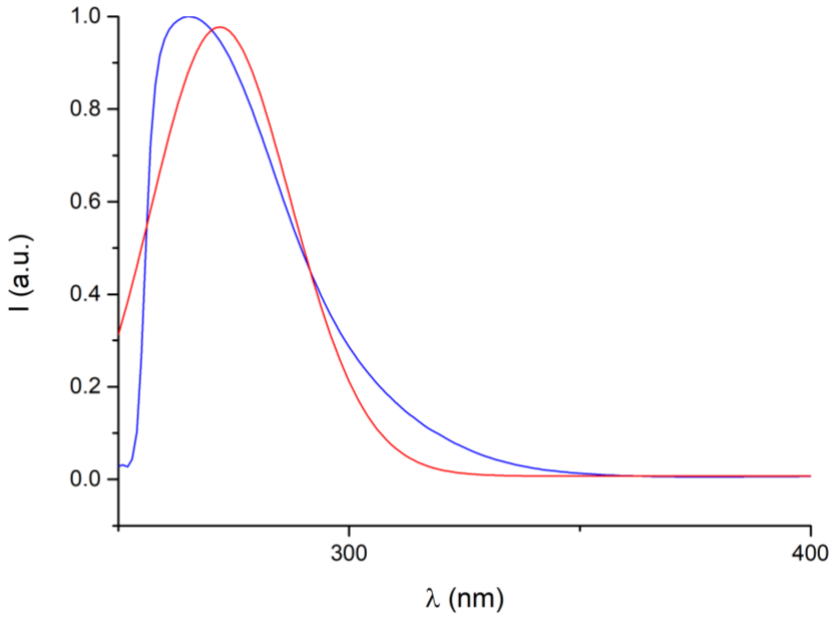

Figure 2.12. Normalised UV-Visible (blue line) and fluorescence emission (red line) spectra of compound **64** in DMSO (25 μM).

Mass spectrometry analysis for compound **64**, reported in Figure 2.13, showed the presence of a peculiar peak at 353.1202 m/z belonging to the dicationic species $[M+^{79}Br]^{2+}$ in which the third positive charge appears to be quenched by the presence of a bromide ion tightly interacting with compound **64**.

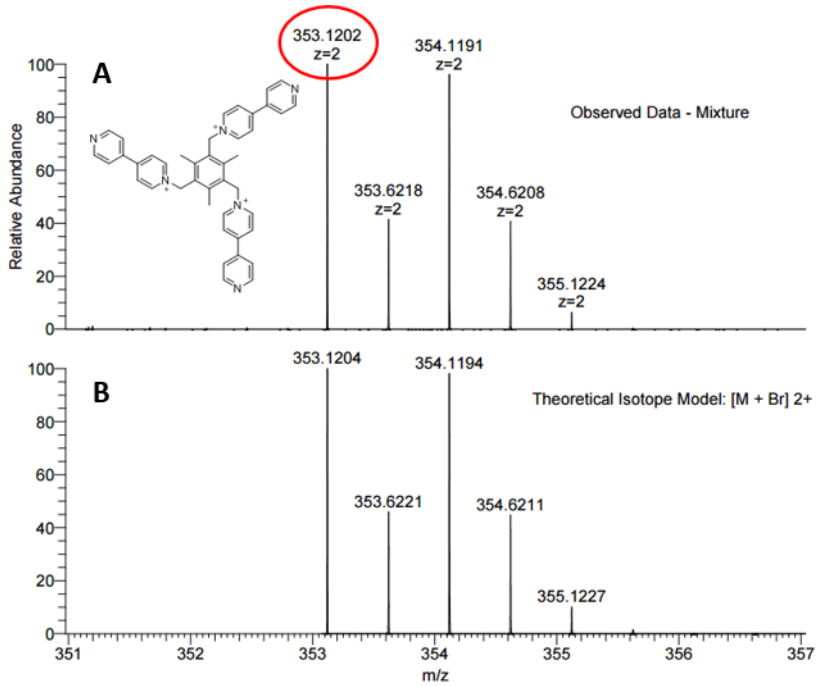

Figure 2.13. Mass spectrum of compound **64** (**A**) and its simulated isotopic pattern (**B**).

Interestingly, Steed and co-workers reported a comparable example of such interaction in a solvent-free crystal structure of compound **65**, shown in Figure 2.14. This acts as a first sphere ligand for bromide by interacting with the anion with CH···Br- hydrogen bonds.[25]

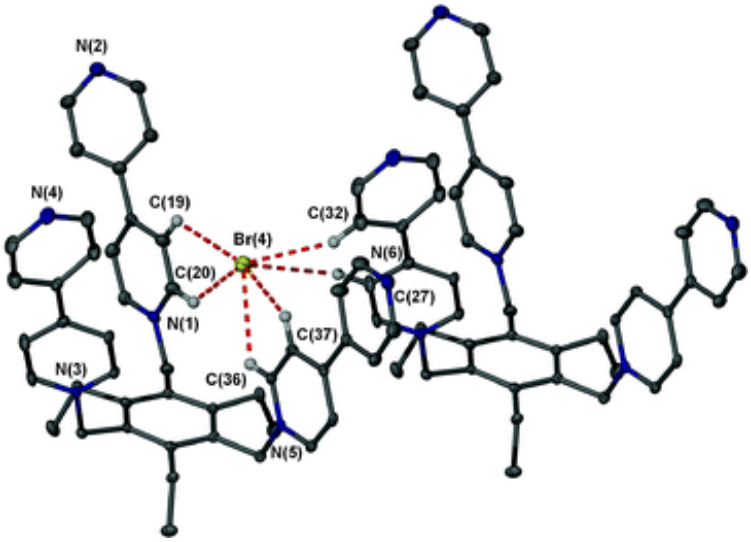

Figure 2.14. Solvent free [**65**⊂Br]$^{2+}$ incorporating CH · Br interactions 2.660–2.977 Å. Adapted from Ref.[25] with permission from The Royal Society of Chemistry.

It was possible to obtain single crystals suitable for X-ray analysis of compound **64** upon slow diffusion of acetonitrile into a concentrated aqueous solution of **64**. Compound **64** crystallises in a P-1 space group and, as for its analogue compound **65**, adopts a C_3 symmetry. From the structure reported in Figure 2.15 it is possible to appreciate the presence of a bromide ion interacting with the ligand *via* CH···Br- hydrogen bonds, found at an average distance between 2.8 and 2.9 Å.

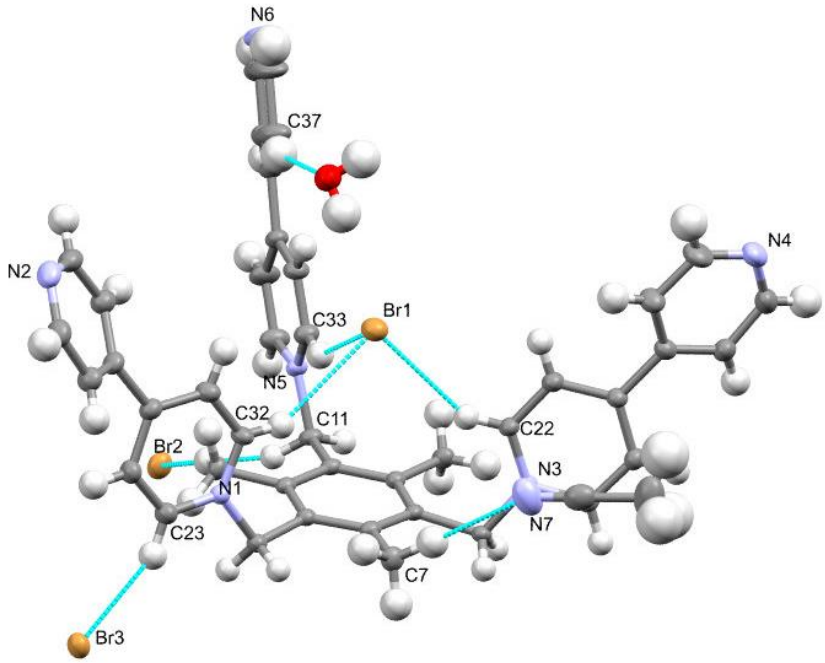

Figure 2.15. Content of the asymmetric unit of compound **64**. Thermal ellipsoids represented at 50% probability.

Interestingly, two molecules of compound **64** were found to form a cage surrounding two bromide ions and two solvent water molecules (Figure 2.16). Such a cage-like structure is similar to the previously reported receptor **B** (Figure 2.4) prepared by Davis and co-workers.[11]

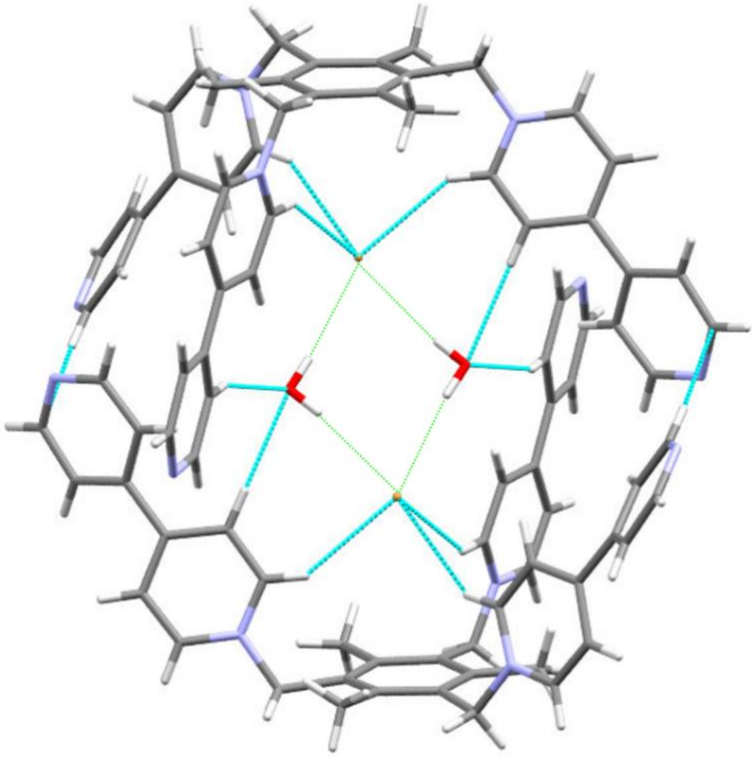

Figure 2.16. Structure of the dimeric cage formed by compound **64** encapsulating two bromide ions and two water molecules.

As for the previous tripodal receptors discussed in this work, the two bipyridine-based compounds **64** and **65** were tested in cell viability assays. In this case, it was of particular interest to assess whether or not the compounds might be taken up by cancer cells, given their lipophilic cationic nature. While compound **65** was found to be nontoxic at all the concentrations studied, PC3 cells incubated with **64** at a concentration of 100 and 250 μM for 30 minutes showed a moderate loss of cell viability. Cell viability only recovered to values above 50% after 72 hours from the initial treatment, suggesting that compound **64** does inhibit cell viability at higher concentrations.

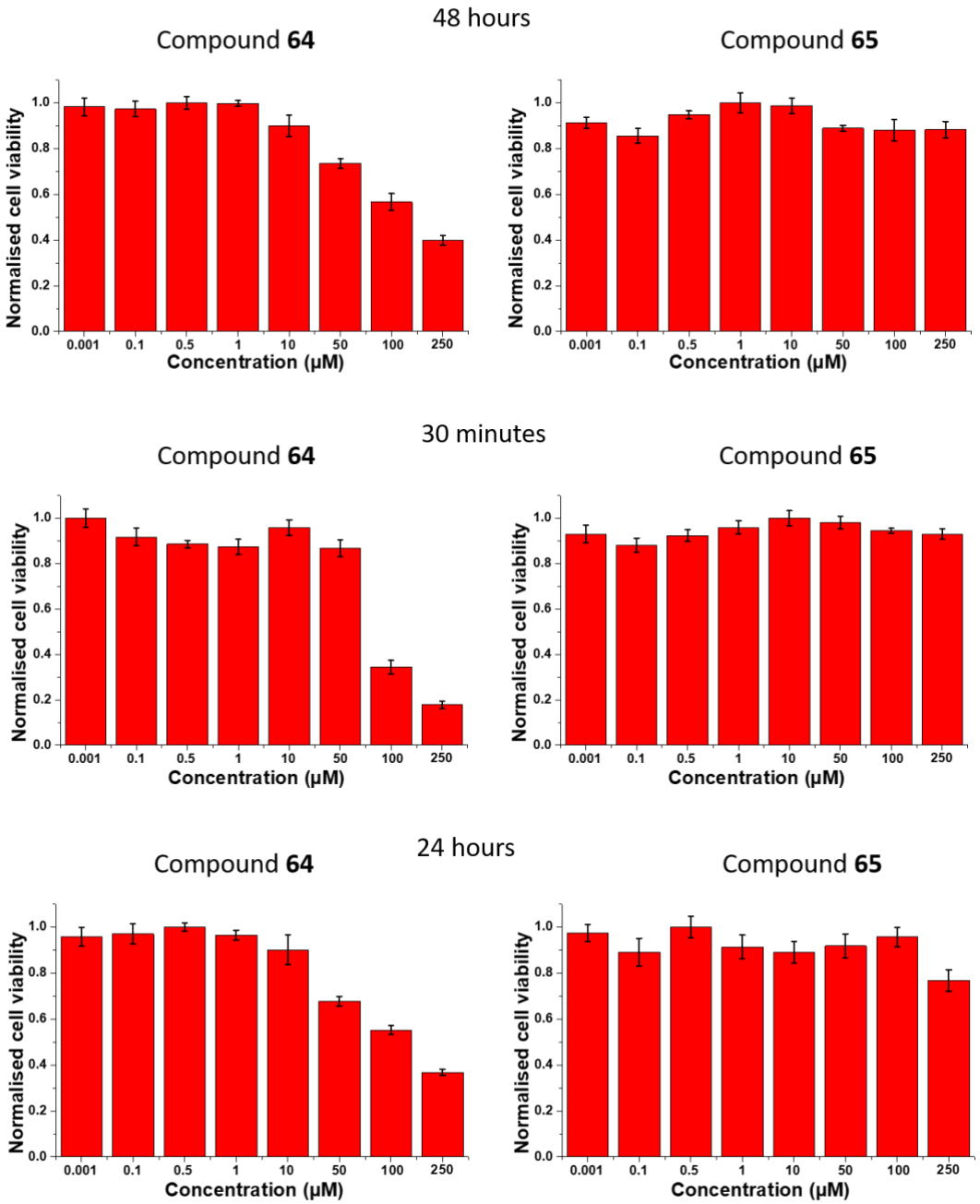

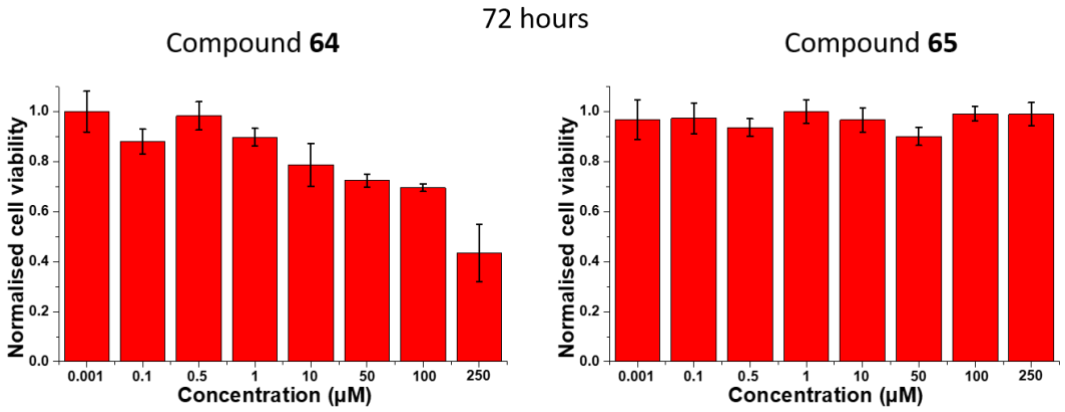

Figure 2.17. Cell viability studies of PC3 cells incubated at 37°C with compounds **64** (left) and **65** (right) for 30 minutes, 24, 48 and 72 hours. (The data were collected from six repeated measurements on the same day, N = 1).

In order to investigate the cellular uptake of the bipyridine-based tripodal ligands and their fluorescence properties within a cellular environment, single-photon laser-scanning confocal microscopy (SLSCM) analysis was performed. PC3 cells were grown following standard culturing methods further described in Chapter 7.

Figure 2.18 shows images taken in the confocal mode of PC3 cells upon 20 min incubation with compound **64**. The images show moderate emission across all the visible wavelengths when the probe was excited at 405 nm ($a_{1\text{-}5}$), while only green-red ($b_{1\text{-}5}$) and red ($c_{1\text{-}5}$) emissions are visible using 488 nm and 561 nm lasers respectively. Compound **64** appears to be taken up in PC3 cells and localise throughout the cytoplasm. Furthermore, there is no emission from the nuclei, suggesting that the compound is unable to cross the nuclear membrane.

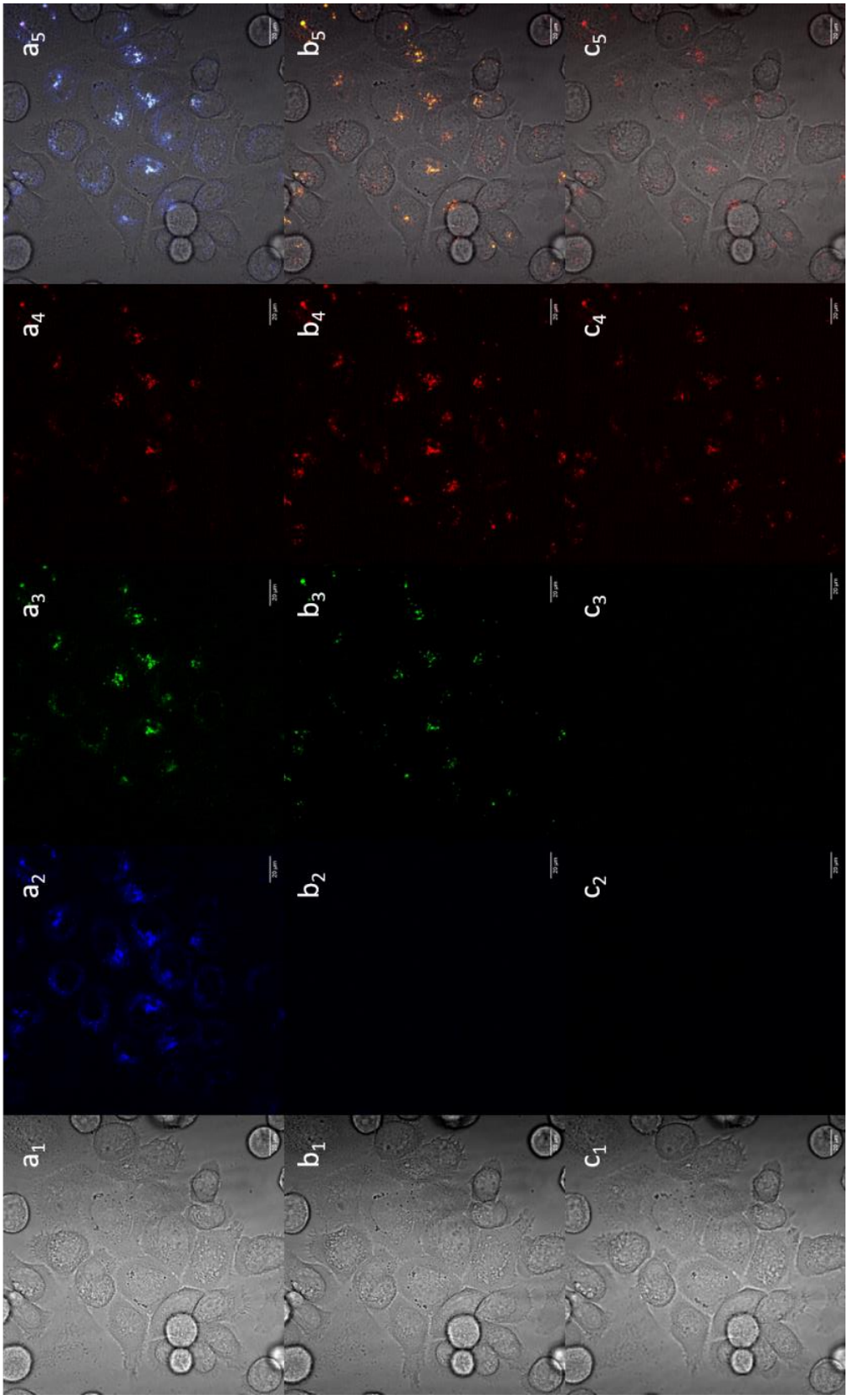

Figure 2.18. Single-photon laser-scanning confocal microscopy images of PC3 cells incubated with compound **64** (10 μg/mL 1% : 99% DMSO : DMEM) at 37 ºC for 20 minutes; λ_{ex} = 405 nm (a_1-a_5), λ_{ex} = 488 nm (b_1-b_5) and λ_{ex} = 561 nm (c_1-c_5). DIC channel (a_1, b_1, c_1), blue channel, λ_{em} = 420-480 nm (a_2, b_2, c_2), green channel, λ_{em} = 516-530 nm (a_3, b_3, c_3), red channel λ_{em} = 615-650 nm (a_4, b_4, c_4), and overlapping of the DIC, blue, green and red channels (a_5, b_5, c_5). Scale bar: 20 μm.

2.4 Tripodal anthracene-thiosemicarbazone based ligands

In this section we describe the syntheses and characterisation of two novel tripodal anthracene-thiosemicarbazone systems bearing the hexasubstituted cores **60** and **61** and anthracene-based arms connected to the core through a thiosemicarbazone linker. The rationale behind those experiments was to develop tripodal ligands characterised by enhanced flexibility and superior emissive properties compared to the bipyridine-based compound **64** and **65**. The tripodal nitrogen-based systems discussed before were promising in terms of cellular interaction, but were weakly or non-fluorescent and also missing some essential cell recognition features such as thiosemicarbazone motif.[26] Furthermore, the novel systems should be theoretically capable of accommodating larger transition metals complexes of relevance to molecular imaging, such as ruthenium or rhenium.

Anthracene is a polycyclic aromatic hydrocarbon (PAH) characterised by intense fluorescence (*e.g.* its quantum yield in acetonitrile is 0.36).[27] Absorption spectra of Anthracene and its derivatives typically show three well-defined bands between 340 and 390 nm, while the emission spectrum is composed of distinct bands around 415 nm.[28] Such interesting luminescent properties, coupled with the commercial availability of many derivatives, make anthracene-based compounds an interesting area of exploration.

The preparation of compound **66** involved an acid-catalysed imine condensation between 9-anthracenecarboxaldehyde and thiosemicarbazide, following a procedure elucidated by Beckford and co-workers.[29] The two reactants were dissolved in anhydrous absolute ethanol, followed by the addition of one or two drops of glacial acetic acid. The reaction mixture was stirred under reflux for four hours and upon cooling a precipitate was formed, which was collected by filtration and washed thoroughly with ethanol and diethyl ether to give compound **66** as a yellow powder. Recrystallization in hot tetrahydrofuran afforded the product as orange crystals in high yield (90%). A detailed mechanism for the reaction is shown in Scheme 2.5 below.

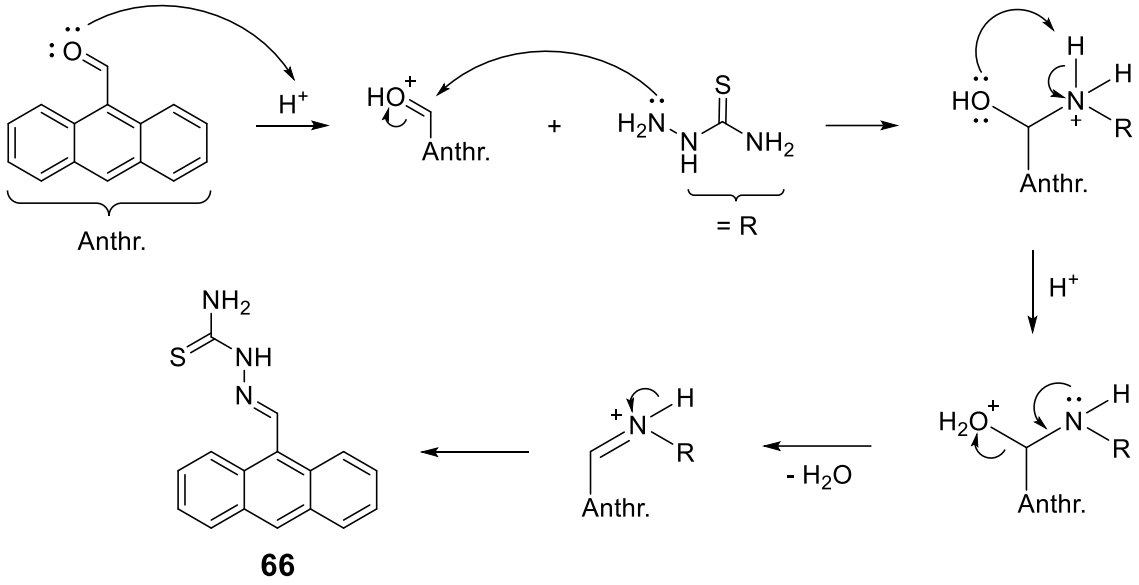

Scheme 2.5. Proposed reaction mechanism of the acid-catalysed imine condensation leading to compound **66**.

^{1}H NMR analysis of compound **66** was performed and the resulting spectrum is reported in Figure 2.19. This shows a resonance at 11.68 ppm assignable to the hydrazinic proton H_1. Such a downshifted resonance is due to the tautomerism of thiosemicarbazones in solution and was reported in a previous study.[30]

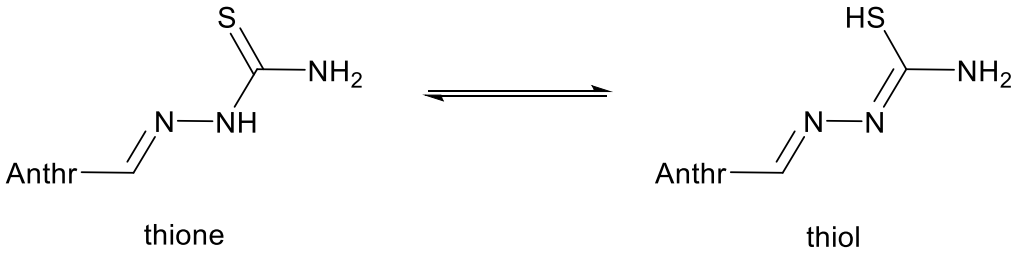

Scheme 2.6. Thione-thiol tautomerism in compound **66**.

Two more resonances, observed at 8.36 and 7.75 ppm, could be attributed to the geminal N-H_2 protons (labelled H_5 and $H_{5'}$ in the spectrum shown in Figure 2.19). Such a shift to downfield resonances appears to be an indication of the hindered rotation due to the SC-NH_2 bond containing a partial double bond character.[29]

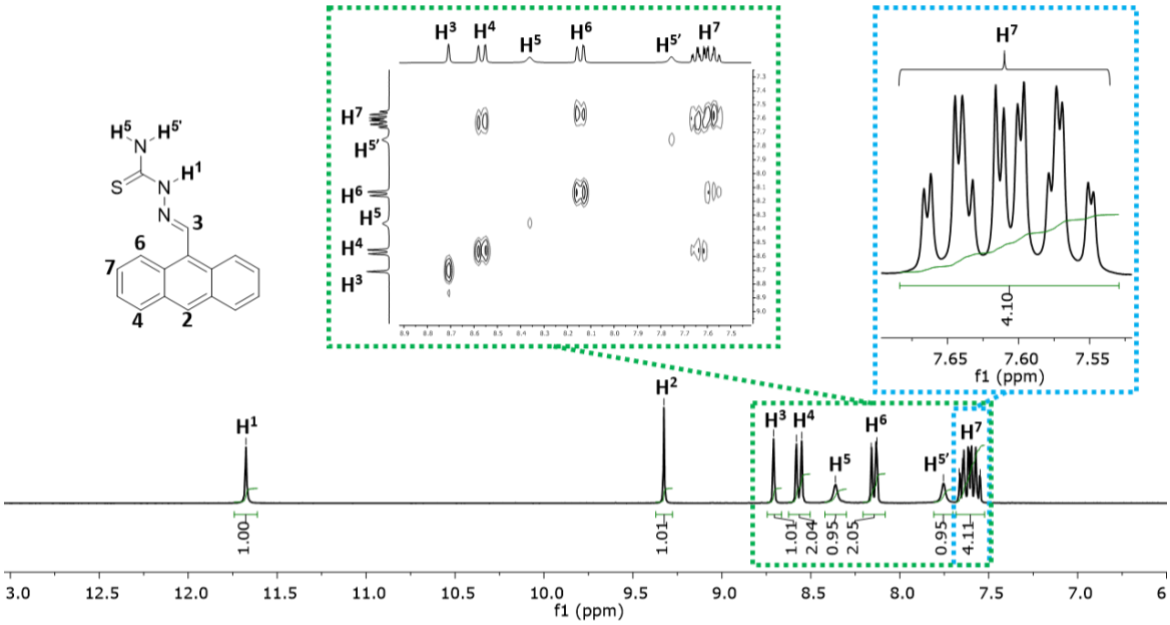

Figure 2.19. $_1$H NMR (300 MHz, DMSO-d$_6$, 298 K) spectrum of compound **66**. Green dotted box: $_1$H-$_1$H COSY NMR (300 MHz, DMSO-d$_6$, 298 K) spectrum expansion highlighting anthracene protons couplings. For clarity, magnetically equivalent nuclei within the same NMR spin system are labelled once.

The syntheses of two tripodal-anthracene-thiosemicarbazone ligands (referred as compounds **67** and **68** throughout this work) was achieved by a nucleophilic substitution on the hexasubstituted cores **60** or **61** with the anthracene-thiosemicarbazone (compound **66**). The reactants were dissolved in dry acetonitrile, and the resulting mixture was refluxed overnight to obtain a yellow precipitate. After cooling to room temperature, in both cases the precipitate was filtered, thoroughly washed with fresh acetonitrile and dried.

Neutralisation of the thiosemicarbazone units was subsequently performed by treating a methanolic solution of the products above with an excess of triethylamine. Upon addition of the base, a bright yellow precipitate immediately formed. The slurry was kept stirring at room temperature for further 24 hours. After that time, the precipitates were filtered, washed extensively with methanol and dried to give the products **67** and **68** in very good yields (94% and 92% respectively).

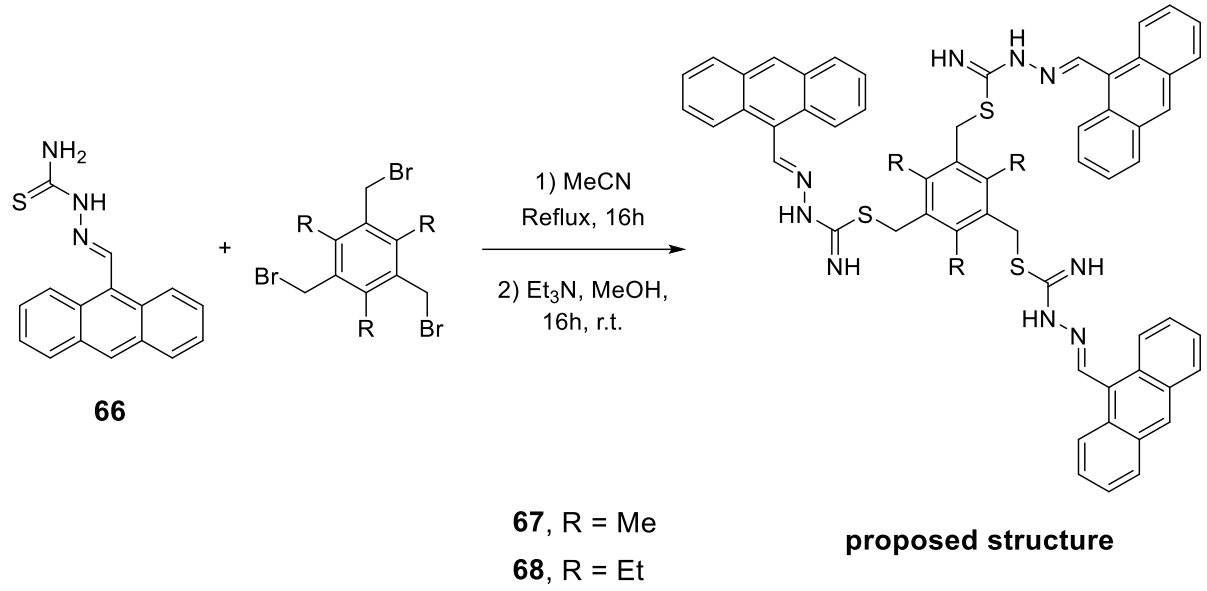

Scheme 2.7. Synthetic pathway for compounds **67** and **68**.

The ^{1}H NMR spectrum of **67**, reported in Figure 2.20, shows a series of eight peaks. A resonance found at 9.62 ppm (integrating for 3H) was attributed to the hydrogen in position 10 of the anthracene ring (entry H_1 in Figure 2.20). The following doublet at 8.68 ppm of intensity 6H was correlated to the anthracene protons in the positions 4 and 5, while the other doublet at 8.03 ppm corresponds to the protons in positions 1 and 8 respectively. To complete the assignment of the signals related to the anthracene, a multiplet positioned between 7.55 and 7.48 ppm was assigned to the four sets of protons in the positions 2,3 and 6,7 respectively. A last significant signal in the aromatic region of the spectrum of **67** is a singlet at 8.49 ppm, integrating for 3H, which was assigned to the H_3-C=N connecting the anthracene tags to the thiosemicarbazone linkers.

Outside the aromatic region, a broad resonance at 5.55 ppm was assigned to the hydrazinic proton (entry H_6, Figure 2.20) while the resonance at 4.65 ppm was assigned to the protons of the methylene linker connecting the anthracene-thiosemicarbazone arms to the aromatic core. Finally, a signal at 2.70 ppm and integrating for 9 protons was assigned to the three mesityl CH_3 resonances.

NMR spectroscopy analysis of compound **68**, with the ^{1}H NMR spectrum reported in Figure 2.21, shows 9 sets of resonances, suggesting that the compound is C_3 symmetric. The spectrum is comparable to the one of the previously synthesised compound **67** with the exception of the two upfield signals (labelled H_8 and H_9 in Figure 2.21), which have been assigned to the two sets of alkyl protons of the three ethyl groups bonded to the central aromatic core.

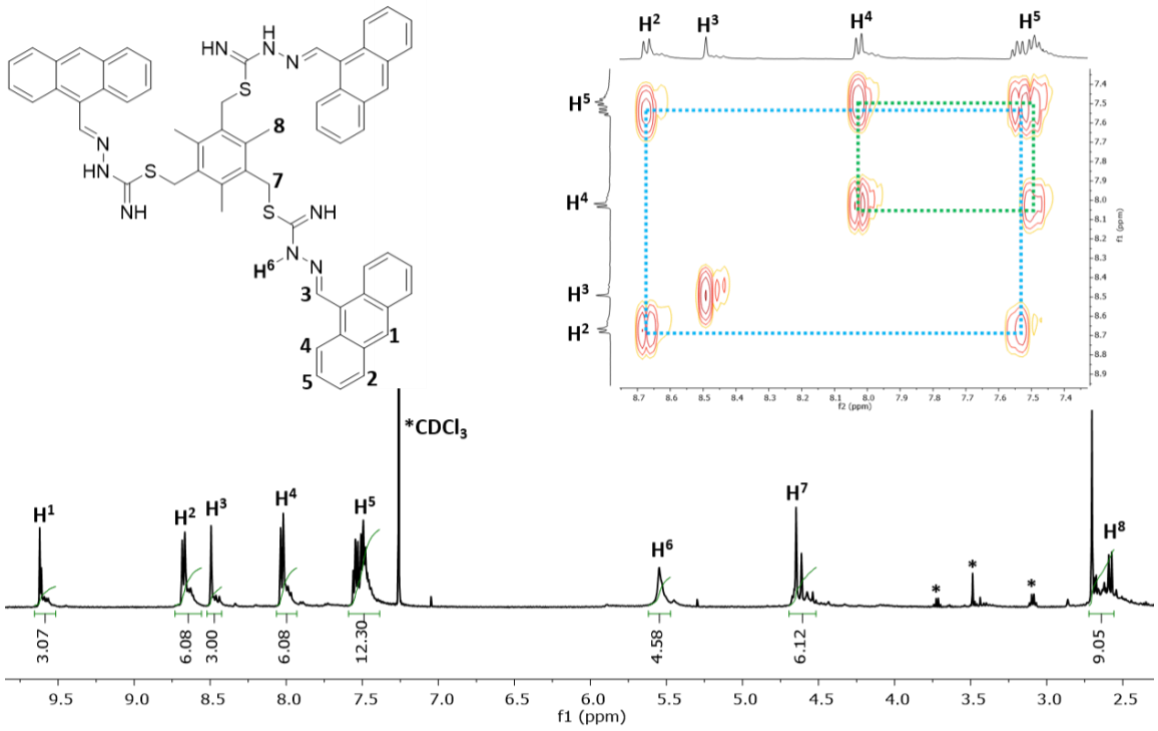

Figure 2.20. 1H NMR (500 MHz, $CDCl_3$, 298 K) spectrum of compound **67** and a detail of the 1H-1H COSY spectrum highlighting the aromatic region. For clarity, magnetically equivalent nuclei within the same NMR spin system are labelled once. * residual solvents and impurities traces.

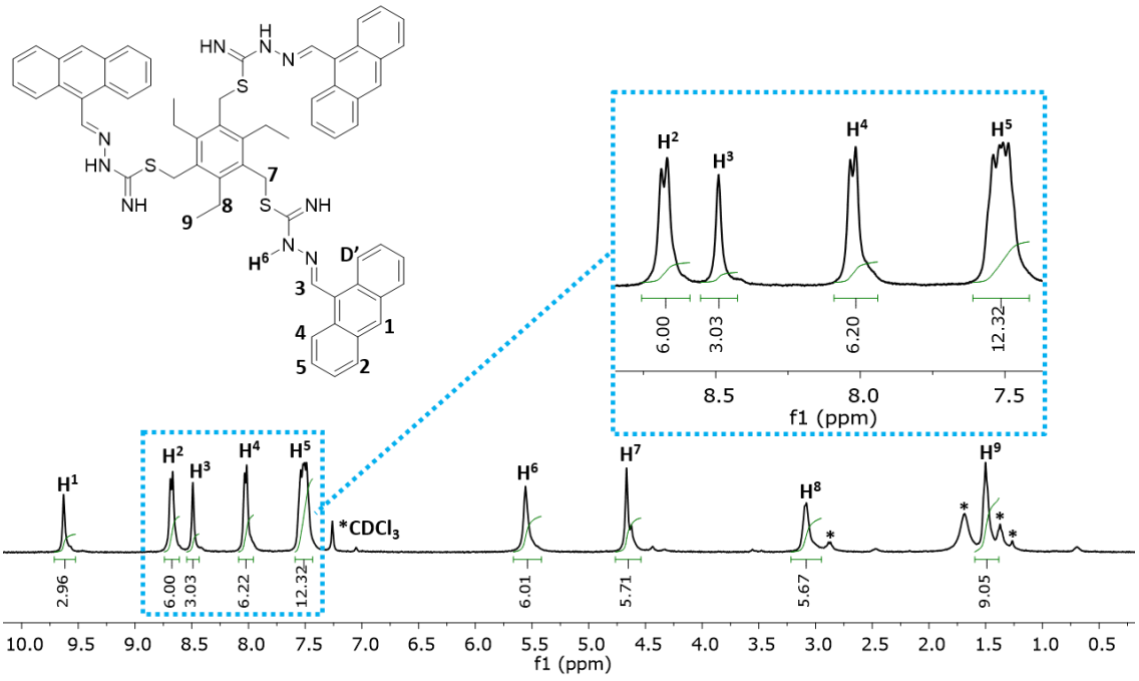

Figure 2.21. 1H NMR (500 MHz, $CDCl_3$, 298 K) spectrum of compound **68**. Blue dotted box: detail of the the aromatic region. For clarity, magnetically equivalent nuclei within the same NMR spin system are labelled once. * residual solvents and impurities traces.

Mass spectrometry analysis performed on compound **67**, acquired at the EPRSC UK National Mass Spectrometry Facility in Swansea, showed a base peak at 994.3497 m/z corresponding to the protonated molecular ion $[M+H]_+$. The mass spectrum **67**, with details of the molecular ion species and assignments are given below, in Figure 2.22.

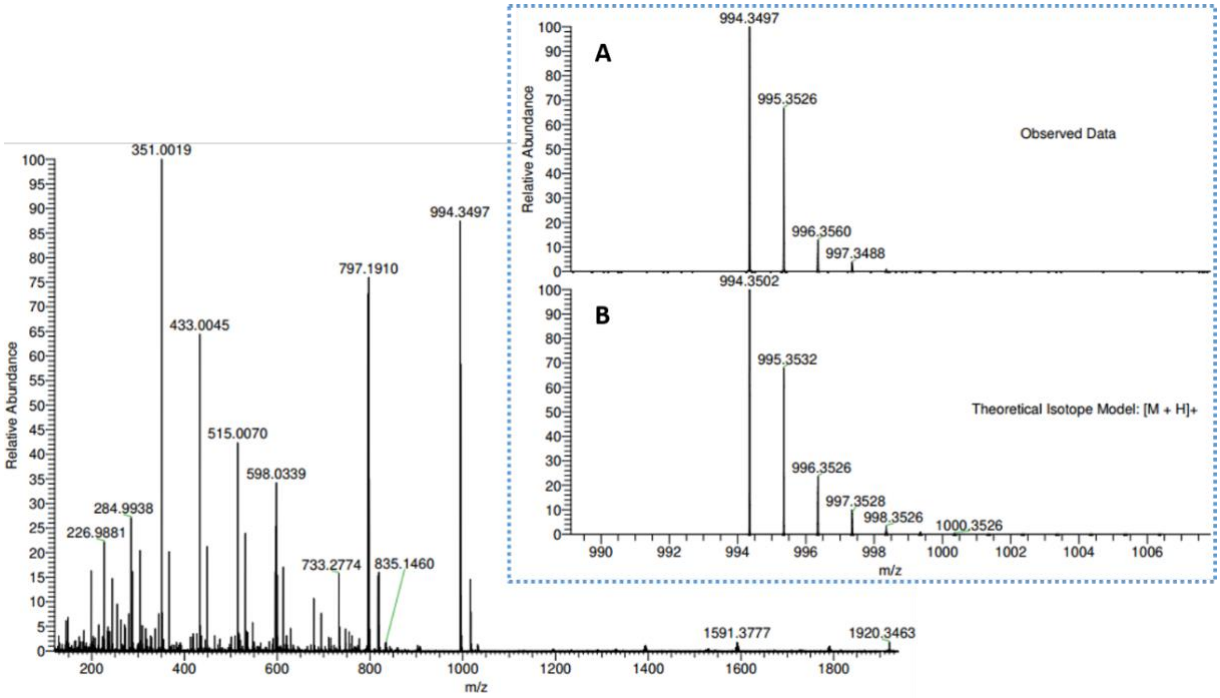

Figure 2.22. Mass spectrum of compound **67**. Blue dotted box: details of the molecular ion (**A**) and its simulated isotopic pattern (**B**).

Analysis of the mass spectrum acquired for compound **68**, reported in Figure 2.23, indicates the presence of a protonated molecular ion $[M+H]_+$ at 1036.4016 m/z, as well as the sodium adduct assignable to $[M+Na]_+$, of m/z = 1058.3903.

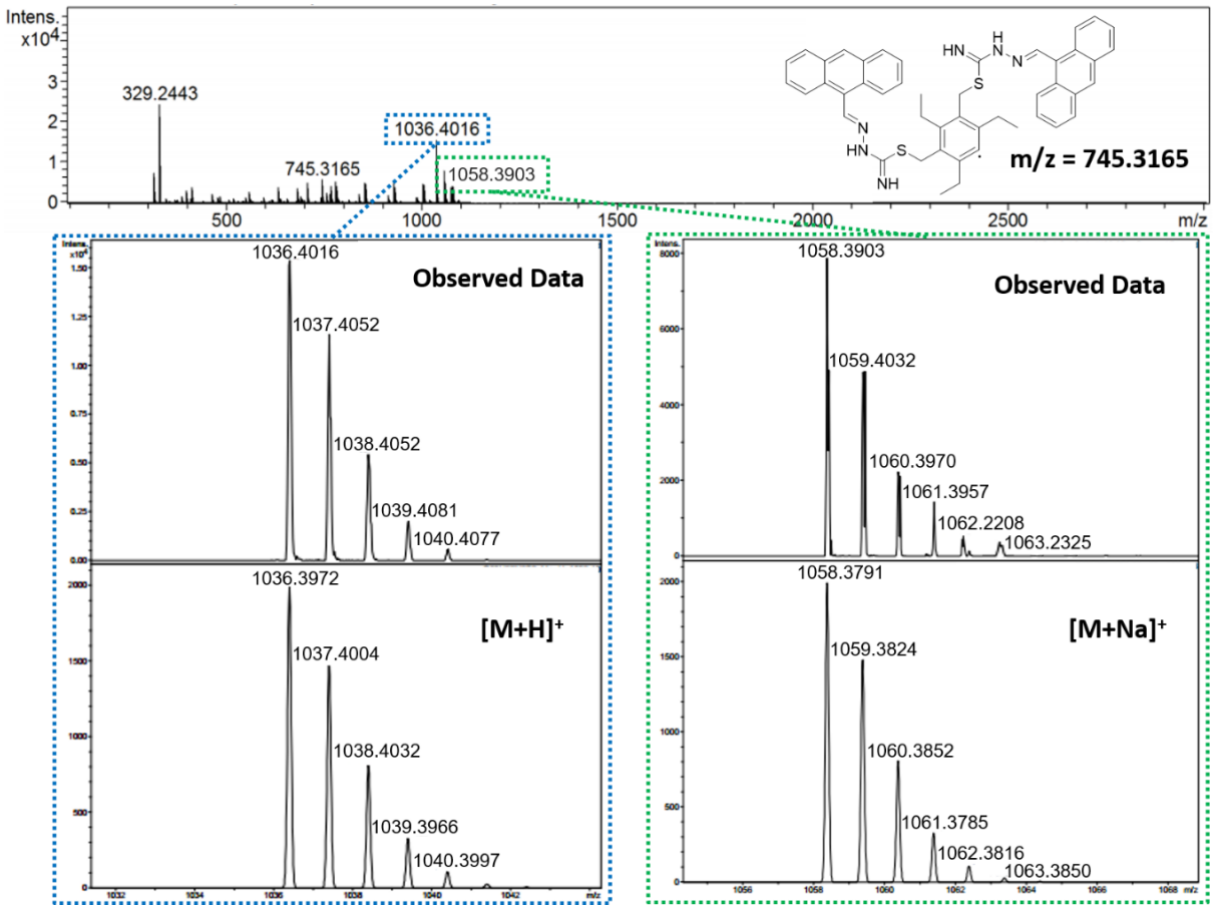

Figure 2.23. Mass spectrum of compound **68**. Blue dotted square: Ion species $[M+H]_+$ at 1036.4016 m/z. Green dotted square: ion species $[M+Na]_+$ at 1058.3903 m/z.

UV-Visible and fluorescence emission spectroscopies were employed to evaluate compounds **67** and **68** as potential imaging agents. Both compounds presented an absorption wavelength maximum at around 400 nm. The absorption spectrum of compound **68** clearly shows the three characteristic bands of the anthracene moiety at 350, 370 and 390 nm. The emission wavelengths for both compounds are in the visible region at around 440 nm (Figure 2.24).

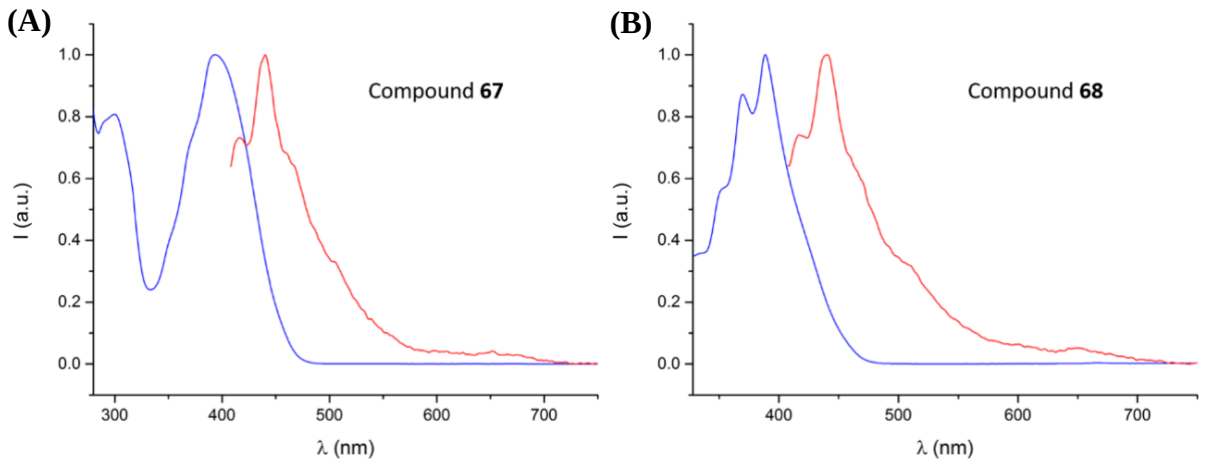

Figure 2.24. (A) Normalised UV-Visible (blue line) and fluorescence emission (red line) spectra of a 12.5 µM THF solution of compound **67**. **(B)** Normalised UV-Visible (blue line) and fluorescence emission (red line) spectra of a 12.5 µM THF solution of compound **68**.

The contour maps of fluorescence emission – excitation were generated to visualise the optical behaviour of the two synthesised compounds across the full excited emission ranges available. This experiment was conducted to gain a preliminary understanding of how such system might respond in cells visualised through confocal microscopy, using the laser wavelengths employed by common microscopes (*e.g.* 305 nm, 488 nm and 561 nm as excitation intensities). If the compounds mimic the autofluorescence of living cells, monitoring their activity would prove to be difficult, therefore it is vital that the two compounds fluoresce in a different region to that of the cells. An emission range of 300-500 nm would be particularly useful.

The fluorescence excitation-emission matrices are shown below in Figure 2.25 for compound **67**, and in Figure 2.26 for compound **68**. The two compounds display emissive properties between 400-500 nm, compound **68** exhibiting a stronger emission compared to **67**, possibly due to a reduced C=N isomerisation in the excited state.

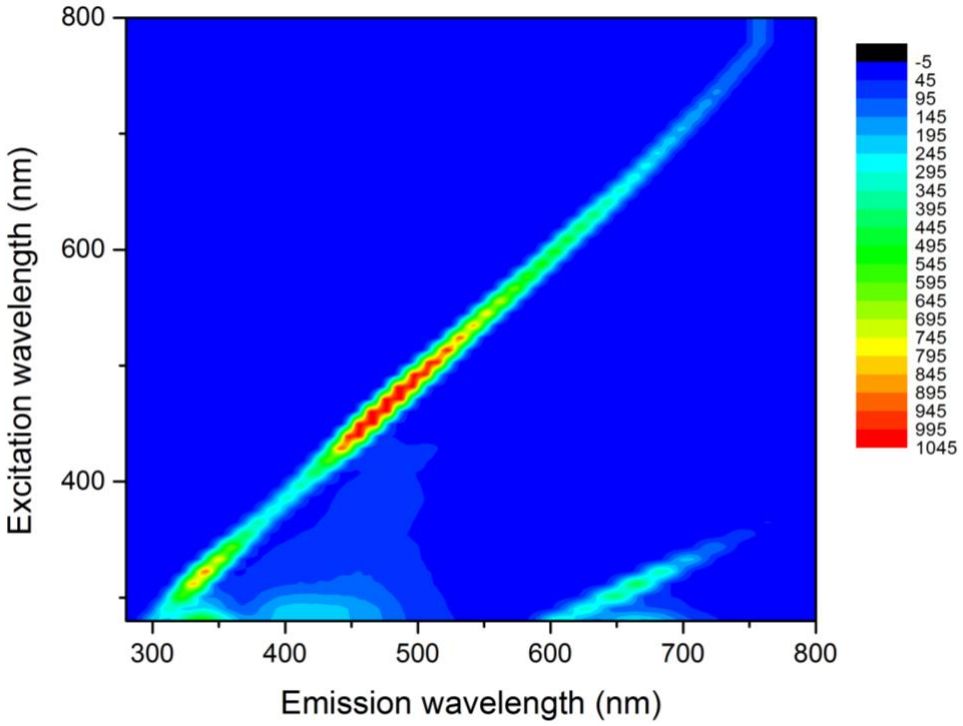

Figure 2.25. 2D fluorescence contour map for compound **67** in THF (25 μM).

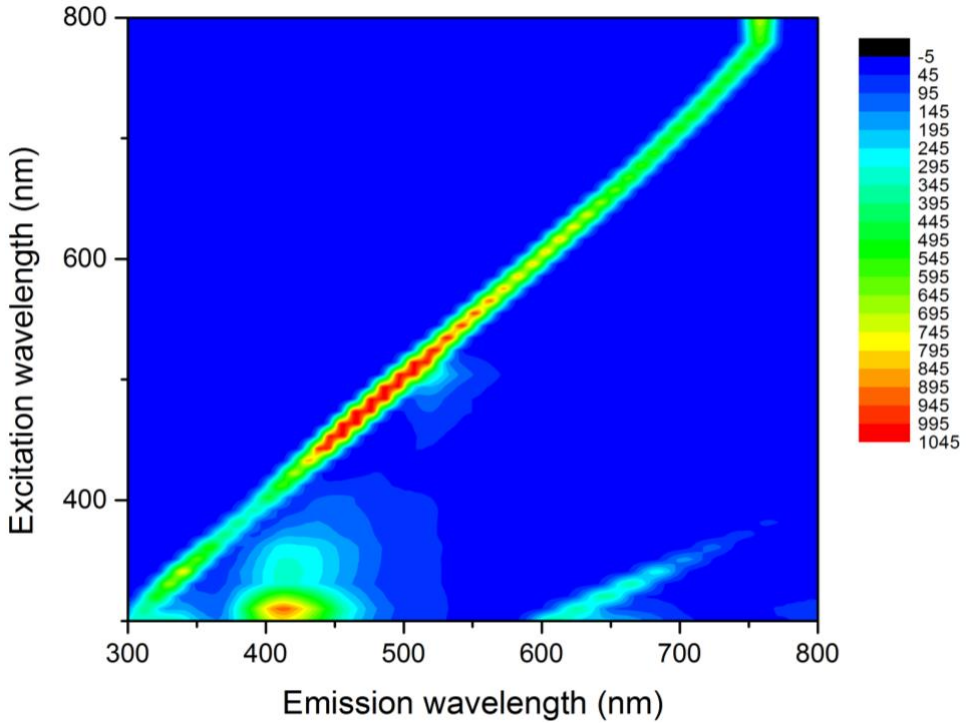

Figure 2.26. 2D fluorescence contour map for compound **68** in THF (25 μM).

2.5 Summary of Chapter 2

In this chapter, three types of tripodal ligands were successfully synthesised and characterised. The products were obtained through nucleophilic substitution of the bromomethyl substituents of the hexasubstituted cores **60** and **61** previously developed with DABCO and 4,4'-bipyridine to achieve compounds **62**, **63**, **64** and **65** in good yields and acceptable purity with minimal work up. Such compounds were characterised spectroscopically, and their biocompatibility probed *via* MTT assay on PC3 prostate cancer cells. While most of the compounds appear to be nontoxic at the highest concentrations recorded, a concentration of 250 μM of compound **64** caused a loss of more than 50% in cell viability. Such inhibition persisted even after 72 hours from the treatment. Further tests will be necessary to determine the factors that promote the loss of cell viability triggered by **64**.

Furthermore, two novel anthracene thiosemicarbazone-based tripodal systems were successfully synthesised in a two-step reaction, beginning with the synthesis of the anthracene thiosemicarbazone, reacting 9-anthraldehyde with thiosemicarbazide, to give compound **66** in excellent yield and high purity

The two tripodal systems were obtained by heating the two tripodal cores **60** and **61** at reflux with an excess of compound **66** in acetonitrile, followed by treatment with triethylamine to give compound **67** and **68** in very high yields. Characterisation of the compounds **67** and **68** revealed that the anthracene thiosemicarbazone "arms" bind to the central aromatic core *via* an unconventional S-alkylation of the bromomethyl moieties of **60** and **61**. The two ligands possess acceptable fluorescent properties with large emission bands around 440 nm, and could therefore be suitable for imaging applications.

2.6 References for Chapter 2

1. J. W. Steed, *Chem. Commun.*, 2006, 2637-2649.
2. A. S. Borovik, *Comments Inorg. Chem.*, 2002, **23**, 45-78.
3. K. J. Wallace, W. J. Belcher, D. R. Turner, K. F. Syed and J. W. Steed, *J. Am. Chem. Soc.*, 2003, **125**, 9699-9715.
4. B. Kuswandi, W. Verboom and D. Reinhoudt, *Sensors*, 2006, **6**, 978-1017.
5. A. Metzger, V. M. Lynch and E. V. Anslyn, *Angew. Chem., Int. Ed.*, 1997, **36**, 862-865.
6. S. K. Sahoo, G.-D. Kim and H.-J. Choi, *J. Photochem. Photobiol. C*, 2016, **27**, 30-53.
7. L. Fabbrizzi, M. Licchelli, G. Rabaioli and A. Taglietti, *Coord. Chem. Rev.*, 2000, **205**, 85-108.
8. T. Gunnlaugsson, M. Glynn, G. M. Tocci, P. E. Kruger and F. M. Pfeffer, *Coord. Chem. Rev.*, 2006, **250**, 3094-3117.
9. L. A. Cabell, M. D. Best, J. J. Lavigne, S. E. Schneider, D. M. Perreault, M.-K. Monahan and E. V. Anslyn, *J. Chem. Soc., Perkin Trans. 2*, 2001, 315-323.
10. N. Busschaert, M. Wenzel, M. E. Light, P. Iglesias-Hernández, R. Pérez-Tomás and P. A. Gale, *J. Am. Chem. Soc.*, 2011, **133**, 14136-14148.
11. H. Valkenier, C. M. Dias, K. L. P. Goff, O. Jurček, R. Puttreddy, K. Rissanen and A. P. Davis, *Chem. Commun.*, 2015, **51**, 14235-14238.
12. P. A. Gale, R. Pérez-Tomás and R. Quesada, *Acc. Chem. Res.*, 2013, **46**, 2801-2813.
13. J. Liu, J. Chen, J. Zhao, Y. Zhao, L. Li and H. Zhang, *Synthesis*, 2003, **2003**, 2661-2666.
14. D. R. Turner, M. J. Paterson and J. W. Steed, *J. Org. Chem.*, 2006, **71**, 1598-1608.
15. A. Van der Made and R. Van der Made, *J. Org. Chem.*, 1993, **58**, 1262-1263.
16. E. Anslyn, K. J. Wallace, R. Hanes, J. Morey, K. V. Kilway and J. Siegel, *Synthesis*, 2005, **2005**, 2080-2083.
17. M. V. Berridge and A. S. Tan, *Arch. Biochem. Biophys.*, 1993, **303**, 474-482.
18. T. Mosmann, *J. Immunol. Methods*, 1983, **65**, 55-63.
19. M. V. Berridge, P. M. Herst and A. S. Tan, *Biotechnol. Annu. Rev.*, 2005, **11**, 127-152.
20. G. Wu, X.-F. Wang, T.-a. Okamura, W.-Y. Sun and N. Ueyama, *Inorg. Chem.*, 2006, **45**, 8523-8532.
21. J. S. Modica-Napolitano and J. R. Aprille, *Adv. Drug Deliv. Rev.*, 2001, **49**, 63-70.
22. M. Kurtoglu and T. J. Lampidis, *Mol. Nutr. Food Res.*, 2009, **53**, 68-75.
23. J. Zielonka, J. Joseph, A. Sikora, M. Hardy, O. Ouari, J. Vasquez-Vivar, G. Cheng, M. Lopez and B. Kalyanaraman, *Chem. Rev.*, 2017, **117**, 10043-10120.
24. H. Chen, J. Wang, X. Feng, M. Zhu, S. Hoffmann, A. Hsu, K. Qian, D. Huang, F. Zhao and W. Liu, *Chem. Sci.*, 2019.
25. W. J. Belcher, M. Fabre, T. Farhan and J. W. Steed, *Org. Biomol. Chem.*, 2006, **4**, 781-786.
26. E. Abel and F. Stone, *Q. Rev. Chem. Soc.*, 1969, **23**, 325-371.
27. W. R. Dawson and M. W. Windsor, *J. Phys. Chem.*, 1968, **72**, 3251-3260.
28. R. Martinez-Manez and F. Sancenón, *Chem. Rev.*, 2003, **103**, 4419-4476.
29. F. A. Beckford, M. Shaloski Jr, G. Leblanc, J. Thessing, L. C. Lewis-Alleyne, A. A. Holder, L. Li and N. P. Seeram, *Dalton Trans.*, 2009, 10757-10764.
30. Z. Afrasiabi, E. Sinn, W. Lin, Y. Ma, C. Campana and S. Padhye, *J. Inorg. Biochem.*, 2005, **99**, 1526-1531.

3. Synthesis, spectroscopic characterisation and X-ray crystallography of novel tripodal pro-carbene derivatives

A new family of tripodal ligands, suitable for the development of novel transition metal complexes, are the tripodal N-heterocyclic carbenes (NHCs). Tripodal N-heterocyclic ligands commonly consist of a central atom or group which acts as an anchor for the three pendant arms bearing the three NHC groups. Several tripodal NHC ligands have been developed with central anchors consisting of boron,[1] carbon,[2] nitrogen,[3] and arene groups.[4] The arms of the tripodal NHC ligand are usually separated from the central anchor by linkers, which generally are small alkyl groups. By alternating these groups, the topological properties of the ligand, such as steric hindrance, bite angle, chirality and fluxional behaviour can be finely tuned.

A tripodal NHC containing a central mesityl group (compound **60**), 1,3,5-[tris(3-tert-butylimidazole-2-ylidene)methyl]-2,4,6-trimethylbenzene (timtmb$_{tBu}$) was first reported in 1994 by Dias and co-workers.[4] As the central arene anchor group *de facto* restricts the extent to which a single metal ion can be accommodated between the three carbene arms, the group was able to bind only the very large thallium atom (Figure 3.1).

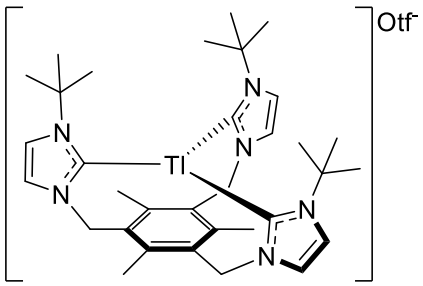

Figure 3.1. the Tl(I)-timtmb$_{tBu}$ complex prepared by Dias and co-workers.

A different approach to the coordination chemistry of such tripodal ligands was reported by Hahn and co-workers in 2010, in which a tripodal NHC bearing a central phenyl group with no linker groups was coordinated to the group 11 transition metals Ag and Au.[5] In these complexes, each NHC arm binds to the metal ion in a monodentate manner, so that each carbene is coordinated to a separate metal centre, leading to a self-assembled *bis*-tripodal NHC complex of structure $[M_3(NHC)_2](PF_6)_3$, with M = Ag, Au, as shown in Figure 3.2.

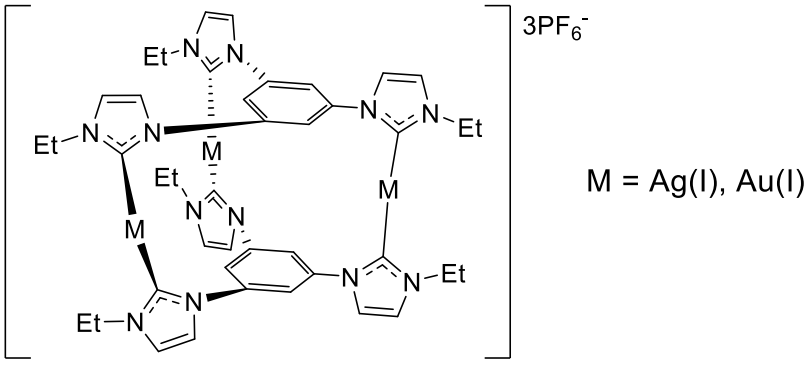

Figure 3.2. Representation of the bis-tripodal carbene complex $[M_3(NHC)_2](PF_6)_3$ prepared by Hahn et al.

Inspired by Hahn's work, Pascu, Whittlesey and co-workers developed a series of tripodal $timteb_{tBu}$ and $timteb_{dipp}$ complexes of palladium(II), whose structures are shown in Figure 3.3.[6] X-Ray analysis showed that the compounds adopt an idealised C_3-symmetrical arrangement with the three Pd-(ICy)I_2 fragments pointing out on the opposite side of the central arene ring to the three ethyl substituents.

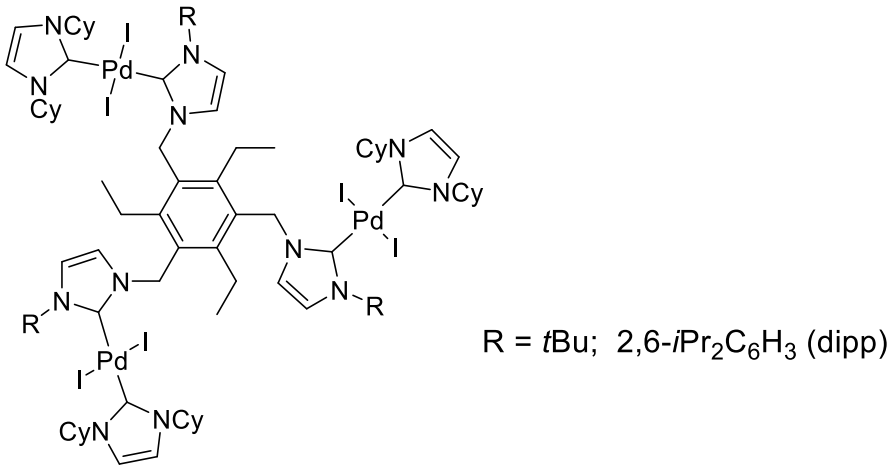

Figure 3.3. Representation of the tripodal $timteb_{tBu}$ and $timteb_{dipp}$ complexes of palladium(II) prepared by Pascu, Whittlesey and co-workers.[6]

In order to gain further understanding of the coordination chemistry of these ligands, the same group attempted the complexation between the $timteb_R$ tripodal ligands and a copper(I) precursor $[Cu(MeCN)_4]PF_6$ *via* a one-pot reaction, by deprotonation of the ligand precursor in THF solution at room temperature using sodium *tert*-butoxide. The reactions gave rise to unexpected *tris*-copper(I) $\mu 3$-oxo complexes $[(timteb_R)Cu_3(\mu 3\text{-}O)]X$ (R = *t*Bu, dipp; X = PF_6, BF_4), both adopting *pseudo* C_3 geometries with an axis directed through the oxygen cap and the centroids of the copper plane and the arene ring (Figure 3.4).

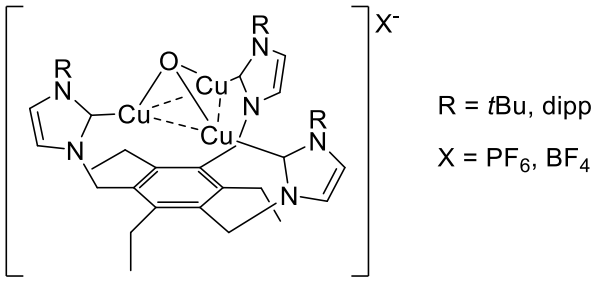

Figure 3.4. Structural representation of the [(timtebR)Cu3(μ3-O)]X complexes prepared by Pascu, Whittlesey and co-workers.

With the aim of further expanding the library of tripodal NHC pro-ligands potentially able to bind transition metal ions, we decided to make further use of the 1,3,5-tris(bromomethyl)-2,4,6-trimethyl benzene anchor **60** and the more rigid scaffold 1,3,5-tris(bromomethyl)-2,4,6-triethyl benzene (compound **61**) with a series of monosubstituted imidazole as arms. A general scheme of the reactions involved is presented below (see Scheme 3.1).

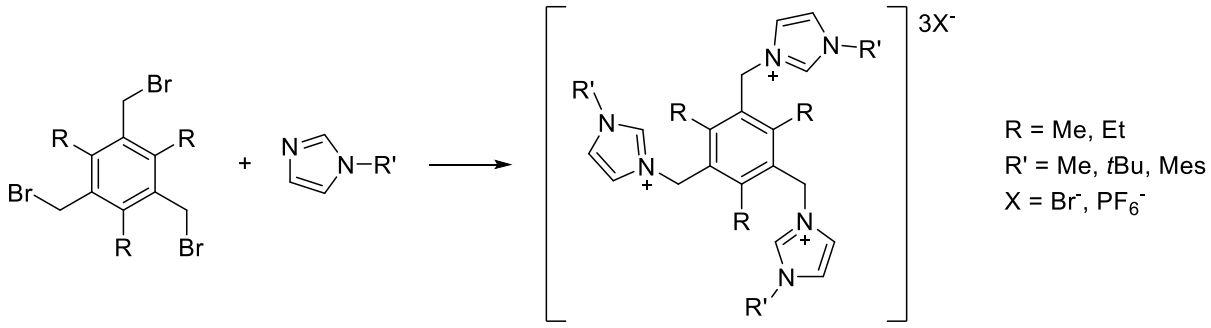

Scheme 3.1. General outline of the synthetic protocols leading to the tripodal imidazolium pro-ligands described in this section.

3.1. Methylimidazole-based tripodal systems

The first tripodal NHC-based pro-ligand, namely compound **69**, was synthesised following a modified procedure from Kumbhar *et al.*[7] by reacting 1,3,5-tri(bromomethyl)-2,4,6-trimethylbenzene (compound **60**) and 3.1 equivalents of the commercially available 1-methyl-H-imidazole in refluxing dry acetonitrile for 24 hours (Scheme 3.2). A cream coloured precipitate was formed, and after recrystallisation of the crude material from a mixture of methanol/diethyl ether, NMR analysis was performed to assess the quality of the product.

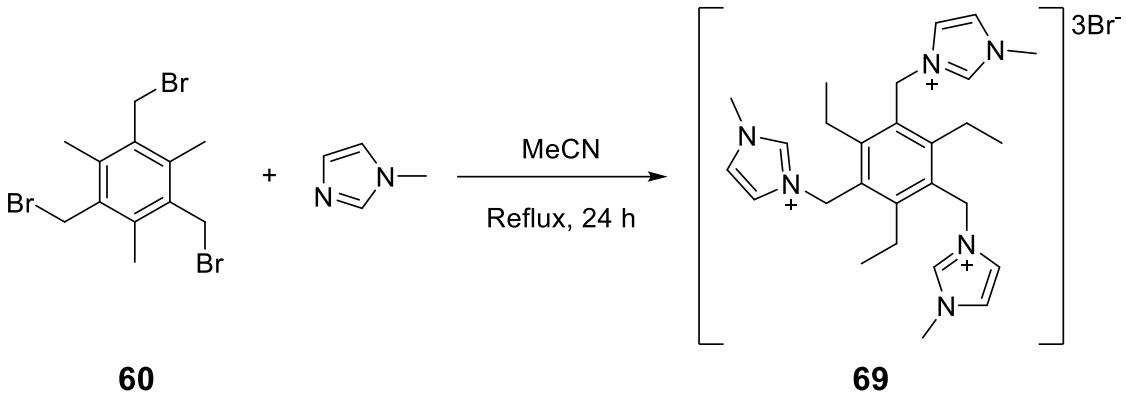

60 **69**

Scheme 3.2. Synthesis of the compound **69**.

The ^{1}H NMR spectrum of compound **69** is shown in Figure 3.5. The spectrum shows two low-field peaks, at 7.73 and 7.62 ppm respectively, corresponding to the imidazolium protons H_2 and H_3. A sharp singlet at 5.61 ppm was assigned to the CH_2 bridging the three imidazolium arms to the mesityl core. The remaining two peaks were assigned to the two sets of CH_3, where the intense signal at 3.96 ppm corresponds to the three methyl units bound to the imidazolium nitrogen, and the sharp singlet at 2.38 ppm was assigned to the 9 protons of the mesitylene core. The absence of the imidazolium C_2-*H* signal (entry 1 in Figure 3.5), expected between 9-10 ppm, may indicate the occurrence of a hydrogen/deuterium exchange between H_1 and O-D of the deuterated solvent.

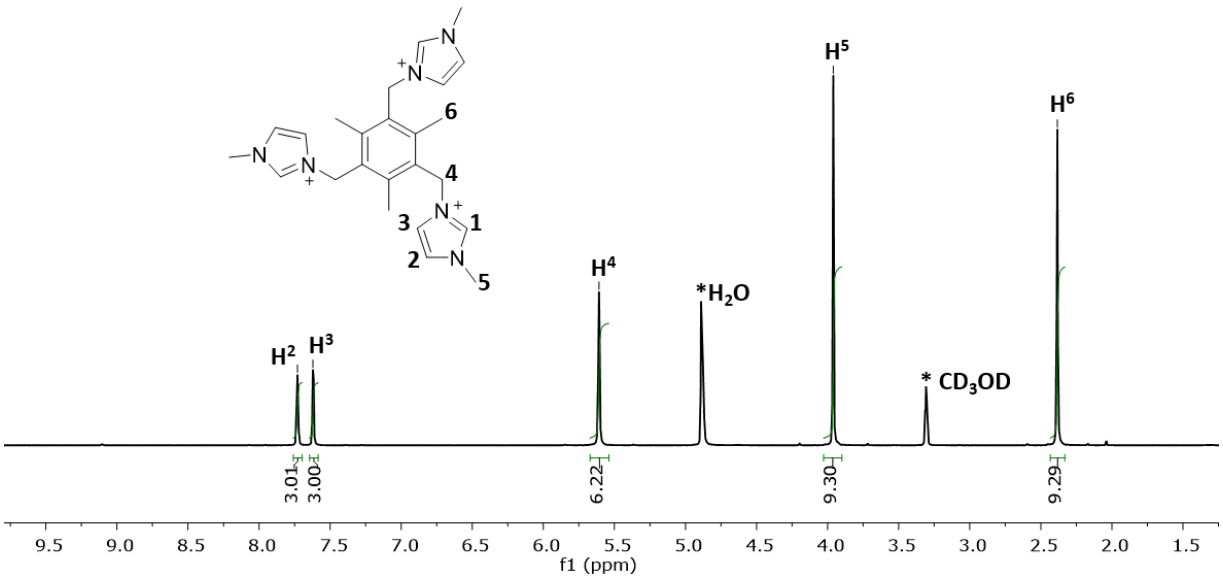

Figure 3.5. 1H NMR (300 MHz, CD_3OD-d_4, 298 K) spectrum of compound **69**. For clarity, magnetically equivalent nuclei within the same NMR spin system are labelled once. * solvent peaks.

The same reaction protocol was carried out using 1,3,5-tri(bromomethyl)-2,4,6-triethylbenzene (compound **61**) as core instead, aiming to obtain a similar compound but with a more rigid conformation. The resulting reaction mixture was refluxed in dry acetonitrile for 24 hours, during which time no precipitate could be observed. After removal of the solvent, a deliquescent grey powder was obtained. The crude mixture was washed thoroughly with diethyl ether and subsequently recrystallised from ethyl acetate. NMR analysis was carried out, revealing an impure product in which the imidazole starting material was still abundant.

A second attempt was carried out by using dry tetrahydrofuran as solvent. After refluxing the mixture overnight, a creamy precipitate was formed. The resulting solid was collected by filtration and washed several times, to give a hygroscopic white powder. Anion metathesis was carried out by treating the product with a saturated solution of potassium hexafluorophosphate (KPF_6) to afford compound **70** in moderate yield (50%). An outline of the synthesis is shown in Scheme 3.3.

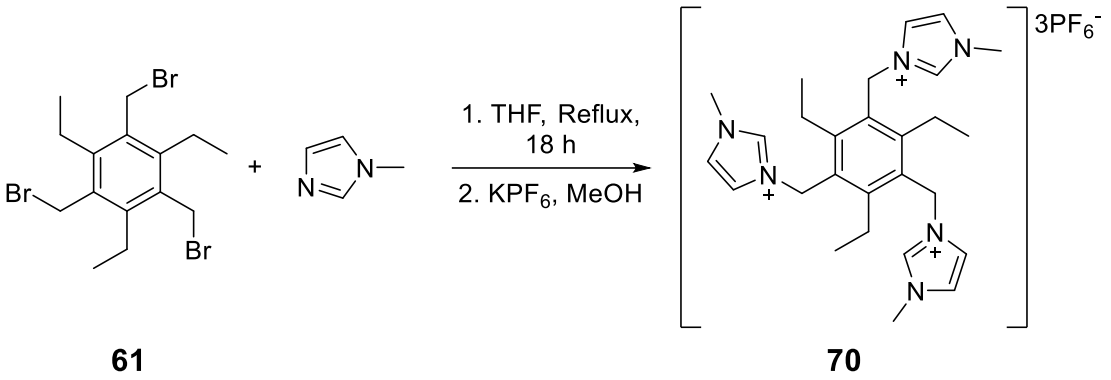

61 **70**

Scheme 3.3. Reaction pathway for compound **70**.

The newly synthesised compound **70** was fully characterised by NMR and mass spectrometry. The ^{1}H NMR spectrum shown, in Figure 3.6, shows a series of 7 signals. A singlet observed at 8.85 ppm, which was assigned to the C$_2$-*H* of the imidazolium arms (entry H$_1$ in Figure 3.6), whilst two triplets at 7.74 and 7.61 ppm respectively correspond to the other two protons of the heterocycle (H$_2$ and H$_3$ in Figure 3.6).

The deshielded protons of the methylene linker between the central aromatic core and the imidazolium arms appear in the spectrum as a sharp singlet at 5.61 ppm, a comparable value to that of the C*H*$_2$ linkers of compound **69**. Another sharp singlet at 3.82 ppm was assigned to the three magnetically equivalent C*H*$_3$ of the methylimidazolium arms. Finally, a quartet integrating to 6H at 2.62 ppm and a triplet integrating to 9H at 0.84 ppm correspond to the three ethylene arms around the central aromatic core.

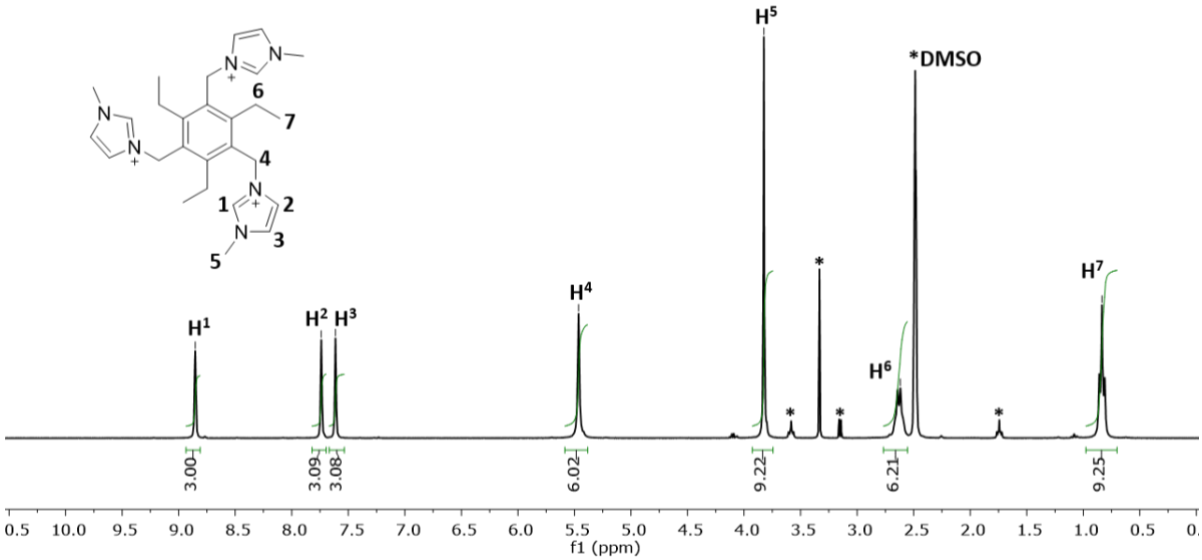

Figure 3.6. ^{1}H NMR (500 MHz, DMSO-d$_6$, 298 K) spectrum of compound **70**. For clarity, magnetically equivalent nuclei within the same NMR spin system are labelled once. * residual solvents and impurities traces.

The proton resonances of compound **70** were assigned also with the help of ^{1}H-^{1}H bidimensional correlation spectroscopy (^{1}H-^{1}H COSY). The COSY NMR spectrum for **70** (Figure 3.7), shows the coupling between the imidazolium protons as well as a weak interaction with the methyl group within the imidazolium arm (H_1-H_2-H_3), and the protons in the ethyl arms (H_6-H_7).

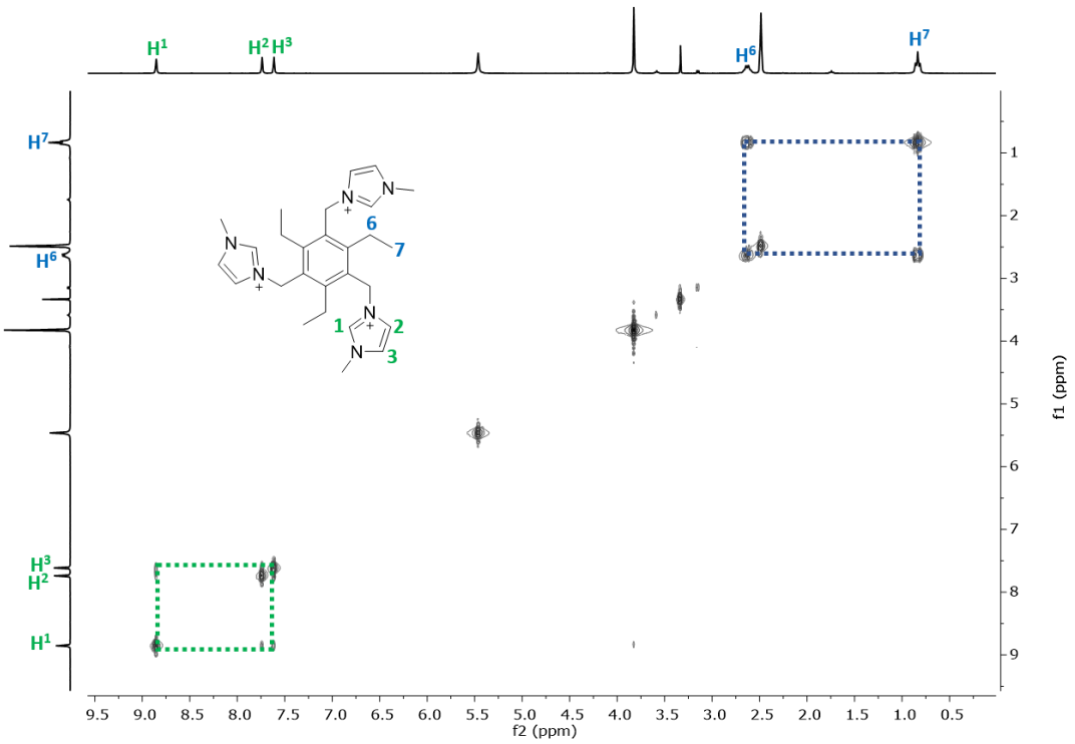

Figure 3.7. ^{1}H-^{1}H COSY NMR (500 MHz, DMSO-d_6, 298 K) spectrum of compound **70**.

Mass spectrometry analysis performed on compound **70**, reported below in Figure 3.8, showed the presence of yet another peculiar molecular ion $[M+2(PF_6)]^+$ at 737.2493 m/z, possibly suggesting the presence of robust interactions between the tripodal system and its counterion.

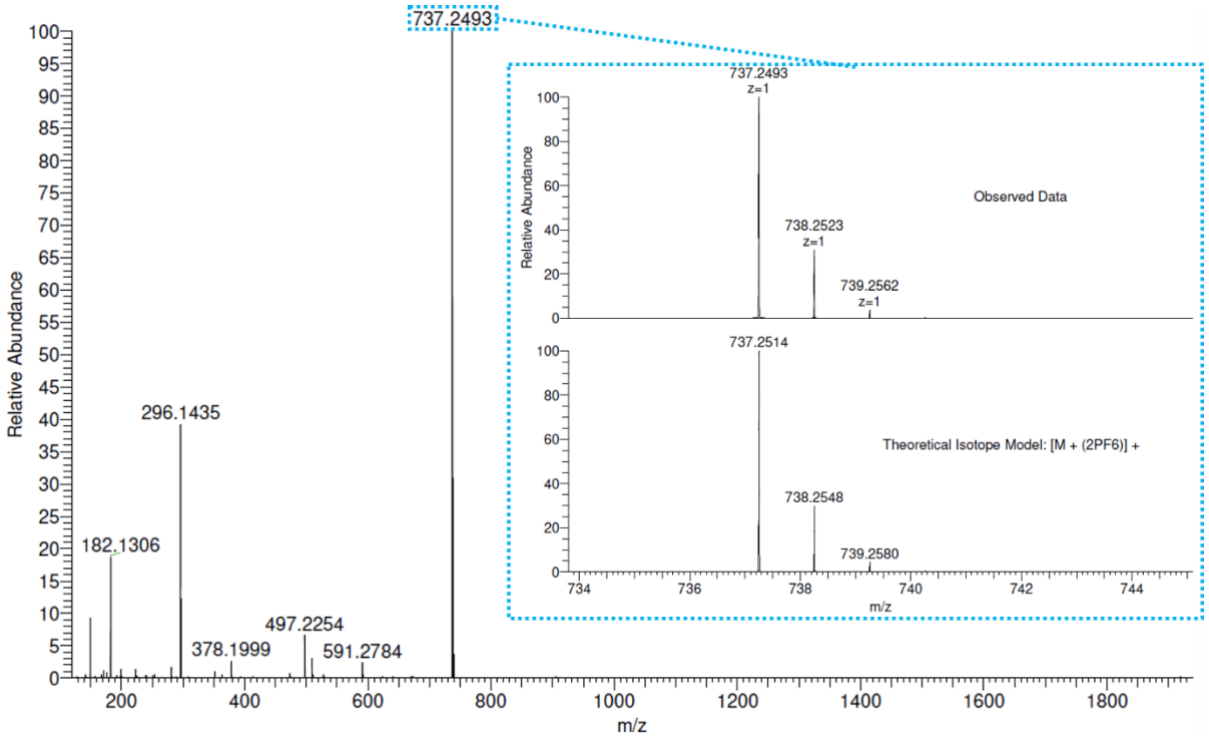

Figure 3.8. Mass spectrum recorded for the compound **70**.

It was possible to develop suitable crystals of compound **70** for X-ray crystallography by slow evaporation of a concentrated solution of **70** in acetonitrile. Compound **70** crystallises in a trigonal P3 space group. From the ORTEP representation shown in Figure 3.9 it is possible to appreciate the presence of the three hexafluorophosphate counterions, one of which appears to be located into the molecule's cavity. Hydrogens bonded to C8 interact with fluorine F3 (see corresponding labelling in Figure 3.9) of the sitting counterion at 2.310 Å, slightly shorter than the H-F "out-of-socket" interactions at an average of 2.5 Å. A representation of the crystal structure of **70**, highlighting the short contact interactions between the imidazolium arms and fluorines from the hexafluorophosphate counterion is shown in Figure 3.10. The imidazolium-bearing arm C1-C3-N4 angle has a value of 113.18°, almost identical to the C2-C10-C11 of the ethylene arm (113.10°). A selection of bonds and angles for compound **70** are presented in Table 3.1 below.

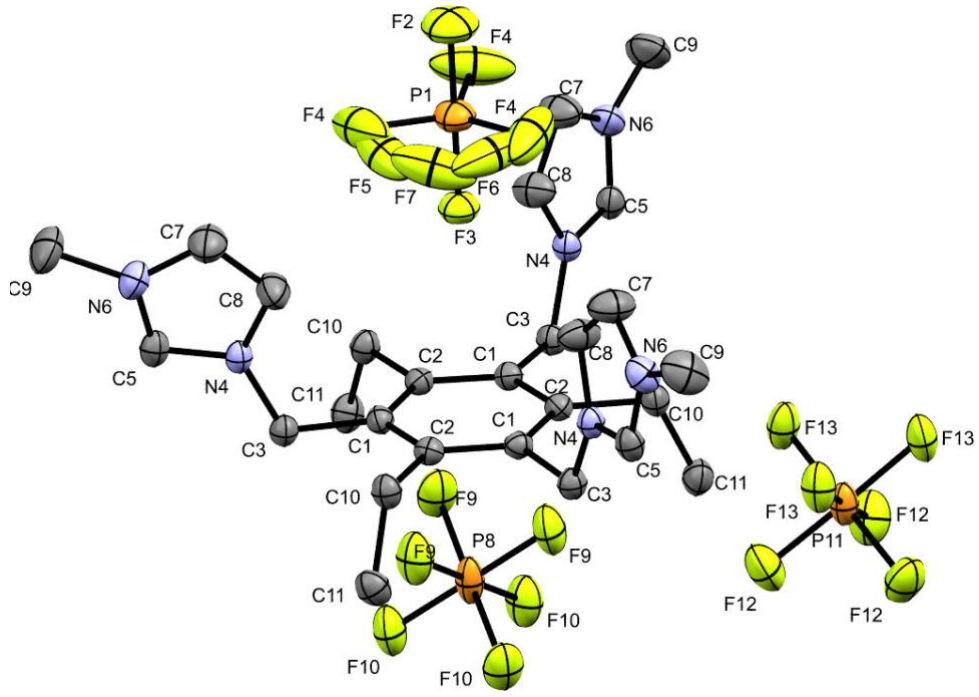

Figure 3.9. Content of the asymmetric unit of compound **70** (ORTEP representation). Thermal ellipsoids represented at 50% probability. Hydrogen atoms have been omitted for clarity.

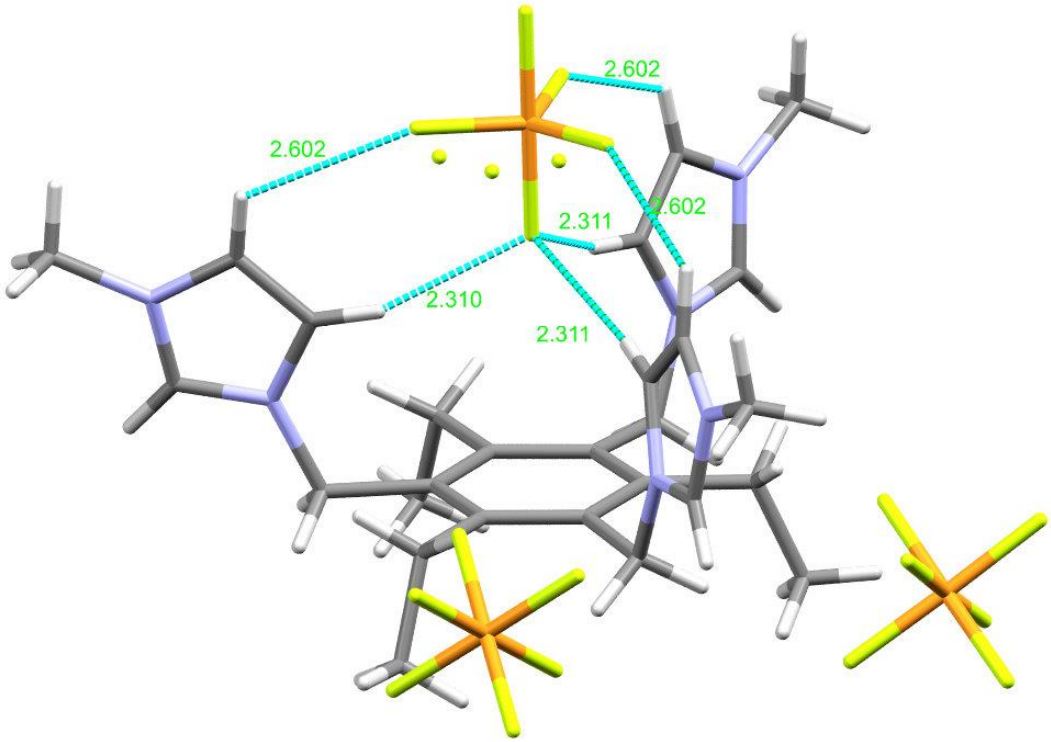

Figure 3.10. Crystal structure of compound **70** highlighting the interactions between the imidazolium arms and fluorines from the hexafluorophosphate counterion.

Table 3.1. Selected bond angles and distances for compound **70**.

Atoms involved	Angle (°) / Distance (Å)
C1-C3-N4	113.18(2)°
C3-N4-C8	127.86(2)°
N4-C5-N6	109.12(2)°
C5-N6-C7	108.37(2)°
N6-C7-C8	107.48(2)°
C7-C8-N4	106.77(2)°
C7-N6-C9	126.31(2)°
C1-C3	1.513(4) Å
C3-N4	1.485(3) Å
C5-N4	1.323(3) Å
C7-C8	1.344(3) Å

The packing unit of compound **70** shows alternate layers, with the molecules of **70** oriented in opposite directions (Figure 3.12). Additionally, multiple interactions between the methylene hydrogens of the linkers and fluorines from the hexafluorophosphate counterions result in polymeric association of the tripodal systems bridged by the counterions (Figure 3.13).

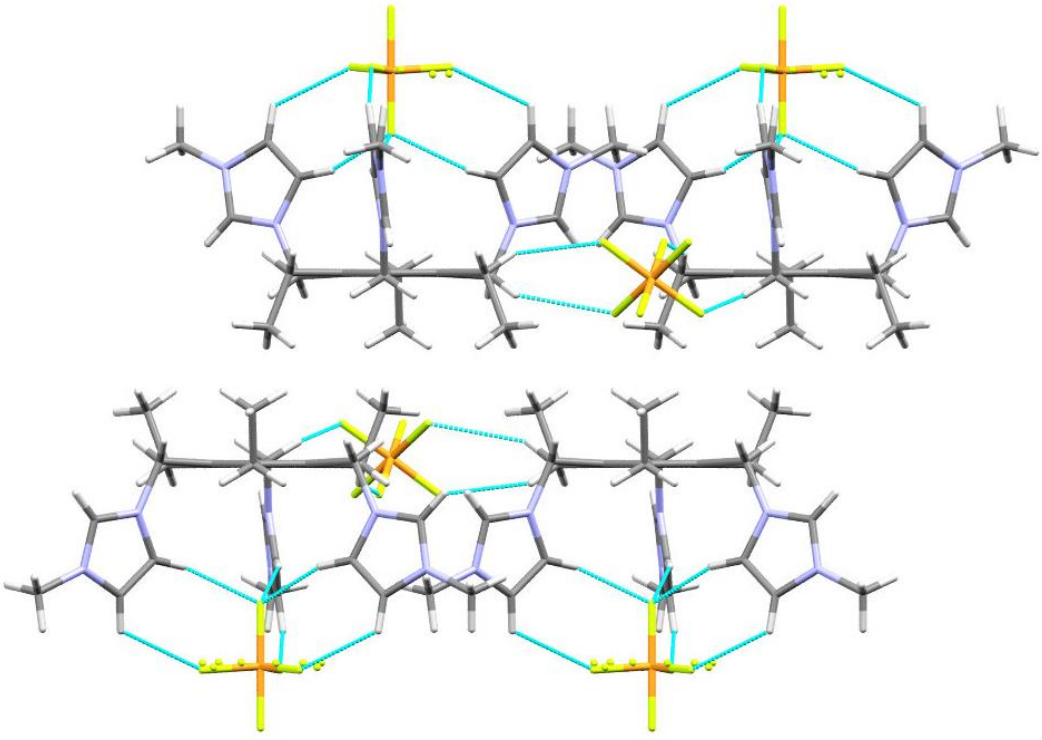

Figure 3.11. Packing units of compound **70**. View along the b axis, highlighting the alternate layers.

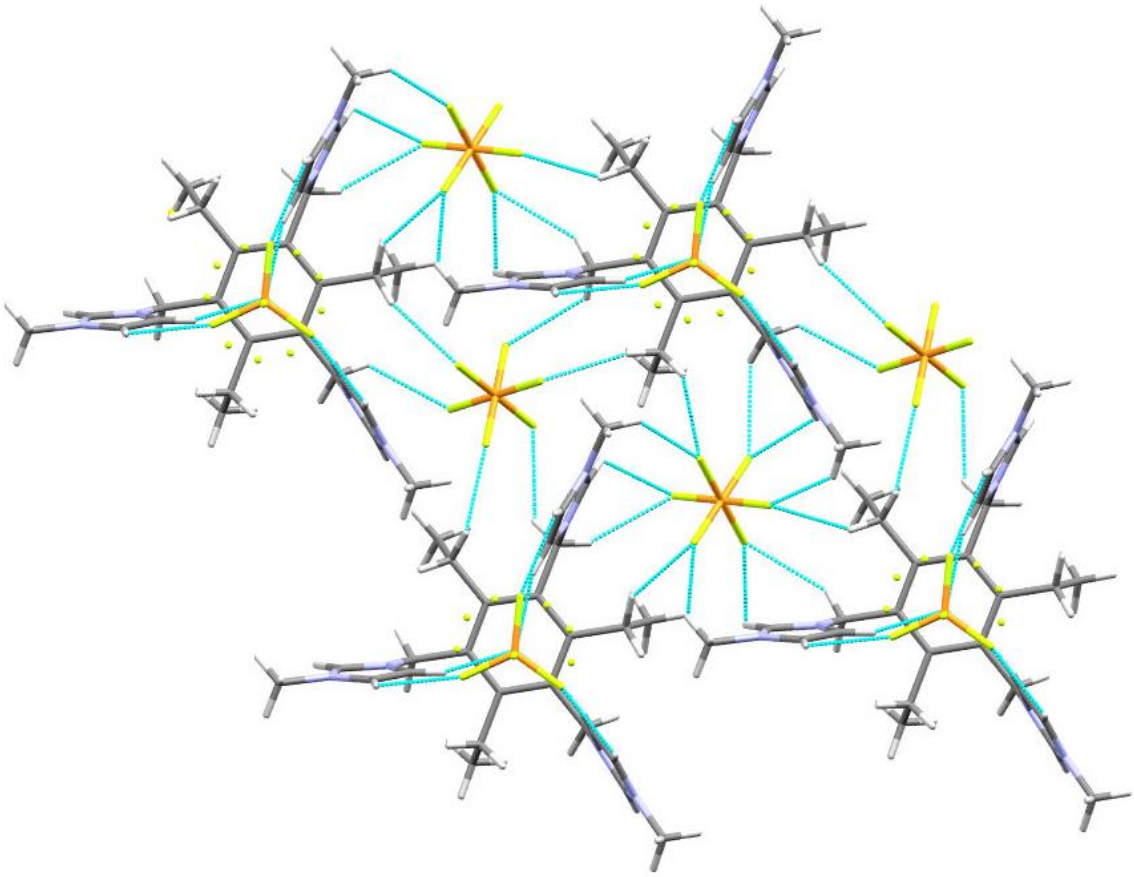

Figure 3.12. Packing units of compound **70**. View along the c axis, highlighting the intermolecular associations between the molecules of **70** and the hexafluorophosphate counterions.

3.2. *Tert*-butylimidazole-based tripodal systems

A second series of tripodal NHC-based ligands, bearing a bulkier *tert*-butyl substituent on the imidazole nitrogen N_6, was also successfully synthesised and is reported below. The first step consisted of the synthesis of the monosubstituted 1-(*tert*-butyl)-1H-imidazole, compound **71**, following a preparation outlined by Cassani and co-workers.[8] This consists of a modification of a Debus-Radziszewski imidazole synthesis in which one equivalent of ammonia is replaced with *tert*-butylamine. An outline of the synthesis is shown in Scheme 3.4. Pure product was afforded after extraction in dichloromethane and subsequent vacuum distillation, to give **71** as a pale-yellow liquid.

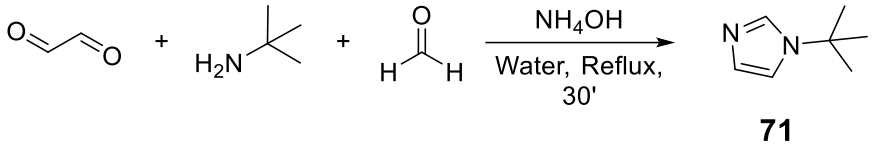

Scheme 3.4. Synthesis of 1-(tert-butyl)-1H-imidazole precursor (compound **71**).

The ^{1}H NMR spectrum of compound **71** (Figure 3.13), showed three signals. The two low-field signals at 7.51 and 6.95 ppm could be assigned to the three protons of the heterocyclic ring, while the intense singlet at 1.46 ppm represents the nine magnetically equivalent protons of the *tert*-butyl substituent (entry H_3 in Figure 3.13). Such values are in agreement with the literature.[8]

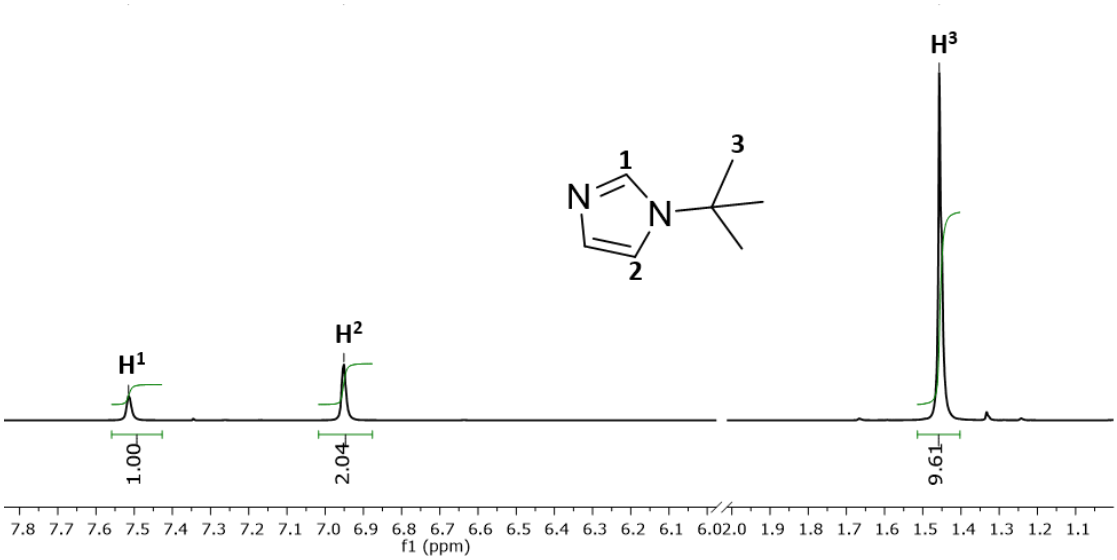

Figure 3.13. ^{1}H NMR (300 MHz, $CDCl_3$, 298 K) spectrum of compound **71**. For clarity, magnetically equivalent nuclei within the same NMR spin system (H_2) are labelled once.

The subsequent step led to the synthesis of two tripodal receptors, compounds **72** and **73**, having as core two hexasubstituted benzene rings (derived from compounds **60** and **61**) and monosubstituted imidazole arms, derived from **71**. An outline of this step is shown in Scheme 3.5. Both syntheses were carried out under anhydrous conditions, using dry acetonitrile as solvent. The reaction mixture was heated at reflux, and the reaction was followed by thin-layer chromatography (TLC) until completion, which occurred in around 48 hours for each compound. After removal of the solvents and recrystallisation, both products were afforded in good yield (84% and 78% respectively) and NMR-level purity, which enabled future reactions to be carried out.

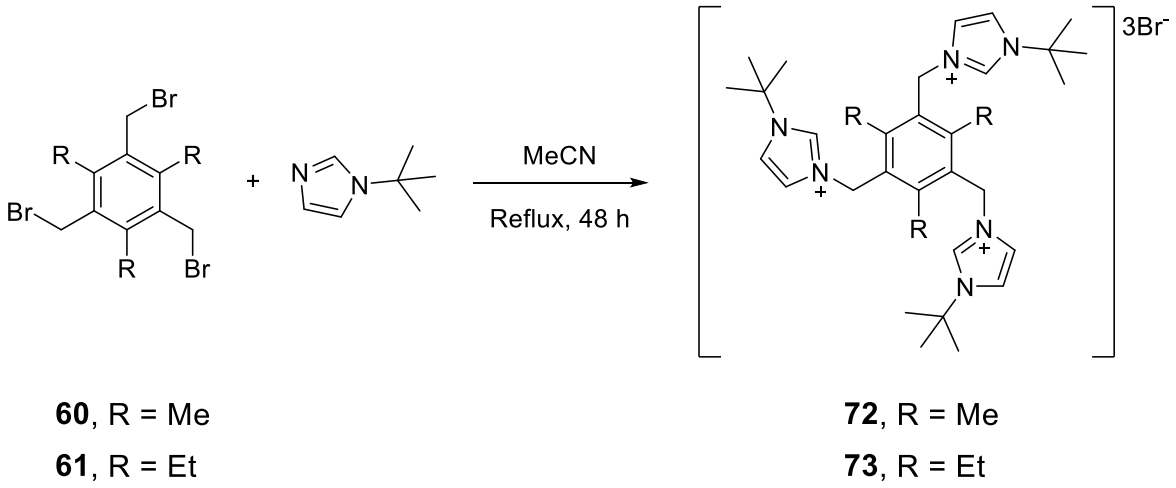

60, R = Me
61, R = Et

72, R = Me
73, R = Et

Scheme 3.5. Synthetic pathway leading to compounds **72** and **73**.

The ^{1}H NMR spectrum of compound **72** (Figure 3.14) shows 6 signals. The signal at 9.53 ppm, integrating for 3H, was assigned to the C$_2$-*H* (H$_1$) of the imidazolium unit that comprises the three arms of **72**. The other two signals between 7 and 8 ppm correspond to the other two sets of protons of the heterocycle (H$_2$ and H$_3$). The singlet integrating to 6H at 5.59 ppm (H$_4$) was assigned to the C*H*$_2$ connecting the *tert*-butyl imidazolium arms to the mesityl core. Another resonance at 2.30 ppm integrating for 9H was assigned to the three magnetically equivalent mesityl C*H*$_3$ groups (H$_5$), and the intense signal at 1.59 ppm was finally assigned to the 27 protons of the three *tert*-butyl substituents of the imidazolium arms (H$_6$). All values are consistent with the literature.[4]

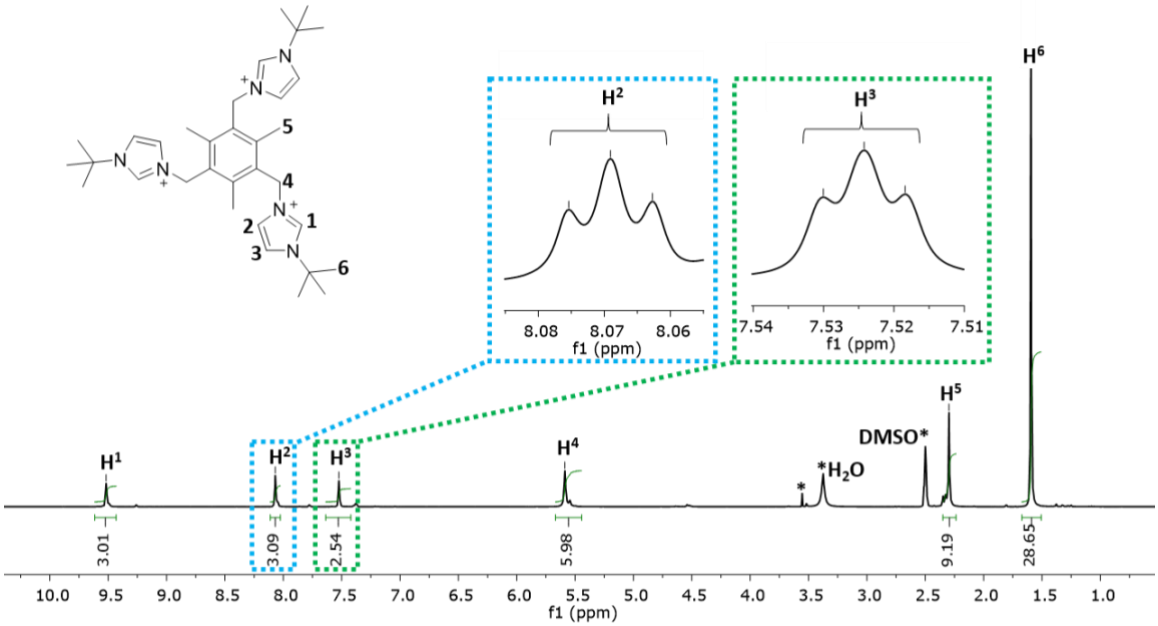

Figure 3.14. 1H NMR (300 MHz, DMSO-d6, 298 K) spectrum of compound **72**. For clarity, magnetically equivalent nuclei within the same NMR spin system are labelled once. * residual solvents and impurities traces.

The 1H NMR spectrum of compound **73** (Figure 3.15) shows seven signals that may be assigned in similar fashion to **72**. The three peaks between 7.5 and 9.5 ppm belong to the three C2-*H* of the imidazolium heterocycle. The singlet at 5.50 ppm, integrating for a total of 6 protons, was assigned to the C*H*2 linking the arms to the triethylbenzene core. The quartet at 2.70 ppm was assigned to the C*H*2 of the ethylene arms. The downfield value for these protons is due to their proximity to the aromatic ring. The intense singlet at 1.60 ppm integrates for 27H and was assigned to the *tert*-butyl groups, in concordance with the values reported for compound **72**. Finally, a triplet of integration 9H placed upfield at 0.74 ppm was correlated to the methyl groups of the three ethylene arms (entry H7 in Figure 3.15).

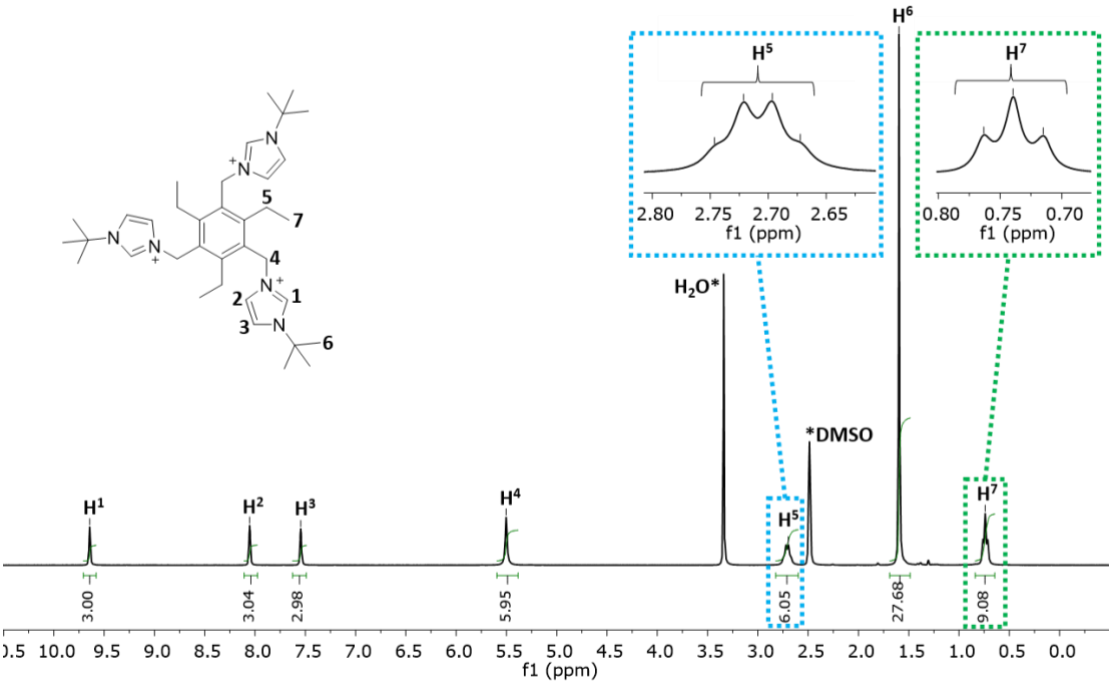

Figure 3.15. 1H NMR (300 MHz, DMSO-d6, 298 K) spectrum of compound **73**. For clarity, magnetically equivalent nuclei within the same NMR spin system are labelled once. * residual solvents and impurities traces.

Prior to mass spectrometry analysis, **73** was subjected to anion metathesis aiming to exchange the bromide counterion to the less coordinating hexafluorophosphate (PF_6^-). Compound **73** was thus treated with a saturated solution of ammonium hexafluorophosphate (NH_4PF_6) in distilled water in open air. The resulting suspension was stirred for a further 2 hours, then filtered and the filter cake was washed thoroughly with aliquots of distilled water. The product (**73·3PF6**) was obtained as a white powder by freeze-drying overnight, and it was fully characterised.

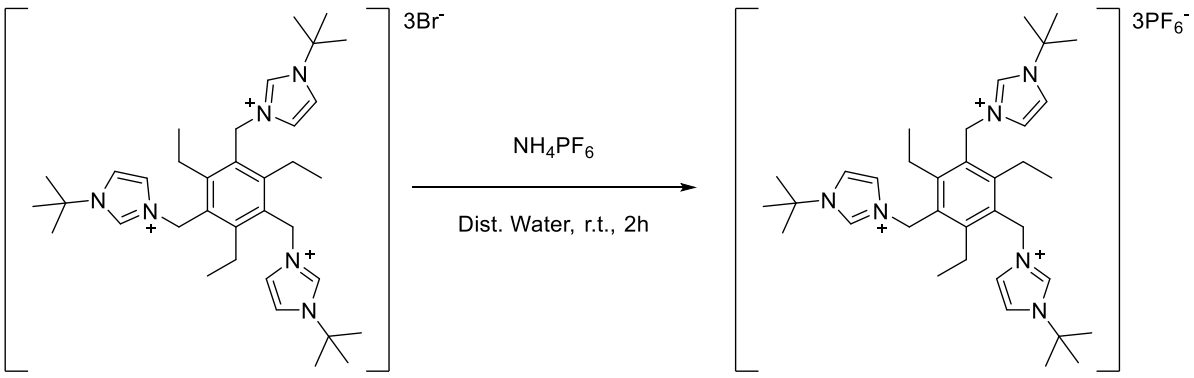

Scheme 3.6. Counterion metathesis for compound **73** to give **73·3PF6**.

Electrospray ionisation mass spectrometry (ESI-MS) carried out for compound **73·3PF6** (Figure 3.16), clearly shows the presence of an intense signal at m/z = 863.3967, corresponding to the ion $[M+2PF_6]^+$. Such singly charged species has also been observed in the mass spectrum recorded for compound **70**. A second peak at m/z = 359.2157 was assigned to the doubly

charged ion $[M+PF_6]^{2+}$. The presence of such a species seems to indicate that tripodal receptors bearing imidazolium arms possess strong affinity for their counterions, effectively acting as chelators for the anions.

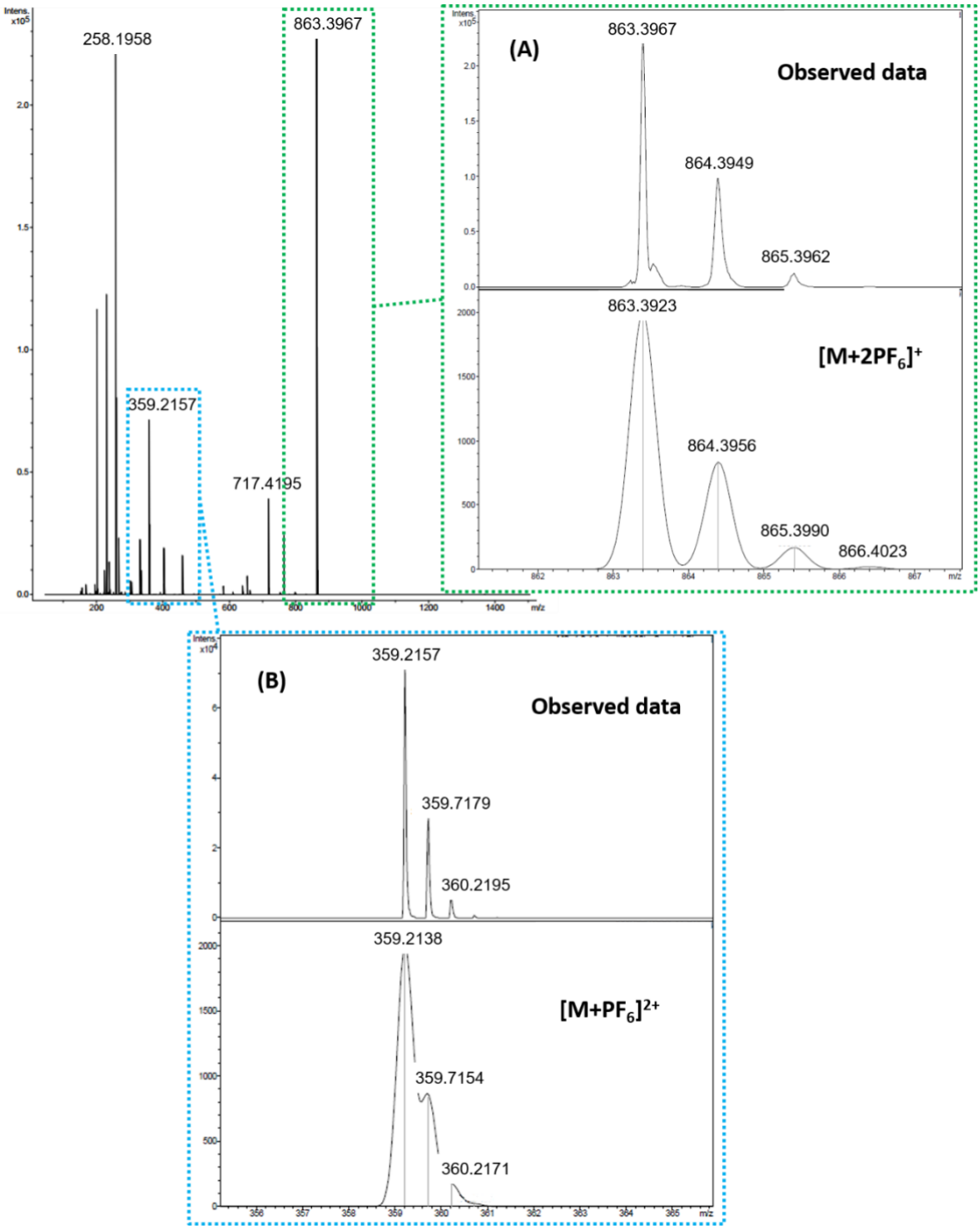

Figure 3.16. Positive-mode ESI-MS for compound **73·3PF6**. **(A)** ion species $[M+2PF_6]^+$ at 863.3967 m/z and below its predicted pattern. **(B)** ion species $[M+PF_6]^{2+}$ at 359.2157 m/z and its predicted pattern.

Suitable single crystals for X-ray diffraction analysis for compound **72** were obtained by slow evaporation of a concentrated solution of **72** in methanol. Compound **72** crystallised in the monoclinic $P2_1/c$ space group. Three molecules of water of crystallisation are present in the structure which interact with the bromide counterions and the imidazolium hydrogens. An ORTEP representation of compound **72** is shown in Figure 3.17.

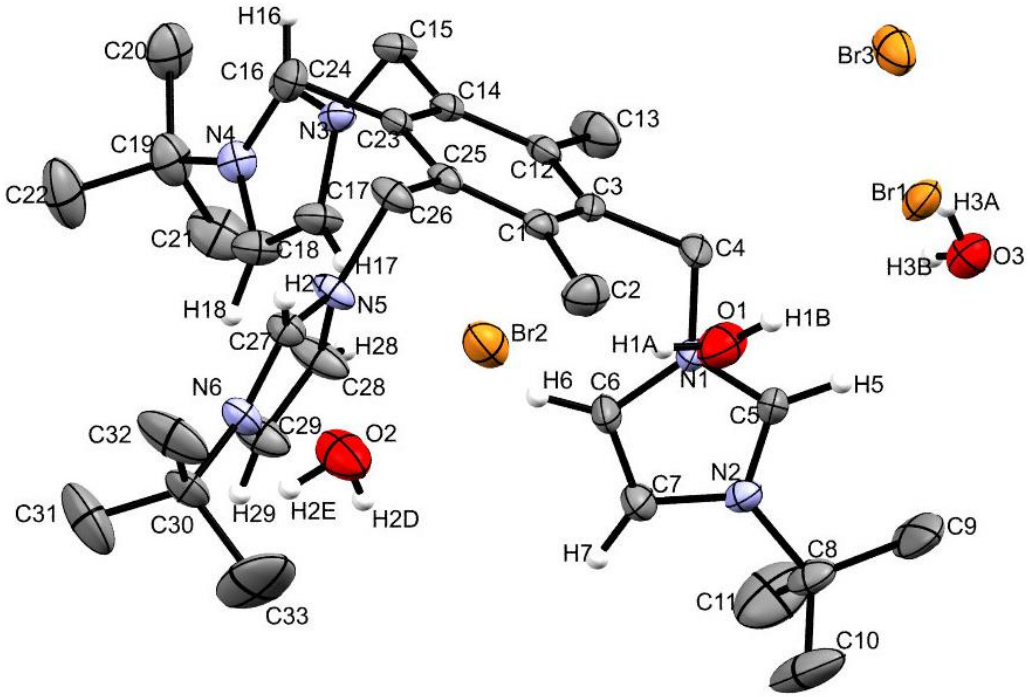

Figure 3.17. X-Ray crystal structure of compound **72** (ORTEP representation). Thermal ellipsoids represented at 50% probability. Some of the hydrogen atoms of **72** have been omitted for clarity.

A summary of the bond lengths is reported below in Table 3.2. Bond lengths and angles for **72** are similar to the related compound **70** and the values are typical of sp2/sp3 hybridised carbons. In the X-ray crystal structure of **72** depicted in Figure 3.18 it is possible to appreciate the presence of a molecule of water interacting with the imidazolium hydrogens within the pocket formed by the *syn* conformation adopted by the three *tert*-butylimidazolium arms at a distance of approximately 2.5 Å.

The encapsulated water molecules have also strong hydrogen bonding interactions with the bromide anions that interact with two or more molecules of **72**. Hydrogen bonding interactions were also observed between the methyl substituents of the hexasubstituted aromatic core of two molecules of **72**. This network of interactions appears to be responsible for the formation of a tetrameric assembly observed in the structure of compound **72** (Figure 3.19)

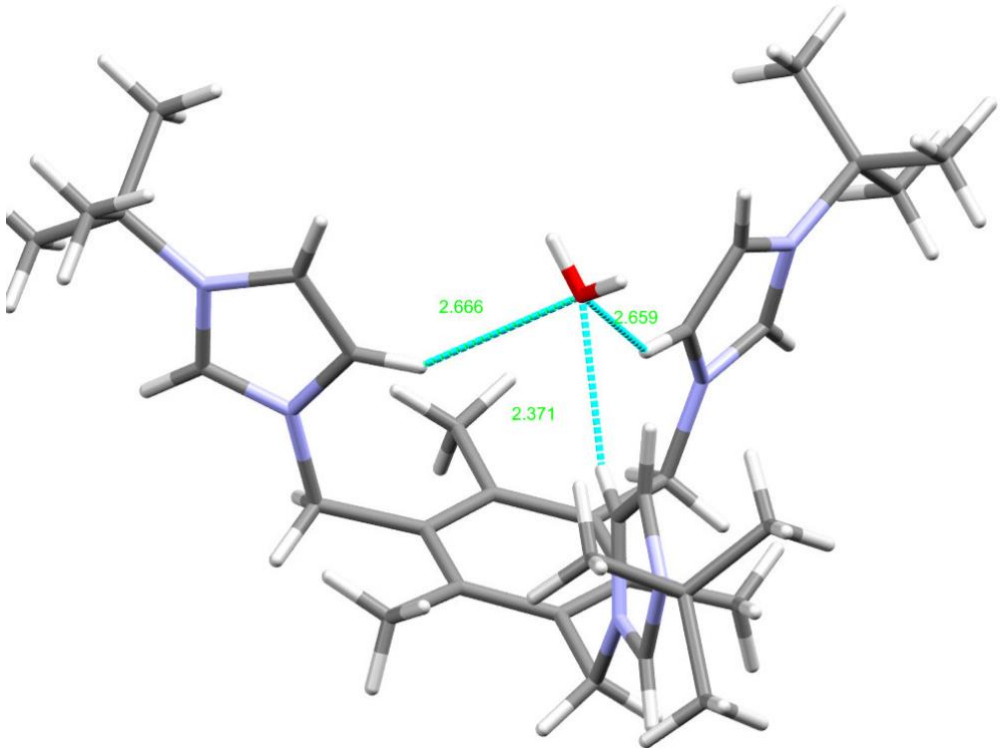

Figure 3.18. Structure of compound **72** highlighting the short contact interactions.

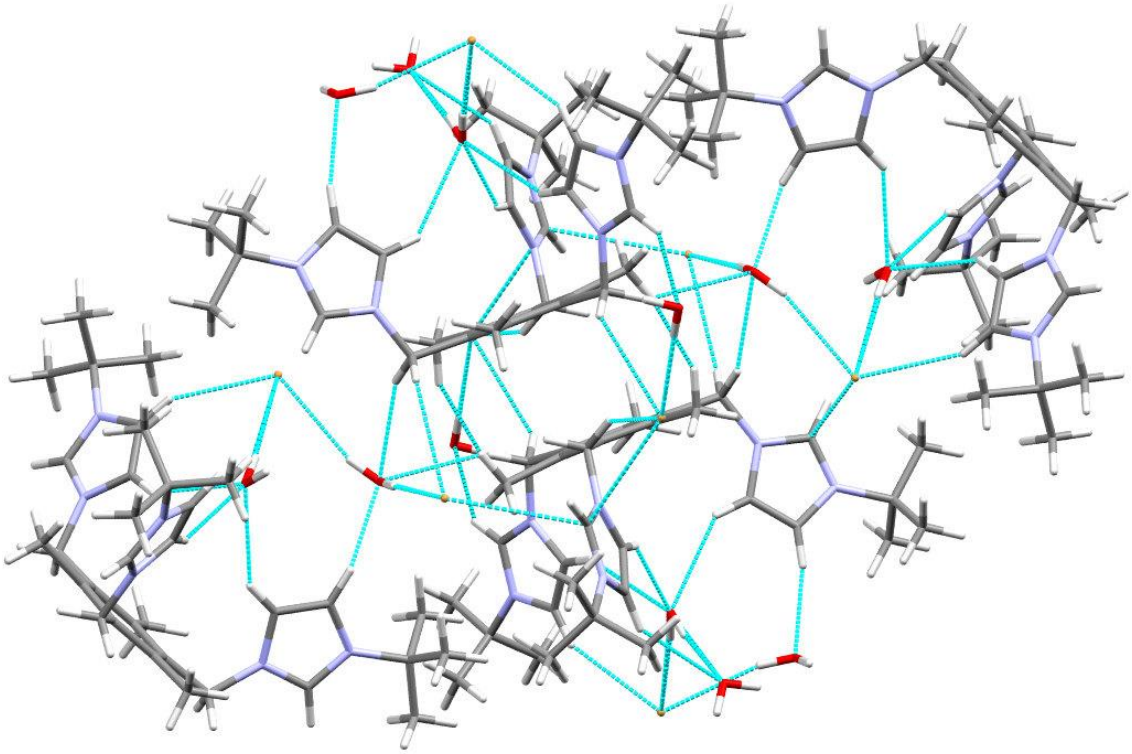

Figure 3.19. Representation of the packing unit of compound **72** highlighting the network of short contact interactions between compound **72**, bromide anions and water molecules.

Table 3.2. Selected bond angles and distances for compound **72**.

Atoms involved	Angle (°) / Distance (Å)
C3-C4-N1	111.7(2)°
N1-C5N2	109.3(2)°
C5-N2-C7	108.2(2)°
N2-C7-C6	107.1(3)°
C7-C6-N1	107.1(3)°
C6-N1-C5	108.3(2)°
C7-N2-C8	125.1(2)°
C1-C2	1.515(4) Å
C4-N1	1.488(4) Å
N1-C5	1.325(3) Å
C6-C7	1.352(4) Å
N1-C6	1.376(4) Å
N2-C8	1.509(4) Å
H6-O2	2.666(5) Å

3.3. Mesitylimidazole-based tripodal systems

With the aim of developing a series of NHC-based receptors containing bulkier steric groups, thus helping the stabilisation of low oxidation state metal centres, a further two new tripodal systems were successfully synthesised and characterised. The pro-ligands described in this section are based upon the previously synthesised hexasubstituted benzene cores **60** and **61**, and the monosubstituted 1-mesityl-1H-imidazole as arms.

The synthesis of the monosubstituted imidazole, compound **74**, consisted of a two-step 1-arylimidazole synthesis performed following a modified procedure from Liu *et al*, which afforded **74** as colourless needles after recrystallisation. ^{1}H NMR spectroscopy analysis performed on the reaction pro duct (Figure 3.20), indicated that the reaction was successful, and the product was obtained with good purity. The spectrum obtained was in agreement with literature data.[9]

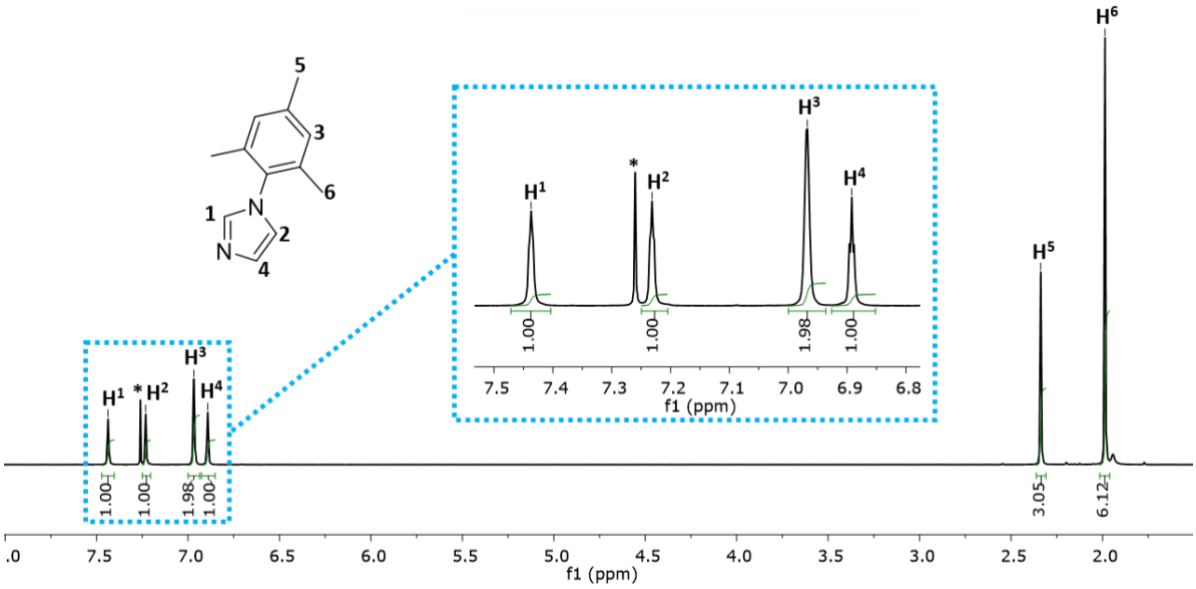

Figure 3.20. ^{1}H NMR (400 MHz, $CDCl_3$, 298 K) spectrum of compound **74**. For clarity, magnetically equivalent nuclei within the same NMR spin system are labelled once. * $CDCl_3$.

The synthesis of two tripodal receptors bearing the monosubstituted imidazole **74** as arms was carried out under similar conditions as for compounds **72** and **73**, exploiting Schlenk techniques and by using dry acetonitrile as solvent (Scheme 3.7). The reaction mixture containing one equivalent of hexasubstituted benzene and an excess of imidazole **74** was stirred under reflux for 48 hours. After cooling down to room temperature, the solvent was removed under vacuum and the crude product was recrystallised from a mixture of tetrahydrofuran/pentane to give **75**,

and a mixture of acetonitrile/diethyl ether to give **76**. Both compounds were obtained with good yields (66-70%).

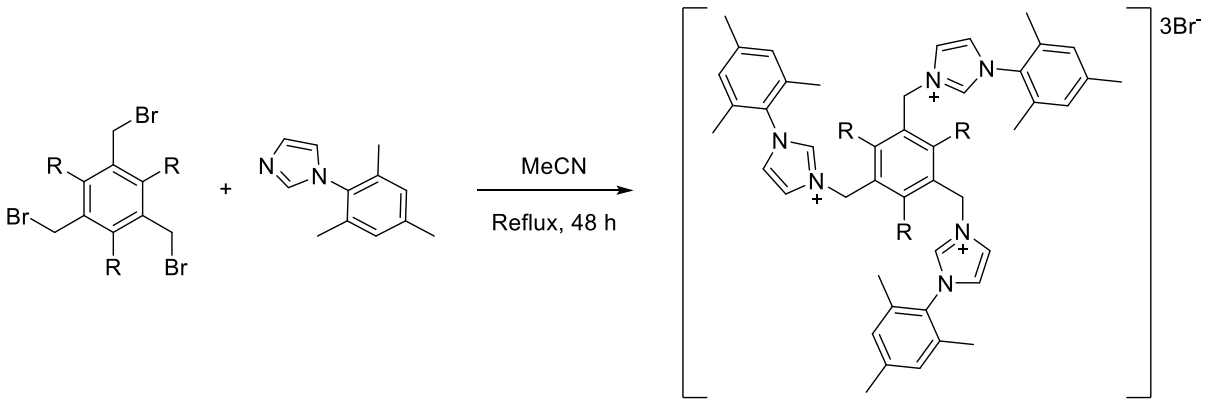

60, R = Me
61, R = Et

75, R = Me
76, R = Et

Scheme 3.7. Synthetic pathway leading to compounds **75** and **76**.

The novel ligands were characterised by routine spectroscopic techniques. ^{1}H NMR spectra of compounds **75** and **76** (see Figure 3.21) were comparable to the previously synthesised imidazolium-based tripodal systems. The mesitylimidazolium arms showed 4 downfield resonances, between 7–10 ppm, which were assigned to the aromatic protons. Two further resonances at 2.3 and 1.9 ppm were correlated to the *para*- and *ortho*- methyl groups of the mesityl substituent respectively.

The mass spectra of compounds **75** and **76** are shown in Appendix B. From the mass spectrum of **75** it was possible to identify a peak at m/z = 239.1537 corresponding to the triply-charged molecular ion $[M]^{3+}$. The mass spectrum of compound **76** showed a peak at m/z = 919.3514 which was assigned to the ion species $[M+2^{79}Br]^{+}$, a further example of how tripodal imidazolium-based systems strongly interact with anions.

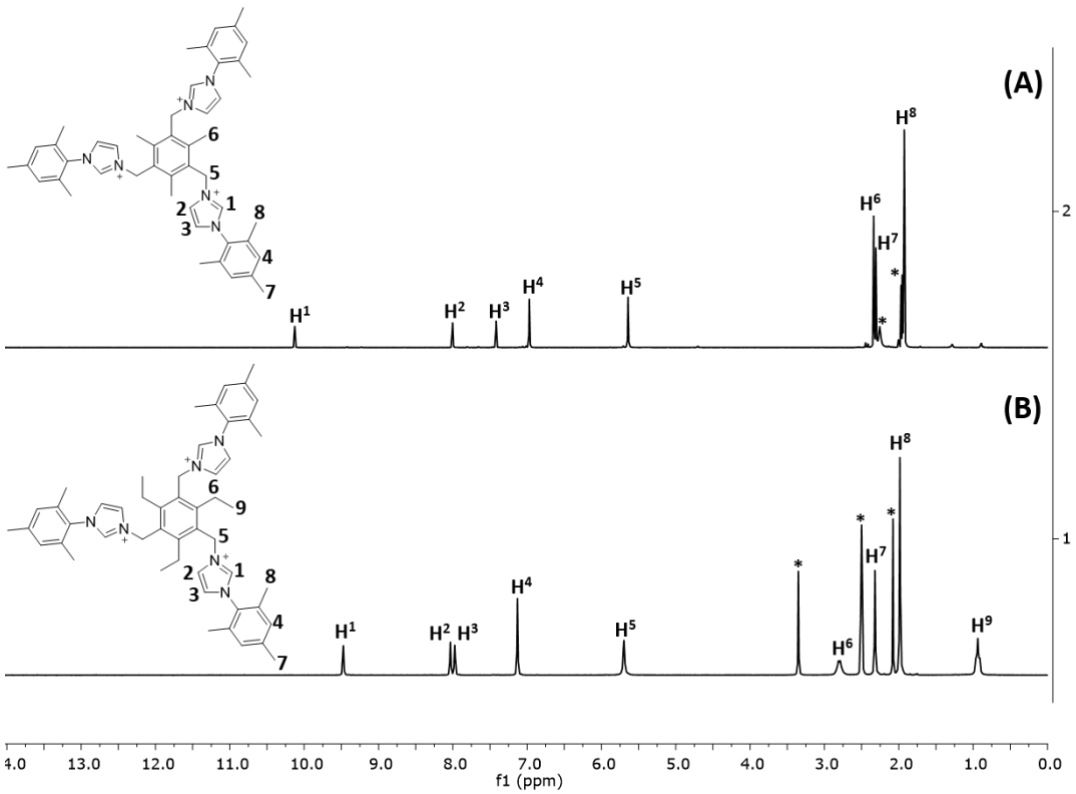

Figure 3.21. 1H NMR (300 MHz, DMSO-d6, 298 K) spectra of mesitylimidazolium-based tripodal ligands. **(A)** Compound **75**, **(B)** compound **76**. * residual solvents and impurities traces.

Using the same reaction protocol as for compound **73**, anion metathesis was performed on both compounds **75** and **76**. The two compounds, **75·3PF6** and **76·3PF6**, were obtained in quantitative yields and the purity was deemed acceptable by NMR spectroscopy, so to enable further reactions to be carried out.

Suitable crystals for X-ray analysis for compound **75·3PF6** were obtained by vapour diffusion using acetonitrile and diethyl ether. Compound **75·3PF6** crystallises in the monoclinic $P2_1/c$ space group and, differently from the previously described tripodal systems, assumes a conformation that has arms in a "two-up one-down" arrangement (Figure 3.22), thus without forming a cage-like structure. The crystal structure shown in Figure 3.23 shows multiple H···F interactions between the fluorines of the counterions and the hydrogens of the mesitylimidazolium moieties at an average distance of 2.5 Å. These interactions are responsible for the polymeric association of molecules of **75·3PF6** along the packing unit (Figure 3.24). A similar type of assembly was observed for the crystal structure of compound **70**.

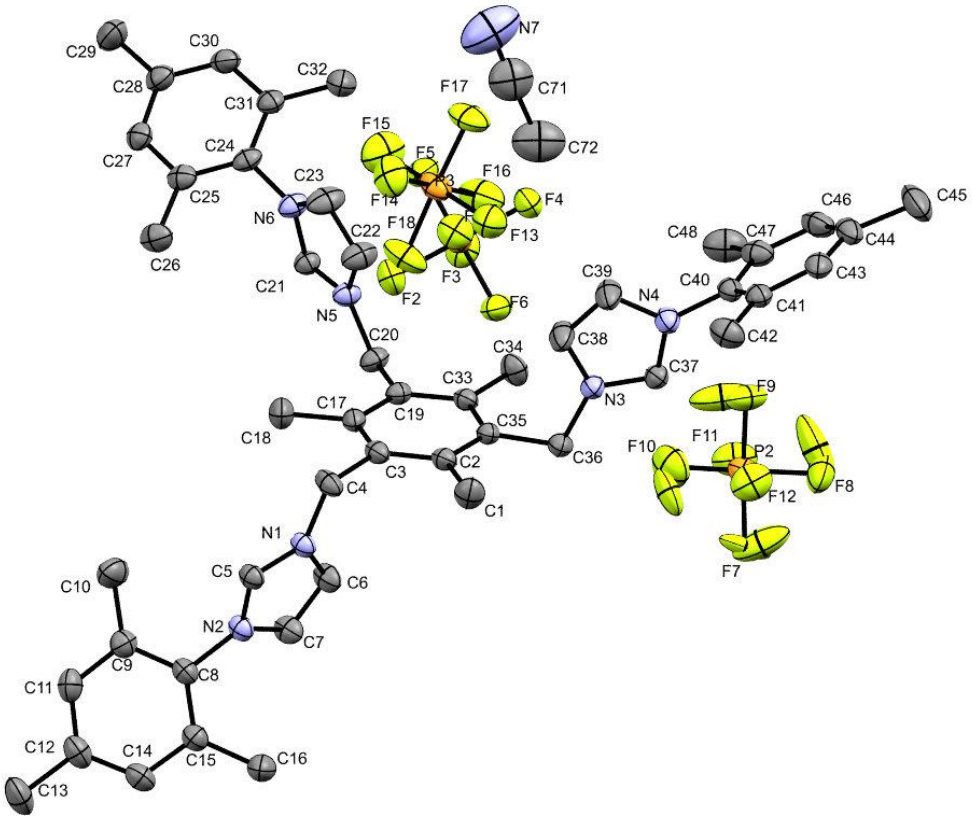

Figure 3.22. X-Ray crystal structure (ORTEP representation) of compound **75·3PF6**. Thermal ellipsoids represented at 50% probability. Hydrogen atoms have been omitted for clarity.

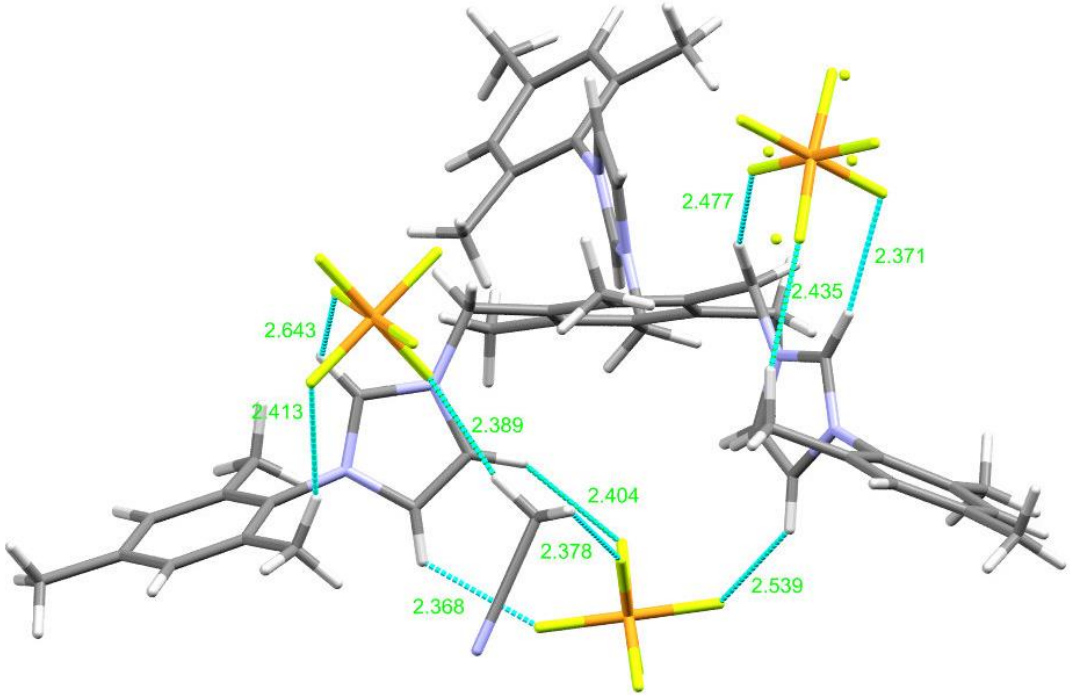

Figure 3.23. Structure of compound **75·3PF6** highlighting the short contact interactions.

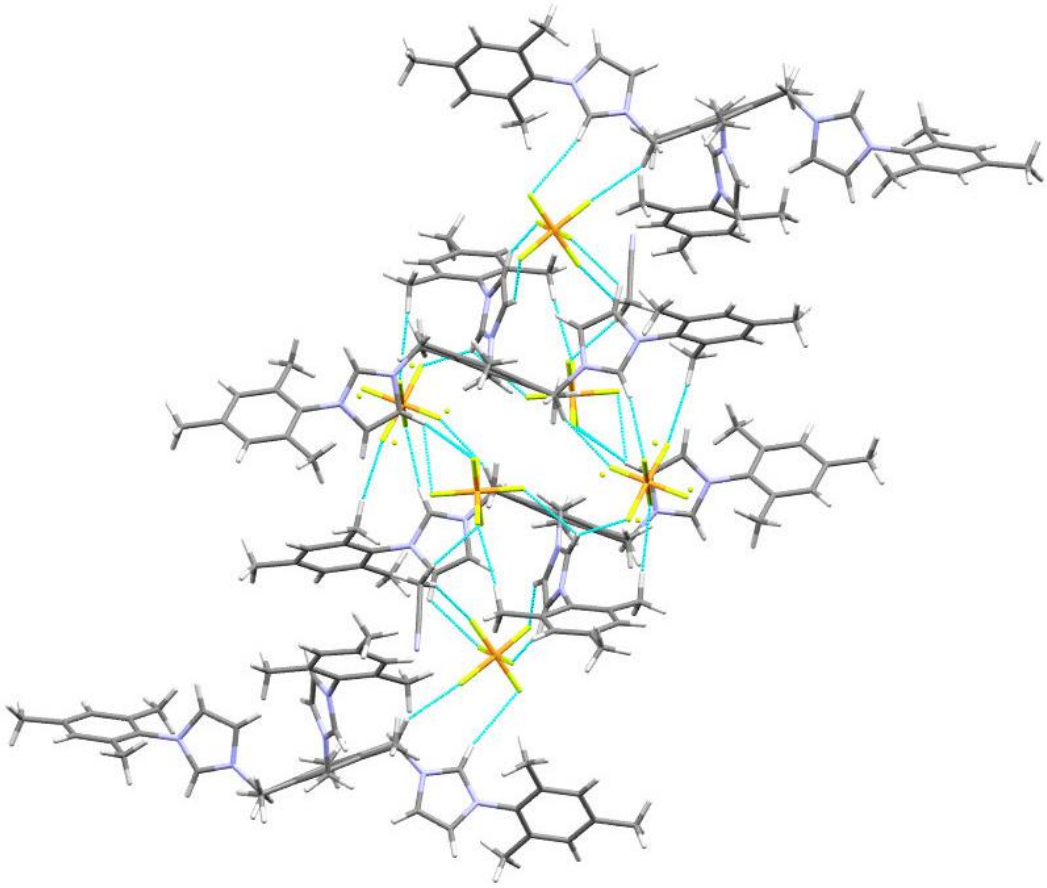

Figure 3.24. Molecular structure of compound **75·3PF$_6$** showing the packing diagram in a fragment of the unit cell.

The angles and bond distances measured for **75·3PF$_6$**, a selection of which are reported in Table 3.3, are comparable to the previously discussed tripodal ligands (*e.g.* compound **70**).

Table 3.3. Selected bond angles and distances for compound **75·3PF$_6$**.

Atoms involved	Angle (°) / Distance (Å)
C3-C4-N1	110.53(2)°
N1-C5-N2	108.70(2)°
C5-N2-C7	108.25(2)°
N2-C7-C6	106.97(2)°
C7-N2-C8	126.07(2)°
C1-C2	1.517(3) Å
C3-C4	1.512(3) Å
C4-N1	1.483(3) Å
N1-C5	1.322(3) Å
C6-C7	1.345(3) Å

Suitable single crystals of compound **76·3PF6** for X-ray diffraction were obtained analogously to compound **75·3PF6**. An ORTEP representation of **76·3PF6** is showed in Figure 3.25. Compound **76·3PF6** crystallises in the orthorhombic Pnma space group. The crystal structure includes solvent molecules filling the intermolecular space, one of which appears to be accommodated in the cavity of **76·3PF6**. Furthermore, N7 of the acetonitrile solvent interacts with the imidazolium hydrogens bonded to the two C6 of the imidazolium heteroatoms facing each other (see Figure 3.25 **B**). It is possible that such interactions are responsible for this cage-like conformation.

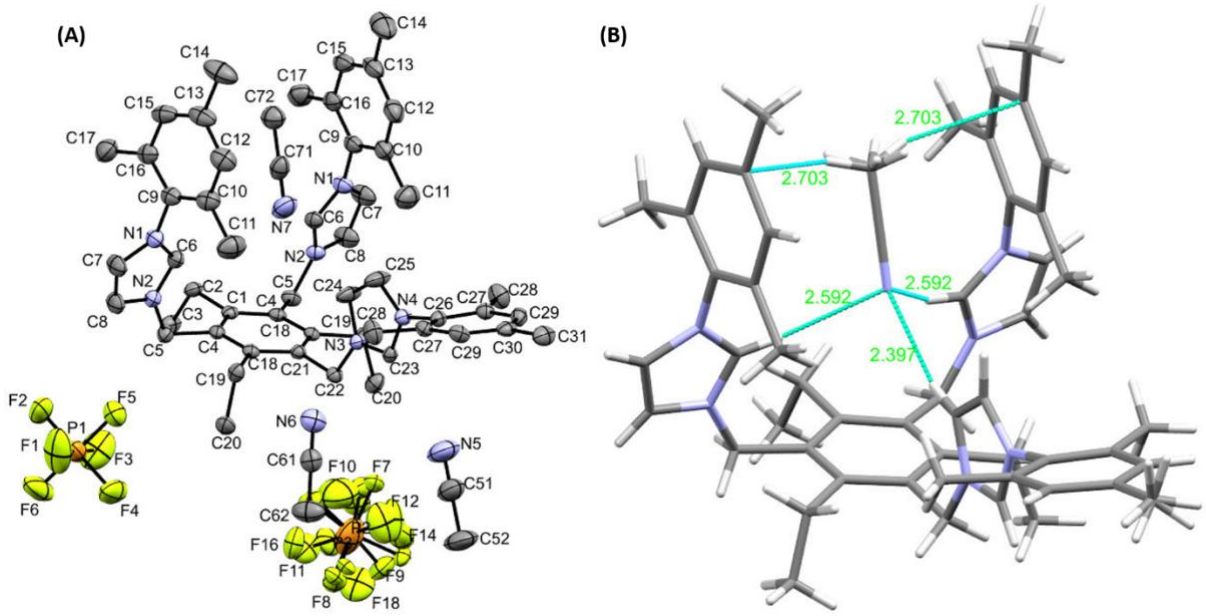

Figure 3.25. X-Ray crystal structure of compound **76·3PF6**. **(A)** ORTEP representation of **76**. Thermal ellipsoids represented at 50% probability. Hydrogen atoms have been omitted for clarity. **(B)** Structure of compound **76** highlighting the short contact interactions between the mesityl imidazolium arms of **76** and one acetonitrile molecule.

Analysis of the unit cell of compound **76·3PF6**, an example of which is shown in Figure 3.26, revealed a closely packed cell unit due to a network of interactions between molecules of **76**, the solvent and the hexafluorophosphate counterion. Particularly crucial to this type of conformation is the presence of the counterion deeply embedded within the pocket of compound **76·3PF6**. A summary of the bond lengths is reported below in Table 3.4.

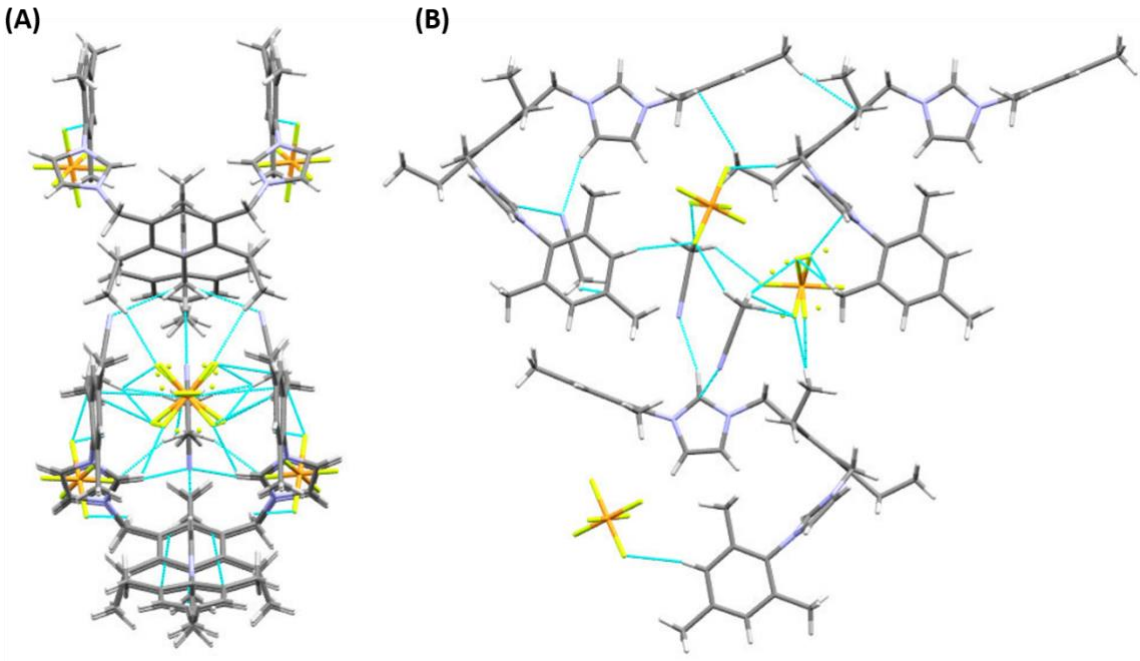

Figure 3.26. Representation of the unit cell of compound **76·3PF6**. **(A)** View along the a-axis, and **(B)** view along the b-axis.

Table 3.4. Selected bond angles and distances for compound **76·3PF6**.

Atoms involved	Angle (°) / Distance (Å)
C1-C2-C3	112.41(2)°
C4-C5-N2	112.56(2)°
C6-N1-C9	125.73(2)°
C23-N4-C26	123.13°
C1-C2	1.527(3) Å
C4-C5	1.509(3) Å
C5-N2	1.489(3) Å
H6-N7 (acetonitrile)	2.592(5) Å
H24-N7 (acetonitrile)	2.397(5) Å

A second batch of crystals of compound **76·3PF6** was obtained by slow evaporation of a concentrated solution of **76·3PF6** in acetonitrile. Compound **76·3PF6** crystallises in the triclinic P-1 space group. The structure, reported in Figure 3.27, is comparable to compound **75** where the molecule assumes an "open" configuration, with the three arms pointing in separate directions. To minimise the steric hindrance, the three ethyl arms adopt a "two-up one-down"

configuration. However, the presence of molecular disorder along one of those arms suggests that such a configuration is a dynamic equilibrium in which the arms of the tripodal system **76·3PF6** can "flip" above and below the plane of the central benzene ring. The packing unit of shows further interactions between the mesityl moieties of two molecules of **76·3PF6** (Figure 3.28), which may be responsible for the "open" conformation adopted by the molecule.

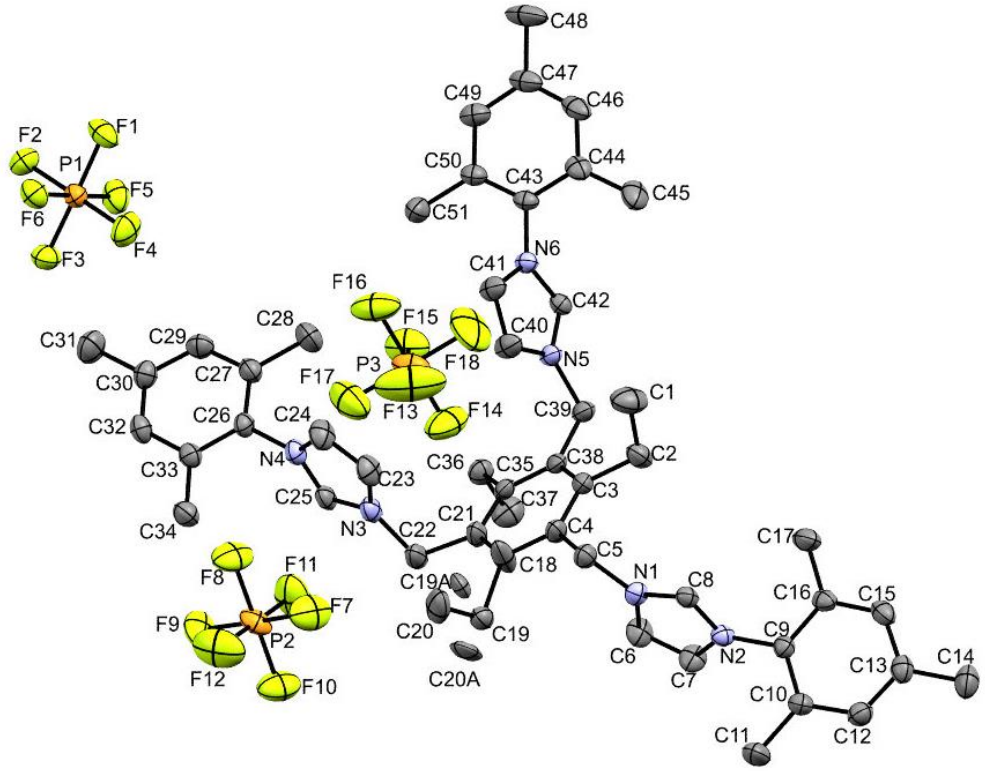

Figure 3.27. X-Ray crystal structure (ORTEP representation) of compound **76·3PF6** in "open configuration". Thermal ellipsoids represented at 50% probability.

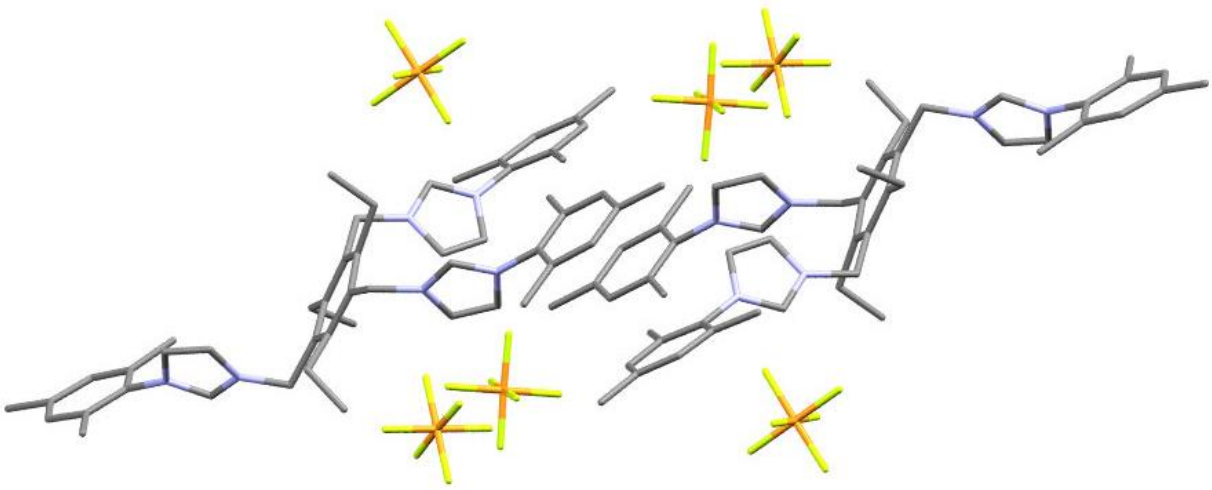

Figure 3.28. Representation of a packing unit of compound **76·3PF6** in "open" configuration. Hydrogen atoms have been omitted for clarity.

From the packing visualisation of the unit cell (Figure 3.29) it was possible to appreciate the presence of short contact interactions, at an average distance of 2.5 Å, between the imidazolium moieties and the hexafluorophosphate anions. Moreover, the "open" configuration assumed by compound **76·3PF$_6$** appear to be due to further interactions between the counterion and the mesitylene groups.

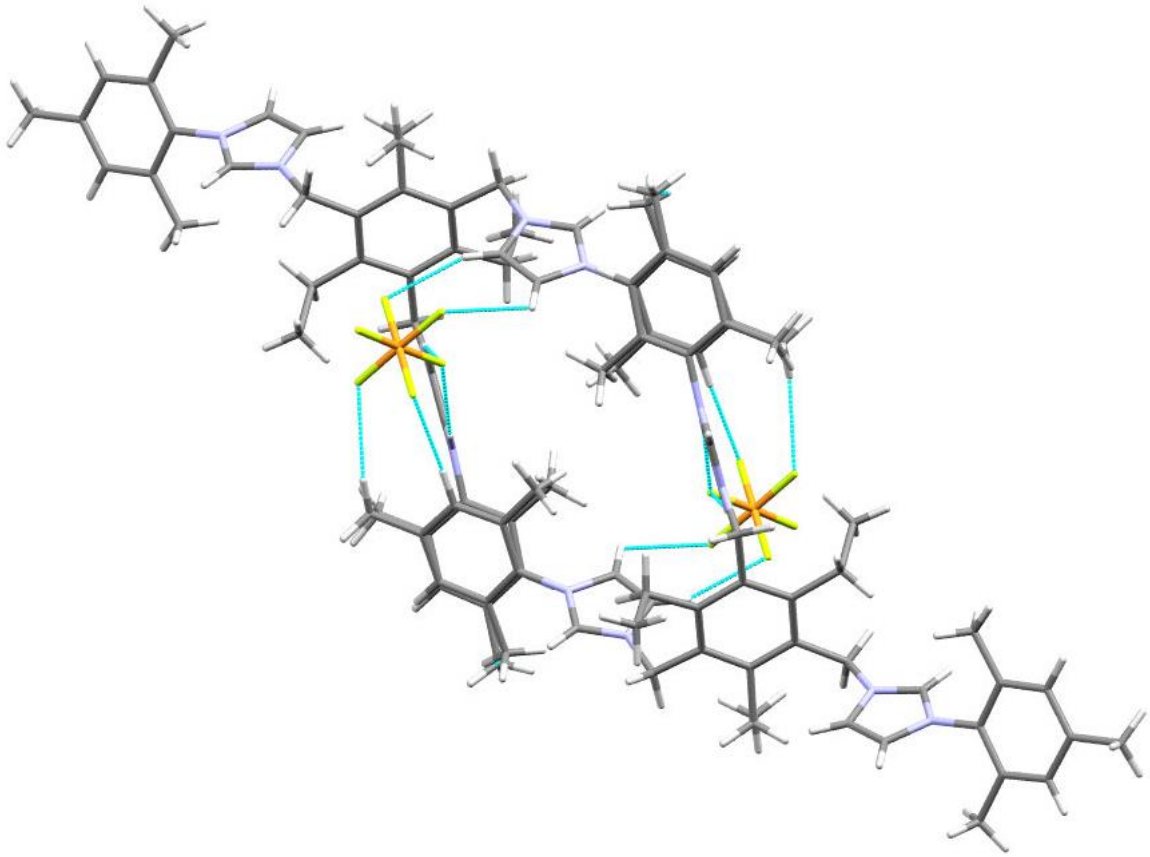

Figure 3.29. Unit cell of compound **76·3PF$_6$** in "open" configuration, highlighting the H···F interaction between the imidazolium and mesityl moieties of **76·3PF$_6$** and the hexafluorophosphate anions.

3.4. Summary of Chapter 3

This chapter described the syntheses of 9 tripodal receptors which are based upon the two hexasubstituted aromatic core **60** and **61** and unsymmetrical imidazole arms with different methyl, *tert*-butyl and mesityl moieties. Initially, we performed the syntheses of two symmetrical tripodal ligands bearing three methylimidazole arms. It was possible to obtain a single crystal suitable for X-ray diffraction analysis for the novel compound **70**, which allowed us to visualise how the three imidazole arms are accommodated towards the same side to form a pocket, which in turn closely interacts with the molecule's counterions. Moreover, these interactions are responsible to the formation of polymeric assemblies.

Furthermore, 4 tripodal ligands based on the bulkier *tert*-butyl and mesityl imidazole were obtained in good yields and purity. Crystal structures were also obtained for the novel compounds **75** and **76**, which have allowed us to gain some understanding of how those systems present a dynamic equilibrium between "open arms" or a "closed arms" configuration and the influence of the counterion in the assembly of these systems.

3.5. References for Chapter 3

1. U. Kernbach, M. Ramm, P. Luger and W. P. Fehlhammer, *Angew. Chem. Int. Ed.*, 1996, **35**, 310-312.
2. E. Mas-Marzá, M. Poyatos, M. Sanaú and E. Peris, *Inorg. Chem.*, 2004, **43**, 2213-2219.
3. X. Hu, I. Castro-Rodriguez and K. Meyer, *J. Am. Chem. Soc.*, 2004, **126**, 13464-13473.
4. H. R. Dias and W. Jin, *Tetrahedron Lett.*, 1994, **35**, 1365-1366.
5. A. Rit, T. Pape and F. E. Hahn, *J. Am. Chem. Soc.*, 2010, **132**, 4572-4573.
6. C. E. Ellul, G. Reed, M. F. Mahon, S. I. Pascu and M. K. Whittlesey, *Organometallics*, 2010, **29**, 4097-4104.
7. A. Kumbhar, S. Jadhav, R. Shejwal, G. Rashinkar and R. Salunkhe, *RSC Advances*, 2016, **6**, 19612-19619.
8. M. C. Cassani, M. A. Brucka, C. Femoni, M. Mancinelli, A. Mazzanti, R. Mazzoni and G. Solinas, *New J. Chem.*, 2014, **38**, 1768-1779.
9. J. Liu, J. Chen, J. Zhao, Y. Zhao, L. Li and H. Zhang, *Synthesis*, 2003, **2003**, 2661-2666.

4. Synthesis, characterisation and cellular interactions of novel *bis*-NHC-based tripodal systems with multifunctional capabilities

The possibility to synthesise a tridentate system with unsymmetrical substituents was also investigated in this work, in order to develop ligands capable of binding metals as well as attaching other functionalities (*e.g.* fluorophores, linkers, targeting peptides). A pictorial representation of a conceptual bis-NHC-based tripodal system is shown below in Figure 4.1.

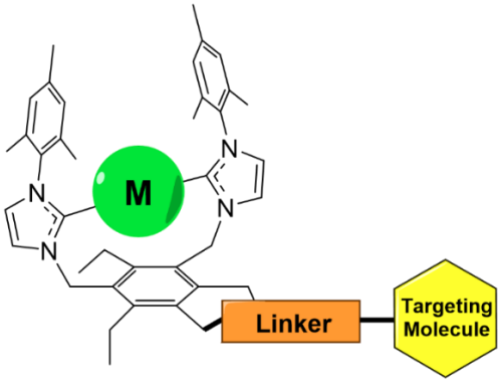

Figure 4.1. Pictorial representation of a conceptual compound based upon a bis-NHC – based tripodal system.

In this chapter, three novel *bis*-NHC-based tripodal receptors bearing different substituents around the hexasubstituted central core were synthesised and characterised. The unsymmetrical *bis*-NHC-based tripodal systems described in this chapter were obtained by replacing one of the imidazolium-based arms of the tripodal ligand **76** (whose synthesis is described in Chapter 3) either with a carboxylic acid-based linker or with an anthracene-thiosemicarbazone moiety. A summary of the functionalities described in this chapter is shown in Scheme 4.1.

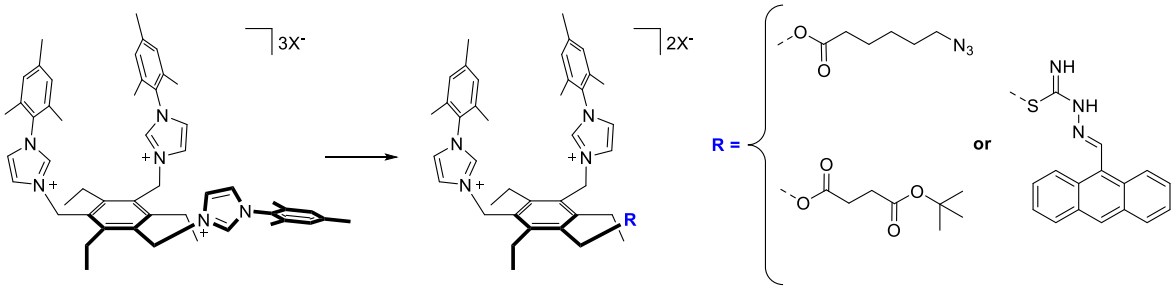

Scheme 4.1. General representation of the unsymmetrical bis-NHC-based tripodal ligands described in this section.

4.1. Bifunctional NHC-based systems bearing a carboxylic linker

The first series of reactions described in this section had the purpose of mono-functionalising the tripodal core (compound **61**). To do so, it was decided to employ linkers bearing carboxylic acids, which are capable of reacting with one of the bromomethyl substituents of the tripodal core *via* a base-catalysed nucleophilic substitution.

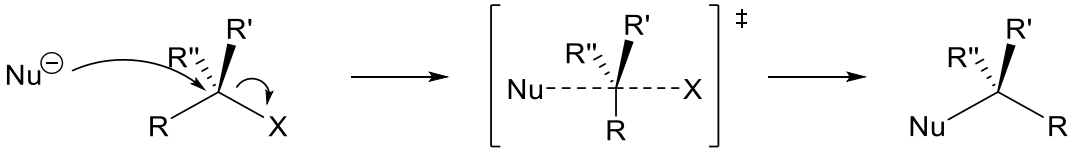

Scheme 4.2. General mechanism of a nucleophilic substitution.

First, compound **61** was treated with the commercially available 4-(tert-butoxy)-4-oxobutanoic acid in presence of potassium carbonate (K_2CO_3) as base, following a procedure previously developed by our group.[1] The reaction was carried out by dissolving compound **61** and the carboxylic acid in acetonitrile, followed by addition of an excess of K_2CO_3. The reaction mixture was stirred under reflux overnight (for a total of 16 hours) before the solvent was removed under vacuum. Following work up, TLC of the organic extract revealed the presence of unreacted starting materials, and thus the product was purified by silica gel chromatography which gave compound **77** as white solid in 29% yield.

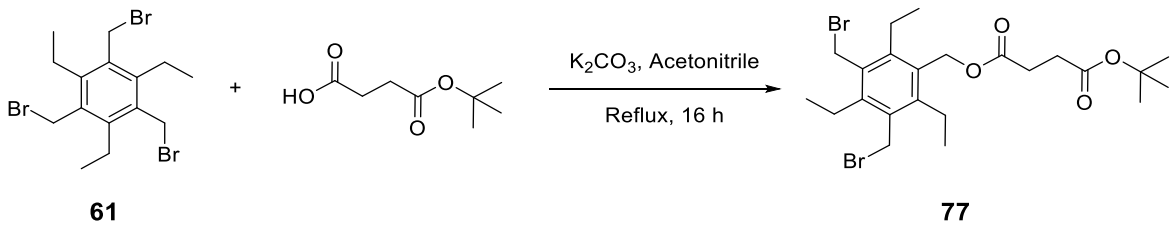

61 **77**

Scheme 4.3. Synthetic pathway leading to compound **77**.

The ^{1}H NMR spectrum recorded for compound **77** (Figure 4.2), showed the presence of nine sets of signals. Two singlets at 5.25 and 4.65 ppm were correlated to the methylene units bridging the 4-(tert-butoxy)-4-oxobutanoate linker (H_1) and the two bromomethyl groups respectively (H_2). Similarly, the two quartets at 2.99-2.93 and 2.87-2.81 ppm were assigned to the C*H*$_2$ of the three ethylene arms around the aromatic core (labelled as H_3 and H_4 in Figure 4.2).

The presence of two sets of signals indicates a magnetically inequivalence between the ethyl arms positioned *para*- and *ortho*- relatively to the linker. Furthermore, the C*H*$_3$ protons belonging to the ethyl arms are subject to the same chemical inequivalence, exhibiting two triplets at 1.40 and 1.31 ppm, assigned to the *para*- and *ortho*- positions respectively (see peaks labelled H$_8$ and H$_9$ in Figure 4.2). Finally, the two multiplets H$_5$ and H$_6$ were assigned to the C*H*$_2$ groups connecting the two carbonyl units of the linker, and the intense singlet H$_7$ at 1.48 ppm was attributed to the nine magnetically equivalent protons of the linker's *tert*-butyl substituent.

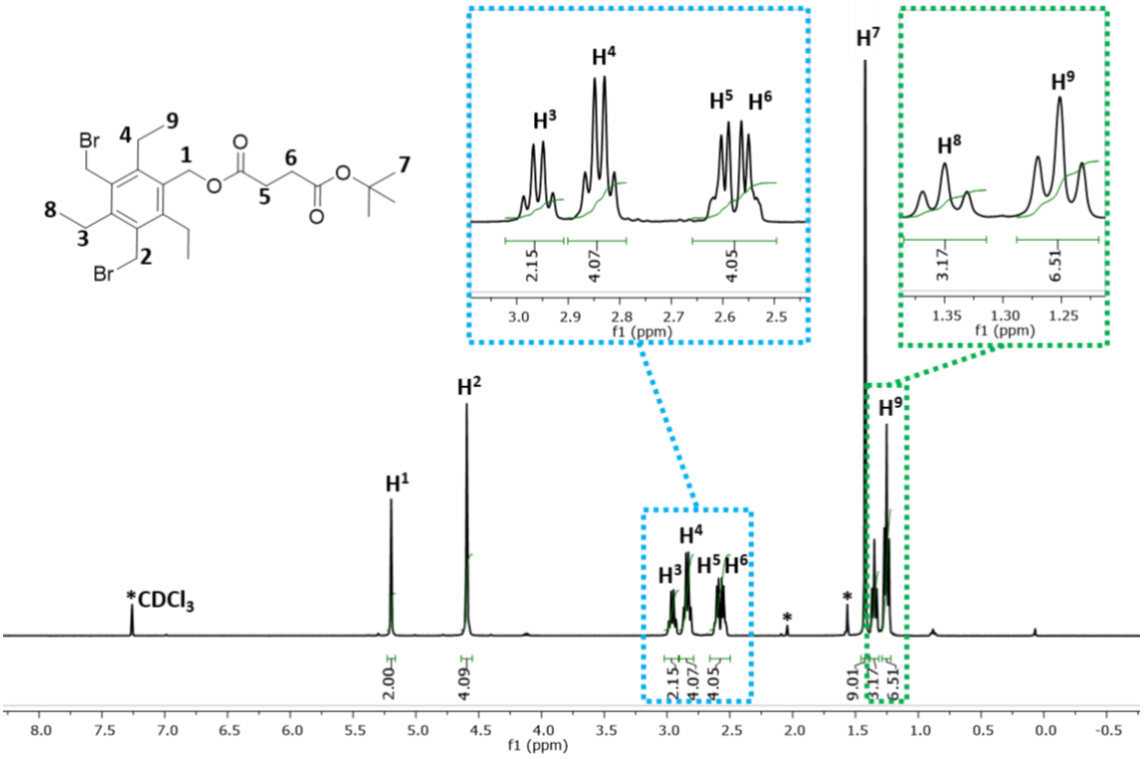

Figure 4.2. $_1$H NMR (400 MHz, CDCl$_3$, 298 K) spectrum of compound **77**. For clarity, magnetically equivalent nuclei within the same NMR spin system are labelled once. * residual solvents and impurities traces.

Following the purification of compound **77** by silica chromatography, the synthesis of the *bis*-imidazolium salt proceeded by reacting **77** with a slight excess of 1-mesityl-1H-imidazole (compound **74**) in dry acetonitrile under reflux conditions. The reaction mixture was monitored by TLC until all of compound **77** was consumed. Finally, recrystallisation from dichloromethane gave rise to compound **78** as a white solid in 83% yield.

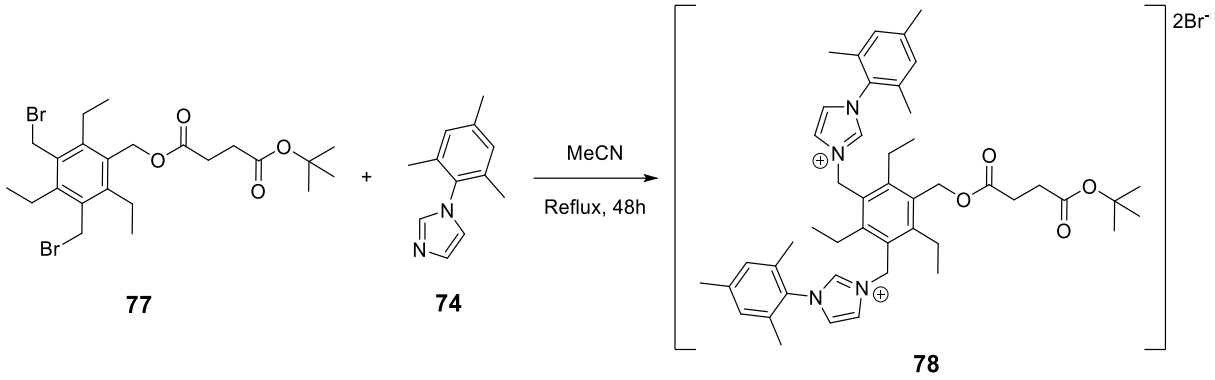

Scheme 4.4. Synthetic pathway leading to compound **78**.

The ^{1}H NMR spectrum of compound **78** (Figure 4.3), shows the characteristic peaks of the bonded imidazolium arms in the downfield part of the spectrum (labelled H_1, H_2 and H_3) and the four aromatic protons of the mesitylene bulky group appear as a singlet at 7.10 ppm (entry H_7 in Figure 4.3). Two more singlets were assigned to the six methyl units of the mesityl groups at 2.29 ppm for the position *para*- (H_9), and 1.95 for the position *ortho*- (H_{10}) relative to the bonded nitrogen.

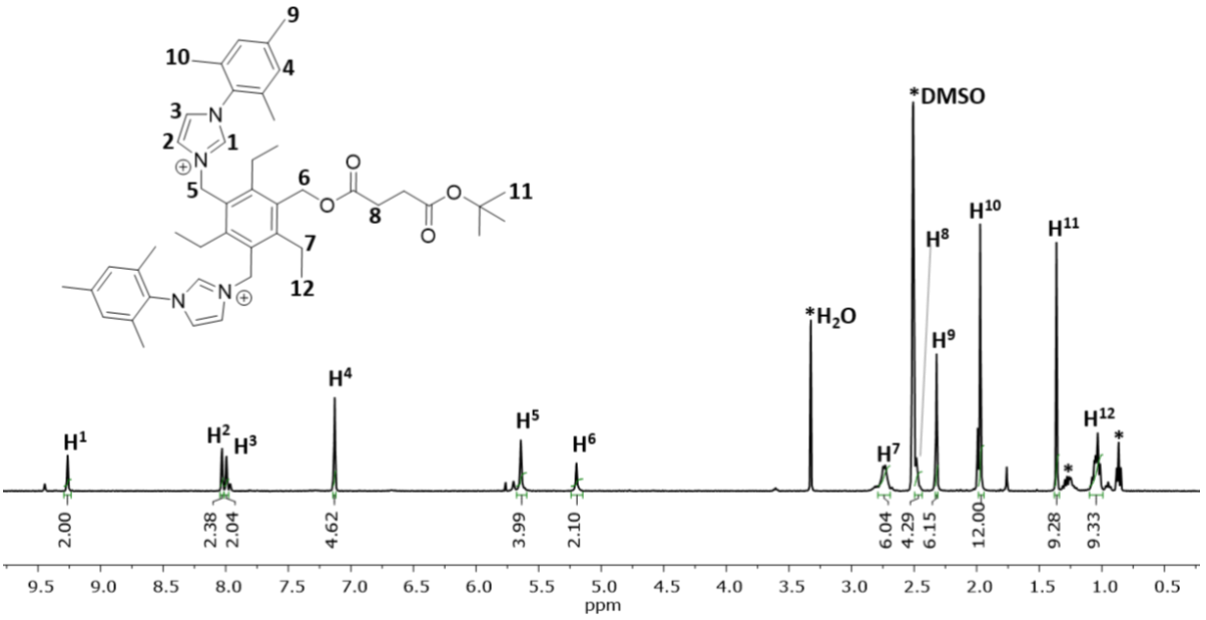

Figure 4.3. ^{1}H NMR (500 MHz, DMSO-d_6, 298 K) spectrum of compound **78**. For clarity, magnetically equivalent nuclei within the same NMR spin system are labelled once. * residual solvents and impurities traces.

The assignment of the ^{1}H NMR spectrum of **78** was carried out using a bidimensional ^{1}H-^{1}H COSY spectrum (Figure 4.4), which displays the correlations among vicinal protons. In this spectrum, three sets of correlating protons were observed: a first set can be identified as the three hydrogens of the imidazolium heterocycle ($H_{1\text{-}2\text{-}3}$); the second set is correlated the

aromatic protons of the mesitylene group with the protons of the methyl substituents situated in the *ortho*- positions (H_9 and H_{10}, compared to the aromatic protons labelled H_4 in both figures 4.3 and 4.4). Finally, the third correlation can be observed between the C*H*$_2$ and C*H*$_3$ protons of the ethyl arms of the tripodal core (H_7 and H_{12}).

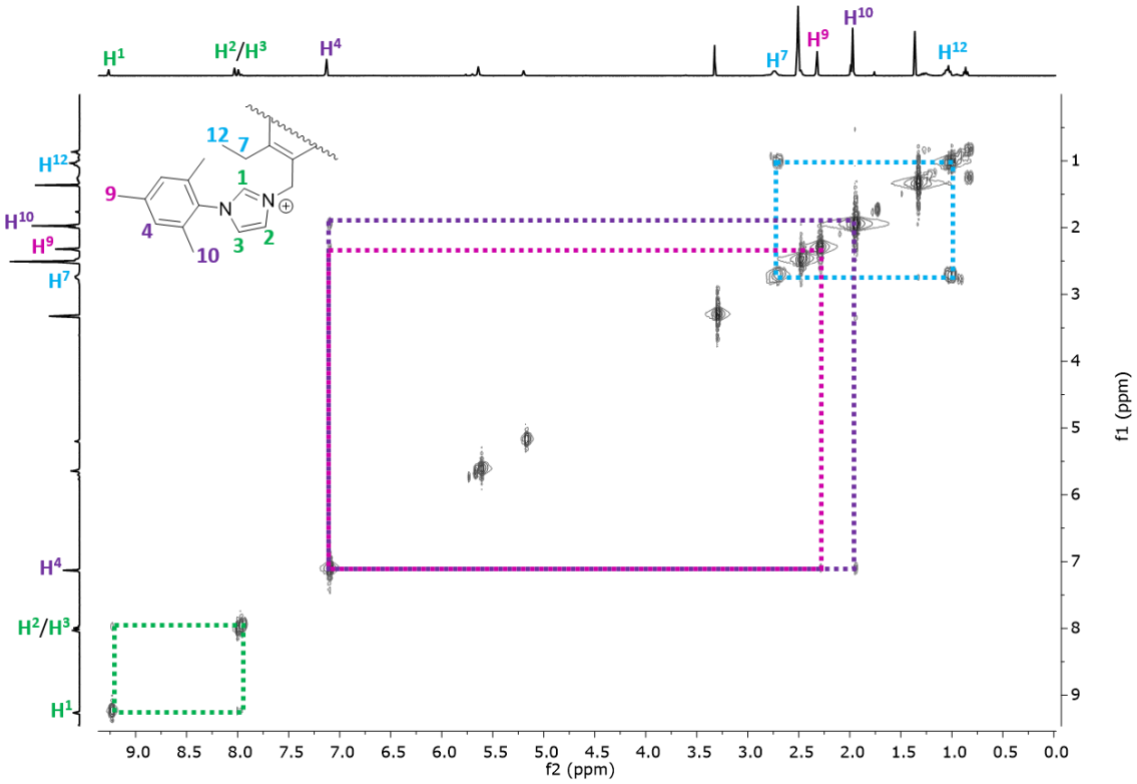

Figure 4.4. ^{1}H-^{1}H COSY NMR (500 MHz, DMSO-d$_6$, 298 K) spectrum of compound **78**.

Mass spectrometry analysis performed on compound **78** (Figure 4.5), shows a peak at m/z = 375.2469, indicating the presence of a dicationic molecular ion $[M]^{2+}$, thus strengthening the hypothesis that compound **78** is a bis-imidazolium salt.

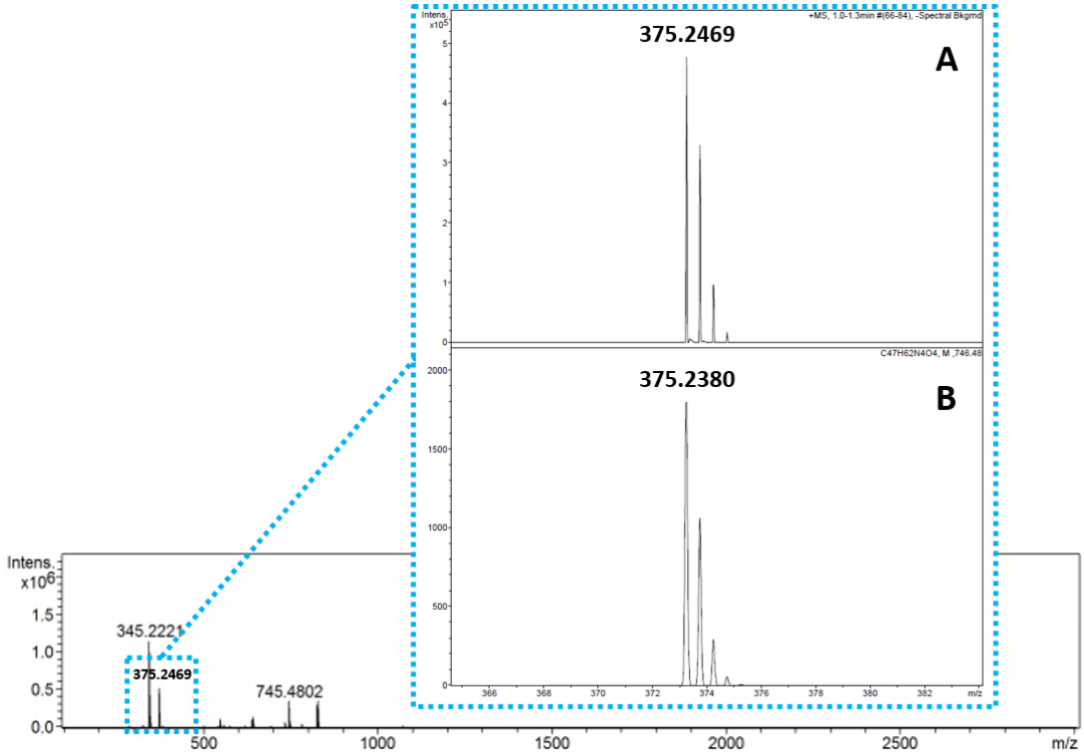

Figure 4.5. Mass spectrum of the compound **78**. A) Ion species $[M]^{2+}$ at m/z = 375.2469, and B) its predicted pattern.

4.2. Bifunctional NHC-based systems bearing a terminal azido linker

A second monofunctionalised tripodal core was obtained by reacting compound **61** with the linker 6-azidohexanoic acid (referred in this work as compound **79**) in refluxing acetonitrile and with potassium carbonate as base. The linker **79** was also synthesised from 6-bromohexanoic acid and sodium azide following an adapted preparation outlined by Travelli and co-workers.[2] A summary of the overall synthesis is reported below in Scheme 4.5.

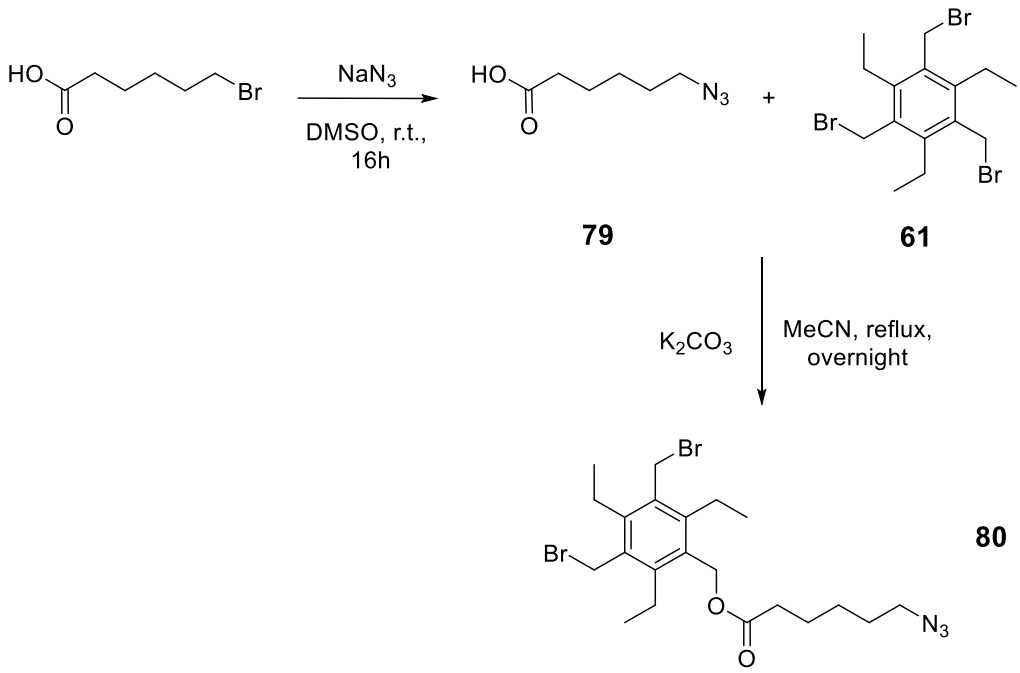

Scheme 4.5. Synthetic pathway leading to the monofunctionalised compound **80**.

As for the previous asymmetric tripodal receptor, compound **80** was treated with a slight excess of mesityl imidazole (compound **74**) in refluxing acetonitrile, affording the dicarbene compound **81** as a white powder in good yield.

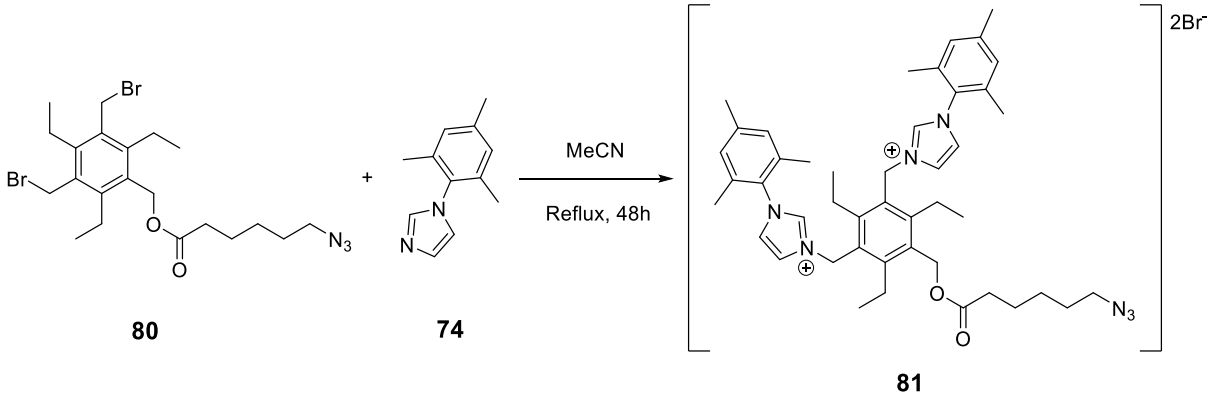

Scheme 4.6. Synthesis of compound **81**.

The ^{1}H NMR spectrum of **81** (Figure 4.6), shows four signals characteristic of the imidazolium arms, between 8.0 and 9.5 ppm. The presence of two singlets at 9.44 and 9.22, assigned to the C2-*H* (labelled H1 in Figure 4.6), may indicate a conformational asymmetry for the two mesityl imidazolium arms or impurity traces in the NMR sample. Resonances assigned to the mesityl substituents were also comparable to the previously synthesised mesityl imidazolium derivatives. Chemical shifts characteristic of the 6-azidohexanoyl linker were also assigned: an expansion of the upfield region is reported in the blue box in Figure 4.6. Such values are in agreement with literature values found for compound **79**.[2]

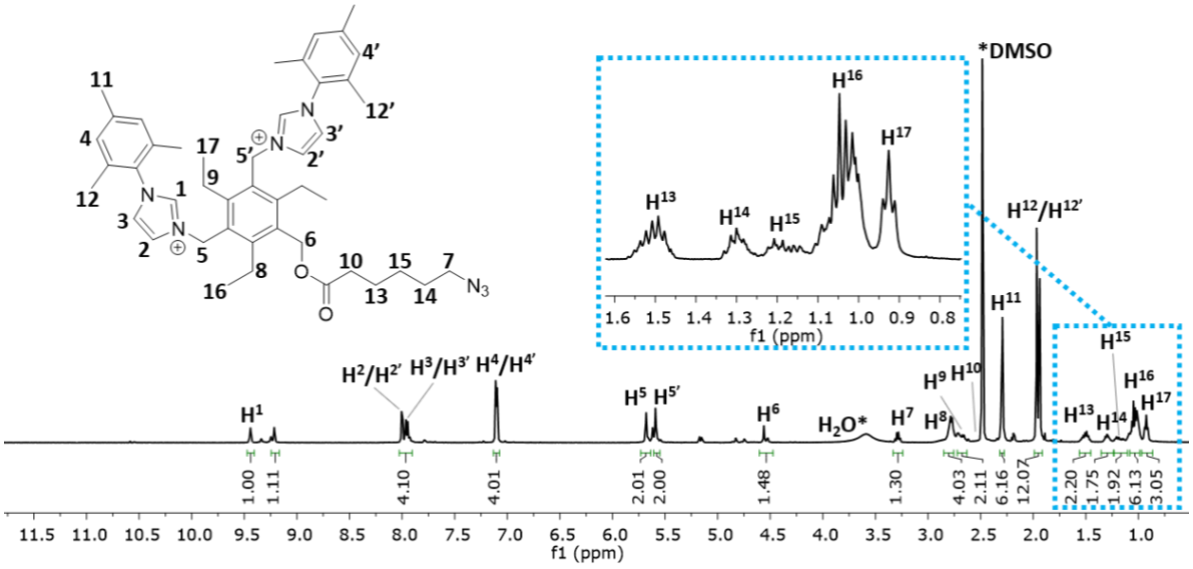

Figure 4.6. ^{1}H NMR (500 MHz, DMSO-d6, 298 K) spectrum of compound **81**. For clarity, magnetically equivalent nuclei within the same NMR spin system are labelled once. * residual solvents and impurities traces.

Mass spectrometry analysis performed on compound **81** confirmed the predicted chemical formula. Positive-mode ESI mass spectrum of **81**, reported in Figure 4.7, shows the presence of a fragment at m/z = 364.7366, indicative of the presence of a doubly-charged molecular ion.

A second fragment with m/z = 810.3881, belonging to a singly-charged species, was attributed to the bromide adduct $[M+^{79}Br]^+$. The base peak of the spectrum of compound **81**, with m/z = 624.2776, appears to be a bromide adduct of the fragmented molecule, where one of the mesityl imidazolium arms is removed (Figure 4.7 **C**).

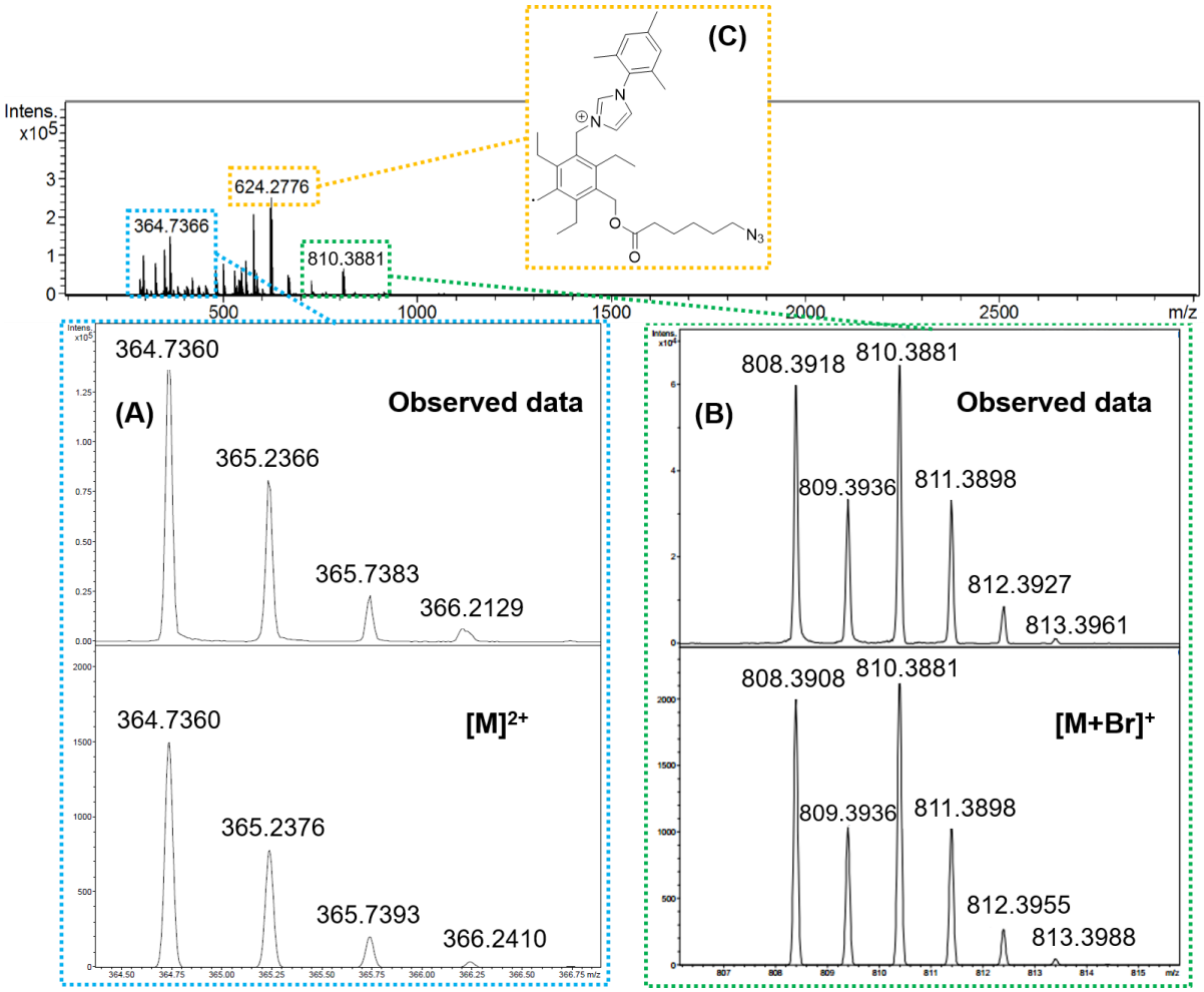

Figure 4.7. Mass spectrum of compound **81**. **(A)** ion species $[M]^{2+}$ of m/z = 364.7360. **(B)** ion species $[M+^{79}Br]^+$ of m/z = 810.3881.

4.3. Synthesis, characterisation and *in vitro* confocal imaging of a *bis*-NHC-based system bearing an anthracene-thiosemicarbazone "arm"

The final part of this chapter describes the development of a new unsymmetrical *bis*-NHC-based tripodal system, designed with the aim of producing a potential ligand that possesses intrinsic fluorescent properties. To achieve this, it was decided to exploit the well-known photophysical properties of anthracene, previously described in Chapter 2.

A second feature of choice was the nature of the linker to be placed between the tripodal core and the fluorophore. We selected thiosemicarbazide, an inexpensive thiourea derivative that is attracting considerable pharmacological interest due to the successful use of the metal complex derivative copper(II)-diacetyl-bis(N(4)-methylthiosemicarbazone (Cu-ATSM) as a hypoxia imaging agent in PET studies.[3] Furthermore, condensation reaction between thiosemicarbazide and aldehydes or ketones gives thiosemicarbazone derivatives which have recently been studied for their anti-tumour properties.[4]

The synthesis was designed to minimise the number of steps so to have the highest overall yield, to use sparingly the reactants and to prevent secondary reactions. The following retrosynthetic analysis (Scheme 4.7) represents the shortest pathway to obtain the final compound **83**.

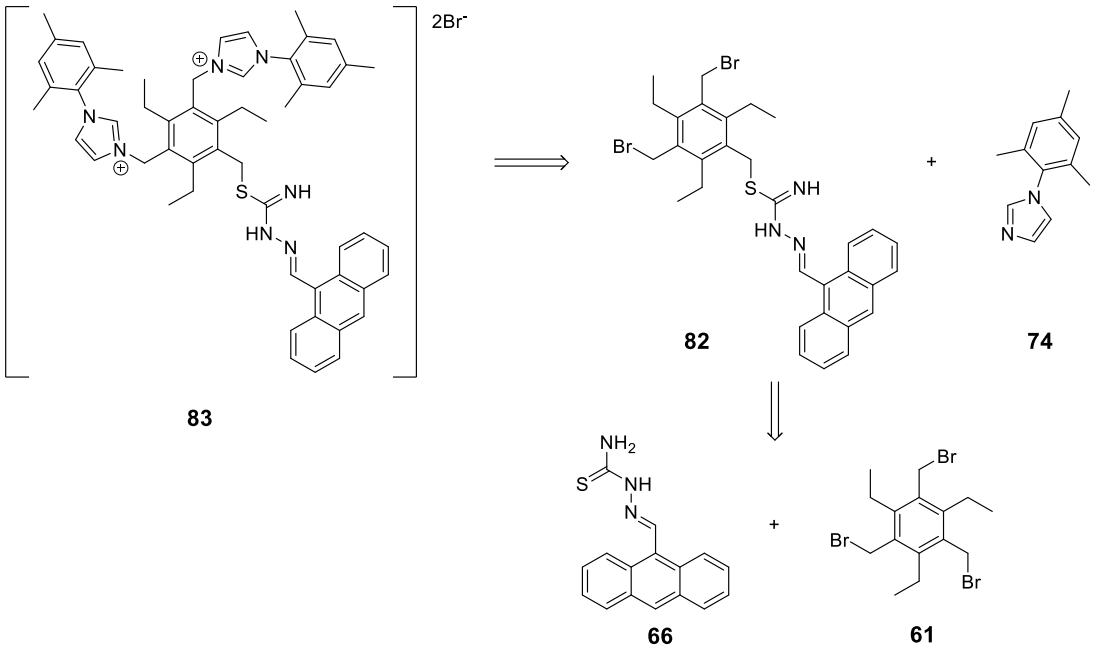

Scheme 4.7. Retrosynthetic analysis leading to compound **83**.

The first disconnection of the tripodal ligand **83** corresponds to a substitution of the two bromide groups of **82** with 1-mesityl-1H-imidazole (compound **74**), which gives the dicationic tripodal ligand. The monosubstituted compound **82** is also product of a substitution of one bromide of compound **61** with anthracene-thiosemicarbazone (compound **66**), whose synthesis is reported in Chapter 2.

The synthesis of the monosubstituted tripodal system **82** was attempted by reacting the core **61** and the linker/fluorophore **66**. The two compounds were dissolved under vigorous stirring in acetonitrile and heated at reflux for 16 hours, leading to the formation of an orange precipitate. After filtering off the orange residue, the mother liquor was concentrated to 1-2 mL and the product was precipitated with diethyl ether to give a bright yellow powder, which was washed copiously to give compound **82** without further purification being required.

The ^{1}H NMR spectrum of **82** (Figure 4.8) shows the triethylbenzene resonances between 1.0 and 3.0 ppm and what appears to be two merged singlets at 4.75 ppm, which we assigned to the six protons of the three methylene groups that connect the two bromo groups and the linker/fluorophore to the core (entry H_6 in Figure 4.8). A second set of resonances, placed between 7.5 and 9.5 ppm, were assigned to the aromatic protons belonging to the anthracene substituent.

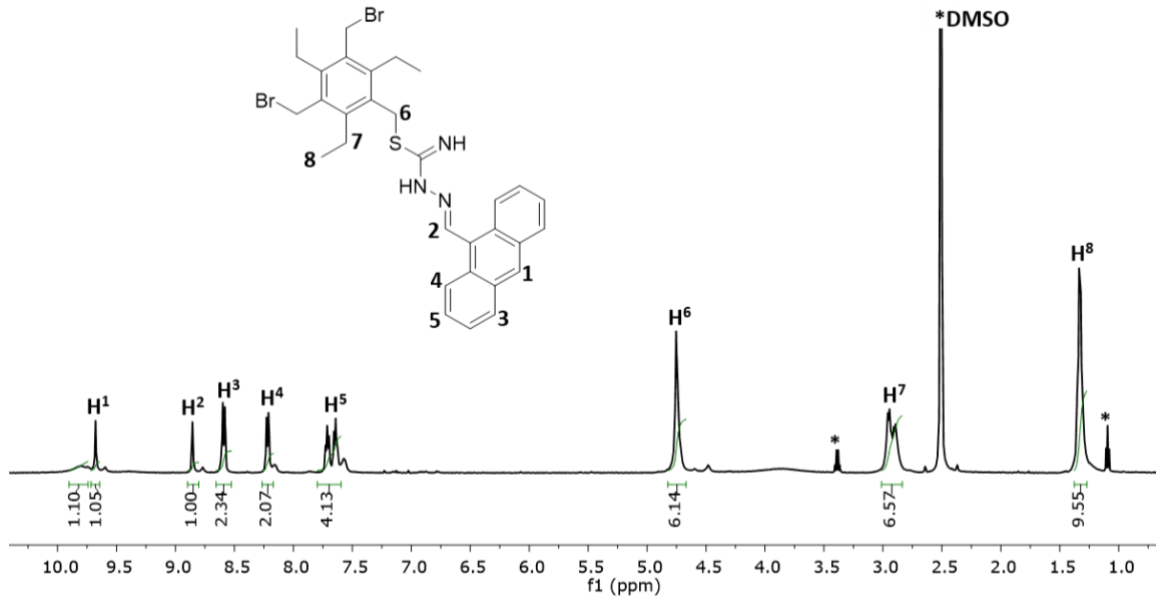

Figure 4.8. 1H NMR (400 MHz, DMSO-d6, 298 K) spectrum of compound **82**. For clarity, magnetically equivalent nuclei within the same NMR spin system are labelled once. * residual solvents and impurities traces.

Mass spectrometry analysis was also performed. Electrospray Ionisation in positive mode for compound **82** (Figure 4.9), shows clearly the presence of two main fragments. The intense peak at m/z = 640.0807 represents the protonated molecular ion $[M+H]^+$, while the less intense signal at m/z = 662.0625 corresponds to the sodium adduct.

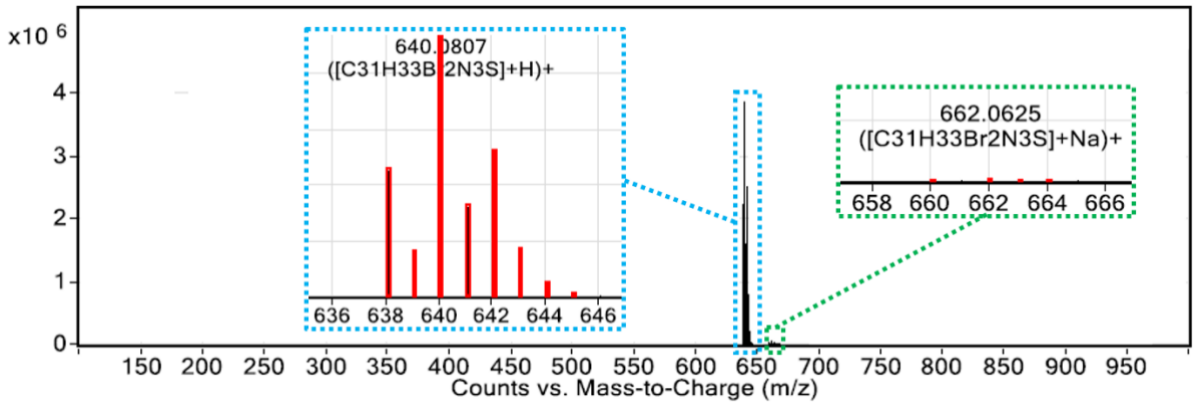

Figure 4.9. Positive-mode ESI-MS for compound **82**. Blue dotted square: Ion species $[M+H]^+$ at m/z = 640.0807. Green dotted square: Ion species $[M+Na]^+$ at m/z = 662.0625.

UV-Visible and fluorescence spectroscopy were also carried out to define the emissive properties of compounds **66** and **82**. Both compounds exhibited broad absorption band in the region 320–460 nm, with structural bands located at 350, 370, and 390 nm, which is typical for transitions between the π-electronic energy levels of the anthracene moiety.[5] Fluorescence emission spectra of both compounds are broad and the resulting Stokes shifts are large, with 107 and 110nm for compounds **66** and **82** respectively (see Figure 4.10).

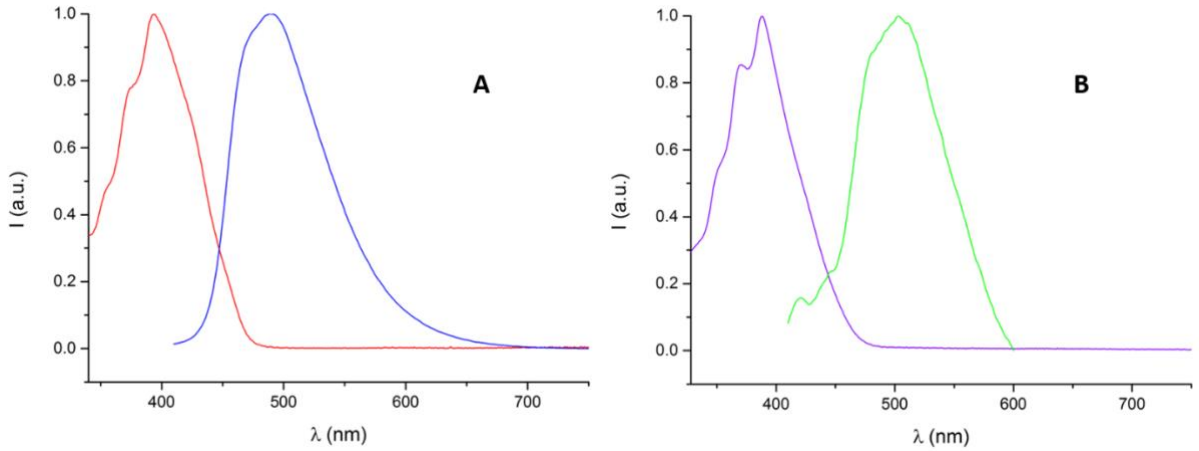

Figure 4.10. A: Normalised UV-Visible (red line) and fluorescence emission (blue line) spectra of compound **66** in CH_2Cl_2 (12.5 µM). **B**: Normalised UV-Visible (violet line) and fluorescence emission (green line) spectra of compound **82** in CH_2Cl_2 (12.5 µM).

To further elucidate the structure of compound **82**, infrared spectroscopy analysis was carried out. The results are shown in Figure 4.11 **B**, along with the FTIR spectrum of the starting material **66** (Figure 4.11 **A**). The spectrum of **66** shows a unique medium-intense band a 3439 cm^{-1} that we assigned to the N-H stretching of the germinal NH_2. The intense band at 1600 cm^{-1} was attributed to the C=N stretching and the strong signal at 1279 cm^{-1} was correlated to the C=S stretching.

In the spectrum of compound **82** (Figure 4.11 **B**) a broad absorption was observed in the higher frequency part of the spectrum, with a strong peak at 2965 cm^{-1}, indicative of the various C-H stretchings from the hexasubstituted benzene core. Two strong signals at 1635 cm^{-1} and 1586 cm^{-1} were correlated to the C=N stretchings of the newly synthesised compound. Coupled with the absence of the C=S stretching previously observed, the IR spectrum of **82** strengthens the hypothesis of the S-alkylation of compound **61** by the thiosemicarbazone **66**, thus reinforcing the case for the proposed structure. A list of the main FT-IR band assignments is for the two compounds is shown in Table 4.1

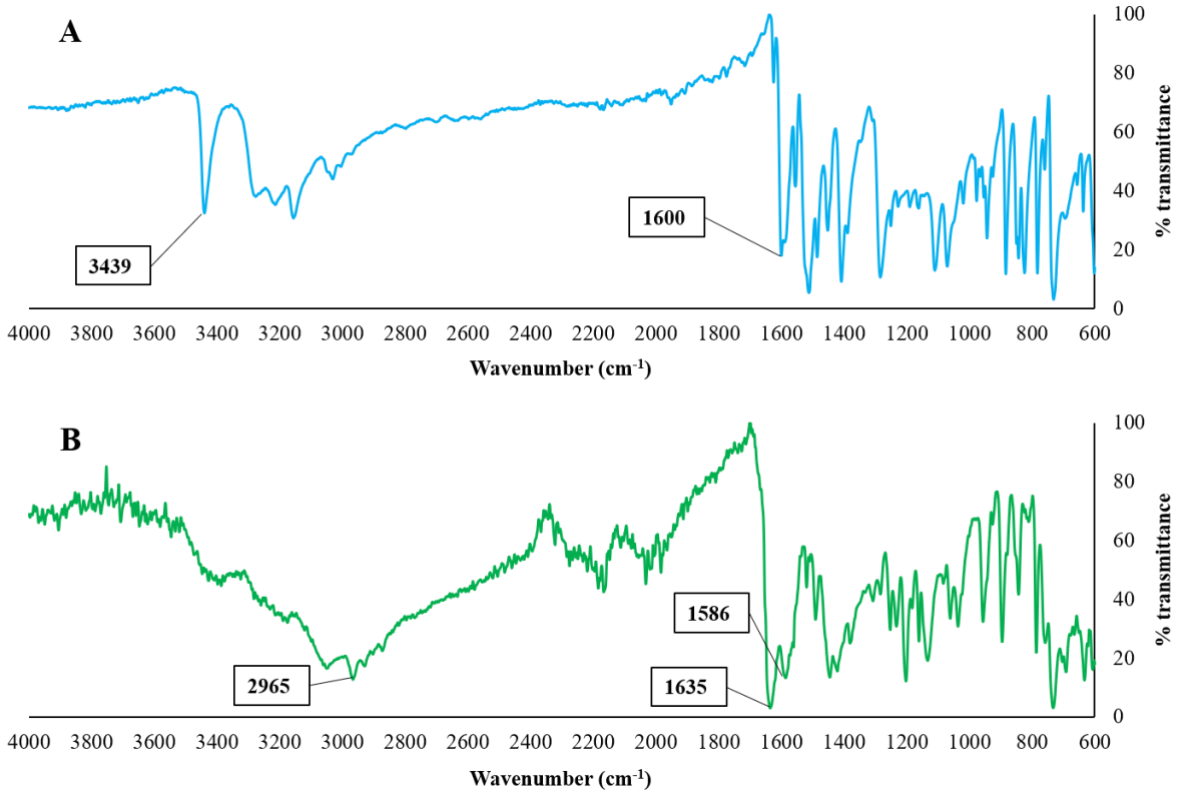

Figure 4.11. Solid state FT-IR spectra of compound **66** (**A**) and compound **82** (**B**).

Table 4.1. Band assignments for the FT-IR spectra of compounds **66** and **82** (Figure 4.10).

Compound	Wavenumber (cm-1)	Vibrational mode
66	3439	N-H st
	3213	
	3155	
	1600	C=N st
	1279	C=S st
	843	
82	2965	C-H st
	1635	C=N st
	1586	
	632	C-S st

The last part of the synthesis consisted of the reaction between the newly synthesised compound **82** and mesityl imidazole (compound **74**) by employing the procedure already exploited for the previously synthesised imidazolium-based receptors. An outline of the synthesis is reported in Scheme 4.8. After standard work up and recrystallisation in chloroform a yellow powder was obtained in a very good yield (87%).

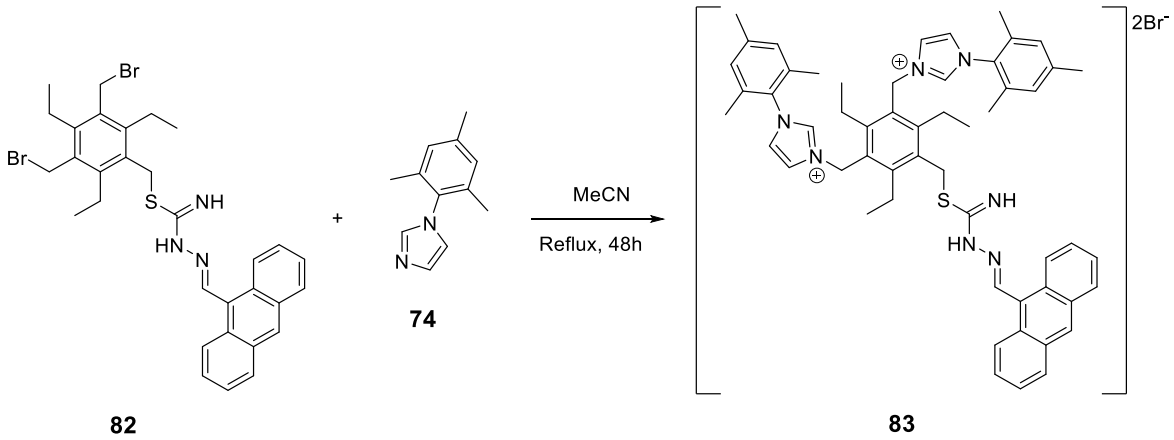

Scheme 4.8. Synthesis of compound **83**.

The ^{1}H NMR spectrum of the reaction product (Figure 4.12), displays resonances comparable to compound **82** as well as the resonances of the bonded imidazolium (signals labelled H_2, $H_7$and H_8). Interestingly, the spectrum of **83** showed a splitting of the resonances attributed to the *ortho*-methyl moieties of the mesityl substituents (labelled H_{13} and $H_{13'}$ in Figure 4.12). As the resonance labelled $H_{13'}$ is partially overlapping with a residual acetone signal, a two-dimensional ^{1}H-^{1}H COSY NMR spectrum was recorded (for the full ^{1}H-^{1}H COSY spectrum of compound **83** see appendix C). As for the previously analysed mesityl imidazolium-based systems, the *ortho*-methyl moieties of the mesityl groups of **83** couple with the aryl C-*H* protons of the mesityl ring (labelled H_{10} in Figure 4.12). In the spectrum of **83**, both resonances labelled H_{13} and $H_{13'}$ couple with H_{10}.

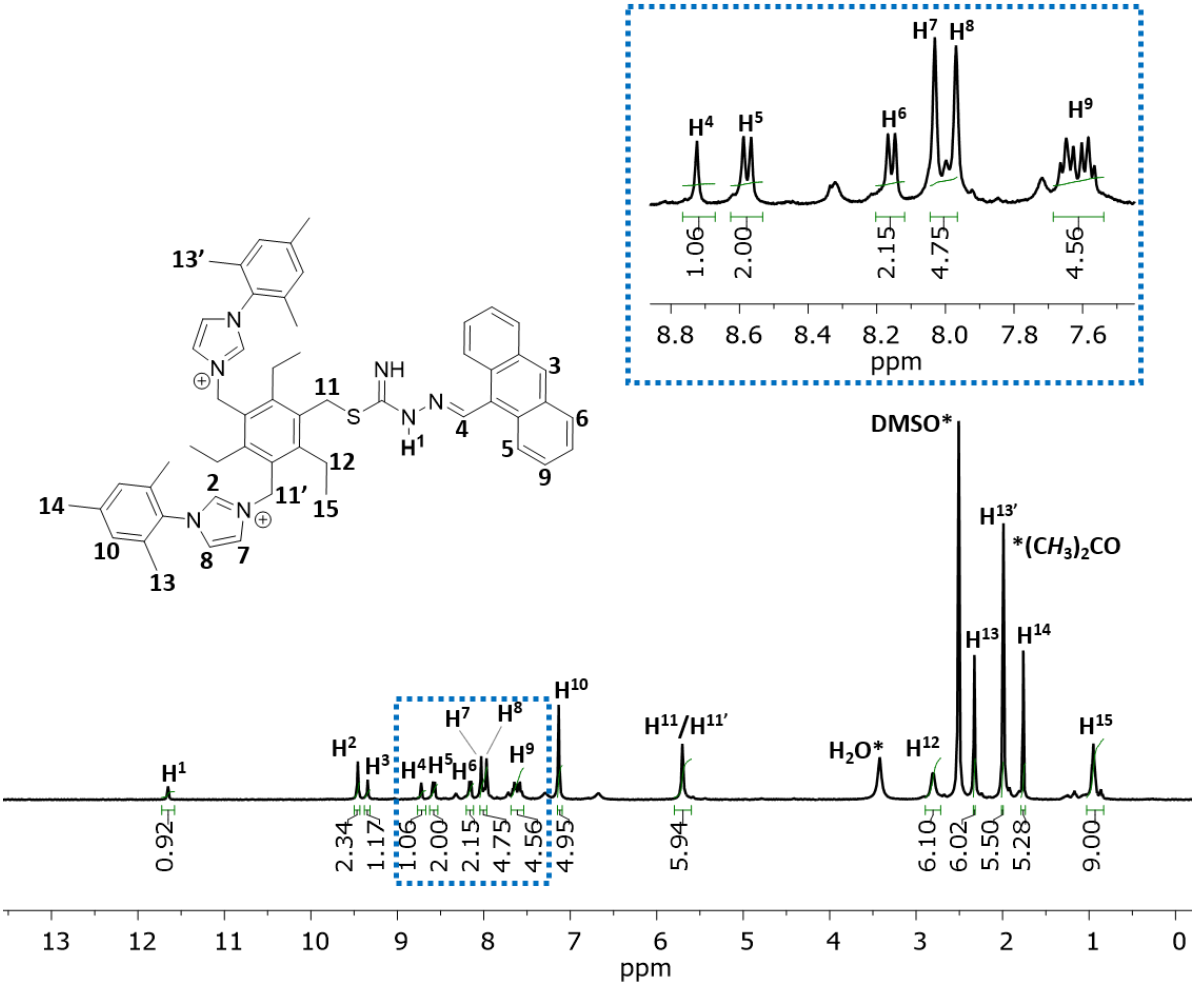

Figure 4.12. $_1$H NMR (400 MHz, DMSO-d$_6$, 298 K) spectrum of compound (**83**). Blue dotted box: expansion of the aromatic region. For clarity, magnetically equivalent nuclei within the same NMR spin system are labelled once.

Further confirmation of the molecular formula came from mass spectrometry analysis. The ESI mass spectrum of compound **83** (Figure 4.13), shows a fragment at m/z = 425.7384, which we assigned to the dicationic molecular ion $[M]^{2+}$.

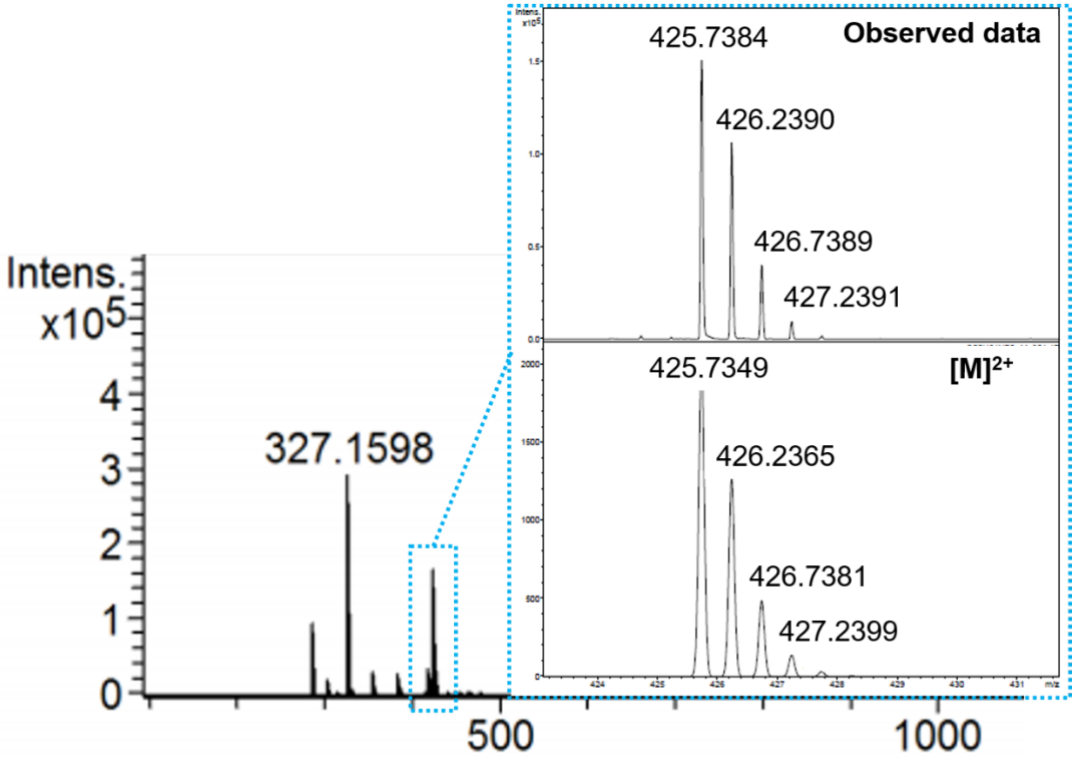

Figure 4.13. Positive-mode ESI-MS spectrum of compound **83**. Blue dotted square: fragment $[M]^{2+}$ at m/z = 425.7384 (**A**), and its simulated pattern (**B**).

UV-Visible spectroscopy performed on a DCM solution of compound **83** produced a similar spectrum compared to its starting material. Compared to **82**, the fluorescence emission spectrum of compound **83** presented a smaller Stokes shift and the presence of three emission bands at 435, 464 and 500 nm. The normalised UV-Vis and fluorescence spectra of **83** are shown in Figure 4.14.

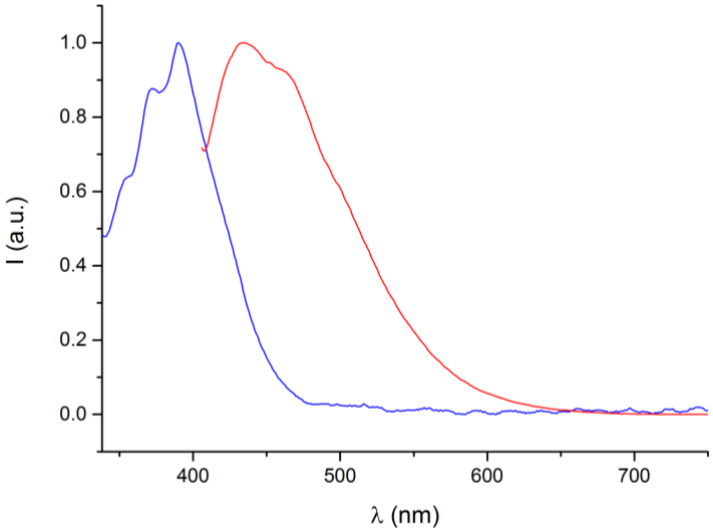

Figure 4.14. Normalised UV-Visible (blue line) and fluorescence emission (red line) spectra of a 12.5 µM solution of compound **83** in CH_2Cl_2.

The optical properties of compounds **82** and **83** were also evaluated using 2D fluorescence contour maps generated by scanning solutions of the two compounds across the full excited emission ranges available (Figure 4.15 and Figure 4.16 respectively). Both compounds display emissions between 450-550 nm, which are particularly intense in the case of compound **83** where the emissive window is blue-shifted towards lower values of 400 nm.

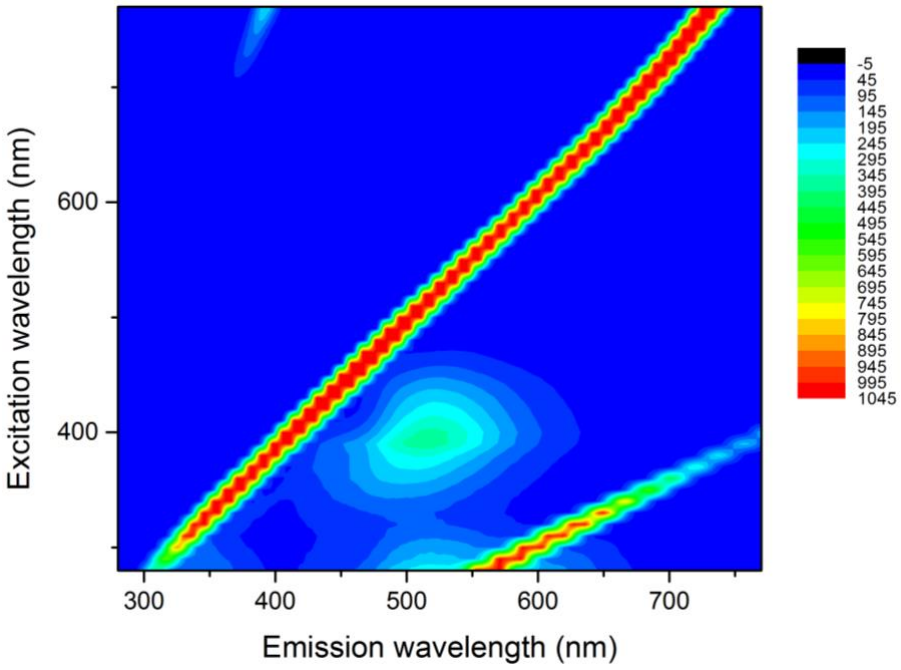

Figure 4.15. 2D fluorescence contour map of compound **82** (12.5 µM in CH_2Cl_2).

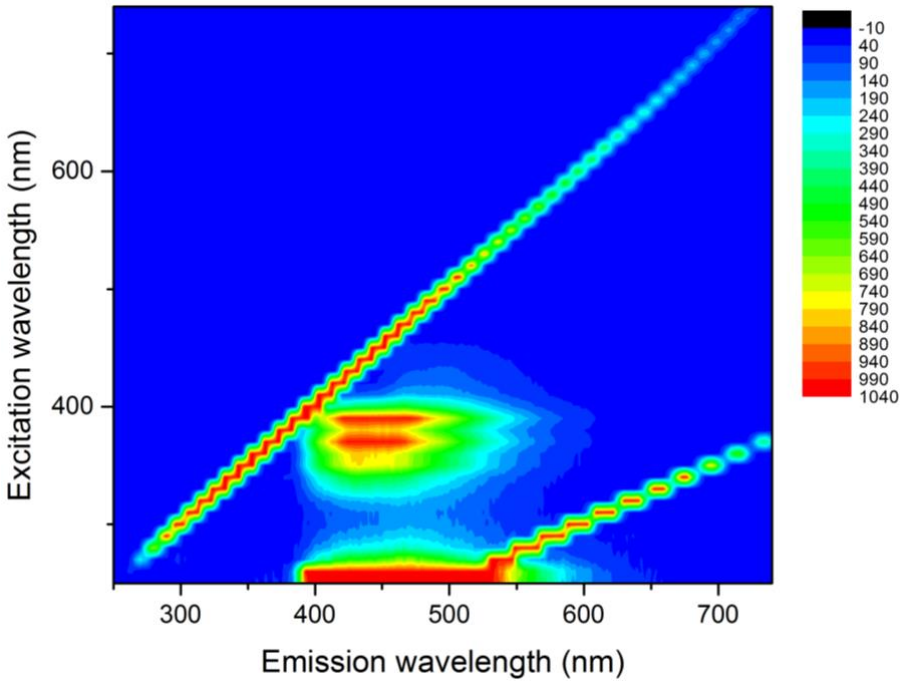

Figure 4.16. 2D fluorescence contour map of compound **83** (12.5 μM in CH_2Cl_2).

4.3.1. Single-photon laser-scanning microscopy investigation of ATSC-based probes in PC3 cancer cells

For the newly synthesised ATSC-based compounds **82** and **83** single-photon laser-scanning confocal microscopy (SLSCM) analysis was performed. PC3 cells were grown according to standard culturing methods, placed onto glass-bottomed dishes and allowed to grow to a suitable confluence.

Figure 4.17 shows the images of PC3 cells incubated for 20 min with compound **82** taken in the confocal mode. The images show broad emission across blue and green channels when the probe is excited at 405 nm ($a_{1\text{-}5}$), while there seems to be no emission using 488 nm and 561 nm lasers respectively. Compound **ss** appear to be taken up in PC3 cells and localises throughout the cytoplasm, whereas no emission appears to originate from the nuclei.

SLSCM analysis of compound **83**, shown in Figure 4.18, revealed broad emissions in all the visible wavelengths when the probe is excited at 405 nm, while only green-red emissions are visible using the 488 nm laser. Interestingly, irradiation of the sample at 561 nm showed a noticeable emission in all three channels. Further tests will be needed to explain such emission at the highest excitation wavelength tested. Compound **83** appeared to localise evenly throughout the cytoplasm, and as for its precursor **82**, no emission could be observed in the cell nuclei.

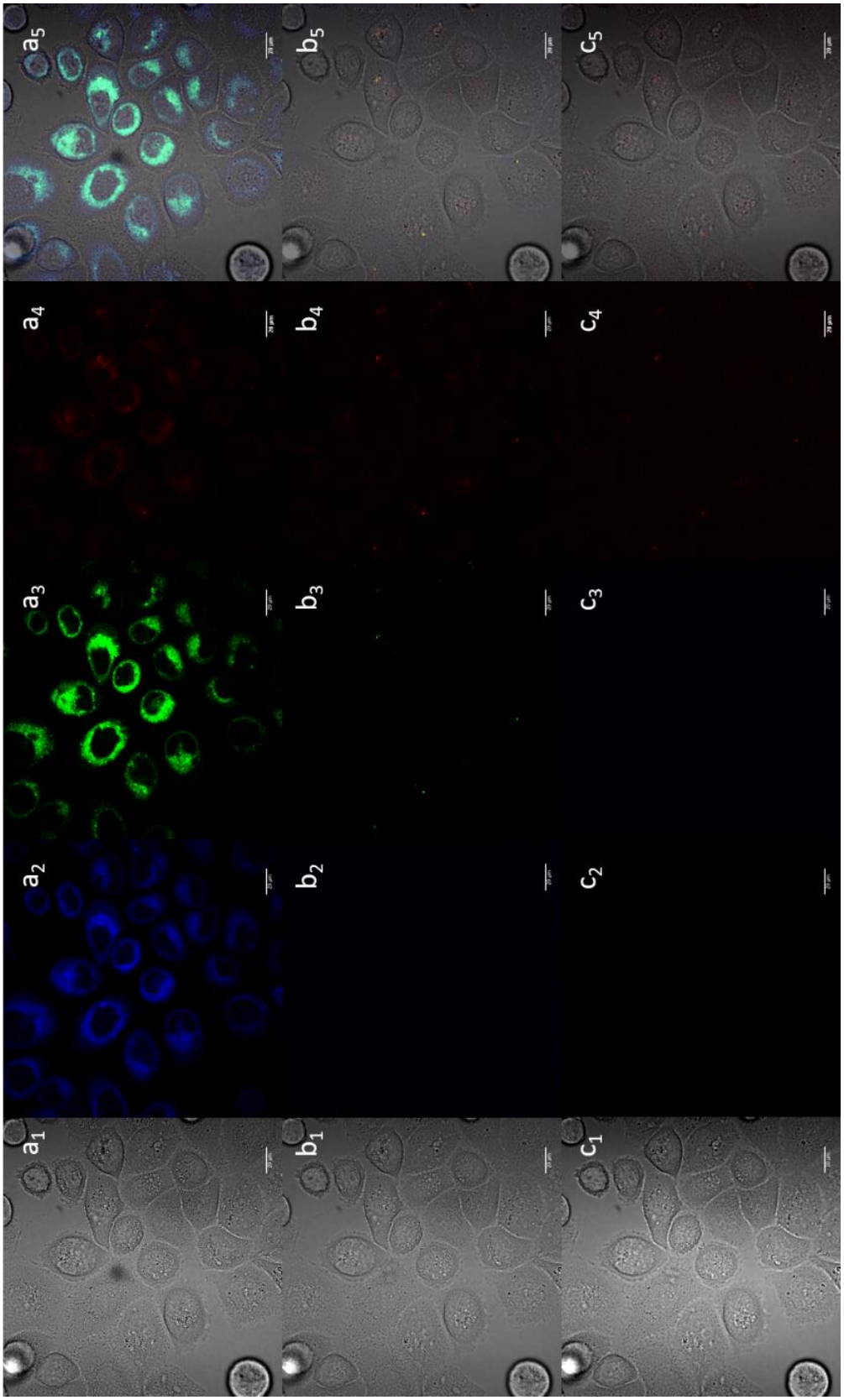

Figure 4.17. Single-photon laser-scanning confocal microscopy images of PC3 cells incubated with compound **82** (10 μg/mL 1% : 99% DMSO : DMEM) at 37 ºC for 20 minutes; λ_{ex} = 405 nm (a_1-a_5), λ_{ex} = 488 nm (b_1-b_5) and λ_{ex} = 561 nm (c_1-c_5). DIC channel (a_1, b_1, c_1), blue channel, λ_{em} = 420-480 nm (a_2, b_2, c_2), green channel, λ_{em} = 516-530 nm (a_3, b_3, c_3), red channel λ_{em} = 615-650 nm (a_4, b_4, c_4), and overlapping of the DIC, blue, green and red channels (a_5, b_5, c_5). Scale bar: 20 μm.

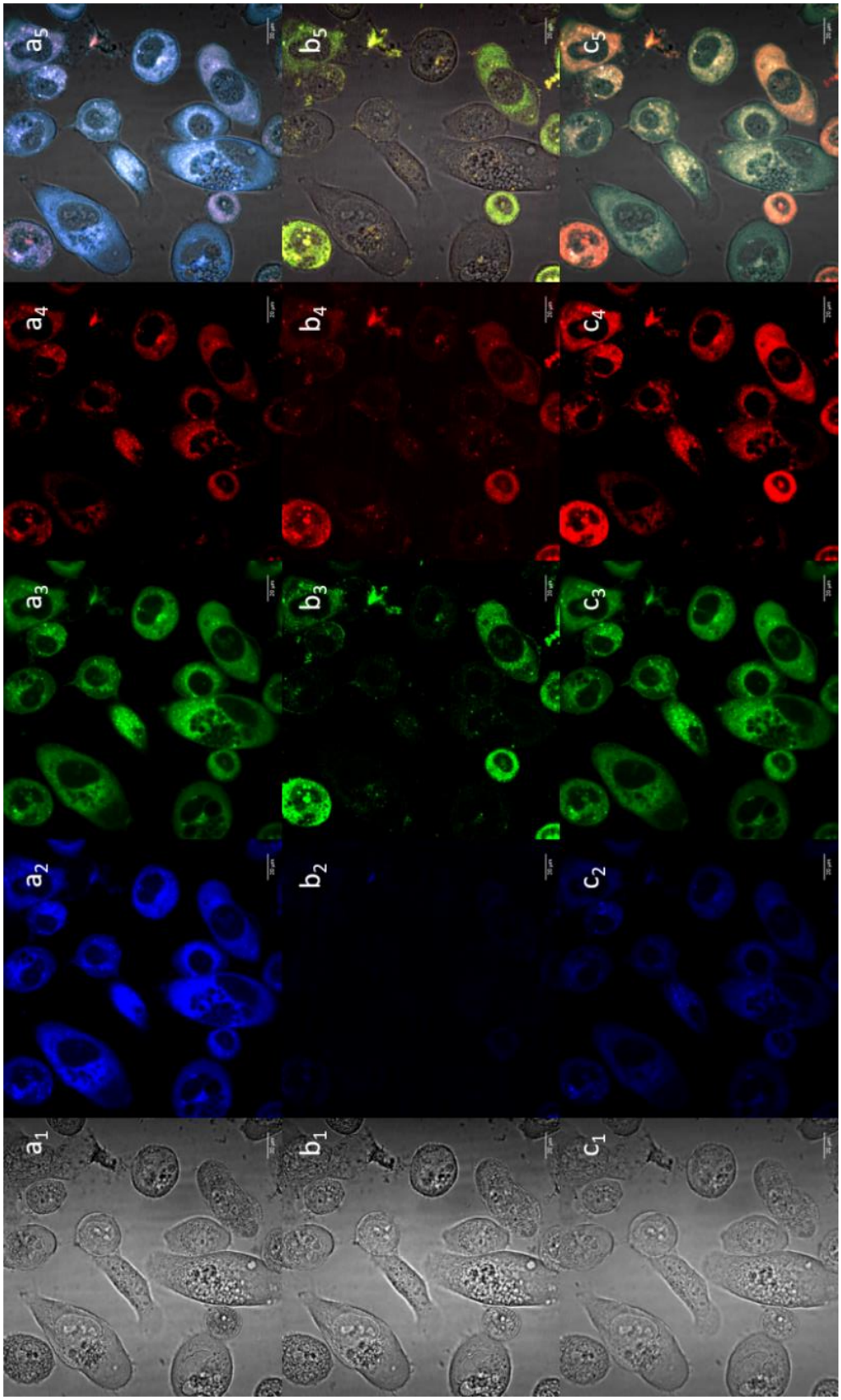

Figure 4.18. Single-photon laser-scanning confocal microscopy images of PC3 cells incubated with compound **83** (10 μg/mL 1% : 99% DMSO : DMEM) at 37 ºC for 20 minutes; λ_{ex} = 405 nm (a_1-a_5), λ_{ex} = 488 nm (b_1-b_5) and λ_{ex} = 561 nm (c_1-c_5). DIC channel (a_1, b_1, c_1), blue channel, λ_{em} = 420-480 nm (a_2, b_2, c_2), green channel, λ_{em} = 516-530 nm (a_3, b_3, c_3), red channel λ_{em} = 615-650 nm (a_4, b_4, c_4), and overlapping of the DIC, blue, green and red channels (a_5, b_5, c_5). Scale bar: 20 μm.

4.4. Summary of Chapter 4

This chapter describes the syntheses of three NHC-based tripodal systems in which one of the three arms has been modified with two carboxylic acid-based linkers (compounds **78** and **81**), as well as with the introduction of an anthracene-thiosemicarbazone derivative as fluorophore (compound **83**).

Compound **83** was obtained in a two-step reaction, firstly by preforming a nucleophilic substitution of one bromomethyl arm of the core **61** with **66**, to give compound **82** after a simple workup. Spectrophotometric analyses of **82** revealed that the preferential mode of substitution of the bromide is through sulphur as for the previously reported compounds **67** and **68**, thus suggesting that thiosemicarbazone compounds are able to S-alkylate the hexasubstituted aromatic cores.

Finally, reaction between mesityl imidazole derivative compound **74** and compound **82** has been performed. The unsymmetrical tripodal system **83** was obtained in acceptable purity and good yield and its fluorescent properties were evaluated by fluorescence spectroscopy. The new compound shows absorption peaks characteristic of the anthracene moiety and a larger fluorescence emission curve between 450-550 nm, which is suitable for cellular imaging applications.

Lastly, single-photon laser-scanning confocal microscopy experiments carried out on PC3 prostate cancer cells incubated with compound **83** revealed that the compound was able to cross the cellular membrane and localise throughout the cytoplasm, where it displayed intense fluorescence when irradiated at 405, 488 and 561 nm.

4.5. References for Chapter 4

1. M. Lledos, PhD Thesis, University of Bath, 2018.
2. C. Travelli, S. Aprile, R. Rahimian, A. A. Grolla, F. Rogati, M. Bertolotti, F. Malagnino, R. Di Paola, D. Impellizzeri and R. Fusco, *J. Med. Chem.*, 2017, **60**, 1768-1792.
3. A. L. Vāvere and J. S. Lewis, *Dalton Trans.*, 2007, 4893-4902.
4. A. G. Quiroga, J. M. Pérez, I. López-Solera, J. R. Masaguer, A. Luque, P. Román, A. Edwards, C. Alonso and C. Navarro-Ranninger, *J. Med. Chem.*, 1998, **41**, 1399-1408.
5. J. Bai, R.-H. Wang, Y. Qiao, A. Wang and C.-J. Fang, *Drug Des. Dev. Ther.*, 2017, **11**, 2227.

5. Incorporation of metallic units onto tripodal synthetic scaffolds

Following the successful syntheses of several tripodal systems, we began to test the possibility of developing novel metal complexes containing metal centres of relevance to imaging and/or therapy. The following chapter reports the complexation attempts between a series of transition metals and few selected tripodal ligands previously discussed.

5.1. Tripodal ATSC-based metal complexes

The focus of this section is the synthesis and evaluation of organometallic complexes composed from the newly synthesised tripodal anthracene-thiosemicarbazone (ATSC) ligands **67** and **68**, previously described in Chapter 2, with a variety of transition metal precursors.

Preliminary radiolabelling experiments with the positron-emitter radiotracer zirconium-89 revealed that **67** was able to coordinate the radionuclide with a very high radio-incorporation factor (see Appendix D). However, subsequent attempts to synthesise the "cold" complex were unsuccessful. Therefore, we opted to make use of other transition metals that act as softer Lewis acids, such as ruthenium and rhenium, to develop a series of coordination compounds with the two tripodal ATSC-based ligands. Given the structural complexity of such tripodal systems, a prediction of the coordination modes between the metal centre and these ligands cannot be made unequivocally. Nonetheless, there are several literature examples that can help to speculate the coordination modalities involving these transition metals and thiosemicarbazone-based ligands.[1-7] A summary of the possible binding modalities between the ATSC-based ligands and the metal centre is shown in Figure 5.1.

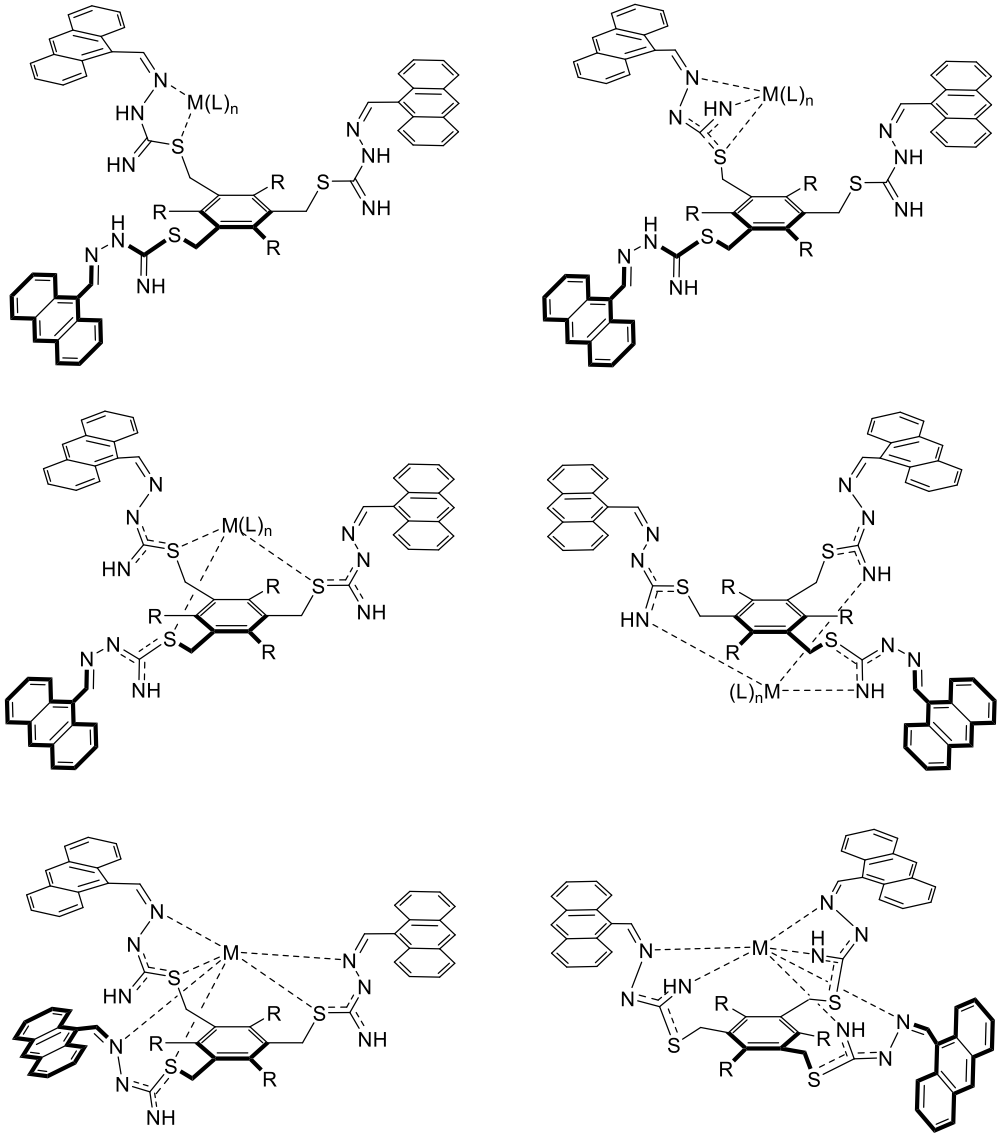

Figure 5.1. Proposed binding modes between the ATSC-based ligands **67** (R = Me), **68** (R = Et) and the transition metal centre (M = Re, Ru).

5.1.1. Rhenium complexes

Rhenium(I) tricarbonyl complexes (of the general formula *fac*-[Re(CO)$_3$L] where "L" is a tridentate ligand) have been demonstrated to exhibit interesting luminescent properties,[8] arising from its octahedral d_6 low-spin configuration. This allows precise detection by confocal microscopy in cells, but also presents some weaknesses such as very low luminescence quantum yield in aqueous medium[9].

Rhenium tricarbonyl complexes are usually obtained by refluxing a mixture of the ligand with the metal precursor in an appropriate solvent for several hours. In this work, a microwave-assisted methodology was investigated in order to obtain the desired products in much shorter times. Equimolar quantities of ligand and the metal precursor halogen-pentacarbonylrhenium(I) ($Re(CO)_5X$, with X = Br or Cl), were dissolved in dry toluene, and placed into a microwave vial and purged with argon. The reaction mixture was heated at 150 ºC for 30 minutes under microwave irradiation, during which time an orange precipitate was formed. The precipitates were filtered and washed several times with fresh toluene and diethyl ether, the products were obtained as orange solids in moderate yields. A general reaction scheme, along with the proposed product structures, is shown below in Scheme 5.1.

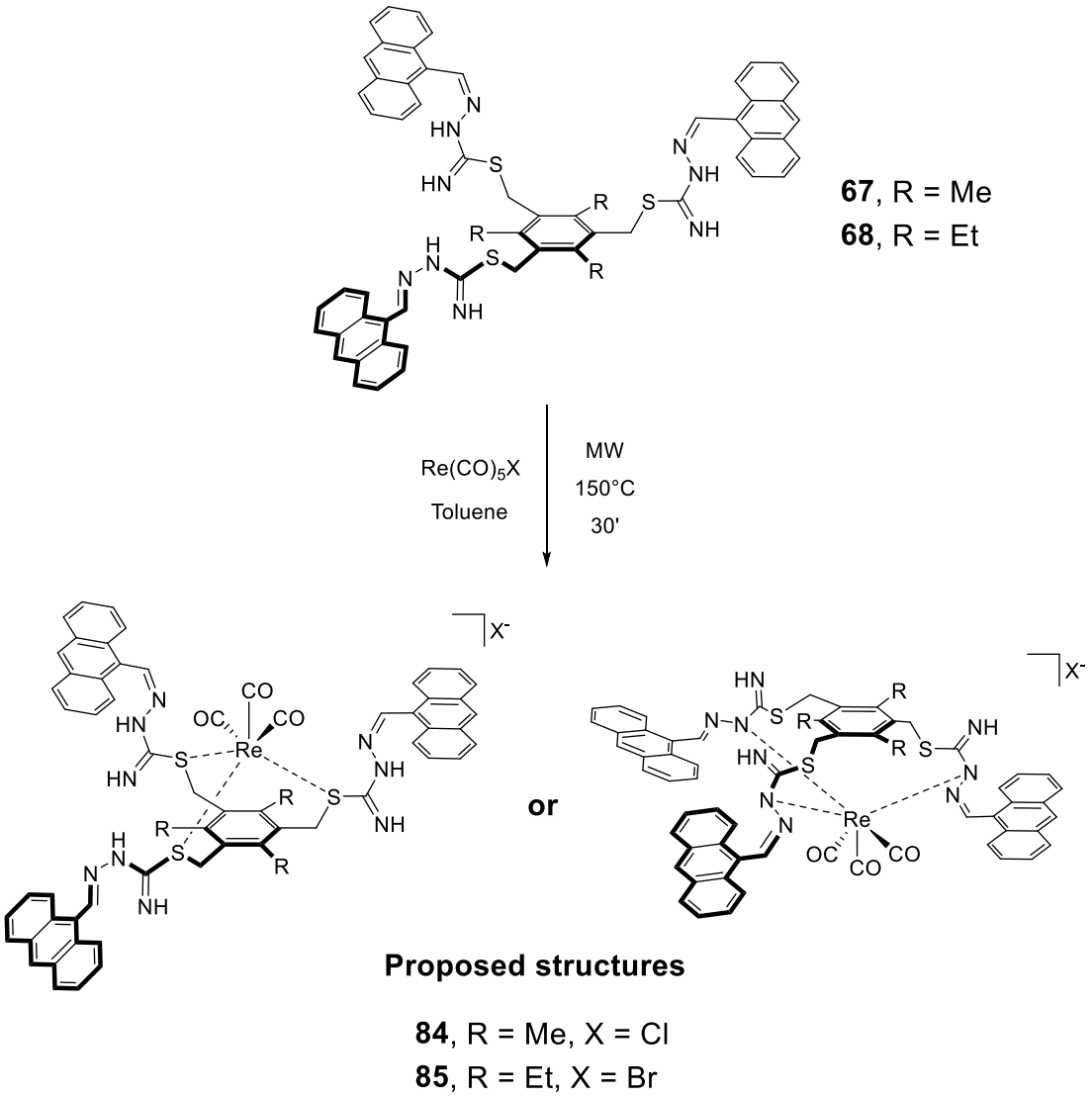

Scheme 5.1. Synthetic pathway leading to rhenium complexes **84** and **85**.

The newly synthesised compounds were analysed with standard spectroscopic techniques. ^{1}H NMR spectra of both metal complexes show little variations in the chemical shifts compared to their ligands. The ^{1}H NMR spectrum of compound **85** is shown in Figure 5.2.

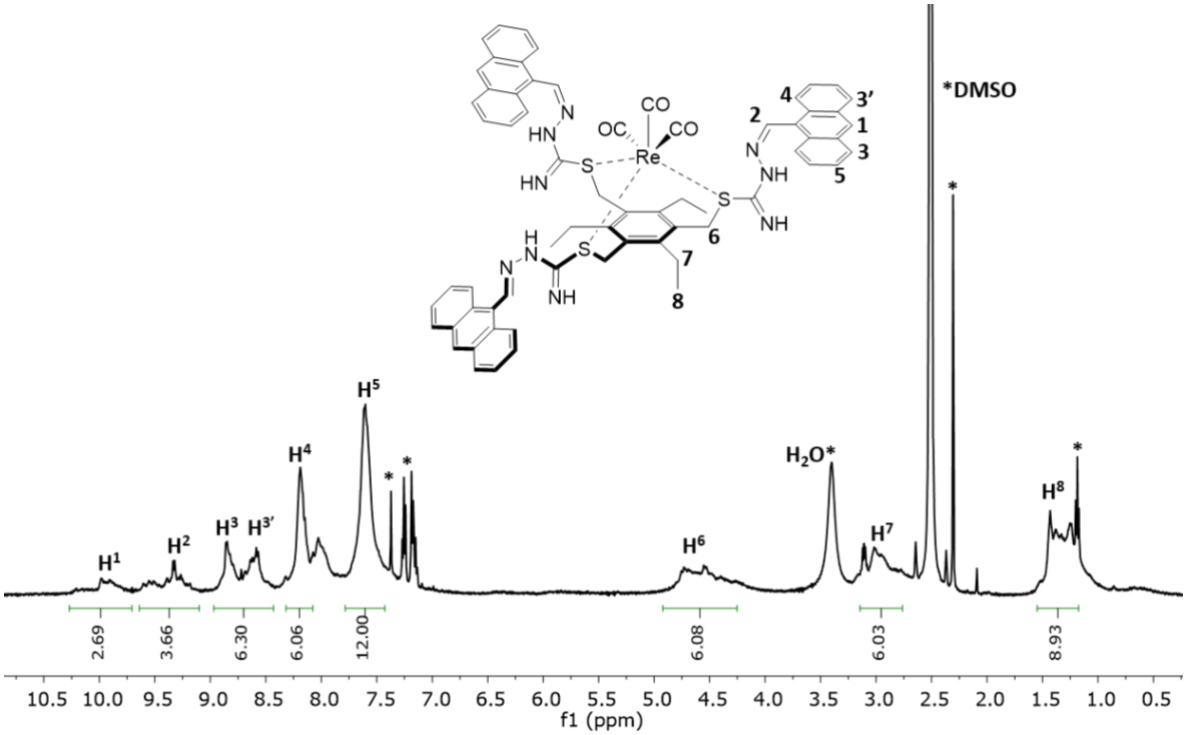

Figure 5.2. ^{1}H NMR (500 MHz, $CDCl_3$, 298 K) spectrum of compound **85**. For clarity, magnetically equivalent nuclei within the same NMR spin system are labelled once. * residual solvents and impurities traces.

Positive-mode ESI mass spectrum of a 1µg/ml solution of compound **84** in methanol was subsequently acquired, revealing the presence of a bi-protonated molecular ion ([M+2H+Cl], with M = $C_{63}H_{51}N_9O_3S_3Re$, corresponding to the proposed structure for compound **84**), along with a chlorine adduct. However, given the complexity of the recorded mass spectrum, as well as the presence of potential alternative rhenium-ligand coordinations (such as the fragment with m/z = 564.2638), it was not possible to unequivocally define the molecular formula of compound **84**. The full spectrum acquired for compound **84** is shown below in Figure 5.3.

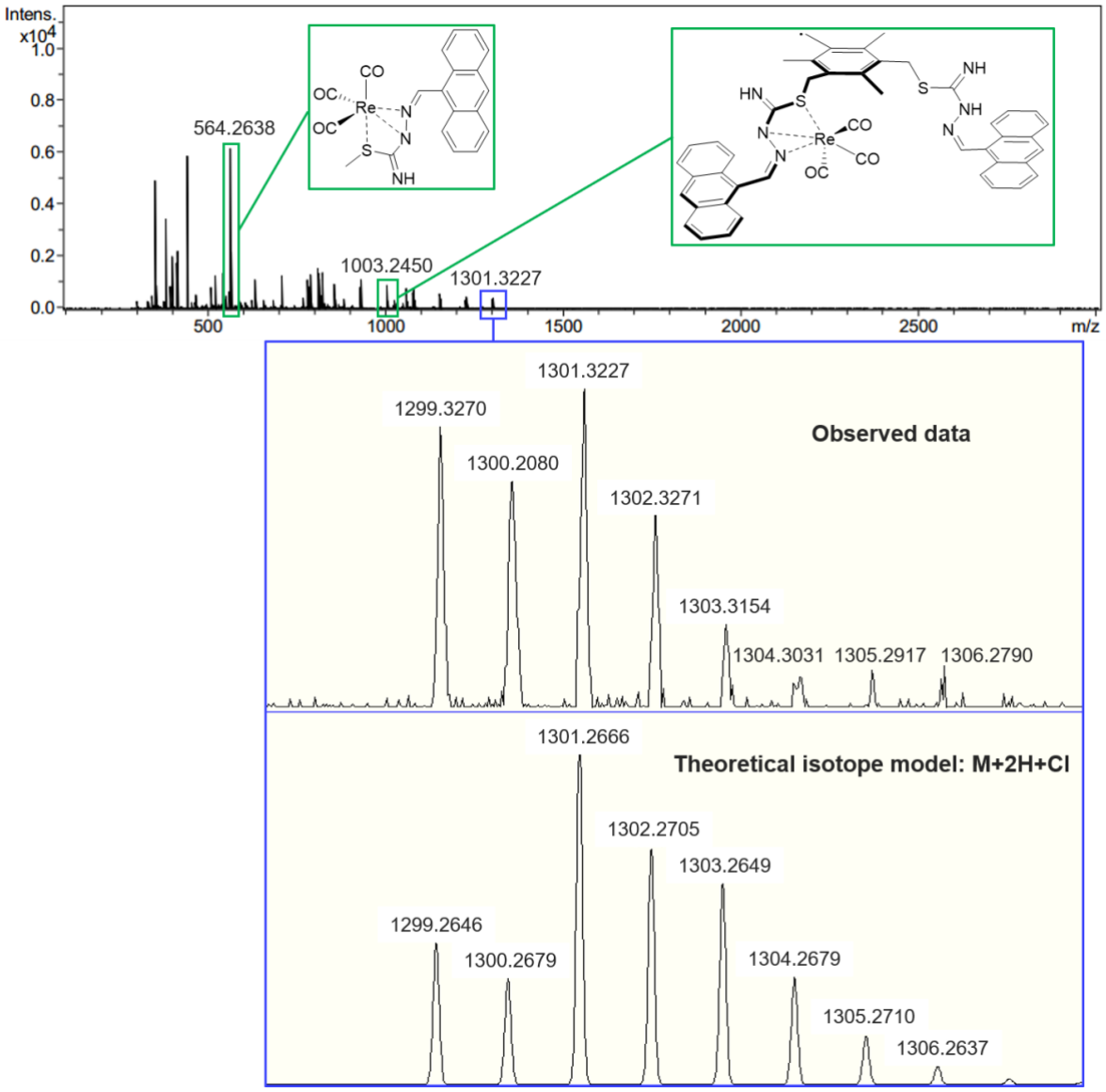

Figure 5.3. Positive-mode ESI-MS for compound **84**. Blue box: Ion species $[M+2H+Cl]^+$ at 1301.3227 m/z.

The presence of chlorine in the ion species with m/z = 1301.3227 in the mass spectrum recorded for compound **84** might be a suggestion of an alternative complexation mode, leading to a Re-arene half-sandwich compound. Previous literature reports have demonstrated the possibility of preparing various half-sandwich compounds of rhenium (Figure 5.4 **A**),[10, 11] while Hogarth and co-workers successfully synthesised a tripodal-based complex of molecular formula $Cr(CO)_3(\eta_6\text{-arene})$ in which the metal centre interacts with the hexasubstituted core of compound **64** (Figure 5.4 **B**).[12]

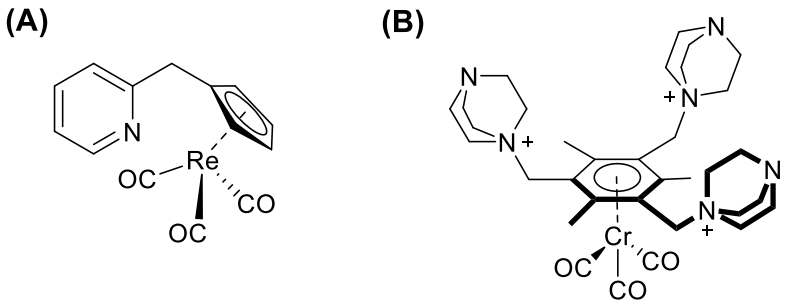

Figure 5.4. Examples of half-sandwich complexes. Adapted from ref.[10] (**A**) and ref.[12] (**B**).

We thus propose an alternative structure for compound **84** of molecular formula $Re(CO)_3(\eta^2$-**67**). This structure could help rationalise the broad peaks observed in the up-field region of the NMR spectrum (the full ^1H NMR spectrum recorded for **84** is shown in appendix D).

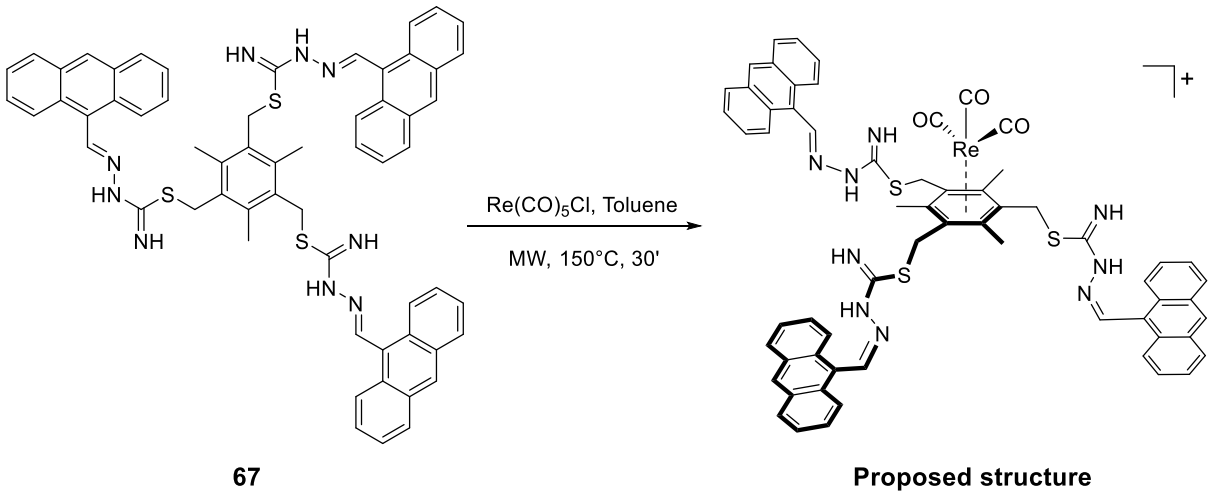

Scheme 5.2. Alternative reaction scheme proposed for compound **84**.

The mass spectrum of compound **85** recorded in positive-mode ESI was acquired at the EPRSC UK National Mass Spectrometry Facility in Swansea. The spectrum, reported in Figure 5.5, shows a peak at 1306.3282 m/z corresponding to the molecular ion $[M]^+$ (where M = $C_{66}H_{57}N_9O_3S_3Re$, corresponding to the proposed structure for compound **85**).

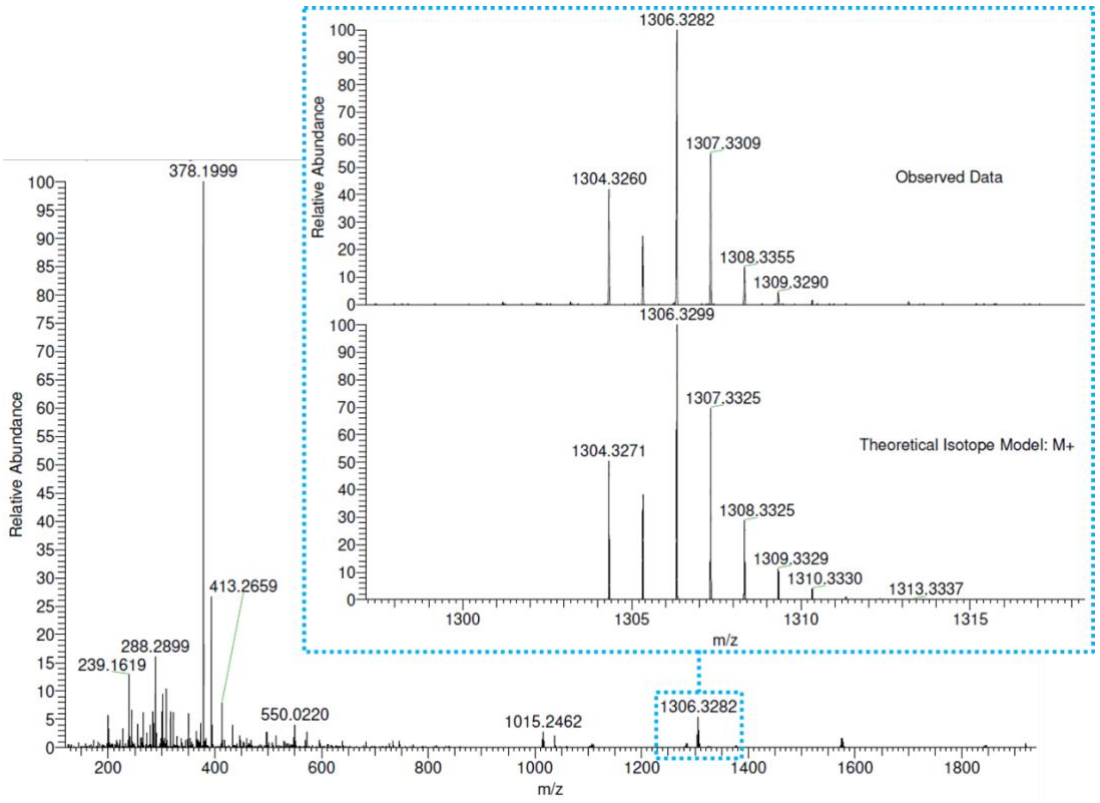

Figure 5.5. Mass spectrum of compound **85**. Blue dotted box: details of the molecular ion $[M]^+$ and its simulated isotopic pattern.

FT-IR analysis was also used to confirm the presence of carbonyl ligands bonded to the metal centre for **84** and **85**. From the spectra shown in Figure 5.7 it is possible to distinguish the presence of three intense bands at 2017, 1907 and 1883 cm^{-1} for the metal complex **84** (Figure 5.7, purple line) and at 2020, 1907 and 1887 cm^{-1} for the analogue **85** (Figure 5.7, green line). The broad bands observed at lower wavenumbers are due to the overlapping E, E' modes (see Figure 5.6 for their composition).[13] These values are in agreement with typical C-O stretching vibrations of carbon monoxide units of a *fac*-$[M(CO)_3]$ metal complex. Furthermore, such lower frequencies suggest the presence of strong π-backbonding between the CO ligand and the Re(I) centre.[14]

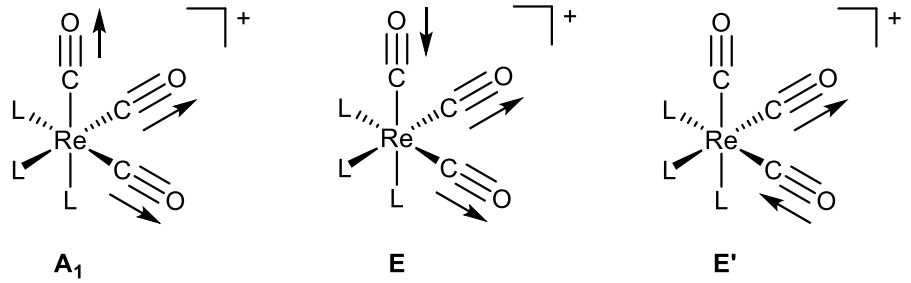

Figure 5.6. A_1, E, and E' vibrational modes in C3v symmetry for complexes **84** and **85**. L = tripodal ligand **67** or **68**.

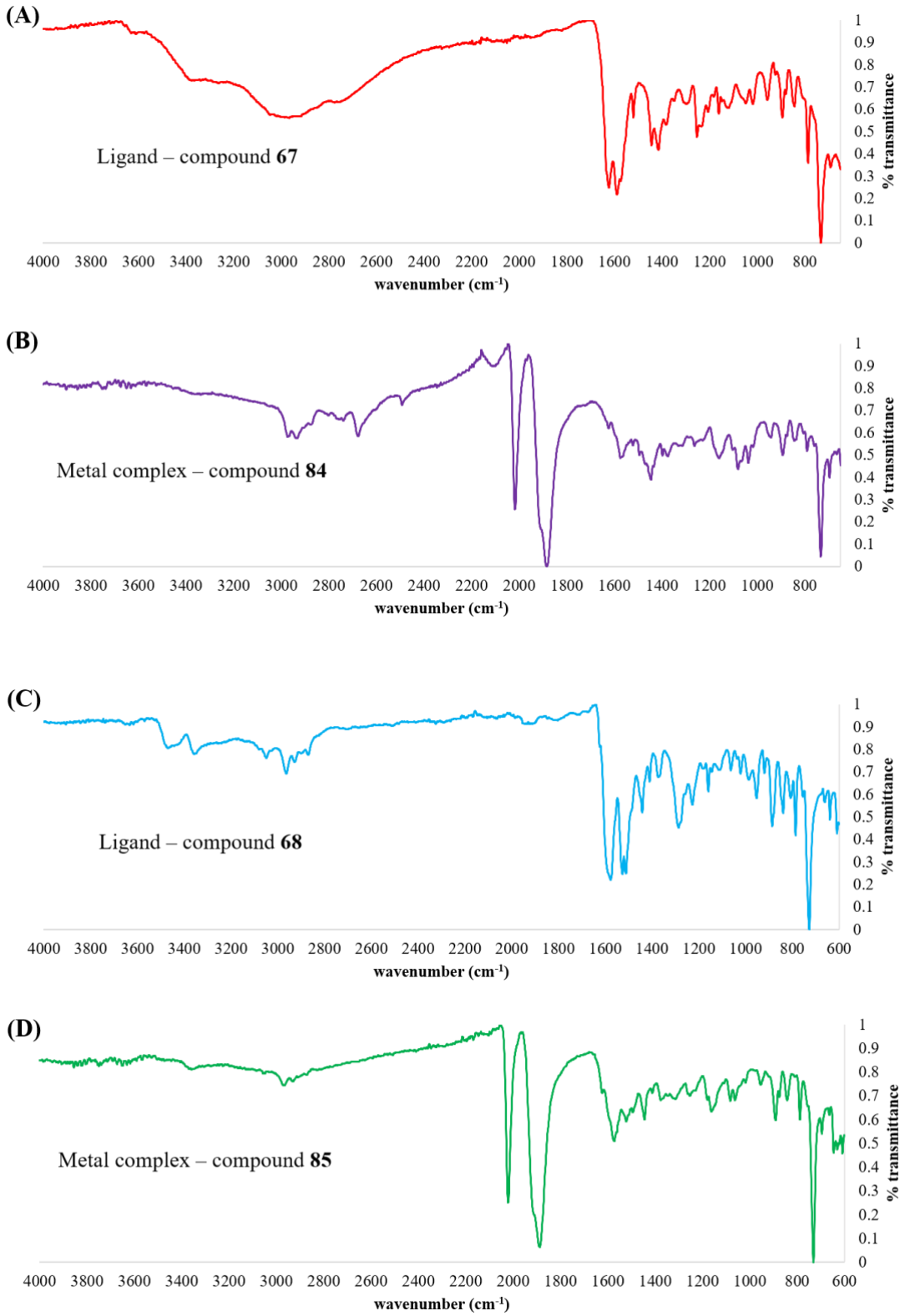

Figure 5.7. Solid-state FT-IR spectra of metal complexes **84** (**B**) and **85** (**D**) and their ligand precursors **67** (**A**) and **68** (**C**).

UV-Visible and fluorescence emission measurements were carried out for both complexes. Normalised spectra for compounds **84** and **85** are shown below in Figure 5.8. The two metal complexes exhibit absorption patterns characteristic of the anthracene moiety, with three distinct bands at 350, 370 and 390 nm. Fluorescence spectra for both metal complexes show large Stokes shifts, with intensity maxima of 441 nm and 475 nm for compound **84** and **85** respectively. Compared to the fluorescence spectra of the starting ligands, reported in this work in Chapter 2, the redshift observed in the spectrum of compound **85** could be due to the presence of metal-to-ligand charge-transfer (MLCT).[15]

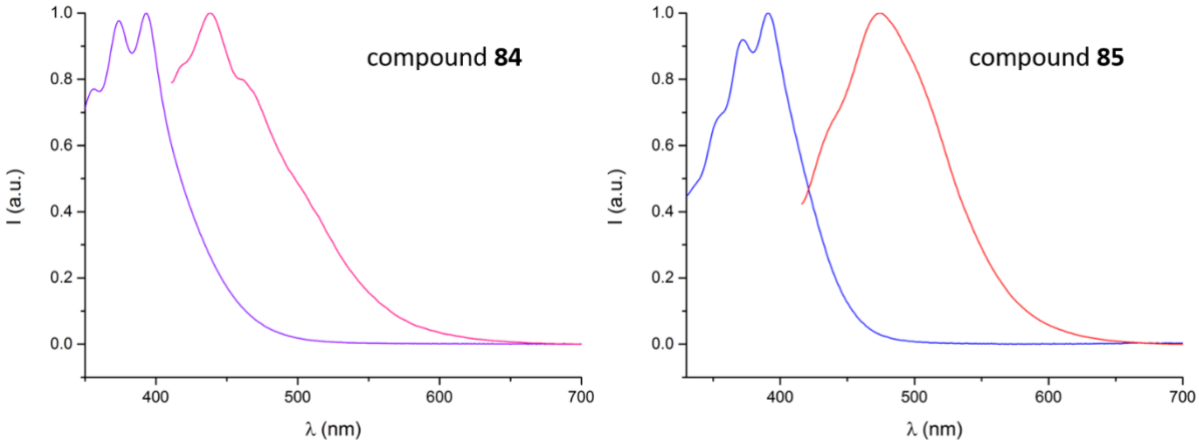

Figure 5.8. Left: normalised UV-visible (purple line) and fluorescence emission (pink line) spectra of compound **84** in THF (12.5 µM). Right: normalised UV-visible (blue line) and fluorescence emission (red line) spectra of compound **85** in THF (12.5 µM).

Analogously for the ligands **67** and **68**, fluorescence contour maps were generated to visualise the optical behaviour of the complexes **84** and **85** across the full excited emission ranges available. Both complexes display emissive properties between 390 to 500-550 nm, which makes them suitable dyes for confocal microscopy of cells. 2D contour maps of the two complexes are shown below in Figure 5.9 for compound **84** and in Figure 5.10 for compound **85**.

Compared to the 2D maps generated for the ligands precursors **67** and **68** shown in Chapter 2, the rhenium complexes **84** and **85** exhibited stronger fluorescence emissions from 370 to 500 nm. The emission intensity is particularly enhanced upon metallation of the ligand precursor **67** (Figure 5.9).

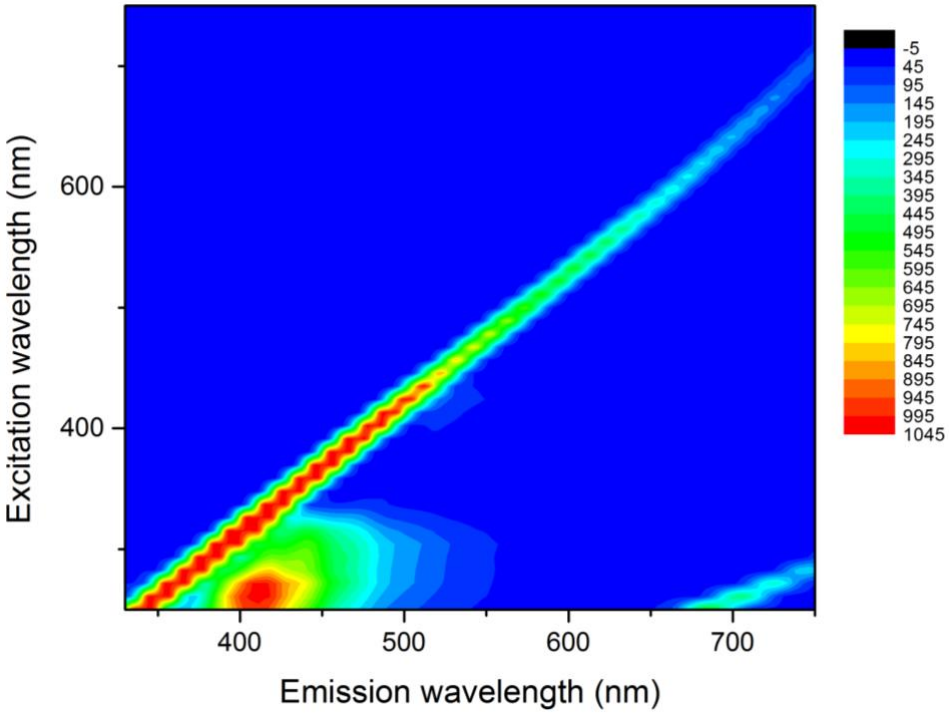

Figure 5.9. 2D fluorescence contour map for compound **84** (5 μM in THF).

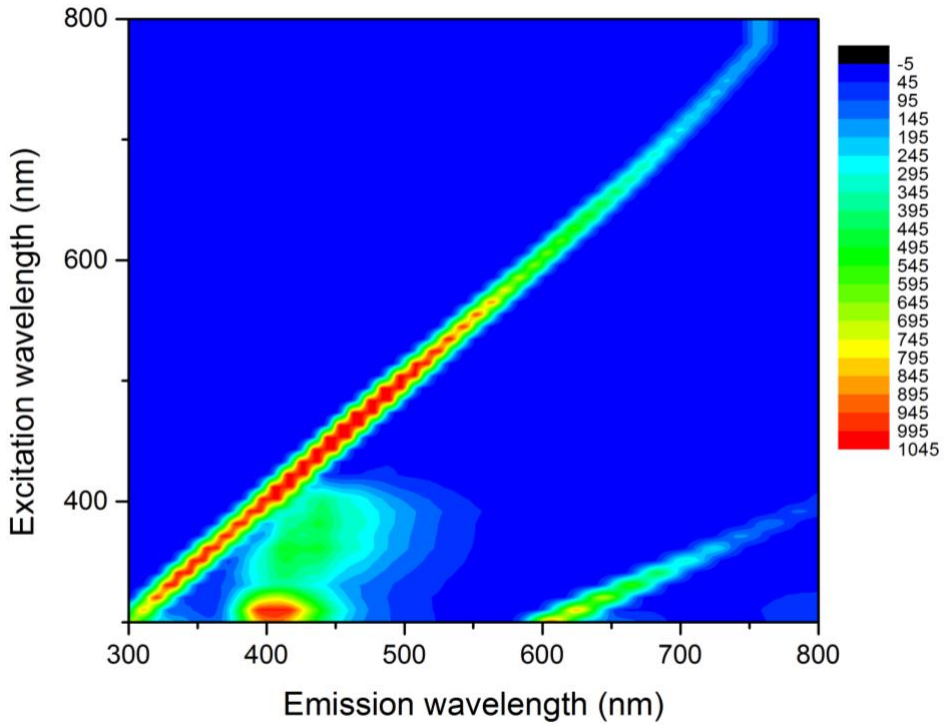

Figure 5.10. 2D fluorescence contour map for compound **85** (5 μM in THF).

5.1.2. Ruthenium complexes

Ruthenium anticancer drugs have attracted increasing interest in the last couple of decades, with two of them (NAMI-A and KP1019) currently undergoing clinical trials in Europe.[16, 17] Compared to cisplatin and congeners, ruthenium complexes often display lower toxicity and are capable of overcoming the resistance induced by platinum drugs in cancer cells.[18]

In this section we report the complexation attempts between tripodal ATSC-based ligands and a ruthenium(II) precursor, so to test the capacity of these new tripodal systems to accept other transition metals with biomedical applications. As for the previous complexation attempts (see section 5.1.1.), we opted to perform the syntheses by exploiting microwave technology to considerably shorten the reaction times.

In an argon-purged microwave vial, equimolar quantities of compound **68** and triruthenium dodecacarbonyl ($Ru_3(CO)_{12}$) were heated in toluene at 150°C for 30 minutes under microwave irradiation. A cloudy, deep red solution was obtained. After removal of the solvent, a red powder was obtained. TLC examination clearly showed the presence of two spots, one of which belonging to the tripodal starting material **68**. Silica gel flash chromatography was performed, and the crude product was eluted with a mixture of chloroform/hexane (60:40) to give the final product as a red solid in moderate yield (44%). A general outline of the synthesis is shown in Scheme 5.3.

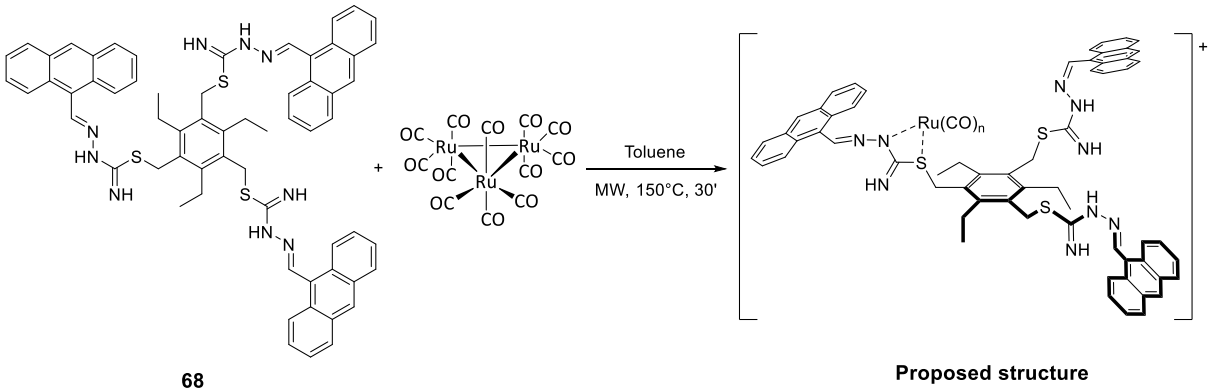

68 Proposed structure

Scheme 5.3. Synthesis of compound **86**.

^{1}H NMR analysis performed on the newly synthesised compound **86** revealed the presence of 8 signals (Figure 5.11). Due to the poor resolution of the multiplets, the assignment of each resonance of the aromatic region (between 7 – 9 ppm) proved to be difficult. However, the assignment of the resonances found in the aliphatic region (1 – 3 ppm) was facilitated by a ^{1}H-

^{1}H COSY analysis which revealed a noticeable shift upfield of the signals belonging to the methylene units **1** and **2**, which is probably due to the complexation of the ligand with the metal centre.

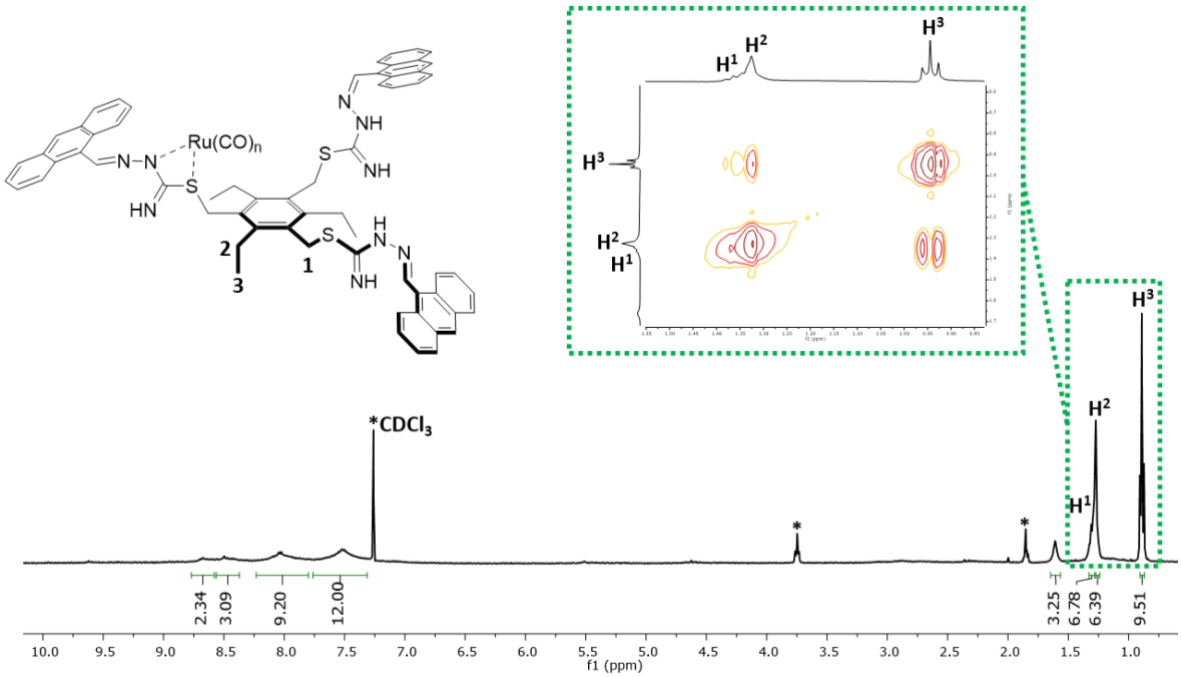

Figure 5.11. ^{1}H NMR (400 MHz, $CDCl_3$, 298 K) spectrum of compound **86** and a detail of the ^{1}H-^{1}H COSY spectrum highlighting the aliphatic region (green dotted box). For clarity, magnetically equivalent nuclei within the same NMR spin system are labelled once. * residual solvents and impurities traces.

Accurate mass spectrometry analysis of compound **86** was carried out and the results shown in Figure 5.12 and in Figure 5.13. The spectrum of **86** revealed the presence of a monometallic ion fragment at m/z = 1194.2958, corresponding to the protonated molecular ion with the loss of one molecule of carbon monoxide $[M+H-CO]^+$ (where M = $C_{66}H_{57}N_9O_3S_3Ru$, corresponding to the initially proposed structure for compound **85** with three CO ligands bound to the ruthenium centre).

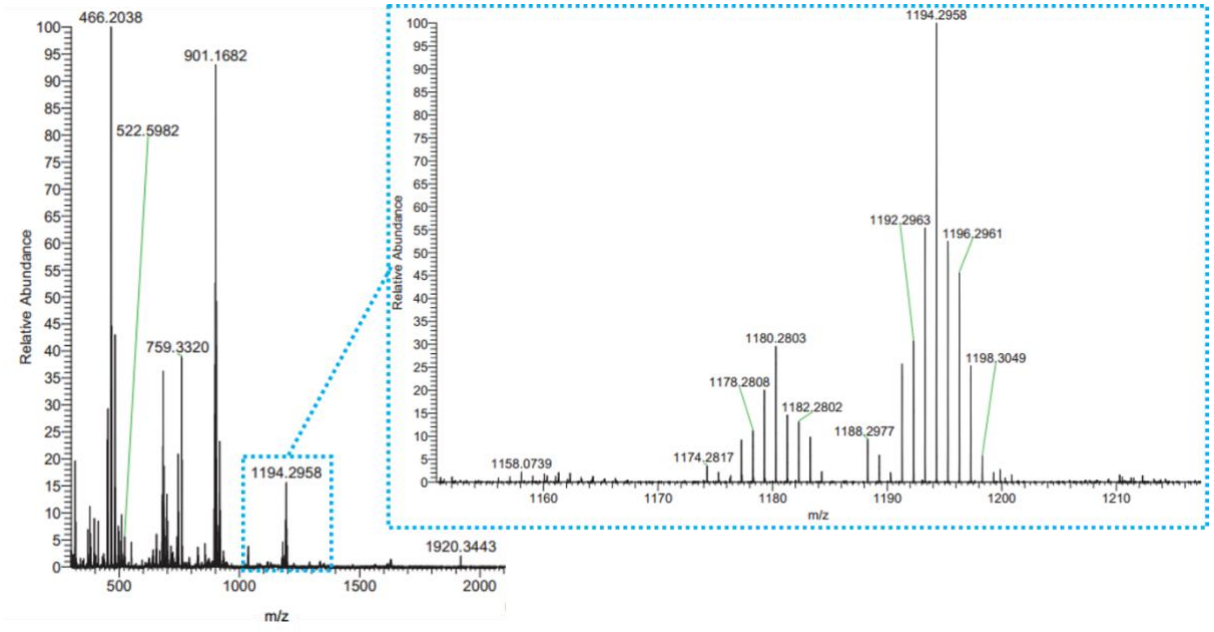

Figure 5.12. Mass spectrum of compound **86**.

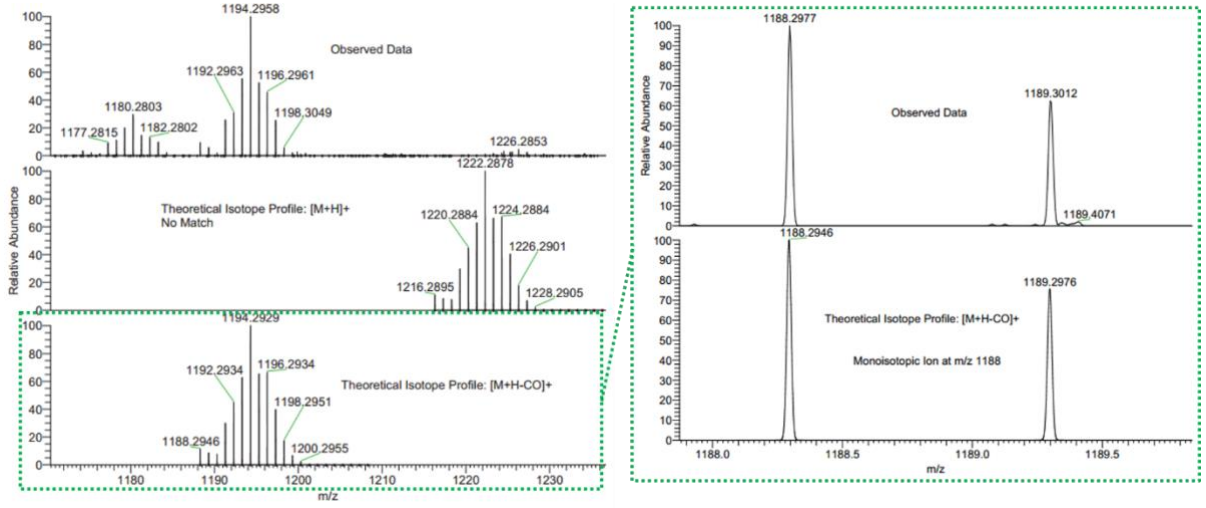

Figure 5.13. Detail of the fragment $[M+H-CO]_+$, along with its predicted isotopic pattern.

The FT-IR spectrum of compound **86**, along with its pro-ligand compound **68**, is shown in Figure 5.14. The IR spectrum of the metal complex clearly shows the presence of strong bands at 2041 cm^{-1} and 1972 cm^{-1} which are indicative of CO stretching vibrations of carbon monoxide units bound to a metal centre.[19] A summary of the band assignments for **86** and the metal precursor $Ru_3(CO)_{12}$ is shown in Table 5.1. We also noted a shift in the C=N bands, positioned at 1586-1526 cm^{-1} in the free ligand, to lower values of 1579-1494 cm^{-1} in the complex. This shift may suggest that the azomethine nitrogens coordinate to the metal.[20]

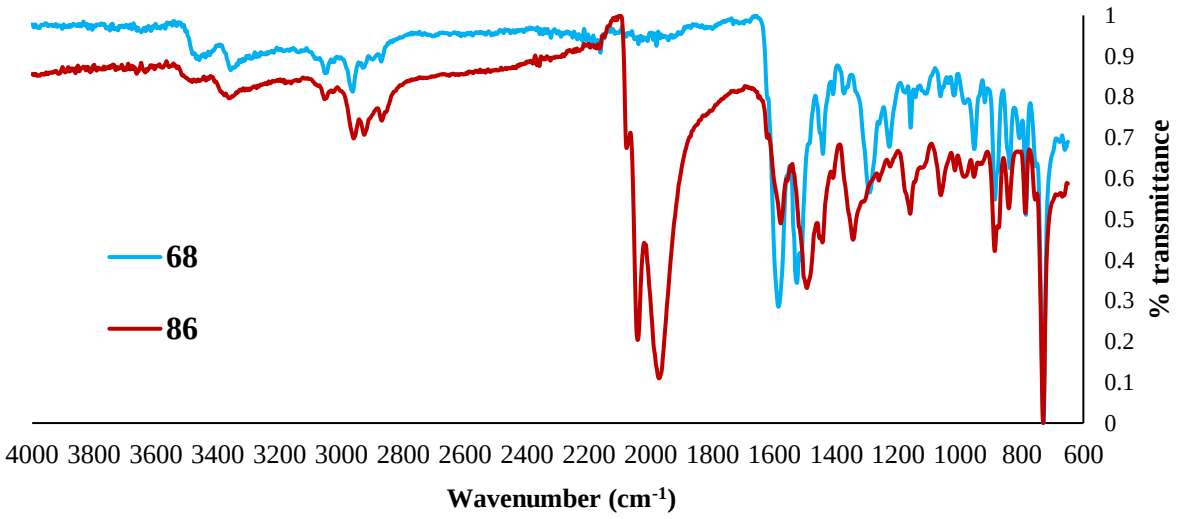

Figure 5.14. Normalised FT-IR spectra of compound **86** (red curve) and its ligand precursor **68** (blue curve).

Table 5.1. Band assignments for the FT-IR spectra of the metal precursor $Ru_3(CO)_{12}$ and **86** (Figure 5.13).

Compound	Wavenumber (cm^{-1})	Vibrational mode
$Ru_3(CO)_{12}$	2047 2010 1990 1982	C-O st
86	2041 1972 1579 1494	C-O st C=N st

The strong, broad bands assigned to the CO stretching in the IR spectrum of compound **86** might also be an indication of the presence of ruthenium clusters. Previous unpublished results from our group involving the reactivity of tripodal NHC ligands with the cluster $Fe_3(CO)_{12}$ led to a compound of formula $[(timteb^{tBu}H_3)_2][\{Fe_2(CO)_8\}_3]$ in which the diiron cluster acts as anion for the protonated tripodal ligand $timteb^{tBu}$ (Figure 5.15).[21]

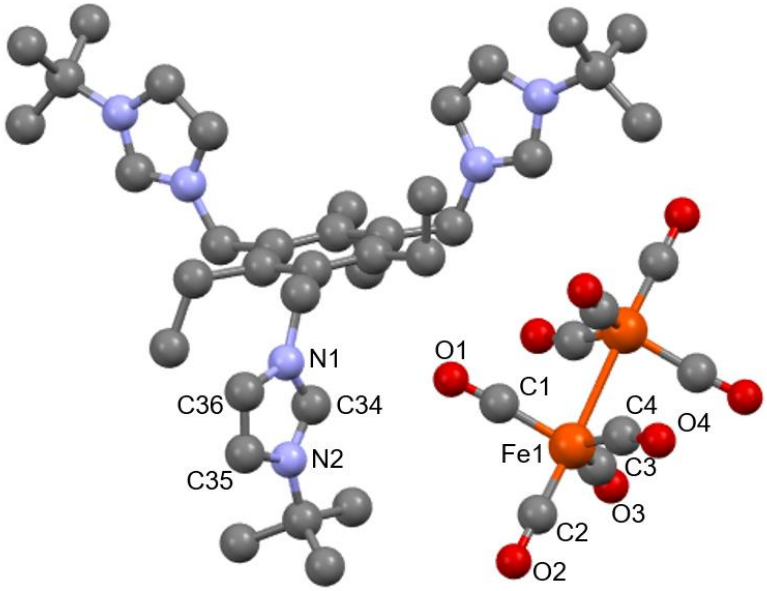

Figure 5.15. Representation of the crystal structure of half a unit cell containing $[(timteb^{tBu}H_3)_2][\{Fe_2(CO)_8\}_3]$.

The results from the ^{1}H NMR analysis of **86** (previously reported in Figure 5.11) led us to consider the possibility of having again obtained an alternative complexation structure that involves a metal-arene interaction. The presence of such broad signals in the low field part of the ^{1}H NMR spectrum of **86** might suggest that the ruthenium centre interacts with the aromatic rings of the anthracene arms, therefore generating an Ru-anthracene "half sandwich compound" (Figure 5.16).

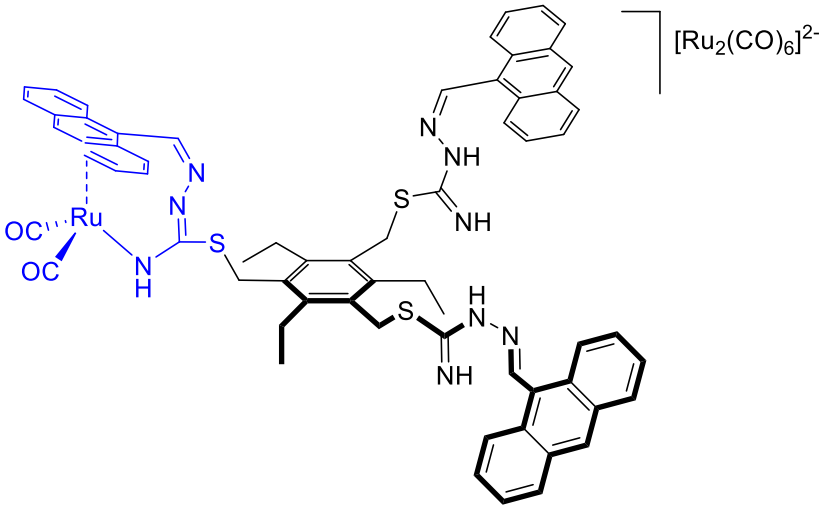

Figure 5.16. Alternative structure proposed for compound **86** involving the arene coordination with the metal centre.

Reports on metal-arene coordination arrangements between ruthenium-carbonyl moieties and aromatic systems (Figure 5.17) have been published by Kraupp,[22] Lin,[23] Casey[24] and Yildirim.[25]

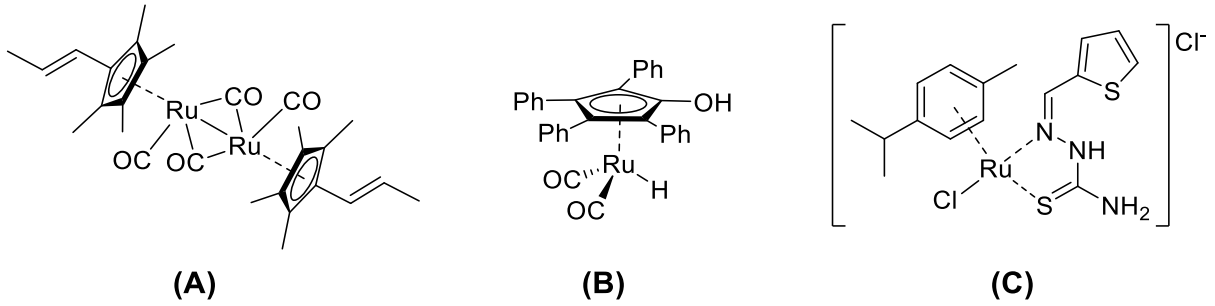

Figure 5.17. Literature examples of Ruthenium "half sandwich" compounds from Lin (**A**), Casey (**B**) and Yildirim (**C**).

The UV-visible and fluorescence spectra of compound **86** are shown in Figure 5.18 **A**. The UV-Vis spectrum (blue curve) shows the characteristic absorption bands of the anthracene moiety at 350, 370 and 390 nm. The fluorescence spectrum (red curve) shows a relatively narrow emission band with an intensity maximum at 441 nm. A fluorescence 2D map was also generated and is in Figure 5.18 **B**. Compound **86** appears to exhibit higher fluorescence emission compared to its ligand precursor **68**, whose spectra is reported in Chapter 2.

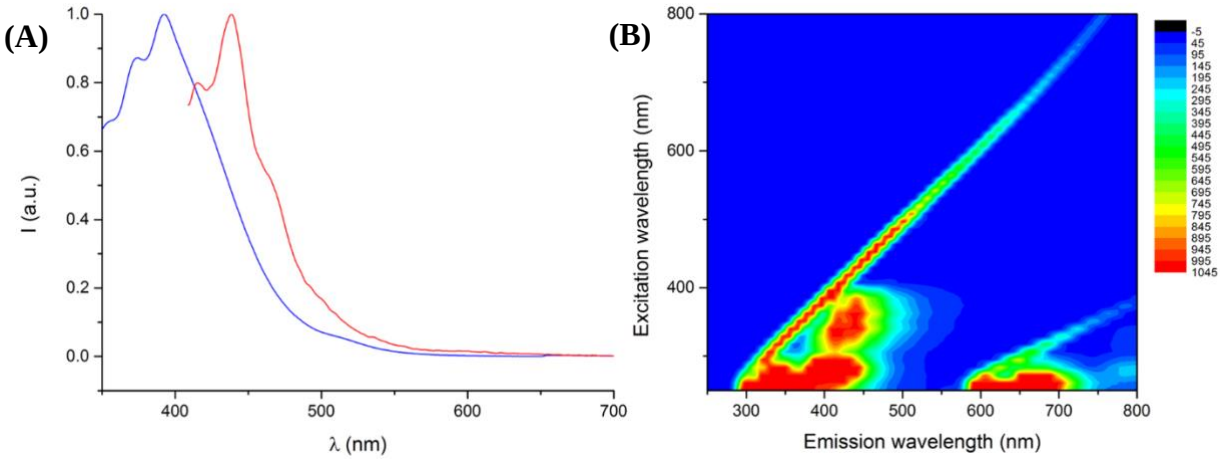

Figure 5.18. (**A**) Normalised UV-Visible (blue line) and fluorescence emission (red line) spectra of compound **86** (5 µM in THF). (**B**) 2D fluorescence contour map (5 µM in THF).

5.2. Metal complexes of tripodal NHC-based ligands

N-Heterocyclic carbenes represent one of the most important classes of ligands in organometallic chemistry. NHCs are good σ-donors and π-acceptors, which makes them able to form strong metal–carbene bonds, thus giving complexes that are stable in biological media.[26]

The aim of this work was to test the ability of few selected tripodal NHC-based ligands to bind transition metals with demonstrated antiproliferative capabilities such as silver,[27] gold,[28] copper[29] and ruthenium.[30]

5.2.1. Silver(I) complexes

Silver and its salts have been exploited as antimicrobial agents and have proved to exhibit low toxicity for humans. Thus, most of the biomedical studies on silver complexes have been conducted on their antimicrobial properties.[31] Youngs and co-workers were the first to report the anticancer activity of Ag(I)-NHC compounds.[32] Since then, several groups have been developing new Ag(I)-NHC complexes which have displayed remarkable activity towards several cancer cell lines.[27, 33]

In this section, we describe various attempts to develop new metal complexes of silver(I) with a few selected ligands synthesised in Chapter 3. In order to synthesise such complexes, we decided to use a method involving the *in situ* deprotonation of the carbene, by simply mixing the ligand precursor with silver(I) oxide (Ag_2O) in an appropriate solvent.[34] This methodology presented several advantages compared to the typical deprotonation-metallation of NHCs, as it did not require solvent pre-treatments (such as solvent drying), anhydrous conditions, and strong bases to deprotonate the C_2 carbon.

After performing a literature review regarding multidentate Ag-NHC complexes, it was decided to attempt the metalation of some selected tripodal systems previously obtained. This would probe whether it would be possible to synthesise trimetallic complexes in which each imidazolium “arm” of the tripodal ligand was bound to a silver atom. A representation of the proposed reaction is shown in Scheme 5.4.

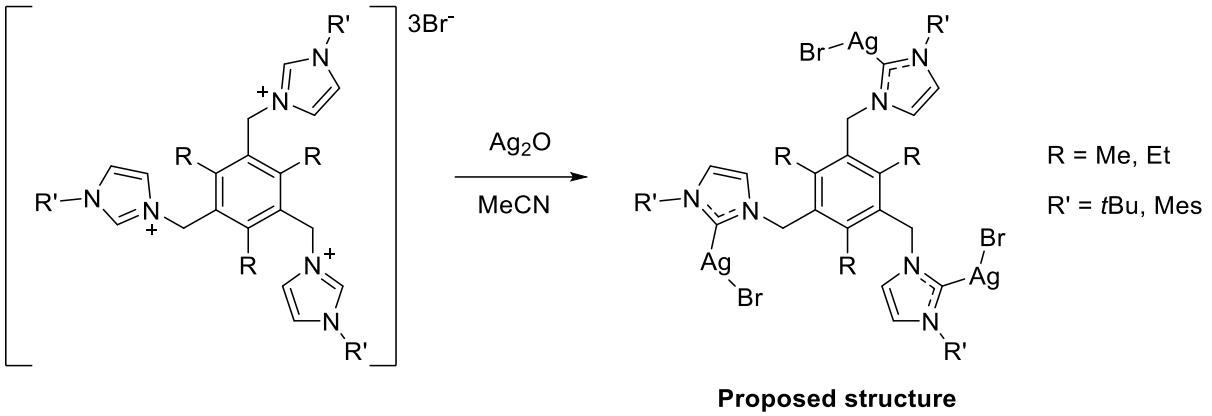

Scheme 5.4. Proposed synthesis of tripodal NHC-Ag_3 complexes.

The first reaction was attempted by mixing a suspension of the ligand precursor compound **76** and a 3-fold excess of Ag_2O in acetonitrile. The reaction vessel was wrapped with tinfoil to prevent photodecomposition, then the slurry was stirred at room temperature and followed *via* TLC. After 48 hours the mixture was filtered through a Celite® pad to remove all the unreacted Ag_2O and the solvent was removed under vacuum to give an off-white powder. However, upon redissolution the crude product quickly turned grey, possibly due to photosensitivity. Nonetheless, a ^{1}H NMR spectrum of the crude product, shown below in Figure 5.19, revealed a small peak at 8.60 ppm, which we attributed to the C_2-*H* proton, indicating an incomplete deprotonation of all three NHC sites.

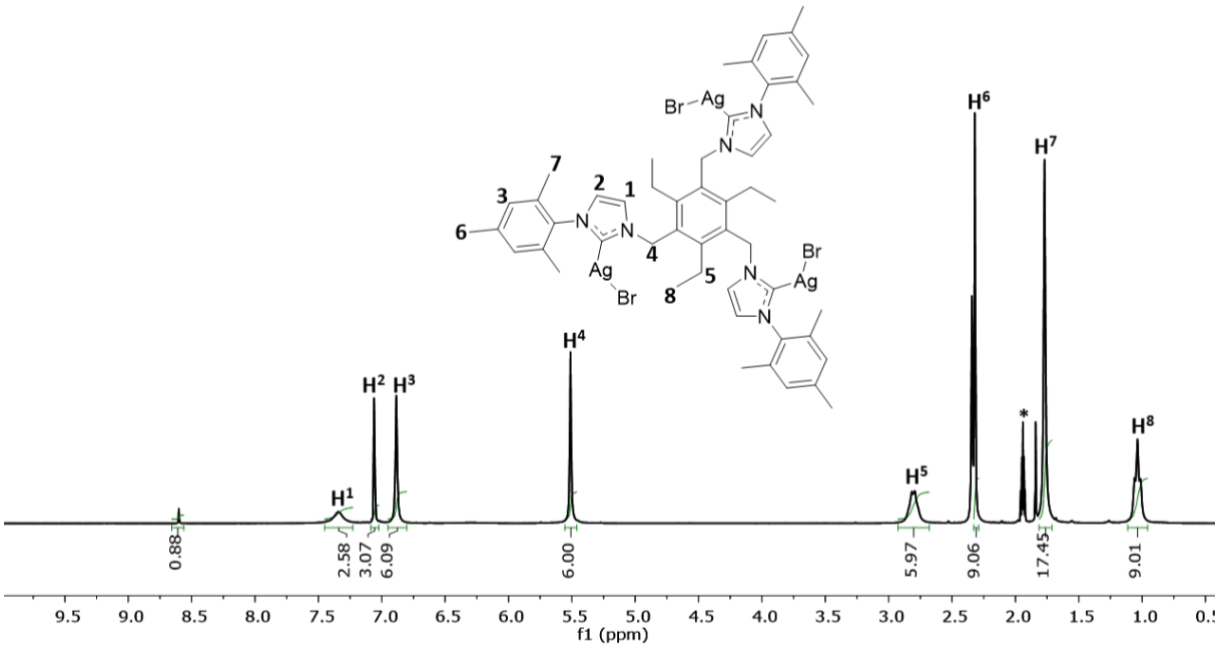

Figure 5.19. ^{1}H NMR (300 MHz, MeCN-d_3, 298 K) spectrum of the reaction product formed between compound **76** and Ag_2O.

Mass spectrometry analysis of the reaction product was carried out. The resulting spectrum (Figure 5.20) shows no traces of a trimetallic pattern. A bimetallic pattern was instead identified with an ion species of m/z = 998.3050, attributable to the formation of a bimetallic complex of formula **76·Ag$_2$Br**. The last assignable peak in the spectrum in Figure 5.20 belongs to the monometallic ion species with m/z = 865.3919, which is presumably indicative of a potential Ag$_1$-NHC species. Unfortunately, attempts to repeat the preparation of this bimetallic compound were unsuccessful.

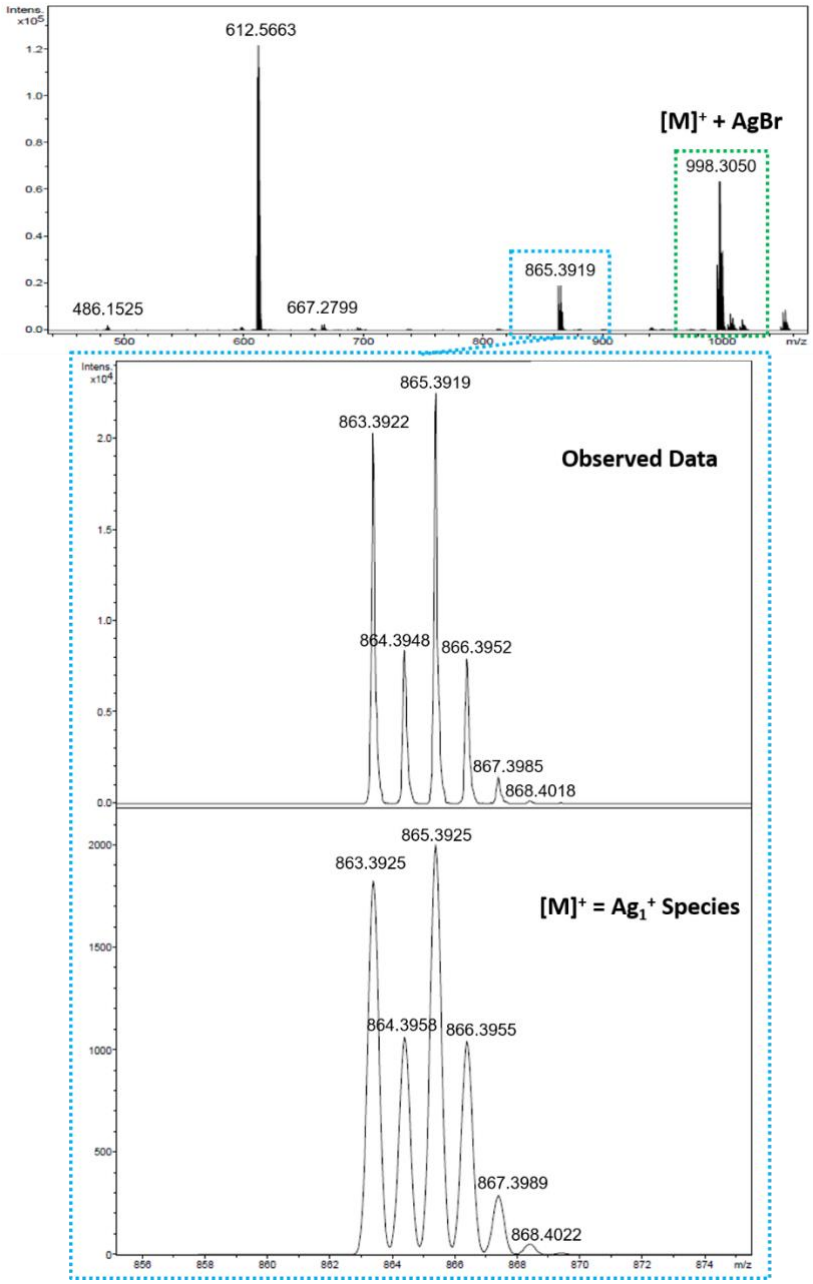

Figure 5.20. Mass spectrum recorded for the product between compound **76** and Ag$_2$O.

Following the unsuccessful initial attempt to obtain a trimetallic complex, we performed subsequent experiments with different equivalents of metal precursor (1, 2, 3.3 and large excess), times (up to 5 days) and solvents. Higher equivalents of Ag_2O appeared to trigger photodecomposition of the samples with a monometallic species formed as by-product, while ratios of 1:1 – 1:2 ligand precursor – Ag_2O seemed to favour the formation of a monometallic species. A paper from Willans and co-workers reported the development of a small tris(imidazolium) cage that reacts with Ag_2O to give an Ag(I) carbene complex, in which one of the imidazolium moieties remains protonated (Figure 5.21).[35]

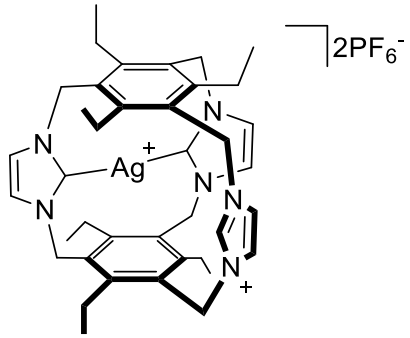

Figure 5.21. Structural representation of the tris(imidazolium) cage complex of Ag(I) prepared by Willans et al.

Based on this precedent and our results above, we therefore decided to further explore the path leading to monometallic species and their properties. The synthesis of the Ag_1-NHC complex, named compound **87** in this work, thus involved mixing the ligand precursor **76·3PF6** and a small excess of Ag_2O in acetonitrile. After stirring for 48 hours at room temperature, the mixture was filtered through a Celite® pad and the solvent removed *via* rotary evaporator. The residue was purified by silica gel chromatography, eluting with dichloromethane, to give an off-white powder in moderate yield (53%).

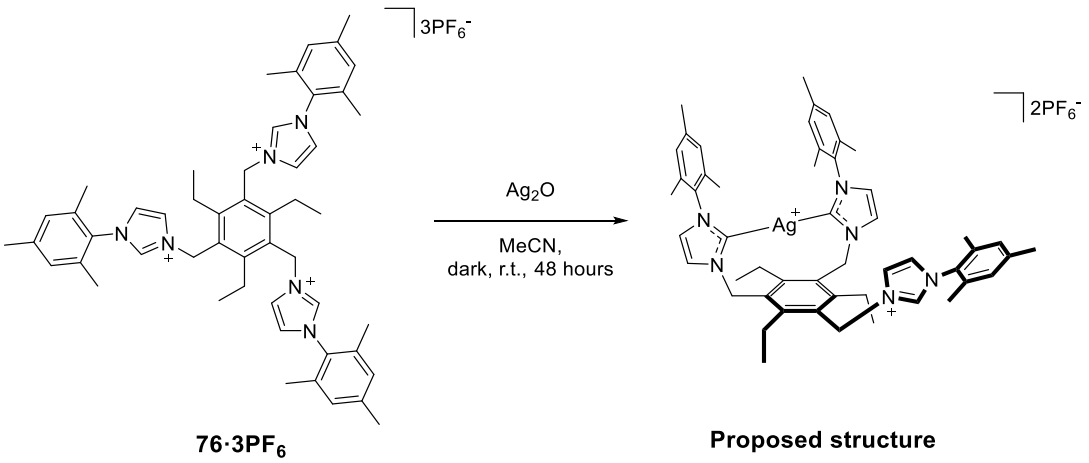

Scheme 5.5. Synthesis of compound **87**.

The ^{1}H NMR spectrum of **87** (Figure 5.22) shows 15 sets of signals. The signal at 9.22 ppm, integrating for 1H, was assigned to the imidazolium C$_2$-*H* proton (entry H$_1$ in Figure 5.22). The two signals at 8.01 and 7.91 ppm, both integrating for 2H, were assigned to the N(C*H*)$_2$N of the imidazol-2-ylidene groups (entries H$_2$ and H$_3$ in Figure 5.22). A up-field shift of the N(C*H*)$_2$N signals (entries H$_6$ and H$_7$, Figure 5.22) of the uncoordinated imidazolium moiety was also observed This shielding effect could be due to the *endo* position of the two imidazolium hydrogens,[36] and as suggested by the "close" configuration assumed by the crystal structure of the ligand **76·3PF$_6$**, reported in Chapter 3 (section 3.3), figure 3.25.

Two resonances at 7.38 and 7.12 ppm, integrating for 2H and 4H respectively, were assigned to the aromatic C-*H* of the mesityl moieties (H$_4$ and H$_5$ in Figure 5.22). Two more signals at 5.63 (H$_8$), integrating for 2H, and 5.56 ppm (H$_9$), integrating for 4H, were correlated to the C*H*$_2$ connecting the mesitylimidazolium arms and the hexasubstituted aromatic core. Compared to the ^{1}H NMR spectrum of the starting material (compound **76·3PF$_6$**, reported in Chapter 3, section 3.3), the splitting of the C*H*$_2$ linkers may be indicating the presence of an asymmetric complex. Additional signal splittings, indicative of such asymmetry, are evident in the shifts of the proton signals of the ethylene arms (entries H$_{10}$, H$_{11}$ and H$_{14}$, H$_{15}$ in Figure 5.22).

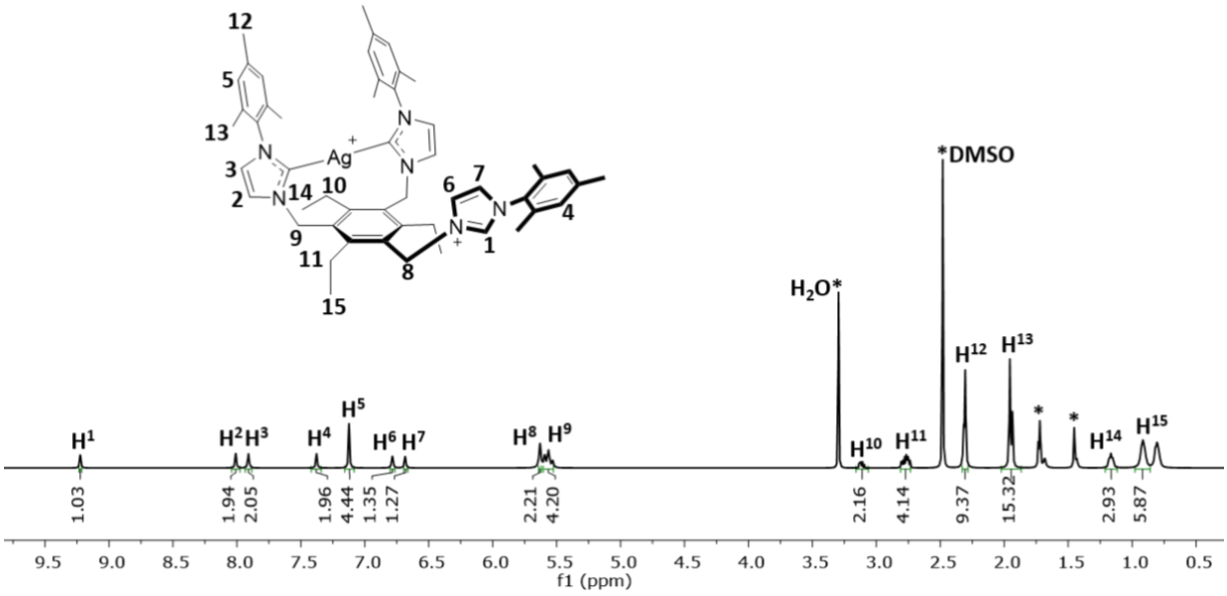

Figure 5.22. ^{1}H NMR (400 MHz, DMSO-d$_6$, 298 K) spectrum of compound **87**. For clarity, magnetically equivalent nuclei within the same NMR spin system are labelled once. * residual solvents and impurities traces.

Electrospray ionisation mass spectrometry performed on compound **87** further strengthened the hypothesis that **87** is a di-cationic, monometallic Ag1-NHC species. In the spectrum of **87**, shown below in Figure 5.23, two main peaks can be identified. The base peak at m/z = 1011.3786 corresponds to the singly charged adduct $[M+PF_6]^+$, while the next most intense peak at m/z = 433.2100 may be assigned to the doubly charged molecular ion, $[M]^{2+}$.

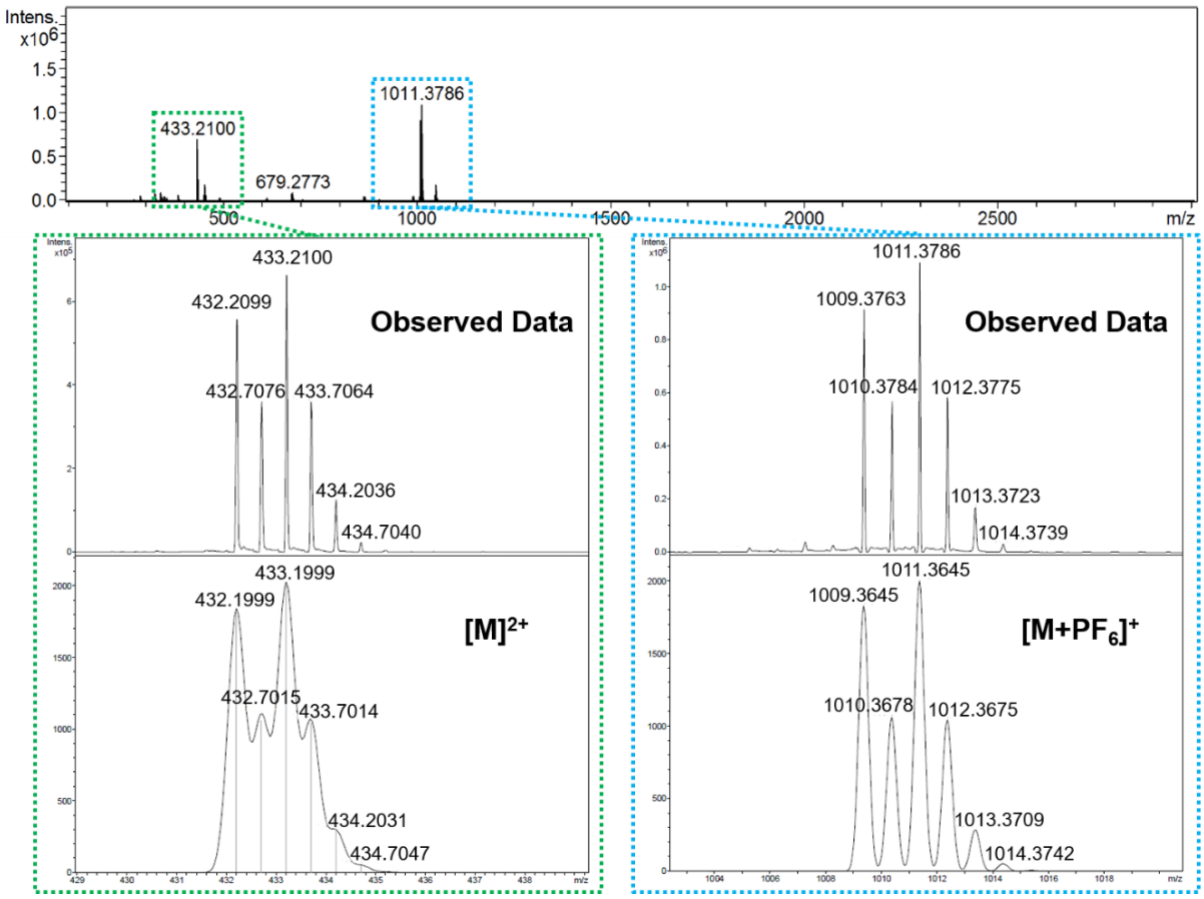

Figure 5.23. Mass spectrum of compound **87**. Green dotted box: ion species $[M]^{2+}$ at 433.2100 m/z. Blue dotted box: ion species $[M+PF_6]^+$ at 1011.3786 m/z.

The UV-visible and fluorescence spectra of compound **87** are shown in Figure 5.24. The UV spectrum (red line) shows an absorption maximum at 280 nm, which is due to the presence of the aromatic units. The fluorescence emission spectrum is broad, with a Stokes shift of several hundred nm and an emission intensity maximum at 431 nm.

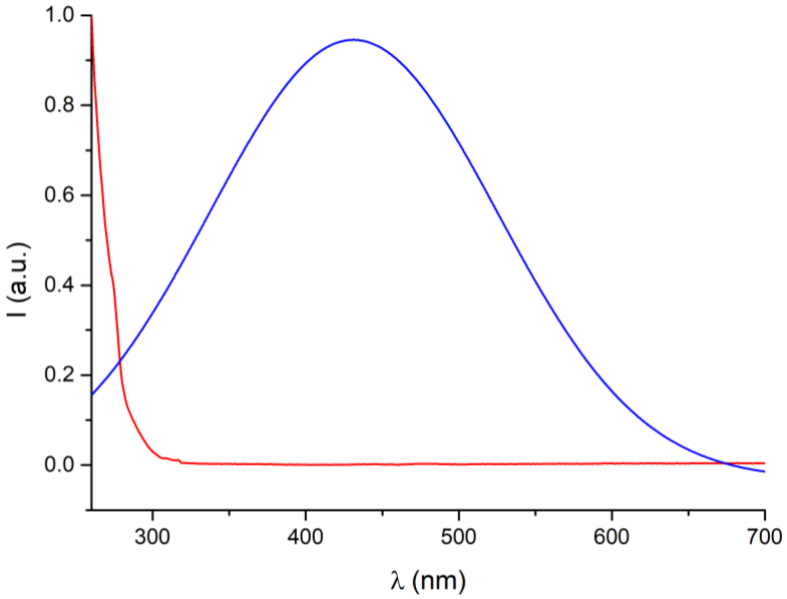

Figure 5.24. Normalised UV-Visible (red line) and fluorescence emission (blue line) spectra of compound **87** (25 μM in CH_2Cl_2).

In order to shorten the reaction time for the preparation of **87**, we considered employing microwave methodology. The use of microwave heating for the synthesis of NHC-based complexes of coinage metals (such as Ag) has been shown to allow for a drastic reduction of the reaction times compared to conventional heating, while affording comparable or better yields of the desired products.[37]

The microwave-assisted synthesis of compound **87** was achieved by dissolving the ligand precursor compound **76·3PF$_6$** in appropriate amount of anhydrous dichloroethane (DCE), followed by a slight excess of Ag_2O. The vial containing the reaction mixture was sealed, purged with argon and heated at 150 °C under microwave irradiation for 42 minutes. After work up and chromatography, the product was obtained as a white solid.

The ^{1}H NMR spectrum of the product of the microwave-assisted reaction is shown in Figure 5.25, along with its ^{1}H-^{1}H COSY spectrum (Figure 5.26). As for the spectrum of the complex obtained by the conventional heating method (Figure 5.22), the same magnetic inequivalence between the aliphatic protons may be observed (entries H_6, H_7, H_8, H_{10} and H_{11} in the ^{1}H NMR spectra reported in Figure 5.25). The methylene groups linking the imidazolium arms and the aromatic core also display such inequivalence: compared to the ligand precursor, with the resonance at around 5.50 ppm being split upon complexation into two signals at 5.52 and 5.29 ppm (labelled as H_4 and H_5 respectively). However, an important difference in the resonance shown by the spectrum of compound **87** (Figure 5.22) and that of the product of the microwave

reaction (Figure 5.25) can be observed in the downfield region: the spectrum of compound **87** clearly shows the presence of the undeprotonated imidazolium proton (H_1 in Figure 5.22), as well as splitting of the signals generated by the remaining protons of the chemically diverse heteroatoms. In the ^1H NMR spectrum of the compound obtained through the microwave reaction (Figure 5.25), such splittings are not observed, and the pro-carbenic proton signal observed for **87** is missing.

Given the obvious differences between the ^1H NMR spectra shown in Figure 5.22 and 5.25, it is possible to conclude that the product of the microwave reaction is not compound **87**. Moreover, the lack of signal attributable to the pro-carbenic proton suggests that the complexation of the metal centre involved all three NHC arms. Several groups reported the synthesis of tri-coordinate complexes of Ag(I) with monodentate tertiary phosphines and multidentate nitrogen donors able to enforce such coordination over the metal centre.[38-42] The proposed structure of the newly synthesised Ag(I) complex, further referred as compound **88**, is shown in Figure 5.25.

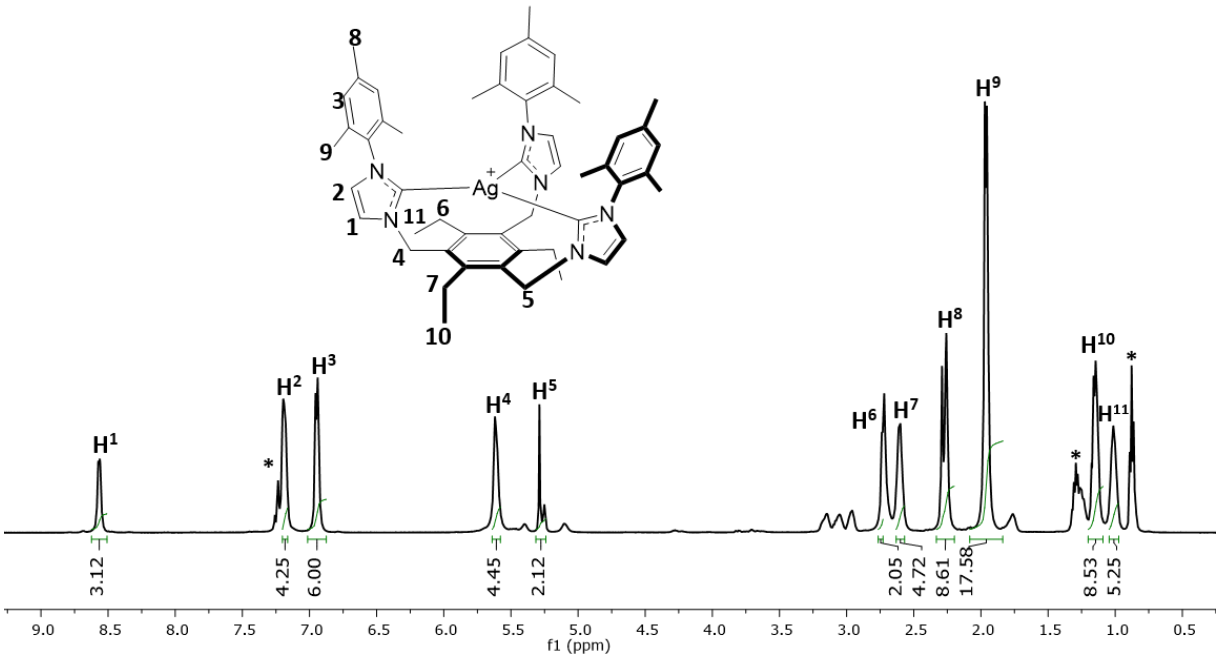

Figure 5.25. ^1H NMR (400 MHz, $CDCl_3$, 298 K) spectrum of compound **88** synthesised via the microwave method. For clarity, magnetically equivalent nuclei within the same NMR spin system are labelled once. * residual solvents and impurities traces.

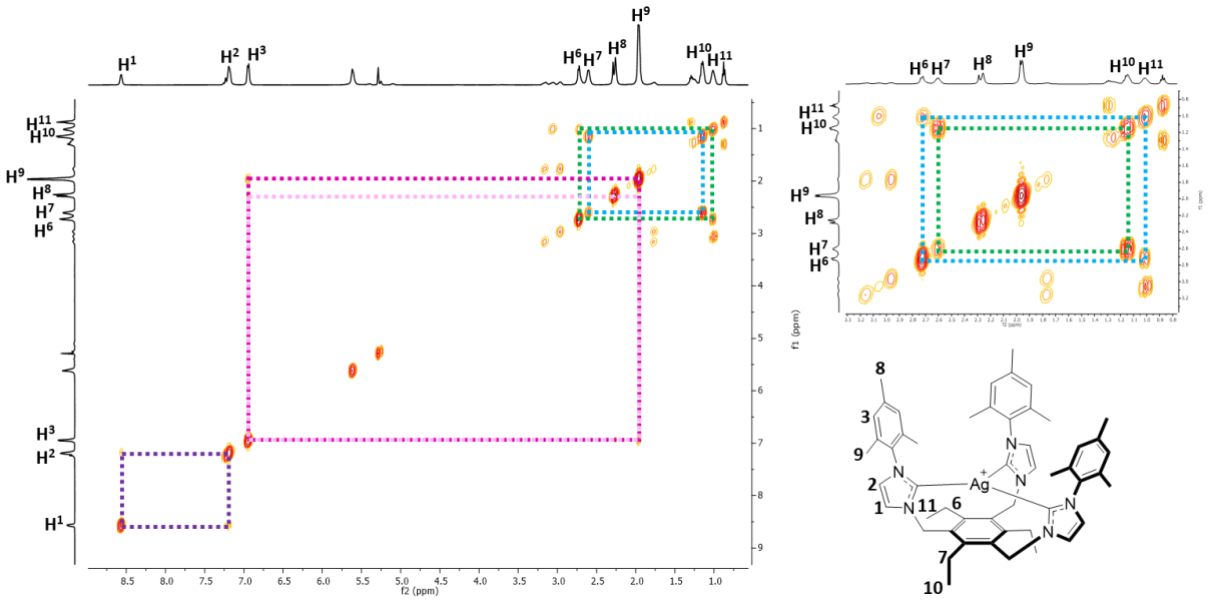

Figure 5.26. ^{1}H-^{1}H COSY (400 MHz, $CDCl_3$, 298 K) spectrum of compound **88**. On the right: detail of the spectrum highlighting the aliphatic region. For clarity, magnetically equivalent nuclei within the same NMR spin system are labelled once.

The mass spectrum of compound **88**, shown in Figure 5.27, clearly shows an intense peak at m/z = 865.3957, corresponding to the molecular ion $[M]^+$ of the mono-metallic complex.

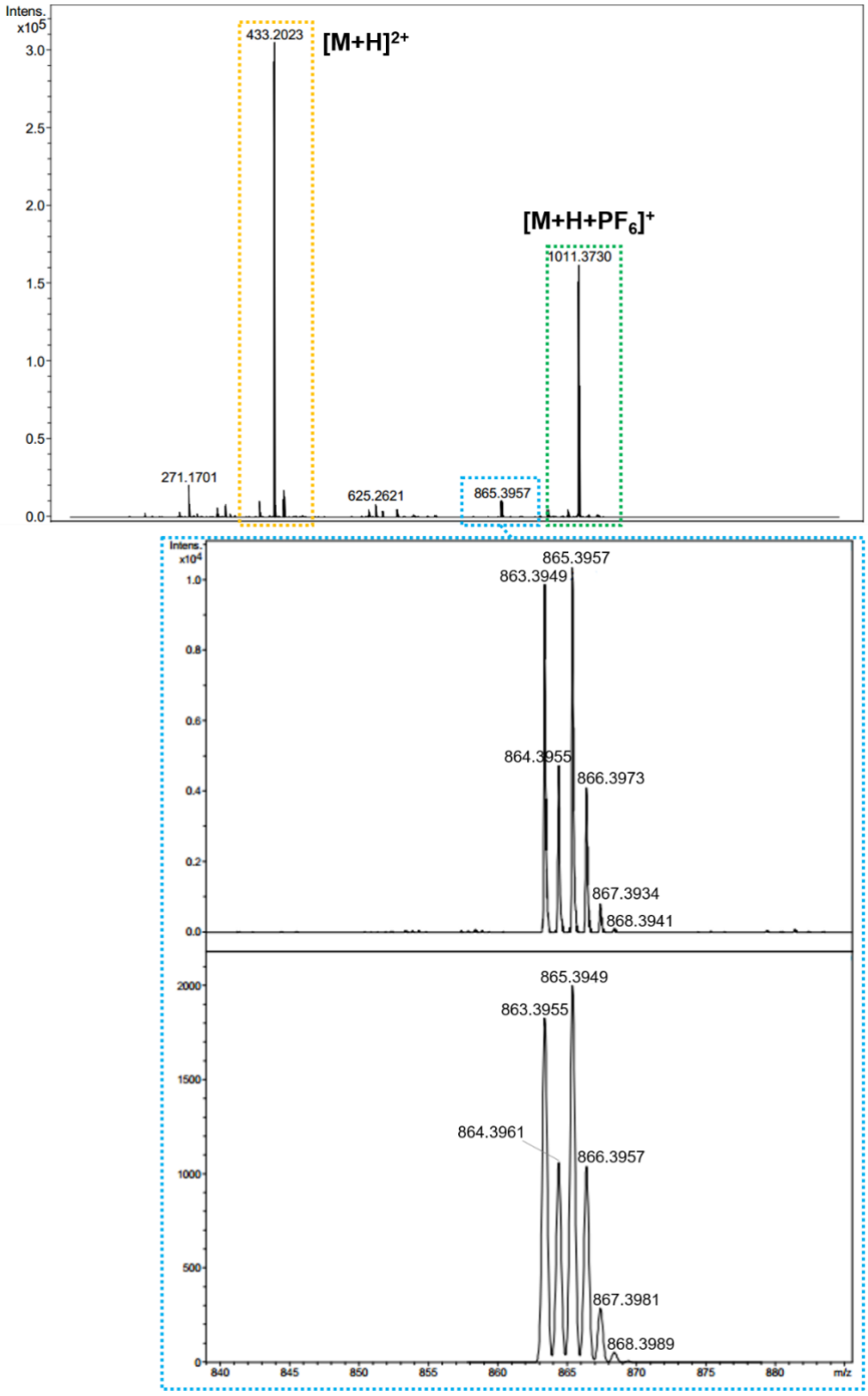

Figure 5.27. Mass spectrum of compound **88**.

The microwave-assisted methodology was employed again to react the tripodal NHC-based compound **75** with the silver precursor Ag_2O. The reaction was carried out by mixing in a microwave vial a dichloroethane solution of ligand precursor **75** and a slight excess of powdered Ag_2O (1.2 equivalents). The reaction vessel was sealed, and the mixture heated at 150°C for 40 minutes. The product was obtained as a pale-yellow powder after recrystallisation from dichloromethane.

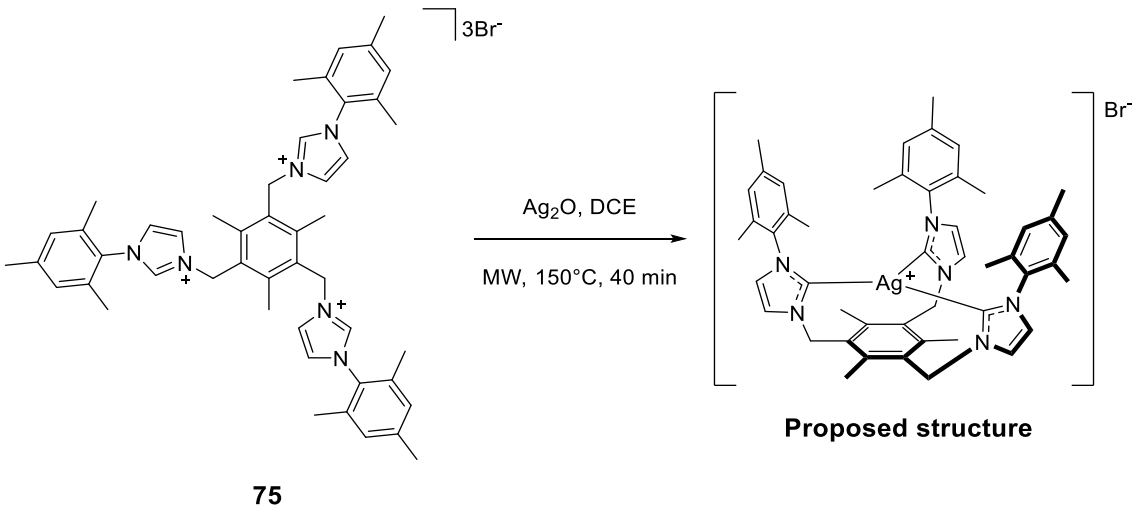

Scheme 5.6. Microwave-assisted synthesis of compound **89**.

The new metal complex, named compound **89**, was characterised with NMR spectroscopy. The ^{1}H NMR spectrum of compound **89** is shown in Figure 5.28. The resonances in the spectrum of **89** were comparable to the ones observed for the ligand precursor **75**, with the sole exception of the pro-carbenic proton signal (C$_2$-*H*), which is usually deshielded to values around 9.5-10.5 ppm. There was also an upfield shift in the signals belonging to the N(C*H*)$_2$N of the imidazol-2-ylidene groups of *ca.* 0.5 ppm, possibly due to complexation.

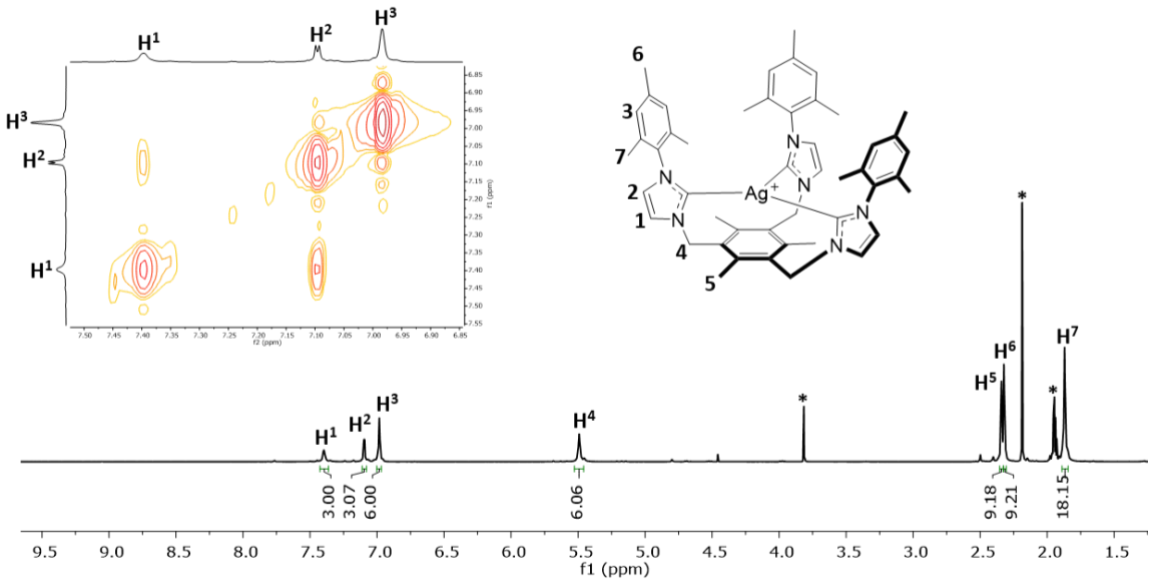

Figure 5.28. ^{1}H NMR (300 MHz, MeCN-d_3, 298 K) spectrum of compound **89** and a detail of the ^{1}H-^{1}H COSY spectrum highlighting the aromatic region. For clarity, magnetically equivalent nuclei within the same NMR spin system are labelled once. * residual solvents and impurities traces.

The mass spectrum of compound **89** (Figure 5.29) displays a peak at m/z = 412.1783, which can be attributed to the protonated, doubly charged molecular ion ($[M+H]^{2+}$, with M = $C_{48}H_{54}N_6Ag$ as molecular formula corresponding to the proposed structure for compound **89**). A second species, with m/z = 823.3513, was correlated with the molecular ion $[M]^{+}$ of the proposed formula for compound **89**. The presence of such a species coupled with the ^{1}H NMR results indicating that the complexation have occurred in all three "arms" of the ligand precursor compound **75**, could be an indication of an alternative coordination modality between the metal centre and compound **75**, which sees the silver ion coordinating the three NHC arms of **75** in a similar fashion as for the previously obtained compound **88**.

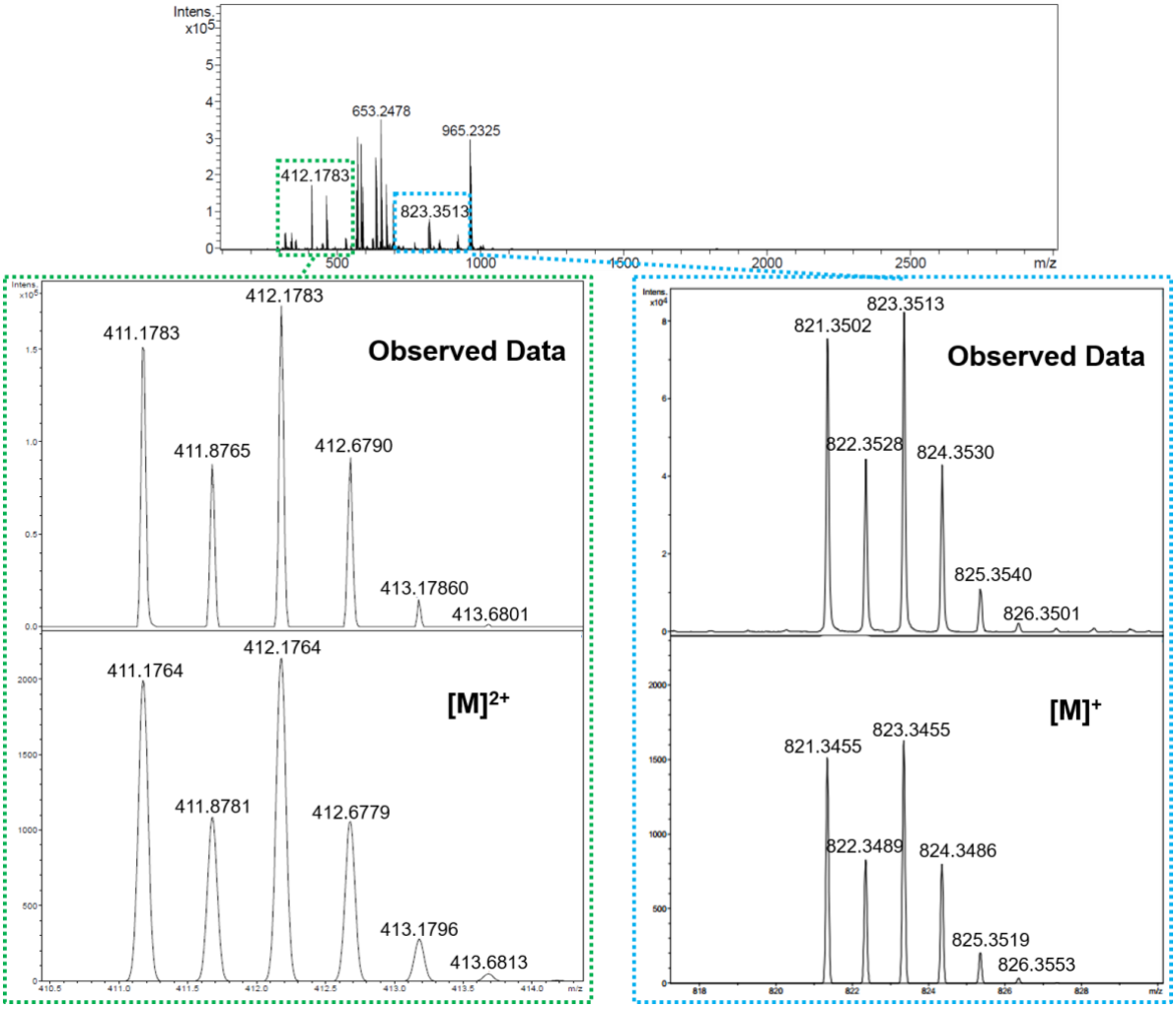

Figure 5.29. Mass spectrum of compound **89**. Green dotted box: ion species $[M+H]^{2+}$ at m/z = 412.1783. Blue dotted box: ion species $[M]^{+}$ at m/z = 823.3513.

Another metalation attempt, using Ag_2O as metal precursor and microwave heating, involved the use of the tripodal *tert*-butylimidazolium-based compound **73**, whose synthesis is reported in Chapter 3, section 3.2. The reaction was carried out by dissolving compound **73** in DCE, followed by addition of a slight excess of finely powdered Ag_2O. The mixture was heated under MW irradiation at 150 °C for 32 minutes, and the product was obtained as a pale orange powder in fair yield (61%).

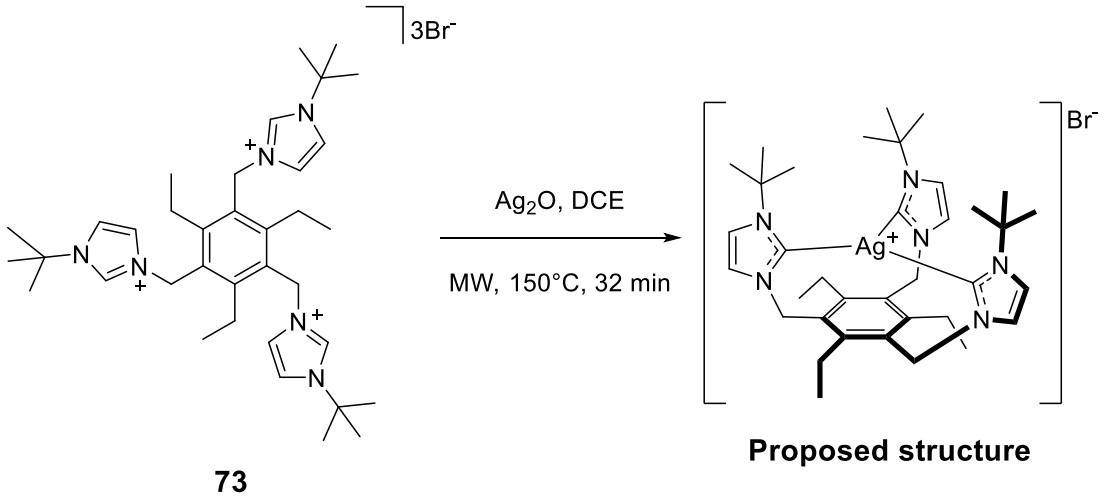

73

Scheme 5.7. Synthesis of compound **90**.

The results of ^{1}H NMR spectroscopy analysis performed on compound **90** are shown in Figure 5.30. The spectrum of **90** shows 9 resonances. Two signals in the aromatic region, at 7.57 and 7.28 ppm respectively, were assigned to the hydrogens of the imidazole-ylidene arms coordinated to the silver centre (H_1 and H_2). The signal at 5.43 ppm was assigned to the three methylene groups linking the aromatic core and the arms (H_3). Finally, the sharp singlet at 1.62 ppm was assigned to the protons of the three *tert*-butyl moieties (H_5) and the signal at 0.74 ppm was assigned to the 15 protons of the three ethylic arms (labelled H_4 and H_6 in Figure 5.30).

The remaining three signals identifiable in the ^{1}H NMR spectrum of **90** were correlated to unreacted ligand **73**: at 9.36 ppm was assigned to the C_2-*H* protons of the un-coordinated *tert*-butyl imidazolium, while the two signals at 7.61 and 7.38 were assigned to the remaining protons of the uncoordinated imidazolium arms (labelled with * in Figure 5.30).

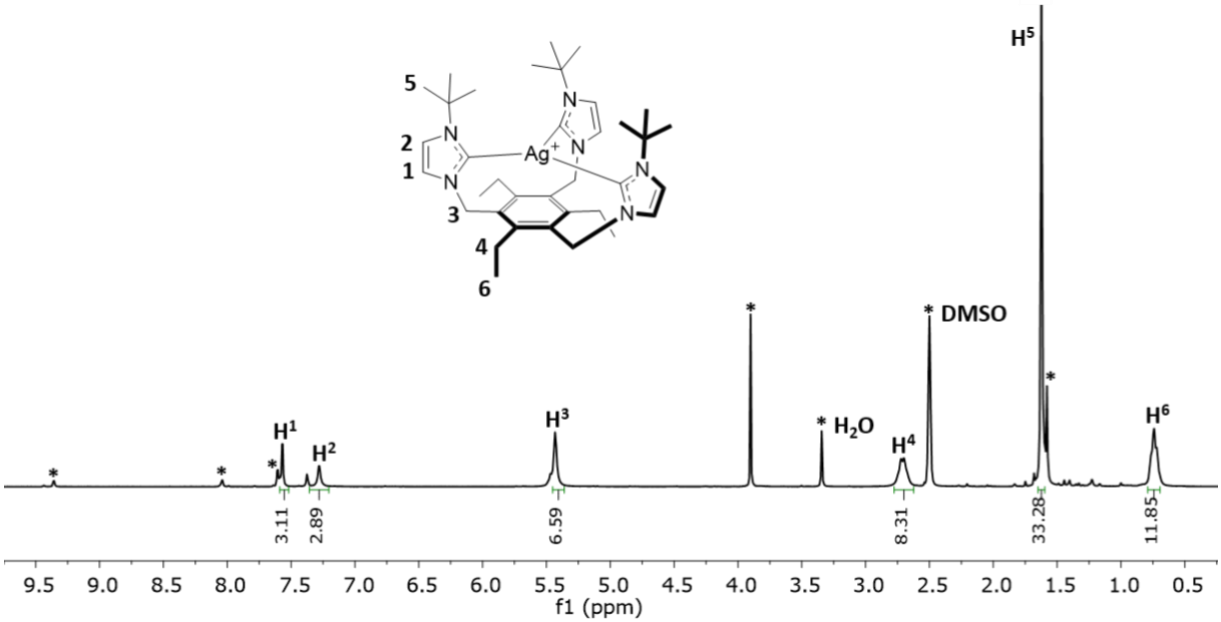

Figure 5.30. 1H NMR (300 MHz, DMSO-d6, 298 K) spectrum of compound **90**. For clarity, magnetically equivalent nuclei within the same NMR spin system are labelled once. * residual solvents and impurities traces.

Mass spectrometry analysis carried out on compound **90** (Figure 5.31) revealed the presence of three species: the first, with m/z = 677.3499 was correlated to the molecular ion $[M]^+$, of the proposed structure, where M corresponds to the molecular formula for compound **90** ($C_{36}H_{54}N_6Ag$). The second ion species found, with m/z = 715.3280, presented unexpectedly the chlorine isotopic pattern and was correlated with the species $[M+Cl]^+$.

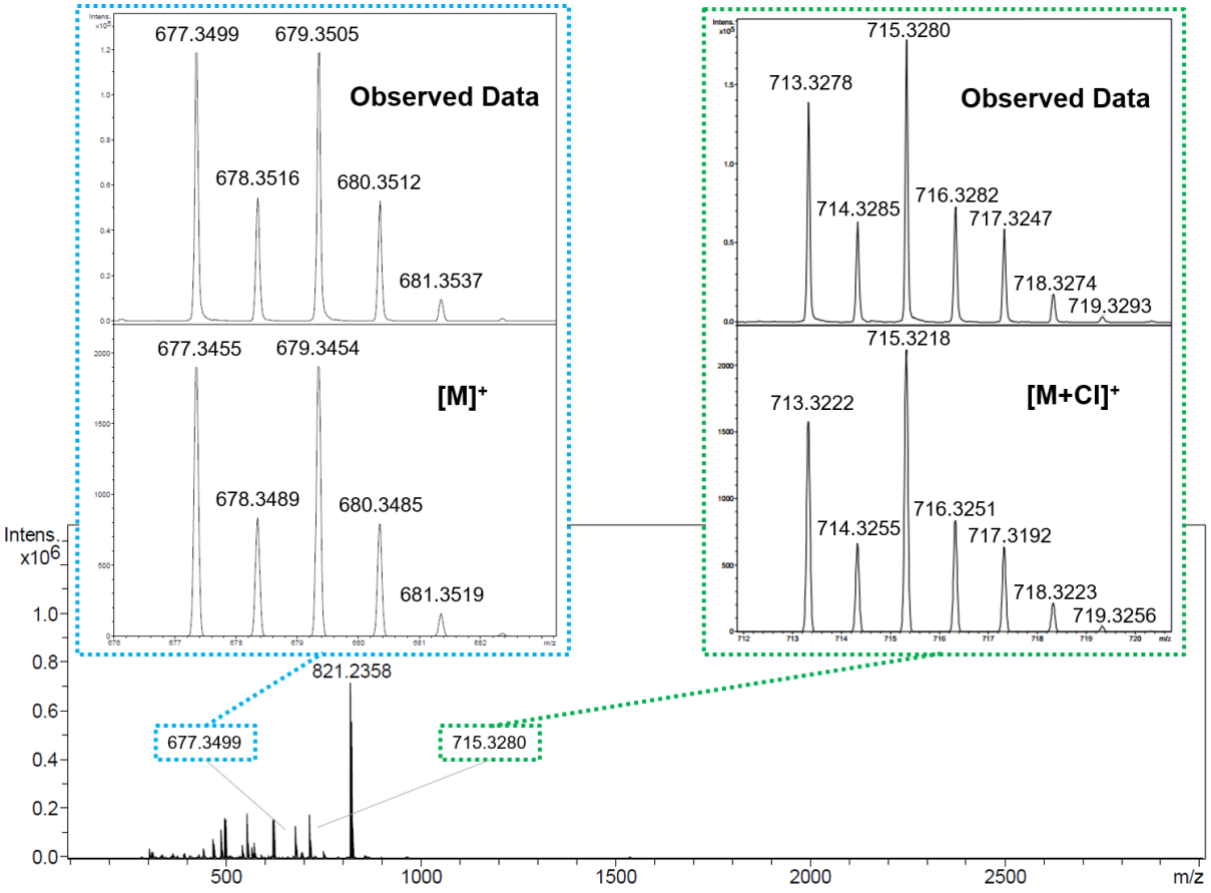

Figure 5.31. Mass spectrum of compound **90**. Blue dotted box: ion species $[M]_+$ at m/z = 677.3499. Green dotted box: ion species $[M+Cl]_+$ at m/z = 715.3280.

5.2.2. Synthesis of a novel gold(I)-carbene complex

Following the discovery of the gold(I) complex auranofin as an antirheumatic reagent in 1985,[43] the usage of gold complexes in medicine has been increasingly explored. More recently, a series of binuclear NHC-based gold(I) complexes displaying attractive anticancer activity was developed by Barnard and co-workers.[44] Carbene ligands have some similarities to phosphines, but metal-carbene complexes are often more stable than similar metal-phosphine complexes.[45] In addition, NHCs are often easier to synthesise than phosphines and their lipophilic/hydrophilic properties can be readily fine-tuned by the incorporation of appropriate functional groups.

It was decided to investigate the possibility to develop a gold(I)-NHC complex from the previously obtained Ag(I)-NHC complex **87**. Silver complexes are known to be effective carbene-transfer agents, often without loss of structure.[34]

The reaction was performed by dissolving the previously synthesised metal complex **87** in dried dichloromethane, followed by the gold(I) precursor chloro(dimethylsulfide)gold(I). The resulting mixture was placed into a Schlenk tube, wrapped in tinfoil to avoid photodecomposition and stirred at room temperature overnight. After work-up by filtration, the product was obtained as an off-white solid.

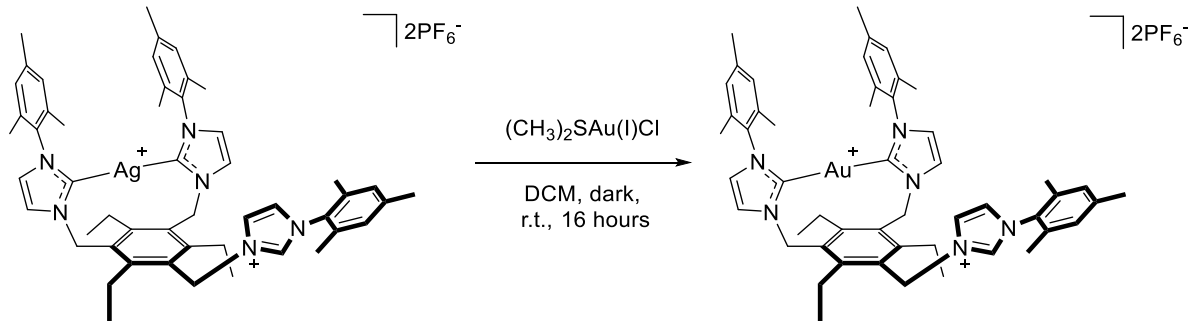

87 **Proposed structure**

Scheme 5.8. Synthesis of compound **91**.

The newly obtained compound **91** was analysed by ^{1}H NMR, but due to the poor resolution of the multiplets it was not possible to assign all the signals found in the ^{1}H NMR spectrum. Subsequent mass spectrometry analysis revealed the presence of two ion signals that were assigned to the presence of the predicted metal complex: a doubly charge species $[M]^{2+}$ at m/z

= 477.1082 and the base peak at m/z = 1098.8146, which was assigned to the singly-charged $[M+PF_6]^+$. The mass spectrum of compound **91** is shown in Figure 5.32.

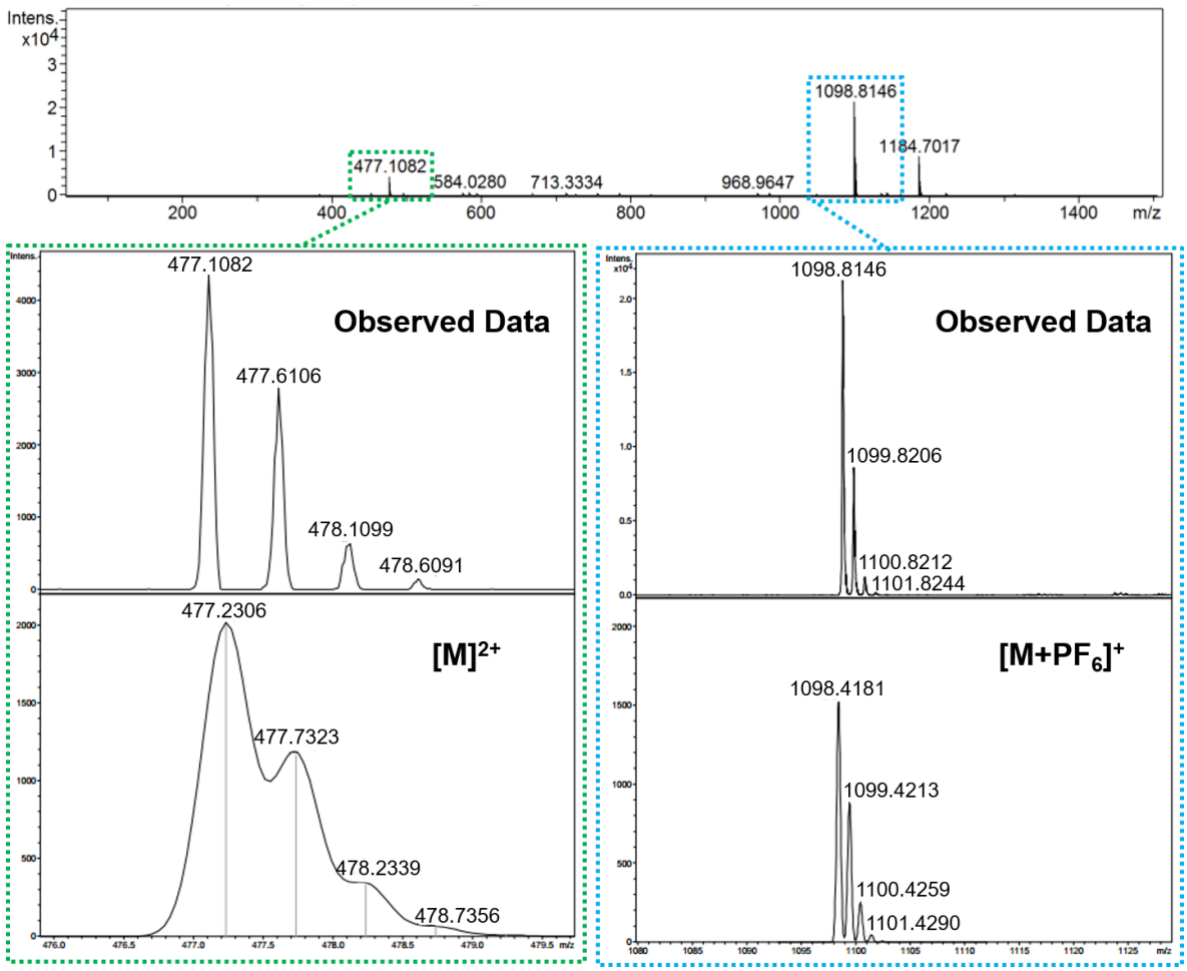

Figure 5.32. Mass spectrum recorded for compound **91**. Green dotted box: ion fragment $[M]^{2+}$ at m/z = 477.1082. Blue dotted box: ion signal $[M+PF_6]^+$ at m/z = 1098.8146.

However, the acquired spectroscopic data are not sufficient to clearly determine the proposed structure. The presence of the hexafluorophosphate counterion in the singly-charged ion species recorded in the mass spectrum of compound **91** might suggest that the counterion is closely interacting with the positive charge of the tripodal ligand. Moreover, the presence of the chloride adduct of the ion species $[M+PF_6]$ of m/z = 1134.3948 might suggest an alternative complexation mode where the metal halide Au(I)Cl is bound to only one NHC arm of the tripodal ligand (see Figure 5.33).

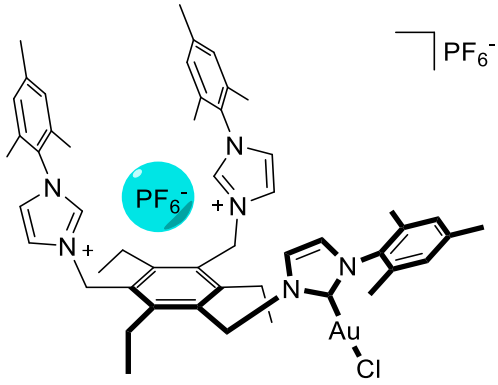

Figure 5.33. Alterative structure proposed for compound **91**.

The UV-visible and fluorescence spectra of compound **91** are shown in Figure 5.34. The UV spectrum (blue line) shows an absorption maximum at 280 nm. The fluorescence emission spectrum, similarly to the silver complex (and precursor) **87** is broad, with an intensity maximum at 419 nm.

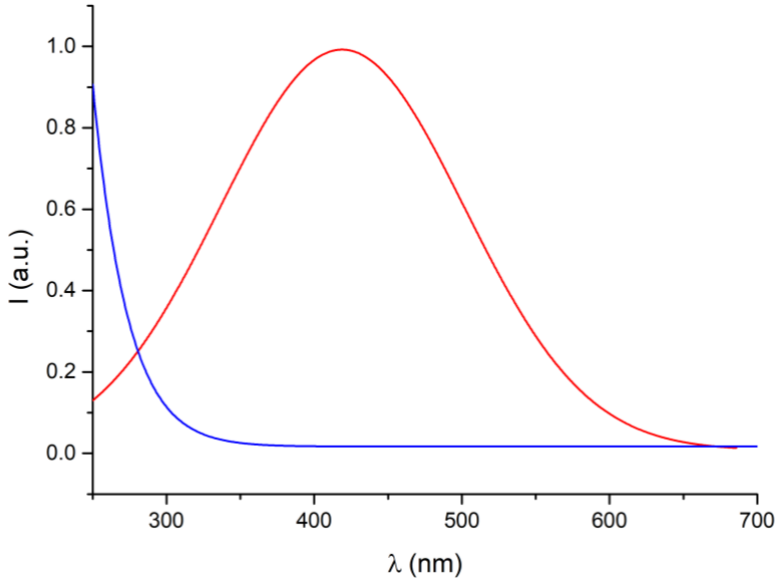

Figure 5.34. Normalised UV-visible (blue line) and fluorescence emission (red line) spectra of compound **91** (25 μM in CH_2Cl_2).

5.2.3. Synthesis of a novel copper(I)-carbene complex

Copper is found in all living organisms and is a crucial trace element in redox chemistry, growth and development.[46] Copper toxicity derives from its ability to produce reactive oxygen species (ROS), displace other metal ions, peroxidise lipids, and directly cleave DNA and RNA.[47]

Most of the reports regarding copper complexes as anti-cancer agents have focused on copper(II), while very few examples of copper(I) species have been examined. Even few reports of Cu(I)-NHC complexes are focused around its capability to act as anticancer compound,[48, 49] thus we decided to investigate the possibility to develop a novel Cu(I)-NHC complex from the silver(I) complex **87**.

The synthesis of the copper(I) complex, named **92** in this work, followed the transmetallation synthetic route between the silver complex **87** and the copper(I) precursor copper(I)*tetrakis*(acetonitrile)hexafluorophosphate (molecular formula = $[(CH_3CN)_4Cu(I)][PF_6]$). The reaction was carried out by stirring the two reactants in anhydrous DCM at room temperature under an inert atmosphere for 16 hours, until a cloudy solution was formed. The copper(I) complex **92** was isolated as a white solid upon filtration and precipitation.

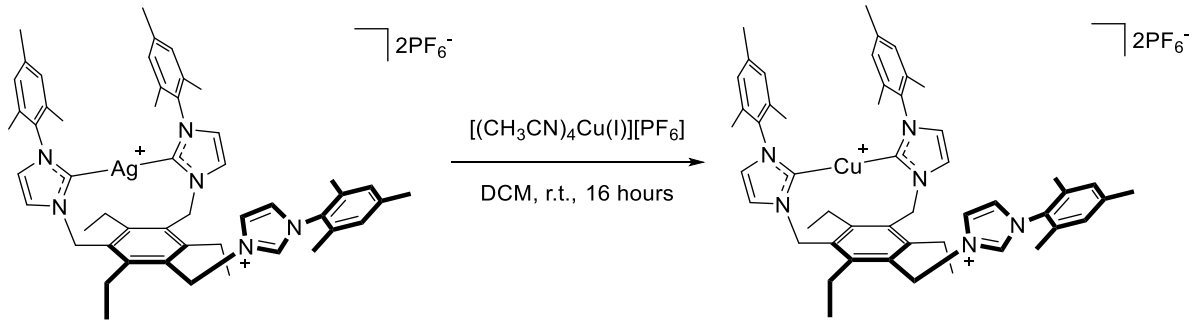

87 **Proposed structure**

Scheme 5.9. Synthesis of compound **92**.

The ^{1}H NMR spectrum of compound **92** (Figure 5.35) shows 16 signals. The signal at 8.82 ppm, integrating for 1H, was assigned to the imidazolium C2-*H* proton (labelled H_1 in Figure 5.35). There are two poorly resolved signals between 7.50 and 7.29 ppm, the first assigned to the $N^+(CH)_2N$ protons (labelled $H_2$and H_3) of the uncoordinated imidazolium arm, the second to the $N(CH)_2N$ protons belonging to the coordinated imidazol-2-ylidene groups (labelled H_4 and H_5). The signal at 7.00 ppm (H_6) was assigned to the four aromatic C-*H* of the mesityl

moieties linked to the coordinated ylidene arms, while the signal at 6.72 ppm, labelled H_7 in Figure 5.35, was correlated to the mesityl C-*H* of the uncoordinated arm.

Two signals at 5.81 ppm and 5.53 ppm were correlated to the methylene moieties linking the coordinated NHC arms and the hexasubstituted aromatic core (labelled H_8 and H_9 in Figure 5.35). Further splittings, which may indicate the presence of an asymmetric system, are evident in the signals assigned to the methyl groups of the mesityl substituents (labelled H_{11} and H_{12} for the *p*-C*H*$_3$, and H_{13} and H_{14} for the *o*-C*H*$_3$); as well as for the proton resonances of the ethylene arms (labelled H_{15} and H_{16} in Figure 5.35).

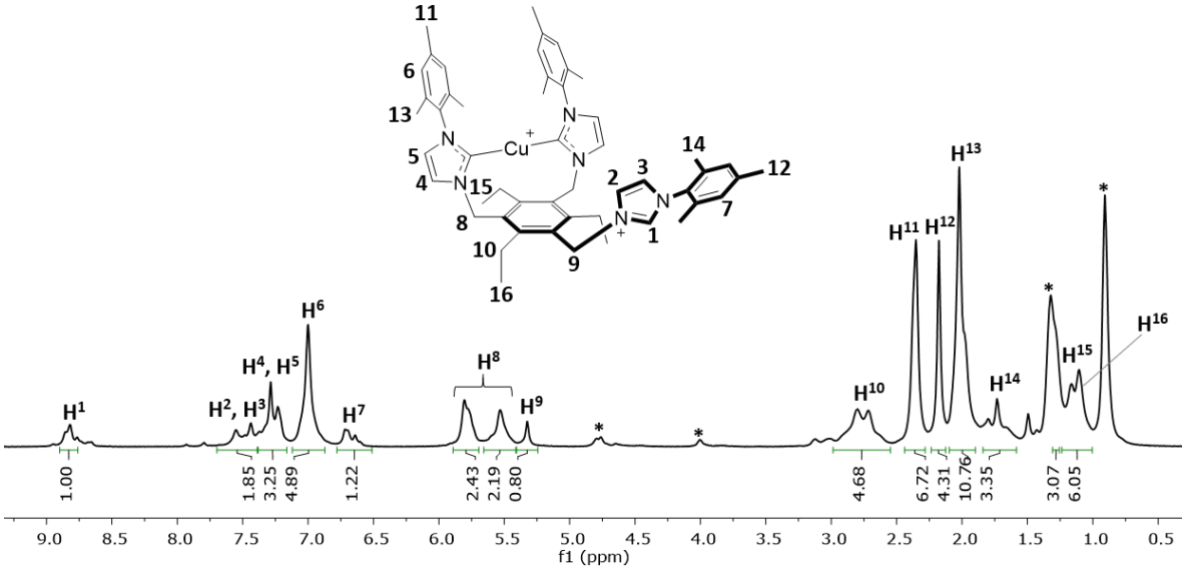

Figure 5.35. $_1$H NMR (400 MHz, $CDCl_3$, 298 K) spectrum of compound **92**. For clarity, magnetically equivalent nuclei within the same NMR spin system are labelled once. * residual solvents and impurities traces.

Mass spectrometry analysis performed on compound **92** revealed the presence of two well defined peaks at m/z = 410.2170 and m/z = 965.3866, which could be attributed to the doubly charged ion species $[M]^{2+}$ and the singly-charged hexafluorophosphate adduct $[M+PF_6]^+$ respectively. The positive mode mass spectrum of **92** is shown below in Figure 5.36.

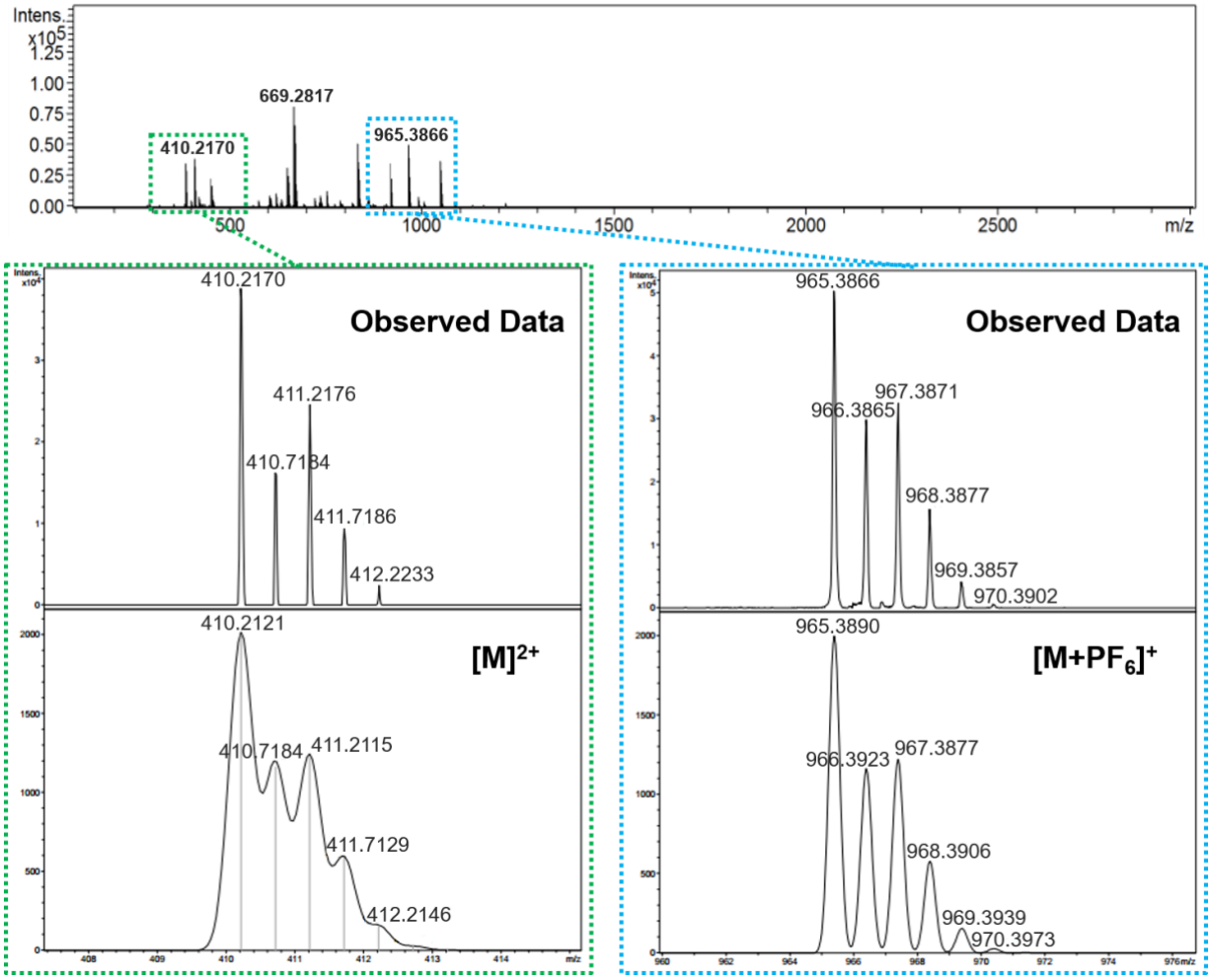

Figure 5.36. Mass spectrum recorded for compound **92**. Green dotted box: the doubly-charged ion species $[M]^{2+}$ at m/z = 410.2170. Blue dotted box: ion species $[M+PF_6]^+$ at m/z = 965.3866.

The normalised UV-visible and fluorescence spectra of compound **92** are reported in Figure 5.38. The UV spectrum (red line) shows an absorption maximum at 280 nm, which is again due to the presence of the aromatic units. As for the previously synthesised metal-NHC complexes **87** and **91**, the fluorescence emission spectrum of compound **92** is broad (see Figure 5.38).

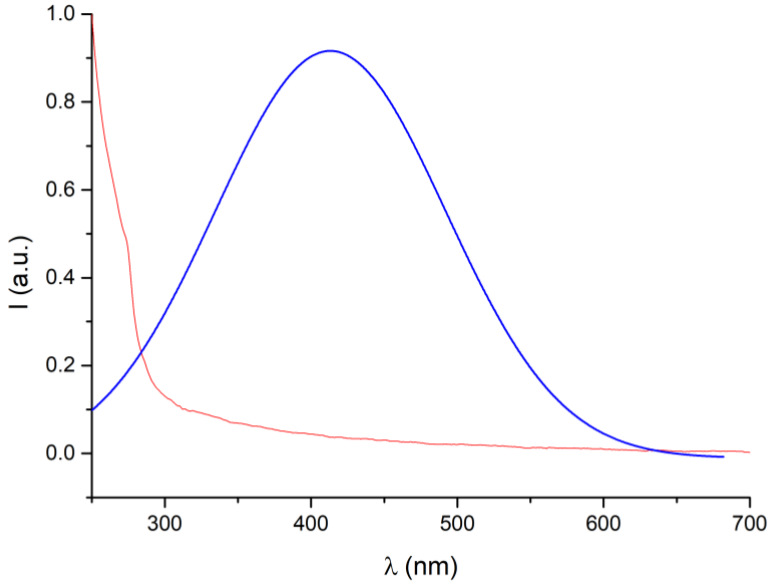

Figure 5.38. Normalised UV-Visible (red line) and fluorescence emission (blue line) spectra of a 25 μM solution of compound **92** in CH_2Cl_2.

5.2.4. Ruthenium complexes

The last series of reactions involving tripodal NHC-based ligands and transition metals discussed in this chapter aimed to develop a trimetallic species by exploiting the ability of the ruthenium cluster $Ru_3(CO)_{12}$ to generate interesting metal complexes with a wide array of N-heterocyclic carbenes.[50-52]

Unpublished work within our group has shown that compound **73** will react with $Fe_3(CO)_{12}$ to form **73**$[Fe(CO)_4]_3$ (Figure 5.39),[53] although no spectroscopic characterisation was obtained to support the X-ray structure. Further attempt to reproduce those results proved unsuccessful, thus it was decided to explore the reactivity of the tripodal ligands with its ruthenium analogue $Ru_3(CO)_{12}$ as more robust metal carbonyl cluster.

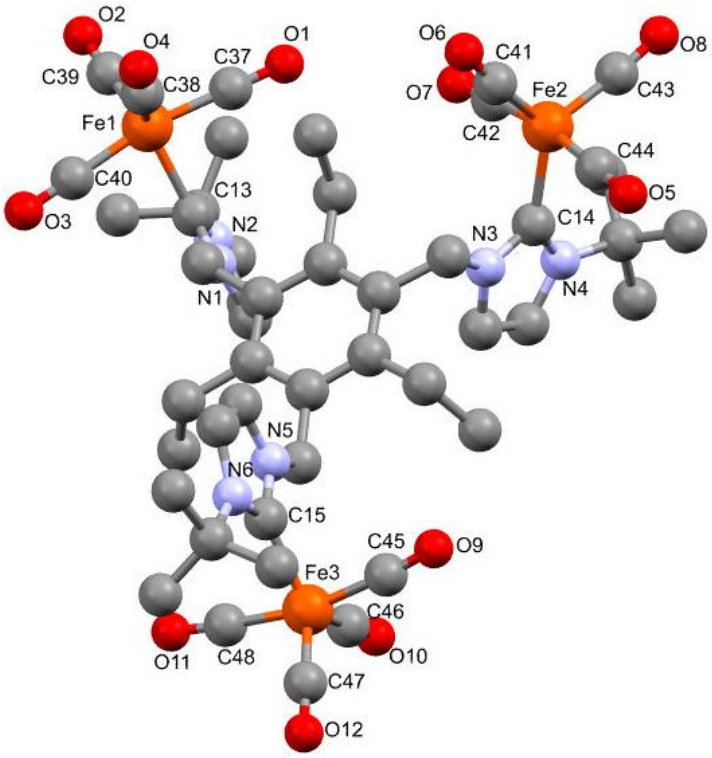

Figure 5.39. Crystal structure of half a unit cell containing **73**$[Fe(CO)_4]_3$. Hydrogen atoms are removed for clarity.

The synthesis of the ruthenium analogue of **73**$[Fe(CO)_4]_3$, compound **93**, was attempted as shown in Scheme 5.10. Treatment of $Ru_3(CO)_{12}$ with compound **73** and potassium *tert*-butoxide (*t*BuOK) in tetrahydrofuran (THF) at room temperature for two hours led to a colour change in the resulting suspension from orange to deep red and, after work up, the isolation of a red solid.

Subsequent ^{1}H NMR analysis, using deuterated methanol as solvent, revealed the presence of the characteristic C_2-*H* signal at 9.78 ppm, likely belonging to unreacted **73**.

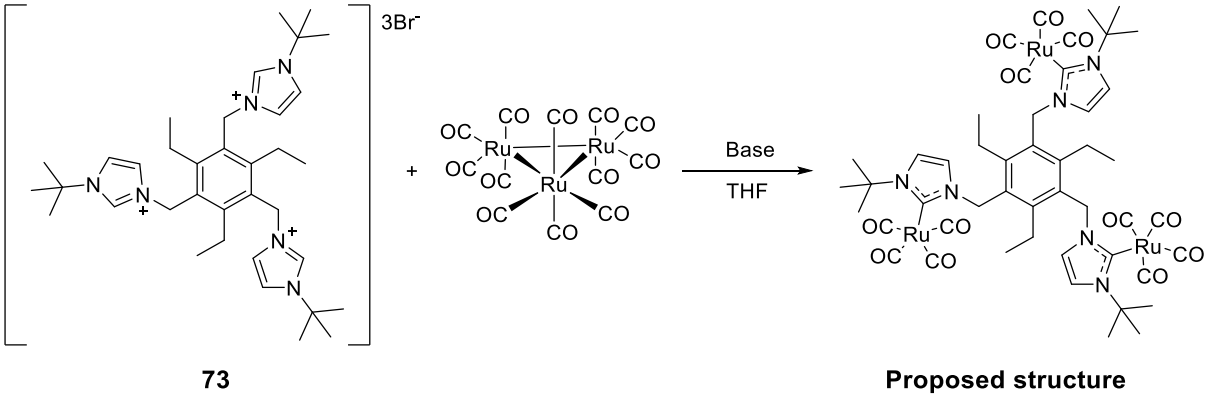

Scheme 5.10. Generic synthetic pathway for the compound **93**.

Further attempts were carried out by varying the reaction times and the type of base for deprotonation. Among the various attempts, pre-treatment of compound **73** with potassium bis(trimethylsilyl) amide in THF and subsequent addition of the deprotonated ligand into a THF solution of $Ru_3(CO)_{12}$ cooled down to -78 ºC gave a bright red suspension, which turned deep red after warming up to room temperature in the course of 16 hours. ^{1}H NMR analysis performed on the dark red product obtained is shown below in Figure 5.40. There are 6 sets of signals with chemical shifts and integrations comparable to the ligand precursor compound **73**. The absence of the low field signal belonging to the C_2-*H* is also evident from the spectrum, suggesting that complexation might have occurred on all three imidazolium "arms".

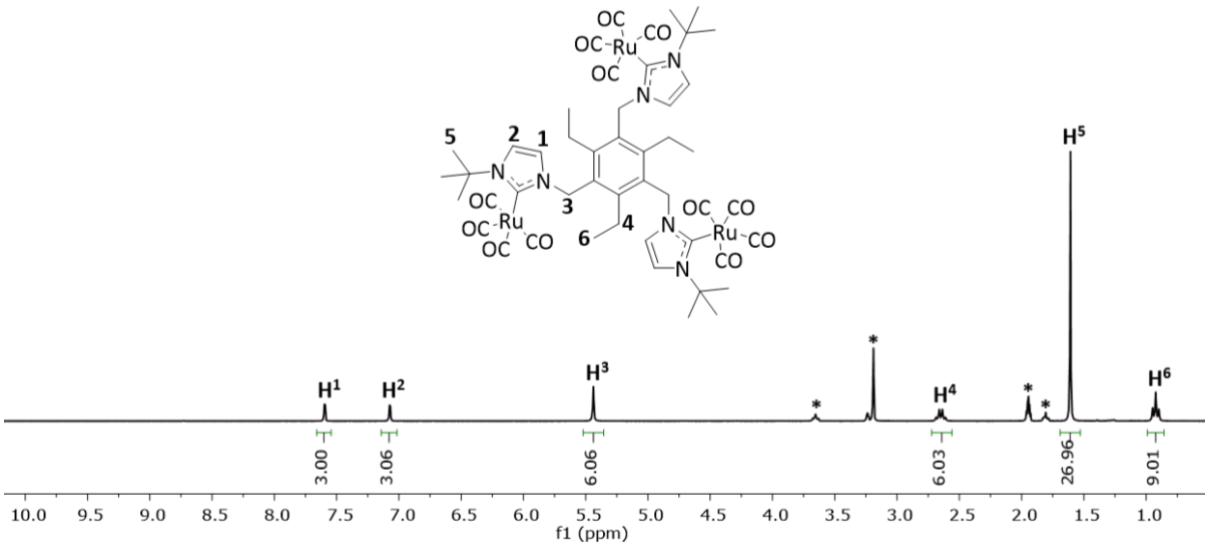

Figure 5.40. ^{1}H NMR (500 MHz, MeCN-d_3, 298 K) spectrum of compound **93**. For clarity, magnetically equivalent nuclei within the same NMR spin system are labelled once. * residual solvents and impurities traces.

Subsequent FT-IR analysis performed on compound **93** is shown in Figure 5.41. The IR spectrum shows a medium, broad band with peaks at 2054, 2011, 1995 and 1979 cm^{-1}, which may be attributed to the C-O stretching of the carbon monoxide ligands. However, such values are not typical of trigonal bipyramidal $[M(CO)_4(L)]$ complexes.[50] A summary of the band assignments for **93** and the metal precursor $Ru_3(CO)_{12}$ is shown in Table 5.2. Further attempts to isolate a defined product proved inconclusive as the product readily decomposed into a brown powder, insoluble in common organic solvents such as CH_2Cl_2, Methanol, THF etc.

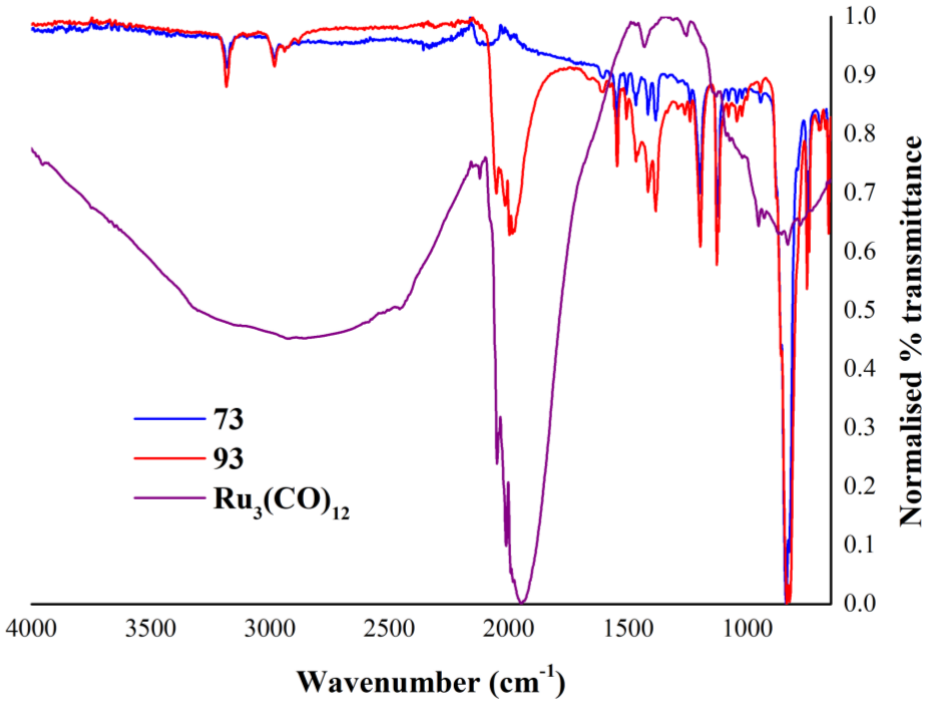

Figure 5.41. Normalised FT-IR spectra of compound **93** (red curve) and its ligand precursor compound **73** (blue curve).

Table 5.2. Band assignments for the FT-IR spectra of the metal precursor $Ru_3(CO)_{12}$ and **93** (Figure 5.41).

Compound	Wavenumber (cm^{-1})	Vibrational mode
$Ru_3(CO)_{12}$	2047 2010 1990 1982	C-O st
93	2054 2011 1995 1979	C-O st

To shed a better light on the reactivity of such tripodal systems with the ruthenium cluster, it was decided to make use of the more flexible methyl-substituted ligand precursor **72**. This experiment aimed to prove whether the rigid conformation of compound **73** was a limitation to its reactivity towards $Ru_3(CO)_{12}$ and if it was possible to generate the trimetallic complex **72**$[Ru(CO)_4]_3$ thanks to the enhanced flexibility of this ligand precursor.

The reaction between compound **72** and $Ru_3(CO)_{12}$ was performed in two steps: first, deprotonation of the compound **72**, by adopting a modified procedure by Dias and co-worker,[54] followed by work up to isolate the free carbene (further referred as compound **94** in this work) as a white solid in good yield (74%). ^{1}H NMR analysis performed on the free carbene (Figure 5.42) revealed that the deprotonation of the three *tert*-butyl imidazolium arms was successful as no signals arising from the C_2-*H* protons were observed. Furthermore, formation of the free carbene was confirmed by ^{13}C NMR analysis of **94** where the resonance of the carbene was found at 214.7 ppm (Appendix D).

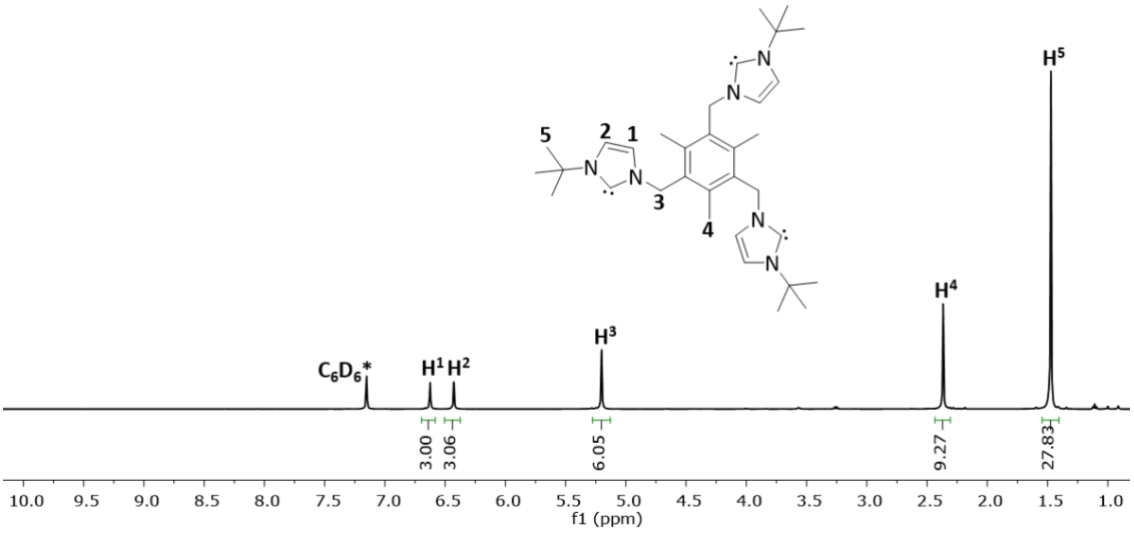

Figure 5.42. ^{1}H NMR (500 MHz, C_6D_6, 298 K) spectrum of compound **94**. For clarity, magnetically equivalent nuclei within the same NMR spin system are labelled once. * C_6D_6.

The second step of the reaction involved the treatment of a THF solution of $Ru_3(CO)_{12}$ with the previously synthesised free carbene **94**. The reaction mixture was kept stirring at room temperature until the formation of a cloudy red solution was observed. IR analysis performed on the THF solution of the product showed the presence of three bands at 2071, 2027 and 2006 cm^{-1} (Figure 5.43).

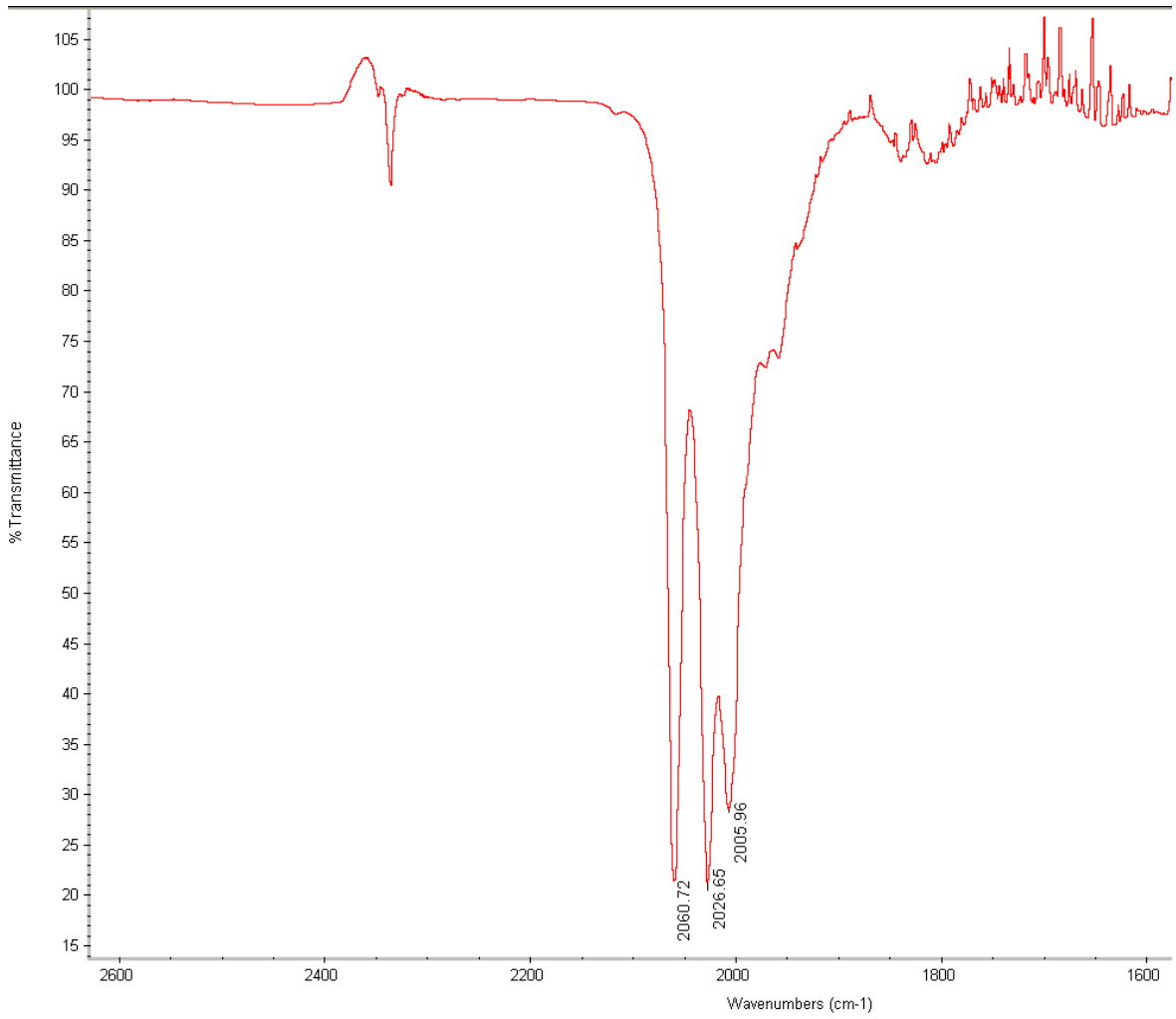

Figure 5.43. FT-IR spectrum recorded form a THF solution of **94**.

Upon cooling the aforementioned solution at -30 ºC, red crystals suitable for X-ray diffraction were isolated. However, due to the poor quality of the crystals, only a partially ordered resolved structure was obtained (Figure 5.45), showing the presence of a rearranged anionic cluster in which compound **72** acts, in its tri-protonated state, as a counterion. There are several disordered solvent units in the unit cell which were only partially refined. Unfortunately, due to the low scale on which the reaction was performed, their high air/moisture sensitivity, and the rather low yield of this reaction in terms of single crystal harvested, further spectroscopic analysis could not be performed to confirm the full identity of the bulk with respect of the single crystal analysed.

From the single crystal X-ray diffraction data and the spectroscopic evidence available, the current interpretation of the partially resolved structure is that a complex salt of the tris-imidazolium salt of the N-heterocyclic carbene **94** was obtained. The salt that results from the

combination of $[H_3\mathbf{94}]^{3+}$ with $Ru_4(CO)_{12}$ fragments and crystallises in the high symmetry space group R-3 and shows severe disorder. A detailed crystallographic analysis was performed with the assistance of Dr Gabriele Kociok Köhn and Professor Paul Raithby. A possible interpretation of the structure is that it consists of two triply-protonated **94** cations and two $[Ru_4(CO)_{12}(\mu_3\text{-}CO)]^{2-}$ anions, the charge balance being complete by the presence of two Br- (disordered) in the asymmetric unit. The availability of HBr (additionally to adventitious water) to assist the formation of this complex may well be assigned to residual impurities of the earliest starting material used in preparing the imidazolium salt precursor.

The $[\mathbf{94}]^{3+}$ cations are in general positions while both the $[Ru_4(CO)_{12}(\mu_3\text{-}CO)]^{2-}$ anions sit on crystallographic 3-fold axes. The Ru-Ru bond lengths within the tetrahedral tetra-metal anions are consistent with the presence of unbridged Ru-Ru single bonds, and the $[Ru_4(CO)_{12}(\mu_3\text{-}CO)]^{2-}$ formulation is consistent with the presence of a *closo*-60 electron species for this counterion, the correct electron count for a Ru_4 tetrahedron by the Effective Atomic Number Rule. The formation of $[Ru_4(CO)_{12}(\mu_3\text{-}CO)]^{2-}$ anions has been observed in the reactions of $Ru_3(CO)_{12}$ with organic reagents previously[55] and has apparently occurred under the reaction conditions used here.

To fully confirm this hypothesis, a further stretching frequency in the IR of the complex salt at around 1750 cm^{-1} would have been expected, which would be consistent with the presence of the μ_3-CO ligand crystallographically observed in the anion,[56] but these signals are often weak and could not be located with certainty in the solution IR recorded hereby (Figure 5.43). Similar examples of such cluster rearrangement, possibly mediated by the bulky nature of the carbene involved and presence of adventitious deprotonated solvents (H_2O, HBr), have been previously reported by the groups of Carty,[55] Whittlesey[57] and Cabeza[51], and are a further indication that tripodal carbene chemistry leads to diversity in the products formation, which present challenges in their spectroscopic characterisation.

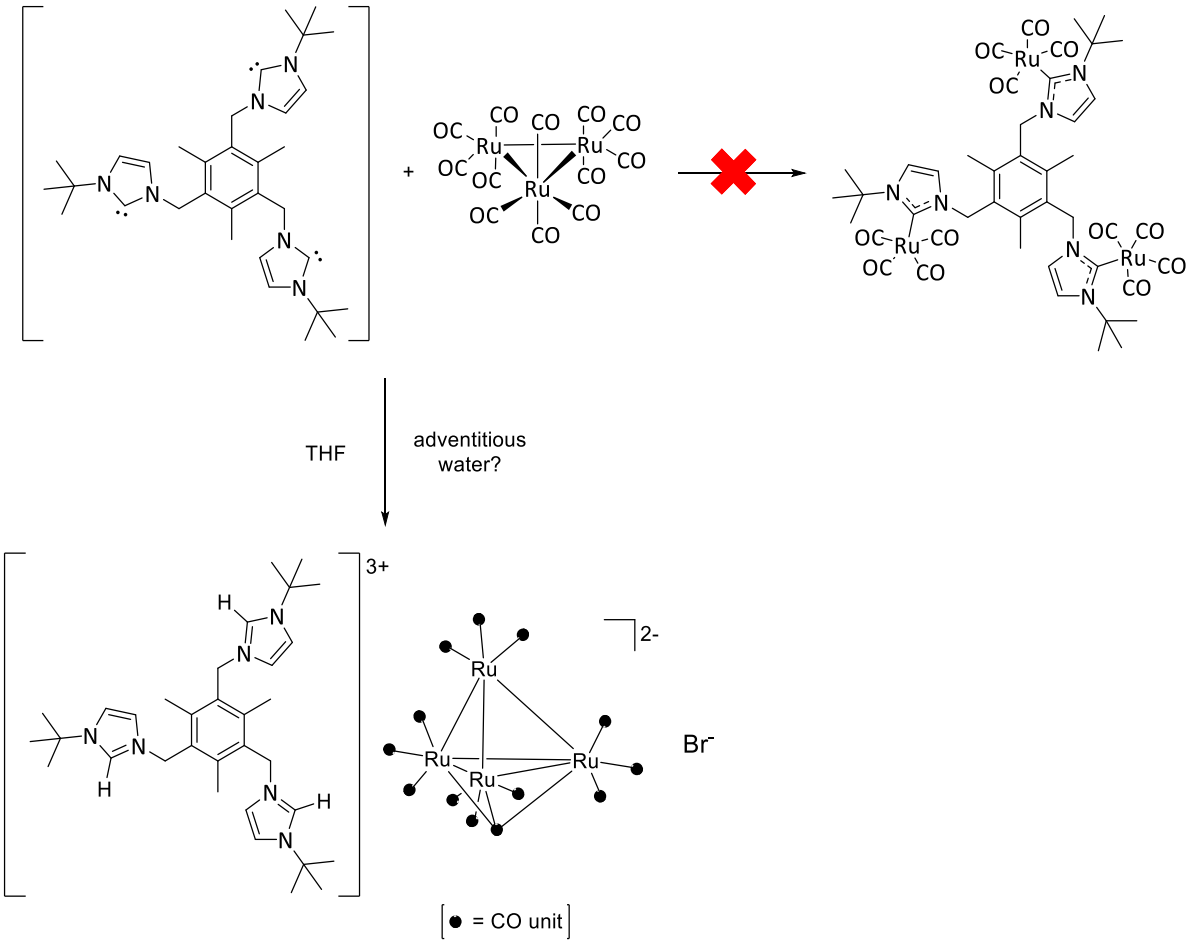

Figure 5.44. Alternative reaction scheme proposed for the reaction between compound **94** and $Ru_3(CO)_{12}$.

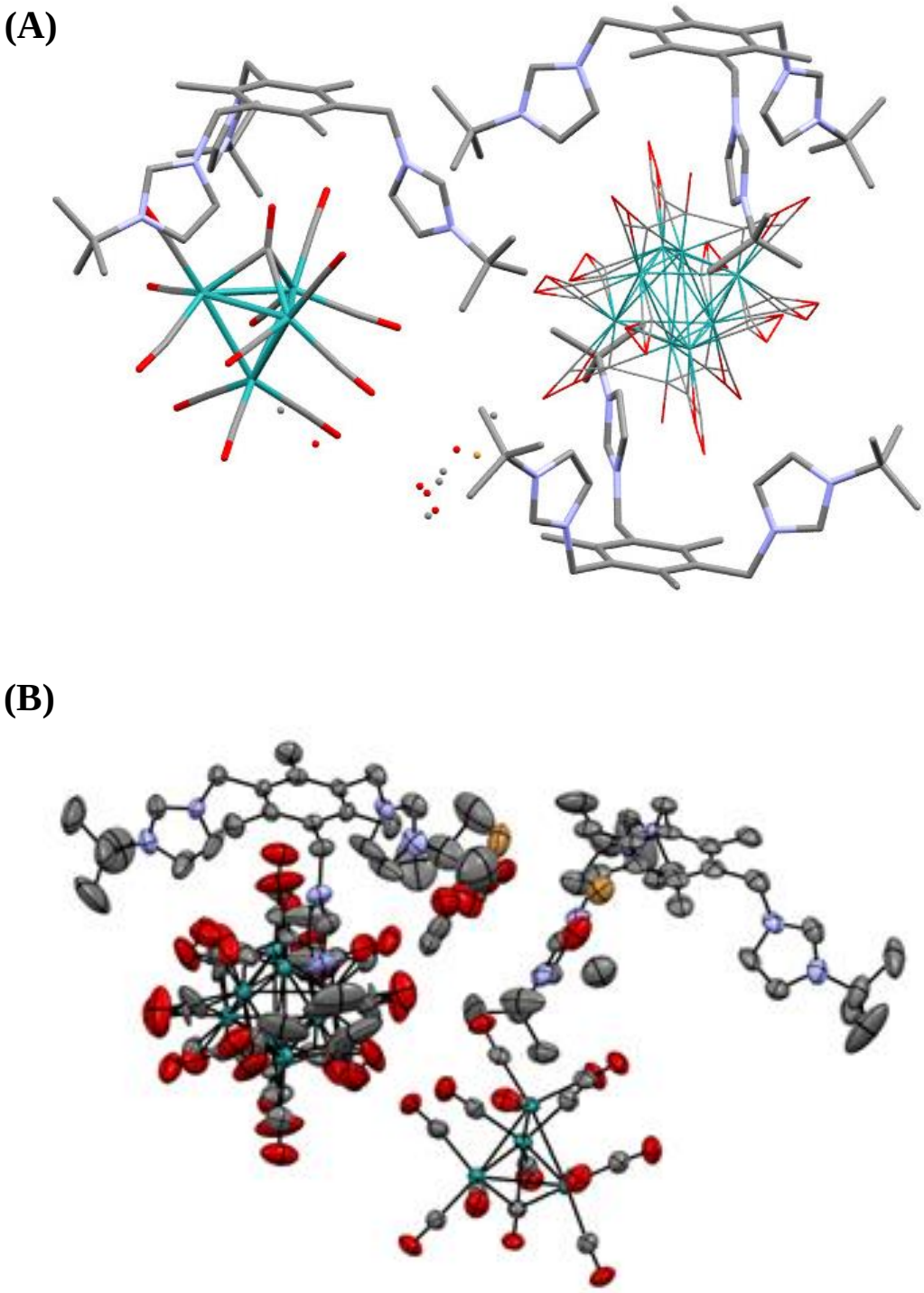

Figure 5.45. The X-ray diffraction study showing the reaction product obtained by the reaction the free carbene compound **94** and $Ru_3(CO)_{12}$ postulated to occur through a cluster rearrangement and ligand protonation. Hydrogen atoms are removed for clarity. (**B**) The content of the asymmetric unit showing the disordered solvent molecules present; the bromine counterions are disordered, whereas the tripodal units are well defined, as is one of the clusters presents.

5.3. Cell viability assays

Cellular viability assays were obtained with the assistance of Dr Haobo Ge whom carried out these evaluations in PC3 cells in Pharmacy and Pharmacology Department, University of Bath. Standard 96 well plates were incubated with compounds **68** and **85** in serum medium (1% DMSO) at different concentrations and times (24, 48 and 72 hours) at 37°C. MTT was then added and the treated cells incubated for 2 hours before recording the absorbance with a plate reader.

The results of MTT assays performed on the ATSC-based ligand precursor **68**, whose synthesis and characterisation were previously reported in Chapter 2, is shown below in Figure 5.46. Treatment of PC3 cells with compound **68** showed a moderate loss in viability at the highest concentration (250 µM) of compound. Interestingly, treatment of PC3 cells with compound **85** did not significantly perturb the cell viability at any concentration tested. Cell viability recovered to pre-treatment levels after 48 hours (see Figure 5.47). This could be due to differences in cellular uptake between the two compounds, with compound **68** being slightly more cytotoxic, possibly due to its uncoordinated thiosemicarbazone arms.

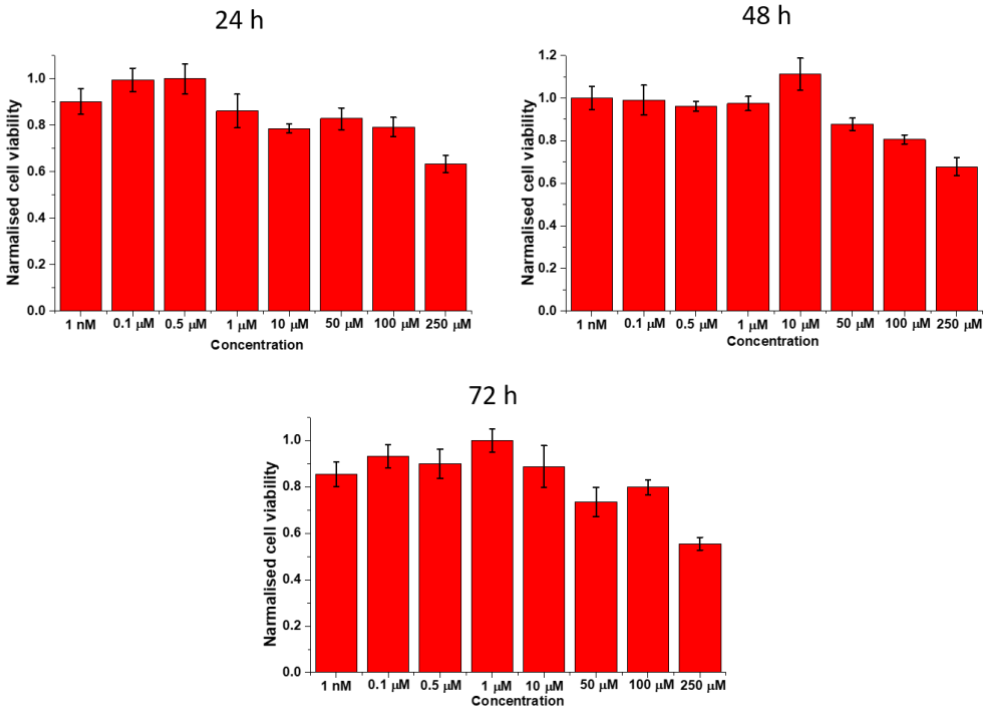

Figure 5.46. Cell viability studies of compound **68** at t = 24, 48 and 72 hours. The data were collected from six repeated measurements on the same day, N = 1

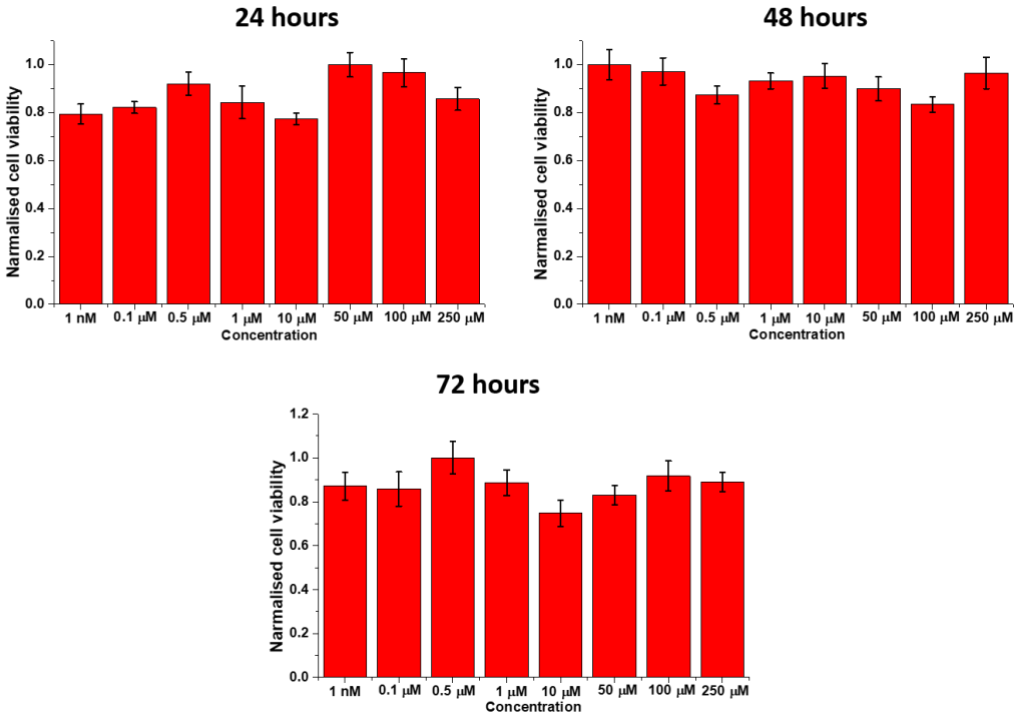

Figure 5.47. Cell viability studies of compound **85** at t = 24, 48 and 72 hours. The data were collected from six repeated measurements on the same day, N = 1

Cellular viability assays were performed by treating PC3 cells with the newly synthesised NHC-based complexes **87**, **91** and **92** to determine the half maximal inhibitory concentration (IC_{50}) values of such complexes (Table 5.3). IC_{50} is a measure that indicates the capacity of a compound to inhibit a specific biological function and it is commonly used to evaluate the capability of a drug to reduce the cell viability by 50%.

In order to calculate IC_{50} values, MTT assays were carried out in 96 well plates containing PC3 cells treated with each of the NHC-based metal complexes at different concentrations for 24 and 48 hours. MTT was then added to the cells and incubated for a further 2 hours. After measuring the absorbance at 570 nm as described previously (Chapter 2), the absorbance readings were plotted as dose-response curves and the IC_{50} of the complexes were calculated (see Table 5.3). It can be seen that the most toxic compound for PC3 cells after 24 hours of treatment, is the gold(I) complex **91**. After 24 hours of treatment, the least cytotoxic compound proved to be the copper(I) complex **92**. Incubation of PC3 cells with the selected compound for 48 hours revealed that the silver(I) complex **87** displayed IC_{50} values comparable to its gold(I) analogue **91**, whereas only a small change of IC_{50} values could be appreciated for compounds **91** and **92**.

Table 5.3. Summary of compounds tested in PC3 cells with MTT assays and its IC_{50} values calculated after incubation of the compound for 24 and 48 hours.

Compound	IC_{50} at 24 hours (mg/mL)	IC_{50} at 48 hours (mg/mL)
87	$(9.7 \pm 0.9)\cdot 10^{-6}$	$(3.1 \pm 0.7)\cdot 10^{-6}$
91	$(3.3 \pm 0.9)\cdot 10^{-6}$	$(3.8 \pm 0.5)\cdot 10^{-6}$
92	$(1.3 \pm 0.1)\cdot 10^{-5}$	$(1.1 \pm 0.1)\cdot 10^{-5}$

5.4. *In vitro* confocal fluorescence investigations of the metal complexes

Epi-fluorescence and single-photon laser scanning confocal microscopy analysis were performed on PC3 cells, treated with selected metal complexes previously described in this section. PC3 cells were grown according to standard culturing methods, placed onto glass-bottomed dishes and allowed to grow to a suitable confluence prior treatment with a DMSO solution (10 mM) of the compound.

Figure 5.48 shows the images of PC3 cells incubated for 20 min with compound **84** taken in the confocal mode. The images show broad emission across blue and green channels when the probe is excited at 405 nm ($a_{1\text{-}5}$), while only green-red and red emissions were observed when using 488 nm and 561 nm lasers respectively ($b_{1\text{-}5}$ and $c_{1\text{-}5}$). Compound **84** appear to be taken up in PC3 cells and localised throughout the cytoplasm, whereas no emission appears to originate from the nucleus.

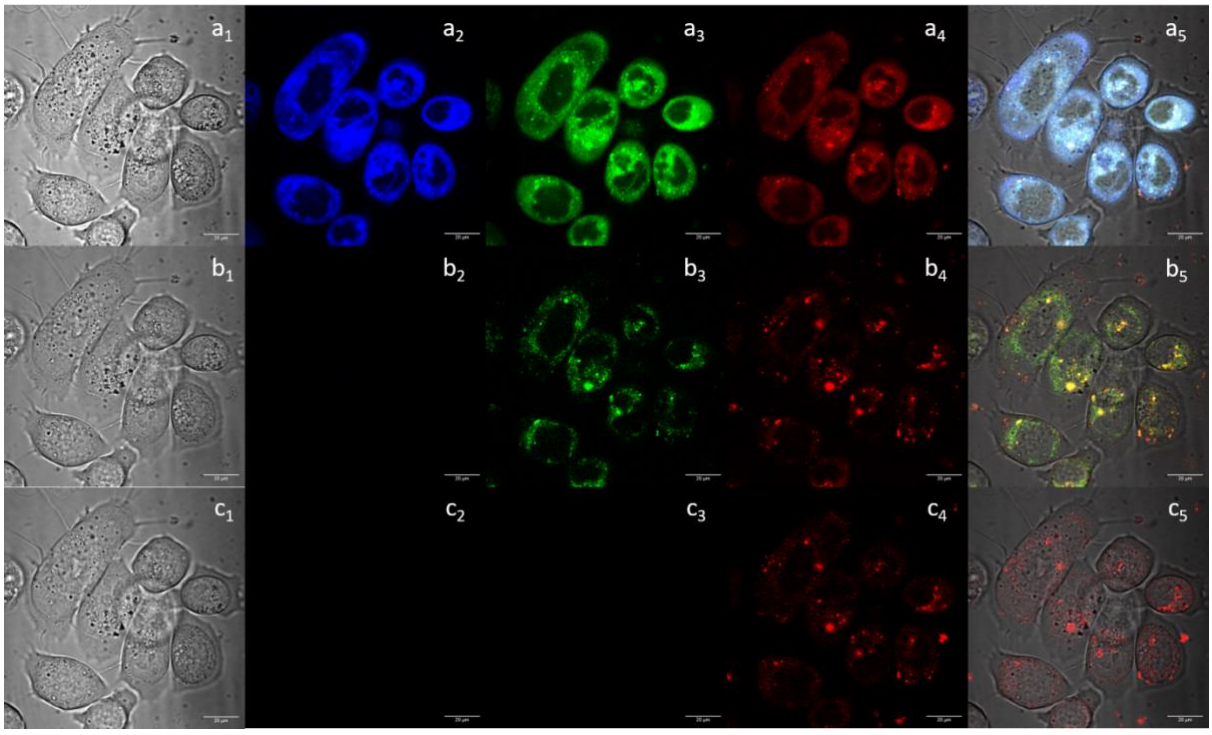

Figure 5.48. Single-photon laser-scanning confocal microscopy images of PC3 cells incubated with compound **84** (10 µg/mL 1% : 99% DMSO : DMEM) at 37 ºC for 20 minutes; λ_{ex} = 405 nm (a_1-a_5), λ_{ex} = 488 nm (b_1-b_5) and λ_{ex} = 561 nm (c_1-c_5). DIC channel (a_1, b_1, c_1), blue channel, λ_{em} = 420-480 nm (a_2, b_2, c_2), green channel, λ_{em} = 516-530 nm (a_3, b_3, c_3), red channel λ_{em} = 615-650 nm (a_4, b_4, c_4), and overlapping of the DIC, blue, green and red channels (a_5, b_5, c_5). Scale bar: 20 µm.

Confocal microscopy analysis of PC3 cells treated with compound **85** is shown below in Figure 5.49. Compound **85** shows comparable emissive properties to its analogue **84**, displaying broad emission in all channels when excited at 405 nm.

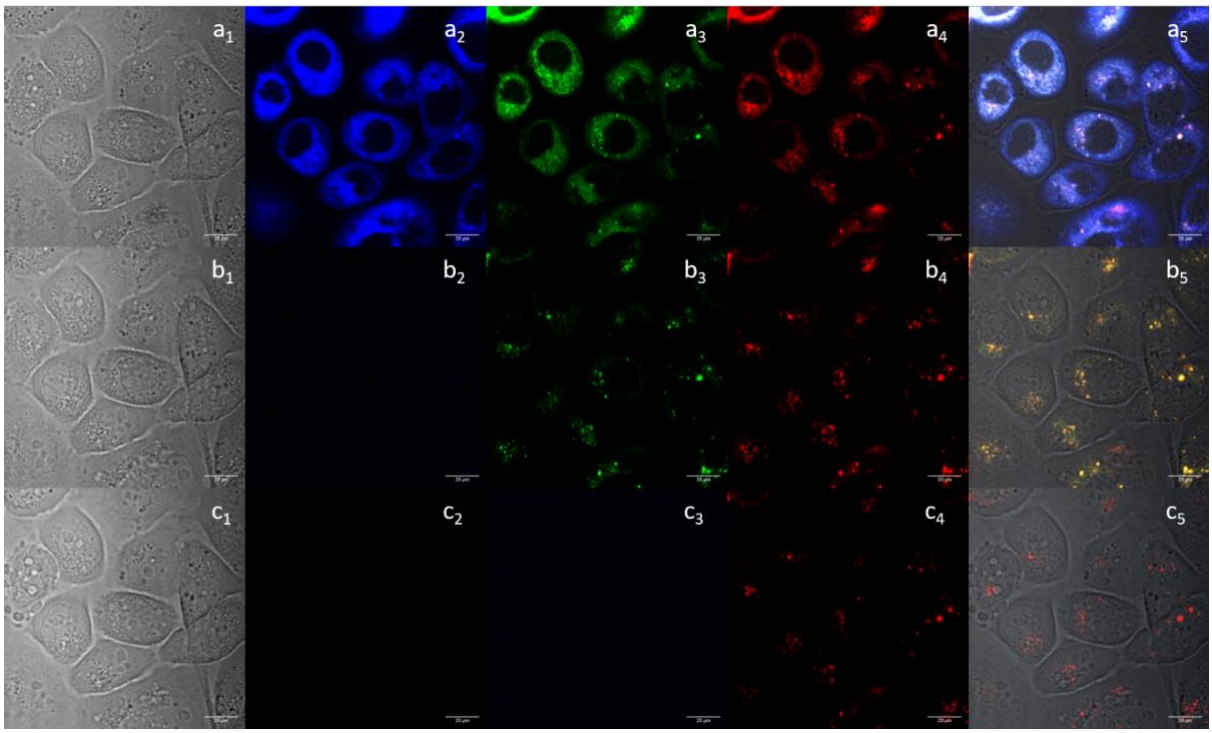

Figure 5.49. Single-photon laser-scanning confocal microscopy images of PC3 cells incubated with compound **85** (10 µg/mL 1% : 99% DMSO : DMEM) at 37 ºC for 20 minutes; λ_{ex} = 405 nm (a_1-a_5), λ_{ex} = 488 nm (b_1-b_5) and λ_{ex} = 561 nm (c_1-c_5). DIC channel (a_1, b_1, c_1), blue channel, λ_{em} = 420-480 nm (a_2, b_2, c_2), green channel, λ_{em} = 516-530 nm (a_3, b_3, c_3), red channel λ_{em} = 615-650 nm (a_4, b_4, c_4), and overlapping of the DIC, blue, green and red channels (a_5, b_5, c_5). Scale bar: 20 µm.

SLSCM analysis performed in PC3 cells treated with the ruthenium-based compound **86** is shown below in Figure 5.50. A homogeneous distribution of **86** is observed in the blue and green channels when the 405 nm laser is employed, while it is visible only in the green and red channels and only in the red, respectively, after irradiating the probe with 488 and 561 nm lasers. As for its rhenium(I)-based analogues discussed before, compound **86** appears to localise mainly in the cytoplasm, with no emission arising from the nuclear region of the cells.

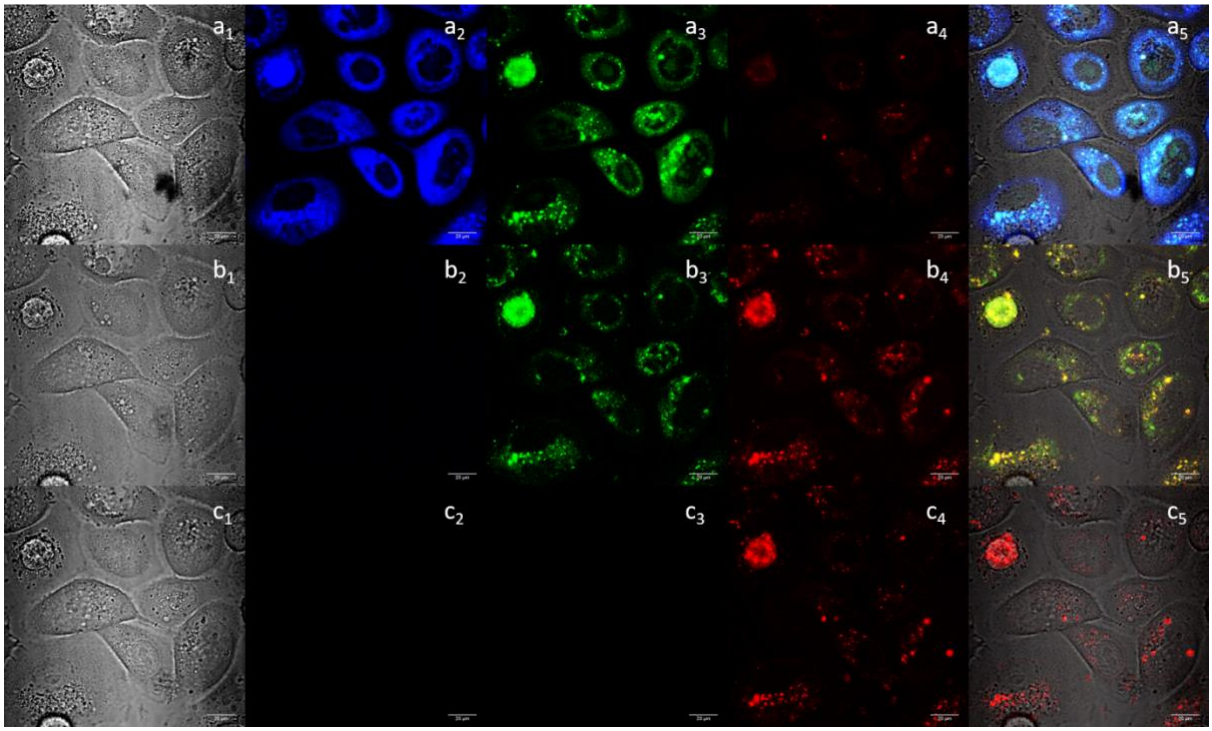

Figure 5.50. Single-photon laser-scanning confocal microscopy images of PC3 cells incubated with compound **86** (10 µg/mL 1% : 99% DMSO : DMEM) at 37 ºC for 20 minutes; λ_{ex} = 405 nm (a_1-a_5), λ_{ex} = 488 nm (b_1-b_5) and λ_{ex} = 561 nm (c_1-c_5). DIC channel (a_1, b_1, c_1), blue channel, λ_{em} = 420-480 nm (a_2, b_2, c_2), green channel, λ_{em} = 516-530 nm (a_3, b_3, c_3), red channel λ_{em} = 615-650 nm (a_4, b_4, c_4), and overlapping of the DIC, blue, green and red channels (a_5, b_5, c_5). Scale bar: 20 µm.

SLSCM (Figure 5.51) and epi-fluorescence microscopy (Figure 5.52) images of fixed PC3 cells incubated with a DMSO : serum-free medium (1:99) solution of 10 mM of the gold(I) complex **91** were acquired following the same protocol as for the previous metal complexes. Compound **91** displayed broad emission in all the channels when the probe was excited at 405 nm, while it is only visible in the green and red and red only after excitation at 488 and 561 nm wavelengths respectively. The complex localises throughout the cytoplasm and some emission appear to originate from the cellular nuclei, although is unclear if such emission is due to compound **91** being able to penetrate the nuclear membrane, whether it actually influences the cell morphology.

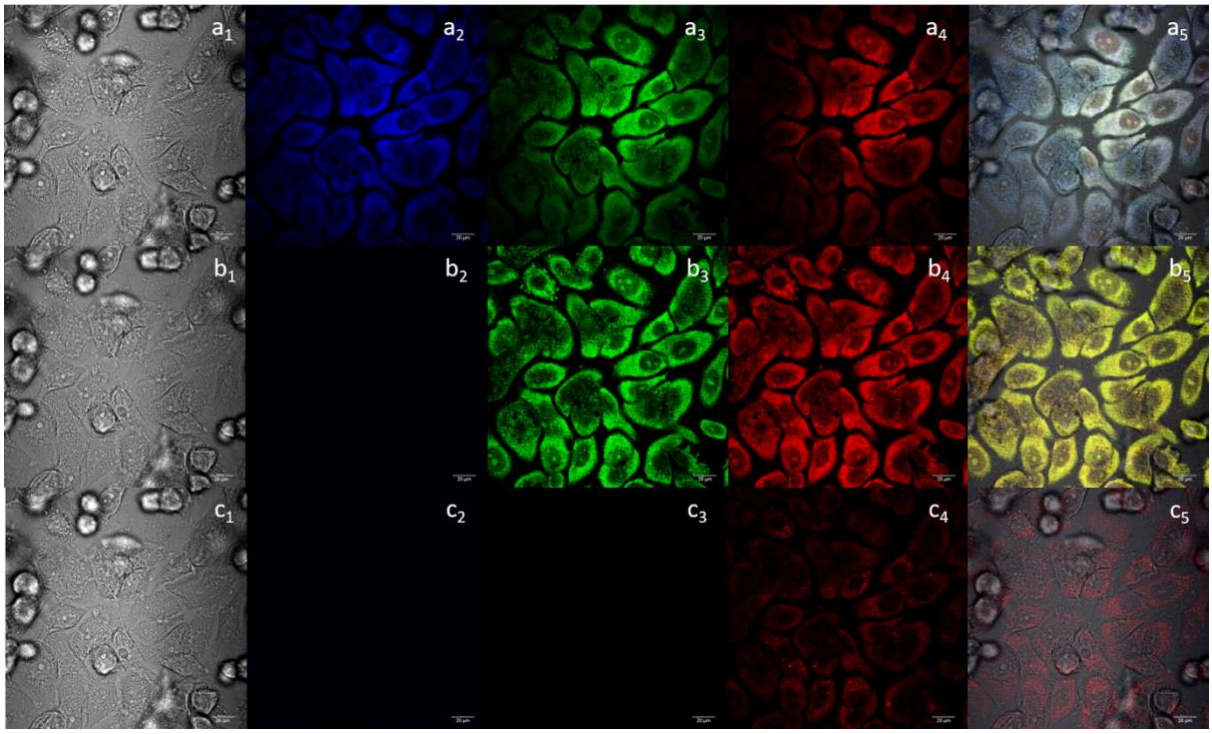

Figure 5.51. Single-photon laser-scanning confocal microscopy images of fixed PC3 cells incubated with compound **91** (10 µg/mL 1% : 99% DMSO : DMEM) at 37 ºC for 20 minutes; λ_{ex} = 405 nm (a_1-a_5), λ_{ex} = 488 nm (b_1-b_5) and λ_{ex} = 561 nm (c_1-c_5). DIC channel (a_1, b_1, c_1), blue channel, λ_{em} = 420-480 nm (a_2, b_2, c_2), green channel, λ_{em} = 516-530 nm (a_3, b_3, c_3), red channel λ_{em} = 615-650 nm (a_4, b_4, c_4), and overlapping of the DIC, blue, green and red channels (a_5, b_5, c_5). Scale bar: 20 µm.

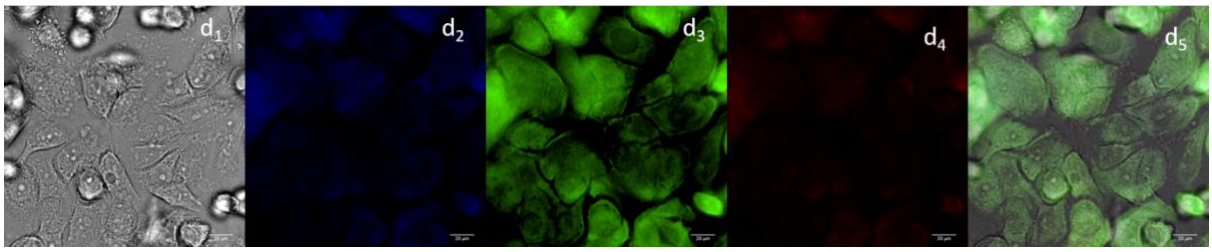

Figure 5.52. Epi-fluorescence acquisition of fixed PC3 cells incubated at 37 ºC for 20 min with compound **91** (10 µg/mL 1% : 99% DMSO : DMEM). DIC channel (d_1), blue channel, λ_{em} = 420-480 nm (d_2), green channel, λ_{em} = 516-530 nm (d_3), red channel λ_{em} = 615-650 nm (d_4), and overlapping of the DIC, blue, green and red channels (d_5). Scale bar: 20 µm.

PC3 cells were also incubated with the copper(I) complex **92**, and SLSCM images were collected (Figure 5.53). Compound **92** strongly emits in the blue channel and more lightly in the green and red channels when excited with a 405 laser, while the emission is less intense and confined to green and red and red only, respectively, when 488 and 561 lasers were employed. Compound **92** is taken up by the cells and localise in the cytoplasm, whereas no emission

appears to originate from the nuclei. Furthermore, treatment of the cells with the complex did not alter the cell morphology.

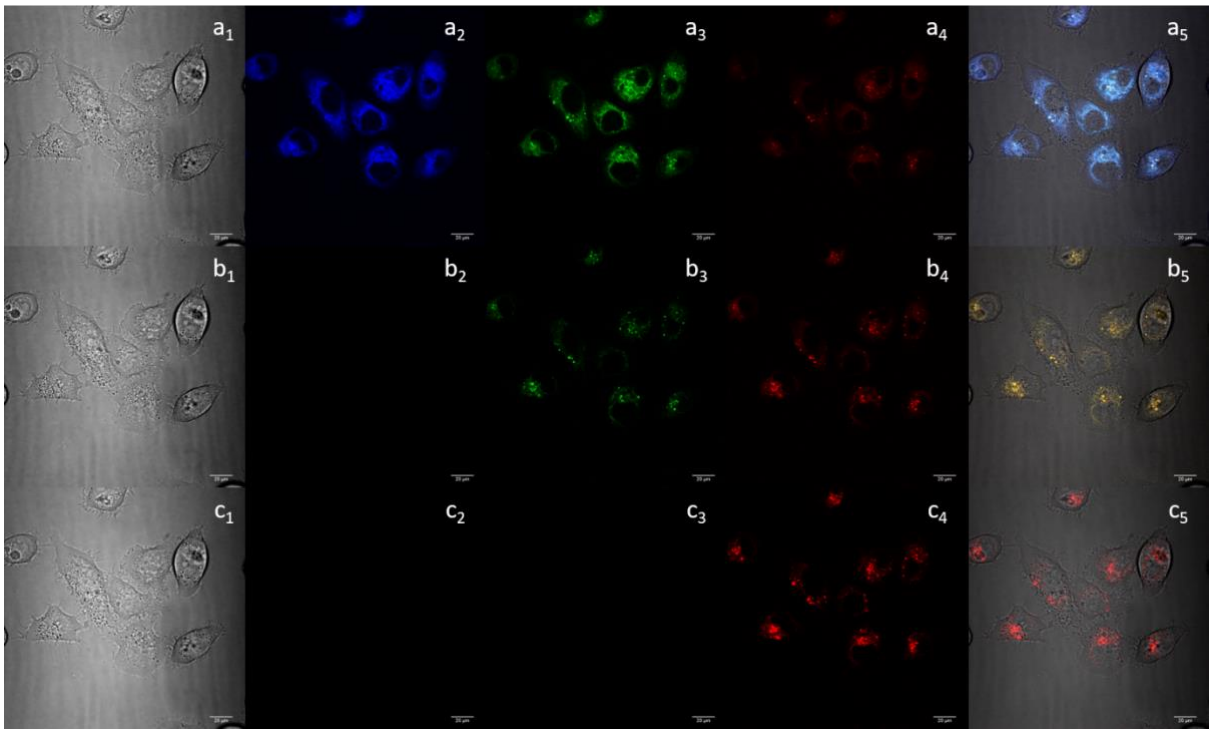

Figure 5.53. Single-photon laser-scanning confocal microscopy images of PC3 cells incubated with compound **92** (10 μg/mL 1% : 99% DMSO : DMEM) at 37 ºC for 20 minutes; λ_{ex} = 405 nm (a_1-a_5), λ_{ex} = 488 nm (b_1-b_5) and λ_{ex} = 561 nm (c_1-c_5). DIC channel (a_1, b_1, c_1), blue channel, λ_{em} = 420-480 nm (a_2, b_2, c_2), green channel, λ_{em} = 516-530 nm (a_3, b_3, c_3), red channel λ_{em} = 615-650 nm (a_4, b_4, c_4), and overlapping of the DIC, blue, green and red channels (a_5, b_5, c_5). Scale bar: 20 μm.

5.5. Summary of Chapter 5

This chapter described the synthesis of several metal complexes deriving from some selected tripodal ligands and their testing as potential imaging agents.

The two tripodal-ATSC ligands **67** and **68** were successfully metallated by exploiting microwave technology to obtain complexes of rhenium(I) (compounds **84** and **85**) and ruthenium(II) (compound **86**). Their emissive properties were evaluated and were found to be suitable for *in-vitro* cellular imaging applications.

Attempts to develop a trimetallic silver(I) complex from the tripodal ligand precursor **76** resulted instead in the formation of the monometallic, NHC-based complex **87**, in which two arms of the tripodal system are bound to the metal centre, while the third arm remains in its protonated state. Attempts made to obtain the same compound *via* a novel microwave-assisted synthesis resulted instead in a new, tri-coordinated Ag(I) compound (**88**), in which the silver centre is coordinated to all the three NHC arms of **76**. The same reaction protocol was employed for the ligand precursors **73** and **75**. Spectroscopic analyses carried out on the reaction products pointed to the formation of tri-coordinated complexes of Ag(I) (compounds **89** and **90**).

As silver(I)-NHC complexes are usually excellent carbene-transfer agents, the possibility to transmetallate the silver(I) centre with other coinage metals was explored. The metal complex **87** was successfully transmetallated with gold(I) and copper(I) precursors to give the new metal complexes **91** and **92** respectively.

The last complexation attempts discussed in this chapter involved the tripodal *tert*-butylimidazolium based ligands **72** and **73** and the ruthenium cluster $Ru_3(CO)_{12}$, aiming to obtain trimetallic metal complexes where each NHC "arm" binds a $[Ru(CO)_4]$ moiety. The various attempts to achieve such complexations proved fruitless, however these experiments demonstrated that tripodal systems are able to induce the rearrangement of the ruthenium cluster. Further experiments will be carried out to explore the fascinating nature of such organometallic reactions.

Cell viability assays were carried out on a few selected metal complexes. While the tripodal ATSC-based rhenium(I) complex **85** was found to be essentially non-toxic towards PC3 cancer cells, the NHC-based complexes **87**, **91** and **92** displayed remarkable toxicity towards the same cell line, with IC_{50} values comparable to the anticancer drug cisplatin.[58]

Finally, cellular imaging experiments on PC3 cells were carried out using single-photon laser scanning microscopy. The confocal microscopy results showed that the selected metal complexes are taken up by the cells and localise primarily in the cytoplasm, where they display interesting emissive properties. Complexes **84**, **85**, **86**, **91** and **92** are therefore suitable for *in vitro* imaging applications.

5.6. References for Chapter 5

1. D. Mishra, S. Naskar, M. G. B. Drew and S. K. Chattopadhyay, *Inorganica Chim. Acta*, 2006, **359**, 585-592.
2. B. Demoro, R. F. M. de Almeida, F. Marques, C. P. Matos, L. Otero, J. Costa Pessoa, I. Santos, A. Rodríguez, V. Moreno, J. Lorenzo, D. Gambino and A. I. Tomaz, *Dalton Trans.*, 2013, **42**, 7131-7146.
3. P. Anitha, P. Viswanathamurthi, D. Kesavan and R. J. Butcher, *J. Coord. Chem.*, 2015, **68**, 321-334.
4. N. Raja, N. Devika, G. Gupta, V. L. Nayak, A. Kamal, N. Nagesh and B. Therrien, *J. Organomet. Chem.*, 2015, **794**, 104-114.
5. Z. Tavsan, P. K. Yaman, E. Subasi and H. A. Kayali, *J. Biol. Inorg. Chem.*, 2018, **23**, 425-435.
6. P. I. d. S. Maia, H. H. Nguyen, A. Hagenbach, S. Bergemann, R. Gust, V. M. Deflon and U. Abram, *Dalton Trans.*, 2013, **42**, 5111-5121.
7. D. K. Nayak, R. Baishya, R. Natarajan, T. Sen and M. C. Debnath, *Dalton Trans.*, 2015, **44**, 16136-16148.
8. L. J. Raszeja, D. Siegmund, A. L. Cordes, J. Güldenhaupt, K. Gerwert, S. Hahn and N. Metzler-Nolte, *Chem. Commun.*, 2017, **53**, 905-908.
9. H. C. Bertrand, S. Clède, R. Guillot, F. Lambert and C. Policar, *Inorg. Chem.*, 2014, **53**, 6204-6223.
10. N. C. Ackroyd and J. A. Katzenellenbogen, *Organometallics*, 2010, **29**, 3669-3671.
11. G. Meola, H. Braband, S. Jordi, T. Fox, O. Blacque, B. Spingler and R. Alberto, *Dalton Trans.*, 2017, **46**, 14631-14637.
12. A. M. Christofi, P. J. Garratt and G. Hogarth, *Tetrahedron*, 2001, **57**, 751-759.
13. D. M. Dattelbaum, R. L. Martin, J. R. Schoonover and T. J. Meyer, *J. Phys. Chem. A*, 2004, **108**, 3518-3526.
14. M. R. Gonçalves and K. P. Frin, *Polyhedron*, 2015, **97**, 112-117.
15. A. F. Stange, S. Tokura and M. Kira, *J. Organomet. Chem.*, 2000, **612**, 117-124.
16. M. Groessl, E. Reisner, C. G. Hartinger, R. Eichinger, O. Semenova, A. R. Timerbaev, M. A. Jakupec, V. B. Arion and B. K. Keppler, *J. Med. Chem.*, 2007, **50**, 2185-2193.
17. C. G. Hartinger, S. Zorbas-Seifried, M. A. Jakupec, B. Kynast, H. Zorbas and B. K. Keppler, *J. Inorg. Biochem.*, 2006, **100**, 891-904.
18. A. Bergamo and G. Sava, *Dalton Trans.*, 2011, **40**, 7817-7823.
19. E. Abel and F. Stone, *Q. Rev. Chem. Soc.*, 1969, **23**, 325-371.
20. S. A. Khan, A. M. Asiri, K. Al-Amry and M. A. Malik, *Sci. World J*, 2014, **2014**.
21. C. E. Ellul, unpublished work.
22. U. Effertz, U. Englert, F. Podewils, A. Salzer, T. Wagner and M. Kaupp, *Organometallics*, 2003, **22**, 264-274.
23. J. Lin, Z.-H. Ma, F. Li, M.-X. Zhao, X.-H. Liu and X.-Z. Zheng, *Transition Met. Chem.*, 2009, **34**, 797-801.
24. C. P. Casey, X. Jiao and I. A. Guzei, *Organometallics*, 2010, **29**, 4829-4836.
25. H. Yildirim, E. Guler, M. Yavuz, N. Ozturk, P. K. Yaman, E. Subasi, E. Sahin and S. Timur, *Mater. Sci. Eng. C*, 2014, **44**, 1-8.
26. C. Hemmert and H. Gornitzka, *Dalton Trans.*, 2016, **45**, 440-447.
27. N. A. Johnson, M. R. Southerland and W. J. Youngs, *Molecules*, 2017, **22**, 1263.
28. B. Dominelli, J. D. Correia and F. E. Kühn, *J. Organomet. Chem.*, 2018, **866**, 153-164.
29. F. Tisato, C. Marzano, M. Porchia, M. Pellei and C. Santini, *Med. Res. Rev.*, 2010, **30**, 708-749.

30. E. Alessio, *Eur. J. Inorg. Chem.*, 2017, **2017**, 1549-1560.
31. A. B. Lansdown, *J Wound Care*, 2002, **11**, 125-130.
32. D. A. Medvetz, K. M. Hindi, M. J. Panzner, A. J. Ditto, Y. H. Yun and W. J. Youngs, *Met.-Based Drugs*, 2008, **2008**.
33. M.-L. Teyssot, A.-S. Jarrousse, M. Manin, A. Chevry, S. Roche, F. Norre, C. Beaudoin, L. Morel, D. Boyer and R. Mahiou, *Dalton Trans.*, 2009, 6894-6902.
34. H. M. Wang and I. J. Lin, *Organometallics*, 1998, **17**, 972-975.
35. C. E. Willans, K. M. Anderson, P. C. Junk, L. J. Barbour and J. W. Steed, *Chem. Commun.*, 2007, 3634-3636.
36. M. V. Baker, M. J. Bosnich, C. C. Williams, B. W. Skelton and A. H. White, *Aust. J. Chem.*, 1999, **52**, 823-826.
37. B. Landers and O. Navarro, *Eur. J. Inorg. Chem.*, 2012, **2012**, 2980-2982.
38. P. F. Barron, J. C. Dyason, P. C. Healy, L. M. Engelhardt, B. W. Skelton and A. H. White, *J. Chem. Soc., Dalton Trans.*, 1986, 1965-1970.
39. D. E. Hibbs, M. B. Hursthouse, K. A. Malik, M. A. Beckett and P. W. Jones, *Acta Crystallogr. Sect. C: Cryst. Struct. Commun.*, 1996, **52**, 884-887.
40. M. Camalli and F. Caruso, *Inorg. Chim. Acta*, 1988, **144**, 205-211.
41. S. Socol, R. Jacobson and J. Verkade, *Inorg. Chem.*, 1984, **23**, 88-94.
42. M. N. McCain, S. Schneider, M. R. Salata and T. J. Marks, *Inorg. Chem.*, 2008, **47**, 2534-2542.
43. C. F. Shaw, *Chem. Rev.*, 1999, **99**, 2589-2600.
44. P. J. Barnard, M. V. Baker, S. J. Berners-Price and D. A. Day, *J. Inorg. Biochem.*, 2004, **98**, 1642-1647.
45. W. A. Herrmann, L. J. Goossen and M. Spiegler, *Organometallics*, 1998, **17**, 2162-2168.
46. M. C. Linder, *Mutat. Res.*, 2001, **475**, 141-152.
47. B. Halliwell and J. M. Gutteridge, in *Methods Enzymol.*, Elsevier, 1990, vol. 186, pp. 1-85.
48. M. L. Teyssot, A. S. Jarrousse, A. Chevry, A. De Haze, C. Beaudoin, M. Manin, S. P. Nolan, S. Díez-González, L. Morel and A. Gautier, *Chem.: Eur. J.*, 2009, **15**, 314-318.
49. W. Liu and R. Gust, *Coord. Chem. Rev.*, 2016, **329**, 191-213.
50. M. I. Bruce, M. L. Cole, R. S. Fung, C. M. Forsyth, M. Hilder, P. C. Junk and K. Konstas, *Dalton Trans.*, 2008, 4118-4128.
51. J. A. Cabeza, I. del Río, D. Miguel, E. Pérez-Carreño and M. G. Sánchez-Vega, *Organometallics*, 2007, **27**, 211-217.
52. C. E. Ellul, M. F. Mahon, O. Saker and M. K. Whittlesey, *Angew. Chem. Int. Ed.*, 2007, **46**, 6343-6345.
53. S. I. Pascu, unpublished work.
54. H. R. Dias and W. Jin, *Tetrahedron Lett.*, 1994, **35**, 1365-1366.
55. A. A. Cherkas, J. F. Corrigan, S. Doherty, S. A. MacLaughlin, F. van Gastel, N. J. Taylor and A. J. Carty, *Inorg. Chem.*, 1993, **32**, 1662-1670.
56. A. A. Bhattacharyya, C. C. Nagel and S. G. Shore, *Organometallics*, 1983, **2**, 1187-1193.
57. C. E. Ellul, O. Saker, M. F. Mahon, D. C. Apperley and M. K. Whittlesey, *Organometallics*, 2007, **27**, 100-108.
58. S. Tardito, C. Isella, E. Medico, L. Marchio, E. Bevilacqua, M. Hatzoglou, O. Bussolati and R. Franchi-Gazzola, *J. Biol. Chem.*, 2009, **284**, 24306-24319.

6. Conclusions and future work

An increasing number of metal complexes are being investigated in a wide array of biomedical applications, such as molecular imaging and the development of new therapies. The focus of this work has been the development of tripodal molecules and their related metal complexes and their biomedical application.

Chapter 2 described the syntheses and characterisation of tripodal systems based upon the hexasubstituted benzene scaffold, and their potential for biomedical applications was probed. In this chapter, three types of tripodal ligands were successfully synthesised and characterised. The products were obtained through nucleophilic substitution of the bromomethyl substituents of the hexasubstituted cores **60** and **61** with DABCO and 4,4'-bipyridine, to give compounds **62**, **63**, **64** and **65** in good yields and acceptable purity with minimal work up. Such compounds were characterised spectroscopically, and their biocompatibility probed *via* MTT assay on PC3 prostate cancer cells. While most of the compounds appear to be nontoxic at the highest concentrations recorded, a concentration of 250 μM of compound **64** caused a loss of more than 50% in cell viability. Such inhibition persisted even after 72 hours from the treatment. Further tests will be necessary to determine the factors that promote the loss of cell viability triggered by **64**.

Furthermore, two novel anthracene-thiosemicarbazone-based tripodal systems were successfully synthesised by a two-step procedure, beginning with the synthesis of the anthracene-thiosemicarbazone (compound **66**), by reacting 9-anthraldehyde with thiosemicarbazide, to give **66** in excellent yield and high purity. Characterisation of the new compounds **67** and **68** indicated that three molecules of **66** bind to the central aromatic core *via* an unconventional S-alkylation of the bromomethyl moieties of **60** and **61**. The two compounds possess acceptable fluorescent properties for cellular imaging experiments, with large emission bands around 440 nm.

Chapter 3 described the development of new tripodal N-heterocyclic carbene-based compounds with the potential to act as ligands for a variety of transition metals. This chapter described the syntheses of nine tripodal systems which are based upon unsymmetrical imidazole arms. Initially, we performed the syntheses of two symmetrical tripodal compounds bearing three methylimidazole arms *via* a nucleophilic substitution of the bromomethyl moieties of **60** and **61** with a small excess of 1-H-methylimidazole. It was possible to obtain crystals suitable for

X-ray diffraction analysis for the novel compound **70**, which allowed us to visualise how the three imidazole arms can be oriented towards the same face of the aromatic core to form a cage around the hexafluorophosphate counterion.

Two tripodal systems based upon the monosubstituted *tert*-butylimidazole were successfully prepared in a two-step reaction. First, the unsymmetrical 1-(*tert*-butyl)-1H-imidazole (referred as compound **71** in this work) was obtained following a modified Debus-Radziszewski imidazole synthesis. The monosubstituted imidazole was then reacted with the two hexasubstituted cores **60** and **61** to give the tripodal systems **72** and **73** respectively in good yields and purities. Moreover, crystals suitable for X-ray diffraction were successfully obtained for compound **72**. The unit cell of **72** shows that the compound is able to form a cage by interacting with the solvent water molecules and can self-assemble *via* hydrogen bond interactions into a tetramer of formula $[(\mathbf{72})_4(H_2O)_{12}][Br]_{12}$.

Finally, two novel mesitylimidazole-based tripodal systems have been prepared and characterised. The two compounds, named **75** and **76** in this thesis, were obtained by reacting an excess of the freshly prepared 1-H-mesitylimidazole (compound **74**) with the two hexasubstituted cores **60** and **61**. Anion metathesis was subsequently performed to give compounds **75·3PF$_6$** and **76·3PF$_6$** respectively in quantitative yields and satisfactory NMR purity. Furthermore, crystal structures were also obtained for the compounds **75·3PF$_6$** and **76·3PF$_6$**, which allowed us to gain some understanding of how those systems present a dynamic equilibrium between "open arms" and "closed arms" configurations, and how these tripodal systems are able to form polymeric associations through the network of interactions between the tripodal systems and their anions.

Chapter 4 explored the possibility of developing a tridentate system with unsymmetrical substituents, so as to develop ligands capable of binding metals as well as other functionalities, thus creating a multimodal system in a single compound. This chapter describes the syntheses of three mesitylimidazolium-based tripodal systems in which one of the three NHC arms was modified with two carboxylic acid-based linkers (compounds **78** and **81**), as well as with the introduction of an anthracene-thiosemicarbazone derivative as fluorophore (compound **83**). The azido group of **81** could be used to bind further functionalities, such as targeting groups (*e.g.* bombesin), so as to enhance the specificity of the tripodal system towards the biological target.

Compound **83** was obtained in a two-step reaction, firstly by preforming a nucleophilic substitution of one bromomethyl arm of the core **61** with the anthracene-thiosemicarbazone **66**,

to give compound **82** after a simple workup. Spectrophotometric analyses performed on **82** suggested that the preferential mode of substitution of the bromide is through sulphur, as for the previously reported compounds **67** and **68**, further indicating that thiosemicarbazone-based compounds are able to S-alkylate the hexasubstituted aromatic cores such as compound **61**. Finally, reaction between the mesitylimidazole derivative **74** and compound **82** was performed. The unsymmetrical tripodal system **83** was obtained in acceptable purity and good yield and its fluorescent properties were evaluated by fluorescence spectroscopy. The new compound showed absorption peaks characteristic of the anthracene moiety and, compared to its precursor **82**, a larger fluorescence emission curve (between 450-550 nm) which is suitable for cellular imaging applications. Lastly, single-photon laser-scanning confocal microscopy experiments carried out on PC3 prostate cancer cells incubated with compound **83** revealed that the compound was able to cross the cellular membrane and localise throughout the cytoplasm, where it displayed intense fluorescence when irradiated at 405, 488 and 561 nm. Given the promising emission properties of **83**, future experiments should involve testing the capacity of this compound to act as a ligand for biologically relevant transition metals

Chapter 5 explored the possibility of developing novel tripodal-based metal complexes containing metal centres of relevance to imaging and/or therapy. The chapter describes the complexation attempts between a series of transition metals and a few selected tripodal ligands previously discussed. The two tripodal-ATSC ligands **67** and **68** were metallated by exploiting microwave technology to obtain complexes of rhenium(I) (compounds **84** and **85**) and ruthenium(II) (compound **86**). Their emissive properties were evaluated and found to be suitable for *in vitro* cellular imaging applications.

Attempts to develop a trimetallic silver(I) complex from the tripodal ligand precursor **76** resulted instead in the formation of the monometallic, *bis* NHC-based complex **87**, in which two arms of the tripodal system are bound to the metal centre, while the third arm remains in its protonated state. The usage of a novel, microwave-assisted synthetic protocol to obtain the Ag(I) complex **87** gave instead a new, tri-coordinated Ag(I) compound (**88**), in which the silver centre is coordinated to all the three NHC arms of **76**. The microwave-assisted synthesis was also employed for the ligand precursors **73** and **75**. Spectroscopic analyses carried out on the reaction products pointed to the formation of tri-coordinated complexes of Ag(I) (compounds **89** and **90**).

As silver(I)-NHC complexes are usually excellent carbene-transfer agents, the possibility to transmetallate the silver(I) centre with other group 11 metals was explored. The silver(I)-based complex **87** was successfully transmetallated with gold(I) and copper(I) precursors to give the new metal complexes **90** and **91** respectively.

The last complexation attempts discussed in this chapter involved the combination of the tripodal *tert*-butylimidazole-based compounds **72** and **73** with the ruthenium cluster $Ru_3(CO)_{12}$, aiming to obtain trimetallic metal complexes where each NHC "arm" is attached to a $[Ru(CO)_4]$ moiety. The various attempts to achieve such complexation modes proved to be fruitless, however these experiments demonstrated that tripodal systems are able to induce the rearrangement of the ruthenium cluster into an anionic species, where the protonated tripodal system acts as a counterion.

Cell viability assays were carried out on a few selected metal complexes from Chapter 5. While the tripodal ATSC-based rhenium(I) complex **85** was found to be essentially non-toxic towards PC3 cancer cells, the NHC-based complexes **87**, **90** and **91** displayed remarkable toxicity towards the same cell line, with IC_{50} values comparable to the anticancer drug cisplatin on PC3 cells. Further experiments will be necessary to elucidate how these complexes are able to elicit their cytotoxic effects. Finally, cellular imaging experiments on PC3 cells were carried out using single-photon laser scanning microscopy. The confocal microscopy results show that the selected metal complexes are taken up by the cells and localise in the cytoplasm. The anthracene-based compounds **84**, **85** and **86** emit preferentially in the blue channel, whereas the gold(I) NHC-based compound **90** appears to be more emissive in the green channel. Further tests will aim to investigate the behaviour of these complexes in a variety of conditions (*e.g.* cellular hypoxia) and to confirm their sub-cellular location through co-localisation studies.

Overall, the work presented in this thesis represents a contribution towards the development of novel multifunctional tripodal-based systems and their metal complexes, which are of relevance for biomedical applications in the context of prostate cancer *in vitro* imaging and therapy.

7. Experimental section

7.1. Materials and methods

Reagents and solvents were obtained from Aldrich Chemical Co., Fluoro Chem and Fisher (Acros) and used without further purification unless otherwise stated.

All reactions involving air- or moisture-sensitive reagents or intermediates were carried out under anhydrous conditions and nitrogen or argon atmosphere, using standard Schlenk techniques, unless otherwise stated.

Microwave reactions were carried out in a Biotage Initiator 2.5 reactor in stirred capped vials.

Chromatography

Thin layer chromatography (TLC) was carried out on Merck silica gel 60 F254 analytical plates (Matrix silica gel with aluminium support and fluorescent indicator 254 nm, 0.2 mm thickness) and visualized by ultraviolet (UV) fluorescence (λ = 254, 366 nm). The elution conditions for TLC varied and are quoted for each compound.

Infrared Spectroscopy

FT-IR spectra in the 4000-650 cm^{-1} range were recorded on a Perkin Elmer Frontier FT-IR instrument.

UV/Visible Spectroscopy

UV-Vis spectra were acquired in 1 cm quartz cuvettes in a Perkin Elmer Lambda 650 UV-Vis spectrometer controlled by UV-Winlab software.

Fluorescence Spectroscopy

Fluorescence spectra were acquired in a 1 cm quartz cuvette in a Perkin Elmer LS55 luminescence spectrometer controlled by FL-Winlab 4.0 software

Nuclear Magnetic Resonance Spectroscopy

$_1$H NMR spectra were recorded on Bruker on a 300 MHz Bruker Avance, 400 MHz Bruker Avance or a 500 MHz Bruker Avance II+ spectrometers operating at 300.130, 400.130 and 500.130 MHz respectively. 13C NMR spectra were recorded on a 500 MHz Bruker Avance II+ spectrometer operating at 125.758 MHz. Chemical shift assignments were made by using standard COSY (cosygpqf) and HMQC (hmqcgpqf) pulse sequences outlined within the Bruker library. Spectra are attributed to the deuterated solvent residual peak, and coupling constants (*J*) are reported in hertz (Hz) with a possible discrepancy ≥ 0.2 Hz. Chemical shifts δ are reported in ppm. Chemical shifts of solvent residues were identified as follows: $CDCl_3$: $_1$H, δ = 7.26, $_{13}$C, δ = 77.23; DMSO-*d*$_6$: $_1$H, δ = 2.50; $_{13}$C, δ = 39.51; CD_3OD: $_1$H, δ = 4.78, 3.31; $_{13}$C, δ = 49.15; CD3CN: δ = 1.94; $_{13}$C, δ = 118.69, 1.39; C_6D_6: $_1$H, δ = 7.16; $_{13}$C, δ = 128.39; D_2O: $_1$H, δ = 4.79). Peak multiplicities are given as follows: *s*, singlet; *d*, doublet; *t*, triplet; *q*, quartet; *m*, multiplet; *dd*, doublet of doublets; *dt*, doublet of triplets; *bs*, broad.

Mass Spectrometry

MS (*m/z*) spectra were recorded on a Bruker Daltonics MicroTOF. Accurate Mass Spectrometry was carried out at the EPSRC National Mass Spectrometry Centre, Swansea University, U.K.. Different techniques were used such as MALDI, ESI and EI (Swansea) and ESI (Bath).

Single Crystal X-Ray Diffraction

X-ray crystallography data were collected at 150 K on an Agilent SuperNova Dual diffractometer, using monochromated Cu-Kα radiation (λ = 1.54184 Å). All structures were solved with SHELXT and refined by a full-matrix least-squares procedure based on F_2. Single crystal X-ray diffraction and structure refinements were carried out by Dr. Gabrielle Kociok-Köhn, Department of Chemistry, University of Bath.

Cell culturing and cell plate preparation

Cells were cultured at 37˚C in 5 % CO_2 atmosphere and diluted once a suitable confluency had been obtained. PC-3 cells were cultured in RPMI 1640 containing 10 % heat activated foetal calf serum (FCS), 0.5 % penicillin/streptomycin (10 gmL^{-1}) and 200 mM of L-glutamine. The medium contained no fluorescent indicator dyes such as phenol red and was therefore suitable for use in fluorescence imaging studies. Excess supernatant containing dead cell constituents

and excess proteins and metabolites was aspirated. The viable live adherent cells were washed with 2 x 10 mL aliquots of PBS to remove residual media containing FCS. Cells were then re-suspended in 10 mL PBS with an additional 2-5 mL Trypsin and incubated for a further 5 minutes at 37°C. After trypsinisation, 5 mL of medium containing 10 % serum was added to inactivate the trypsin and the suspension was centrifuged for 5 minutes (1000 rpm) to remove residual dead cell constituents. The resulting supernatant was aspirated, and 5 mL of medium was added. Cells were counted using a haemocytometer and seeded as appropriate. Fresh DMEM (10% FCS) was added to the suspended cells to give a sufficient concentration of cells (ca. 300000 cells mL^{-1}). The cells were plated in a Petri dish with a glass cover slip (*MaTek*) and left for 24 hours to adhere before fluorescence imaging measurements were made. Cell culturing and studies were carried out by Dr. Haobo Ge, Department of Chemistry, University of Bath.

Laser Scanning Confocal Microscopy

Confocal microscopy images were acquired in a Nikon Eclipse Ti instrument equipped with 405/488/561 nm excitation lasers. The images were processed using a Nikon NIS elements-AR Analysis 4.30.02 software.

MTT Assays

Cell viability assays (MTT) were performed with the assistance of Dr Haobo Ge in the Department of Pharmacy and Pharmacology, University of Bath, by culturing cells at 37˚C in RPMI medium in 96 well plates (*ca.* $5x10^4$ cells mL^{-1}). The cells were incubated for 48 hours to adhere and then the compounds of interest were added in different concentrations in RPMI medium (1% DMSO). The concentrations used were 0.25, 0.1, 0.05, 0.01, $1x10^{-3}$, $0.5x10^{-3}$, $1x10^{-4}$, $1x10^{-6}$ mM. The compounds were incubated for different times at 37˚C, to be subsequently washed with PBS before the MTT reagent was added. The tetrazolium compound was incubated for 2 hours, then the cell media was removed and DMSO was added. The absorbance of the generated colour was measured using a Molecular Devices Versa Max ELISA plate reader. Data were calculated from at least six consistent results and IC_{50} values were calculated from the fitting obtained with the software Origin 9.0. The error reported corresponds to the error of the mean.

7.2. Experimental procedures

7.2.1. Synthesis of compounds from Chapter 2

1,3,5-*Tris*(bromomethyl)-2,4,6-trimethylbenzene (compound 60)

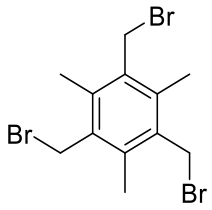

To a stirring mixture of mesitylene (12.0 g, 0.10 mol) and paraformaldehyde (10 g, 0.33 mol) in 50 mL of glacial acetic acid, 70 mL of hydrogen bromide in acetic acid (33% wt) were added. The mixture was stirred for 4 hours at 50°C, then poured into 100 mL of distilled water to afford a precipitate, which was filtered, washed with aliquots of distilled water and dried in a freeze drier to give the product as a white powder (36.2 g, 91%).

^{1}H NMR (300 MHz, $CDCl_3$, 298 K) δ 4.58 (6H, *s*, CH_2Br), 2.47 (9H, *s*, CH_3).

This analysis was consistent with literature data[1] and further characterisation was not performed.

1,3,5-*Tris*(bromomethyl)-2,4,6-triethylbenzene (compound 61)

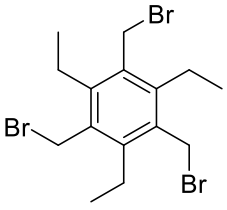

In a 500 mL round-bottomed flask connected to a condenser, zinc powder (5.0 g, 76.0 mmol) and acetic acid (glacial, 50 mL) were added in the open air. At room temperature, to the stirring reaction mixture, hydrogen bromide in acetic acid (33% wt, 50 mL) was added slowly over the course of 30 minutes. The reaction mixture was stirred until all the zinc powder had dissolved, leading to an orange-coloured solution. To this solution, 1,3,5-triethylbenzene (10.0 g, 8.62 mL,

62.0 mmol), paraformaldehyde (15 g, 93.0 mmol) and hydrogen bromide in acetic acid (33% wt, 148 mL) were added together and the resulting slurry was heated to 90°C for 48 hours, resulting in a dark brown solution. The solution was cooled down to room temperature with continuous stirring, where upon a white precipitate was formed. The solid was filtered and washed with water (3 x 20 mL). The remaining solution was collected and reheated at 90°C for a further 24 hours, allowing the formation of a second crop of product (total recovery: 28.2 g, 97%).

^{1}H NMR (300 MHz, $CDCl_3$, 298 K) δ 4.58 (6H, *s*, C*H*$_2$Br), 2.94 (6H, *q*, *J* = 7.6 Hz, C*H*$_2$CH$_3$), 1.34 (9H, *t*, *J* = 7.6 Hz, CH$_2$C*H*$_3$).

Analysis consistent with literature data.[2]

1,1',1''-((2,4,6-Trimethylbenzene-1,3,5-triyl)*tris*(methylene))*tris*(1,4-diazabicyclo[2.2.2]octan-1-ium) tribromide (compound 62)

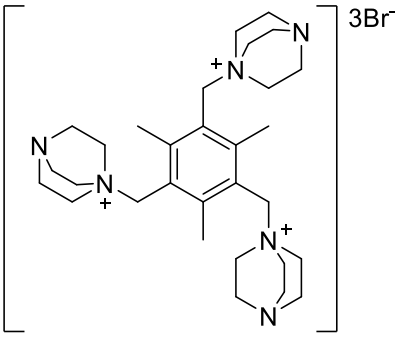

In a 250 mL two-necked round bottomed flask compound **60** (0.500 g, 1.25 mmol) and diazabicyclo[2.2.2]octane (DABCO, 1.41 g, 12.6 mmol) were dissolved in dry acetonitrile (100 mL) and refluxed under anhydrous conditions (N_2) for 24 hours, during which time a precipitate formed. The solid was collected by filtration, washed with acetonitrile, diethyl ether (3 times, 50 mL each), and dried in order to obtain a white powder (0.785 g, 85%).

^{1}H NMR (300 MHz, DMSO-*d*$_6$, 298 K) δ 4.79 (6H, *s*, C*H*$_2$N), 3.51 (18H, *t*, *J* = 7.1 Hz, N$^+$C*H*$_2$CH$_2$N), 2.97 (18H, *t*, *J* = 7.1 Hz, N$^+$CH$_2$C*H*$_2$N), 2.59 (9H, *s*, C*H*$_3$).

^{13}C NMR (75 MHz, DMSO-*d*$_6$, 298 K) δ 146.5 (*C*CH$_2$), 127.1 (*C*CH$_3$), 62.5 (*C*H$_2$N), 51.1 (N$^+$CH$_2$*C*H$_2$N), 45.5 (N$^+$*C*H$_2$CH$_2$N), 21.6 (*C*H$_3$).

ESI-MS calculated for $C_{30}H_{51}N_6Br_2^+$ $[M+^{79}Br]^{2+}$ 287.1674, found 287.1673.

1,1',1''-((2,4,6-Triethylbenzene-1,3,5-triyl)*tris*(methylene))*tris*(1,4-diazabicyclo[2.2.2]octan-1-ium) tribromide (compound 63)

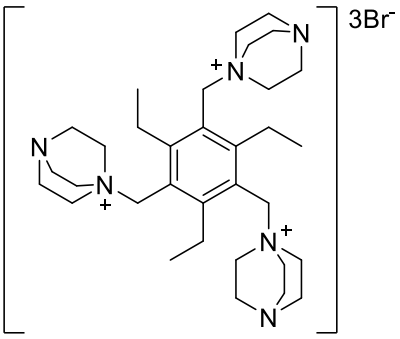

Under anhydrous conditions (N$_2$ atmosphere), compound **60** (0.500 g, 1.13 mmol) and 1.27 g (11.3 mmol) of diazabicyclo[2.2.2]octane (DABCO) were refluxed in dry acetonitrile (100 mL) for 36 hours, during which time a precipitate occurred. The precipitate was collected by filtration, washed with acetonitrile, diethyl ether and dried to give the product as a hygroscopic white powder (0.876 g, 73%).

^{1}H NMR (300 MHz, DMSO-*d*$_6$, 298 K) δ 4.69 (6H, *s*, C*H*$_2$N), 3.57 (18H, *t*, *J* = 7.3 Hz, N$^+$C*H*$_2$CH$_2$N), 3.19 (6H, *d*, *J* = 7.7 Hz, C*H*$_2$CH$_3$), 2.98 (18H, *t*, *J* = 7.2 Hz, N$^+$CH$_2$C*H*$_2$N), 0.82 (9H, *t*, CH$_2$C*H*$_3$).

^{13}C NMR (75 MHz, DMSO-*d*$_6$, 298 K) δ 154.9 (*C*CH$_2$CH$_3$), 122.7 (*C*CH$_2$N$^+$), 59.9 (*C*H$_2$N), 50.5 (N$^+$CH$_2$*C*H$_2$N), 45.1 (N$^+$*C*H$_2$CH$_2$N), 25.6 (*C*H$_2$CH$_3$), 18.2 (*C*H$_3$).

ESI-MS calculated for $C_{33}H_{57}N_6Br_2^+$ $[M+2^{79}Br]^+$ 697.2988, found 697.3017.

1,1'',1''''-((2,4,6-Trimethylbenzene-1,3,5-triyl)*tris*(methylene))*tris*([4,4'-bipyridin]-1-ium) tribromide (compound 64)

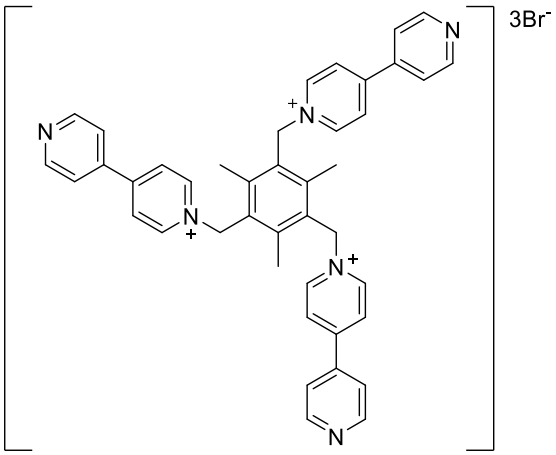

Under anhydrous conditions in a nitrogen atmosphere, compound **60** (0.500 g, 1.25 mmol) and 4,4'-bipyridine (1.77 g, 11.3 mmol) were dissolved in dry dichloromethane (100 mL). The resulting solution was stirred at reflux for 24 hours. After that time, a yellow precipitate was produced and collected by filtration, washed with aliquots of dichloromethane and diethyl ether to afford the product as a pale-yellow powder (0.736 g, 71%).

^{1}H NMR (300 MHz, DMSO-d_6, 298 K) δ 9.11 (6H, *d*, *J* = 6.9 Hz, $N^{+}CH_2CH_2N$), 8.86 (6H, *dd*, *J* = 7.1, 2.9 Hz, $N^{+}CH_2CH_2N$), 8.60 (6H, *d*, *J* = 6.5 Hz, CH_2CH_2N), 8.02 (6H, *dd*, *J* = 8.7, 4.1 Hz, CH_2CH_2N), 6.19 (6H, *s*, CH_2N), 2.39 (9H, *s*, CCH_3).

^{13}C NMR (75 MHz, DMSO-d_6, 298 K) δ 151.3 (*C*-C BiPy), 144.9 (*C*HN), 141.2 ($N^{+}CH$), 128.8 (C-*C* BiPy), 126.1 (C*C*HCHN), 122.3 (NCH*C*HC), 58.6 ($N^{+}CH_2$), 16.5 (CH_3).

ESI-MS calculated for $C_{42}H_{39}N_6Br^{2+}$ $[M+Br]^{2+}$ 353.1204, found 353.1202.

1,1'',1''''-((2,4,6-Triethylbenzene-1,3,5-triyl)*tris*(methylene))*tris*([4,4'-bipyridin]-1-ium) tribromide (compound 65)

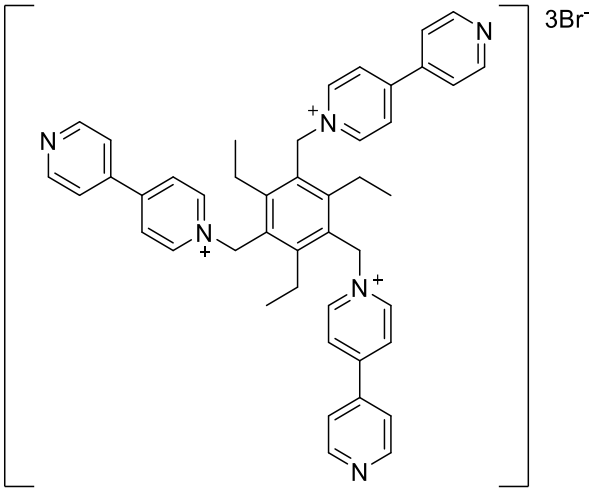

In a 250 mL round bottom flask, compound **61** (0.500 g, 1.13 mmol) and 4,4'-bipyridine (1.96 g, 12.5 mmol) were dissolved in dry dichloromethane (150 mL). The resulting solution was stirred at reflux under anhydrous conditions for 24 hours. After that time, a pale-yellow precipitate was produced and subsequently collected by filtration, washed with dichloromethane (3 x 50 mL) and diethyl ether (3 x 50 mL) to afford the product as a yellow deliquescent powder (0.882 g, 76%).

$_1$H NMR (300 MHz, DMSO-*d*$_6$, 298 K) δ 9.43 (6H, *d*, *J* = 52.2 Hz, N$^+$C*H*$_2$CH$_2$N), 8.86-8.63 (6H, *m*, N$^+$CH$_2$C*H*$_2$N), 8.62 (6H, *bs*, CH$_2$C*H*$_2$N), 7.96 (6H, *bs*, C*H*$_2$CH$_2$N), 6.16 (6H, *s*, C*H*$_2$N), 2.66 (6H, b*s*, C*H*$_2$CH$_3$), 0.97 9H, *s*, CH$_2$C*H*$_3$).

$_{13}$C NMR (75 MHz, DMSO-*d*$_6$, 298 K) δ 152.6 (*C*-C BiPy), 151.3 (*C*HN), 150.8 (N$^+$*C*H), 149.3 (C-*C* BiPy), 145.3 (*C*CH$_2$CH$_3$), 141.3 (*C*CH$_2$N$^+$), 126.0 (C*C*HCHN$^+$), 122.2 (C*C*HCHN), 57.2 (N$^+$*C*H$_2$), 23.9 (*C*H$_2$CH$_3$), 15.9 (*C*H$_3$).

ESI-MS calculated for C$_{45}$H$_{45}$N$_6^{3+}$ [M]$^{3+}$ 223.1230, found 223.1230.

2-(Anthracen-9-ylmethylene)hydrazine-1-carbothioamide (compound 66)

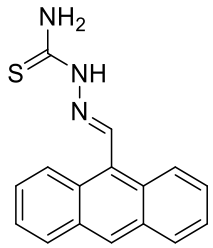

In a 100 mL round-bottomed flask, 9-anthracenecarboxaldehyde (0.500 g, 2.42 mmol), and thiosemicarbazide (0.221 g, 2.42 mmol) were suspended in 30 mL of anhydrous absolute ethanol containing 1-2 drops of acetic acid. The reaction mixture was stirred at reflux for 3.5 hours. After cooling down to room temperature, the resulting precipitate was collected by filtration and washed thoroughly with ethanol, diethyl ether and dried (0.609 g, 90%).

^{1}H NMR (300 MHz, DMSO-*d*$_6$, 298 K) δ 11.68 (1H, *s*, C*H*NNH), 9.33 (1H, *s*, C(10)*H*), 8.71 (1H, *s*, C*H*=N), 8.58-8.55 (2H, *m*, C(4,5)*H*), 8.36 (1H, *s*, SCN*H*H), 8.16-8.13 (2H, *m*, C(1,8)*H*), 7.75 (1H, *s*, SCNH*H*), 7.67-7.55 (4H, *m*, C(2,3-6,7)*H*).

Analysis consistent with literature data.[3]

(2,4,6-Trimethylbenzene-1,3,5-triyl)*tris*(methylene) (2,2',2'')-*tris*(2-(anthracen-9-ylmethylene)hydrazine-1-carbimidothioate) (compound 67)

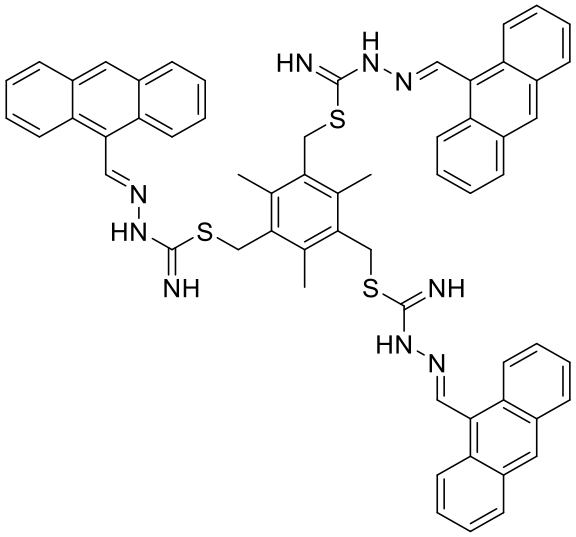

In a round-bottomed flask connected to a condenser a mixture of compound **66** (0.463 g, 1.66 mmol) and compound **60** (0.200 g, 0.50 mmol) were dissolved in 100 mL of dry acetonitrile. The reaction mixture was stirred under reflux for 16 hours. After cooling down to room temperature, the resulting precipitate was filtered and washed with acetonitrile and diethyl ether to give an orange-yellow powder, which was re-dissolved in 100 mL of methanol. To the vigorously stirring solution, an excess of triethylamine was added dropwise, resulting in the formation of a cloudy solution. The slurry was kept stirring for further 24 hours. The solvent was removed *via* rotary evaporator, tetrahydrofuran was added, and the resulting mixture was filtered (to remove the insoluble triethylamine hydrobromide) and washed thoroughly with further THF. The final product was afforded, after evaporation of the solvent, as a bright yellow powder (0.463 g, 94%).

^{1}H NMR (500 MHz, $CDCl_3$, 298 K) δ 9.62 (3H, *bs*, C(10)*H*), 8.71-8.67 (6H, *m*, C(4,5)*H*), 8.49 (3H, *s*, C(9)-C*H*=NNH), 8.05-7.99 (6H, *m*, C(1,8)*H*), 7.56-7.48 (12H, *m*, C(2,3-6,7)*H*), 5.55 (3H, *bs*, NN*H*CNHS), 4.65 (6H, *s*, CH_2S), 2.70 (9H, *s*, CH_3).

^{13}C NMR (125 MHz, $CDCl_3$, 298 K) δ 162.4 (S*C*NHNH), 153.4 (C(9)*C*HN), 137.6 (*C*CH_2S), 135.7 (*C*CH_3), 131.5 (C(4)*C*C(10), C(10)*C*C(5)), 130.5 (C(1)*C*C(9), C(8)*C*C(9)), 129.3 (*C*(9)), 128.9 (*C*(1,8)), 126.9 (*C*(4,5), 125.6 (*C*(10)) 125.4 (*C*(2,3,6,7), 31.1 (*C*H_2S), 16.7 (*C*H_3).

ESI-MS calculated for $C_{60}H_{51}N_9S_3$ $[M+H]^+$ 994.3502, found 994.3497.

(2,4,6-Triethylbenzene-1,3,5-triyl)*tris*(methylene) (2,2',2'')-*tris*(2-(anthracen-9-ylmethylene)hydrazine-1-carbimidothioate) (compound 68)

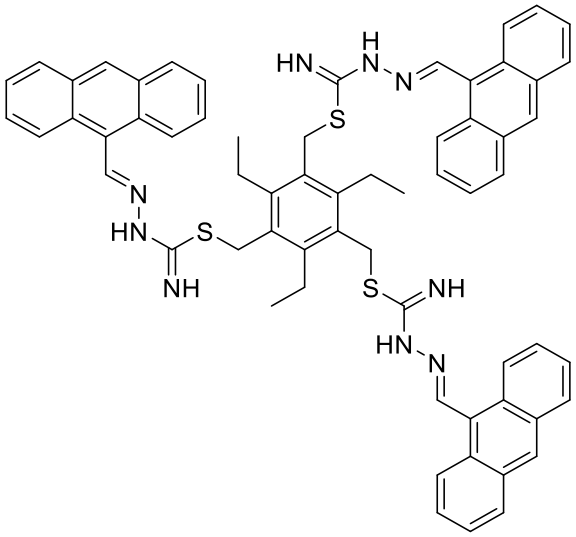

In a round-bottomed flask connected to a condenser a mixture of compound **66** (0.418 g, 1.49 mmol) and compound **61** (0.200 g, 0.45 mmol) were dissolved in 100 mL of dry acetonitrile. The reaction mixture was stirred under reflux for 18 hours. After cooling down to room temperature, the resulting precipitate was filtered and washed with acetonitrile and diethyl ether to give an orange-yellow powder, which was re-dissolved in 100 mL of methanol. To the vigorously stirring solution, an excess of triethylamine was added dropwise, resulting in the formation of a precipitate. The slurry was kept stirring for further 24 hours. The precipitate was finally filtered, washed with methanol and dried to give the final product as a yellow powder (0.431 g, 92%).

^{1}H NMR (500 MHz, $CDCl_3$, 298 K) δ 9.63 (3H, *s*, C(10)*H*), 8.71-8.66 (6H, *m*, C(4,5)*H*), 8.49 (3H, *s*, C(9)-C*H*=NNH), 8.05-7.99 (6H, *m*, C(1,8)*H*), 7.54-7.49 (12H, *m*, C(2,3-6,7)*H*), 5.56 (6H, *s*, SC=NH-N*H*), 4.67 (6H, *s*, CH_2S), 3.08 (6H, *q*, *J* = 7.4 Hz, C$H_2$$CH_3$), 1.50 (9H, *t*, *J* = 7.4 Hz, CH_2CH_3).

^{13}C NMR (125 MHz, $CDCl_3$, 298 K) δ 162.3 (S*C*NHNH), 153.4 (C(9)*C*HN), 144.4 (*C*CH_2S), 143.9 (*C*$CH_2$$CH_3$), 131.5 (C(4)*C*C(10), C(10)*C*C(5)), 130.5 (*C*(9)), 130.3 (C(1)*C*C(9), C(8)*C*C(9)), 128.9 (*C*(1,8)), 126.6 (*C*(4,5), 125.6 (*C*(10)) 125.4 (*C*(2,3,6,7), 29.6 (*C*H_2S), 23.6 (*C*$H_2$$CH_3$), 16.5 ($CH_2$*C*$H_3$).

ESI-MS calculated for $C_{63}H_{57}N_9S_3$ $[M+H]^+$ 1036.3972, found 1036.4016.

7.2.2. Synthesis of compounds from Chapter 3

3,3',3''-((2,4,6-Trimethylbenzene-1,3,5-triyl)*tris*(methylene))*tris*(1-methyl-1H-imidazol-3-ium) tribromide (compound 69)

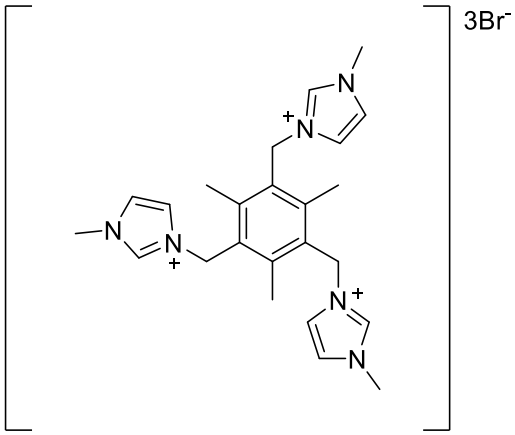

To a stirring solution of compound **60** (1.00 g, 2.51 mmol) in 250 mL of dry acetonitrile, 1-methyl-1H-imidazole (0.650 mL, 8.27 mmol) was added. The resulting mixture was refluxed under an argon atmosphere for 24 hours. Following the formation of a white precipitate, the mixture was cooled down to room temperature, filtered and the precipitate washed with aliquots of acetonitrile and diethyl ether. The pure product was obtained after recrystallization form a methanol/diethyl ether mixture as colourless needles (1.21 g, 75%).

^{1}H NMR (400 MHz, CD_3OD, 298 K) δ 7.73 (3H, *t*, *J* = 1.8 Hz, NC*H*=CHN), 7.62 (3H, *t*, *J* = 1.8 Hz, NCH=C*H*N), 5.61 (6H, *s*, CH_2N), 3.96 (*s*, 9 H, N-CH_3), 2.38 (9H, *s*, Ar-CH_3).

Analysis consistent with literature data.[4]

3,3',3''-((2,4,6-Triethylbenzene-1,3,5-triyl)*tris*(methylene))*tris*(1-methyl-1H-imidazol-3-ium) tris(hexafluorophosphate) (compound 70)

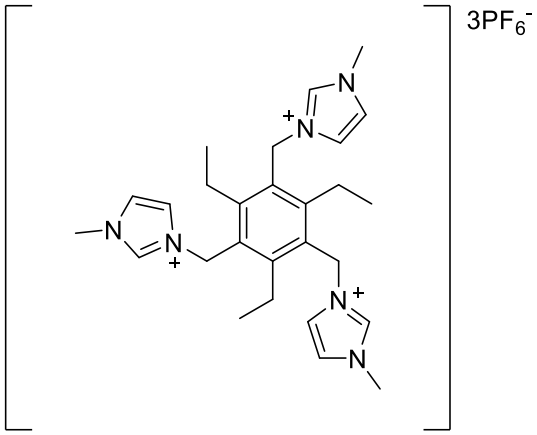

In a 250 mL two necked round bottomed flask compound **61** (1.00 g, 2.27 mmol) was dissolved in 100 mL of dry tetrahydrofuran under vigorous stirring. To this solution, 1-methyl-1H-imidazole (0.636 mL, 7.48 mmol) was added. The resulting mixture was heated at reflux under an argon atmosphere for 18 hours, resulting in the formation of a light beige precipitate, which was filtered and washed with aliquots of tetrahydrofuran. The resulting hygroscopic powder was dissolved in 100 mL of methanol and treated with a saturated solution of potassium hexafluorophosphate in methanol, which gave the pure product as a white powder (1.11 g, 50%).

^{1}H NMR (500 MHz, DMSO-*d*$_6$ 298 K) δ 8.85 (*s*, 3H, NC*H*N) 7.74 (3H, *t*, *J* = 1.8 Hz, NC*H*=CHN), 7.61 (3H, *t*, *J* = 1.8 Hz, NCH=C*H*N), 5.46 (6H, *s*, C*H*$_2$N), 3.82 (*s*, 9 H, N-C*H*$_3$), 2.62 (6H, *q*, *J* = 7.4 Hz, C*H*$_2$CH$_3$), 0.84 (9H, *t*, *J* = 7.4 Hz, CH$_2$C*H*$_3$).

^{13}C NMR (125 MHz, DMSO-*d*$_6$, 298 K) δ 148.0 (N*C*HN), 136.4 (*C*CH$_2$CH$_3$), 128.9 (*C*CH$_2$N$^+$), 124.2 (N*C*H=CHN), 123.2 (NCH=*C*HN), 47.2 (*C*H$_2$N), 36.3 (N-*C*H$_3$), 23.5 (*C*H$_2$CH$_3$), 16.0 (CH$_2$*C*H$_3$).

ESI-MS calculated for $C_{27}H_{39}N_6P_2F_{12}^+$ $[M+2PF_6]^+$ 737.2514, found 737.2493.

1-(*tert*-Butyl)-1H-imidazole (compound 71)

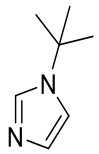

Distilled water (50 mL) was placed in a 250 mL 3-necked flask connected to two dropping funnels and a condenser. One dropping funnel contained a mixture of aqueous glyoxal (11.5 mL, 0.10 mol, 40% w/v) and aqueous formaldehyde (8.10 ml, 0.10 mol, 40% conc.); the other dropping funnel *tert*-butylamine (10.6 mL, 0.10 mol) and aqueous ammonia (6.80 mL, 0.10 mol, 25% w/v). The water was heated to reflux and then the contents of both dropping funnels were added dropwise and simultaneously. The reaction mixture turned brown and after the addition was complete, it was subsequently stirred for 30 minutes at 100°C. The solution was cooled to room temperature and the solvent was removed under reduced pressure to give a brown oil, which was extracted into dichloromethane (150 mL) and then it was washed with a saturated solution of sodium chloride (3 x 150 mL). The organic layer was dried over sodium sulphate and the solvent removed under reduced pressure. The pure product was purified by Kugelröhr distillation to give a very pale-yellow oil (b.p.116°C) (5.77 g, 44%).

$_1$H NMR (300 MHz, $CDCl_3$, 298 K) δ 7.52 (1H, *s*, NC*H*N), 6.95 (2H, *s*, NC*H*=C*H*N), 1.46 (9H, *s*, *t*Bu-C*H*$_3$).

$_{13}$C NMR (75 MHz, $CDCl_3$, 298 K) δ 134.2 (N*C*HN), 128.9 (NCH=*C*HN), 116.2 (N*C*H=HCN), 54.6 (*t*Bu-*C*), 30.5 (*t*Bu-*C*H$_3$).

Analysis consistent with literature data.[5]

3,3',3''-((2,4,6-Trimethylbenzene-1,3,5-triyl)*tris*(methylene))*tris*(1-(tert-butyl)-1H-imidazol-3-ium) tribromide (compound 72)

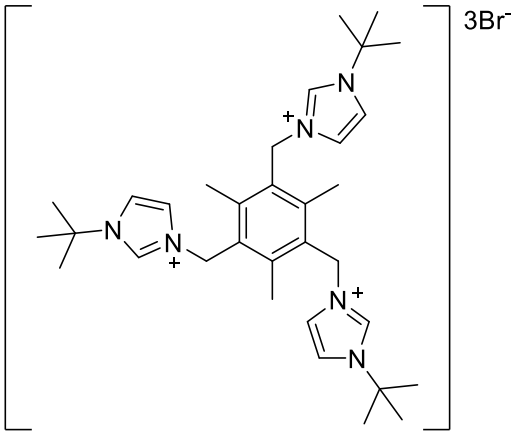

In a 250 mL two necked round bottomed flask compound **60** (5.00 g, 12.6 mmol) and compound **71** (5.16 g, 41.6 mmol) were dissolved in dry acetonitrile (100 mL) and refluxed under dinitrogen atmosphere for 48 hours. After removal of the solvent under vacuum, the solid was washed with diethyl ether and the product was recrystallized from a dichloromethane/diethyl ether mixture to give a white microcrystalline solid (8.13 g, 84%).

^{1}H NMR (300 MHz, DMSO-*d*$_6$, 298 K) δ 9.50 (3H, *t*, *J* = 1.7 Hz, NC*H*N), 8.06 (3H, *t*, *J* = 1.9 Hz, NC*H*=CHN), 7.51 (3H, *t*, *J* = 1.8 Hz, NCH=C*H*N), 5.57 (6H, *s*, C*H*$_2$N), 2.28 (9H, *s*, Ar-C*H*$_3$), 1.58 (27H, *s*, C(C*H*$_3$)$_3$).

^{13}C NMR (125 MHz, DMSO-*d*$_6$, 298 K) δ 141.4 (*C*CH$_2$N), 134.9 (N*C*HN), 129.7 (N*C*H=CHN), 122.3 (Ar-*C*), 120.9 (NCH=*C*HN), 60.2 (N*C*(CH$_3$)$_3$), 48.2 (*C*H$_2$N), 29.5 (C(*C*H$_3$)$_3$), 16.9 (*C*H$_3$).

Analysis consistent with literature data.[6]

3,3',3''-((2,4,6-Triethylbenzene-1,3,5-triyl)*tris*(methylene))*tris*-1-(tert-butyl)-1H-imidazol-3-ium) tribromide (compound 73)

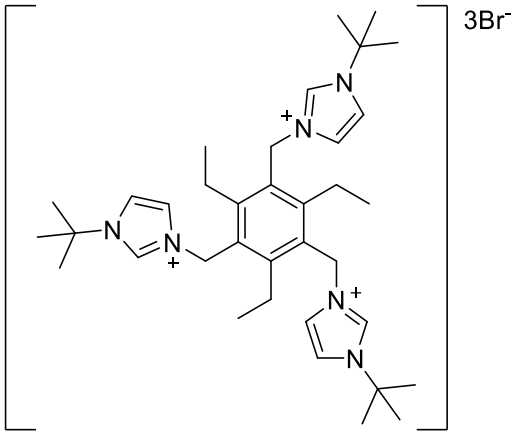

In a 500 mL two-necked round bottomed flask compound **61** (1.18 g, 2.67 mmol) and compound **71** (1 g, 8.1 mmol) were mixed in anhydrous conditions under flux of nitrogen. 250 mL of anhydrous acetonitrile were added, the resulting reaction mixture was stirred under reflux for 48 hours. The reaction mixture was cooled down and a white-grey precipitate was obtained. The solid was filtered, washed with aliquots of acetonitrile and dried. Counterion metathesis was performed by treating a rapidly stirring aqueous suspension of the product with ammonium hexafluorophosphate. Following recrystallization from tetrahydrofuran/*n*-pentane, the product was obtained as a white powder (1.695 g, 78%).

^{1}H NMR (300 MHz, DMSO-d_6, 298 K) δ 9.64 (3H, *t*, *J* = 1.7 Hz, NC*H*N), 8.05 (3H, *t*, *J* = 1.9 Hz, NC*H*=CHN), 7.55 (3H, *t*, *J* = 1.9 Hz, NCH=C*H*N), 5.50 (6H, *s*, CH_2N), 2.71 (6H, *q*, *J* = 7.4 Hz, CH_2CH$_3$), 1.60 (27H, *s*, C(CH_3)$_3$), 0.74 (9H, *t*, *J* = 7.2 Hz, CH$_2$CH_3).

^{13}C NMR (75 MHz, DMSO-d_6, 298 K) δ 147.7 (*C*CH$_2$CH$_3$ or *C*CH$_2$N), 136.2 (N*C*HN), 122.3 (*C*CH$_2$CH$_3$ or *C*CH$_2$N), 128.9 (N*C*H=CHN), 120.8 (NCH=*C*HN), 60.1 (N*C*(CH$_3$)$_3$), 48.9 (*C*H$_2$N), 29.5 (C(*C*H$_3$)$_3$), 23.6 (*C*H$_2$CH$_3$), 15.2 (CH$_2$*C*H$_3$).

3,3',3''-((2,4,6-Triethylbenzene-1,3,5-triyl)*tris*(methylene))*tris*-1-(tert-butyl)-1H-imidazol-3-ium) *tris*-hexafluorophosphate (compound 73·3PF$_6$)

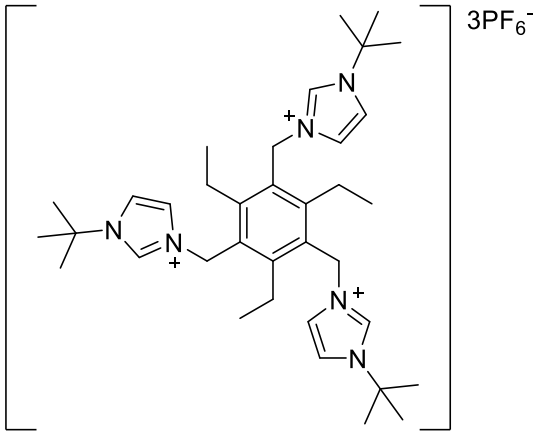

Compound **73·3PF$_6$** was obtained by treating a rapidly stirring aqueous suspension of compound **73** (0.100 g, 0.12 mmol) with an excess ammonium hexafluorophosphate (0.053 g, 0.33 mmol). The suspension was filtered and dried in a freeze drier to give the product as a white powder (0.117 g, 99%).

^{1}H NMR (300 MHz, DMSO-*d*$_6$, 298 K) δ 9.58 (3H, *t*, *J* = 1.7 Hz, NC*H*N), 8.00 (3H, *t*, *J* = 1.9 Hz, NC*H*=CHN), 7.51 (3H, *t*, *J* = 1.8 Hz, NCH=C*H*N), 5.52 (6H, *s*, C*H*$_2$N), 2.73 (6H, *q*, *J* = 7.3 Hz, C*H*$_2$CH$_3$), 1.62 (27H, *s*, C(C*H*$_3$)$_3$), 0.76 (9H, *t*, *J* = 7.2 Hz, CH$_2$C*H*$_3$).

^{13}C NMR (75 MHz, DMSO-*d*$_6$, 298 K) δ 148.3 (*C*CH$_2$CH$_3$ or *C*CH$_2$N), 137.4 (N*C*HN), 121.9 (*C*CH$_2$CH$_3$ or *C*CH$_2$N), 127.5 (N*C*H=CHN), 121.2 (NCH=*C*HN), 59.1 (N*C*(CH$_3$)$_3$), 48.4 (*C*H$_2$N), 29.2 (C(*C*H$_3$)$_3$), 23.1 (*C*H$_2$CH$_3$), 15.4 (CH$_2$*C*H$_3$).

ESI-MS calculated for $C_{36}H_{57}N_6P_2F_{12}^+$ $[M+2PF_6]^+$ 863.3923, found 863.3967.

1-Mesityl-1H-imidazole (compound 74)

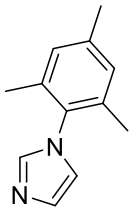

In a 1 L round-bottom flask, a solution of 2,4,6-trimethylaniline (37.7 mL, 0.10 mol) in methanol (50 mL) was treated with 30% aqueous glyoxal (16.2 mL, 0.10 mol) for 16 hours at room temperature. A pale-yellow solution was formed. Ammonium chloride (10.7 g, 0.20 mol) was added, followed by 37% aqueous formaldehyde (16 mL, 0.20 mol). The mixture was diluted with methanol (400 mL) and refluxed for 1 hour. Phosphoric acid (14 mL, 85% wt) was slowly added dropwise over a period of 10 minutes. The resulting mixture was stirred at reflux for further 8 hours. After removal of the solvent, the dark brown residue was poured onto ice (300 g) and neutralised with a 40% wt potassium hydroxide solution until pH 9. The resulting slurry was extracted with diethyl ether (5 x 150 mL). The organic phases were combined and washed with distilled water, brine and dried over sodium sulphate. After removal of the solvent, the pure compound was afforded following recrystallization from a concentrated solution of ethyl acetate as colourless needles (26.9 g, 71%).

$_1$H NMR (300 MHz, $CDCl_3$, 298 K) δ 7.44 (1H, *t*, *J* = 1.2 Hz, NC*H*N), 7.23 (1H, *t*, *J* = 1.1 Hz, NCH=C*H*N), 7.00-6.94 (2H, *m*, Ar-C*H*), 6.89 (1H, *t*, *J* = 1.3 Hz, NC*H*=CHN), 2.34 (3H, *s*, *p*-C*H*$_3$), 1.99 (6H, *s*, *o*-C*H*$_3$).

Analysis consistent with literature data.[7]

3,3',3''-((2,4,6-Trimethylbenzene-1,3,5-triyl)*tris*(methylene))*tris*(1-mesityl-1H-imidazol-3-ium) tribromide (compound 75)

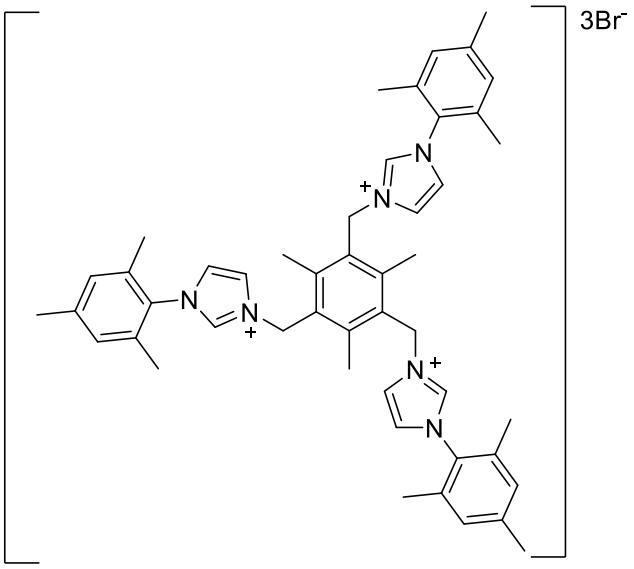

In a 250 mL two-necked round-bottomed flask compound **60** (0.505 g, 1.27 mmol) and compound **74** (0.712 g, 3.82 mmol) were mixed under nitrogen. 100 mL of dry acetonitrile was added, and the resulting reaction mixture was stirred under reflux for 48 hours. After two days, the reaction mixture was cooled down and a pale-yellow precipitate was obtained. The precipitate was recrystallized from tetrahydrofuran/*n*-pentane to give the pure product as a white powder (0.688 g, 70%).

^{1}H NMR (300 MHz, CD_3CN, 298 K) δ 10.13 (3H, *t*, *J* = 1.6 Hz, NC*H*N), 8.00 (3H, *s*, *J* = 1.8 Hz, NC*H*=CHN), 7.42 (3H, *t*, *J* = 1.8 Hz, NCH=C*H*N), 6.97 (6H, *s*, *m*-C*H*), 5.64 (6H, *s*, CH_2N), 2.34 (9H, *s*, Ar-CH_3), 2.31 (9H, *s*, *p*-CH_3) 1.93 (18H, *s*, *o*-CH_3).

^{13}C NMR (75 MHz, DMSO-*d*$_6$, 298 K) δ 149.7 (CH_2-*p*-Me), 140.1 (NCHN), 136.4 (*C*CH_3), 134.7 (*C*H_2-*o*-Me), 130.6 (*C*CH_2N) 129.7 (*C*H Mes), 128.2 (*C*N), 124.8 (NCH=CHN), 122.7 (NCH=*C*HN), 21.3 (*C*H_3), 19.9 (*p*-*C*H_3), 17.3 (*o*-*C*H_3).

ESI-MS calculated for $C_{48}H_{57}N_6^{3+}$ $[M]^{3+}$ 239.1543, found 239.1537.

3,3',3''-((2,4,6-Triethylbenzene-1,3,5-triyl)*tris*(methylene))*tris*(1-mesityl-1H-imidazol-3-ium) tribromide (compound 76)

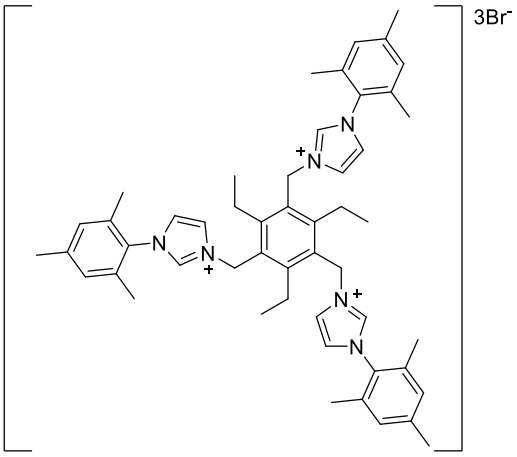

In a 250 mL Schlenk tube, compound **61** (0.362 g, 0.82 mmol) and compound **74** (0.459 g, 2.46 mmol) were stirred in anhydrous conditions under nitrogen. 100 mL of anhydrous acetonitrile was added, and the reaction mixture was stirred under reflux for 48 hours. After cooling down to room temperature, the solution was concentrated to ~2-3 mL before layering it with diethyl ether. The pure product was obtained as colourless crystals (0.413 g, 66%).

^{1}H NMR (300 MHz, DMSO-d_6, 298 K) δ 9.38 (3H, *s*, NC*H*N), 8.02 (3H, *t*, *J* = 1.8 Hz, NC*H*=CHN), 7.93 (3H, *t*, *J* = 1.8 Hz, NCH=C*H*N), 7.12 (6H, *s*, *m*-C*H*), 5.66 (6H, *s*, CH_2N), 2.77 (6H, *q*, *J* = 7.5 Hz, CH_2CH$_3$), 2.31 (9H, *s*, *p*-CH_3) 1.96 (18H, *s*, *o*-CH_3), 0.92 (9H, *t*, *J* = 7.2 Hz, CH$_2$CH_3).

^{13}C NMR (75 MHz, DMSO-d_6, 298 K) δ 148.2 (*C*H$_2$-*p*-Me), 140.6 (N*C*HN), 137.1 (*C*CH$_2$CH$_3$), 134.5 (*C*H$_2$-*o*-Me), 131.5 (*C*CH$_2$N) 129.6 (*C*H Mes), 128.9 (*C*N), 124.5 (N*C*H=CHN), 123.5 (NCH=*C*HN), 20.9 (*p*-*C*H$_3$), 17.4 (*o*-*C*H$_3$), 16.0 (CH$_2$*C*H$_3$).

ESI-MS calculated for $C_{51}H_{61}N_6Br_2^+$ [M+2^{79}Br]$^+$ 919.8960, found 919.3525.

3,3',3''-((2,4,6-Triethylbenzene-1,3,5-triyl)*tris*(methylene))*tris*(1-mesityl-1H-imidazol-3-ium) *tris*-hexafluorophosphate (compound 76·3PF$_6$)

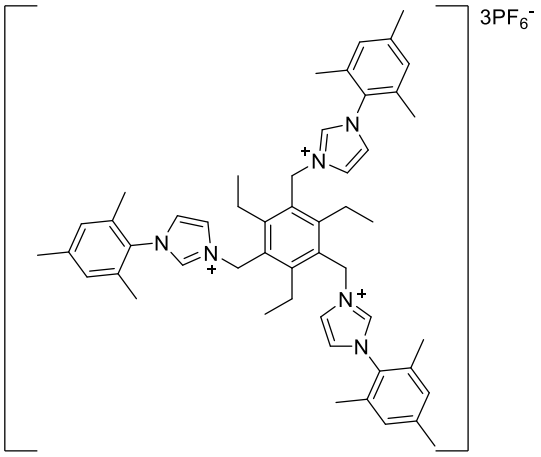

Compound **76·3PF$_6$** was obtained by treating a rapidly stirring aqueous suspension of compound **76** (0.100 g, 0.10 mmol) with an excess ammonium hexafluorophosphate (0.054 g, 0.33 mmol). The suspension was filtered and dried in a freeze drier to give the product as a white powder (0.118 g, 99%).

^{1}H NMR (300 MHz, DMSO-*d*$_6$, 298 K) δ 9.47 (3H, *s*, NC*H*N), 8.04 (3H, *t*, *J* = 1.8 Hz, NC*H*=CHN), 7.98 (3H, *t*, *J* = 1.8 Hz, NCH=C*H*N), 7.13 (6H, *s*, *m*-C*H*), 5.70 (6H, *s*, C*H*$_2$N), 2.81 (6H, *q*, *J* = 7.4 Hz, C*H*$_2$CH$_3$), 2.32 (9H, *s*, *p*-C*H*$_3$) 1.99 (18H, *s*, *o*-C*H*$_3$), 0.93 (9H, *t*, *J* = 7.2 Hz, CH$_2$C*H*$_3$).

^{13}C NMR (75 MHz, DMSO-*d*$_6$, 298 K) δ 148.8 (*C*H$_2$-*p*-Me), 139.8 (N*C*HN), 136.7 (*C*CH$_2$CH$_3$), 134.8 (*C*H$_2$-*o*-Me), 131.8 (*C*CH$_2$N) 130.1 (*C*H Mes), 128.5 (*C*N), 124.1 (N*C*H=CHN), 122.9 (NCH=*C*HN), 21.0 (*p*-*C*H$_3$), 17.5 (*o*-*C*H$_3$), 16.1 (CH$_2$*C*H$_3$).

7.2.3. Synthesis of compounds from Chapter 4

3,5-*Bis*(bromomethyl)-2,4,6-triethylbenzyl *tert*-butyl succinate (compound 77)

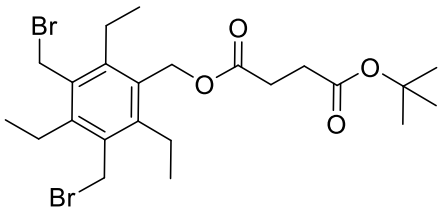

In a 100 mL round-bottomed flask connected to a condenser compound **60** (0.500 g, 1.13 mmol) and 4-(*tert*-butoxy)-4-oxobutanoic acid (0.198 g, 1.13 mmol) were dissolved in 50 mL of acetonitrile. To the stirring solution, potassium carbonate (0.235 g, 1.70 mmol) was added and the resulting mixture was refluxed for 18 hours. After cooling down to room temperature, the solvent was removed under vacuum and dichloromethane was added. The resulting mixture was washed three times with a sodium hydroxide 1M solution, the organic phase dried over magnesium sulphate and the solvent was removed. Pure product was afforded after purification *via* silica gel flash chromatography with a solvent system of 10% ethyl acetate/hexane (0.176 g, 29%).

^{1}H NMR (400 MHz, $CDCl_3$, 298 K) δ 5.25 (2H, *s*, C*H*$_2$O) 4.65 (4H, *s*, C*H*$_2$Br), 3.00 (2H, *q*, *J* = 7.5 Hz, p-C*H*$_2$CH$_3$), 2.89 (2H, *q*, *J* = 7.5 Hz, o-C*H*$_2$CH$_3$), 2.62-2.59 (2H, *m*, COC*H*$_2$), 2.56-2.53 (2H, *m*, C*H*$_2$CO), 1.48 (9H, *s*, C(C*H*$_3$)), 1.40 (3H, *t*, *J* = 7.6 Hz, p-CH$_2$C*H*$_3$), 1.31 (6H, *t*, *J* = 7.6 Hz, o-CH$_2$C*H*$_3$).

^{13}C NMR (125 MHz, $CDCl_3$, 298 K) δ 173.1 (CH$_2$OO*C*CH$_2$), 171.7 (*C*OO*t*Bu), 144.3 (*p*-Ar-*C*CH$_2$CH$_3$), 143.8 (*o*-Ar-*C*CH$_2$CH$_3$), 132.4 (Ar-*C*CH$_2$O), 130.6 (Ar-*C*CH$_2$Br), 81.4 (*C*(CH$_3$)$_3$), 61.6 (*C*H$_2$O), 30.6 (*C*H$_2$COO*t*Bu), 29.1 (*C*H$_2$CH$_2$COO*t*Bu), 28.4 ((C(*C*H$_3$)$_3$), 23.3 (*o*-Ar-C*C*H$_2$CH$_3$), 22.7 (*p*-Ar-C*C*H$_2$CH$_3$), 16.0 (*o*-CH$_2$*C*H$_3$), 15.6 (*p*-CH$_2$*C*H$_3$).

ESI-MS calculated for $C_{23}H_3O_4Br_2$ $[M+NH_4]^+$ 552.1143, found 552.1128.

3,3'-((5-(((4-(*Tert*-butoxy)-4-oxobutanoyl)oxy)methyl)-2,4,6-triethyl-1,3-phenylene)*bis*(methylene))*bis*(1-mesityl-1H-imidazol-3-ium) dibromide (compound 78)

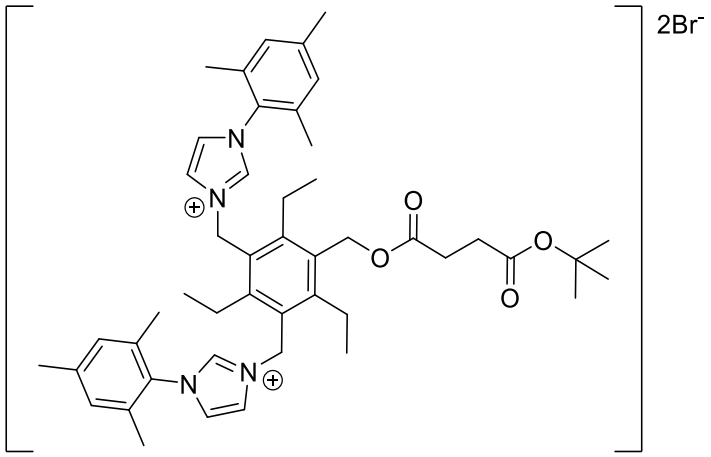

In a 250 mL round-bottomed flask equipped with a magnetic stirrer and a condenser, a mixture of compound **77** (0.730 g, 1.37 mmol) and the monosubstituted imidazole (compound **74**) (0.534 g, 2.88 mmol) were dissolved in 100 mL of dry acetonitrile. The reaction mixture was refluxed under an argon atmosphere for 48 hours. After cooling down to room temperature, the solvent was removed under reduced pressure and the crude product was recrystallized from a mixture of dichloromethane/*n*-pentane to give the title compound as a white powder (1.04 g, 83%).

^{1}H NMR (500 MHz, DMSO-d_6, 298 K) δ 9.30 (2H, *s*, NC*H*N), 8.00 (4H, *s*, NC*H*CHN), 7.98 (4H, *s*, NCHC*H*N), 7.10 (4H, *s*, Mes-C*H*), 5.64 (4H, *s*, CH_2N), 5.17 (2H, *s*, CH_2O), 2.72 (6H, *q*, *J* = 7.4 Hz, CH_2CH$_3$), 2.48-2.46 (4H, *m*, COCH_2CH_2CO), 2.29 (6H, s, Mes-*p*-CH_3), 1.95 (12H, *s*, Mes-*o*-CH_3), 1.33 (9H, *s*, C(CH_3)), 1.08-1.02 (9H, *m*, CH$_2$CH_3).

^{13}C NMR (125 MHz, DMSO-d_6, 298 K) δ 172.0 (CH$_2$OO*C*CH$_2$), 171.1 (*C*OO*t*Bu), 147.6 (Mes-*p*-*C*CH$_3$), 146.6 (*p*-Ar-*C*CH$_2$CH$_3$), 140.3 (*o*-Ar-*C*CH$_2$CH$_3$), 136.5 (N*C*HN), 134.2 (Mes-*o*-*C*CH$_3$), 131.2 (*C*CH$_2$N), 129.2 (Mes-*o*-*C*CH$_3$), 124.2 (N*C*H=CHN), 123.4 (NCH=*C*HN), 79.9 (*C*(CH$_3$)$_3$), 60.2 (*C*H$_2$O), 47.3 (*C*H$_2$N), 29.7 (*C*H$_2$COO*t*Bu), 28.8 (*C*H$_2$CH$_2$COO*t*Bu), 27.8 (C(*C*H$_3$)$_3$), 23.0 (*p*-Ar-C*C*H$_2$CH$_3$), 22.5 (*o*-Ar-C*C*H$_2$CH$_3$), 20.5 (Mes-*p*-C*C*H$_3$), 17.0 (Mes-*o*-*C*CH$_3$), 16.8 (*p*-CH$_2$*C*H$_3$), 15.7 (*o*-CH$_2$*C*H$_3$).

ESI-MS calculated for $C_{47}H_{62}N_4O_4$ $[M]^{2+}$ 373.2380, found 373.2469.

6-Azidohexanoic acid (compound 79)

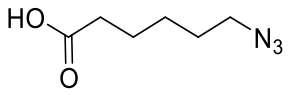

In a 250 mL round-bottomed flask 6-bromohexanoic acid (1.00 g 5.13 mmol) was dissolved in 80 mL of dimethyl sulfoxide. To the stirring solution, sodium azide (0.500 g, 7.69 mmol) was added and the resulting mixture was stirred at room temperature for 16 hours. After this time, 200 mL of distilled water was added, and the crude product was extracted with diethyl ether (5 x 150 mL). The organic phases were combined and dried over magnesium sulphate, filtered and the solvent removed under reduced pressure to give the pure product as a pale-yellow oil (0.503g, 72%).

$_1$H NMR (300 MHz, $CDCl_3$, 298 K) δ 10.76 (1H, *s*, COO*H*), 3.23 (2H, *t*, *J* = 6.9 Hz, C*H*$_2$N$_3$), 2.31 (2H, *t*, *J* = 7.3 Hz, C*H*$_2$COOH), 1.68-1.65 (2H, *m*, C*H*$_2$CH$_2$N$_3$), 1.59-1.56 (2H, *m*, C*H*$_2$CH$_2$COOH), 1.46-1.42 (2H, *m*, N$_3$CH$_2$CH$_2$C*H*$_2$).

Analysis consistent with literature data.[8]

3,5-*Bis*(bromomethyl)-2,4,6-triethylbenzyl 6-azidohexanoate (compound 80)

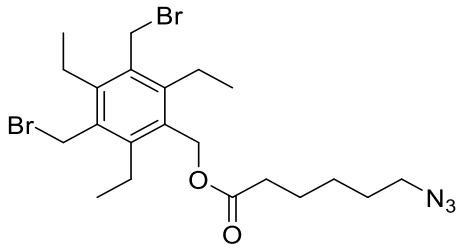

In a 100 mL round-bottomed flask connected to a condenser compound **61** (0.500 g, 1.13 mmol) was dissolved in 50 mL of acetonitrile. To the stirring solution, potassium carbonate (0.235 g, 1.70 mmol) and compound **79** (0.178 g, 1.13 mmol) were added and the resulting mixture was refluxed for 16 hours. After cooling down to room temperature, the solvent was removed under reduced pressure and dichloromethane was added. The resulting mixture was washed three times with 1M sodium hydroxide solution, the organic phase dried over magnesium sulphate, and the solvent removed. Pure product was afforded after purification *via* silica gel flash chromatography with a solvent system of 2-20% ethyl acetate/hexane (0.181 g, 32%).

^{1}H NMR (500 MHz, $CDCl_3$, 298 K) δ 5.16 (2H, *s*, C*H*$_2$O), 4.60 (4H, *s*, C*H*$_2$Br), 3.21 (2H, *t*, *J* = 6.9 Hz, C*H*$_2$N$_3$), 2.96 (2H, *q*, *J* = 7.5 Hz, p-C*H*$_2$CH$_3$) 2.79 (2H, *q*, *J* = 7.6 Hz, o-C*H*$_2$CH$_3$) 2.36 (2H, *t*, *J* = 7.5 Hz, COC*H*$_2$), 1.70-1.63 (2H, *m*, COCH$_2$C*H*$_2$), 1.61-1.54 (2H, *m*, C*H*$_2$CH$_2$N$_3$), 1.45-1.38 (2H, m, N$_3$CH$_2$CH$_2$C*H*$_2$), 1.35 (3H, *t*, *J* = 7.6 Hz, p-CH$_2$C*H*$_3$), 1.23 (6H, *t*, *J* = 7.7 Hz, o-CH$_2$C*H*$_3$).

^{13}C NMR (125 MHz, $CDCl_3$, 298 K) δ 173.1 (*C*OOCH$_2$), 143.6 (*p*-Ar-*C*CH$_2$CH$_3$), 142.7 (*o*-Ar-*C*CH$_2$CH$_3$), 132.5 (Ar-*C*CH$_2$O), 130.7 (Ar-*C*CH$_2$Br), 60.8 (*C*H$_2$O), 49.5 (*C*H$_2$N$_3$), 34.2 (OC*C*H$_2$), 30.1 (*C*H$_2$Br), 29.6 (*C*H$_2$CH$_2$N$_3$), 23.4 (*o*-Ar-C*C*H$_2$CH$_3$), 22.0 (*p*-Ar-C*C*H$_2$CH$_3$), 16.3 (*o*-CH$_2$*C*H$_3$), 15.7 (*p*-CH$_2$*C*H$_3$).

ESI-MS calculated for $C_{21}H_{31}N_3O_2Br_2$ $[M+NH_4]^+$ 535.1102, found 535.1091.

3,3'-((5-(((6-Azidohexanoyl)oxy)methyl)-2,4,6-triethyl-1,3-phenylene)*bis*(methylene))*bis*(1-mesityl-1H-imidazol-3-ium) dibromide (compound 81)

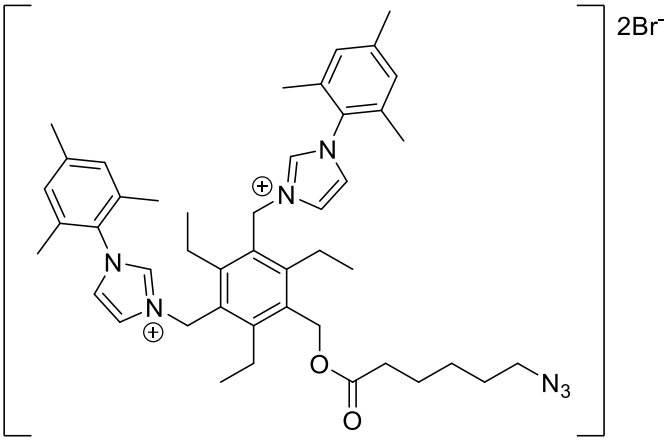

In a 250 mL round-bottomed flask a mixture of compound **80** (0.300 g, 0.58 mmol) and compound **74** (0.227 g, 1.22 mmol) were dissolved in 80 mL of dry acetonitrile. The reaction mixture was refluxed under anhydrous atmosphere for 48 hours. After cooling down to room temperature, the solvent was removed under reduced pressure and the crude product was recrystallized from a mixture of dichloromethane/hexane to give the compound **81** as a white powder (0.398 g, 77%).

^{1}H NMR (500 MHz, DMSO-*d*$_6$, 298 K) δ 9.44 (1H, *s*, NC*H*N), 9.22 (1H, *s*, NC*H*N), 8.03-7.99 (2H, *m*, NC*H*=CHN), 7.96-7.92 (2H, *m*, NCH=C*H*N), 7.11 (4H, *s*, Mes *m*-C*H*), 5.68, 5.59 (4H, *s*, CH_2N), 4.56 (2H, *s*, CH_2O), 3.28 (2H, *t*, *J* = 7.2 Hz, CH_2N$_3$), 2.81-2.76 (4H, *m*, o-CH_2CH$_3$), 2.73-2.70 (2H, *m*, p-CH_2CH$_3$), 2.54 (2H, *bs*, COCH_2), 2.29 (6H, *s*, Mes *p*-CH_3), 1.97,1.94 (12H, *s*, Mes *o*-CH_3), 1.56-1.53 (2H, *m*, COCH$_2$CH_2), 1.33-1.26 (2H, *m*, CH_2CH$_2$N$_3$), 1.22-1.14 (2H, *m*, N$_3$CH$_2$CH$_2$CH_2) 1.07-1.03 (6H, *m*, *o*-CH$_2$CH_3), 0.93 (3H, *t*, *J* = 7.3 Hz, *p*-CH$_2$CH_3).

^{13}C NMR (125 MHz, CDCl$_3$, 298 K) δ 173.8 (*C*OOCH$_2$), 147.1 (*p*-Ar-*C*CH$_2$CH$_3$), 146.2 (Mes-*p*-*C*CH$_3$), 143.9 (*p*-Ar-*C*CH$_2$CH$_3$), 142.3 (*o*-Ar-*C*CH$_2$CH$_3$), 137.5 (N*C*HN), 133.9 (Mes-*o*-*C*CH$_3$), 132.3 (Ar-*C*CH$_2$O), 131.8 (*C*CH$_2$N), 125.2 (N*C*H=CHN), 124.7 (NCH=*C*HN), 62.4 (C̲H$_2$O), 50.0 (*C*H$_2$N$_3$), 34.6 (OCC̲H$_2$), 28.9 (*C*H$_2$CH$_2$N$_3$), 22.8 (*o*-Ar-C*C*H$_2$CH$_3$), 22.3 (*p*-Ar-C*C*H$_2$CH$_3$), 16.1 (*o*-CH$_2$*C*H$_3$), 15.8 (*p*-CH$_2$*C*H$_3$).

ESI-MS calculated for C$_{45}$H$_{59}$N$_7$O$_{22+}$ [M]$^{2+}$ 364.7360, found 364.7366.

3,5-*Bis*(bromomethyl)-2,4,6-triethylbenzyl-2-(anthracen-9-ylmethylene)hydrazine-1-carbimidothioate (compound 82)

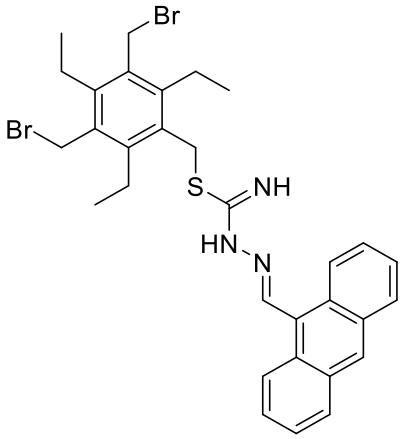

In a 250 mL two-necked round-bottomed flask connected to a condenser, compound **61** (0.500 g, 1.13 mmol) was dissolved in 100 mL of dry acetonitrile. To this solution, compound **66** (0.158 g, 0.57 mmol) was added. The resulting suspension was heated to reflux and stirred for 16 hours. After cooling down to room temperature, the reaction mixture was filtered, the filtrate concentrated to 1-2 mL and diethyl ether was added to precipitate the title compound, which was washed with further aliquots of diethyl ether and dried to give a bright yellow powder (0.142 g, 39%).

^{1}H NMR (400 MHz, DMSO-*d*$_6$, 298 K) δ 9.81 (1H, *s*, C=N*H*), 9.68 (1H, *s*, C(10)*H*), 8.86 (1H, *s*, C*H*NNH), 8.60-8.58 (2H, *m*, C(4,5)*H*), 8.23-8.21 (2H, *m*, C(1,8)*H*), 7.71-7.64 (4H, *m*, C(2,3-6,7)*H*), 4.75 (4H, *s*, C*H*$_2$Br), 4.73 (2H, *s*, C*H*$_2$S), 2.95-2.91 (6H, *m*, C*H*$_2$CH$_3$), 0.87-0.81 (9H, *m*, CH$_2$C*H*$_3$).

^{13}C NMR (125 MHz, DMSO-*d*$_6$, 298 K) δ 164.1 (S*C*NHNH), 143.9 (C(9)*C*HN), 137.8 (*C*CH$_2$S), 136.9 (*C*-*p*-CH$_2$CH$_3$), 133.3 (*C*-*o*-CH$_2$CH$_3$), 131.1 (C(4)*C*C(10), C(10)*C*C(5)), 130.3 (*C*CH$_2$Br), 129.6 (*C*(9)), 129.5 (C(1)*C*C(9), C(8)*C*C(9)), 128.3 (*C*(1,8, 4,5)), 126.27 (*C*(2,3,6,7)), 125.14 (*C*(10)), 31.2 (*C*H$_2$S), 30.7 (*C*H$_2$Br), 23.1 (*o*-*C*H$_2$CH$_3$), 22.9 (*p*-*C*H$_2$CH$_3$), 16.6 (CH$_2$*C*H$_3$).

ESI-MS calculated for C$_{31}$H$_{33}$N$_3$S$_1$Br$_2$ [M+H$^+$] 640.0788, found 640.0807.

3,3'-((5-((((2-(Anthracen-9-ylmethylene)hydrazineyl)(imino)methyl)thio)methyl)-2,4,6-triethyl-1,3-phenylene)*bis*(methylene))*bis*(1-mesityl-1H-imidazol-3-ium) dibromide (compound 83)

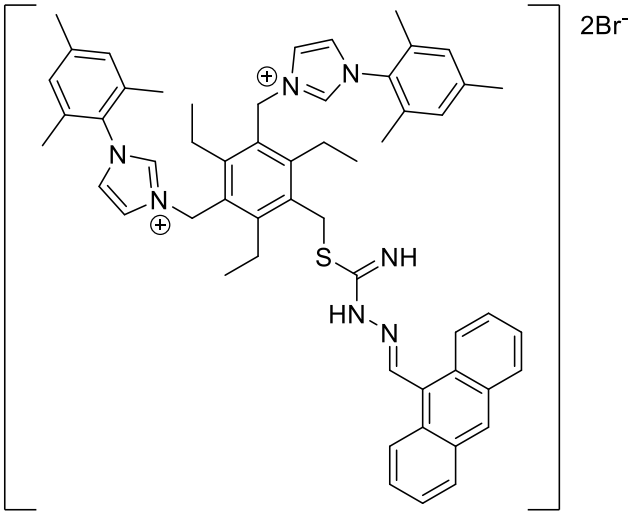

In an oven-dried, argon-purged two-necked round-bottomed flask connected to a condenser, compound **82** (0.100 g, 0.16 mmol) and compound **74** (0.061 g, 0.33 mmol) were dissolved in 50 mL of dry acetonitrile. The reaction mixture was refluxed for 48 hours. After cooling to room temperature, the solvent was evaporated under reduced pressure and the product recrystallized from a mixture of chloroform/*n*-pentane to give the title compound as a yellow powder (0.141 g, 87%).

^{1}H NMR (400 MHz, DMSO-d_6, 298 K) δ 11.65 (1H, *s*, C*H*NNH), 9.46 (2H, *s*, NC*H*N), 9.34 (1H, *s*, C(10)*H*), 8.72 (1H, *s*, C*H*NNH), 8.58 (2H, *d*, *J* = 8.8 Hz, C(1,8)*H*), 8.16 (2H, *d*, *J* = 8.3 Hz, C(4,5)*H*), 8.03, 7.97 (4H, *bs*, NC*H*C*H*N), 7.65 (4H, *dt*, *J* = 7.5, 2.5 Hz, C(2,3-6,7)*H*), 7.13 (4H, *s*, Mes-C*H*), 5.70 (6H, *s*, CH_2N, CH_2S), 2.81 (6H, *q*, *J* = 7.1 Hz, CH_2CH$_3$), 2.33 (6H, s, Mes-*p*-CH_3), 1.99 (12H, *s*, Mes-*o*-CH_3), 1.33 (9H, *s*, C(CH_3)), 0.95 (9H, *t*, *J* = 6.9 Hz, CH$_2$CH_3).

^{13}C NMR (125 MHz, DMSO-d_6, 298 K) δ 177.9 (S*C*NHNH), 147.8 (C(9)*C*HN), 142.1 (*C*CH$_2$S), 140.2 (Mes *o*-*C*CH$_3$), 136.8 (N*C*HN), 134.3 (*C*-*p*-CH$_2$CH$_3$), 134.1 (*C*CH$_2$N), 131.6 (*C*-*o*-CH$_2$CH$_3$), 131.3 (Mes *C*-*o*-CH$_3$), 129.6 (C(1)*C*C(9), C(8)*C*C(9)), 129.6 (*C*(9)), 129.4 (C(4)*C*C(10), C(10)*C*C(5)), 128.9 (Mes *C*H), 128.5 (Mes *C*N), 127.2 (*C*(1,8, 4,5)), 125.3 (*C*(2,3,6,7)), 124.9 (*C*(10)), 124.1 (N*C*H=CHN), 123.1 (NCH=*C*HN), 47.7 (*C*H$_2$N), 30.5 (*C*H$_2$S), 23.4 (*C*H$_2$CH$_3$), 21.0 (Mes *p*-*C*H$_3$), 17.5 (Mes *o*-*C*H$_3$), 16.1 (CH$_2$*C*H$_3$).

ESI-MS calculated for $C_{55}H_{61}N_7S_1$ [M^{2+}] 425.7349, found 425.7384.

7.2.4. Synthesis of compounds from Chapter 5

$Re(CO)_3$ (2,4,6-trimethylbenzene-1,3,5-triyl)*tris*(methylene) (2,2',2'')-*tris*(2-(anthracen-9-ylmethylene)hydrazine-1-carbimidothioate) (compound 84)

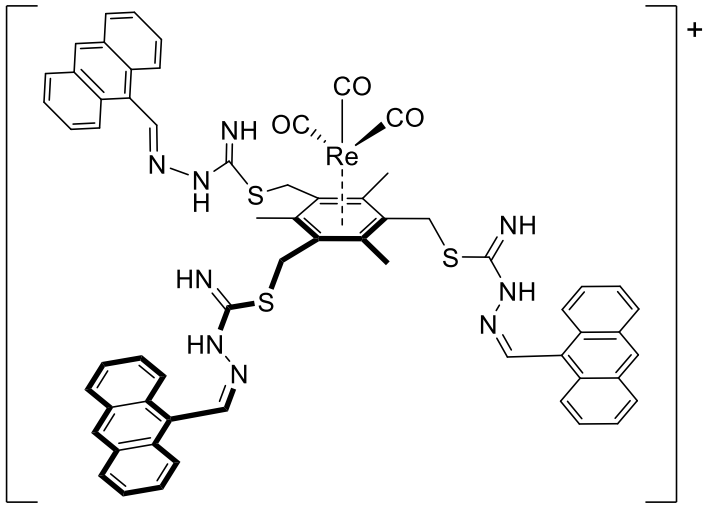

Proposed Structure

In a 10 mL microwave vial equipped with a stirring magnet equimolar amounts of compound **67** (0.115 g, 0.12 mmol) and chloropentacarbonylrhenium(I) (0.047 g, 0.12 mmol) were added. The reaction vessel was sealed and saturated with argon for 15 minutes, then 8 mL of dry toluene was added. The reaction mixture was heated at 150°C for 30 minutes under microwave irradiation, during which time an orange precipitate was formed. The suspension was filtered, and the filter cake washed with aliquots of fresh toluene, diethyl ether and dried to give the title compound as an orange solid (0.051 g, 34%).

^{1}H NMR (400 MHz, DMSO-*d*$_6$, 298 K) δ 9.86 (3H, *bs*, C(10)*H*), 8.87 (3H, *s*, C(9)-C*H*=NNH), 8.62 (6H, *m*, C(4,5)*H*), 8.28-8.22 (6H, *m*, C(1,8)*H*), 7.72-7.65 (12H, *m*, C(2,3-6,7)*H*), 4.92 (6H, *bs*, CH_2S), 2.71 (9H, *s*, CH_3).

^{13}C NMR (125 MHz, $CDCl_3$, 298 K) δ 162.87 (S*C*NHNH), 151.3 (C(9)*C*HN), 138.1 (*C*CH_2S), 133.2 (*C*CH_3), 131.0 (C(4)*C*C(10), C(10)*C*C(5)), 130.7 (C(1)*C*C(9), C(8)*C*C(9)), 128.1 (*C*(9)), 127.5 (*C*(1,8)), 126.7 (*C*(4,5), 125.8 (*C*(10)) 125.3 (*C*(2,3,6,7), 31.0 (*C*H_2S), 16.4 (*C*H_3).

ESI-MS calculated for $C_{63}H_{51}N_9O_3S_3Re$ $[M+H+Na]^+$ 1286.3069, found 1286.3334.

Solid-state (powder) FT-IR (cm^{-1}) 2017, 1907, 1883.

***fac*-Re(CO)$_3$(2,4,6-triethylbenzene-1,3,5-triyl)*tris*(methylene) (2,2',2'')-*tris*(2-(anthracen-9-ylmethylene)hydrazine-1-carbimidothioate) (compound 85)**

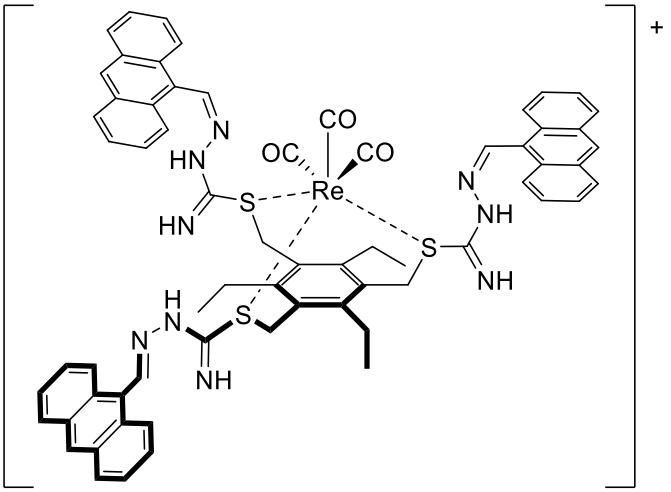

Proposed structure

Compound **85** was synthesised following the experimental procedure for compound **84**. Compound **68** (0.050 g, 0.05 mmol) and bromopentacarbonylrhenium(I) (0.021 g, 0.05 mmol) were heated in toluene at 150°C for 30 minutes under microwave irradiation. The product was obtained as an orange solid (0.041 g, 62%).

^{1}H NMR (400 MHz, DMSO-d_6, 298 K) δ 9.89 (3H, *s*, C(10)*H*), 9.32 (3H, *s*, C(9)-C*H*=NNH), 8.86-8.59 (6H, *m*, C(4,5)*H*), 8.18-8.06 (6H, *m*, C(1,8)*H*), 7.63-7.57 (12H, *m*, C(2,3-6,7)*H*), 4.55 (6H, *s*, CH_2S), 3.03-2.98 (6H, *m*, CH_2CH$_3$), 1.37-1.33 (9H, *m*, CH$_2$CH_3).

^{13}C NMR (125 MHz, $CDCl_3$, 298 K) δ 183.8 (*C*O), 164.5 (S*C*NHNH), 155.1 (C(9)*C*HN), 147.6 (*C*CH$_2$S), 144.5 (*C*CH$_2$CH$_3$), 131.7 (C(4)*C*C(10), C(10)*C*C(5)), 131.2 (*C*(9)), 130.8 (C(1)*C*C(9), C(8)*C*C(9)), 129.6 (*C*(1,8)), 125.7 (*C*(4,5), 125.2 (*C*(10)) 124.8 (*C*(2,3,6,7), 30.7 (*C*H$_2$S), 24.0 (*C*H$_2$CH$_3$), 16.3 (CH$_2$*C*H$_3$).

ESI-MS calculated for $C_{66}H_{57}N_9O_3S_3Re$ $[M]^+$ 1306.3299, found 1306.3282.

Solid-state (powder) FT-IR (cm^{-1}) 2020, 1907, 1887.

Ru(CO)$_2$(2,4,6-triethylbenzene-1,3,5-triyl)*tris*(methylene) (2,2',2'')-*tris*(2-(anthracen-9-ylmethylene)hydrazine-1-carbimidothioate) (compound 86)

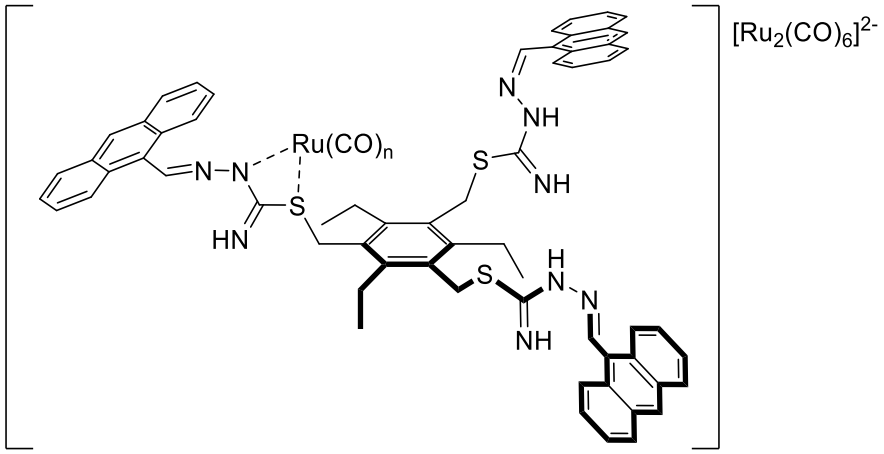

Proposed structure

Compound **86** was synthesised following the experimental procedure for compound **84**. Compound **68** (0.050 g, 0.05 mmol) and triruthenium dodecacarbonyl (0.031 g, 0.05 mmol) were heated in toluene at 150°C for 30 minutes under microwave irradiation. A cloudy, deep red solution was obtained. The mixture was filtered, and the solution was evaporated under vacuum to give a red solid. The product was eluted with chloroform/hexane (60:40). After removal of the solvents, the title compound was afforded as a red solid. (0.027 g, 44%)

^{1}H NMR (400 MHz, DMSO-*d*$_6$, 298 K) δ 9.62 (3H, *s*, C(10)*H*), 8.56 (3H, *s*, C(9)-C*H*=NNH), 8.22-7.80 (6H, *m*, C(4,5)*H*), 8.18-8.06 (6H, *m*, C(1,8)*H*), 7.70-7.33 (12H, *m*, C(2,3-6,7)*H*), 1.31 (6H, *s*, C*H*$_2$S), 1.30-1.24 (6H, *m*, C*H*$_2$CH$_3$), 0.95-0.87 (9H, *m*, CH$_2$C*H*$_3$).

ESI-MS calculated for $C_{66}H_{57}N_9O_3S_3Ru$ $[M+H-CO]^+$ 1194.2929, found 1194.2958.

UV-Visible (THF): 350, 370 and 390 nm

Fluorescence emission (Maximum, THF): 441 nm

Solid-state (powder) FT-IR (cm^{-1}) 2041, 1972, 1579, 1494.

3,3'-((2,4,6-Triethyl-5-((1-mesityl-1H-imidazol-3-ium-3-yl)methyl)-1,3-phenylene)*bis*(methylene))*bis*(1-mesityl-2,3-dihydro-1H-imidazol-2-ide) silver(I) *bis*-hexafluorophosphate (compound 87)

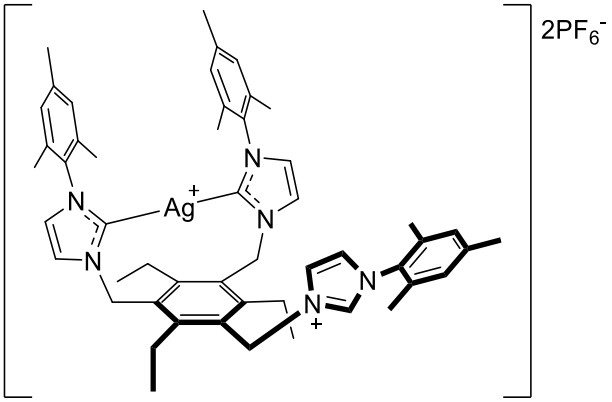

Proposed structure

To a 50 mL round-bottomed flask compound **76·3PF6** (0.148 g, 0.12 mmol) and silver(I) oxide (0.034 g, 0.15 mmol), 20 mL acetonitrile was added. The resulting mixture was wrapped in tinfoil to prevent photodecomposition and stirred at room temperature for 48 hours. The reaction mixture was subsequently filtered through a Celite® pad and the solution was evaporated under reduced pressure. The final product was obtained *via* column chromatography, eluting with dichloromethane, as an off-white solid (0.074 g, 53%).

^{1}H NMR (400 MHz, $CDCl_3$, 298 K) δ 9.22 (1H, *s*, NC*H*N), 8.01 (2H, *s*, N*H*C=CHN), 7.91 (2H, *s*, NHC=C*H*N), 7.38 (2H, *s*, Mes-C*H*), 7.12 (4H, *s*, Mes-C*H*), 6.78 (1H, *s*, N*H*C=CHN), 6.68 (1H, *s*, NHC=C*H*N), 5.63 (2H, *s*, CH_2N^+), 5.56 (4H, *s*, CH_2N), 3.14-3.09 (2H, *m*, *p*-CH_2CH_3), 2.82-2.74 (4H, *m*, *o*-CH_2CH_3), 2.30 (9H, *s*, *p*-CH_3), 1.96 (18H, *s*, *o*-CH_3), 1.18-1.15 (3H, *m*, *p*-CH_2CH_3), 0.93-0.90 (6H, *m*, *o*-CH_2CH_3).

^{13}C NMR (125 MHz, $CDCl_3$, 298 K) δ 186.7 (*C*) 147.3 (*C*H), 141.2 (*C*H), 134.2 (*C*), 134.1 (*C*), 129.7 (*C*), 125.8 (*C*H), 124.4 (*C*H), 122.6 (*C*H), 54.2 (*C*H_2), 47.1 (*C*H_2), 26.0 (*C*H_2), 22.3 (*C*H_2), 21.0 (*C*H_3), 17.0 (*C*H_3), 16.9 (*C*H_3), 15.9 (*C*H_3), 15.0 (*C*H_3), 14.0 (*C*H_3).

ESI-MS calculated for $C_{51}H_{61}N_6PF_6Ag^+$ $[M+PF_6]^+$ 1011.3645, found 1011.3786.

3,3',3''-((2,4,6-Triethyl-1,3,5-phenylene)*tris*(methylene))*tris*(1-mesityl-2,3-dihydro-1H-imidazol-2-ide) silver(I) hexafluorophosphate (compound 88)

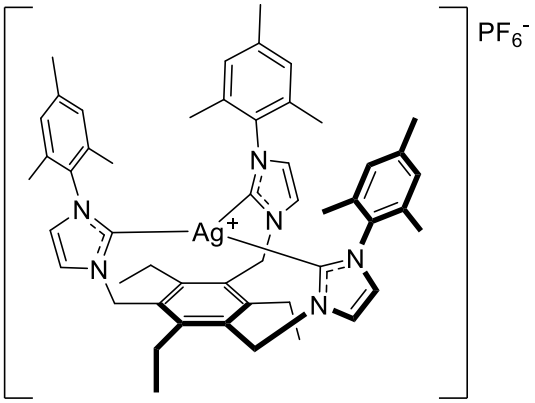

Proposed structure

In a 20 mL microwave vial equipped with a stirring magnet equimolar amounts of compound **76·3PF6** (0.100 g, 0.08 mmol) and silver(I) oxide (0.023 g, 0.10 mmol) were added. The reaction vessel was sealed and saturated with argon for 15 minutes, then 15 mL of dichloroethane (DCE) were added. the resulting mixture was heated for 40 minutes at 150°C under microwave irradiation. The reaction mixture was subsequently filtered through a Celite® pad and the solution was evaporated under reduced pressure. The final product was obtained *via* column chromatography, eluting with dichloromethane, as a white solid (0.039 g, 48%).

^{1}H NMR (400 MHz, $CDCl_3$, 298 K) δ 8.57 (3H, *bs*, N*H*C=CHN), 7.20 (3H, *bs*, NHC=C*H*N), 6.94 (6H, *bs*, Mes-C*H*), 5.62 (4H, *bs*, CH_2N), 5.20 (2H, *s*, CH_2N_+), 2.75-2.73 (2H, *m*, *p*-CH_2CH_3), 2.63-2.58 (4H, *m*, *o*-CH_2CH_3), 2.29 (3H, *s*, Mes-*p*-CH_3), 2.26 (6H, *s*, Mes-*p*-CH_3), 1.97 (6H, *s*, Mes-*o*-CH_3), 1.96 (12H, *s*, Mes-*o*-CH_3), 1.18-1.13 (6H, *m*, *o*-CH_2CH_3), 1.03-0.99 (3H, *m*, *p*-CH_2CH_3).

^{13}C NMR (125 MHz, $CDCl_3$, 298 K) δ 148.1 (*C*H), 140.4 (*C*H), 136.6 (*C*), 131.2 (*C*), 126.4 (*C*H), 125.8 (*C*H), 56.7 (*C*H_2), 25.1 (*C*H_2), 23.0 (*C*H_2), 21.0 (*C*H_3), 17.0 (*C*H_3), 16.9 (*C*H_3), 15.9 (*C*H_3), 15.0 (*C*H_3), 14.0 (*C*H_3).

ESI-MS calculated for $C_{51}H_{60}N_6Ag$ $[M]_+$ 865.3925, found 865.3957.

3,3',3''-((2,4,6-Trimethyl-1,3,5-phenylene)*tris*(methylene))*tris*(1-mesityl-2,3-dihydro-1H-imidazol-2-ide) silver(I) bromide (compound 89)

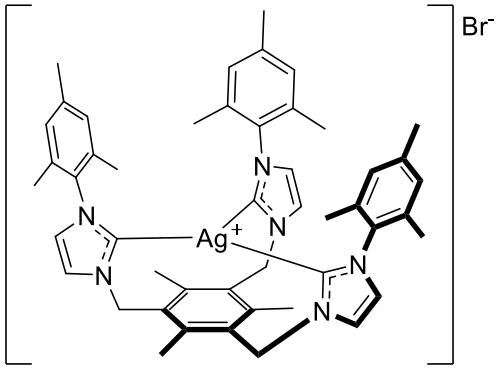

Proposed structure

Compound **89** was synthesised following the experimental procedure for compound **89**. Compound **75** (0.100 g, 0.09 mmol) and silver(I) oxide (0.066 g, 0.28 mmol) were heated in dichloroethane at 150°C for 40 minutes under microwave irradiation. The product was obtained as a pale yellow solid (0.058 g, 66%).

^{1}H NMR (400 MHz, CD_3CN, 298 K) δ 7.40 (3H, *s*, N*H*C=CHN), 7.10 (3H, *d*, *J* = 1.7 Hz, NHC=C*H*N), 6.98 (6H, *s*, Mes-C*H*), 5.49 (6H, *s*, CH_2N), 2.34 (9H, *s*, *core*-Ar-CH_3), 2.32 (9H, *s*, Mes-*p*-CH_3), 1.87 (18H, *s*, Mes-*o*-CH_3).

^{13}C NMR (125 MHz, DMSO-d_6, 298 K) δ 148.4 (CH_2-*p*-Me), 135.9 (*C*CH_3), 134.4 (*C*H_2-*o*-Me), 130.2 (*C*CH_2N) 129.2 (*C*H Mes), 127.8 (*C*N), 123.1 (N*C*H=CHN), 122.8 (NCH=*C*HN), 21.4 (*C*H_3), 19.7 (*p*-*C*H_3), 17.4 (*o*-*C*H_3).

ESI-MS calculated for $C_{48}H_{54}N_6Ag$ $[M]^+$ 823.3455, found 823.3513.

3,3'-((2,4,6-Triethyl-5-((1-*tert*-butyl-1H-imidazol-3-ium-3-yl)methyl)-1,3-phenylene)*bis*(methylene))*bis*(1-*tert*-butyl-1H-imidazol-2-ide) silver(I) bromide (compound 90)

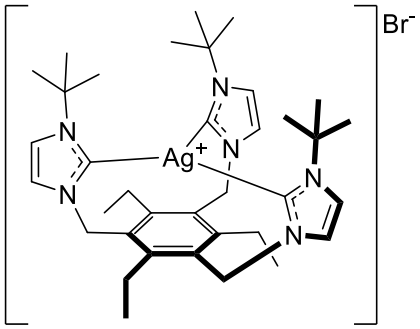

Proposed structure

Compound **90** was synthesised following the experimental procedure of compound **88**. Compound **73** (0.100 g, 0.12 mmol) and silver(I) oxide (0.034 g, 0.15 mmol) were heated in dichloroethane at 150°C for 32 minutes under microwave irradiation. The product was obtained as a pale orange solid (0.061 g, 61%).

^{1}H NMR (300 MHz, DMSO-d_6, 298 K) δ 7.57 (3H, *s*, NC*H*=CHN), 7.28 (3H, *s*, NCH=C*H*N), 5.43 (6H, *s*, CH_2N), 2.71 (6H, *q*, *J* = 8.2 Hz, CH_2CH$_3$), 1.62 (27H, *s*, C(CH_3)$_3$), 0.76-0.71 (9H, *m*, CH$_2$CH_3).

^{13}C NMR (75 MHz, DMSO-d_6, 298 K) δ 147.7 (*C*CH$_2$CH$_3$ or *C*CH$_2$N), 136.2 (N*C*HN), 122.3 (*C*CH$_2$CH$_3$ or *C*CH$_2$N), 128.9 (N*C*H=CHN), 120.8 (NCH=*C*HN), 60.1 (N*C*(CH$_3$)$_3$), 48.9 (*C*H$_2$N), 29.5 (C(*C*H$_3$)$_3$), 23.6 (*C*H$_2$CH$_3$), 15.2 (CH$_2$*C*H$_3$).

ESI-MS calculated for $C_{36}H_{54}N_6Ag^+$ $[M]^+$ 677.3455, found 677.3499.

3,3'-((2,4,6-Triethyl-5-((1-mesityl-1H-imidazol-3-ium-3-yl)methyl)-1,3-phenylene)*bis*(methylene))*bis*(1-mesityl-2,3-dihydro-1H-imidazol-2-ide) gold(I) *bis*-hexafluorophosphate (compound 91)

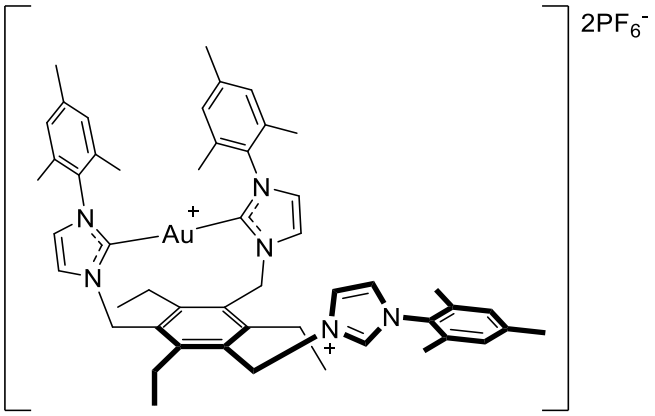

Proposed structure

In an oven-dried, argon-purged Schlenk flask, compound **87** (0.10 g, 0.09 mmol) and chloro(dimethylsulfide)gold(I) (0.026 g, 0.090 mmol) were dissolved in 20 mL of dry dichloromethane. The reaction mixture was stirred in the dark for 16 hours. The resulting cloudy solution was filtered through a Celite® pad, and the solution was treated with a saturated aqueous solution of ammonium hexafluorophosphate. After filtering off the precipitates, the clear solution was evaporated under reduced pressure to give the title compound as an off-white solid (0.068 g, 61%).

ESI-MS calculated for $C_{51}H_{61}N_6AuPF_6$ $[M+PF_6]_+$ 1098.4181, found 1098.8146.

UV-Visible (MeCN): 280 nm

Fluorescence emission (Maximum, MeCN): 419 nm

3,3'-((2,4,6-Triethyl-5-((1-mesityl-1H-imidazol-3-ium-3-yl)methyl)-1,3-phenylene)*bis*(methylene))*bis*(1-mesityl-2,3-dihydro-1H-imidazol-2-ide) copper(I) *bis*-hexafluorophosphate (compound 92)

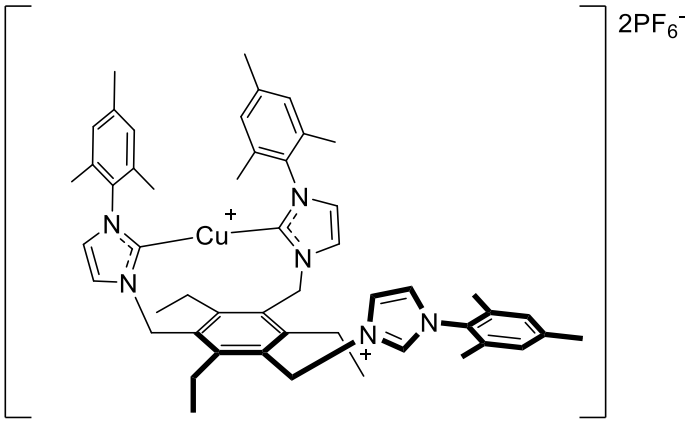

Proposed structure

Compound **92** was prepared following the experimental procedure for compound **91**. Compound **87** (0.100 g, 0.09 mmol) and *tetrakis*(acetonitrile)copper(I) hexafluorophosphate (0.027 g, 0.09 mmol) were dissolved in dry dichloromethane. After recrystallization from a mixture of dichloromethane/*n*-pentane, the product was afforded as a white solid (0.057 mg, 57%).

^{1}H NMR (400 MHz, $CDCl_3$, 298 K) δ 8.82 (1H, *s*, N^+CHN), 7.50 (2H, *bs*, $N^+HC{=}CHN$), 7.29 (4H, *bs*, $N^+HC{=}CHN$), 7.00 (4H, *s*, yliden-Mes-C*H*), 6.72 (6H, *bs*, Mes-C*H*), 5.81 (2H, *bs*, CH_2N), 5.53 (2H, *bs*, CH_2N), 5.32 (2H, *s*, CH_2N^+), 2.79-2.75 (6H, *m*, CH_2CH_3), 2.35 (6H, *s*, yliden-Mes-*p*-CH_3), 2.18 (3H, *s*, Mes-*p*-CH_3), 2.02 (12H, *bs*, yliden-Mes-*o*-CH_3), 1.73 (6H, *bs*, Mes-*o*-CH_3), 1.34-1.31 (3H, *m*, *p*-CH_2CH_3), 1.15-1.08 (6H, *m*, *o*-CH_2CH_3).

ESI-MS calculated for $C_{51}H_{61}N_6CuPF_6$ $[M+PF_6]^+$ 965.3890, found 965.3866.

UV-Visible (MeCN): 280 nm

Fluorescence emission (Maximum, MeCN): 425 nm

Reaction between compound 73 and $Ru_3(CO)_{12}$ to give compound 93

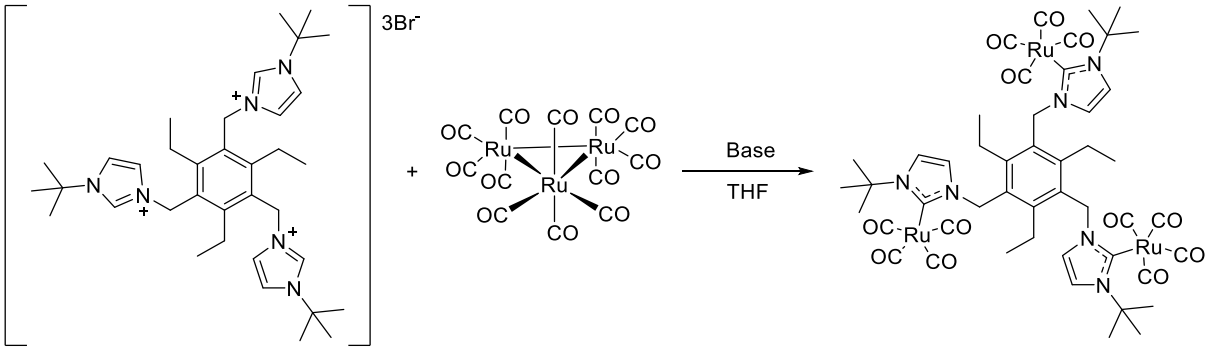

Compound **73** **Proposed structure**

1) One-pot reaction: Under anhydrous conditions with argon, triruthenium dodecarbonyl (0.039 g, 0.061 mmol), compound **73** (0.050 g, 0.061 mmol) and potassium *tert*-butoxide (*t*BuOK, 0.023 g, 0.20 mmol) were mixed in a Schlenk flask and solubilised in 8 mL of anhydrous THF. The reaction mixture was stirred for 48 hours until a dark orange solid precipitated. The solvent was removed and the solid was recrystallized from diethyl ether to give a brown solid (0.035 g).

2) One-pot reaction: Same procedure as before, but with potassium *bis*(trimethylsilyl)amide (KHMDS) as base. The ^{1}H NMR analysis performed on the dark red product showed no reaction had occurred between the Ru cluster and compound **73**.

3) Two step reaction:

A) Formation of the free carbene: Under anhydrous conditions with argon, compound **73** (0.050 g, 0.061 mmol) and potassium *bis*(trimethylsilyl) amide (0.038 g, 0.19 mmol) were dissolved in 10 mL of dry THF and stirred under anhydrous condition for 16 hours. During this time the white, cloudy reaction mixture turned to a pale-yellow solution.

B) Formation of the metal complex: A solution of triruthenium dodecarbonyl (0.039 g, 0.061 mmol) in 5 mL of dry THF was slowly cannulated into the reaction mixture from the previous passage. The solution turned orange and was stirred for a further 12 hours. After that time, the solid residue was separated from the solution by using a filter cannula and the resulting red solution was concentrated under vacuum. 20 mL of dry diethyl ether was added, then the two phases were separated and dried under *vacuo*. ^{1}H NMR analysis performed on both fractions revealed the presence of large amounts of the starting compounds.

4) Two step reaction:

A) Formation of the free carbene: Under anhydrous conditions of argon compound **73** (0.050 g, 0.061 mmol) and potassium *bis*(trimethylsilyl) amide (0.038 g, 0.19 mmol) were dissolved in 15 mL of dry THF and stirred under anhydrous condition for 16 hours. During this time the white, cloudy reaction mixture turned to a pale-yellow solution.

B) Formation of the metal complex: The reaction mixture containing the carbene was cooled down to -78°C and a solution of $Ru_3(CO)_{12}$ (0.039 g, 0.061 mmol) in 5 mL of dry THF was slowly cannulated to the reaction mixture. The solution turned orange and was stirred for 16 hours until the mixture reached room temperature. After that time, the solid residue was separated from the solution by using a filter cannula and the resulting red solution was concentrated under vacuum to *.ca* 1-2 mL before layering it with diethyl ether. The product was obtained as a red solid after filtration of the precipitated (0.032 g).

^{1}H NMR (400 MHz, CD_3CN, 298 K) δ 7.59 (3H, *s*, $N^+C\mathit{H}$=CHN), 7.08 (3H, *s*, $NC\mathit{H}$=CHN^+), 5.44 (6H, *s*, $C\mathit{H}_2N$), 2.64 (6H, *q*, *J* = 7.5 Hz, $C\mathit{H}_2CH_3$), 1.61 (27H, *s*, $C(C\mathit{H}_3)_3$), 0.92 (9H, *t*, *J* = 7.5 Hz, $CH_2C\mathit{H}_3$).

Solid-state (powder) FT-IR (cm^{-1}) 2054, 2011, 1995, 1979.

3,3',3''-((2,4,6-Trimethylbenzene-1,3,5-triyl)*tris*(methylene))*tris*(1-(tert-butyl)-1H-imidazol-3-ium-2-ide) (compound 94)

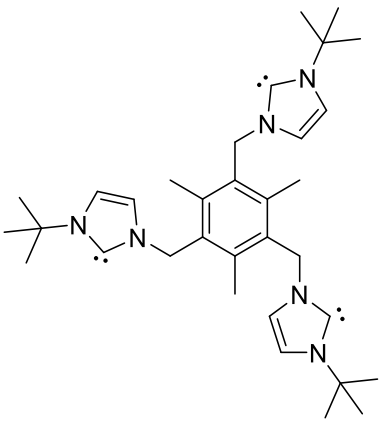

A Schlenk tube was charged with compound **72** (0.502 g, 0.65 mmol) and potassium *bis*(trimethylsilyl)amide (KHMDS) (0.388 g, 1.95 mmol). 15 mL of freshly distilled tetrahydrofuran was added, and the mixture was stirred at room temperature for 1.5 hours. The reaction mixture was filtered through a Celite® pad, the solvent removed under vacuum and the resulting oily yellow solid was washed with small aliquots of dry diethyl ether (3 x 5 mL) to give the desired product as a white powder (0.211 g, 74%).

^{1}H NMR (500 MHz, C_6D_6, 298 K) δ 6.63 (3H, *s*, NC*H*=CHN), 6.43 (3H, *s*, NCH=C*H*N), 5.20 (6H, *s*, CH_2N), 2.37 (9H, *s*, CH_3), 1.47 (27H, *s*, C(CH_3)$_3$).

^{13}C NMR (125 MHz, C_6D_6, 298 K) δ 214.7 (N*C*N), 138.1 (Ar-*C*), 133.2 (Ar-*C*), 116.7 (N*C*H=CHN), 115.0 (NCH=*C*HN), 55.4 (N*C*(CH$_3$)$_3$), 49.6 (*C*H$_2$N), 31.2 (C(*C*H$_3$)$_3$), 16.4 (Ar-*C*H$_3$).

Analysis consistent with literature data.[9]

Reaction between compound 94 and $Ru_3(CO)_{12}$

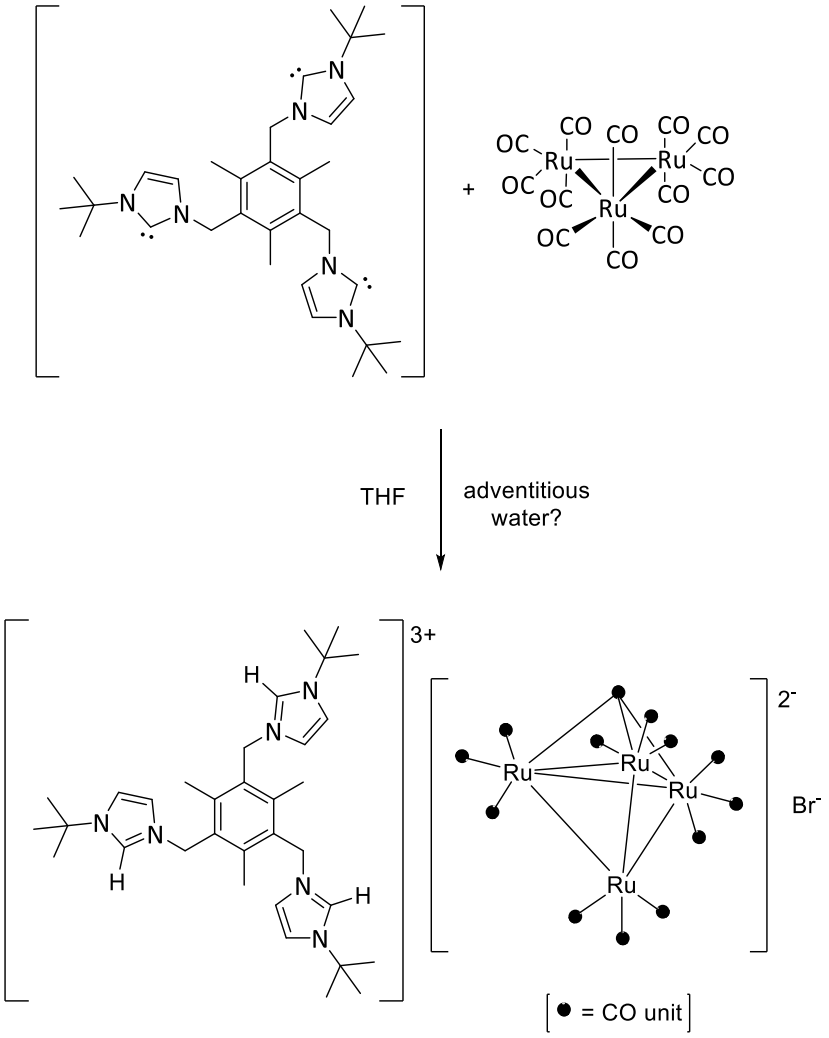

To a solution of triruthenium dodecarbonyl (0.041 g, 0.065 mmol) in 15 mL of dry THF, powdered compound **94** (0.050 g, 0.065 mmol) was added. The mixture immediately turned bright red. The reaction slurry was stirred for further 12 hours. After that time, the deep red solution was filtered and cooled to -30°C until formation of red crystals occurred (0.022 g).

FT-IR (CH_2Cl_2, cm^{-1}) 2071, 2027, 2006.

7.3. References for Chapter 7

1. A. Van der Made and R. Van der Made, *J. Org. Chem.*, 1993, **58**, 1262-1263.
2. A. Vacca, C. Nativi, M. Cacciarini, R. Pergoli and S. Roelens, *J. Am. Chem. Soc.*, 2004, **126**, 16456-16465.
3. J. Bai, R.-H. Wang, Y. Qiao, A. Wang and C.-J. Fang, *Drug Des. Dev. Ther.*, 2017, **11**, 2227.
4. T. Fahlbusch, M. Frank, J. Schatz and H. Schmaderer, *Eur. J. Org. Chem.*, 2006, **2006**, 1899-1903.
5. M. C. Cassani, M. A. Brucka, C. Femoni, M. Mancinelli, A. Mazzanti, R. Mazzoni and G. Solinas, *New J. Chem.*, 2014, **38**, 1768-1779.
6. H. R. Dias and W. Jin, *Tetrahedron Lett.*, 1994, **35**, 1365-1366.
7. J. Liu, J. Chen, J. Zhao, Y. Zhao, L. Li and H. Zhang, *Synthesis*, 2003, **2003**, 2661-2666.
8. C. Travelli, S. Aprile, R. Rahimian, A. A. Grolla, F. Rogati, M. Bertolotti, F. Malagnino, R. di Paola, D. Impellizzeri, R. Fusco, V. Mercalli, A. Massarotti, G. Stortini, S. Terrazzino, E. Del Grosso, G. Fakhfouri, M. P. Troiani, M. A. Alisi, G. Grosa, G. Sorba, P. L. Canonico, G. Orsomando, S. Cuzzocrea, A. A. Genazzani, U. Galli and G. C. Tron, *J. Med. Chem.*, 2017, **60**, 1768-1792.
9. H. R. Dias and W. Jin, *Tetrahedron Lett.*, 1994, **35**, 1365-1366.

Appendix A (Chapter 2)

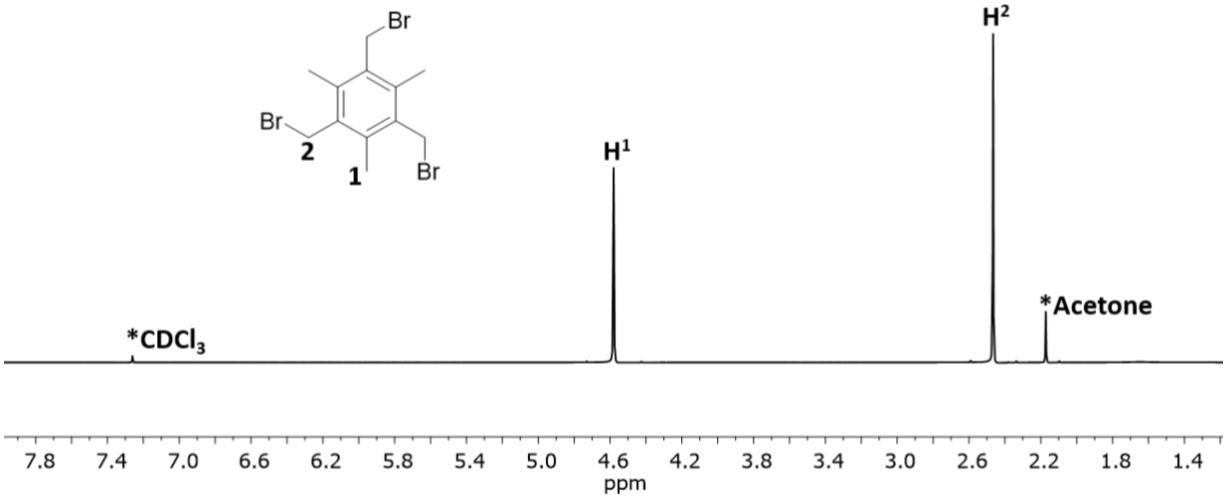

Figure A.1. 1H NMR (500 MHz, $CDCl_3$, 298 K) spectrum of compound **60**. For clarity, magnetically equivalent nuclei within the same NMR spin system are labelled once. * residual solvents and impurities traces.

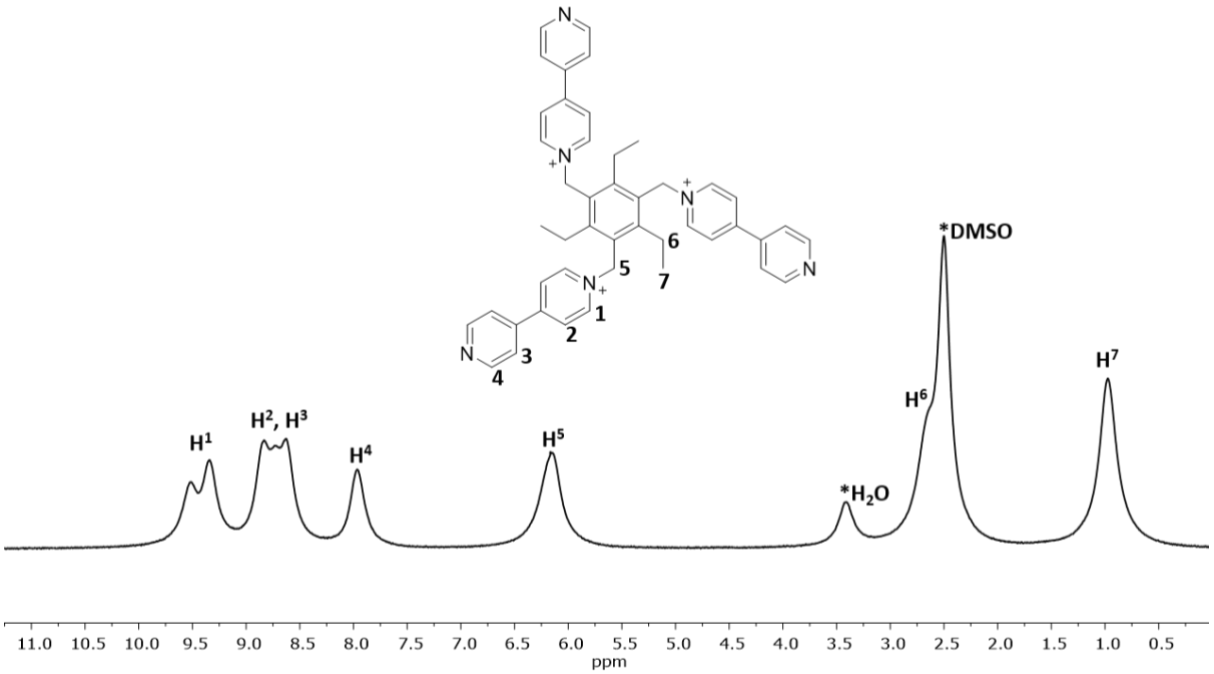

Figure A.2. 1H NMR (300 MHz, DMSO-d_6, 298 K) spectrum of compound **65**. For clarity, magnetically equivalent nuclei within the same NMR spin system are labelled once. * residual solvents and impurities traces.

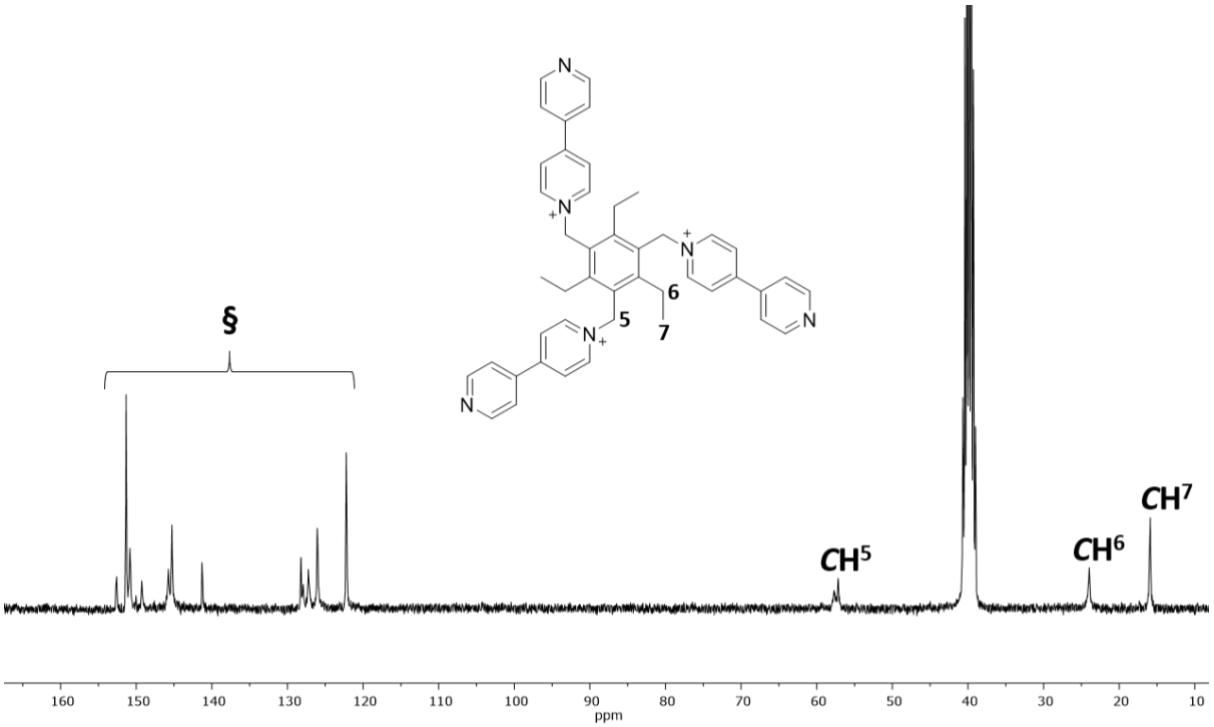

Figure A.3. ^{13}C NMR (75 MHz, DMSO-d_6, 298 K) spectrum of compound **65**. **§** refers to aromatic **C** within the aromatic rings. For clarity, magnetically equivalent nuclei within the same NMR spin system are labelled once.

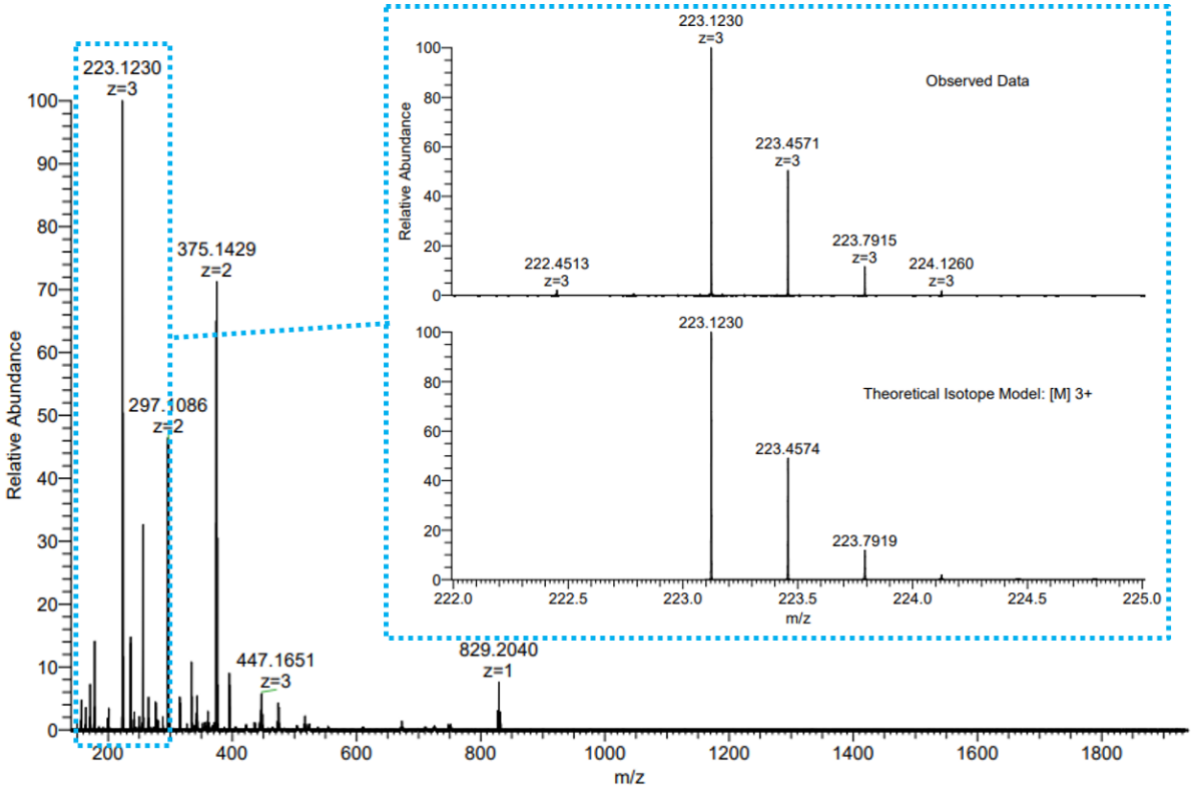

Figure A.4. Mass spectrum of compound **65**. Blue dotted box: ion species $[M]^{3+}$ at m/z = 223.1230.

Table A.1. Crystal data and structure refinement for compound **64**.

Identification code	ox058	
Empirical formula*	C44 H44 Br7 N7 O1	
Formula weight	926.59	
Temperature	293 K	
Wavelength	0.69110 Å	
Crystal system	Triclinic	
Space group	P-1	
Unit cell dimensions	a = 11.4638(3) Å	α = 93.770(1)°
	b = 13.5483(7) Å	β = 105.543(1)°
	c = 16.9684(9) Å	γ = 108.461(1)°
Volume	2073.11(19) $Å_3$	
Z	2	
Density	1.449 Mg/m_3	
Absorption coefficient	2.962 mm^{-1}	
F(000)	940	
Crystal size	-	
Theta range for data collection	1.228 to 31.003°	
Index ranges	-14<=h<=14, -19<=k<=19, -24<=l<=24	
Reflections collected	24216	
Independent reflections	12843 [R(int) = 0.064]	
Absorption correction	Semi-empirical from equivalents	
Max. and min. transmission	1.00000 and 1.00000	
Completeness to theta = 67.684°	100%	
Refinement method	Full-matrix least-squares on F_2	
Data / restraints / parameters	8993 / 0 / 496	
Goodness-of-fit F_2	1.0796	
Final R indices [I>2sigma(I)]	R1 = 0.0500, wR2 = 0.0592	
R indices (all data)	R1 = 0.0653, wR2 = 0.0665	
Extinction coefficient	n/a	
Largest diff. peak and hole	1.15 and -0.80 $e.Å^{-3}$	

*** Moiety formula** (estimated from "checkcif"): C42 H39 N6, C2 H3 N, 3(Br), H2 O.

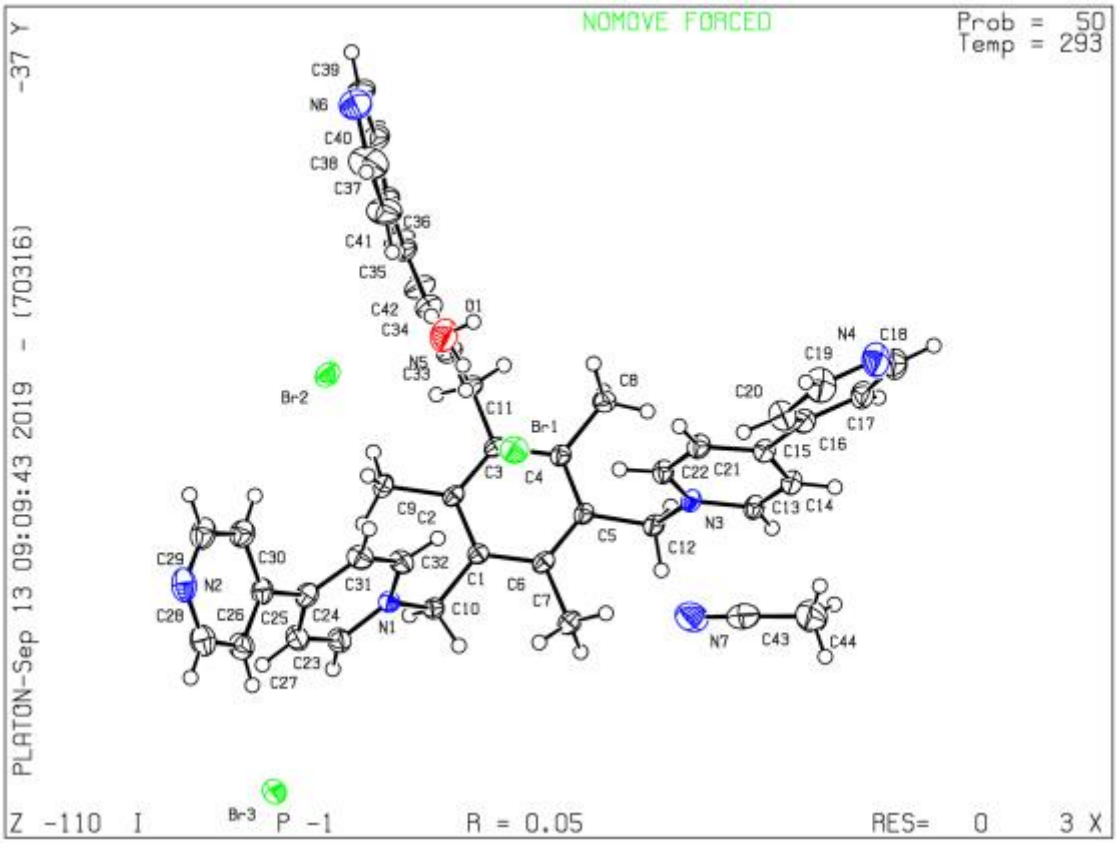

Figure A.5. Crystal structure of compound **64** (generated from “checkcif”).

Appendix B (Chapter 3)

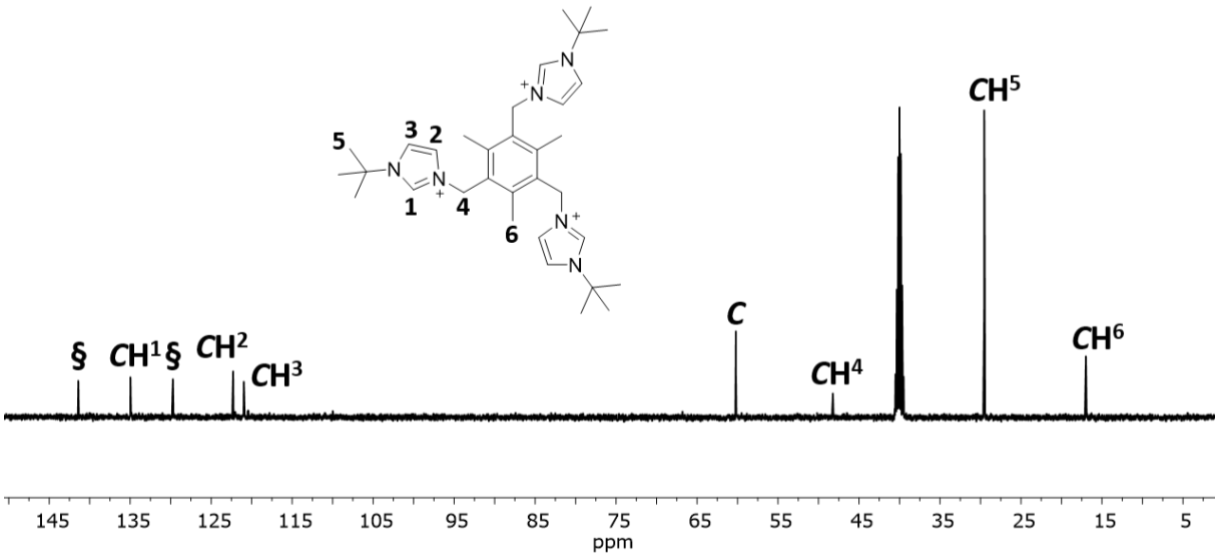

Figure B.1. ^{13}C NMR (75 MHz, DMSO-d$_6$, 298 K) spectrum of compound **72**. **§** refers to aromatic **C** within the aromatic ring. For clarity, magnetically equivalent nuclei within the same NMR spin system are labelled once.

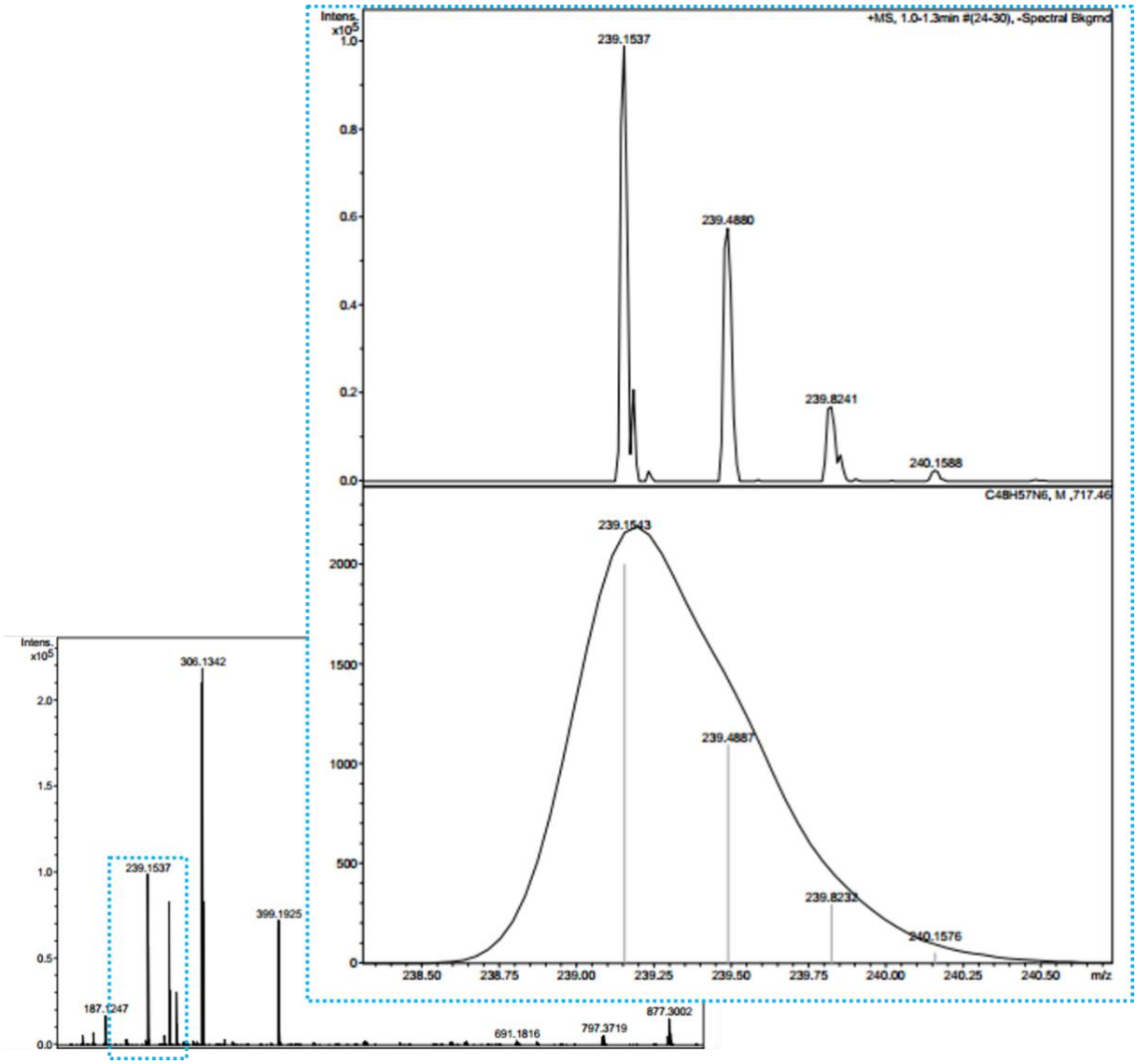

Figure B.2. Mass spectrum of compound **75**. Blue dotted box: ion species $[M]^{3+}$ at m/z = 239.1537.

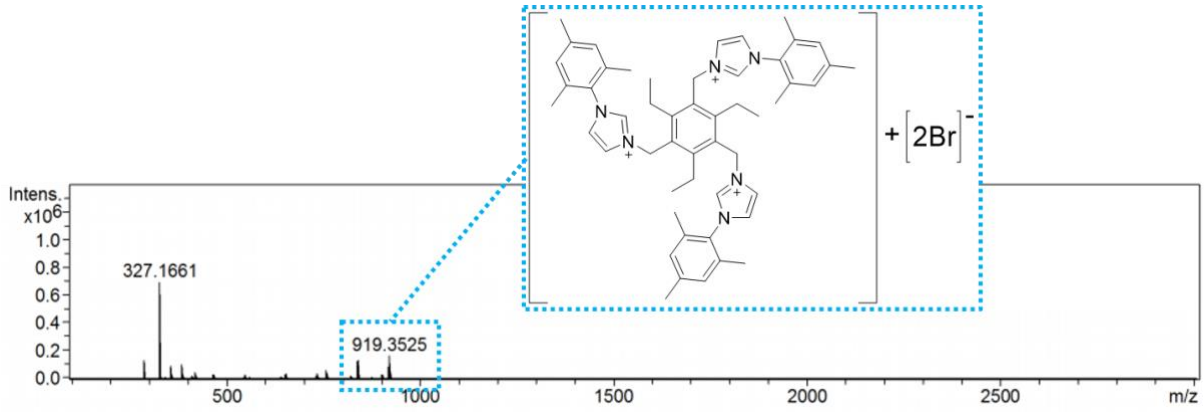

Figure B.3. Mass spectrum of compound **76**. Blue dotted box: ion species $[M+2^{79}Br]^{+}$ at m/z = 919.3525.

Table B.1. Crystal data and structure refinement for compound **70**.

Identification code	p18prr225_sq	
Empirical formula*	C27 H39 F18 N6 P3	
Formula weight	882.56	
Temperature	150 K	
Wavelength	0.71073 Å	
Crystal system	Trigonal	
Space group	P-3	
Unit cell dimensions	a = 11.6941(4) Å	α = 90°
	b = 11.6941(4) Å	β = 90°
	c = 16.2196(6) Å	γ = 120°
Volume	1920.90(15) $Å^3$	
Z	2	
Density	1.526 Mg/m^3	
Absorption coefficient	0.272 mm^{-1}	
F(000)	900.0	
Crystal size	0.47 x 0.27 x 0.16 mm^3	
Theta range for data collection	3.218 to 26.349°	
Index ranges	-10<=h<=14, -14<=k<=12, -20<=l<=20	
Reflections collected	11040	
Independent reflections	2626 [R(int) = 0.0375]	
Absorption correction	Semi-empirical from equivalents	
Max. and min. transmission	1.00000 and 1.00000	
Completeness to theta = 67.684°	100%	
Refinement method	Full-matrix least-squares on F^2	
Data / restraints / parameters	2626 / 15 / 189	
Goodness-of-fit F^2	1.036	
Final R indices [I>2sigma(I)]	R1 = 0.0396, wR2 = 0.0592	
R indices (all data)	R1 = 0.1015, wR2 = 0.0923	
Extinction coefficient	n/a	
Largest diff. peak and hole	0.277 and -0.331 $e.Å^{-3}$	

*** Moiety formula** (estimated from "checkcif"): C27 H39 N6, 3(F6 P).

Table B.2. Crystal data and structure refinement for compound **75·3PF$_6$**.

Identification code	s18p7	
Empirical formula*	C50 H60 F18 N7 P3	
Formula weight	1193.96	
Temperature	150.0(2) K	
Wavelength	1.54184 Å	
Crystal system	Monoclinic	
Space group	P 2_1/c	
Unit cell dimensions	a = 11.72750(10) Å	α = 90°
	b = 28.2893(3) Å	β = 106.309(10)°
	c = 17.1865(2) Å	γ = 90°
Volume	5472.40(10) Å^3	
Z	4	
Density	1.449 Mg/m^3	
Absorption coefficient	1.926 mm^{-1}	
F(000)	2464	
Crystal size	0.326 x 0.127 x 0.053 mm^3	
Theta range for data collection	3.124 to 73.132°	
Index ranges	-8<=h<=14, -32<=k<=34, -21<=l<=21	
Reflections collected	43265	
Independent reflections	10860 [R(int) = 0.0407]	
Absorption correction	Semi-empirical from equivalents	
Max. and min. transmission	1.00000 and 0.69900	
Completeness to theta = 67.684°	100%	
Refinement method	Full-matrix least-squares on F^2	
Data / restraints / parameters	10860 / 0 / 753	
Goodness-of-fit F^2	1.037	
Final R indices [I>2sigma(I)]	R1 = 0.0455, wR2 = 0.1145	
R indices (all data)	R1 = 0.0552, wR2 = 0.1210	
Extinction coefficient	n/a	
Largest diff. peak and hole	0.386 and -0.342 e.Å^{-3}	

*** Moiety formula** (estimated from "checkcif"): C48 H57 N6, 3(F6 P), C2 H3 N C48 H57 N6, 3(F6 P), C2 H3 N.

Table B.3. Crystal data and structure refinement for compound **76·3PF$_6$** in "closed arms" conformation".

Identification code	e17sip1
Empirical formula*	C59 H75 F18 N10 P3
Formula weight	1359.20
Temperature	150.0(3) K
Wavelength	0.71073 Å
Crystal system	Orthorhombic
Space group	Pnma
Unit cell dimensions	a = 24.1394(9) Å α = 90° b = 21.1348(10) Å β = 90° c = 12.8990(6) Å γ = 90°
Volume	6580.8(5) Å^3
Z	4
Density	1.372 Mg/m^3
Absorption coefficient	0.187 mm^{-1}
F(000)	2824
Crystal size	0.480 x 0.270 x 0.100 mm^3
Theta range for data collection	3.269 to 26.448°
Index ranges	-30<=h<=30, -26<=k<=26, -16<=l<=16
Reflections collected	82739
Independent reflections	6926 [R(int) = 0.0983]
Absorption correction	Analytical
Max. and min. transmission	0.987 and 0.957
Completeness to theta = 67.684°	99.8%
Refinement method	Full-matrix least-squares on F^2
Data / restraints / parameters	6926 / 72 / 532
Goodness-of-fit F^2	1.017
Final R indices [I>2sigma(I)]	R1 = 0.0545, wR2 = 0.1153
R indices (all data)	R1 = 0.0967, wR2 = 0.1331
Extinction coefficient	n/a
Largest diff. peak and hole	0.368 and -0.363 e.Å^{-3}

*** Moiety formula** (estimated from "checkcif"): C51 H63 N6, F2.40 P0.40, 2(F6 P), 2(F1.80 P0.30), 4(C2 H3 N).

Table B.4. Crystal data and structure refinement for compound **76·3PF$_6$** in "open arms" conformation".

Identification code	e17sip3	
Empirical formula*	C51 H63 F18 N6 P3	
Formula weight	1194.98	
Temperature	150.0(3) K	
Wavelength	0.71073 Å	
Crystal system	Triclinic	
Space group	P-1	
Unit cell dimensions	a = 10.1987(4) Å	α = 110.980(4)°
	b = 16.8351(7) Å	β = 96.945(4)°
	c = 17.7222(9) Å	γ = 97.767(4)°
Volume	2767.5(2) Å^3	
Z	2	
Density	1.434 Mg/m^3	
Absorption coefficient	0.210 mm^{-1}	
F(000)	1236	
Crystal size	0.600 x 0.180 x 0.090 mm^3	
Theta range for data collection	3.373 to 29.746°	
Index ranges	-13<=h<=14, -23<=k<=22, -22<=l<=24	
Reflections collected	48157	
Independent reflections	13603 [R(int) = 0.0478]	
Absorption correction	Semi-empirical from equivalents	
Max. and min. transmission	1.00000 and 0.86805	
Completeness to theta = 67.684°	99.8%	
Refinement method	Full-matrix least-squares on F^2	
Data / restraints / parameters	13603 / 0 / 735	
Goodness-of-fit F^2	1.014	
Final R indices [I>2sigma(I)]	R1 = 0.0691, wR2 = 0.1329	
R indices (all data)	R1 = 0.1186, wR2 = 0.1537	
Extinction coefficient	n/a	
Largest diff. peak and hole	0.460 and -0.427 e.Å^{-3}	

*** Moiety formula** (estimated from "checkcif"): C51 H63 N6, 3(F6 P).

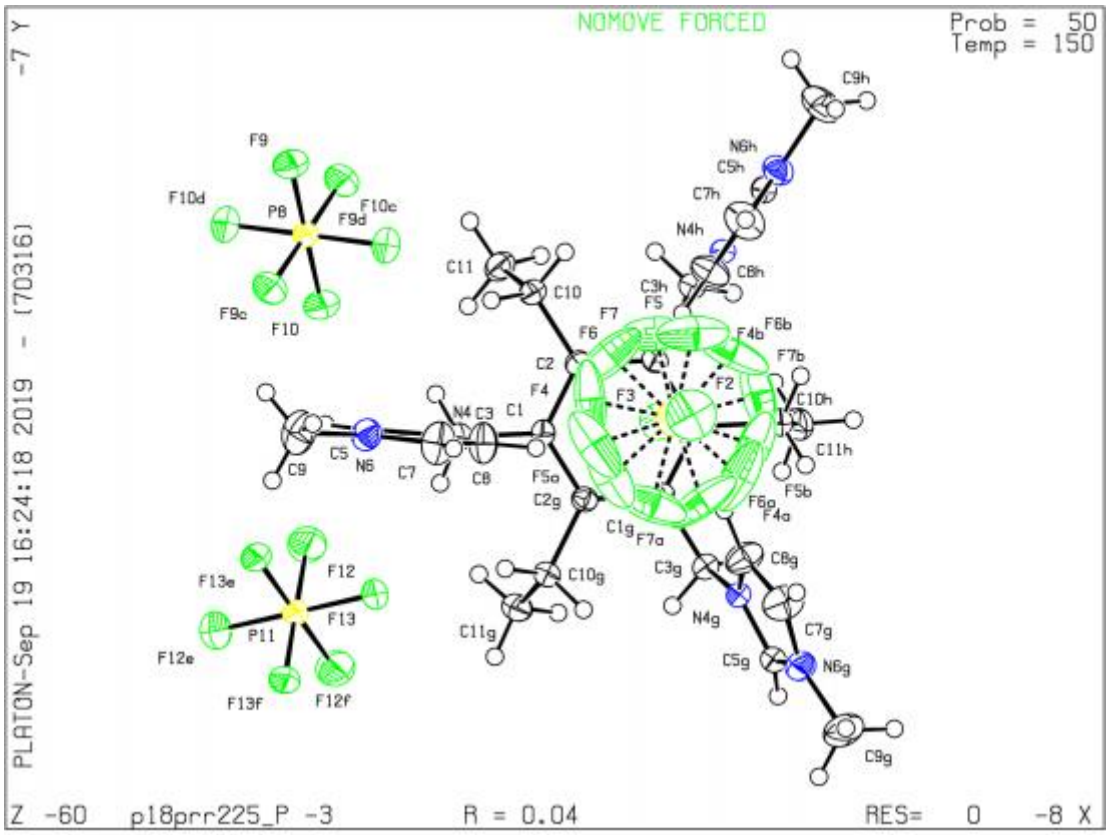

Figure B.4. Crystal structure of compound **70** (generated from "checkcif").

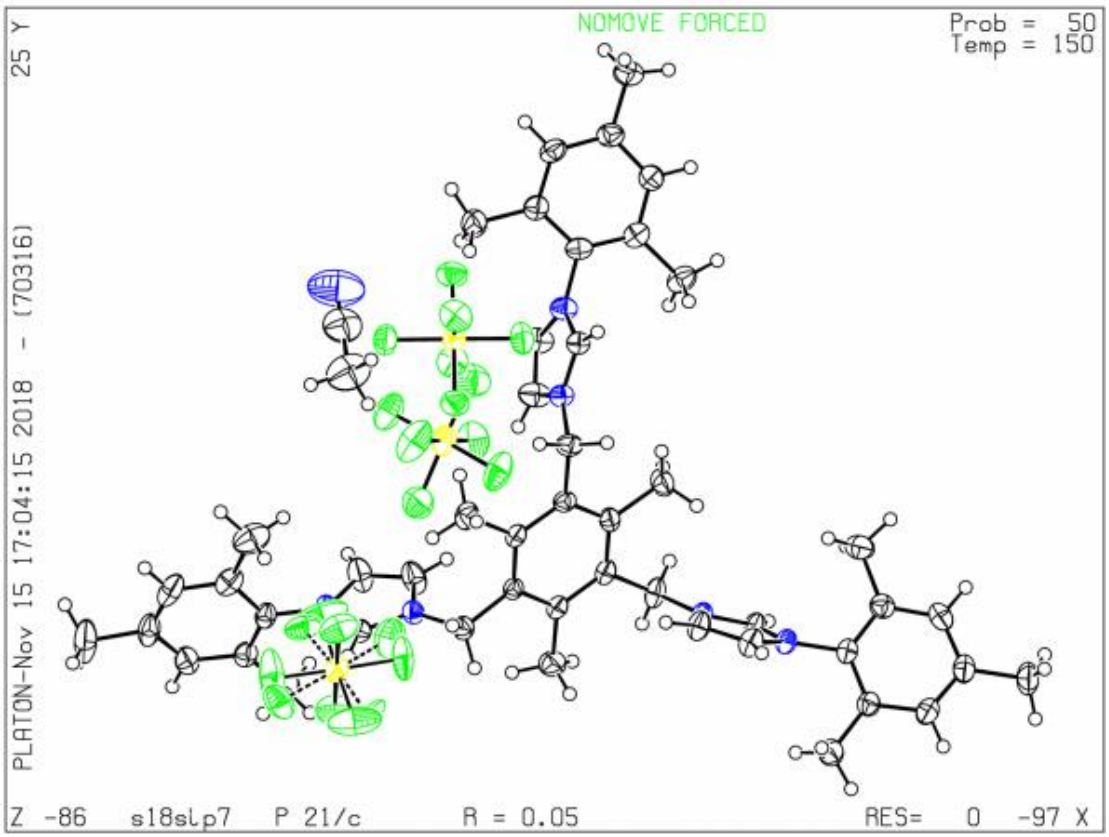

Figure B.5. Crystal structure of compound **75·3PF$_6$** (generated from "checkcif").

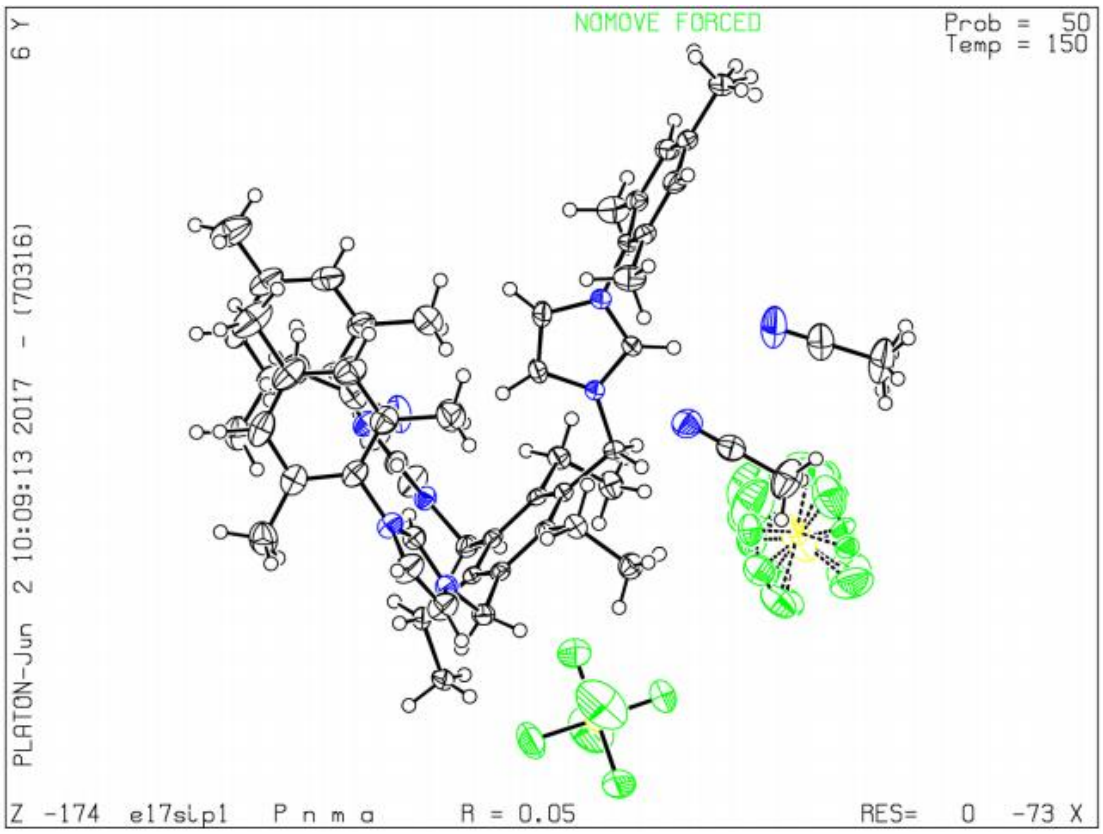

Figure B.6. Crystal structure of compound **76·3PF$_6$** in "closed arms" conformation (generated from "checkcif").

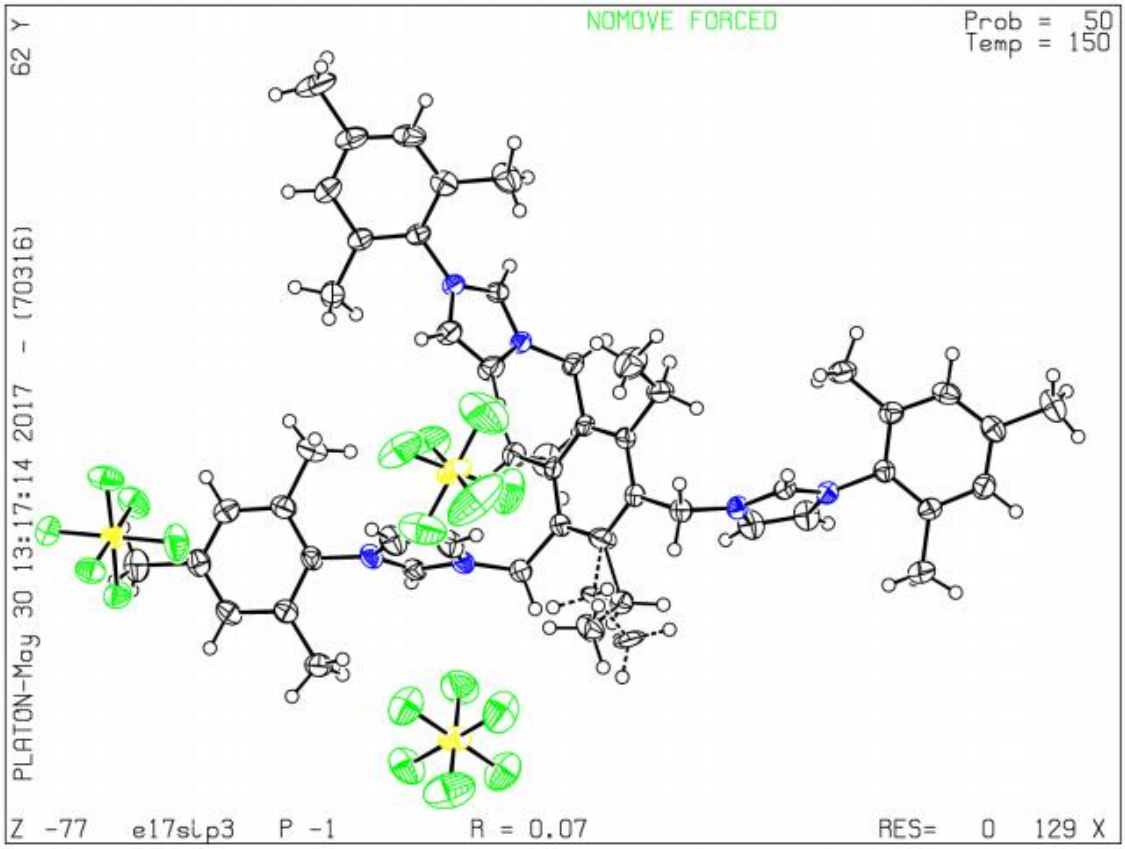

Figure B.7. Crystal structure of compound **76·3PF$_6$** in "open arms" conformation (generated from "checkcif").

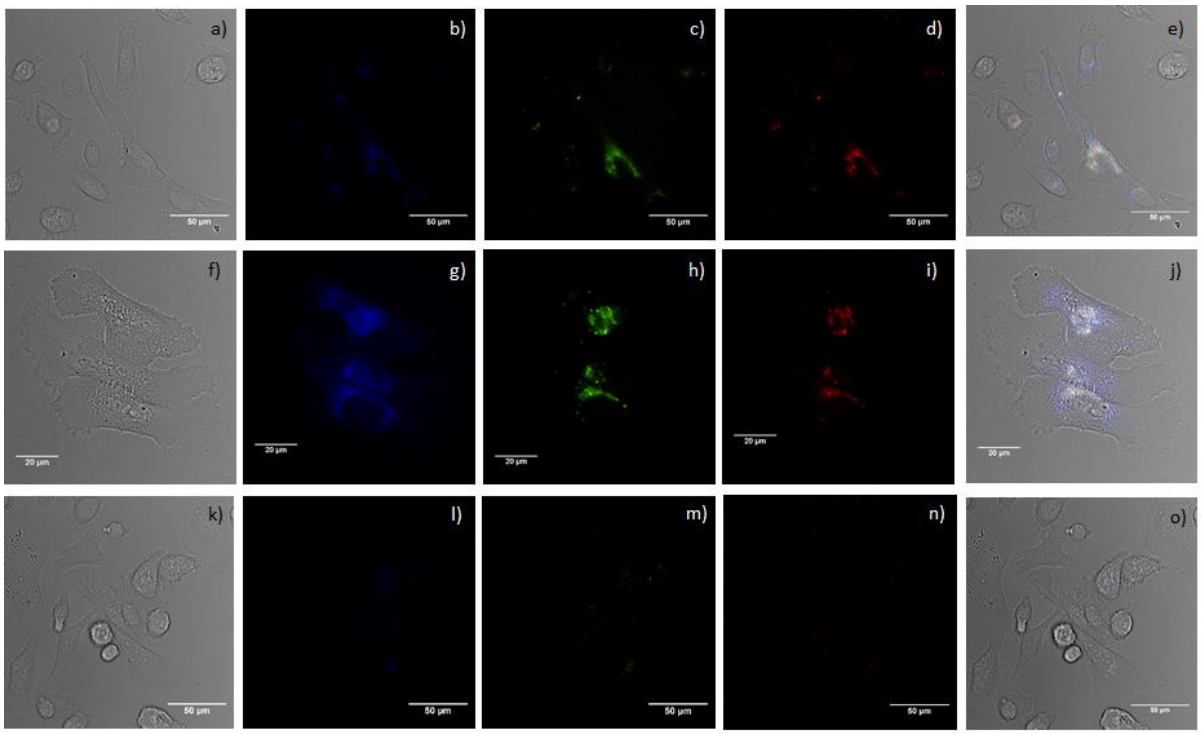

Figure B.8. Epi-fluorescence acquisition of PC3 cells incubated for 15 min with compound **76** (a-e), compound **73** (f-j), and DMSO control (k-o). Final concentrations 50 × 10^{-6} M in 5:95 DMSO:serum-free medium at 37°C. a,f) DIC channel; b,g) blue channel, λ_{em} = 460.0 nm; c,h) green channel λ_{em} = 525.0 nm; d,i) red channel λ_{em} = 629.5 nm; e,j) overlay of DIC-blue-green-red channels. Scale bars: 50 μm a-e) and k-o), 20 μm f-j).

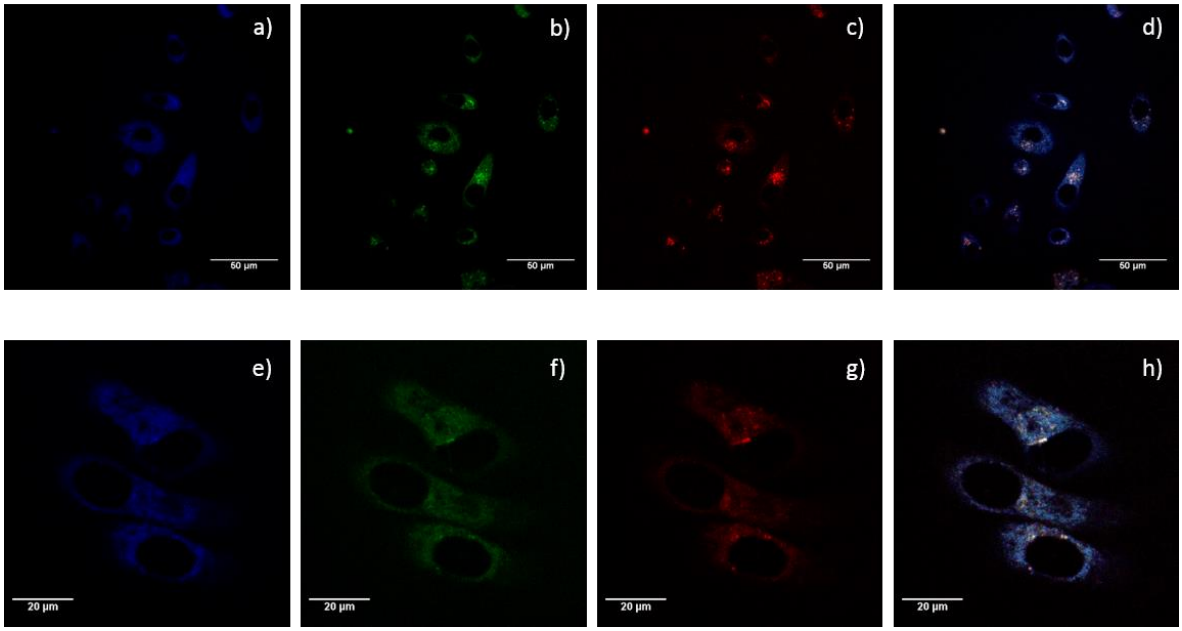

Figure B.9. Single-photon laser-scanning confocal microscopy of PC-3 cells incubated at 37°C for 15 min with compound **76** (a–d), and compound **73** (e–h) (50 × 10^{-6} M, in 5:95 DMSO:serum-free medium). a,e) blue channel (417–477 nm); b,f) green channel (500–550 nm); and c,g) red channel (570–750 nm); d,h) overlay of the blue–green–red channels. λ_{ex} = 405.0, 488.0, and 561.0 nm. Scale bars: 50 μm (a-d), 20 μm (e-h).

Appendix C (Chapter 4)

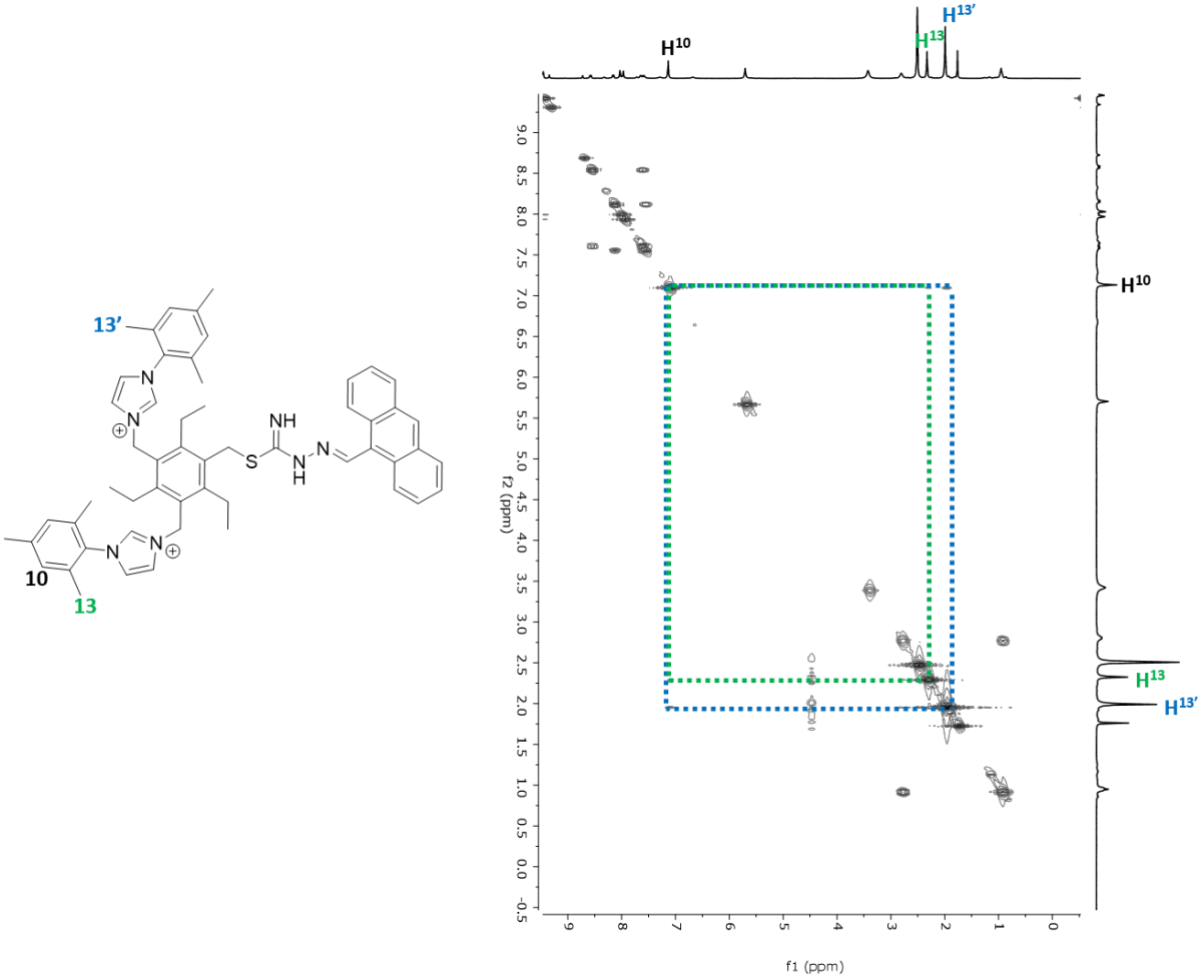

Figure C.1. $_1$H-$_1$H COSY NMR (400 MHz, DMSO-d$_6$, 298 K) spectrum of compound **83**.

Appendix D (Chapter 5)

Radiolabelling of tripodal ATSC-based ligands with zirconium-89

The positron-emitter radiotracer zirconium-89 was generated at the Wales Research and Diagnostic Positron Emission Tomography Imaging Centre (PETIC) via the ^{89}Y(p,n)-^{89}Zr reaction using the cyclotron CYCLONE 18/9. ^{89}Zr was obtained as a 1 M solution in oxalic acid, which was neutralised to pH 7 with a 1 M aqueous solution of sodium carbonate. To this, a 1 mM solution of compound **84** in 1:1 DMSO:water was added. The reaction mixture was stirred at 60°C for 16 hours. The radiolabelling activity was probed by radio-TLC using a 50 mM solution of diethylenetriaminepentaacetic acid (DTPA) to chelate all the free $^{89}Zr^{4+}$ ions. The chelate ^{89}Zr-DTPA elute with the solvent front with a Rf > 0.9 (Figure D.1).

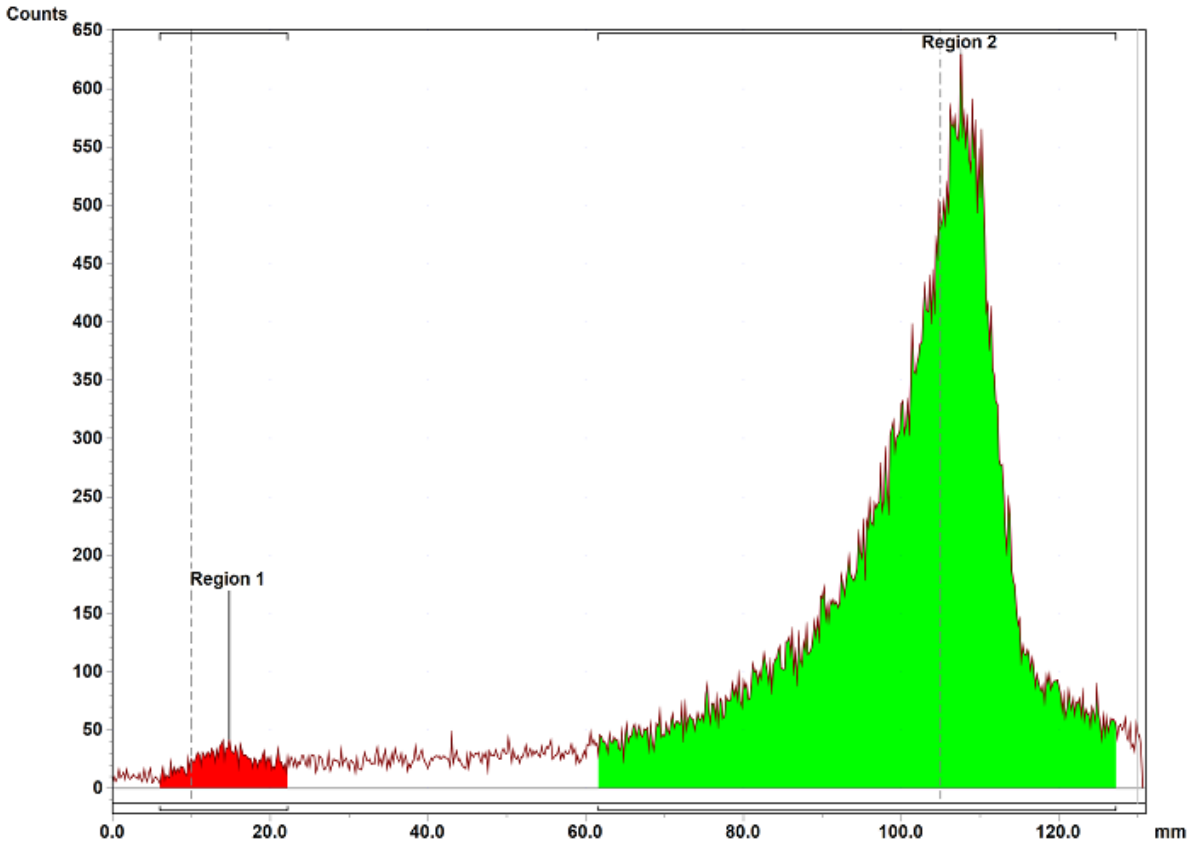

Figure D.1. Radio-TLC chromatogram of the ^{89}Zr-DTPA chelate (Region 2).

Radio-TLC analysis of the reaction product (Figure D.2) showed that the radiolabelling efficiency was ≥ 99.9%. These preliminary data suggest that **84** may be a potential new chelator for the radioisotope ^{89}Zr.

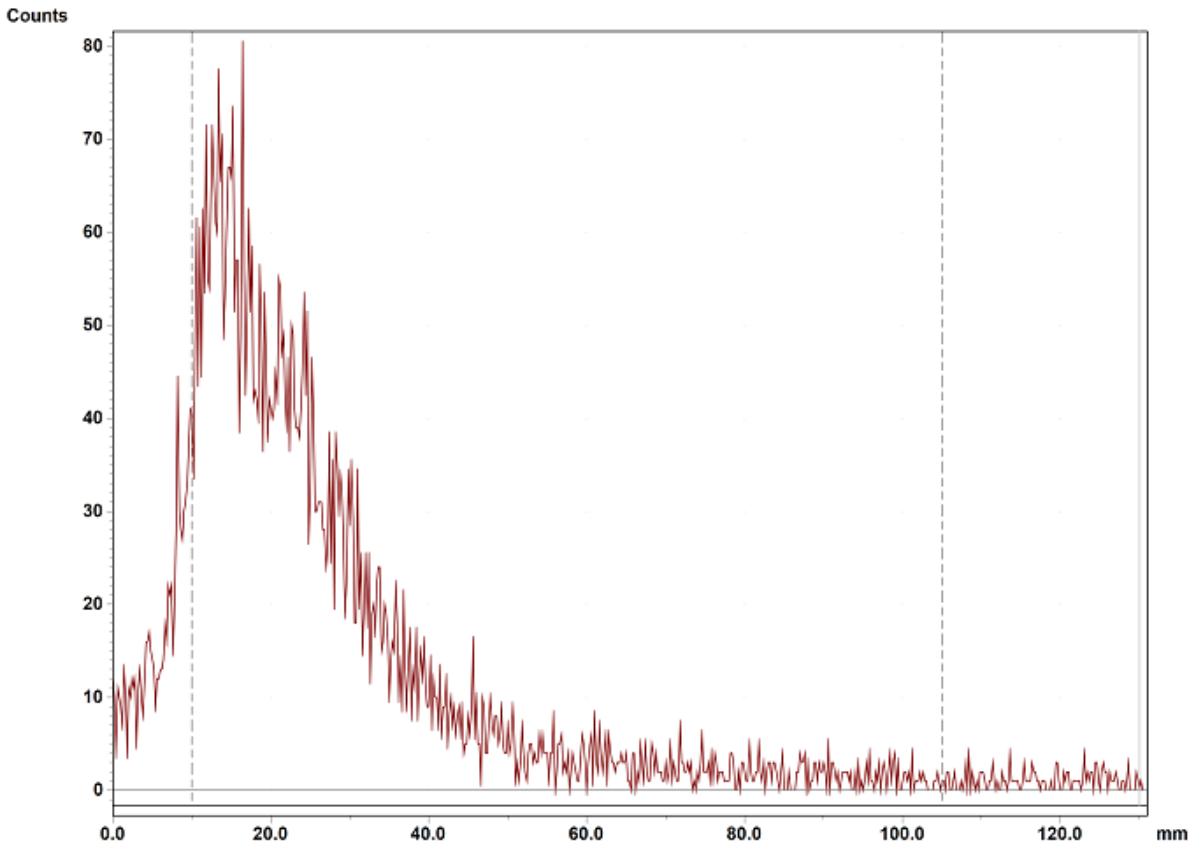

Figure D.2. Radio-TLC chromatogram of **84** with ^{89}Zr. The radio-TLC was eluted using 50 mM DTPA solution as the mobile phase.

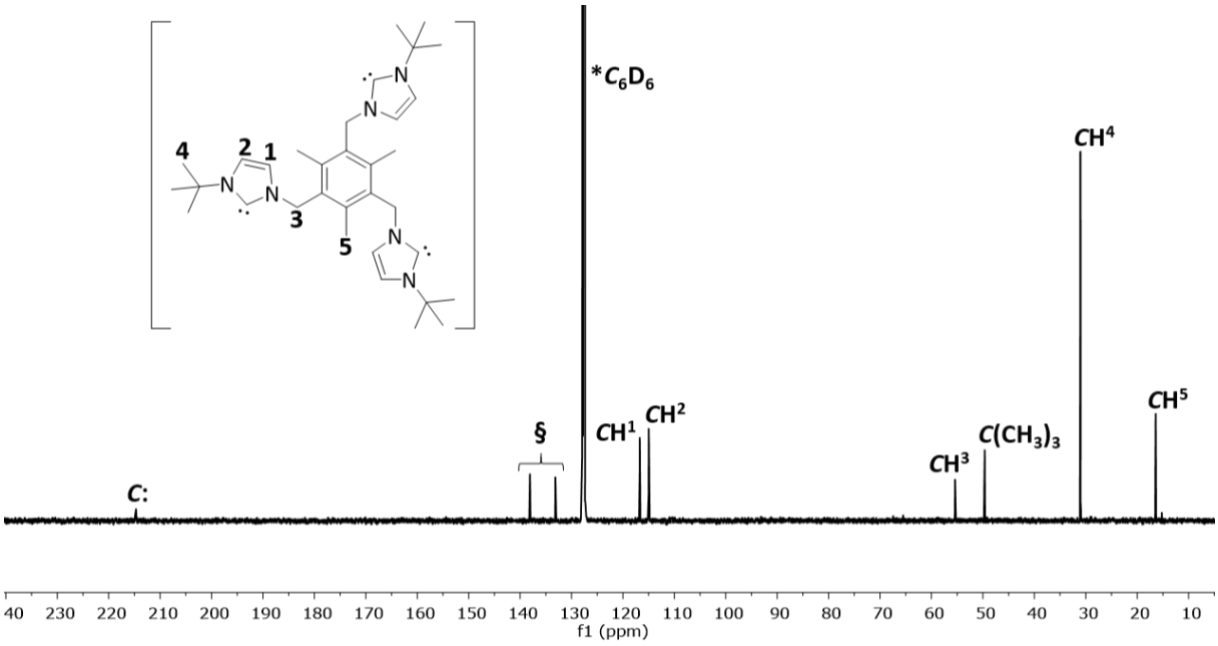

Figure D.3. ^{13}C NMR (75 MHz, DMSO-d_6, 298 K) spectrum of the deprotonated compound **72**. **C:** refers to the carbene, **§** refers to aromatic **C** within the aromatic ring. For clarity, magnetically equivalent nuclei within the same NMR spin system are labelled once.

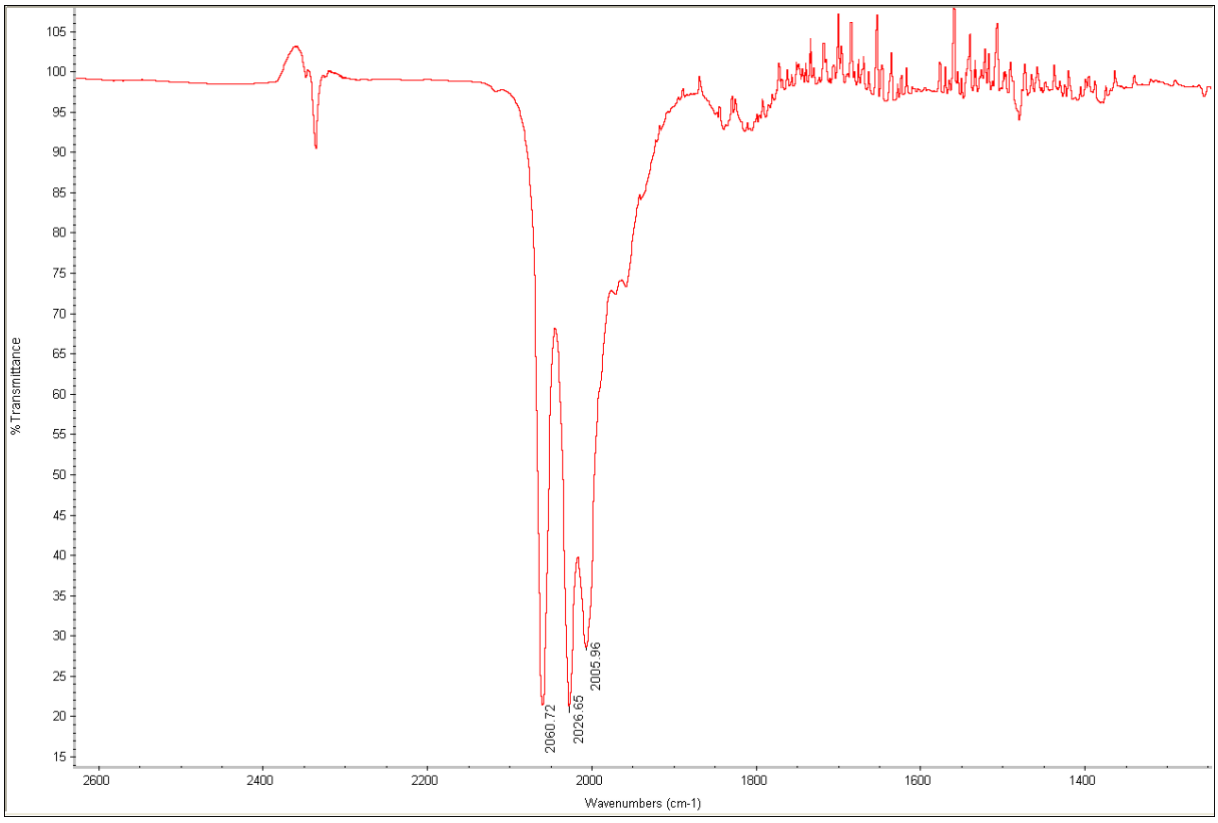

Figure D.4. FT-IR spectrum (THF) of the reaction product between compound **94** and $Ru_3(CO)_{12}$.

Table D.1. Crystal data and structure refinement for the reaction product between compound **94** and $Ru_3(CO)_{12}$.

Identification code	e17sip7
Empirical formula*	C181.80 H247.20 Br6 N24 O49.80 Ru12
Formula weight	5257.91
Temperature	149.97(10) K
Wavelength	0.71073 Å
Crystal system	Trigonal
Space group	R-3
Unit cell dimensions	a = 20.5077(8) Å α = 90° b = 20.5077(8) Å β = 90° c = 43.7192(13) Å γ = 120°
Volume	15923.4(13) $Å^3$
Z	3
Density	1.645 Mg/m^3
Absorption coefficient	2.035 mm^{-1}
F(000)	7927
Crystal size	0.370 x 0.130 x 0.080 mm^3
Theta range for data collection	3.430 to 27.528°
Index ranges	-26<=h<=21, -22<=k<=25, -56<=l<=55
Reflections collected	38075
Independent reflections	8095 [R(int) = 0.0625]
Absorption correction	Semi-empirical from equivalents
Max. and min. transmission	1.00000 and 0.76511
Completeness to theta = 67.684°	99.7%
Refinement method	Full-matrix least-squares on F^2
Data / restraints / parameters	8095 / 62 / 541
Goodness-of-fit F^2	1.029
Final R indices [I>2sigma(I)]	R1 = 0.0498, wR2 = 0.1064
R indices (all data)	R1 = 0.0949, wR2 = 0.1254
Extinction coefficient	n/a
Largest diff. peak and hole	0.679 and -0.638 $e.Å^{-3}$

*** Moiety formula** (estimated from "checkcif"): 3(C13 O13 Ru4), 4(C33 H51N6), 10.8(C H4 O), 6(Br).

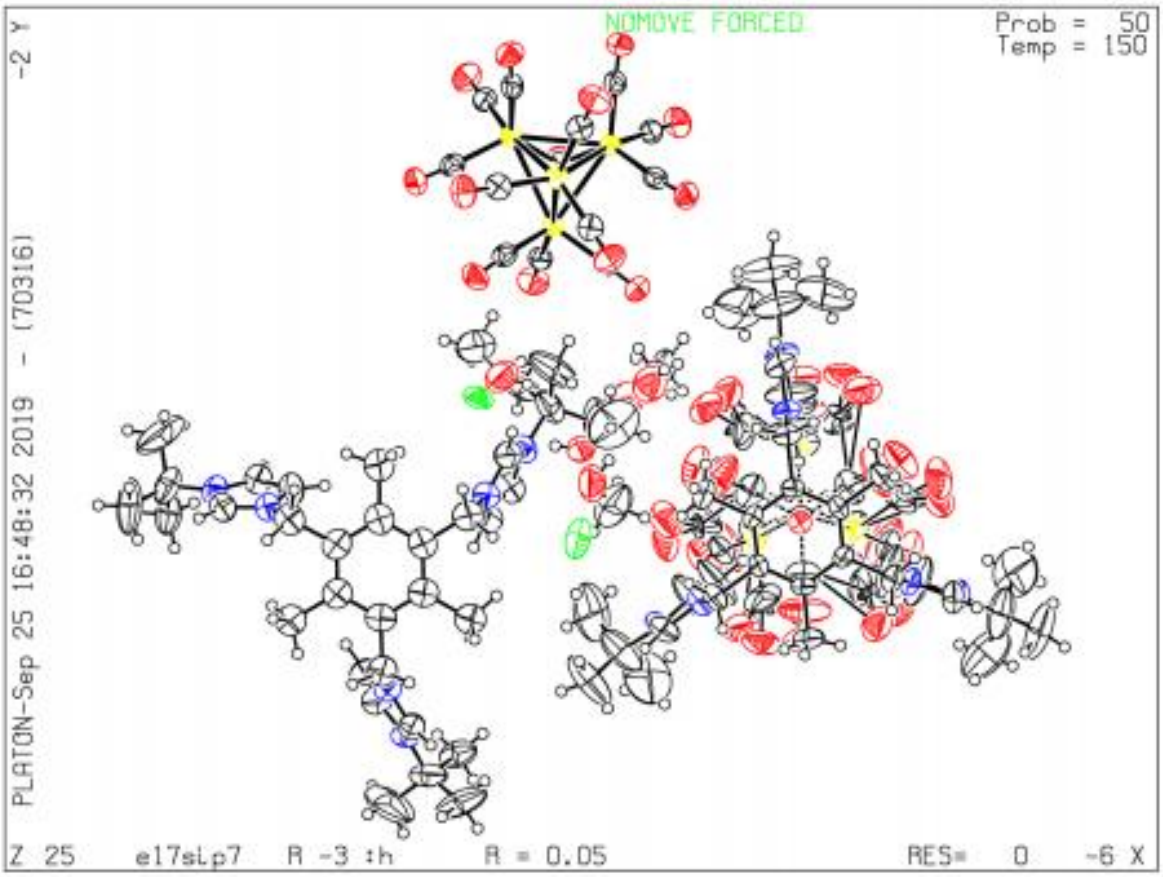

Figure D.5. Crystal structure of the reaction product between compound **94** and $Ru_3(CO)_{12}$. (generated from "checkcif").

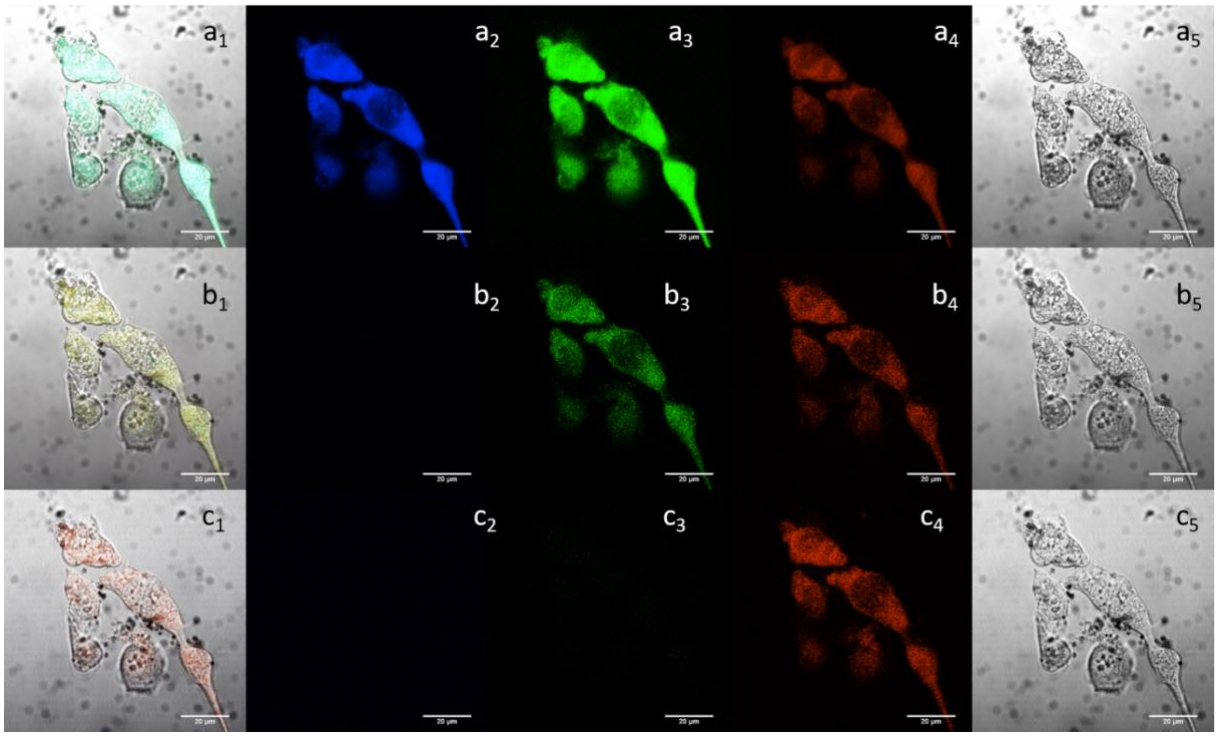

Figure D.6. Single-photon laser-scanning confocal microscopy images of Chinese hamster ovary cells (CHO) incubated with compound **87** (10 µg/mL 1% : 99% DMSO : DMEM) at 37 ºC for 16 hours; λ_{ex} = 405 nm (a_1-a_5), λ_{ex} = 488 nm (b_1-b_5) and λ_{ex} = 561 nm (c_1-c_5). Overlapping of the DIC, blue, green and red channels (a_1, b_1, c_1), blue channel, λ_{em} = 420-480 nm (a_2, b_2, c_2), green channel, λ_{em} = 516-530 nm (a_3, b_3, c_3), red channel λ_{em} = 615-650 nm (a_4, b_4, c_4), and DIC channel (a_5, b_5, c_5). Scale bar: 20 µm.

Two-photon fluorescence lifetime imaging microscopy of tripodal metal complexes

Fluorescence lifetime, defined as the average time in which a fluorescent molecule remains in an excited state before returning to the ground state by releasing a photon, is an intrinsic property of every fluorophore and is influenced by fluorescence intensity and concentration. Fluorescence lifetime imaging (FLIM) is an optical imaging technique that relies on the fluorescence lifetime of an individual fluorophore (*e.g.* in a biological sample) rather than its emission spectrum.

Preliminary FLIM experiments were carried out on selected metal complexes (described in Chapter 5) in order to study their lifetime characteristics in solution and in human breast cancer cells (MCF7). Prior to *in-vitro* experiments, time-correlated single-photo counting (TCSPC) measurements were carried out to test the lifetime of the selected metal complexes in solution, using DMSO as solvent. TCSPC and FLIM experiments were carried out at the Rutherford Appleton Laboratory (RAL), in the Central Laser Facility (CLF) by Dr Fernando Cortezon Tamarit and Dr Haobo Ge.

TCSPC decay curves were generated for compounds **85** (Figure D.7) and **87** (Figure D.8). In TCSPC, each photon detected was plotted to calculate the fluorescence lifetime. The results consist of three components: the quality of fit χ_2, the lifetime τ_n (ns), and the lifetime percentage a_n (%). TCSPC results for **87** are shown below in Table D.2.

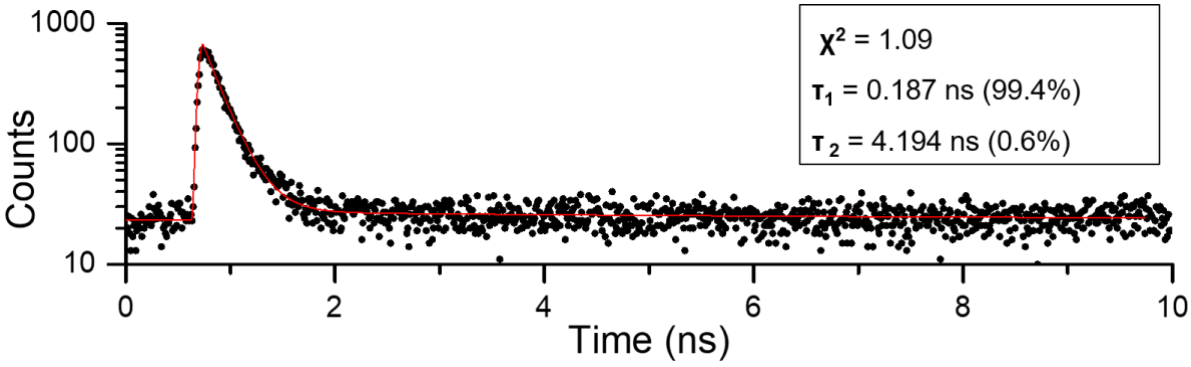

Figure D.7. TCSPC decay and fitting curves for compound **85** (10 mM in DMSO, excited at 810 nm with a laser power of 0.2 mW for 10 s).

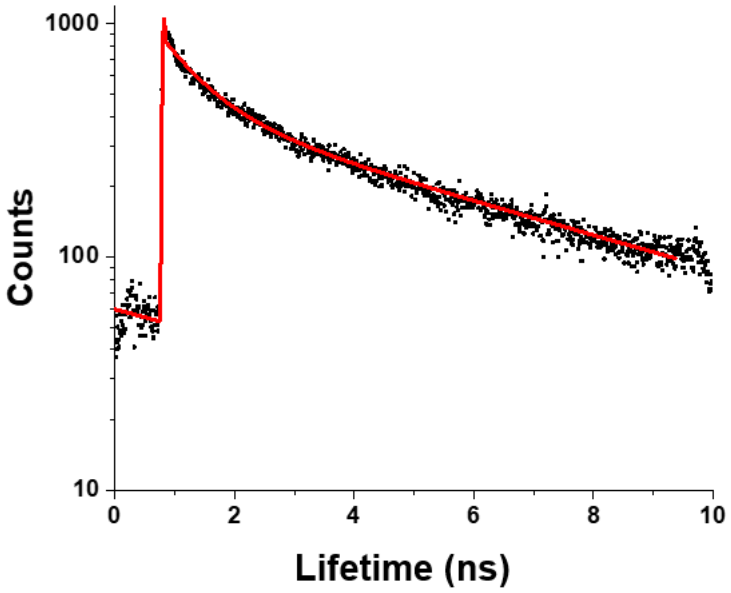

Figure D.8. TCSPC decay and fitting curves for compound **87** (10 mM in DMSO, excited at 810 nm with a laser power of 3 mW for 10 s). The data were collected from three repeated measurements on the same day.

Table D.2. TCSPC data for compound **87**.

Compound	χ^2	τ_1 (ns)	a_1 (%).	τ_2 (ns)	a_2 (%).	τ_m (ns)
87	1.16	0.69	51.63	5.30	48.37	2.92

Two-photon FLIM mapping and intensities in MCF7 cells were produced for compounds **85** and **86**. From the two-photon fluorescence intensity diagrams (Figure D.9 **(A)** and Figure D.10 **(A)**) and the fluorescence lifetime mapping in MCF7 cells (Figure D.9 **(B)** and Figure D.10 **(B)**), it was possible to observe that the compounds are able to accumulate into the cell membrane and no emission appears to originate from the nuclei. From the fluorescence lifetime mappings, it was possible to generate fluorescence lifetime distribution curves (Figure D.9 **(C)** and Figure D.10 **(C)**), which represent the overall fluorescence lifetime of the compounds in MCF7 cells. The distribution of these curves is proportional to the individual lifetimes recorded for each lifetime component. For compound **85**, the average lifetime distribution is around 1.5 ns, while for compound **86** τ_m is only 0.15 ns and at an intensity maximum of 140 A.U.

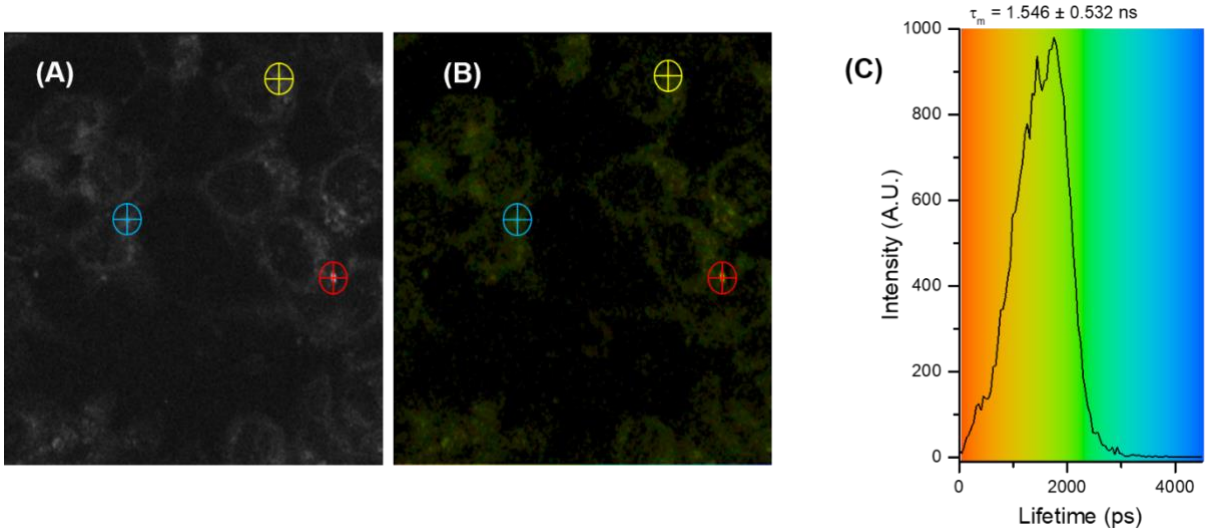

Figure D.9. (A) Two-photon intensity diagram; **(B)** fluorescence lifetime mapping of τ_m and **(C)** fluorescence lifetime distribution curve of MCF7 cells treated with 0.1 mM solution of **85** in DMSO (incubation time = 1h, laser power = 5.3 mW, acquisition time = 90 sec, λex = 810nm).

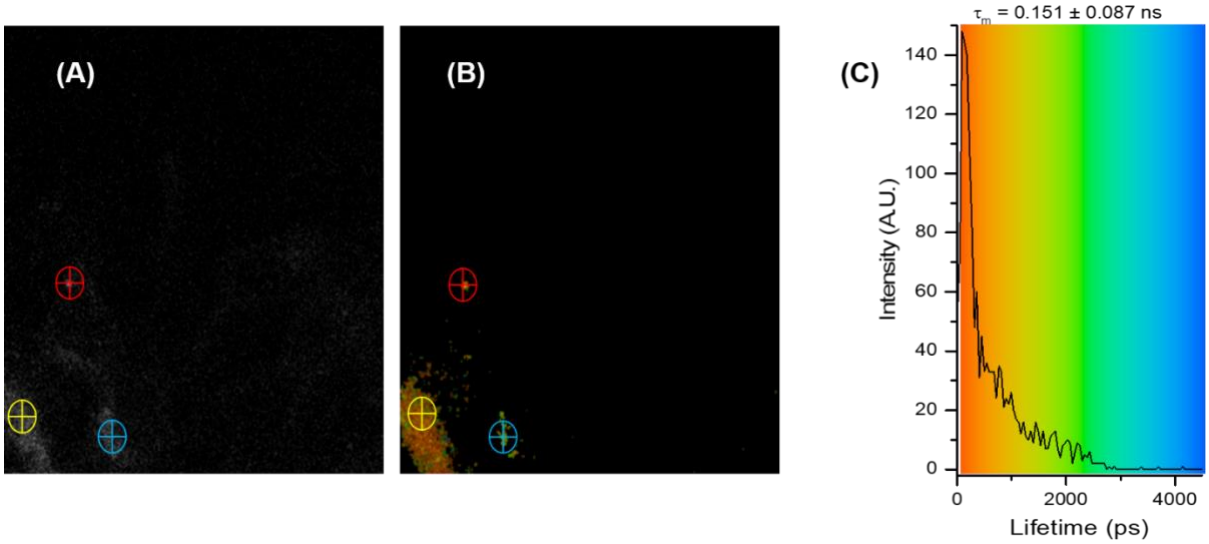

Figure D.10. Two-photon intensity diagram; **(B)** fluorescence lifetime mapping of τ_m and **(C)** fluorescence lifetime distribution curve of MCF7 cells treated with 0.1 mM solution of **86** in DMSO (incubation time = 1h, laser power = 7.3 mW, acquisition time = 90 sec, λex = 810nm).

Experimental procedures for the fluorescence lifetime measurements

Time-correlated single photon counting (TCSPC). Lifetime measurements were recorded using TCSPC with an excitation wavelength of 910 nm and the emission measured at 360-580 nm. The measurement of compounds **85** and **87** were carried out in DMSO/ water solvent with concentration of 10 mM. Emission spectral detection was carried out using an Acton Research Component 275 spectrograph and an Andor iDus 740-BU CCD camera.

Confocal microscopy. Fluorescence microscopy images were captured on a Nikon eclipse TE2000 epifluorescence or a Zeiss LSM510META microscope at University of Bath, whereas at the Rutherford Appleton Laboratory a modified Nikon TE2000-U was utilised. MCF7 cells were cultured and plated in a glass bottomed petri dish (35 mm diameter and 1.5 mm thickness) at 1.5×10^5 -2.5×10^5 cells per dish depending on the culture time. In general, MCF7 cells needed 48 hours to adhere. Prior to the microscopy observation, cultured cells were washed with PBS three times and refilled with 990 μL of serum free medium. Subsequently, a small volume of compound (10 μL) in DMSO was loaded to make the final volume 1 mL at the appropriate concentration. The final concentration on the plate were usually at 100 μM with 1% - 5% DMSO depending on the compound solubility. After 1 hour of incubation at 37 °C, cells were washed with HBSS three times and refilled with fresh SFM (1 mL). Confocal images were captured immediately afterwards.

Fluorescence lifetime imaging microscopy (FLIM). Cell uptake studies were performed using MCF7 cells. The cells were plated on a glass petri dishes and left to attach for 12-24 hours, depending on the growth rate. Control FLIM were recorded before the addition of the compounds. Plates were then mounted on the microscope stage and kept at 37ºC.

The compounds were dissolved in DMSO and added to cells to achieve final concentration of 100μM in DMEM/RPMI medium containing 1% of DMSO. The cells were incubated for 1 hour prior to confocal imaging, FLIM was carried out immediately after the microscopy experiments. The fluorescence decay curve is well fitted to a multiexponential function as:

$$I(t)=\sum_i a_i exp\left(\frac{-t}{t1}\right)$$

Appendix E

Synthesis of the peptide fragment [7-13]-bombesin

As already mentioned in Chapter 1, the possibility to develop nanotherapeutics that can also display specificity for the cancer cells is crucial for both diagnosis and therapy. Hence, we decided to develop a small targeting peptide that can be easily conjugated to the luminescent metal complex. Thus, we opted for the fragment 7-13 of the bombesin, a short peptide involved in cancer growth. The bombesin displays high affinity for the Gastrin-releasing peptide receptor (GRPR), a member of the family of the G-protein, which is found to be overexpressed in various types of prostate cancers.

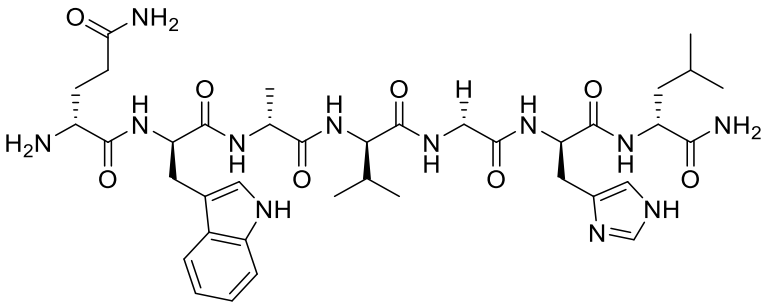

Figure E.1. Structural representation of the D-[7,13]-bombesin fragment.

We decided to perform a solid phase synthesis of the sequence 7-13 of the bombesin peptide. Furthermore, we also chose to synthesise the D-[7-13]-bombesin fragment (Figure E.1) in order to achieve a targeting molecule less susceptible to proteolytic degradation and digestion compared to the natural L-version. A general scheme of the synthetic pathway for the synthesis of the peptide fragment is reported in Figure E.2.

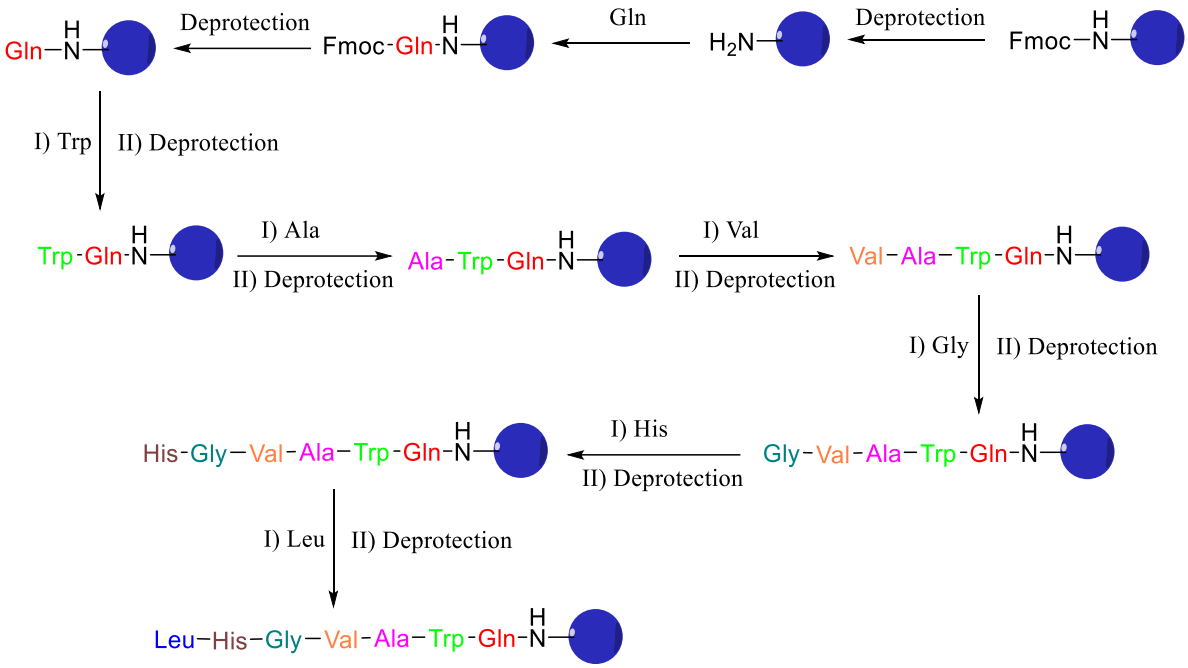

Figure E.2. Synthetic steps for the [7-13]-bombesin peptide fragment.

The characterisation of the D-[7-13]-bombesin fragment was performed using reverse phase HPLC and electrospray ionisation mass spectrometry (ESI-MS) techniques. The results, shown in Figure E.3 and Figure E.4, showed that the synthesis was successful, and the product was obtained with high purity. This work was carried out in collaboration under the supervision of Dr Ruggero Dondi, at the Department of Pharmacy & Pharmacology, University of Bath.

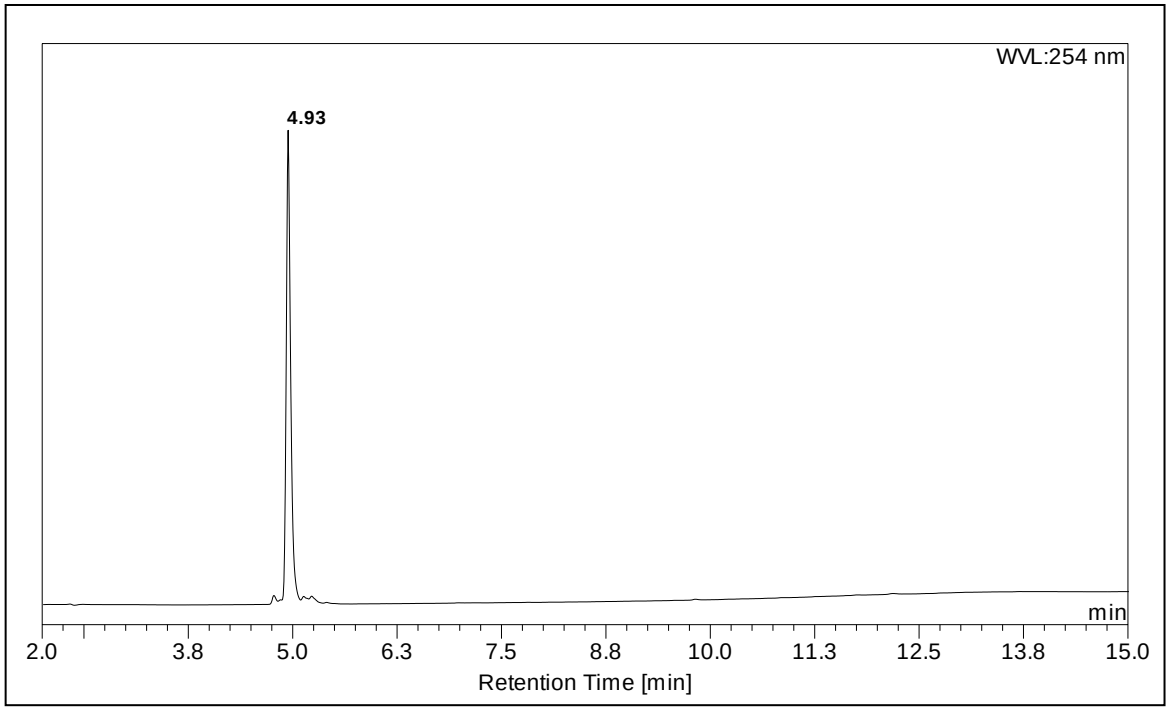

Figure E.3. HPLC chromatogram of the purified D-[7-13]-bombesin fragment.

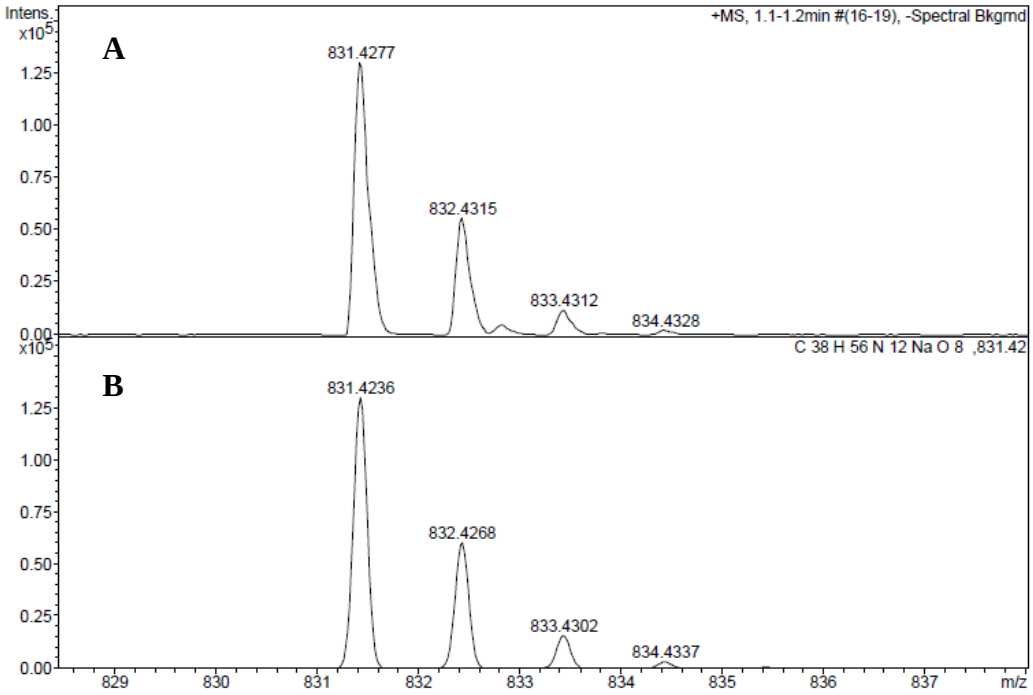

Figure E.4. ESI-MS spectrum of the D-[7-13]-bombesin fragment. **A**: m/z value found. **B**: m/z value calculated.

Experimental procedure for the synthesis of the [7-13]-bombesin

The peptide fragment [7-13]-bombesin was assembled by Fmoc solid phase peptide synthesis on *Rink Amide MBHA Resin* (Novabiochem, 200-400 mesh, assumed 0.6 mmolg^{-1} loading) using an *Activotec Activo-P11* automated peptide synthesizer. The first residue was attached to the resin manually as follows. The resin (250 mg, 0.15 mmol) was placed in a 10 ml plastic reactor and was swollen in dimethylformamide DMF (15 min). The Fmoc protection was removed by treatment with 20% piperidine/DMF (3 cycles, 12 minutes and two rounds of 3 minutes each). After washing thoroughly with DMF to remove traces of piperidine, the deprotection was confirmed by a positive Kaiser test. Fmoc-Gln-OH (251 mg, 0.59 mmol, 4 eq) in DMF (2.5 ml) was preactivated by treatment with *N,N′*-diisopropylcarbodiimide **(**DIC, 94 μL, 0.96 mmol, 6 eq.) and HOBt (81 mg, 0.59 mmol, 4 eq). After 3 h, this solution was added to the deprotected resin, followed by DIEA (157 μL, 0.96 mmol, 6 eq) and the vessel was shaken for 45 min. The vessel was then transferred to the automated synthesiser, and the reaction vessel was fitted with a heating jacket (60^{o}C). Subsequent Fmoc deprotection steps were performed using 20% piperidine/DMF (3 ml, 5 + 10 min). Amino acid couplings were performed with 3 eq of each Fmoc-protected amino acid, 3 eq. of PyBop (0.2 M) and 6 eq. of DIEA (0.4 M) in DMF. No final Fmoc deprotection step was performed to allow for subsequent elaboration of the peptide on the resin. After the synthesis, cleavage of the peptide from the resin was performed by mixing a small amount of the resin with a mixture of TFA/TIS/H_2O (95:25:25) for 2 h. The resin beads were removed by filtration and the peptide was precipitated by addition of anhydrous Et_2O. The white precipitate was collected by centrifugation and washed with further Et_2O (3 x 1.5 ml). The solvent was removed, and the product was obtained as a white solid

Rt = 4.93 min;

ESI-MS calculated for $C_{38}H_{56}N_{12}NaO_8$ m/z $[M+H]^+$ 831.4236, found 831.4277